Modern Geotechnical Codes of Practice and New Design Challenges Using Numerical Methods for Supported Excavations

Department of Civil, Environmental and Geomatic Engineering

University College London

Georgios Katsigiannis

A thesis submitted in partial fulfilment of the requirements for the award of the degree Doctor of Engineering (EngD) at the University of London

June 2017

To Mitra, for all her love and support.

Declaration

I, Georgios Katsigiannis confirm that the work presented in this thesis is my own. Where information has been derived from other sources, I confirm that this has been indicated in the thesis.

Signature

Georgios Katsigiannis

Date

01/06/2017

Acknowledgements

First and foremost, I would like to thank my academic supervisors, Dr Pedro Ferreira and Dr Raul Fuentes for always steering me in the right direction. Their passionate participation and input and the continuous encouragement have been precious all these years. I am also grateful to Arup Geotechnics for the excellent technical guidance and financial support, and especially to Anton Pillai, Duncan Nicholson and Stuart Hardy for guiding my research for the past several years. I would like particularly to express my deepest gratitude to Dr Brian Simpson who was always willing to help, share his knowledge and give his best suggestions. Special thanks are extended to Professor Helmut Schweiger for all his help and the excellent collaboration during and after my 2-month visit at Graz University of Technology in Austria and Dr. Andrew Bond and the members of the EC7 Evolution Groups, particularly the EG4 on numerical methods and the EG9 on water pressures for all the fruitful discussions. I would like also to thank the Urban Sustainability and Resilience Centre at UCL and particularly the Director of the Centre, Dr Helena Titheridge for the continuous support. Working at University College London has been a great experience and I would like to thank all the research staff and students in the Civil, Environmental and Geomatic Engineering Department for making this journey so special. Finally, I am grateful to the EPSRC for funding this research project and the UCL European Institute for awarding me three years in a row the Junior Researcher Grant.

Abstract

Eurocode 7 (EC7), which is the geotechnical engineering design standard in Europe, introduces the concept of partial safety factors and distinguishes between Serviceability Limit State (SLS) and Ultimate Limit State (ULS). While EC7 allows the use of Finite Element Methods (FEM) for ULS, there is limited guidance in a number of issues.

The thesis focuses on a number of constitutive models of increasing complexity and both the characteristic and design values of the model parameters are derived for the London Clay and a soft Marine clay. The challenges associated with factoring the undrained shear strength when using total and effective stress parameters are discussed.

The use of FEM for ULS design of supported excavations, is highlighted using simple excavation examples and two deep excavation case histories; the Moorgate Crossrail Station and the Exhibition Road Building of the Victoria & Albert Museum. The different factoring combinations and strategies, required by EC7, are compared in terms of the calculated design internal structural forces, illustrating that the use of more advanced models can have significant advantages. Moreover, comparisons are made between the design prop loads calculated from the FEM and a number of empirical methods.

The HYD limit state, as described in EC7, relates to the upward flow of water through the soil towards a free surface. The HYD verification, using FEM, can be performed with two approaches; the soil block approach by calculating the equilibrium of a rectangular soil block and the integration point approach by checking that the equilibrium is satisfied at each integration point. Thorough comparisons between the two approaches using benchmark geometries illustrate the benefits of using more advanced approaches for such stability verifications.

Keywords

Eurocode 7, ULS design, FE analysis, deep excavations, Hardening Soil, Hardening Soil Small, BRICK, HYD, water pressures.

Table of Contents

List of Figures

List of Appendix Figures

List of Tables

INTRODUCTION

Background

The Structural Eurocodes are design codes for buildings and civil engineering works and now have been established as the current European Standards. They replaced the old National Standards and their use became mandatory across Europe since 2010. Eurocode 7 (EC7) is the European Standard for geotechnical design. The code is based on the principles of *limit state* design, making a distinction between *Serviceability Limit State (SLS)* and *Ultimate Limit State (ULS)*. It also uses a *partial factor* format and thus, it represents an advance over the old standards as it factors the uncertainty at source.

The development of advanced geotechnical software, together with the introduction of cutting edge and less expensive hardware has resulted in 2D and 3D Finite Element Methods (FEMs) being routinely used in the Geotechnical Engineering field. Moreover, the introduction of advanced constitutive models that allow a better simulation of the soil behaviour has resulted in the increasing use of FEM in geotechnical engineering to obtain better deformation predictions and check for SLS.

Eurocode 7 allows the use of FEM for ULS, but gives no guidance to the designer on several important issues. These issues have triggered an important debate in the geotechnical engineering community over the feasibility of the routine use of FEM with soil models of increasing complexity, for ULS checks.

Aims and objectives

This research aims to contribute to this debate by addressing the most critical issues that are either directly code related or wider numerical analysis issues brought into light, again, after the introduction of the EC7, to the extent that the former have knock-on effects on the latter. A more specific set of objectives has been developed and is listed below:

- Review the most common challenges associated with the use of FEM for the analysis of supported excavations in accordance with EC7.
- Identify advanced constitutive models suitable to model the behaviour of London Clay and derive a set of appropriate parameters, based on available test data in the literature and a typical soil profile in the London area. Perform a sensitivity

analysis to investigate the effect of the parameters that have a high level of uncertainty.

- Provide guidance on what partial factors should be applied on the soil strength for undrained analysis, using effective stress parameters and how designers can verify that the undrained shear strength computed by the soil model is consistent with the EC7 requirements.

- Develop methodologies for the application of partial factors to constitutive soil models of high complexity, such as the BRICK model, in compliance with EC7.

- Compare the FE results from the two DA1 Combinations and the different DA1-2 Strategies for the ULS analysis of a wide range of supported excavations of increasing depth and number of prop levels, in order to better understand their advantages and limitations.

- Identify critical parameters (e.g. initial stresses, soil stiffness, prop stiffness etc.) to the SLS and ULS analysis of supported excavations and highlight their influence on the discrepancies in the results between the different EC7 factoring combinations and methods.

- Review common empirical methods for deriving the design prop loads in the UK and elsewhere and compare with the FEM results, assessing the conservatism of the methodology when comparing the results.

- Investigate the feasibility of the use of advanced constitutive models for the ULS FE analysis and highlight any potential advantages.

- Identify and model, in FEM, deep excavation case histories, in the Greater London area, and extend the conclusions from the simple examples to these more realistic cases.

- Review the current guidance in the UK and elsewhere on the accidental single prop loss effect and investigate ways for this effect to be taken into account in the 2D and 3D FEM analysis.

- Review the current EC7 requirements on the stability verification against the HYD Limit State, which particularly relates to the ground movement of a free surface caused by a vertical upward flow of water (e.g. at the base of the excavation), address common misconceptions on how partial factors are applied and develop

a methodology for HYD verification using advanced numerical methods in compliance with EC7.

Overall, the impact of the research is vast as this is a problem affecting not only the European countries but all the countries that have adopted the Eurocodes. The outcomes of the project enable the geotechnical community to better understand the benefits and limitations of implementing Eurocode 7 in advanced numerical analysis, and consequently produce code compliant and effective designs. This will, in turn, generate consequential benefits in both life expectancy and embodied energy of infrastructure projects and thereby a reduction in energy consumption. The research outcome represent a step forward in achieving more sustainable design in the construction industry.

Structure of the thesis

The research work presented in this document was structured according to the research pursued.

Chapter 1 describes the main definitions and concepts, listed in the Eurocode 7 and important to this work, together with the plans for the development of the next generation of the code. This Chapter also discusses the challenges associated with the use of advanced numerical methods for routine Ultimate Limit State verifications

In Chapter 2, the formulation and the main features of the constitutive models, used in this thesis for modelling the behaviour of the soil in supported excavation problems, are described. The constitutive models range from simple linear elastic perfectly plastic to more advanced models. Both characteristic and design values of the model parameters are derived for a stiff over-consolidated clay such as the London Clay while the challenges associated with factoring the undrained shear strength of the material, when using total and effective stress parameters are discussed in detail.

In Chapter 3, the challenges of the Serviceability Limit State (SLS) and Ultimate Limit State (ULS) analysis of embedded walls supporting a range of typical excavations in the greater London area using plane strain (2D) Finite Element analysis with the well-known Mohr-Coulomb model, are discussed and highlighted. In all cases, the effect of a number of factors critical to the design such as the earth coefficient at rest, soil stiffness and prop stiffness on the resulting discrepancies is illustrated. The design prop loads, calculated from the FE analyses, are compared with the values derived from a number of empirical methods (e.g. CIRIA C517, EAB) for all the geometries considered in this study. Moreover, the challenges of accounting for the accidental single prop loss in FE

methods are highlighted using a three-dimensional excavation geometry and comparisons are made with the two-dimensional cases. Finally, the FE analysis is repeated for a deep excavation in a typical Singapore soil profile, to investigate the effect of the material strength on the differences in the results between the different EC7 factoring combinations and strategies for a soft clay.

In Chapter 4, the analyses are repeated for all excavation geometries, using more advanced constitutive models such as the Hardening Soil (HS), Hardening Soil Small (HSS) and BRICK. The SLS and ULS FE analysis challenges are discussed while the effect of the soil model on the resulting discrepancies is investigated. The type of results presented is the same as for the Mohr-Coulomb analysis to allow for comparisons and discussion.

In Chapter 5, the ULS FE challenges of deep supported excavations in London Clay, are illustrated and discussed using two deep excavation case histories. The first project is the Moorgate Crossrail Station excavation, which is part of one of the largest infrastructure projects currently under construction in London. The second project, referred to as the Exhibition Road Building, is a new exhibition space currently being constructed within the courtyard area of the Victoria & Albert Museum.

Finally, Chapter 6 focuses on the HYD limit state which, as described in EC7, is related to the upward flow of water through the soil towards a free surface, such as in front of a retaining wall or in the base of an excavation. The HYD verification using FEM can be performed with two different approaches, namely the *soil block* approach and the *integration point* approach. Comparisons made using benchmark geometries illustrate that the HYD verification using FEM is very promising. Thorough comparisons between the factors from the two approaches, allow designers to better understand the benefits of using more advanced and robust approaches for such stability verifications.

In Appendix A, the BRICK Test program is briefly described and discussed.

In Appendix B, the detailed calculations of the design prop loads are presented based on the empirical pressure diagrams proposed by the CIRIA C517 and the EAB guide.

Finally, in Appendix C, the full list of the contours for the parametric analysis discussed in Chapter 6, are included for completeness.

CHAPTER 1

EC7 and other geotechnical codes of practice

1.1 Introduction

The Structural Eurocodes are the current European design standards for buildings and construction works covering a wide range of structural materials and fields of civil engineering. Eurocode 7 (EC7), which is the standard for geotechnical engineering design in Europe, introduces the concepts of *limit state design* and *partial safety factor*s distinguishing between Serviceability Limit States (SLSs) and Ultimate Limit States (ULSs). In this Chapter, the main definitions and principles of the code are described and discussed, while the plans for the development of the next generation of the EC7 are introduced. Other relevant geotechnical codes of practice, including British Standards and CIRIA guides, are also addressed while the effect of an accidental design situation such as the loss of an individual prop during construction in supported excavations, is discussed and the guidance provided by current standards is reviewed. Moreover, while EC7 allows the use of advanced numerical analysis for ULS, there is limited guidance to designers in a number of critical issues (e.g. when and how the partial factors of safety should be applied). These challenges, which have triggered an ongoing debate among designers over the feasible use of advanced numerical methods for routine ULS verifications, are also reviewed in this chapter.

1.2 The Structural Eurocodes

The Eurocodes represent a set of standards, covering a wide range of structural materials and fields of structural engineering. The current version of the standards were published in 2010, superseding the previous National Standards. The use of Eurocodes became compulsory in all the EU Member States. The National Standards Bodies (NSBs) of each European Union Member State, have the responsibility to translate and publish the standards, together with their National Annexes. The National Annexes provide values for the parameters that need to be specified and are referred to as Nationally Determined Parameters (NDPs). They also need to include country-specific practices, data and any complementary non-conflicting documents (Bond and Harris, 2008).

The Structural Eurocodes consist of the following 10 standards:

- EN 1990: Eurocode - Basis of Structural Design
- EN 1991: Eurocode 1 - Actions on Structures
- EN 1992: Eurocode 2 - Design of Concrete Structures
- EN 1993: Eurocode 3 - Design of Steel Structures
- EN 1994: Eurocode 4 - Design of Composite Steel and Concrete Structures
- EN 1995: Eurocode 5 - Design of Timber Structures
- EN 1996: Eurocode 6 - Design of Masonry Structures
- EN 1997: Eurocode 7 - Geotechnical Design
- EN 1998: Eurocode 8 - Design of Structures for Earthquake Resistance
- EN 1999: Eurocode 9 - Design of Aluminium Structures

The Structural Eurocodes have continuously evolved in the last few decades. The Commission of the European Community, aspiring to strengthen the Construction sector, which accounts for 9% of the EU GDP and represents the largest industrial employer (European Commission, 2016), took the initiative to harmonize the technical standards among the EU countries by introducing the first version of the civil engineering standards. The harmonization intends to provide a common set of technical rules to European engineers while enhancing worldwide competitiveness of European construction companies, fostering innovation and facilitating the trade of engineering services and products (JRC Science for Policy Report, 2015).

The National Standards Bodies of the member countries of the European Economic Community (EEC) and the European Free Trade Association (EFTA) established the European Committee for Standardization or CEN (Comité Européen de Normalisation) in Brussels in 1961. CEN had the responsibility to translate the Eurocodes into English, French and German which are the three official languages of the organisation, and deliver them to all National Standard Bodies. There are over 260 CEN Technical Committees. TC250 is responsible for all the ECs and Sub Committee 7 (SC7) is responsible for EC7 (Frank, 2006; JRC Science for Policy Report, 2015).

In 1989, CEN became responsible for the development of the Eurocodes. The first draft versions of the standards were published in the 1990's as ENVs (EuroNorm Vornorms). While the use of the ENVs was not mandatory and the standards were used along with the National Standards, valuable experience was gained during the trial period so the draft versions could be later updated (Orr, 2007; Bond and Harris, 2008). After

the pre-standards period, the Structural Eurocodes were developed in the final form and published as ENs (EuroNorms) (Frank, 2006).

Many countries outside EU (e.g. Singapore, Malaysia, South Africa, Vietnam etc.) have also adopted the Eurocodes recognising that they are the most advanced, fully integrated set of standards that offer flexibility and address a wide range of construction materials being relevant to all major fields of structural Engineering (Anagnostopoulos and Frank, 2010; JRC Science for Policy Report, 2015).

1.3 Main Principles of Eurocode 7

Eurocode 7 (EC7) or EN1997 is the geotechnical engineering design standard in Europe. The code consists of two parts: EN1997 Part 1- General Rules and EN1997 Part 2 - Ground Investigation and Testing and it is based on the *limit state design* approach which suggests the use of *partial factors* of safety. Therefore, EC7 represents a significant deviation over the previous standards as it applies safety factors to the source of uncertainty and aspires to provide enhanced safety levels while focusing more on sustainability and economy of resources.

1.3.1 Serviceability and Ultimate Limit States

The Limit States are defined as design conditions that shall not be exceeded. The Structural Eurocodes make a distinction between Serviceability Limit States which are concerned with the user comfort and the structure's functioning and appearance, and Ultimate Limit States which are generally concerned with the safety of users and the safety of the structure against collapse. Designers are, therefore, required to ensure that both Limit States are sufficiently unlikely to be exceeded. Typical serviceability states relate to conditions like excessive settlements and differential settlements, unacceptable vibration, noise and water flow, while 5 different types of Ultimate Limit States are introduced in the code:

- **GEO** defined as *failure or excessive deformation of the ground, in which the strength of soil or rock is significant in providing resistance* (BS EN 1997-1 §2.4.7.1(1)P)

- **STR** is defined as *internal failure or excessive deformation of the structure or structural elements… in which the strength of structural material is providing resistance* (BS EN 1997-1 §2.4.7.1(1)P)

- **EQU** is defined as *loss of equilibrium of the structure or the ground, considered as a rigid body… in which the strengths of structural materials and the ground*

are insignificant in providing resistance (BS EN 1997-1 §2.4.7.1(1)P and BS EN 1990 §6.4.1(1)P)

- **UPL** is defined as *loss of equilibrium of the structure or the ground, due to uplift by water pressure (buoyancy) or other vertical actions* (BS EN 1997-1 §2.4.7.1(1)P)

- **HYD** is defined as *hydraulic heave, internal erosion and piping in the ground caused by hydraulic gradients* (BS EN1997-1 §2.4.7.1(1)P)

Some examples of the GEO Ultimate State are shown in Figures 1.1b, 1.1c, 1.1e and 1.1f where the strength of the soil is critical for the design. Figures 1.1a and 1.1d show examples of the STR Limit State where the strength of the structural elements is critical for the design. Moreover, examples of the EQU, UPL and HYD Ultimate Limit States are presented in Figure 1.2.

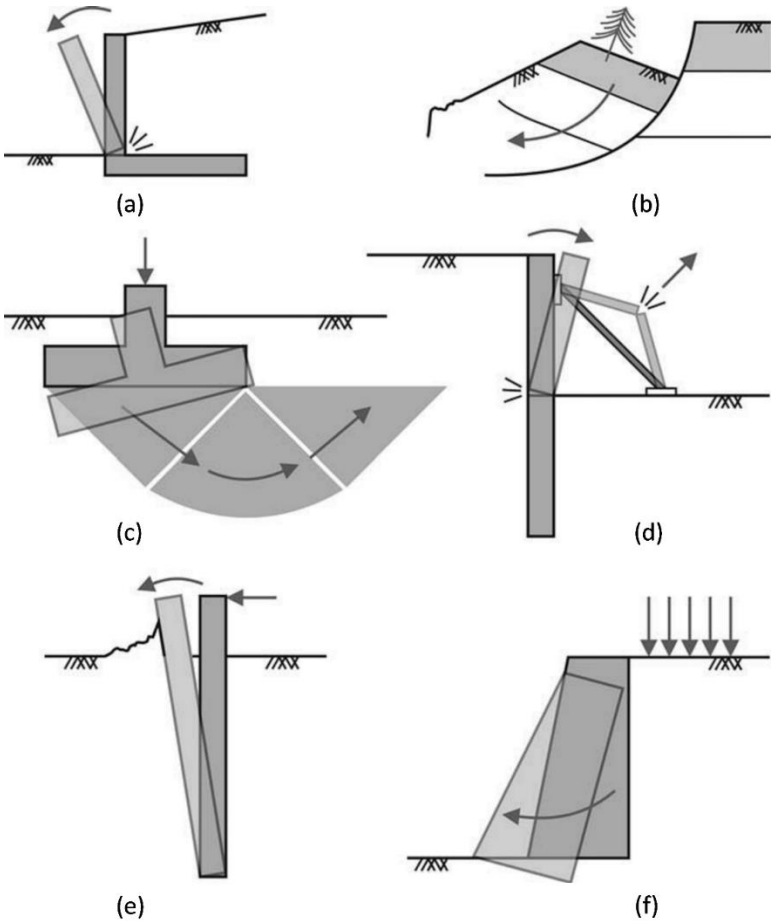

Figure 1.1: Examples of GEO and STR Limit States (after Bond and Harris, 2008)

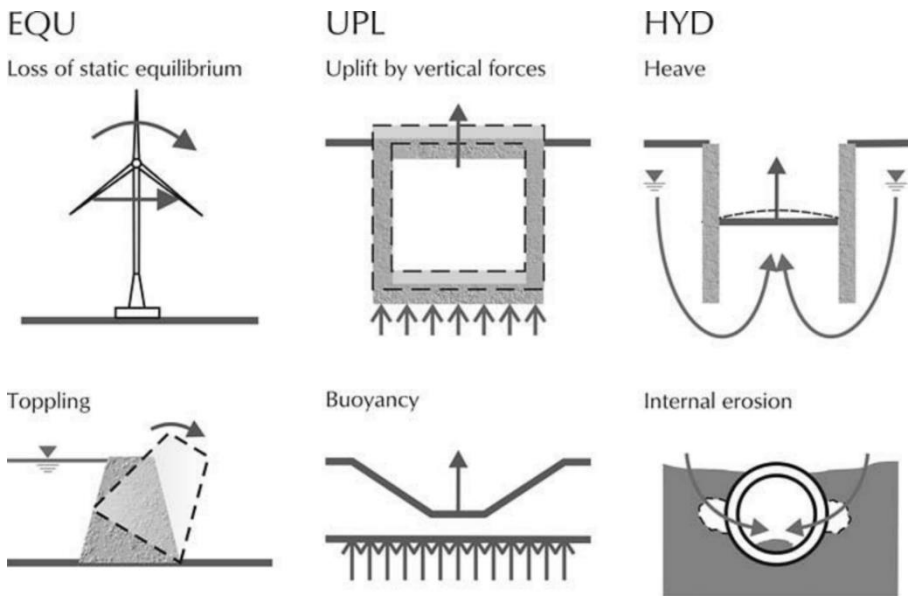

Figure 1.2: Examples of EQU, UPL and HYD Limit States (after Bond and Harris, 2008)

1.3.2 Development of Limit States and Partial Factors

Terzaghi (1943) made a distinction between the stability of geotechnical problems, related to conditions immediately before the ultimate failure is reached and elasticity problems of those associated with the deformations of the soil. These definitions of stability and elasticity conditions have similarities with the ULS and SLS definitions in Eurocodes. For stability problems, the use of a safety factor to prevent failure was first suggested by Bélidor (1729) and Coulomb (1773). In geotechnical engineering, the use of a global safety factor has been common practice in order to ensure safety and take into account all the uncertainties involved in the calculation and construction process. Taylor (1948) and Brinch Hansen (1956) proposed that different partial safety factors need to be applied to actions and material properties. This was widely adopted and had a huge impact in geotechnical engineering design in the European countries.

The aim of the partial factor format is to apply safety margins to the source of uncertainty and illustrate that different uncertainty levels are usually involved in different design aspects. However, as the global safety factor approach had been used for several decades, the values of the partial factors were selected to result in consistent designs with the previous good practice and experience and facilitate the transition (Meyerhof, 1994).

1.3.3 Working State vs Limit State Approach

Another approach that has been quite popular among designers but differs significantly from the Limit State Design, is the Working State Approach. The Working State is defined as the state where the structure performs successfully under working conditions (loads and material parameters). Designers are required to check that the mobilised degree of the soil strength or resistance under these conditions is acceptable (Simpson and Hocombe, 2010).

As the Working State relates to expected conditions rather than unrealistic ultimate limit states, it might seem easier for designers to comprehend it. However, some authors argue that the Working State Design might fail to take into account extreme but critical design conditions (Simpson and Hocombe, 2010).

Advocates of the Working State approach argue that safety factors need to be applied to the peak soil strength in order to ensure safety against expected soil deformations. Designers are required to perform calculations using the mobilised soil strength τ_{mob} which accounts for small and large shear strains and is defined as the lowest value of the ultimate strength, τ_{ult} and the maximum strength divided by the mobilisation factor, τ_{max}/M (Bolton, 1993b). In this approach, both stability and serviceability conditions are verified in one calculation while the Limit State approach requires separate calculations for ultimate and serviceability conditions.

When a structure becomes unstable, SLS is usually surpassed before ULS, so it would make sense that if SLS is avoided, ULS is also avoided. However, avoidance of the serviceability state cannot sufficiently guarantee avoidance of the much more critical ULS. In some cases, ULS occurs suddenly, immediately after SLS. For example, in tension pile problems there is limited displacement before the sudden failure: ULS and SLS occur simultaneously.

There has also been an ongoing debate on whether safety factors need to be applied to the critical state angle of shearing resistance. Some authors argue that reliable measurement of the critical state soil strength is easier than measurement of the peak soil strength so there is no need to factor it (Bolton 1993a). According to Eurocode 7, designers are required to use not the peak soil strength but the soil strength which is relevant to the specific design situation. For example, critical state angle of shearing resistance is relevant at the soil/structures interfaces. It has also been common practice for many designers not to use the actual peak soil strength, which could be quite high for dense soils but unstable, and often leads to progressive failure.

1.3.4 New Terminology of Eurocodes

The Structural Eurocodes introduced some new terminology and definitions that might not have sounded familiar to practising engineers in the United Kingdom. In EN 1990 - Basis of Design the terms of *Actions*, *Action Effects* and *Resistances* are defined.

EN 1990 distinguishes between ***direct actions*** defined as *a set of forces (loads) applied to the structure* and ***indirect actions*** defined as *a set of imposed deformations or accelerations caused, for example, by temperature changes, moisture variation, uneven settlement or earthquakes* (BS EN 1990 §1.5.3.1)

The term ***geotechnical action*** refers to an *action transmitted to the structure by the ground, fill, standing water or ground-water* (BS EN 1997-1 §1.5.2.1).

The term ***effects of actions*** typically refers to internal forces, bending moments, stresses and strains in the structural elements as well as to any deflection or rotation of the structure as a whole (BS EN 1990 §1.5.3.2).

The definition of the ***resistance*** of a structural member is BS EN 1990 as the *capacity of a member or component, or cross-section of a member or component of a structure, to withstand actions without mechanical failure* (BS EN 1990 §1.5.2.15)

1.3.5 Design Situations

The Structural Eurocodes make a distinction between persistent, transient, accidental and seismic design situations. Designers need to consider, for each construction problem, the relevant design situations (BS EN 1990 §3.2(2) P). The values of partial factors are equal to 1.0 for seismic and accidental design situations. Values greater than 1.0, typically 1.2 to 1.5, are used when persistent and transient conditions are considered.

1.3.6 Characteristic Values

The term characteristic value of a material parameter refers to the unfactored value, before the application of the partial safety factor, and is defined in BS EN 1990 as: *«…where a low value… is unfavourable, the characteristic values should be defined as the 5% fractile value; where a high value… is unfavourable,… as the 95% fractile value»* (BS EN 1990 §4.2(3)). A typical normal distribution is presented in Figure 1.3 together with the definition of the mean and characteristic (inferior and superior) value of a material parameter.

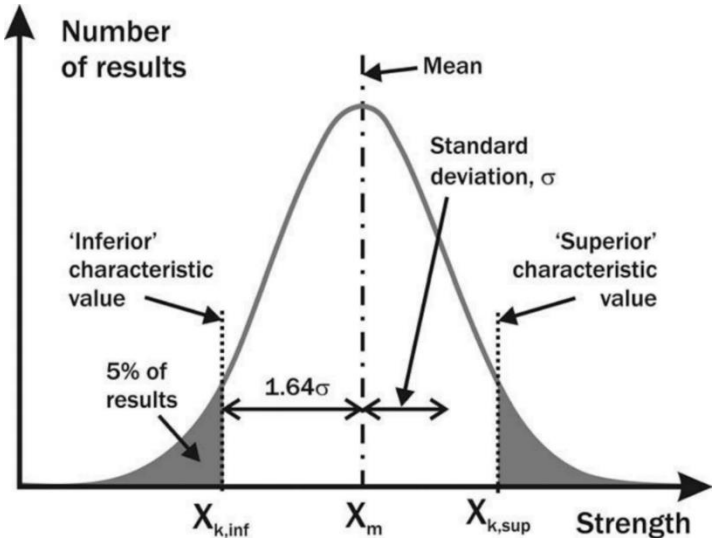

Figure 1.3: Statistical definition of the characteristic material parameter (after Bond and Harris, 2008)

While the statistical definition given in EN 1990 might be relevant for most of the materials (e.g. steel, concrete etc.) where the uncertainty in loads and material parameters is low and the material properties can be accurately measured, the application of the definition is far from straightforward in geotechnical engineering where there is high variability in the soil parameters (Orr, 2000). For this reason, in EN 1997, the characteristic value is defined as *a cautious estimate of the value affecting the occurrence of the limit state* …while… *the choice of characteristic values shall be based on results and derived values from laboratory and field tests, complemented by well-established experience* (BS EN 1997-1 §2.4.5.2(1)P). The stages for deriving the characteristic values from field and laboratory test results have been described in detail by Orr and Farrell (1999), Orr (2000) and Orr (2017).

1.3.7 Partial Factors vs Global Factors of Safety

In geotechnical design, the main variables, and also inputs in the analysis, include the loads, the material parameters and the geometrical properties of the problem. Geotechnical engineers have been traditionally entered a global factor of safety in the calculations to take into account all the type of uncertainties involved. The Structural Eurocodes replaced the well-established concept of the global safety factor and introduced the partial factors which are applied closer to the source of uncertainty.

EC7 requires application of partial factors to actions and material properties. Safety can also be introduced in the geometry of the problem (e.g. unplanned excavation). The standard also allows for applying factors to the effects of actions and resistance instead of actions and soil strength. In that case, the partial factors are applied at the end of the calculation process (see Section 1.3.10).

1.3.8 Design Values

The design values of the material parameters are the values that are used in the analysis and calculated by applying the partial factors to the characteristic values.

Actions

The actions, denoted *F* in EN1990*,* can be categorised in permanent actions *G*, variable actions *Q*, pre-stresses *P* and accidental actions *A*. The design action F_d is equal to the representative action F_{rep} multiplied by the corresponding partial factor γ_F. The definition is given in Equation 1.1.

$$F_d = \gamma_F \, F_{rep} \tag{1.1}$$

The representative action F_{rep} is defined as the sum of any combinations of characteristics values of actions F_k using combination factors ψ (equal to or less than 1.0). An example of the definition is shown in Equation 1.2 for a single characteristic action.

$$F_{rep} = \psi \, F_k \tag{1.2}$$

Material Properties

The material properties are denoted by the symbol *X*. The design material property X_d, which is defined in Equation 1.3 below, is equal to the characteristic value X_k divided by the corresponding material partial factor γ_M.

$$X_d = \frac{X_k}{\gamma_M} \tag{1.3}$$

Geometrical Parameters

The definition of the design value of the dimensions of the problem, denoted α_d in EN1990, is presented in Equation 1.4 and is equal to the nominal value, α_{nom} after any relevant modification (tolerance $\Delta\alpha$). A typical example of such geometrical modifications that account for uncertainty in the value of the dimension, is the increase in the depth of excavation to account for any overdig (unplanned excavation).

$$\alpha_d = \alpha_{nom} \pm \Delta\alpha \tag{1.4}$$

Action Effects and Resistances

As mentioned before, the code allows for the application of factors to the action effects at the end of the calculations. The definition of the design value of the action effect is given in Equation 1.5 as a function of the design values of actions, material strength and dimensions, multiplied by the corresponding partial safety factor.

$$E_d = \gamma_E \, E\{F_d, X_d, a_d\} \tag{1.5}$$

Eurocode 7 also allows for the application of factors to the resistance instead of the soil strength. The definition of the design value of the resistance is given in Equation 1.6 as a function of the design values of actions, material strength and dimensions, reduced by the corresponding partial safety factor. Note that in structural design, resistances are only a function of the material properties and dimensions and not actions.

$$R_d = \frac{R\{F_d, X_d, a_d\}}{\gamma_R} \tag{1.6}$$

1.3.9 EC7 Verifications

According to EC7, designers are required to verify that the existence of any relevant limit state becomes sufficiently unlikely. A distinction can be made between strength and stability verifications.

Strength Verification

The verification of strength relates to the GEO and STR Ultimate Limit States and is shown in Equation 1.7. EC7 requires that the design action effect, E_d, must be equal to or lower than the corresponding design resistance R_d:

$$E_d \leq R_d \tag{1.7}$$

Stability Verification

The verification of stability relates to the EQU and UPL Ultimate Limit States and is given in Equation 1.8. The code requires that the design destabilising action effects $E_{d,dst}$ must be equal to or lower than the sum of the design stabilising action effects $E_{d,stb}$ and the design resistance R_d.

$$E_{d,dst} \leq E_{d,stb} + R_d \tag{1.8}$$

Verification against the HYD Limit State

The safety verification against hydraulic heave and piping relates to the HYD Ultimate Limit State. Eurocode 7 requires verification of an equation in two different forms. Equation 1.9 (EC7 Equation 2.9a) requires that the design value of the pore water pressure $u_{d,dst}$ must be equal or lower than the design total vertical stress $\sigma_{d,stb}$ at the bottom of any relevant soil column while Equation 1.10 (EC7 Equation 2.9b) requires that the design seepage force S' must be equal or lower than the design buoyant weight $G'_{stb,d}$ of any relevant soil column. The HYD verifications will be reviewed in more detail in a following chapter.

$$u_{dst;d} \leq \sigma_{stb;d} \tag{1.9}$$

$$S' \leq G'_{stb;d} \tag{1.10}$$

1.3.10 Design Approaches

Eurocode 7 suggests three different Design Approaches (combinations of partial factors), as shown in Table 1.1. This probably can be explained as an attempt to accommodate the different design practices across the European continent and make the use of the standards more flexible and attractive. In some Member States, the Material Factoring Approach (MFA) has been traditionally used while in others the Load and Resistance Factoring Approach (LRFA) has been more popular.

The main concept of the MFA is to apply the partial safety factors closer to the uncertainty source (loads and material parameters). This method was first applied in Denmark in the 1960's and it was adopted in some early Danish codes of practice (DS 415: 1965). In the following years, the method was also used in many other European countries (e.g. BS 8002, 1994 in the United Kingdom).

On the other hand, the philosophy of LRFA is to factor the results of the calculations (i.e. action effects and resistances). The method's influence is apparent in countries in Northern America and has been referred to in a number of documents (e.g. AASHTO, 2007; American Petroleum Institute, 2003; Canadian Geotechnical Society, 2006). The partial safety factors on the resistance take into account the uncertainty in the material properties but also the uncertainties involved in the method of analysis, the ground investigation techniques and the geometry of the problem. Thus, higher values have been traditionally used when compared to the partial safety factors applied to the material parameters (Meyerhof, 1994).

Eurocode 7 allows for each Member State to select one of the three Design Approaches and specify values for the partial factors in its National Annex (Anagnostopoulos and Frank, 2010; Orr, 2013).

Design Approach 1

The Design Approach 1 (DA1) consists of two sets of partial safety factors (see Table 1.1). In Combination 1 (DA1-1), designers enter design values for the actions in the calculations while no factors are applied to the material parameters. On the other hand, in Combination 2 (DA1-2), partial factors are applied to the soil strength and variable loads (e.g. surcharge) are factored by 1.3. The combination that gives the most adverse results is more critical for the design. DA1 is a Material Factoring Approach as the input parameters are factored.

Design Approach 2

The Design Approach 2 (DA2) consists of one set of partial factors and hence it requires only one check by designers (see Table 1.1). In this approach, the actions and the resistances need to be factored, thus it is a LRFA as partial factors are introduced at the end of the calculations. Eurocode 7 also allows the application of factors to the effects of actions. Such an approach, where the actions effects are factored instead of the actions, is usually referred to as the *star approach* (Frank et al., 2004).

Design Approach 3

In Design Approach 3 (DA3) factoring of both actions and soil strength parameters in one combination is required (see Table 1.1). Hence, designers carry out only one check for ULS. However, in DA3 a distinction is made between geotechnical and structural actions. While factoring of the structural actions is required, for geotechnical actions, values of partial factors equal to 1 are suggested for permanent geotechnical actions and 1.3 for variable geotechnical actions.

The Design Approach 1 has been adopted in the United Kingdom and a few other Member States (see Table 1.2). The majority of the European countries have chosen Design Approach 2 for the design of spread and pile foundations and retaining structures while Design Approach 3 has been widely adopted for slope stability problems (Orr, 2012). In some Member States where the national choice is the DA2, the use of DA3 is allowed for numerical analysis while in only two countries (Ireland and Czech Republic) the use of any Design Approach is permitted (Orr, 2012).

Table 1.1: Design Approaches and partial factors (after Simpson, 2012)

			DA1			DA2	DA3
			Comb 1	Comb 2	Piles		
Actions	Permanent	unfav	1,35			1,35	1,35
		fav					
	Variable	unfav	1,5	1,3	1,3	1,5	1,5/1,3*
Soil	tan φ'			1,25			1,25
	Effective cohesion			1,25			1,25
	Undrained strength			1,4			1,4
	Unconfined strength			1,4			1,4
	Weight density						
Spread	Bearing					1,4	
footings	Sliding					1,1	
Driven	Base				1,3	1,1	
piles	Shaft (compression)				1,3	1,1	
	Total/combined (compression)				1,3	1,1	
	Shaft in tension		1,25		1,6	1,15	1,1

Note: Values of all other factors are 1.0. Further resistance factors are provided for other types of piles, anchors etc.

* 1.5 for structural loads; 1.3 for loads derived from the ground.

Simpson (2007) gives a good review of the DA1 and discuss the advantages of the approach. The Design Approach can be routinely applied with a number of calculation models ranging from simple analytical models to more advanced numerical analysis. Although extra calculation time and effort might be needed for DA1, as two separate verifications, with different sets of partial factors, are required. Overall, DA1 provides sufficient levels of safety, rigor and economy and reasonably consistent levels of reliability can be achieved for a wide range of construction problems (Simpson, 2007).

Further harmonization and ease-of-use represents the biggest challenge for the next version of the Eurocode 7. Possibly, this will be achieved by reducing or even eliminating the current DAs and the NDPs. It has become clear that the DA1 or DA3 (MFA) has been already chosen by most of the European countries for slope stability problems and DA2 (LRFA) for pile design (Bond, 2013). Therefore, the Design Approaches could be eliminated if the code attempts to treat each construction problem in a separate way. This would definitely represent an advance over the current version of the code.

Table 1.2: Choice of Design Approach by the CEN Member countries (after Orr, 2012)

Type of design	DA1	DA2		DA3	DA1, DA2 or DA3	Not known
		DA2	DA2*			
Spread foundations	B, IS, I, LT, P, RO, UK	F, EST	A, CR, CY, D, E, FIN, GR, H, I, PL, SK, SLO	CH, DK, F, N, NL, S	CZ, IRL	BU, L, LV, MK, MT, TU
Pile foundations	B, I, LT, P, RO, UK	A, CH, CR, CY, D, DK, E, EST, F, FIN, GR, H, I, IS, N, PL, S, SK, SLO		NL, S	CZ, IRL	BU, L, LV, MK, MT, TU
Retaining structures	B, IS I, LT, P, UK	A, CH, CR, CY, D, E, EST, F, FIN, GR, H, I, PL, SK, SLO		A, DK, F, N, NL, RO, S	CZ, IRL	BU, L, LV, MK, MT, TU
Slopes	B, IS, EST, LT, P, UK	E, F		A, CH, CR, CY, D, DK, E, F, FIN, GR, H, I, N, NL, PL, RO, S, SK, SLO	CZ, IRL	BU, L, LV, MK, MT, TU
Overall	6–7	2–19		2–19	2	6

Note: A = Austria; B = Belgium; BU = Bulgaria; CH = Switzerland; CR = Croatia; CZ = Czech Republic; CY = Cyprus; D = Germany; DK = Denmark; E = Spain; EST = Estonia; F = France; FIN = Finland; GR = Greece; H = Hungary; I = Italy; IRL = Ireland; IS = Iceland; L = Luxembourg; LI = Lithuania; LV = Latvia; MK = The Former Yugoslav Republic of Macedonia; MT = Malta; N = Norway; NL = the Netherlands; P = Poland; PL = Portugal; RO = Romania; S = Sweden; SK = Slovakia; SLO = Slovenia; TU = Turkey; UK = UK.

1.4 Development plans of Eurocode 7

Working towards the second generation of Structural Eurocodes, the European Commission issued a Mandate (M/515, 2012) in December 2012 for *«amending existing Eurocodes and extending the scope of Structural Eurocodes»*. The Mandate was focused not only on the development of new standards or new parts of existing standards, but also on the introduction of new performance requirements, user-friendly design methods and a technical report on taking into account the challenges of climate change.

CEN responding to this Mandate (CEN/TC 250, 2013) submitted a proposal to undertake the work, including the creation of three new Eurocodes and the update of the existing ones based on recent research developments, reduction in the number of the Nationally Determined Parameters and more focus on easy-of-use and sustainability (Bond, 2013). The European Commission approved funding of €4.5M to support Phase 1 of the project, with two more phases underway. It is anticipated that the total cost will exceed €10M by the end of 2019 (Bond, 2016). In Figure 1.4, the roadmap for the development of the next version of Eurocodes is presented over the period between 2010 and 2020.

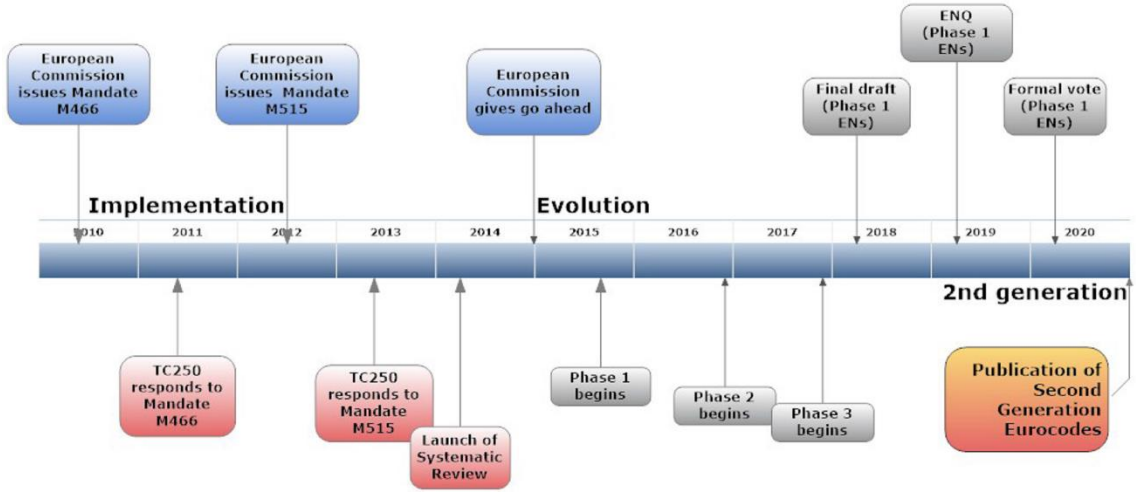

Figure 1.4: Timeline for development of the next generation of Eurocodes (after Bond, 2016)

However, plans for the development of Eurocode 7 had been already underway since March 2011, when the TC250/SC7 made a decision to create a number of Evolution Groups (EGs) to work on the technical issues that require enhanced coverage in the second version of the code (Bond, 2013). These Evolution Groups, which combined expertise by bringing together a large number of volunteering geotechnical engineers from different countries, had been focusing on different issues that need update and more research until the submission of their final reports in December 2015. The complete list with the titles of the SC7's Groups is given in Figure 1.5.

The research, whose outcomes are presented in this thesis, involved collaboration with a number of Evolution Groups, especially with the Evolution Group 4, chaired by Andrew Lees, focusing on the challenges of the use of numerical methods with EC7 and the Evolution Group 9, chaired by Norbert Vogt, looking at the challenges of factoring water pressures.

In order to meet the work requirements outlined in Mandate M/515, SC7 has identified six main tasks:

1. Harmonization and ease-of-use of Eurocode 7
2. Improvements to Eurocode 7 Part 1 – General Rules
3. Improvements to Eurocode 7 Part 2 – Ground Investigation
4. Creation of Eurocode 7 Part 3 – Geotechnical Constructions (slopes and spread and pile foundations)
5. Creation of Eurocode 7 Part 3 – Geotechnical Constructions (retaining structures, anchors, reinforced soil structures and ground improvement)
6. Improved treatment of Rock Mechanics and Dynamic Design

Tasks 1 and 2 will be part of the project Phase 1, Tasks 3 to 5 of Phase 2 and Task 6 of Phase 3. The main responsibility of the Project Team for Task 1 is to divide the code in three parts:

- EN1997-1 Eurocode 7 – Geotechnical Design: Part 1 – General Rules
- EN1997-2 Eurocode 7 – Geotechnical Design: Part 2 – Ground Investigation
- EN1997-3 Eurocode 7 – Geotechnical Design: Part 3 – Geotechnical Constructions

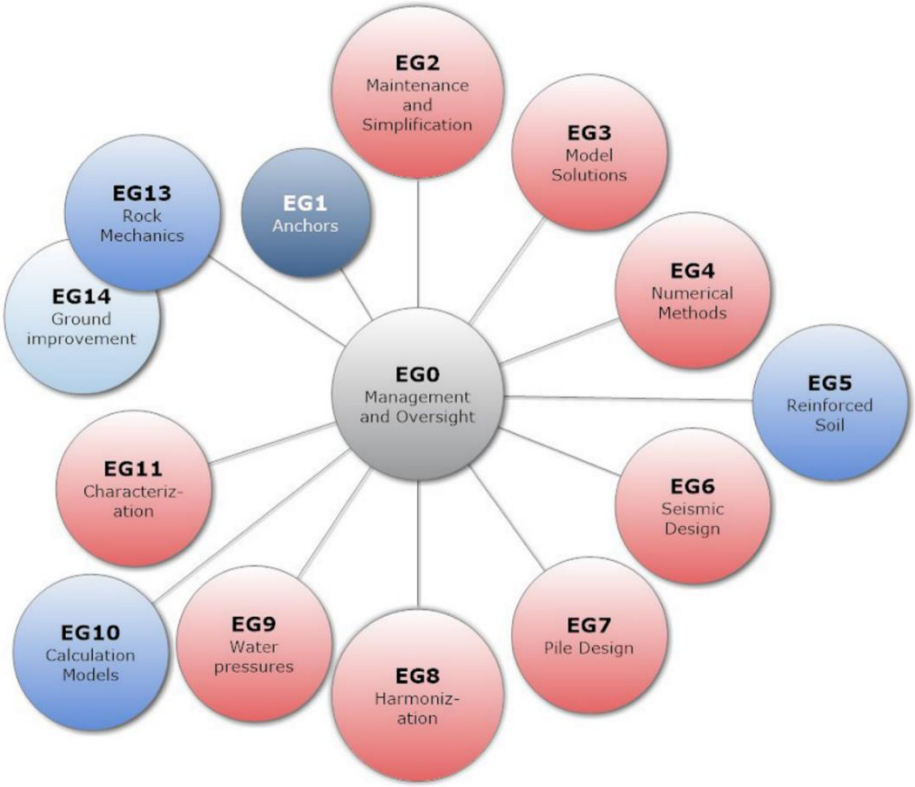

Figure 1.5: SC7's Evolution Groups 2011-2015 (after Bond, 2016)

The proposed new structures for each of the three parts of the code are shown in Figures 1.6 to 1.8. For Part 3, different *Design Combinations* are envisaged for different types of geotechnical structures being designed.

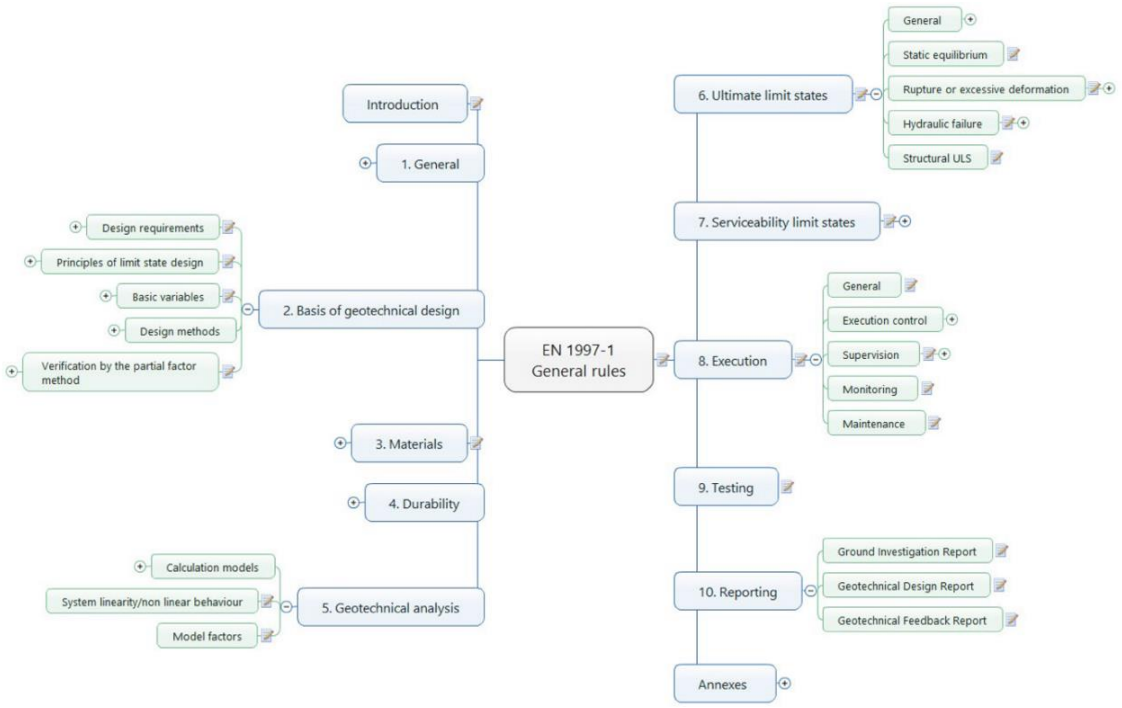

Figure 1.6: Proposed new structure for Eurocode 7: Part 1-General Rules (after Bond, 2016)

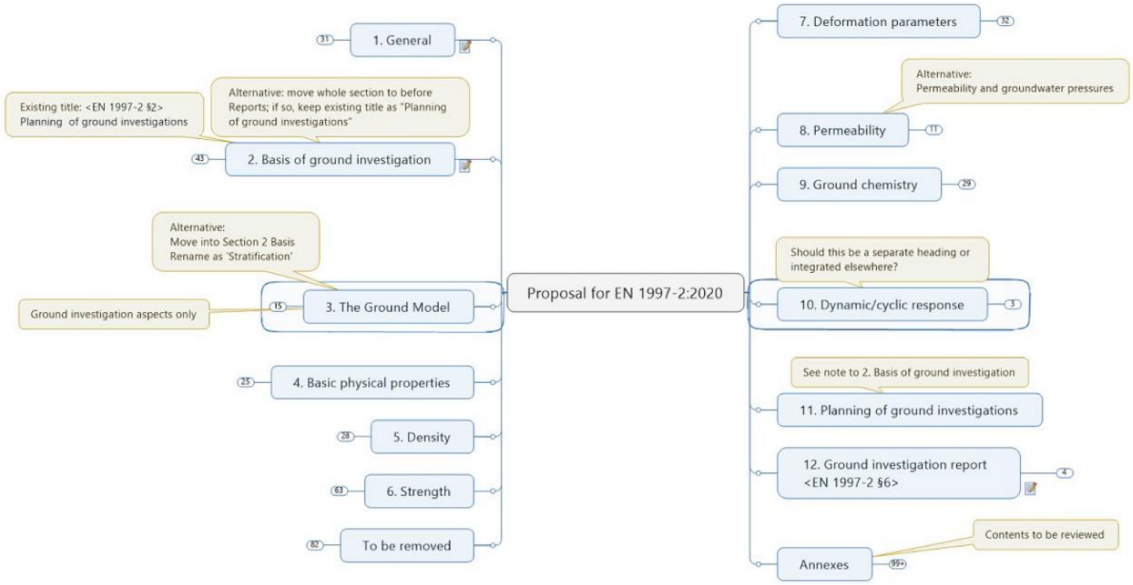

Figure 1.7: Proposed new structure for Eurocode 7: Part 2-Ground Investigation (after Bond, 2016)

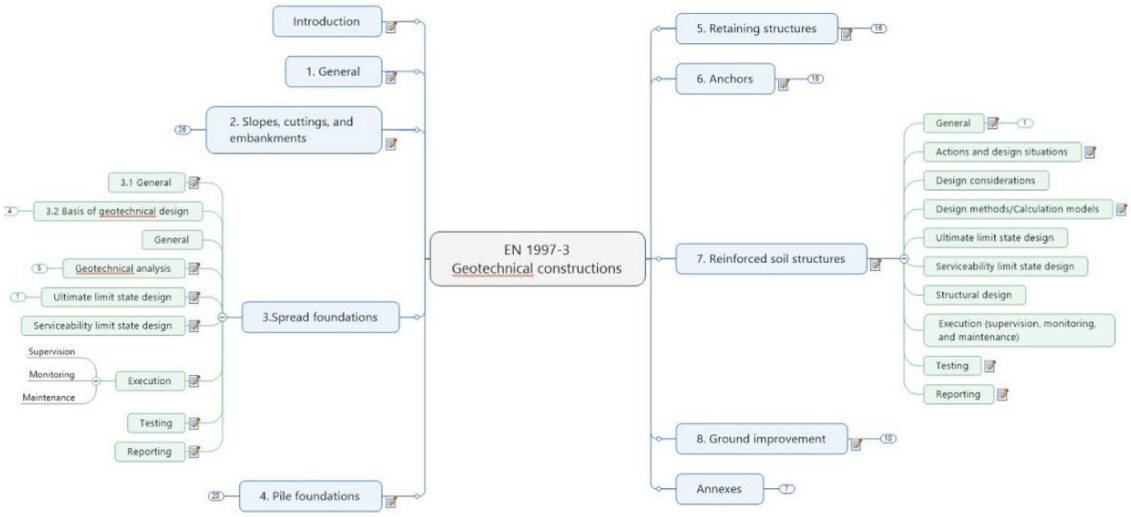

Figure 1.8: Proposed new structure for Eurocode 7: Part 3-Geotechnical Constructions (after Bond, 2016)

SC7 has created three Working Groups (WGs) in charge of each of the three parts of the new code. Several Task Groups have also been created within these WGs to focus on specific technical issues (Bond, 2016). In total, more than 200 engineers will be involved in what, there is no doubt, represents a very ambitious and challenging project, aiming to deliver a significantly improved, more consistent, user-friendly and in tune with the climate change challenges and sustainability requirements, Eurocode 7.

1.5 Other relevant British Standards

As mentioned previously, each Member State is required to publish in its National Annex any non-contradictory national documents and old codes of practice. These documents, which are referred to as Non Contradictory Complementary Information (NCCI), have a supportive role to the Eurocode 7 by addressing issues not covered in the standard (Bond and Harris, 2008). When the use of Structural Eurocodes became compulsory in the United Kingdom, several important geotechnical codes of practice were withdrawn; these included:

- BS 8004:1986, Code of practice for foundations
- BS 8002:1994, Code of practice for earth retaining structures

Other standards remained in use and included in the UK National Annex as NCCI but are not quite consistent with Eurocode 7:

- CIRIA C580 (Gaba et al, 2003), Embedded retaining walls – guidance for economic design

- BS 8081:1989, Code of practice for ground anchorages (renamed 'grouted anchors')

1.5.1 CIRIA C580 - Embedded Retaining Walls

The CIRIA Report C580 is included in the UK National Annex as NCCI and is applicable to cantilever and multi-propped walls embedded in stiff clay and other competent materials. This guide was hugely influenced by the much older CIRIA Report R104 - Design of retaining walls embedded in stiff clay, which was applicable to cantilever and singly propped walls (Padfield and Mair, 1984).

The guide was introduced during the ENV1997 period and before the current version of EC7 was published. It suggests the use of A, B and C design methods which relate to moderately conservative, worst credible and most probable conditions respectively and hence, differ from the Eurocode's Design Approaches (Gaba et al., 2003). The values of the required partial factors are also different while the C580 is probably the only report that suggests factoring the soil stiffness by a factor of 2. Hence, CIRIA C580 is not compatible with Eurocode 7 but only with the old British Standards on structural design of embedded walls. According to Bond and Harris (2008), when there are discrepancies between old national documents and Eurocode 7, the designers shall always comply with the Eurocode's requirements.

An update to the CIRIA guidance has been recently published (Gaba et al., 2016) and extends its applicability beyond stiff clays and competent soils to include soft clays and weak rocks. This new document also aims at updating and extending the current ground movement database and providing guidance on the use of 2D and 3D numerical modelling and analysis, as well as king post wall design and rock socket design and maintenance, inspection and monitoring. The update, which was published in 2016, is consistent with EC7 and proposes changes in the current design practices with the intention to influence the future development of the code.

1.5.2 BS 8002 - Code of Practice for Earth Retaining Structures

BS 8002, which is now obsolete, was introduced in 1994 aiming to provide guidance on the design of retaining structures in the United Kingdom. The guide refers to representative soil parameters which are defined as *"conservative estimates... of the properties of the soil as it exists in situ… properly applicable to the part of the design for which it is intended"* (BS 8002, 1994). It is obvious that this definition has similarities with the way characteristic parameters are defined in Eurocode 7.

BS 8002 suggested the use of mobilization factors to be applied to the strength of the soil in order to limit the soil deformations while no application of factors is required for the actions. The standard suggests factoring the undrained shear strength and the drained strength parameters by mobilization factors of 1.5 and 1.2 respectively (BS 8002, 1994). While factoring the action effects was not required by the guide, it had been common practice for some engineers to apply safety factors to the calculated bending moments (Simpson et al., 2011). Beeby and Simpson (2001) suggested that no factors need to be applied to action effects for embedded walls designed using the prescribed overdig allowances. For all other cases, the authors suggested the use of a factor of 1.2.

An update of BS 8002 was recently undetaken (together with other British Standards, e.g. BS 8004, 2015 and BS 8081, 2015) sponsored by High Speed 2 (HS2) Limited. The update of the standard intends to improve the design of embedded walls, clarify the application of partial factors from Design Approach 1, Combination 1 (i.e. apply 1.11 to variable actions and 1.35 to effects of actions), re-introduce a model factor on prop/anchor loads, depending on method of analysis and clearly map design effects of actions from retaining wall design to design actions used for subsequent anchor design ($F_{ULS,d}$, $F_{Serv,d}$, $F_{Serv,k}$) (BS 8002, 2015). The revised document is intended to complement the current version of Eurocode 7 and its National Annexes, provide clarification of Eurocode 7's requirements, be future-proof against future changes to Eurocode 7 and update 20 to 30 years old technical information contained in the withdrawn codes.

1.6 Accidental Design Situations

As discussed in Section 1.3.5, the Eurocodes make a distinction between persistent, transient, accidental and seismic design situations. In deep supported excavations, the most typical example of an accidental design situation is the loss of an individual prop during the construction or the operation stages, which can trigger progressive failure with severe consequences for the safety of the people and the structure. However, the prop loss effect has been usually overlooked during the design. In this section, current standards relating to accidental design situations including Eurocodes, CIRIA reports, Singapore and Hong Kong codes are reviewed highlighting that there is a need for more consistent and complete guidance for practising engineers.

1.6.1 UK standards

In the United Kingdom, the Code of Practice for Earth Retaining Structures (BS 8002, 1994) highlights that the prop design should make allowance for accidental construction loadings, suggesting that «*the design should accommodate the possible*

failure of an individual strut tie rod or anchor. The wall and walings should be capable of redistributing the load from the failed tie rod or anchor».

In 1999, the CIRIA C517 Temporary Propping of Deep Excavations-Guidance on Design (Twine and Roscoe, 1999) was published including the study of many case histories of supporting excavations and a more extensive discussion on the accidental prop loss case. The guidance suggests that **«***unless the risk of losing of a prop by accident can be eliminated, the design should consider progressive failure. Individual elements of the support system should fail in a ductile rather than in a brittle manner or, if this is not achievable, factors of safety should be increased».* Moreover, the causes and modes of prop failure are discussed: props can be damaged on site from falling objects, excavator buckets and crane loads. In two case histories (i.e. AF2 and AF8), a prop was knocked out by the crane-mounted crab while in the AF2 excavation, the same prop was knocked out twice. This highlights how important is that the design accounts for a single prop loss ensuring that a sudden failure is sufficiently unlikely to occur.

In general, the authors favour the use of the largest possible prop spacing with fewer props but with increased size of sections to reduce the risk of accidental damage due to construction operations and unexpected loads. However, the degree of redundancy within the propping system is reduced and the risk of progressive failure increases. The authors recommend considering possible prop loss in the design «*unless positive steps are taken in the management and operation of the site to eliminate effectively the risk of accidental of loss of a prop*». In any case, designers should thoroughly consider and evaluate the risk and consequences of failure (Twine and Roscoe, 1999). Overall, the CIRIA C517 proposes two different ways of accounting for the prop loss:

- Incorporating the loss of prop into the design of the support system with reduced partial safety factors, reflecting the accidental nature of the loading.

- A risk assessment and management strategy to eliminate the risk of accidentally damaging/removing a prop.

Finally, the CIRIA Report C580 also describes the accidental load cases including the loss of a prop, as extreme cases which can occur any time during the construction works and operational stage. In any case, designers must ensure that the propping system can efficiently withstand the accidental prop loss without excessive movements and progressive failure (Gaba et al., 2003). Similar to the CIRIA C517, the authors make

a distinction between the two ways that accidental prop loss can be taken into account: 1) incorporate prop loss in the design and 2) adequately mitigate prop loss risk through a robust construction management strategy (Gaba et al., 2003).

A summary of the two strategies of accounting for single prop loss, as described in the CIRIA C517 and C580 documents, is given in Table 6.1.

Table 1.3: CIRIA C517 and C580 strategies of accounting for prop loss

Strategy 1	Strategy 2
Incorporate prop loss in design	Mitigate risk of prop loss
▪ Use of reduced partial safety factors. ▪ Not clear in the code what partial factor values should be used. ▪ Additional computational effort and time as many parametric and sensitivity analyses are required.	▪ Risk assessment and management. ▪ Strategy should be specified in tender documents. ▪ Widely differing viewpoints are often expressed between concerned parties. ▪ Lack of consistent and complete guidance.

1.6.2 Singapore standards

The Technical Reference on Deep Excavation TR26 (2010), provides guidance on design checks against one prop/anchor/structural member failure: «*The design for deep excavations should accommodate possible failure of any individual strut, tie rod, ground anchor, structural member or connection at each stage of the construction works*». In any case, the support system should be able to redistribute the load from the failed member and continue to be safe without causing any danger to the adjacent structures.

The Land Transport Authority (LTA) Civil Design Criteria for Road and Rail Transit Systems (LTA, 2010) refers to the design requirements of Temporary Earth Retaining Structures (TERS): «*The TERS shall be designed to accommodate the possible failure of an individual strut, tie rod or ground anchor at each and every stage of the construction works, in accordance with BS 8002*». Moreover, the guidance suggests that «*the design of the support system shall allow for: 1) Accidental load not less than 50kN applied normal to the strut at any point in any direction, unless otherwise demonstrated by risk assessment and 2) one-strut failure*».

1.6.3 The Eurocodes

BS EN 1990-Basis of Structural Design suggests that «*a structure shall be designed and executed in such a way that it will not be damaged by events such as explosion, impact and the consequences of human errors to an extent disproportionate of the original cause*» (BS EN 1990, 2002). Moreover, potential damage shall be avoided or limited among others by: «*selecting a structural form and design that can survive adequately the accidental removal of an individual member or a limited part of the structure, or the occurrence of acceptable localized damage and avoiding as far as possible structural systems that can collapse without warning*» (BS EN 1990, 2002).

The UK National Annex of Eurocode 1 suggests that «*a localized failure due to accidental actions may be acceptable, provided it will not endanger the stability of the whole structure and that the overall load-bearing capacity of the structure is maintained and allows necessary emergency measures to be taken*» (BS NA EN 1991-1-7, 2006). Measures that should be taken to mitigate the risk of accidental actions include: preventing the action from occurring, protecting the structure from the action affects and «*ensuring that the structure has sufficient robustness by incorporating sufficient redundancy in the structure to facilitate the transfer of actions to alternative load paths following an accidental event*» (BS NA EN 1991-1-7, 2006).

Finally, in Eurocode 7, a list of limit states that shall be considered is provided, including «*failure of a structural element such as a wall, anchorage, wale or strut or failure of the connection between such elements*» (BS EN 1997-1, 2004).

1.7 Finite Element Methods and EC7

In recent years, it has been common practice for geotechnical engineers to use advanced numerical methods, such as Finite Element Methods (FEM), to calculate deformations and verify serviceability. For the ULS analysis, designers often just apply load factors to the structural forces (e.g. bending moments and prop loads) at the end of the calculation process, as in many cases, factoring soil strength or resistance is less straightforward.

While the use of FE methods for ULS verifications is suggested in EC7, there is a lack of more detailed guidance. There is no doubt that there is still a number of issues that need to be better understood before the ULS verifications can be routinely carried out using FE Methods (Simpson, 2012). In this section, the challenges related to the ULS FE analysis are discussed.

1.7.1 FE Methods and Design Approaches

ULS FEM analysis cannot be easily performed with all the Design Approaches and the challenges involved have been studied and discussed by many authors (e.g. Schweiger, 2009 and 2014; Lees and Perdikou, 2010; Lees, 2013; Lees, 2016). DA1-2 and DA3 are both Material Factoring Approaches (MFAs) so they can both be easily applied with FEM when simple constitutive models are used as the partial factors are introduced to the input parameters (e.g. actions and material strength). However, DA2 is a Load Resistance Factoring Approach (LRFA) where resistance factoring is required (e.g. bearing resistance, active or passive earth pressures). Because these parameters are not input in the numerical calculations and their factoring is far from straightforward, the majority of the Member States that have adopted DA2, suggest the use of DA3 for numerical analysis. However, the combined use of both these approaches might raise legal issues in cases where the design complies with only one approach (Simpson, 2012).

In retaining wall problems and tunnels, the earth pressures are the actions acting on the structure. Although, DA1-1 requires application of factors to the earth pressures, this is not easy in FEM where the earth pressure is an output and not an input in the calculations. An alternative approach allowed by EC7 involves the application of partial factors to the action effects and not the actions. More specifically, the variable unfavourable actions are factored by γ_G/γ_Q = 1.35/1.5 = 1.1 and the design values of structural forces are obtained by applying a load factor (i.e. by 1.35) at the end of the analysis (Frank et al., 2004). The use of this approach, which is typically referred to as the *star approach* has been highlighted by many authors (e.g. Schweiger, 2010; Lees and Perdikou, 2010, Brinkgreve and Post, 2015). Overall, it is clear that, in one way or another, both combinations of the DA1 can be used with advanced numerical methods.

Other authors suggest the star approach as an alternative to Design Approach 2 with numerical methods (Frank et al., 2004). For retaining wall design, for example, DA2* requires that the active earth pressures enter the analysis with characteristic values while any variable surcharge is factored by γ_G/γ_Q = 1.35/1.5 = 1.1. The passive earth resistances need to be factored by the resistance factor γ_R and the load factor γ_G. The design values of the structural forces are obtained at the end of the analysis, after factoring the outputs by the load factor, γ_G (Frank et al, 2004; Heibaum and Herten, 2010). While, the use of DA2* seems to be straightforward for simple methods of analysis such as Limit Equilibrium, factoring the passive earth resistance is not an easy task in numerical analysis. Lees and Perdikou (2010) studying a simple embedded wall example

with FEM, proposed factoring the available resistance by reducing the value of the passive lateral earth pressure coefficient, K_p through manipulation of ϕ' and c of soils on the excavated side of the wall only. However, designers often calculate the mobilised design passive resistance and then compare that with the available design passive resistance obtained with hand calculations. This is a tedious task that involves both numerical and hand calculations, practically preventing its application. Another approach is the one discussed by Heibaum and Herten (2009; 2010) according to which the actions and effects of actions obtained from the FE output should be factored at the end of the analysis while the design resistances can be calculated from simple analytical methods.

1.7.2 Constitutive models and EC7

Eurocode 7 proposes values of partial factors focusing mostly on conventional analytical calculation models. Factoring the strength of the soil requires the application of partial safety factors to the drained strength parameters c' and φ' and to the undrained shear strength c_u. Therefore, when using FEM, factoring soil strength is an easy task only for models that include the basic strength parameters in their user defined inputs. While the use of more advanced soil models allows more accurate predictions of the soil behaviour, models such as the Modified Cam-Clay (Roscoe and Burland, 1968) and BRICK (Simpson, 1992), do not have the common strength parameters as inputs and, as a consequence, factoring the soil strength can be particularly challenging.

When advanced constitutive models are used it has been common practice for designers to perform serviceability checks using the advanced model parameters and then switch to the design values of Mohr-Coulomb parameters to verify safety against the Ultimate States. ULS verification using more complex constitutive model parameters still involves significant challenges for users. Moreover, when the shear strength is calculated by the model (e.g. undrained conditions with effective stress parameters) it is not clear whether the partial factor value for undrained shear strength should be used or not (Simpson, 2012).

Only a few authors have attempted to use advanced soil models for ULS design (e.g. Schweiger, 2009; Yeow, 2014) thus there is no doubt that more research is needed to improve the understanding of the challenges involved and the benefits of using advanced models for ULS.

1.7.3 Material Factoring Strategies

In FE Methods, there is a number of different ways to reduce the material strength but EC7 provides no guidance as which one is preferable. Simpson (2011) and Katsigiannis et al. (2014, 2015a and 2015b) provided a detailed review and illustrated the benefits and limitations of the two popular Material Factoring Strategies in numerical analysis. As shown in Figure 1.9, in Strategy 1, users are required to apply the partial factors to the material parameters right from the start of the analysis and the calculations are carried out using the design values of the parameters. In Strategy 2, the requirement is for the characteristic values of the material parameters to enter the calculations, and at critical stages, the user switches to the design values for the ULS verifications. Many authors seem to prefer using the Strategy 2 (including the members of the EG4) despite the apparent advantage and simplicity of the Strategy 1. This is mainly because in cases when no modifications are required to the geometry, the surcharge load or the water level, users can verify safety against both SLS and ULS with one numerical analysis when adopting Strategy 2. Moreover, Strategy 2 can be easily used in conjunction with the stepwise soil strength reduction technique (Simpson, 2012), discussed in detail in Section 1.7.4.

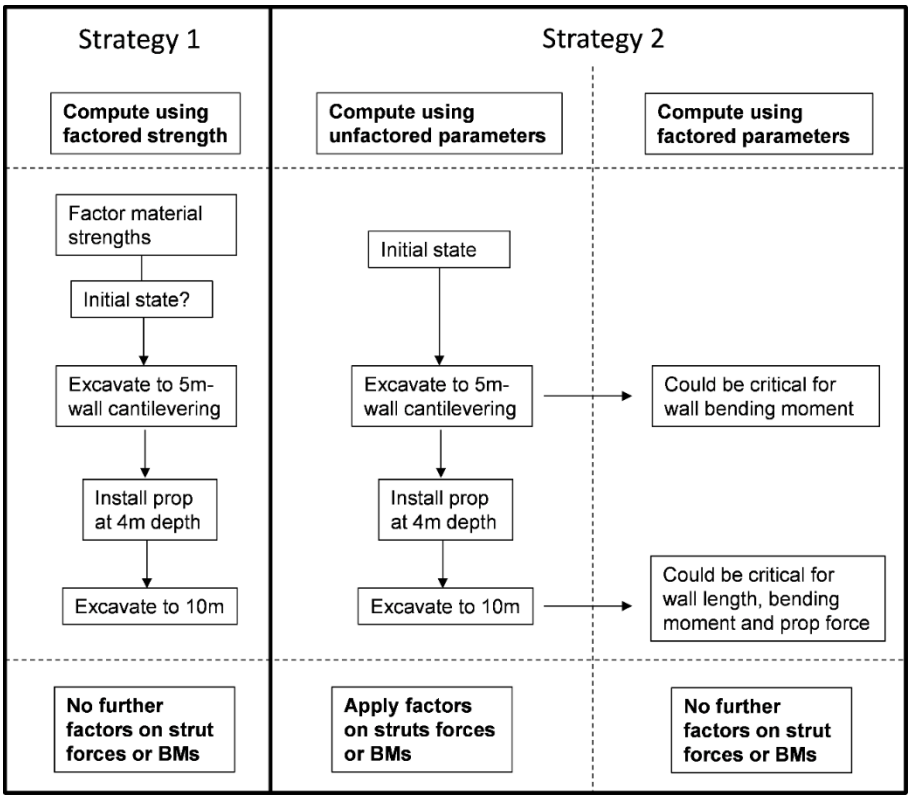

Figure 1.9: Material Factoring Strategies after Simpson (2011)

A limited number of comparisons between the two Material Factoring Strategies in staged excavation problems, using numerical analysis, have been performed in the recent years. Bauduin et al. (2000) analysed a singly supported sheet pile wall and a multi-propped diaphragm wall, and suggested that the Strategy 2 (i.e. material factoring at critical stages) results in only slightly more onerous values of the design structural forces. Simpson and Yazdchi (2003), considering a supported excavation with multiple props, suggested that the DA1-1 results in more adverse results when the wall length has not been optimised by performing a stability analysis first. The authors also show that the Material Factoring Strategies 1 and 2 provide quite different results. Simpson and Driscoll (1998) pointed out that in some cases, Strategy 2 can govern the design. Schweiger (2005), studying a supported excavation with one prop level, highlighted that the difference in the results from both Material Factoring Strategies is small, with the Strategy 2 resulting in just slightly more critical values. Simpson and Hocombe (2010), analysing the Florence High Speed Station case study, compared the two Strategies and concluded that the Strategy 2 gives the most onerous results.

While it is shown that many authors suggest that Strategy 2 might be more critical for the design of the structural elements, the reasons for the discrepancy in the results between the two Strategies have not been well understood.

1.7.4 Stepwise soil strength reduction

Most geotechnical engineering software packages have introduced an analysis option referred to as stepwise material strength (i.e. *c*-*φ*') reduction. By using this option, users are able to drive the system to failure by decreasing gradually the values of the material parameters and calculate the corresponding factor of safety (Brinkgreve and Bakker, 1991). If the value of the factor obtained exceeds the value required by the code, designers can modify the model and carry out the numerical calculations again (Simpson, 2012). Schweiger (2005) highlighted the use of the automatic *c*-*φ*' reduction for slopes and tunnel face stability problems and a single propped excavation. The majority of the software packages apply the stepwise soil strength reduction in combination with a simple linear elastic-perfectly plastic model (Bauduin et al., 2005). More recently, Potts and Zdravkovic (2012) suggested a strength reduction approach that can be used in combination with both simple and advanced constitutive models.

The philosophy of the stepwise soil strength reduction method is to enable users to gain an estimate of safety (and economy) at the final stage or at each critical stage of the analysis. However, the philosophy of Eurocode 7 is to check that the Ultimate Limit State becomes sufficiently unlikely to exist for the required sets of partial factors and not

to deal with a fully mobilised mechanism. The obvious disadvantage of the automatic *c-φ*' reduction method is that no useful information is provided regarding the design values of the structural forces (STR ULS). Some designers in the UK have often misinterpreted the code requirements and have the impression that DA1 Combination 1 is used for verification of the STR Limit State and DA1 Combination 2 for verification of the GEO Limit State. This is a misunderstanding of the code requirements and designers must check both DA1 Combinations for both GEO and STR ULSs. Nevertheless, the automatic *c-φ'* reduction method can be a valuable tool when performed as an additional calculation to obtain the critical failure mechanism and the achieved level of safety. However, users should be aware that Eurocode 7 does not implicitly require this.

1.8 Conclusions

In this Chapter, the evolution history and implementation of the Eurocode 7 were briefly discussed and the main definitions and concepts of the code were described while the plans for the development of the next generation of the standards were introduced. Other relevant British Standards currently in use or recently updated were also discussed. Finally, the most common issues and challenges associated with the routine use of advanced numerical methods for ULS design were reviewed. Overall, it is clear that further research is needed to facilitate the use of FEM for EC7 compliant design and investigate and highlight the potential advantages.

CHAPTER 2

Constitutive models and derivation of ULS parameters

2.1 Introduction

The use of advanced numerical analysis such as the Finite Element Method (FEM) has become increasingly popular in recent years amongst geotechnical engineers. In this chapter, the formulation and the main features of the constitutive models used in this thesis for modelling the behaviour of the soil in supported excavation problems, are described. The constitutive models range from simple linear elastic perfectly plastic such as the Mohr-Coulomb, to more advanced ones such as the Hardening Soil, the Hardening Soil Small (Benz, 2007) and the BRICK (Simpson, 1992) models. Both characteristic and design values of the model parameters are derived for a stiff over-consolidated clay such as the London Clay while the challenges associated with factoring the undrained shear strength of the material, when using total and effective stress parameters are discussed in detail.

2.2 FE Analysis in Geotechnical Engineering

The aim of Engineering is to comprehend the physical world using Mathematics. While geotechnical engineers had been traditionally using empirical or simplified methods of analysis, the recent and continuous advances in hardware and software, enable designers to use more complicated and realistic methods of analysis and analyse more and more complicated and challenging construction problems and understand better the mechanisms of soil-structure interaction (Potts and Zdravkovic, 1999; Carter et al., 2000).

Any theoretical solution should meet 4 fundamental requirements: Equilibrium, Compatibility, Constitutive behaviour and Boundary conditions (forces and displacements). The only method of analysis that satisfies all the theoretical requirements and provides rigorous solutions is the full Numerical Analysis such as the FEM, which is probably the most used numerical analysis method in our field to date. (Potts, 2003). The main advantages of the FEM include the modelling of non-linear and time-dependent soil behaviour and the more accurate simulation of the soil-structure

interaction in staged excavation and seepage problems (Carter et al., 2000). More complicated 3D Finite Element models can be used for problems that cannot be simplified under the assumption of either plane strain or axisymmetric conditions.

There is no doubt that the FEM has been an increasingly popular method of simulating soil-structure interaction problems among researchers and practising engineers. FEM can be used in combination with a variety of constitutive models and boundary conditions that can more accurately predict the real soil behaviour. However, the complexity of FE methods requires high levels of experience and expertise. Users need to have excellent knowledge of both the theory of FE and soil mechanics and be aware of the advantages and limitations of the constitutive models used to simulate the soil behaviour.

2.3 Constitutive Models

The stress-strain relationship of the soil is defined by the specified constitutive behaviour shown in Equation 2.1, where $\{\Delta\sigma\}$ and $\{\Delta\varepsilon\}$ are the vectors of incremental stresses and strains respectively and $[D]$ is the constitutive matrix.

$$\{\Delta\sigma\} = [D]\,\{\Delta\varepsilon\} \tag{2.1}$$

2.3.1 Theory of Elasto-plasticity

Constitutive models formulated within the framework of elasto-plasticity theory have been widely used as they are generally considered to reasonably predict the real soil behaviour. Three essential elements are required in order to define an elasto-plastic constitutive model: a) a yield function, f which distinguishes between purely elastic and plastic behaviour; b) a plastic potential (i.e. flow rule) which defines the direction of plastic strains; and c) a hardening or softening rule which describes how the yield stress, σ'_y, which is the stress that corresponds to the yield state, varies with plastic strains.

As shown in Figure 2.1a, when F < 0, the stress state is within the yield curve and the soil behaviour is elastic and the elastic strains, ε^e, are reversible. The simplest type of elastic behaviour, is linear and isotropic. Significant advances over the linear models include the linear cross-anisotropic models that can capture the anisotropy of the stiffness and the non-linear elastic models with stress or strain dependent soil parameters (Potts and Zdravkovic, 1999). When F = 0, the stress increment touches the yield curve (i.e. the stress becomes equal to the yield stress σ'_y) and plastics strains occur. The plastic strains, ε^p, are irreversible. Stress states outside the yield curve (i.e.

F > 0) are impossible to occur. The total strain consists of the elastic and plastic component as shown in Equation 2.2.

$$\varepsilon = \varepsilon^e + \varepsilon^p \tag{2.2}$$

When the yield and plastic potential functions are the same and the corresponding surfaces coincide as shown in Figure 2.1b, the model is said to have an *associated* flow rule and the constitutive and global finite element matrices are symmetric. When the functions are not similar, the flow rule is said to be *non-associated* and the matrices are non-symmetric, resulting in additional computation resources being required for FEM analysis.

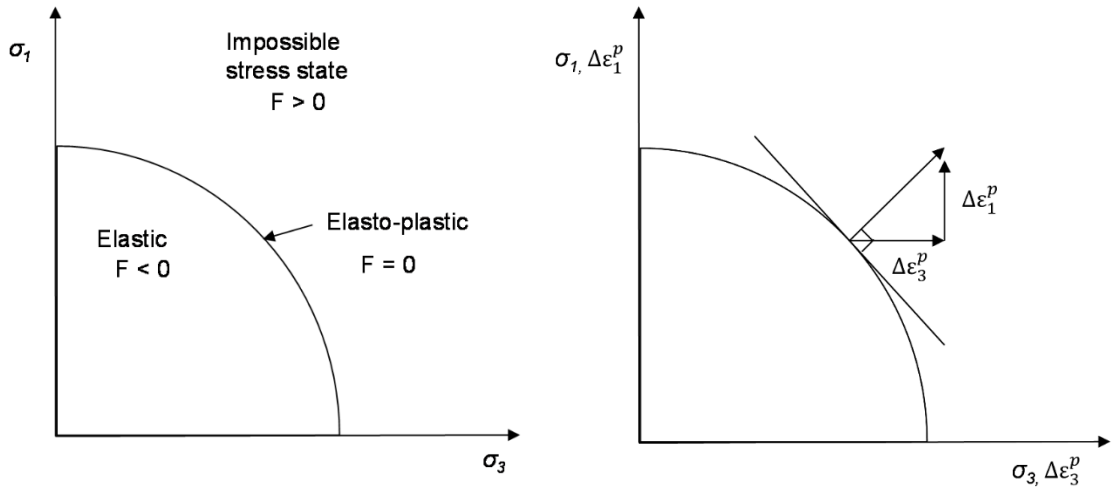

(a) (b)

Figure 2.1: Definition of (a) yield curve and (b) plastic potential function

In general, there are three main types of constitutive models involving plasticity: perfectly-plastic, hardening and softening behaviour. In a perfectly plastic material, the yield stress, σ'_y remains constant and strain occurs at constant stress. The assumption of perfectly-plastic behaviour is not realistic as real soil behaviour usually involves hardening and softening (see Figure 2.2). In a hardening material, the yield stress increases during plastic straining while in a softening material, the yield stress decreases during plastic straining. Regardless of the type of plastic behaviour, all elasto-plastic models assume elastic behaviour prior to yield.

Overall, as all constitutive models have limitations, designers should have a solid understanding of what aspects of the behaviour of the soil can be better predicted by the

models they are using. Depending on the construction problem and/or the type of soil, different constitutive models might be used to improve the quality of the predictions.

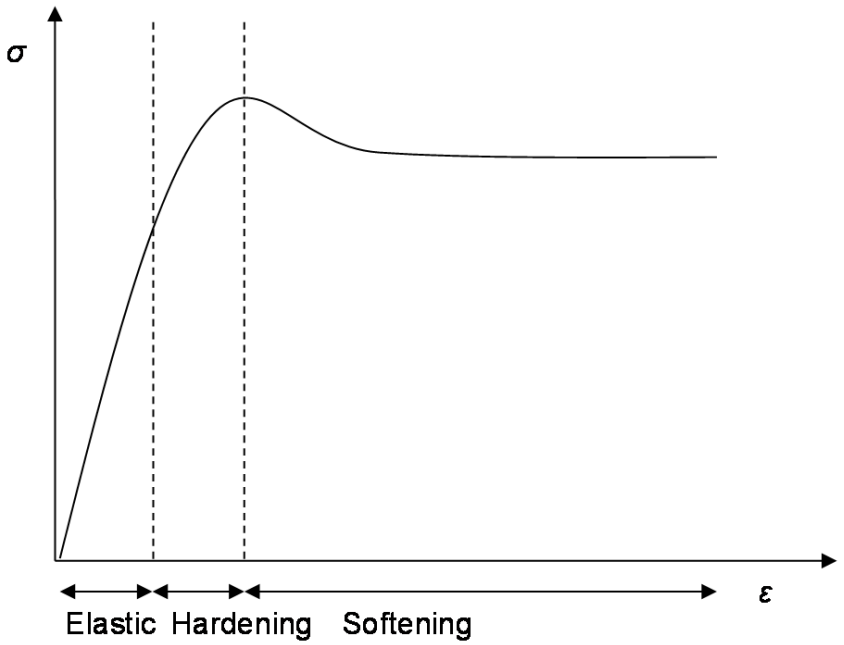

Figure 2.2: Real soil behaviour including hardening and softening

2.3.2 The Mohr-Coulomb model

The simplest and most widely used constitutive model in soil mechanics is the Mohr-Coulomb model, which, at its simplest form, is a linear elastic, perfectly plastic material model. The yield surface of such a perfectly plastic model is fixed which means that it does not vary with plastic strains (i.e. no hardening or softening). In Figure 2.3, it can be seen that for stresses lower than the yield stress, the behaviour is purely elastic and the elastic strains, ε^e, are reversible. When the yield stress is reached, the behaviour becomes perfectly plastic and the plastic strains, ε^p, increase indefinitely under the constant yield stress, σ'_y.

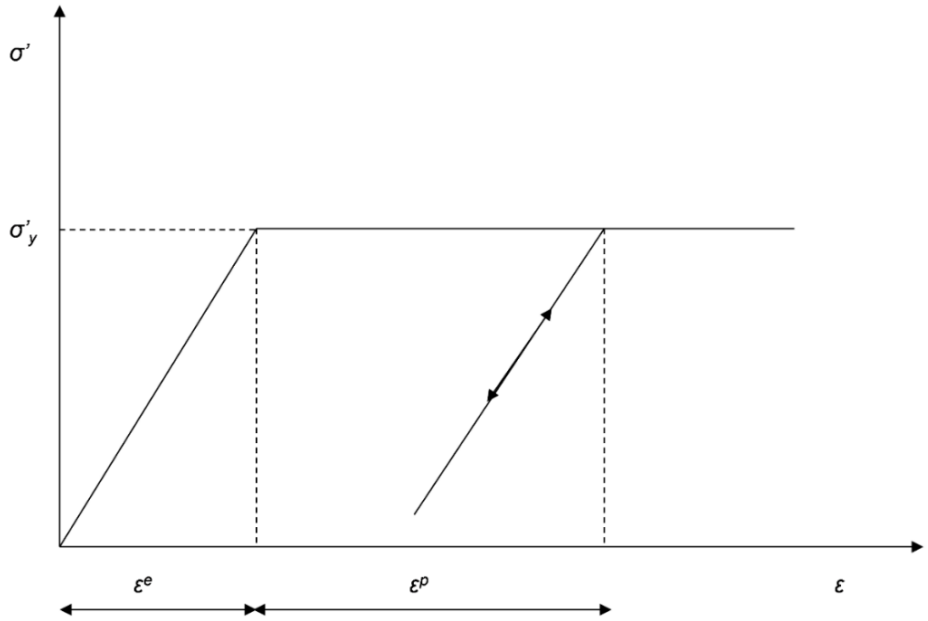

Figure 2.3*:* Linear elastic-perfectly plastic behaviour

For effective stress analysis, the effective friction of the soil is modelled by the angle of shearing resistance, *φ'* and the effective cohesion, *c'* (see Figure 2.4). For total stress analysis, the Mohr-Coulomb failure envelope reduces to the widely used Tresca failure envelope, shown in Figure 2.5 where the cohesion, *c*, is equal to the undrained shear strength, c_u and the angle of shearing resistance, *φ*' is equal to zero.

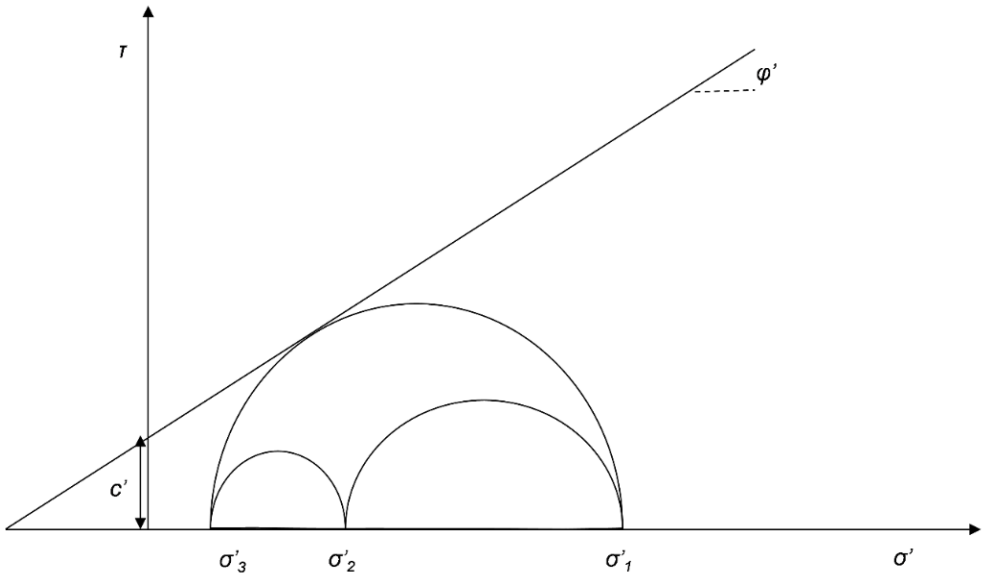

Figure 2.4: Mohr's circles and failure line using effective stress parameters (Mohr-Coulomb criterion)

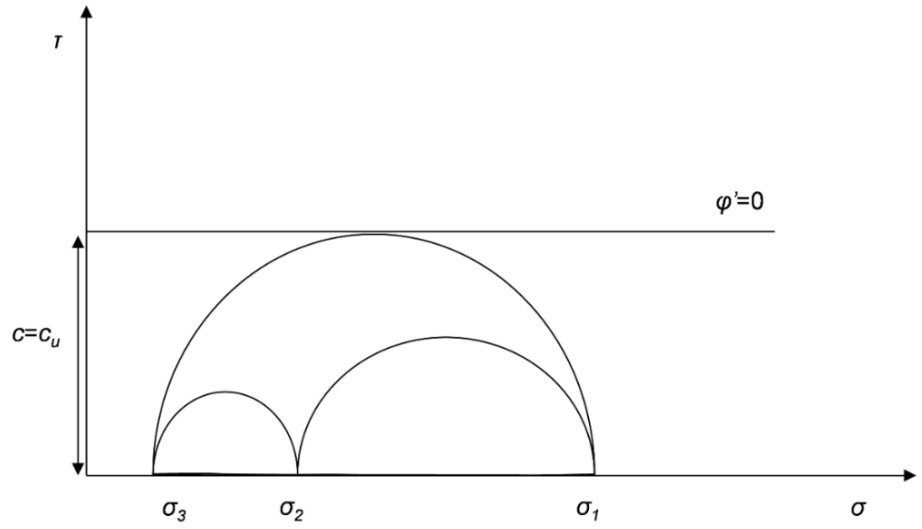

Figure 2.5: Mohr's circles and failure line using total stress parameters (Tresca criterion)

The yield surfaces of the Mohr-Coulomb and the Tresca models are represented by a fixed hexagonal cone and a regular hexagonal cylinder in the principal stress space, as shown in Figures 2.6 and 2.7 respectively. The *space diagonal* is defined as the line where the principal stresses are equal (i.e. $\sigma_1 = \sigma_2 = \sigma_3$).

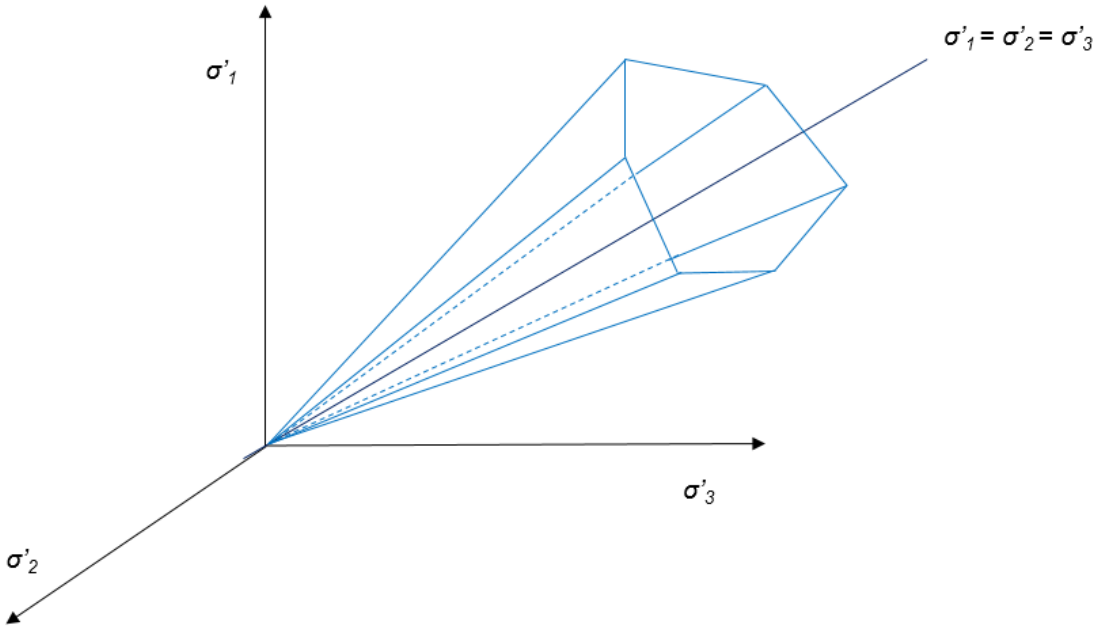

Figure 2.6: The yield surface of the Mohr-Coulomb model in the principal stress space for cohesionless material

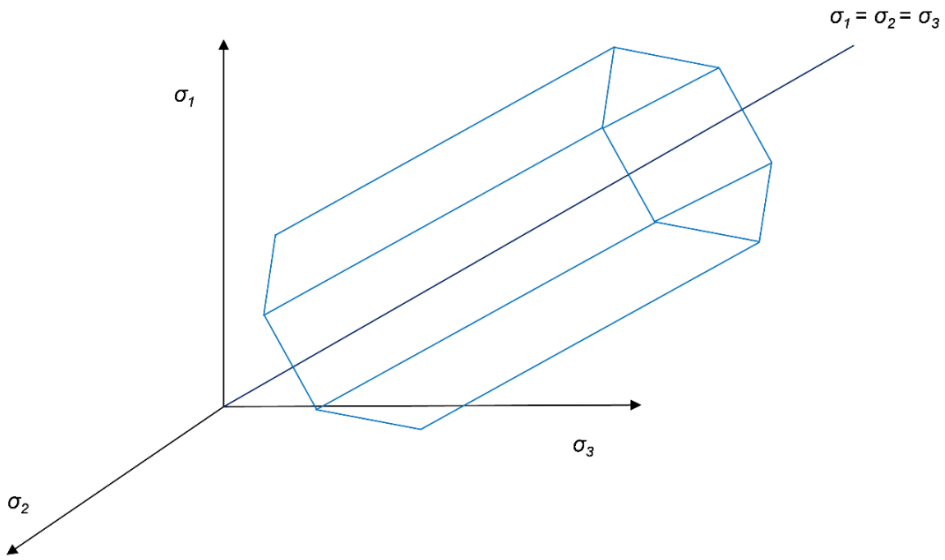

Figure 2.7: The yield surface of the Tresca model in the principal stress space for cohesionless material

Mohr-Coulomb parameters

A total of 5 basic input parameters are required for the Mohr-Coulomb model which are listed below along with their standard units.

- Young's modulus, E (kN/m^2)
- Poisson's ratio, v (-)
- Angle of internal friction, φ' (°)
- Cohesion, c' (kN/m^2)
- Angle of dilatancy, ψ (°)

The Young's modulus, E and the Poisson's ratio, v are the elastic parameters while the angle of internal friction, φ' and the cohesion, c' are the plastic parameters included in the yield function of the model which define the soil strength. The angle of dilatancy, ψ, is another plasticity parameter which appears in the plastic potential function to model increments of plastic volumetric strain. Additional parameters of the model include the increase of the soil stiffness with the depth, E_{inc}, and the increase of cohesion with depth, c_{inc}, which are defined in Equations 2.3 and 2.4 respectively, where E_{ref} and c_{ref} are the values of Young's modulus and cohesion at a reference depth y_{ref}.

$$E(y) = E_{ref} + (y_{ref} - y)E_{inc} \quad (2.3)$$

$$c(y) = c_{ref} + (y_{ref} - y)c_{inc} \quad (2.4)$$

2.3.3 The Hardening Soil model

The Hardening Soil model, which was first introduced by Schanz (1998) and Schanz et al. (1999), is a double hardening model with the yield surface expanding due to plastic straining. The model makes a distinction between two different hardening types; shear stress hardening which models irreversible plastic strains due to primary deviatoric loading, and compression hardening which models irreversible plastic strains due to primary compression in oedometer loading (Schanz et al, 1999).

The model is based on a deviatoric stress, q and axial strain, ε_1 relation that can be approximated with a hyperbolic function for triaxial compression stress paths as shown in Figure 2.8 (Duncan and Chang, 1970). The soil stiffness in primary loading is better defined by the secant modulus, E_{50} than by the initial tangent modulus, E_i, which value can be more difficult to derive from standard laboratory tests. A linear unloading/reloading soil behaviour is assumed within the yield function where the unloading/reloading stiffness, E_{ur} relates elastic stress to elastic strain (Benz, 2007). Following the deviatoric hardening, the deviatoric stress, q, finally becomes equal to the ultimate deviatoric stress, q_f, the failure criterion is satisfied and perfectly plastic yielding occurs. It can be seen in Figure 2.8 that the asymptote deviatoric stress, q_a is higher than the ultimate deviatoric stress, q_f. The failure ratio, defined as $R_f = q_f/q_a$, is equal to 0.9 by default in the model.

The yield surface of the model in the principal stress space is shown for a cohesionless material in Figure 2.9. This consists of the Mohr-Coulomb hexagonal cone, shown previously in Figure 2.6, and a cap yield surface.

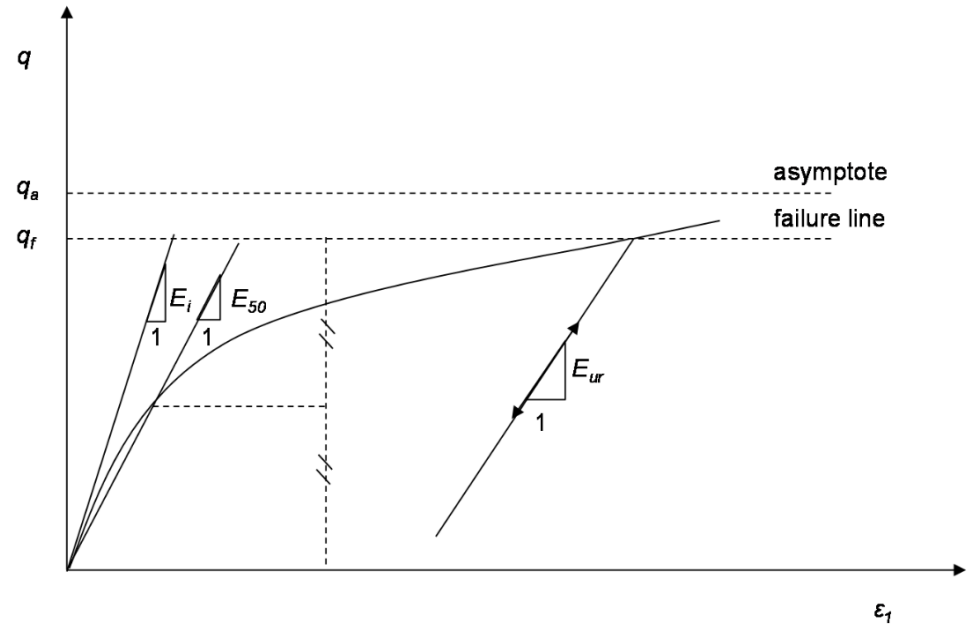

Figure 2.8: Hyperbolic relationship of deviatoric stress and axial strain in primary loading for triaxial test (after Duncan and Chang, 1970)

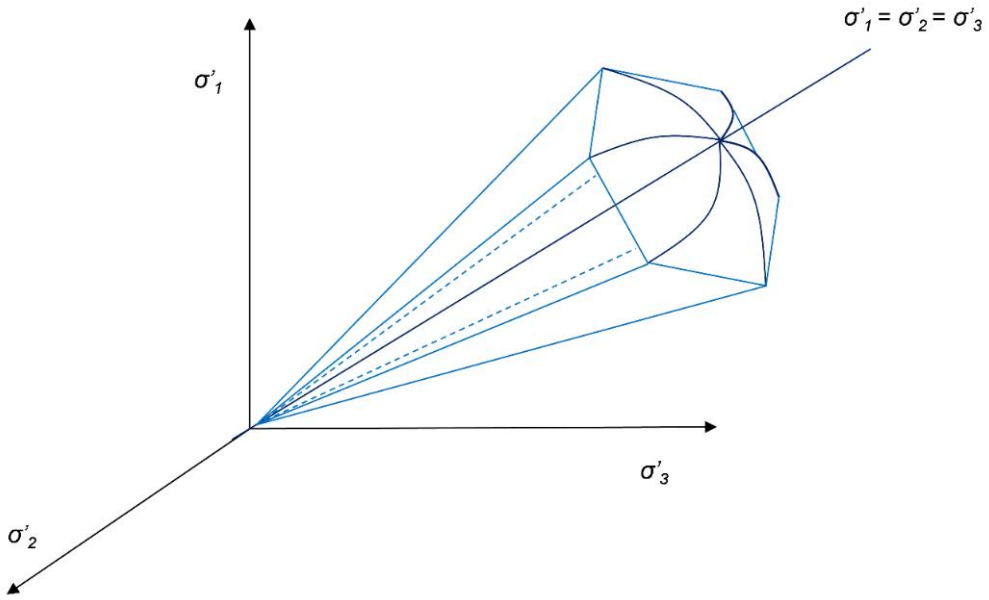

Figure 2.9: The yield surface of the HS model in the principal stress space for cohesionless material (after Schanz et al., 1999)

Hardening Soil model parameters

- Angle of internal friction, φ' (°)
- Cohesion, c (kN/m^2)
- Angle of dilatancy, ψ (°)
- Secant stiffness in standard drained triaxial test, E^{ref}_{50} (kN/m^2)

- Tangent stiffness for primary oedometer loading, E^{ref}_{oed} (kN/m^2)
- Unloading/reloading stiffness, E^{ref}_{ur} (kN/m^2)
- Power for stress-level dependency of stiffness, m (-)

Additional Parameters

- Poisson's ratio for unloading-reloading, v_{ur} (-)
- Reference stress for stiffness, p^{ref} (kN/m^2)
- K_0 for normal consolidation, K_0^{nc} (-)
- Failure ratio, q_a/q_r (-)
- Tensile strength, σ_{tens} (kN/m^2)
- Increase of cohesion, c_{inc} (kN/m^3)

The secant modulus for primary loading, E^{ref}_{50}, is derived from the triaxial stress-strain curve for a mobilisation of 50% of the deviatoric stress at failure, q_f. The modulus for unloading and reloading, E^{ref}_{ur}, corresponds to the triaxial unload/reload path which is modelled as purely linear elastic. The derivation of the tangent modulus for primary oedometer loading, E^{ref}_{oed}, is illustrated in Figure 2.10. Overall, E^{ref}_{50} controls the shear plastic strains and E^{ref}_{oed} controls the volumetric plastic strains (Schanz et al., 1999). Note that the soil stiffness parameters correspond to the reference mean stress, p^{ref}. The stress dependency of the soil stiffness parameters is defined in Equations 2.5 to 2.7 where the minor principal stress, σ'_3, which is the effective confining stress in a triaxial test, defines the actual stress state of the material and the parameter m is the power law exponent which controls the stress-dependency. Overall, the introduction of three different input stiffness parameters, enables the HS model to better predict soil deformations when compared to the Mohr-Coulomb model. This is because different soil stiffness values are relevant to different loading conditions. For example, in excavation problems, due to the removal of soil, there is vertical unloading at the bottom of the excavation and hence the unloading Young's modulus E_{ur} becomes relevant.

$$E_{50} = E_{50}^{ref}\left(\frac{c\,cos\varphi - \sigma'_3 sin\varphi}{c\,cos\varphi + p^{ref} sin\varphi}\right)^m \tag{2.5}$$

$$E_{ur} = E_{ur}^{ref}\left(\frac{c\,cos\varphi - \sigma'_3 sin\varphi}{c\,cos\varphi + p^{ref} sin\varphi}\right)^m \tag{2.6}$$

$$E_{oed} = E_{oed}^{ref}\left(\frac{c\ cos\varphi - \frac{\sigma'_3}{K_0^{nc}} sin\varphi}{c\ cos\varphi + p^{ref} sin\varphi}\right)^m \tag{2.7}$$

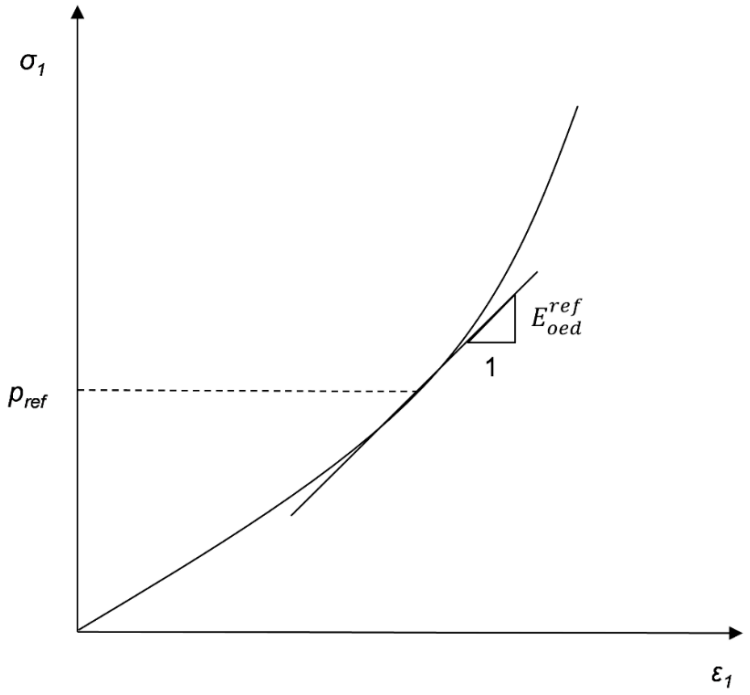

Figure 2.10: Definition of E^{ref}_{oed} in oedometer test results

Figure 2.11 shows examples of the yield surface of the HS model for varying levels of hardening. It can be seen that the yield surface is not fixed but gradually expands until it reaches the ultimate yield surface defined by the Mohr-Coulomb failure criterion.

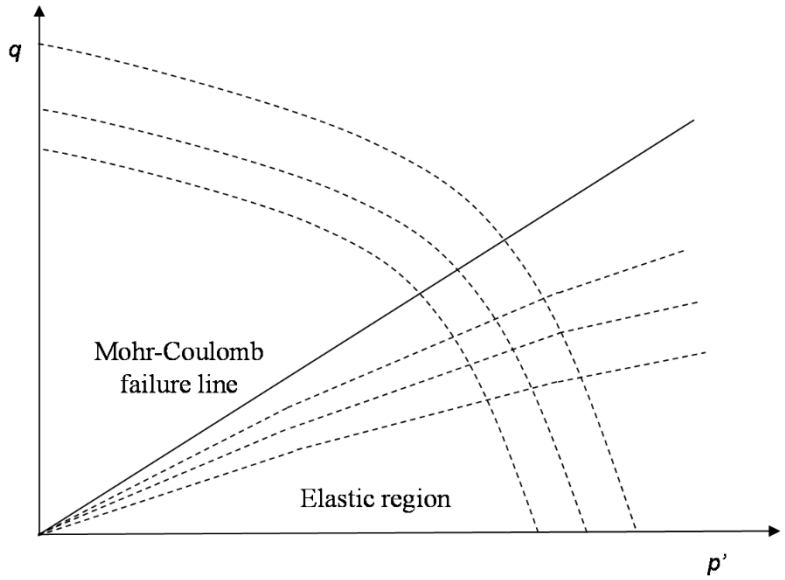

Figure 2.11: Examples of the HS yield surface for varying levels of hardening (after Schanz, 1998)

Shear hardening flow rule

The relationship between the plastic volumetric strain, e_v^p and the plastic shear strain, γ^p is shown in Equation 2.8 below where ψ_m is the mobilised dilatancy angle.

$$e_v^p = sin\psi_m \, \gamma^p \tag{2.8}$$

The mobilised dilatancy angle is calculated from relations based on the well-known stress dilatancy theory by Rowe (1962). For small mobilised friction angles and negative ψ_m as calculated by Rowe's formula, ψ_m in the HS model is taken as zero (Plaxis, 2015).

2.3.4 The Hardening Soil Small model

Attention was first brought to the soil small strain stiffness after comparisons between measured stiffness in the laboratory and those obtained by back-calculation from field observations of soil deformations (St John, 1975). It was observed that the soil stiffness derived from field observations was significantly higher than those measured in the laboratory, probably due to the inability of standard tests to accurately measure the stiffness of the soil in the small strain region.

The importance of the soil stiffness in small strains was highlighted by Simpson et al. (1979), Simpson (1992), Burland (1989) and others. Simpson et al. (1979) observed that in many types of construction problems, such as deep excavations, retaining walls, piled foundations and rigid footings, the shear strains are typically less than 0.1%. Jardine et al. (1986) also illustrated the significance of strains lower than 0.1% around

rigid footings and piled foundations. Jardine et al. (1984 and 1986) successfully modelled the small-strain soil stiffness behaviour based on experimental data: in triaxial testing, soil stiffness is higher in the small strain region and reduces significantly with increasing strains. In Figure 2.12, a typical soil stiffness degradation curve is shown where the stiffness varies depending on the strain level (Atkinson and Sallfors, 1991).

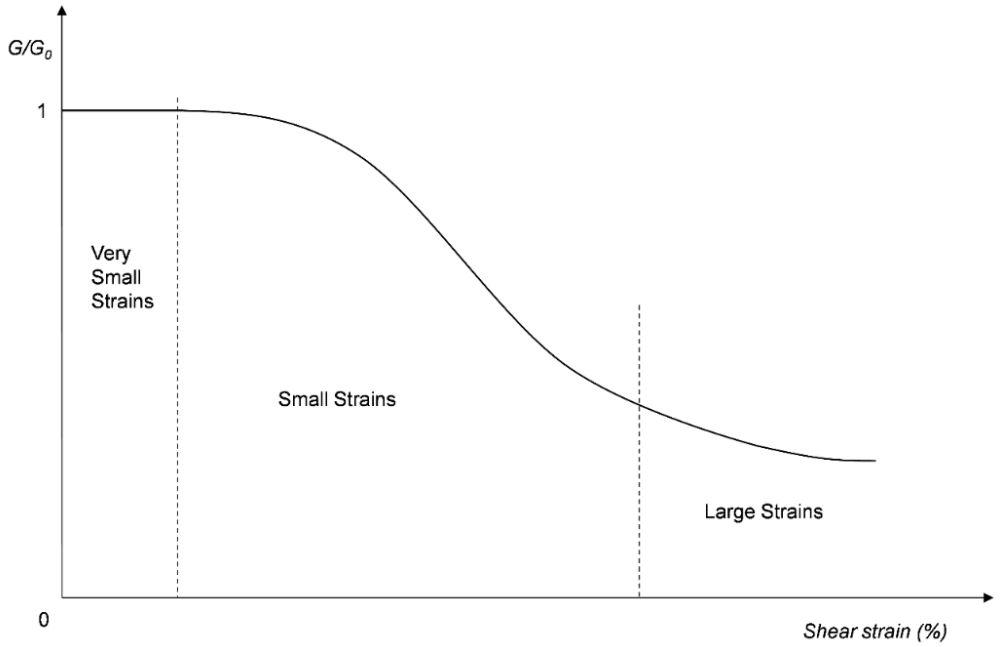

Figure 2.12: Typical soil stiffness degradation curve (after Atkinson and Sallfors, 1991)

The Hardening Soil Small (HSS) model (Benz, 2007) which represents an advance over the Hardening Soil model, introduces the variation of the soil stiffness with shear strain (S-shaped curve) and a hysteretic, nonlinear elastic stress-strain relationship in the small strain range. These features enable the HSS model to more accurately predict soil displacements which is particularly important for dynamic applications or for typical unloading problems such as excavations supported by retaining walls.

Hardening Soil Small additional parameters

The Hardening Soil Small model introduces two additional parameters to define the soil stiffness behaviour in small strains:

- Reference shear modulus at very small strains ($\varepsilon < 10^{-6}$), G_0^{ref}

- Shear strain, $\gamma_{0.7}$

The initial shear modulus, G_0^{ref} is defined for the reference mean stress, p^{ref}, and the stress dependency of the shear modulus, G_0, is shown in Equation 2.9. The shear strain $\gamma_{0.7}$ is independent of the mean stress and is the strain at which the secant shear modulus is reduced to 72.2% of its initial value, G_0 (Benz, 2007). The hyperbolic and hysteretic, nonlinear elastic stress-strain relationship of the model is presented in Figure 2.13.

$$G_0 = G_0^{ref}\left(\frac{c\ cos\varphi - \sigma'_1 sin\varphi}{c\ cos\varphi + p^{ref} sin\varphi}\right)^m \tag{2.9}$$

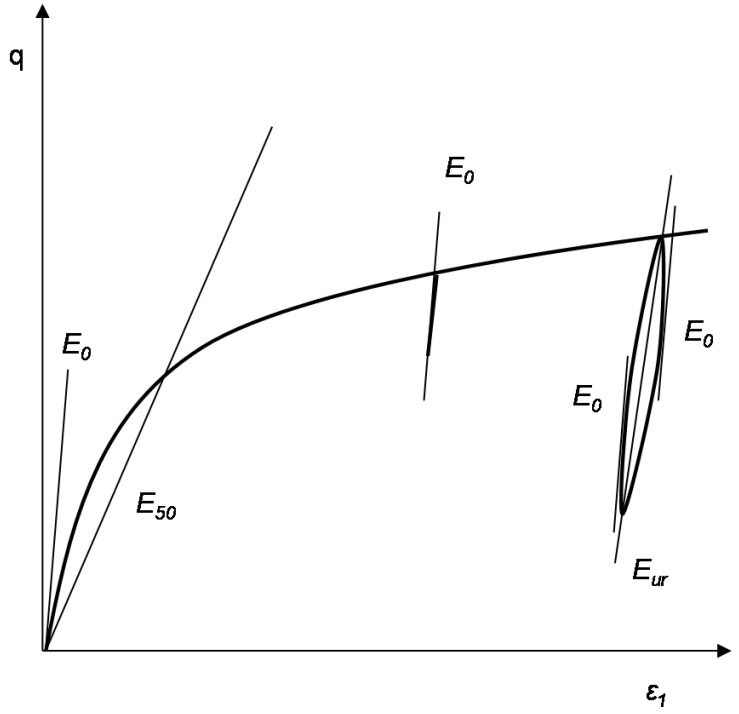

Figure 2.13: The hyperbolic and hysteretic, nonlinear elastic stress-strain relationship of the HSS in standard triaxial test (after Plaxis, 2015)

The degradation curve of the secant shear modulus, G_s, is defined for all materials by Equation 2.10 proposed by Santos and Correia (2001), which is a modification of the relationship originally proposed by Hardin and Drnevich (1972). The relationship shows that the decay of the small strain stiffness depends on the shear strain, γ. Based on the definition of the secant modulus G_s, the shear stress-strain relationship can be re-arranged as shown in Equation 2.11. The tangent shear modulus G_t, can then be derived from Equation 2.11 by taking the derivative with respect to the shear strain (Brinkgreve

et al., 2007). This results in the degradation curve relationship of the tangent modulus given by Equation 2.12.

As shown in Figure 2.14, the curve is bound by a certain lower limit which is introduced at the shear strain $\gamma_{cut\text{-}off}$ where the tangent shear stiffness is reduced to the unloading reloading stiffness, G_{ur} (Benz, 2007). The $\gamma_{cut\text{-}off}$ is defined by Equation 2.13 while the unloading/reloading shear modulus, G_{ur}, relates to E_{ur} and v_{ur} as shown in Equation 2.14.

Finally, another important feature of the HSS soil model is the multi-axial extension of the stiffness decay curve as proposed by Benz (2007). According to the extension, the soil stiffness recovers its initial maximum value every time the loading direction is reversed and then during the loading in the new direction, the stiffness decreases again.

$$\frac{G_s}{G_0} = \frac{1}{1+0.385\frac{\gamma}{\gamma_{0.7}}} \tag{2.10}$$

$$\tau = G_s\gamma = \frac{G_0\,\gamma}{1+0.385\frac{\gamma}{\gamma_{0.7}}} \tag{2.11}$$

$$\frac{G_t}{G_0} = \frac{1}{(1+0.385\frac{\gamma}{\gamma_{0.7}})^2} \tag{2.12}$$

$$\gamma_{cut-off} = \frac{1}{0.385}\left(\sqrt{\frac{G_0}{G_{ur}}} - 1\right)\gamma_{0.7} \tag{2.13}$$

$$E_{ur} = 2\,(1+\nu)\,G_{ur} \tag{2.14}$$

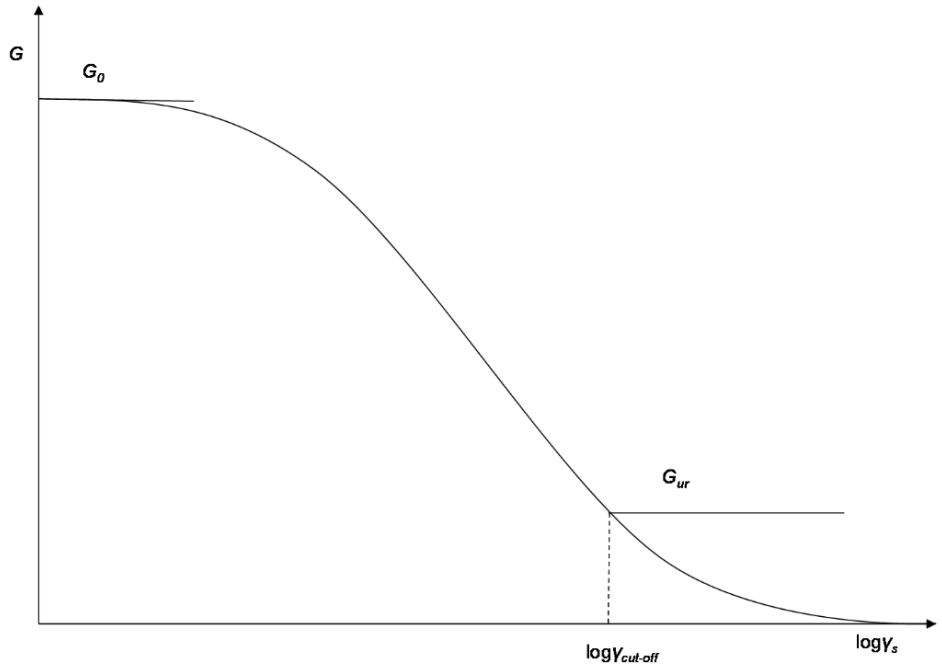

Figure 2.14: Cut-off in the tangent shear modulus degradation curve as used in the HSS model (after Benz, 2007)

Shear hardening flow rule

The shear hardening flow rule in the HSS model is the same as in the HS model, described by Equation 2.8. However, the HSS differs in the way the mobilised dilatancy, ψ_m is calculated. More specifically, the model adapts a simplified approach of the void ratio dependent relation proposed by Li and Dafalias (2000) whenever ψ_m, as computed by Rowe's formula, is negative. This is because it is shown that limiting the minimum value of ψ_m can sometimes result in the generation of too little plastic volumetric strains (Benz, 2007).

2.3.5 The BRICK model

While the yield surfaces of the majority of the most widely used elasto-plastic models for soil behaviour have been defined in the principal stress space, many authors proposed constitutive models formulated in the strain space. Some examples include the hypoplastic models (e.g. Kolymbas, 1991; Niemunis and Herle, 1997), the hyperplastic models (e.g. Houlsby, 1981; Collins and Kelly, 2002) and the BRICK series of models (e.g. Simpson, 1992; Clarke, 2009; and Ellison et al., 2012). The selection of the strain space instead of the stress space can result in significant theoretical and practical advantages.

From a theoretical point of view, the critical mechanisms governing the soil behaviour can be described better in strain space. For example, the accumulation of elastic and plastic strains reflects better the loading history of the soil (Ellison et al., 2012). Practical advantages include: natural compatibility with FEM, more consistent basis for modelling, no assumptions are required about the intersection of yield surfaces and certain aspects of behaviour such as creep and rate effects; as these can be more easily taken into account in the strain space (Ellison et al., 2010 and 2012).

The BRICK model has been continuously utilised and developed within Arup for many years, particularly in its application to model the heavily consolidated London Clay. Simpson (1992) introduced the 2D version of BRICK which was reviewed by Pillai (1996); while the 3D version was later proposed by Lehane and Simpson (2000). Recently, a novel framework has been developed to introduce stiffness anisotropy in this strain space model by modifying the coordinate system in which the model is based (Ellison et al., 2012). Many authors have highlighted the advantages of using the BRICK model (e.g. Fuentes et al., 2010; Yeow et al., 2006; Jovicic et al., 2006; and Powrie et al., 1999).

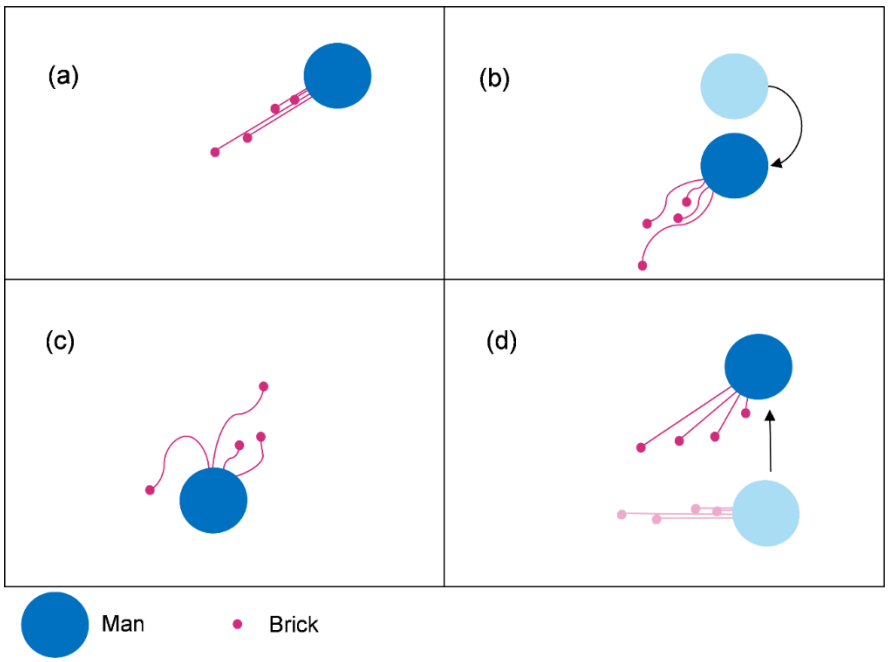

Figure 2.15: The analogue of the man pulling bricks attached to strings (after Simpson, 1992)

The philosophy of BRICK is to capture the material behaviour by employing the analogue of a man pulling bricks on strings in a strain space (see Figure 2.15). The location of the man relates to the current strain state and each brick corresponds to a fixed proportion of the soil behaviour. The movement of each brick directly relates to plastic strain development for the corresponding proportion of the soil. Therefore, the

material behaviour is purely elastic when all strings are loose and purely plastic when all strings are taut and the bricks are lined up behind the man in the direction of the strain increment (Simpson, 1992).

The BRICK model is based on the following main assumptions (Simpson, 1992):

- Stiffness depends on strains, not stresses. Therefore, the stiffness degradation curve is approximated with the use of strings lengths (strain) and proportions of material (change in stiffness).
- The stress increment is derived only from the elastic strain increments.

BRICK is able to model the different stiffness degradation curves during shearing after different stress paths. In other words, the soil model recognises stress path and is capable of modelling the non-linear degradation behaviour of soils (Pillai, 1996). The approximated BRICK soil stiffness degradation curve is shown in Figure 2.16.

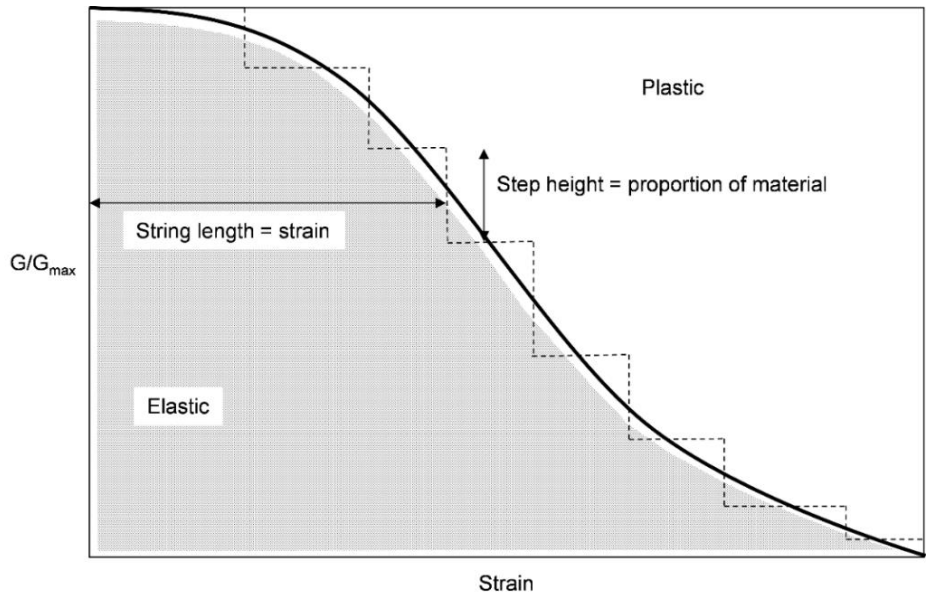

Figure 2.16: Approximation of the S-shaped stiffness-strain curve for the BRICK model

The parameters of the BRICK model are listed below:

- Slope of the isotropic NCL in ε_{vol} - ln$p$ space, λ
- Slope of the isotropic swelling line in ε_{vol} - ln$p$ space, κ
- Stiffness gain parameter due to consolidation, β^G
- Strength gain parameter due to consolidation, β^Φ

- Elastic stiffness parameter, *ı*
- Poisson's ratio on the NCL, *v*
- Parameter controlling string length modifications due to Lode angle, *μ*
- Array of material proportions for each brick, $\{R_b\}$
- Array of initial string lengths for each brick, $\{L_b^0\}$

The parameters R_b and L_b represent the material proportions and string lengths respectively, assigned to each brick, *b* where $\Sigma_{b=1}^{B} R_b$ = 1 and *B* is the total number of bricks. These arrays define discrete lines of string lengths against the tangent shear modulus reduction (G/G_0) that approximate the typical stiffness curve and control the soil stiffness degradation with the development of shear strains (see Figure 2.16). The area within the stiffness curve relates to the soil strength (i.e. it is equal to sinφ'). While any number of bricks can be used, the choice of *B* = 10 represents a reasonable compromise between achieving a sufficiently smooth curve and acceptable levels of computational effort and time (Ellison et al., 2012). Each pair of strings and bricks defines a yield surface for that particular proportion of material. The yield function is a Modified Drucker-Prager yield surface which is achieved by modifying the lengths of the strings as a function of the Lode angle in the strain space. The parameter that controls these string length modifications is *μ*.

The parameters *λ* and *κ,* which are used to specify the virgin compression line and the unloading/reloading lines, correspond to the parameters *λ** and *κ** defined by Houlsby and Wroth (1991). However, the BRICK introduces a new parameter, *ı* that provides a higher stiffness at small strains in the unloading/reloading region.

Moreover, the parameters β^G and β^Φ enable BRICK to model an increase in soil strength and stiffness due to its state of over-consolidation (Clarke, 2009 and Ellison, 2012). The state of over-consolidation is defined by the difference in volumetric strain between a state on the normal consolidation line (NCL) and the current state for a particular mean effective stress, *p'*. Based on the model parameters β^G and β^φ, the parameters χ^G and χ^φ are defined as shown in Equation 2.15 and 2.16 respectively, where the subscripts NC and 0 refer to a state on the NCL and the initial reference state for the NCL respectively (Ellison et al, 2012).

The elastic shear modulus, G_0 is then calculated from Equation 2.17 where K_0 is the elastic bulk modulus and v_{NC} the Poisson's ratio for a state on the NCL. The parameter χ^G has the effect of increasing the initial height of the shear modulus degradation curve (Simpson, 1992).

The increase in soil strength due to the state of over-consolidation is introduced by increasing the string lengths, as shown in Equation 2.18, and hence the area under the shear modulus degradation curve which relates to the soil strength and is controlled by the parameter χ^{φ} (Simpson, 1992; Ellison, 2012).

$$\chi^G = \frac{G_0}{G_{0,NC}} = 1 + \beta^G(\varepsilon_v - \varepsilon_{v,0} - \lambda \ln\left(\frac{p}{p_0}\right)) \tag{2.15}$$

$$\chi^{\varphi} = \frac{\int_0^{\infty} G(\gamma)\vartheta\gamma}{\int_0^{\infty} G_{NC}(\gamma)\vartheta\gamma} = 1 + \beta^{\varphi}(\varepsilon_v - \varepsilon_{v,0} - \lambda \ln\left(\frac{p}{p_0}\right)) \tag{2.16}$$

$$G_0 = \chi^G \, K_0 \frac{3\,(1-2\nu_{NC})}{2\,(1+\nu_{NC})} \tag{2.17}$$

$$L_b = L_b^0 \frac{\chi^{\varphi}}{\chi^G} \tag{2.18}$$

Finally, the in-situ stresses are modelled in BRICK by simulating the soil's geological history from a slurry state to the current state. For example, London Clay was deposited from slurry, then overlain by about 200m of soil which was subjected to erosion and then again overlain by the current deposits as confirmed by, for instance Chandler (2000) and Hight et al. (2007). More details about the calculation of K_0 using this approach is given by Simpson (1992) while a number of other studies provide evidence of the success of the method (SCOUT, 2007; Yeow and Feltham, 20008; Ellison et al., 2012).

2.4 The London Clay formation

2.4.1 Introduction

A typical soil profile in the west of London consists of Made Ground overlaying Terrace Gravels and the London Clay formation while deeper formations include the Lambeth Group, the Thanet sand and the Chalk (Bishop et al., 1965; Hight et al., 2003). Typical below-ground structures in the Greater London area are constructed within the London Clay formation. Hence, studies have been primarily focused on deriving the properties and understanding the complex behaviour of this soil.

The London Clay is classified as a heavily over-consolidated, fissured stiff clay of marine origin. It has high plasticity and generally experiences high horizontal stresses. While it seems that the formation of the material resulted as a sequence of complicated deposition and erosion stages, it is generally assumed that erosion and other physical and geological processes occurred after the end of the deposition period (Gasparre, 2005). Thus, a distinction can be made in the formation's geological history between three major stages referred to as the *geotechnical cycle* by Chandler (2000): deposition, erosion and re-deposition of Quaternary sediments.

2.4.2 Depositional environment

The London Clay formation which belongs to the Thames Group, was deposited in a marine environment in the Eocene epoch about 50 million years ago (Pantelidou and Simpson, 2007). As shown in Figure 2.17, there are two main areas in the south of England where the London Clay formation can be encountered: the Hampshire Basin and the London Basin. King (1981) observed a correlation between the non-uniformities within the London Clay formations and the variation of the sea level. These sea level variations had a profound effect in the deposition conditions. In the Hampshire Basin, the London Clay was deposited in relatively shallow, high energy marine conditions while in the London Basin, it was deposited in a much deeper and low energy marine environment. The stratigraphy of the deposited soil reflects these variations in the depositional conditions as coarser materials were deposited when the sea levels were falling. However, these depositional sequences are more apparent in the Hampshire Basin than in the London Basin. The material is currently about 50-150m thick in the London Basin and 50-130m thick in the Hampshire Basin. A decrease of thickness westwards can be observed in both basins (King, 1991; British Geological Survey, 2004).

2.4.3 Post-Depositional processes

Following the deposition stage, erosion of a significant amount of the material occurred in the Tertiary and Pleistocene epochs. Assessment of the thickness of the eroded material is important for the estimation of the over-consolidation ratio (OCR) and the in-situ horizontal stresses. Geological evidence based on oedometer test results suggests that about 152-213m of the upper part of the London Clay formation were subjected to erosion before the deposition of Terrace Gravels in Central London (Skempton and Henkel, 1957). Skempton (1961) suggested the thickness of Tertiary strata removed by erosion is 150m in Bradwell, Essex, about 80km north-east of London, while Burland et al. (1979) suggested a thickness of 170m in Central London. Henkel (1957) reported a range of 150 to 210m thick strata being eroded in North London while Bishop et al. (1965) estimated a thickness as high as 350m in Ashford Common, about 20km west of London, a value which is not supported by the geological evidence (Pantelidou and Simpson, 2007).

In the Thames Valley, the erosion was followed by the deposition of levels of late Quaternary gravels (King, 1981). The re-deposition stage had an impact not only on the stress history of the material but also on the prevention of weathering. In the Thames Valley, where the formation is covered by Terrace Gravels, the weathering effects are only apparent to a very small zone directly below the gravel base (Hight et al., 2003; Tan et al., 2003). On the contrary, wherever the material had been exposed, the upper 5 to 10m of the formation seems to be weathered (e.g. Skempton and Henkel, 1957; Skempton and LaRochelle, 1965; Skempton, 1961). Weathering is indicated by the change in the colour of the clay. The weathered clay is usually referred to as brown London Clay, due to oxidation, while the un-weathered material is often called blue (or grey) London Clay (Chandler and Apted, 1988).

Overall, based on these studies reported by various authors, the total thickness of the eroded strata is assumed in this thesis to be 200m, with negligible re-deposition of late Quaternary strata. However, the effect of the overburden on the geotechnical parameters will be examined and discussed further.

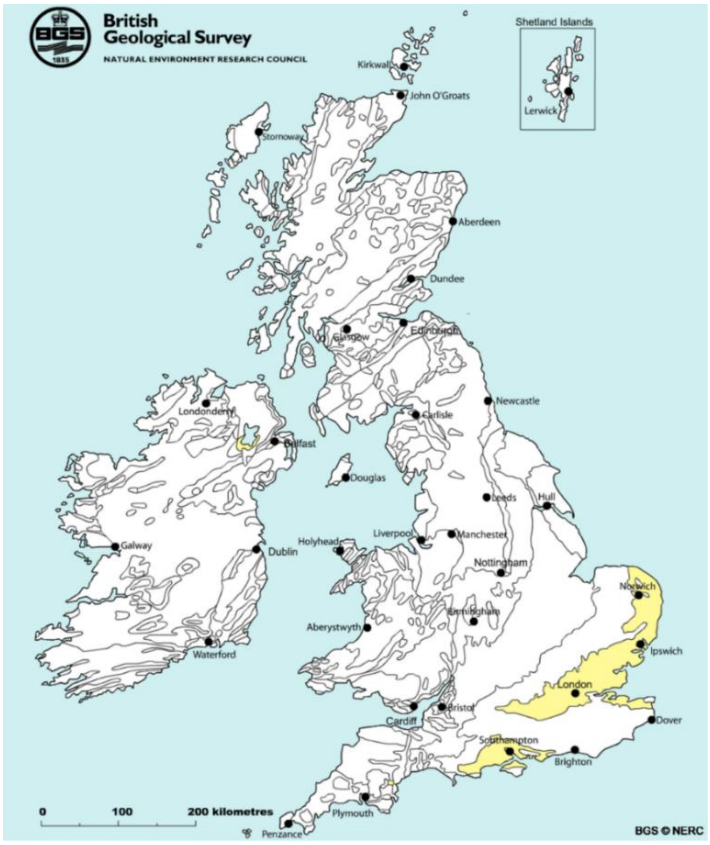

Figure 2.17: The London and Hampshire Basins (Reproduced from the online geological map of the British Geological Survey, ***http://www.bgs.ac.uk/***)

2.4.4 Hydrogeology

Another important characteristic of the geological history is the existence of two aquifers in the London Basin. There is a perched water table situated in the River Terrace Deposits and a deep aquifer in the Chalk layer underneath the London Clay/Lambeth group. The upper aquifer is mostly recharged from the Thames and precipitation and is affected by ground surface activities and shallow drainage (Water Resources Board, 1972; Gray and Foster, 1972; Price and Reed, 1989). In the mid-19th century, when the advances of technology enabled the construction of deep wells, boreholes in the lower aquifer contributed significantly to water supply in central London. Excessive pumping until the middle of the 20th century resulted in a substantial drop of the piezometric level of the Chalk aquifer and the formation of the under-drained pore water pressure profile within the London Clay formation (Water Resources Board, 1972; Royse et al., 2012). Hight and Jardine (1993) also highlighted the effect of draining tunnels on the reduced piezometric profiles in London Clay. The lower aquifer piezometric level reached its minimum between 1950 and 1970, by which time most wells in central London became obsolete (Royse et al., 2012), and it has started rising ever since (Simpson et al., 1989).

2.4.5 Geotechnical parameters

Detailed studies on the material properties (e.g. shear strength, stiffness, initial stresses were undertaken as early as in the 1960s by Ward et al. (1959, 1965), Bishop et al. (1965), Skempton et al. (1969) and Webb (1964). This research was mainly focused on a number of areas in the west of London such as Ashford Common, Wraysbury District and Prospect Park. Hight and Jardine (1993) analysed samples from a number of central London sites and Standing and Burland (2005) highlighted the impact of the geological properties of London Clay on engineering problems. Hight et al. (2003; 2007) provided new insights on the characteristics of the clay by analysing tests carried out for the Heathrow T5 project. Nishimura (2005) provides a detailed chronicle of the numerous studies on London Clay since the 1950s. The main characteristics of the London Clay in the London area, based on these and other studies, will be briefly discussed below.

2.4.5.1 Coefficient of earth pressure at rest

For normally consolidated (NC) soils, Jaky (1944) proposed his well-known relation between the angle of shearing resistance, φ', and the coefficient of earth pressure at rest, K_0. However, because this relation cannot be applied for over-consolidated (OC) soils, a correlation was later introduced by Mayne and Kulhawy (1982) taking into account the over-consolidation ratio (OCR). Other correlations for over-consolidated clays have been proposed by Brooker and Ireland (1965), Simpson et al. (1979) and Shohet (1995). These empirical correlations though cannot capture entirely the behaviour of materials with complex geological history of loading and unloading and a non-linear under-drained pore water pressure profile such as the London Clay, for which, K_0 is one of the most difficult parameters to measure (Hight et al., 2003).

Due to its high over-consolidation, the London clay generally experiences high horizontal stresses and the values of the earth coefficient at rest, K_0, are typically higher than unity. According to Skempton and La Rochelle (1965) and Skempton (1961), K_0 ranges from 2 to 2.5 in the upper 10 m of the material, and then decreases to 1.5 at a depth of about 30 m. Similar K_0 values were reported from various London sites by Shohet (1995). Moreover, published data from the Heathrow Terminal 5, Ashford Common, Paddington and Waterloo sites (Webb, 1964; Bishop et al., 1965; Hight et al., 2003; Hight et al., 2007), shown here in Figure 2.18, are generally in good agreement with the values reported by Skempton.

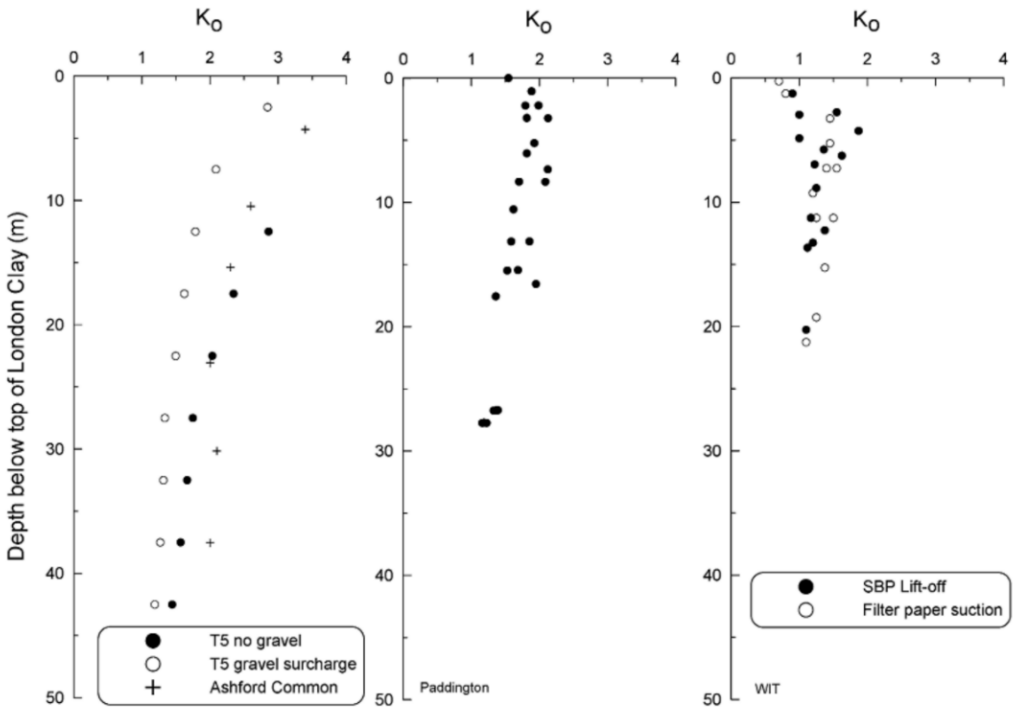

Figure 2.18: K_0 profiles for London Clay at Ashford Common, Heathrow Terminal 5, Paddington and Waterloo (after Hight et al, 2007; Hight et al. 2003)

2.4.5.2 Undrained shear strength

Over-consolidated soils tend to exhibit strain hardening until they reach their peak shear strength. After the peak, they experience strain softening typically with the appearance of shear bands. Thus, shear strength can be defined at different strain levels (e.g. critical state, post-rupture strength, residual strength (Skempton, 1964)). In this thesis, shear strength mainly refers to the peak strength which is inherently more variable than the rest and hence a material partial factor needs to be applied to account for this uncertainty. However, applying a partial factor to a cautious estimate of the critical state soil strength may be too conservative (Bond and Harris, 2008).

Hewitt (1989) carried out research for the Ove Arup and Partners development fund performing a series of back analyses of the total settlements of rafts and piled foundations using 20 case histories in London Clay which he went on to write up as part of his MEng dissertation. The same author also published data from unconsolidated undrained triaxial tests on both small (38mm) and large (100mm) samples tested at confining pressures equal to the corresponding in-situ effective stresses. The distributions of undrained shear strength for each of the 20 case histories considered in his study are shown in Figure 2.19.

Patel (1992) compiled triaxial test data on 100mm samples of London Clay from Ove Arup and Partners' records spanning over two decades. These data were obtained from 23 different sites in the greater London area. The undrained shear strength profiles were then plotted, as presented in Figure 2.20, showing the variability of the undrained shear strength from site to site.

More recently, extensive research has been carried out on the behaviour of London Clay, prompted by the construction of the new Heathrow Terminal 5 (e.g. Gasparre et al., 2007a, 2007b; Nishimura et al., 2007; Hight et al., 2007). The profiles of the undrained shear strength obtained with triaxial compression (Gasparre, 2005) are shown in Figure 2.21 with the level of London Clay being about 6m below ground level. Typically, specimens of 100mm diameter were used for the triaxial tests.

Moreover, in Figure 2.22, unpublished undrained shear strength data are plotted from unconsolidated undrained triaxial tests as well as from correlations with in situ SPT. The data was obtained from a site in South-West London, where a large-scale residential development is currently under construction. It can be seen that the triaxial test data correspond well to the SPT results although the scatter becomes more significant for both the triaxial and SPT values below 20mOD.

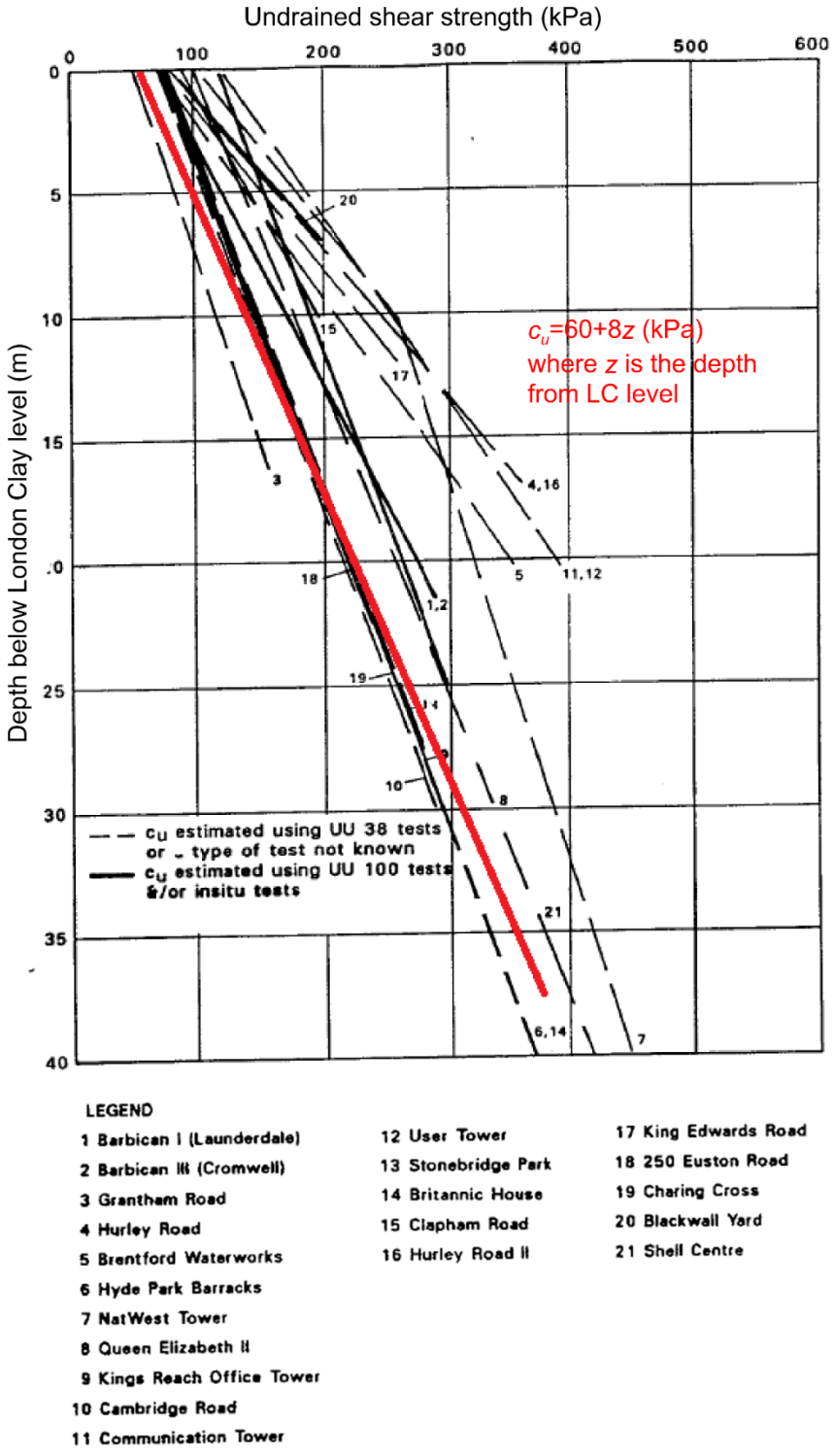

Figure 2.19: Characteristic undrained shear strength profile for London Clay based on the results from Hewitt (1989)

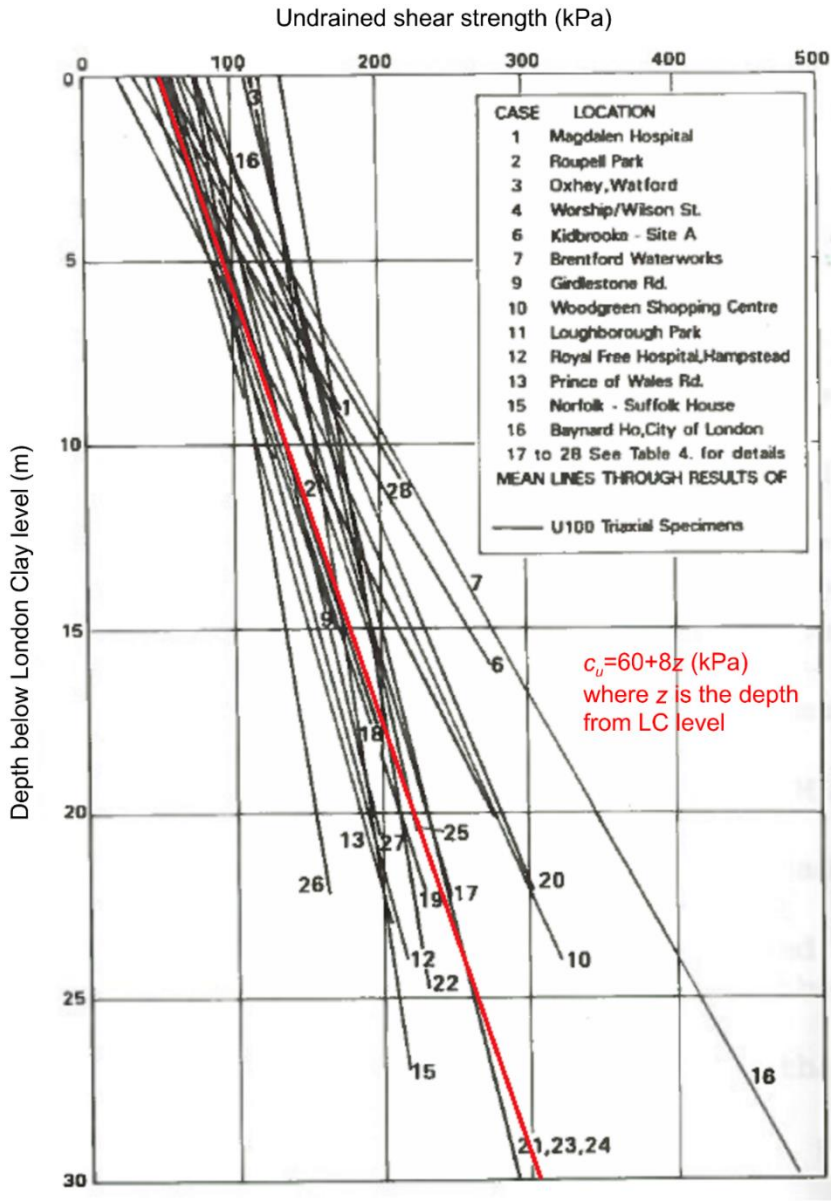

Figure 2.20: Characteristic undrained shear strength profile for London Clay based on the results from Patel (1992)

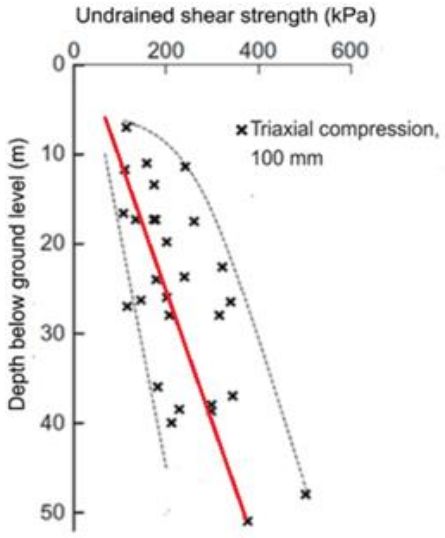

Figure 2.21: Undrained shear strength results from triaxial compression tests for London Clay (after Gasparre, 2005)

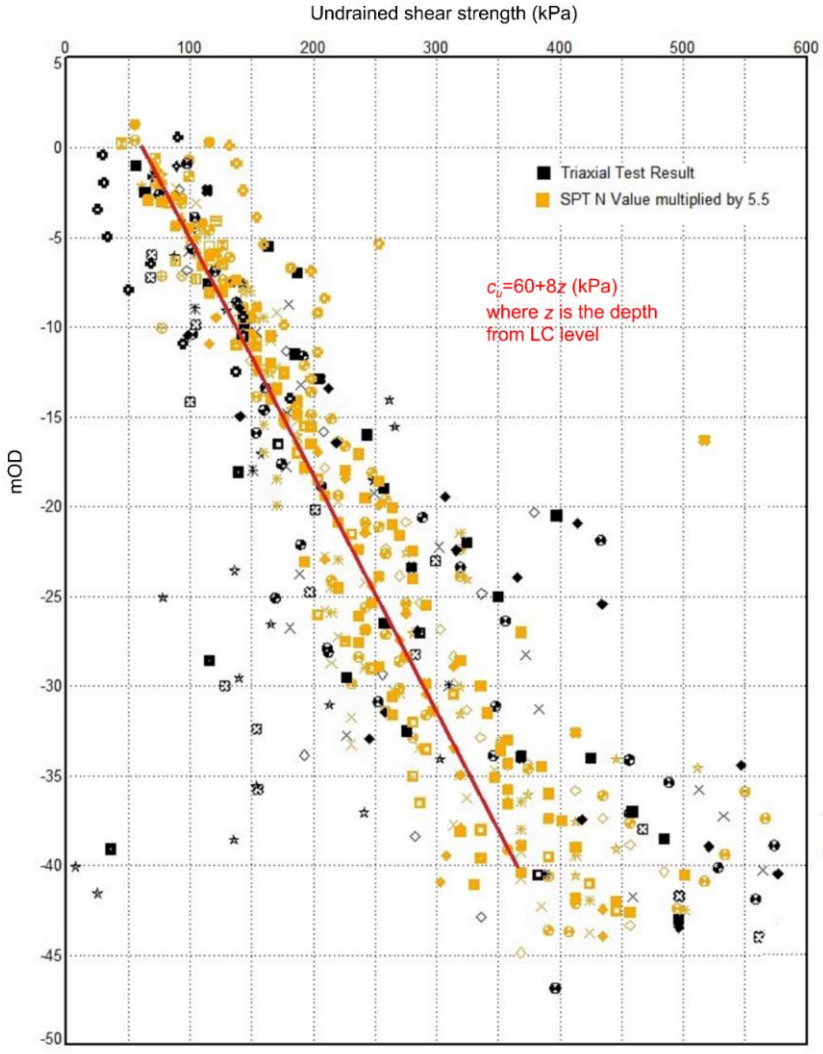

Figure 2.22: Characteristic undrained shear strength profile for London Clay based on the results from a central London project

Based on all these studies, the characteristic undrained shear strength distribution of London Clay has been assessed as a cautious estimate of the published data. The profile adopted in this thesis is described by Equation 2.19 and shown as a red solid line in Figures 2.19 to 2.22.

$$c_u = 60 + 8z \ (kPa) \tag{2.19}$$

where *z*(m) is the depth below London Clay level

2.4.5.3 Soil stiffness

In the past, engineers were often required to make estimates of the undrained and drained stiffness of London Clay without the benefit of reliable field or laboratory measurements. Because obtaining undisturbed samples can be really challenging for such highly stiff and fissured material, the usual practice was to estimate the drained and undrained Young's moduli from back analyses based on previously measured settlements and correlations with undrained shear strength, rather than to rely on low quality test results (Simpson et al., 1981).

As monitoring of building movements is generally undertaken on the foundations, Hewitt (1989) back analysed the total settlements for rafts and piled foundations using 20 case histories in London Clay. Comparisons between the calculated and maximum observed values of total settlement, enabled the author to derive the drained Young's modulus, *E'* values which fitted the data for structures founded on London Clay. Ken Ho (Arup, 1991), following the same methodology but considering only the end of construction settlements from 26 sites in London, derived correlations between the undrained Young's modulus, E_u, and the undrained shear strength, c_u and suggested an average E_u/c_u ratio of 400. This work expanded upon previous back analyses carried out by Arup Geotechnics and reported by Hooper (1974) and Butler (1975) where E_u/c_u ratio values of 310 to 480 were proposed while even older studies reported average ratio values as low as 140 (Cooling and Skempton, 1942; Skempton and Henkel, 1957). Moreover, back calculated values of the undrained Young's modulus for London Clay, based on a number of cases studies as summarised by Burland and Kalra (1986) and re-plotted by Hewitt (1989), are presented in Figure 2.23. Overall, these correlations were extensively applied over the following years for a wide range of problems, beyond the scope of the simple (one-dimensional) vertical loading problems for which the parameters were typically derived.

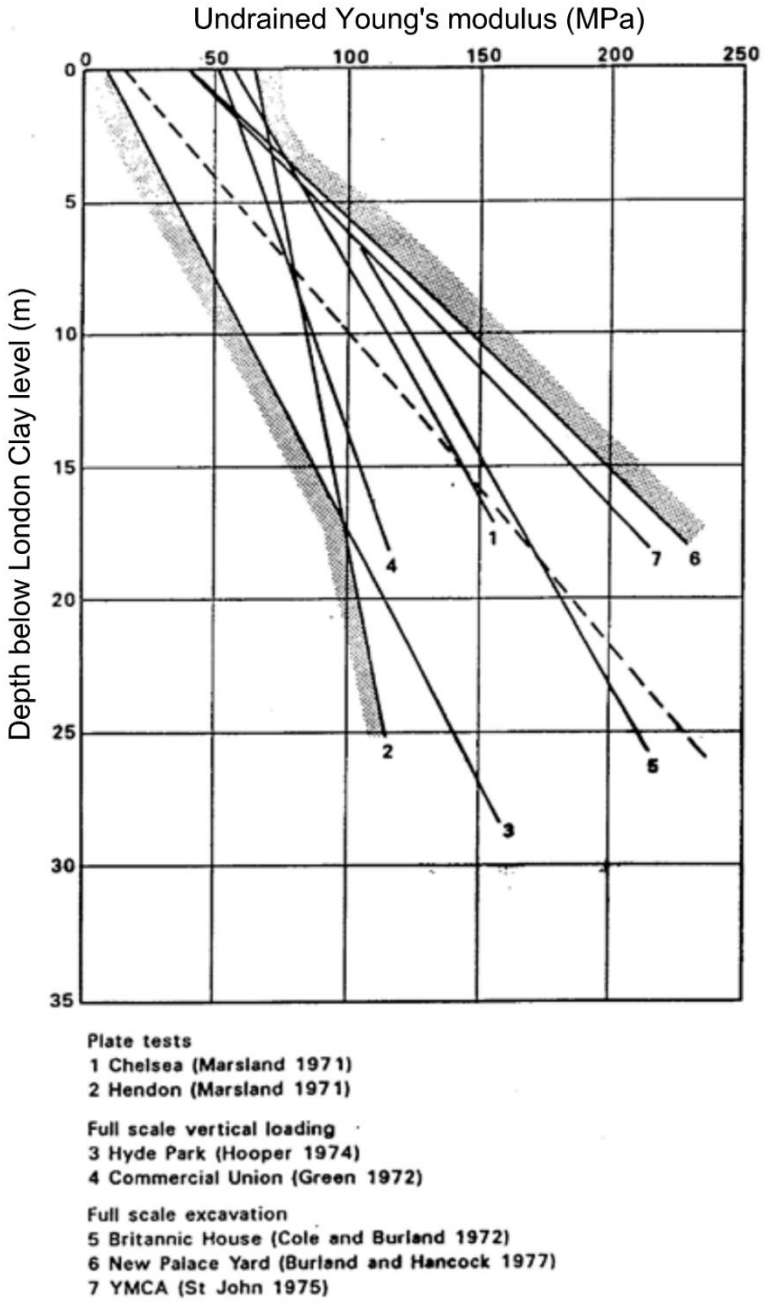

Figure 2.23: Distributions of undrained Young's modulus for London Clay from various sites (after Burland and Kalra, 1986; Hewitt, 1989)

More recent advances in field and laboratory tests and intact specimen extraction methods have enabled researchers to achieve more reliable measurements of the London Clay soil stiffness and a better understanding of its anisotropic behaviour. For example, advanced laboratory tests on intact specimens obtained from rotary boreholes and blocks cut by hand in excavations at Heathrow T5, enabled researchers at Imperial College to determine more reliable values of the drained and undrained Young's moduli. These results are plotted in Figure 2.24 against the depth below the London Clay level. The laboratory tests included both Hollow Cylinder Apparatus (HCA) and triaxial (TX)

tests. Detailed descriptions and illustrations of the HCA tests are given by Minh (2006), Nishimura (2005) and Nishimura et al. (2007). For the triaxial tests, 100 mm diameter and 200 mm high London Clay samples were used, fitted with high-resolution axial and radial strain LVDT sensors (Gasparre et al., 2007b). The values of the undrained Young's modulus, E_u measured from consolidated anisotropic undrained (CAU) triaxial compression tests accord well with those calculated from the combination of other measured elastic independent parameters with the discrepancy between the calculated and measured values being generally below 10%. Overall, the results highlight the strong anisotropy of both the undrained and drained Young's modulus, showing higher values in the horizontal than in the vertical direction.

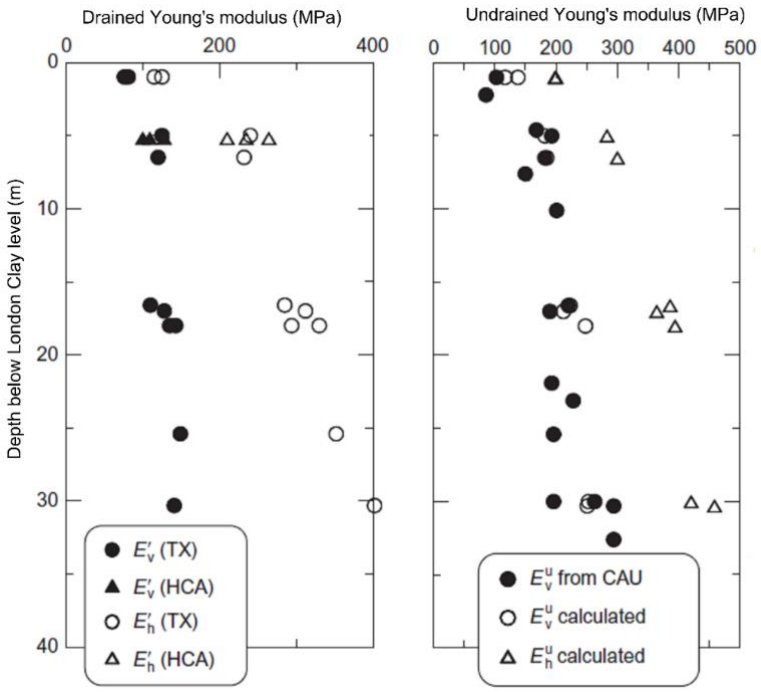

Figure 2.24: Drained and Undrained Young's moduli results for London Clay (after Gasparre, 2007b)

The effect of the soil stiffness anisotropy is particularly important for the design of retaining walls and the assessment of the lateral response of piles to lateral loads and moments where the horizontal drained and undrained Young's moduli become relevant. Based on the more reliable measurements of the soil stiffness and a better understanding of its anisotropy, revised correlations between the horizontal undrained Young's Modulus and the undrained shear strength have been adopted for London Clay in the last two decades with E_u/c_u ratio values typically ranging from 750 to 1250 (O'Brien and Sharp, 2001; Yeow and Feltham, 2008). Based on these studies, the horizontal undrained and drained Young's modulus profiles adopted in this thesis, for the analysis

of supported excavations in London Clay, are described by the Equations 2.20 and 2.21 respectively.

$$E_u = 1000\ c_u\ (kPa) \tag{2.20}$$

$$E' = 750\ c_u\ (kPa) \tag{2.21}$$

Where c_u is the undrained shear strength as defined in Equation 2.19.

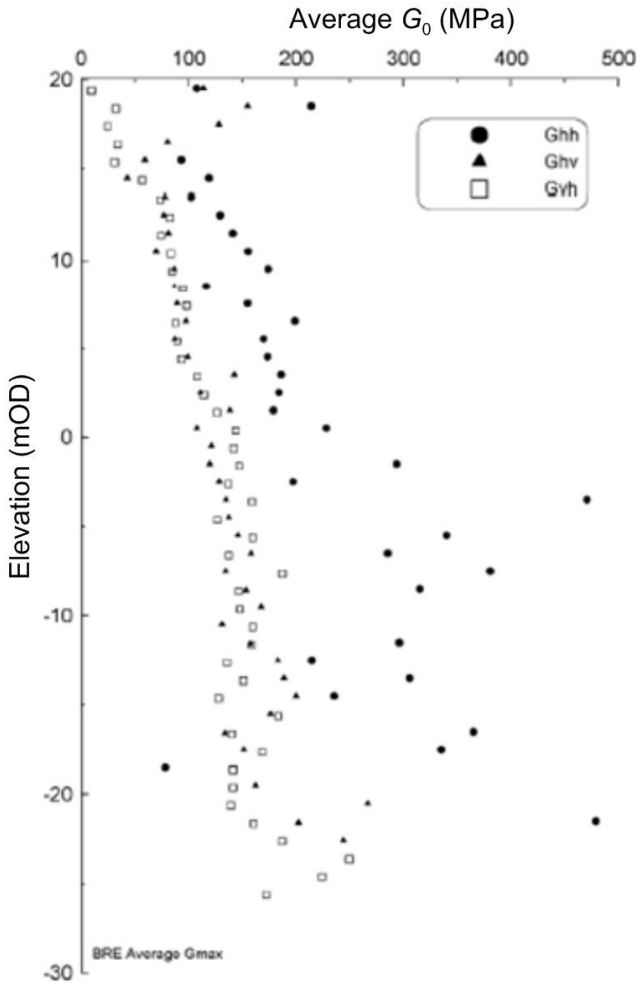

Figure 2.25: In-situ measurements of dynamic shear moduli for London Clay at Heathrow Terminal 5 (after Hight et al., 2007)

Moreover, the Building Research Establishment (BRE) carried out both downhole and crosshole tests in three boreholes at Heathrow Terminal 5 to measure the shear wave velocities, V_{hv}, V_{hh} and V_{vh}. The Imperial College researchers used these measurements to derive the values of G_{vh}, G_{hv} and G_{hh} from two different sets of shear wave velocities, and the average values, as summarised by Hight et al. (2007), are presented in Figure 2.25, where the scatter in the values illustrates the strong anisotropy

of the shear modulus in small strains. Based on these published data, the small strain shear modulus will be later derived for the HSS model.

2.5 MC, HS and HSS model parameters for London Clay

The strength and stiffness parameters for London Clay, used for the design of supported excavations in this thesis, are based on the results of the studies discussed above. In this section, the material parameters are derived for the Mohr-Coulomb, Hardening Soil and Hardening Soil Small constitutive models. These soil models are readily available with Plaxis 2015.02 (Plaxis, 2015), a highly advanced commercial finite element software which was used for all the numerical calculations in this thesis.

2.5.1 Mohr-Coulomb model parameters

The characteristic values of the Mohr-Coulomb model parameters for London Clay are listed in Table 2.1. For total stress analysis, the E_u/c_u ratio is assumed to be equal to 1000. However, a sensitivity analysis will be later performed to investigate the effect of varying E_u/c_u. For effective stress analysis, the effective cohesion, c' is taken as zero and the peak angle of shearing resistance φ' is taken equal to 25° (Simpson, 1992; Pantelidou and Simpson, 2007).

Table 2.1: Mohr-Coulomb parameters for London Clay

Total stress parameters	
γ_{sat} (kN/m^3)	20
c_u (kPa)	60 + 8 z
E_u (MPa)	60 + 8 z
Effective stress parameters	
c' (kPa)	0
φ' (°)	25
ψ (°)	0
E' (MPa)	45 + 6 z
where z(m) is the depth from the top of London Clay	

2.5.2 HS and HSS model parameters

There is limited reference in literature as to what soil parameters are appropriate for London Clay when using the HS and HSS models. Although, the undrained shear strength can also be an input parameter in the HS and HSS models, the soil stiffness parameters lose their stress dependency, which is an important feature of these models (Benz, 2007; Schanz et al., 1999). For this reason, the effective stress analysis with the effective cohesion and internal friction angle as input is typically preferred when these

soil models are used. These effective strength parameters are assumed to be the same as in the Mohr-Coulomb model (see Table 2.1) while the dilatancy angle is taken as zero because dilatant behaviour leads to a significant increase of undrained strength which is highly unrealistic (Schweiger, 2002).

There is a limited number of studies on what input soil stiffness parameter values are appropriate for London Clay. For example, Chambers et al. (2016), using the HSS model for the study of the temporary support at Crossrail Paddington station, adopted values for the maximum shear modulus based on a correlation with undrained shear strength proposed by Vardenega and Bolton (2011) but ignored an important feature of the model which is the stress dependency of the soil stiffness. Similarly, Katsigiannis et al. (2015a), using the HS and HSS soil model for the study of typical supported excavations in London Clay, proposed high values for the input soil stiffness parameters to account for the loss of the stress dependency when using the undrained shear strength as input in the numerical analysis. Wagner (2007) also attempted to estimate values for the HS and HSS stiffness parameters for the study of a deep excavation in London Clay. However, the parameters were estimated by carrying out a series of sensitivity analyses rather than determining them from soil strength and stiffness published data.

In this study, a reference value for the shear modulus at small strains G_0^{ref} is first selected that results in a G_0 distribution that matches the in-situ measurements reported by Hight et al. (2007) and shown in Figure 2.25. As the shear modulus at small strains parameter, G_0, is stress-dependent, the effective stress profile needs first to be defined. The stress distribution is dependent on the soil profile, the value of the earth pressure coefficient at rest and the groundwater regime. For this study, the vertical and horizontal total and effective stress profiles, plotted in Figure 2.26, are considered. They are based on a value of the earth pressure coefficient at rest, K_0, equal to 1.5, constant with depth which is assumed to be a reasonable approximation of the published data for London Clay shown in Figure 2.18. The simplified soil profile consists of a 4m thick layer of Made Ground overlaying the London Clay formation, while the ground water table is assumed to be at 2m below the ground level. The pore water pressure distribution, which is considered to be under-drained (60% hydrostatic) in London Clay, is described by Equation 2.22. This is assumed to realistically account for the under-drainage due to the deep Chalk aquifer as discussed previously.

$$u = 20 + 6z\ (kPa) \tag{2.22}$$

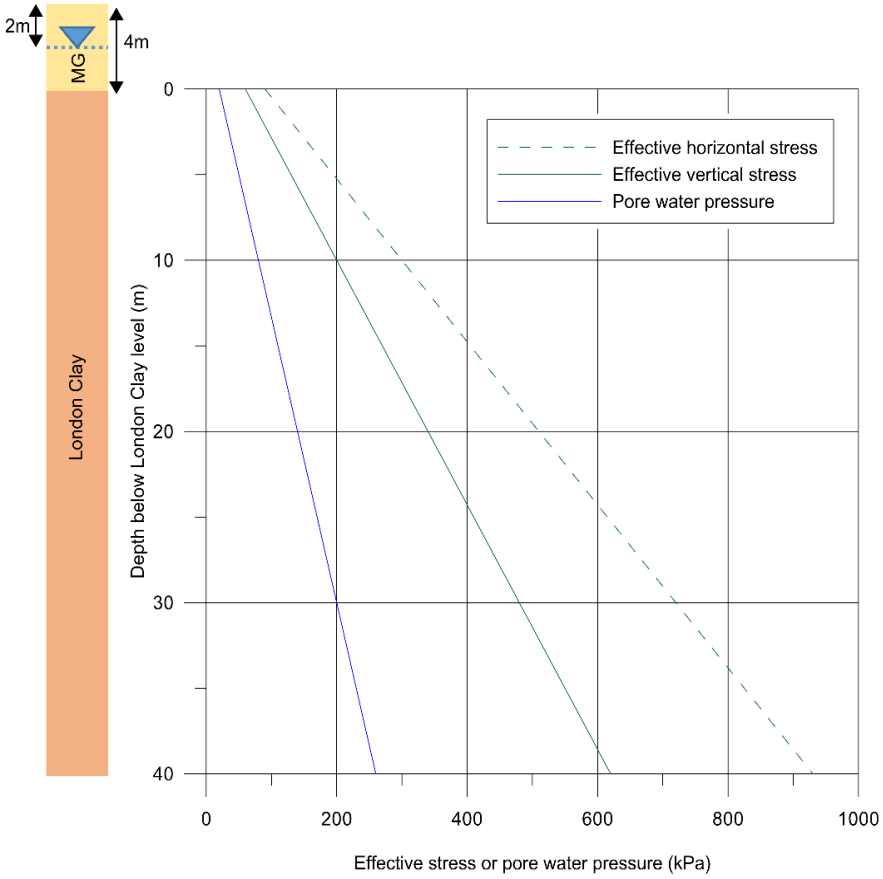

Figure 2.26: Effective stress and pore water pressure profiles

As mentioned above, the effective strength parameters for the HS and HSS model are assumed to be the same as shown in Table 2.1 for the Mohr-Coulomb model. Hence, for cohesion *c'* = 0, Equation 2.9 reduces to Equation 2.23, which in principle means that G_0 depends on the stress level and not the soil strength parameters.

$$G_0 = G_0^{ref}\left(\frac{-\sigma'_1}{p^{ref}}\right)^m \tag{2.23}$$

Based on the effective stress profile shown in Figure 2.26, a value for the G_0^{ref} equal to 60MPa (for p^{ref} = 100kPa) is required to produce a G_0 profile that matches the published values as shown in Figure 2.27. In the figure, the different distributions of G_0 are plotted for m = 0.7, 0.85 and 1 highlighting the effect of the power law exponent m on scaling the stiffness parameters. It can be seen that this range of m values, which is assumed to be typical for clay materials (Benz, 2007), results in a different match with the G_0 data published by Hight et al. (2007). Although, a value of 1 is adopted for the power law exponent because it results in a G_0 distribution according with the published

horizontal shear modulus values, a sensitivity analysis will be later carried out to investigate the effect of varying *m*.

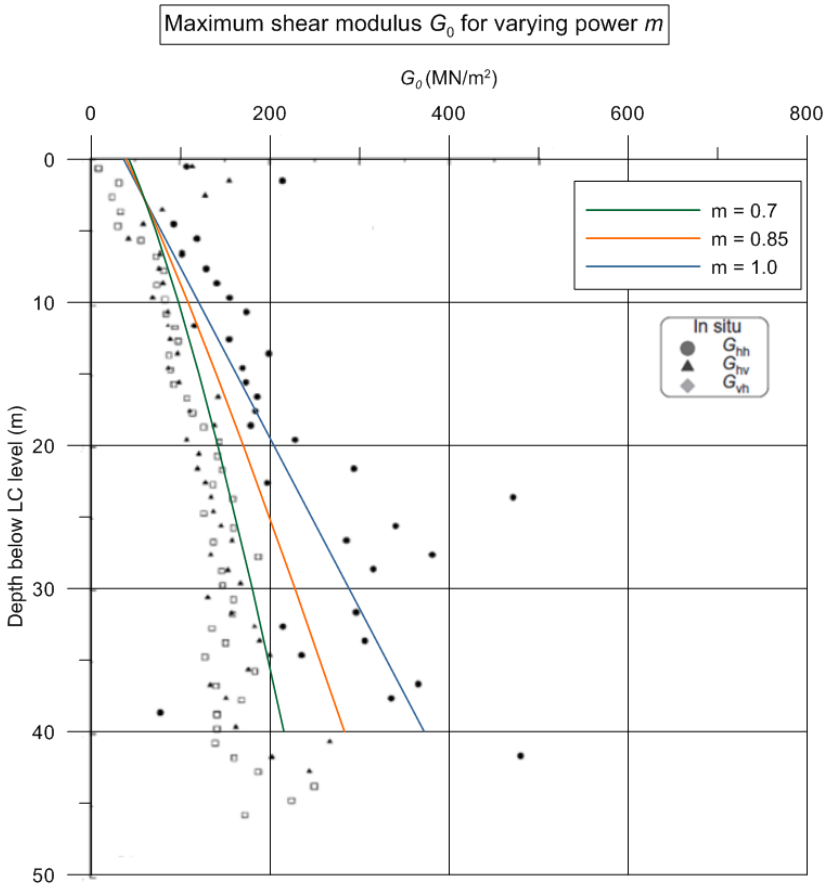

Figure 2.27: G_0 profile for the HSS with varying m based on the results published by Hight et al. (2007)

The effect of $\gamma_{0.7}$ on the tangent shear modulus decay curves is highlighted in Figure 2.28 where the tangent shear modulus degradation curves are shown for $\gamma_{0.7}$ = 0.001, 0.0002, 0.0001 and 0.00001. The resulting shear strain values at the cut-off level in the tangent shear modulus degradation curves are 0.0026, 0.00052, 0.00026 and 0.000026 respectively. It can be seen that $\gamma_{0.7}$ = 0.00001 is an extreme case where the initial shear modulus reduces rapidly to the G_{ur} value at a very small strain level after which the soil behaviour becomes the same as with the HS model case. A value of 0.0001 for the $\gamma_{0.7}$ is generally considered to result in more realistic stiffness degradation curve shapes for a wide range of materials (Brinkgreve et al., 2007). In order to confirm this, in Figure 2.29, the secant shear modulus degradation curves, predicted by the HSS model for m = 1 and $\gamma_{0.7}$ = 0.0001, are plotted at 3 different depths: 4m, 15m and 40m below London Clay. The curves are compared with the secant shear modulus values measured at the same depths from undrained compression triaxial tests on London Clay

samples reported by Pantelidou and Simpson (2007). It can be seen that the HSS predictions are in good agreement with the laboratory results, hence for the shear strain $\gamma_{0.7}$, a value of 0.0001 has been adopted in this thesis.

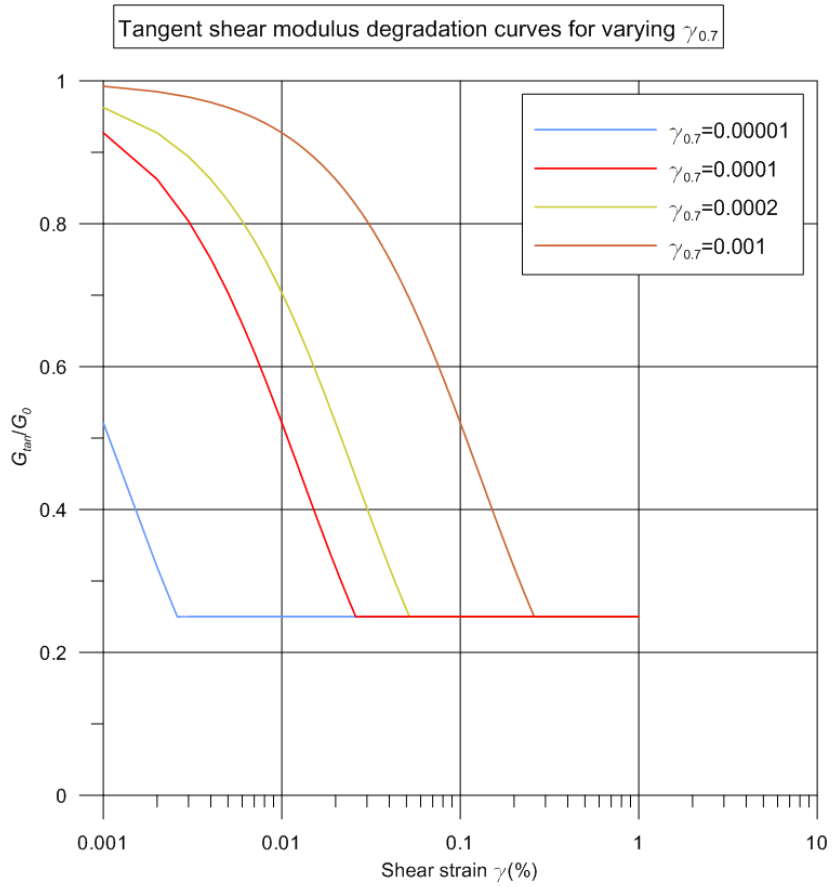

Figure 2.28: Tangent shear modulus degradation curves with varying $\gamma_{0.7}$

Once the value of G^{ref}_0 is derived, the corresponding value of G^{ref}_{ur} can then be calculated using the relation between the initial small strain Young's modulus, E_0 and the Young's modulus for unloading/reloading, E_{ur} shown in Figure 2.30 proposed by Alpan (1970). From this, a value can be derived for the ratio E_0/E_{ur} which is equal to G_0/G_{ur}. For $G_0/G_{ur} = 4$, the reference unloading/reloading shear modulus, G^{ref}_{ur} is equal to 15MPa.

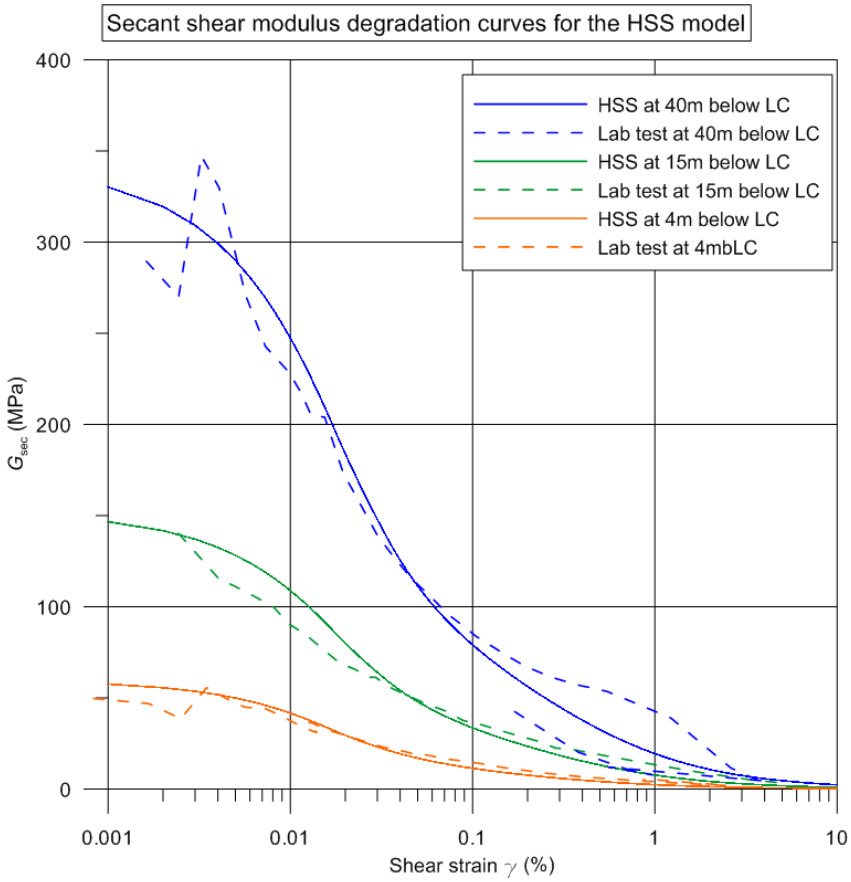

Figure 2.29: Secant shear modulus degradation curves for the HSS with m = 1 and $\gamma_{0.7}$ = 0.0001 and triaxial test results after Pantelidou and Simpson (2007)

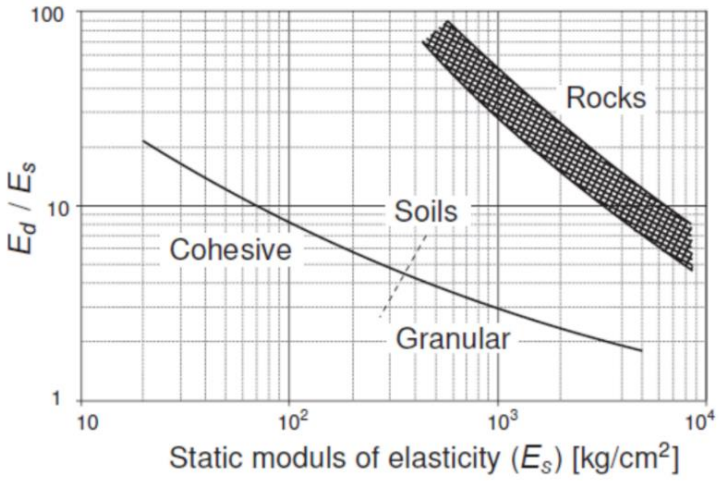

Figure 2.30: Relation between dynamic ($E_d = E_0$) and static soil stiffness ($E_s = E_{ur}$) after Alpan (1970)

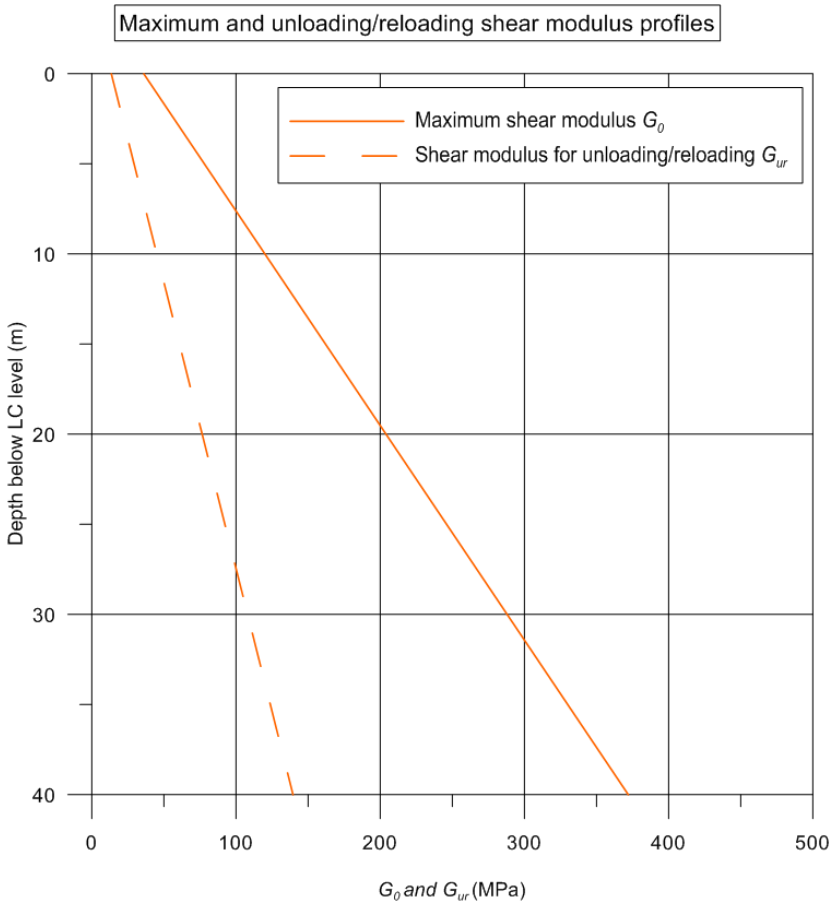

Figure 2.31: G_0 and G_{ur} profiles for the HSS for London Clay

The distributions of the small strain shear modulus, G_0 and the unloading/reloading shear modulus, G_{ur} are plotted in Figure 2.31, based on Equation 2.23 and a power law exponent m = 1. Moreover, for G^{ref}_{ur} = 15MPa, the reference value of the unloading/reloading Young's modulus can then be derived from Equation 2.14 which gives E^{ref}_{ur} = 36MPa. The values of the other two soil stiffness parameters E^{ref}_{50} and E^{ref}_{oed} are taken as 15MPa, which is assumed to be reasonable for the material modelled (Wagner, 2007). A sensitivity analysis will be performed later to verify the values used. The distributions of all the soil stiffness parameters with depth below the level of London Clay are plotted in Figure 2.32.

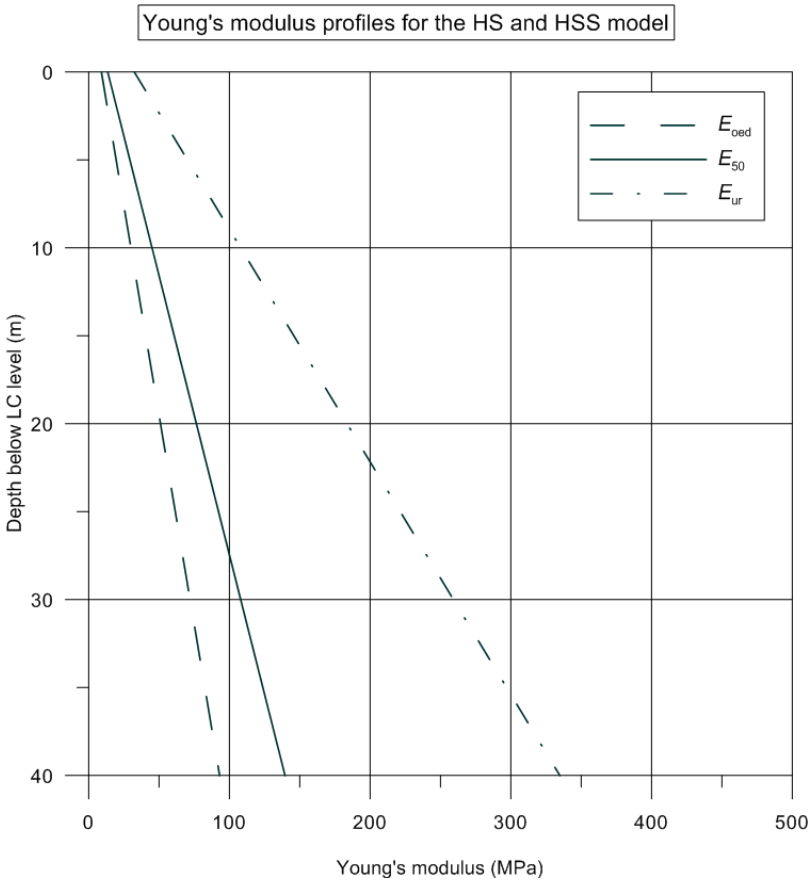

Figure 2.32: Young's modulus profiles for the HS and HSS model for London Clay

As the parameters are stress-dependent, the stiffness profiles are based on the effective stress profiles shown in Figure 2.26 and a power law exponent *m* = 1. Again for *c'* = 0, Equations 2.5, 2.6 and 2.7 reduce to Equations 2.24, 2.25 and 2.26 respectively where the soil stiffness parameters are dependent only on the stress level as expressed by the minor principal effective stress, σ'_3.

$$E_{50} = E_{50}^{ref}\left(\frac{-\sigma'_3}{p^{ref}}\right)^m \tag{2.24}$$

$$E_{ur} = E_{ur}^{ref}\left(\frac{-\sigma'_3}{p^{ref}}\right)^m \tag{2.25}$$

$$E_{oed} = E_{oed}^{ref}\left(\frac{-\frac{\sigma'_3}{K_0^{nc}}}{p^{ref}}\right)^m \tag{2.26}$$

A summary of the parameters discussed above for the Hardening Soil and Hardening Soil Small effective stress models is given in Table 2.2.

Table 2.2: HS and HSS model parameters for London Clay

Effective stress parameters	
γ_{sat} (kN/m^3)	20
E^{ref}_{50} (MPa)	15
E^{ref}_{oed} (MPa)	15
E^{ref}_{ur} (MPa)	36
power m	1
R_f	0.9
p^{ref} (kPa)	100
σ_{tens} (kPa)	15
ν'_{ur}	0.2
c' (kPa)	0
φ' (°)	25
ψ (°)	0
Additional HSS model parameters	
G_0 (MPa)	60
$\gamma_{0.7}$	0.0001

2.5.3 Undrained strength with effective stress parameters

In FEM, it is possible to model undrained behaviour using effective strength parameters. An explicit distinction is then made between effective stresses and excess pore water pressures while the undrained Young's and bulk moduli are automatically calculated from the drained moduli using the Hooke's law of elasticity.

The widely used stress invariants in geotechnical practice are the mean stress p, and the deviatoric stress, q. The mean stress is defined in Equation 2.27, where σ_1, σ_2 and σ_3 are the major, intermediate and minor principal total stresses respectively. The effective mean stress, p', is equal to difference of the total mean stress and the pore water pressure, u, as shown in Equation 2.28. The deviatoric stress q is defined in Equation 2.29 again as a function of the total principal stresses. However, for the special cases of triaxial compression where $\sigma_2 = \sigma_3$ and triaxial extension where $\sigma_1 = \sigma_2$, Equation 2.29 is reduced to Equation 2.30 (Plaxis, 2015). The ratio of the deviatoric and effective mean stress at the critical state, M is defined by Equation 2.31, as a function of the angle of shearing resistance, φ'.

$$p = \frac{1}{3}(\sigma_1 + \sigma_2 + \sigma_3) \tag{2.27}$$

$$p' = p - u \tag{2.28}$$

$$q = \sqrt{\frac{1}{2}[(\sigma_1 - \sigma_3)^2 + (\sigma_2 - \sigma_3)^2 + (\sigma_3 - \sigma_1)^2]} \tag{2.29}$$

$$q = \sigma_1 - \sigma_3 \tag{2.30}$$

$$M = \frac{q}{p\prime} = \frac{6sin\varphi\prime}{3+sin\varphi\prime} \tag{2.31}$$

The pore water pressure in soil, u, consists, as shown in Equation 2.32, of the excess pore pressure, u_{excess} caused by undrained loading and the steady state pore pressure, u_{steady}. The time derivative of the pore water pressure, $\dot{u}$, and the excess pore water pressure $\dot{u}_{excess}$, are equal, as shown in Equation 2.33, as the time derivative of the steady state component is zero.

$$u = u_{steady} + u_{excess} \tag{2.32}$$

$$\dot{u} = \dot{u}_{excess} \tag{2.33}$$

The time derivative of the excess pore water pressure $\dot{u}$ is calculated by Equation 2.34, where $\dot{\varepsilon_v}$ is the derivative of the volumetric strain; K_w is the bulk modulus of the water and n is the porosity of the soil which relates to the initial void ratio e_0 as shown in Equation 2.35. The bulk modulus of water, K_w is obtained from Equation 2.36 for incompressible soil grains where K' is the effective bulk modulus of the soil. It can be seen that the bulk modulus depends on the soil stiffness. The calculated value is always equal to or less than the real bulk modulus of water, K_w = 2000MPa (Plaxis, 2015).

Fully incompressible behaviour of the soil body is obtained for an undrained Poisson's ratio, v_u equal to 0.5. Because, in numerical analysis, this causes a singularity of the stiffness matrix, v_u is taken as 0.495 in order to avoid numerical instability, which results in a slightly compressible undrained behaviour (Plaxis, 2015). Substituting for v_u

= 0.495 and *v'* = 0.2, Equation 2.36 reduces to Equation 2.37 shown below for the MC model and Equation 2.38 for the HS and HSS models. In Equation 2.38, K_w^{ref} is the reference value of the bulk modulus at the default reference pressure p^{ref} = 100kPa.

$$\dot{u} = \frac{K_w}{n}\,\dot{\varepsilon_v} \tag{2.34}$$

$$n = \frac{e_0}{1+e_0} \tag{2.35}$$

$$\frac{K_w}{n} = \frac{3\,(\nu_u - \nu')}{(1-2\,\nu_u)(1+\nu')}\,K' \tag{2.36}$$

$$\frac{K_w}{n} = 73.75\,K' = 40.972\,E' \tag{2.37}$$

$$\frac{K_w}{n}^{ref} = 73.75\,K_{ur}^{ref} = 40.972\,E_{ur}^{ref} \tag{2.38}$$

For undrained conditions, Skempton's pore pressure parameters A and B (Skempton, 1954) are typically used to relate the excess pore pressures with the total principal stresses. For triaxial conditions, Skempton's relation is shown in Equation 2.39 where $\dot{\sigma}_1$ and $\dot{\sigma}_3$ are the derivatives of the total minor and major principal stress respectively. When the material is fully saturated, and the pore water is incompressible, the parameter B is equal to 1.0. However, a value slightly less than unity is typically generated in FEM by Equation 2.40, allowing for slight compressibility of water for numerical stability (Schweiger, 2002). By combining Equations 2.37 and 2.40, the Skempton's parameter B is obtained, which is equal to 0.9866 for *v'* = 0.2. Moreover, by re-arranging Equation 2.39 and assuming B = 1.0, the parameter A is defined as shown in Equation 2.41.

$$\dot{u} = B[\dot{\sigma}_3 + A\,(\dot{\sigma}_1 - \dot{\sigma}_3)] \tag{2.39}$$

$$B = \frac{1}{1+n\frac{K\prime}{Kw}} \tag{2.40}$$

$$A = \frac{\dot{u} - \dot{\sigma}_3}{\dot{\sigma}_1 - \dot{\sigma}_3} \tag{2.41}$$

2.5.3.1 Triaxial tests using Plaxis SoilTest

Most geotechnical engineering software packages offer to users the option to run soil tests to simulate standard tests performed in the laboratory. The option enables designers to gain insights into the modelled behaviour of the material, derive the stress paths and calculate the undrained shear strength based on the input effective stress model parameters. For this study, the SoilTest option, available with Plaxis 2015.02 (Plaxis, 2015), was used which is available for both standard and user-defined constitutive models.

A series of triaxial undrained compression tests are performed with Plaxis SoilTest at different stress levels (corresponding to 0.5, 2, 5, 10, 15, 20, 30 and 40m below the London Clay level) using the MC, HS and HSS soil models. Two different cases are considered: the anisotropically consolidated undrained (CAU) triaxial test where the soil specimen is first consolidated from a slurry state under K_0 conditions (K_0 = 1.5) to its current state and then sheared under undrained triaxial conditions until failure, and the isotropically consolidated undrained (CIU) triaxial test where triaxial shearing follows isotropic consolidation. Moreover, a pre-consolidation pressure, p_c = 2000kPa is applied in all cases to account for 200m overburden. While this test configuration is relevant to the geological history of London Clay, the tests are also repeated for zero pre-consolidation pressure to allow for comparisons between the stress paths predicted by the different soil models and a better understanding of the soil's behaviour under triaxial conditions.

An example of the output summary of the Plaxis triaxial test, which typically includes the stress paths, stress-strain behaviour and excess pore water pressure generation in the undrained case, is presented in Figure 2.33. In the following figures, the results of the Plaxis triaxial tests are presented for the MC, HS and HSS model parameters and for a confining effective pressure equal to 300kPa which corresponds to a depth of 10m below the top of London Clay.

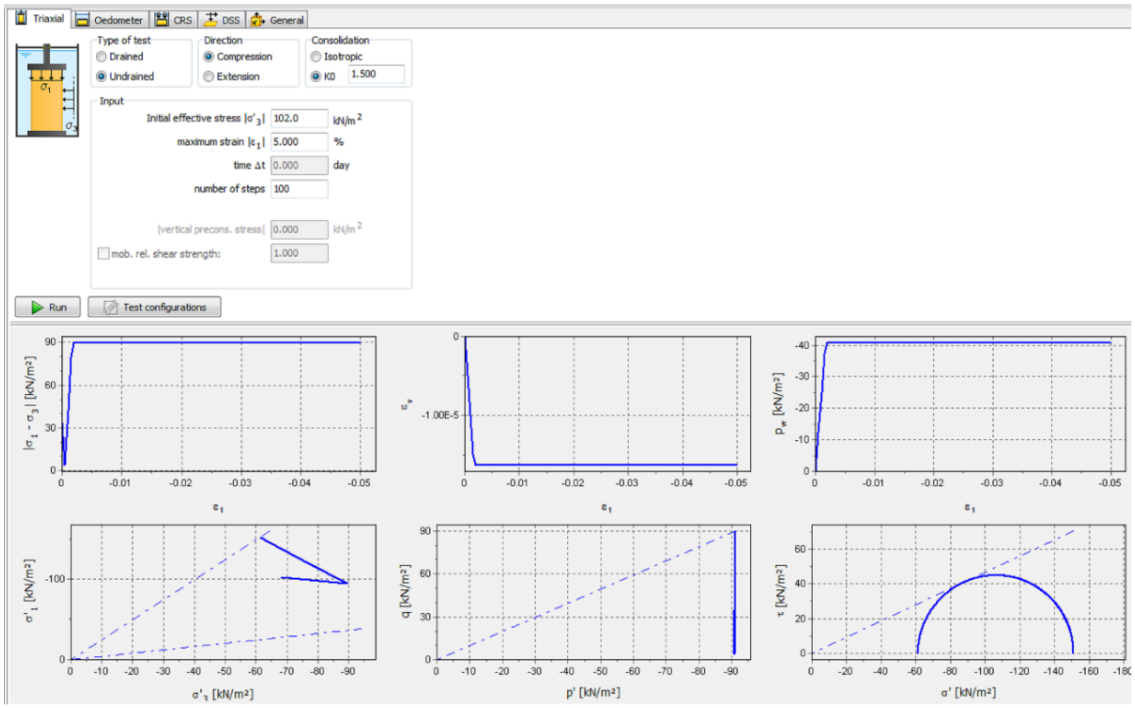

Figure 2.33: Plaxis SoilTest output: summary of graphs

In Figures 2.34 and 2.35, the normalised deviatoric stress is plotted against the principal axial strain, ε_1 for the CAU and CIU triaxial test respectively. It can be seen that in both cases, the MC, HS and HSS curves finally converge to a stress ratio M equal to about 0.98.

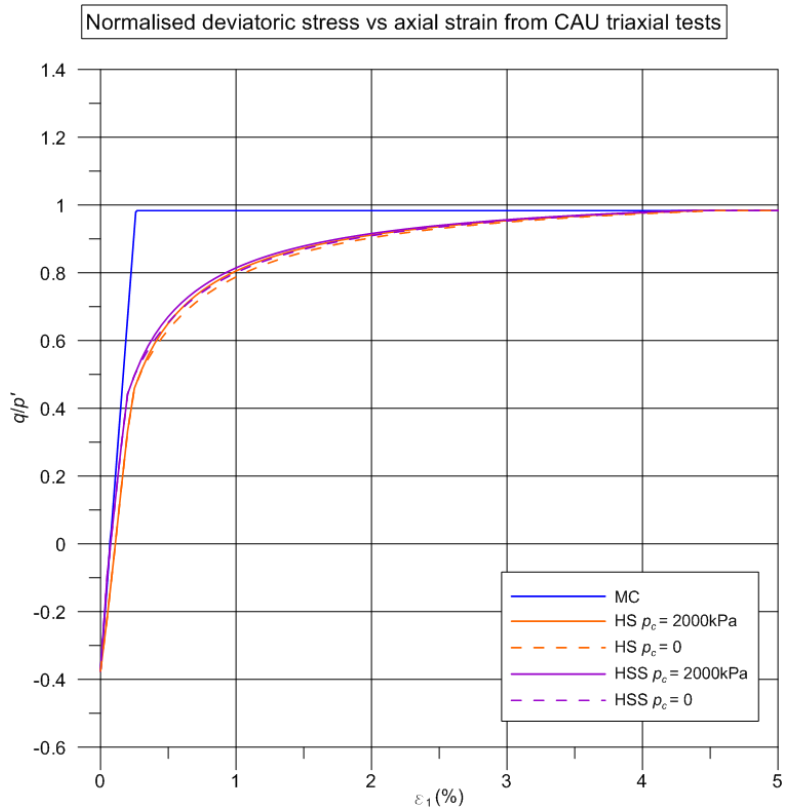

Figure 2.34: Normalised deviatoric stress vs axial strain from CAU triaxial tests at 10m below LC stress level for the MC, HS and HSS

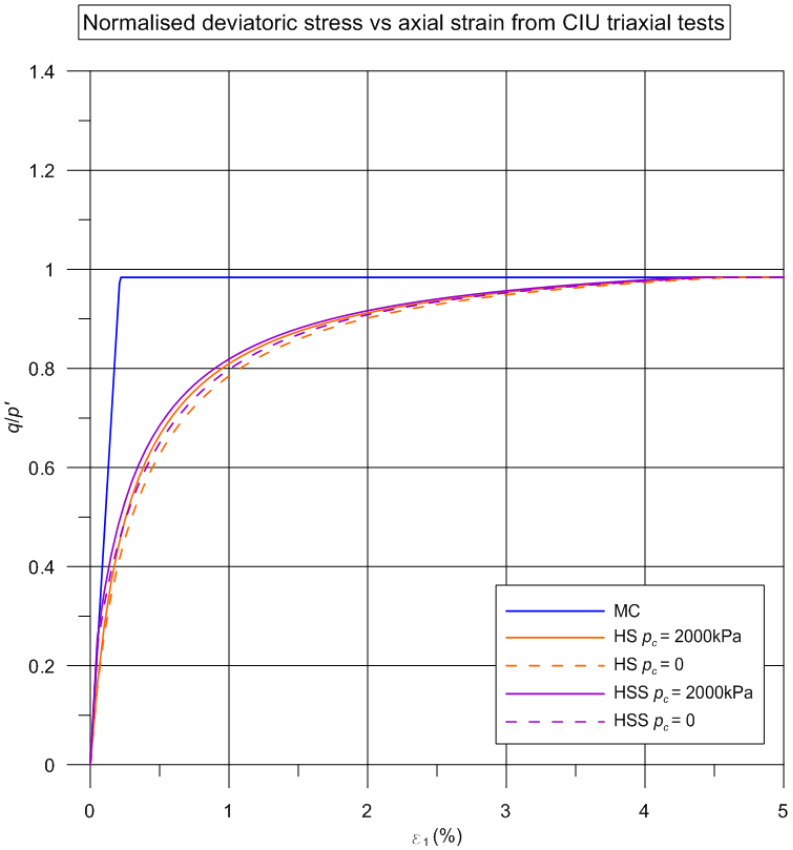

Figure 2.35: Normalised deviatoric stress vs axial strain from CIU triaxial tests at 10m below LC stress level for the MC, HS and HSS

In Figure 2.36, the calculated undrained stress paths in the deviatoric stress and mean effective stress space are plotted for the CAU triaxial tests. Note that the undrained shear strength, c_u is by definition equal to half the value of the deviatoric stress, q. The HS and HSS stress paths for zero pre-consolidation pressure, p_c are also included in the plot, shown as dashed lines, to allow for a better understanding of the effect of the pre-consolidation pressure on the triaxial soil behaviour. The MC stress path is vertical in the q - p' space because the model remains in the elastic range and thus no change in effective mean normal stress occurs (Schweiger, 2002). For p_c = 2000kPa, the HS stress path is also vertical resulting in the same undrained strength, c_u = 132kPa. However, the stress path that corresponds to the Hardening Soil Small model bends slightly to the left, resulting in about 7% lower undrained shear strength. For p_c = 0, both the HS and HSS stress paths bend to the left with the HSS resulting in about 9% lower undrained shear strength.

Overall, a pre-consolidation pressure as high as 2000kPa has, as expected, a profound effect on the stress path and the resulting undrained strength for the more advanced soil models. Also note that while the effective strength input parameters are the same for both the HS and HSS model, the calculated undrained shear strength differs due to the different stress paths predicted by the models.

Similarly, in Figure 2.37, the undrained stress paths in the q - p' space are plotted for CIU triaxial tests for p_c = 0 and 2000kPa. Again it can be seen that the MC stress path and the HS stress path for p_c = 2000kPa are both vertical resulting in c_u = 148kPa, while the HSS results in about 12% lower undrained shear strength. For p_c = 0, both the HS and HSS stress paths again bend to the left with the HSS resulting in about 8% lower undrained strength than the HS.

The excess pore water pressure generated during the CAU triaxial test is plotted against the axial strain in Figure 2.38. It can be seen that the MC and HS model for p_c = 2000kPa result in similar excess pore water pressure equal to about 120kPa while the HSS predicts a 15% higher pressure. For p_c = 0, the excess pore water pressure is 133kPa and 147kPa for the HS and HSS respectively. For isotropic consolidation, the MC and HS for p_c = 2000kPa result in u_{excess} = 97kPa, while the HSS for p_c = 2000kPa predicts u_{excess} = 119.5kPa as shown in Figure 2.39. For p_c = 0, the calculated excess pore water pressure is 120.5kPa and 137kPa for the HS and HSS respectively.

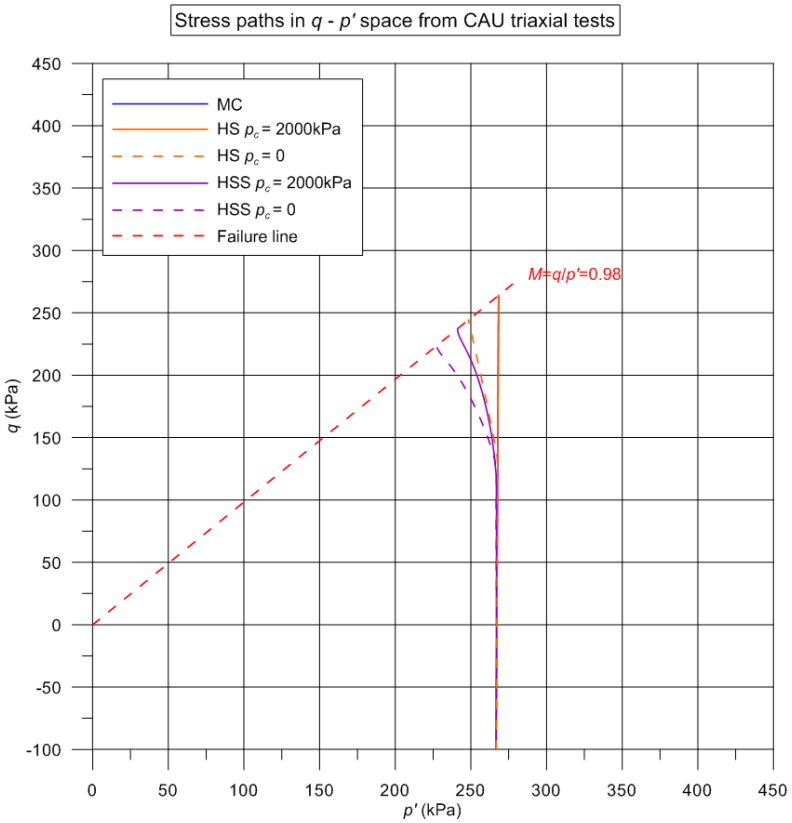

Figure 2.36: Stress paths in q - p' space from CAU triaxial tests at 10m below LC stress level for the MC, HS and HSS

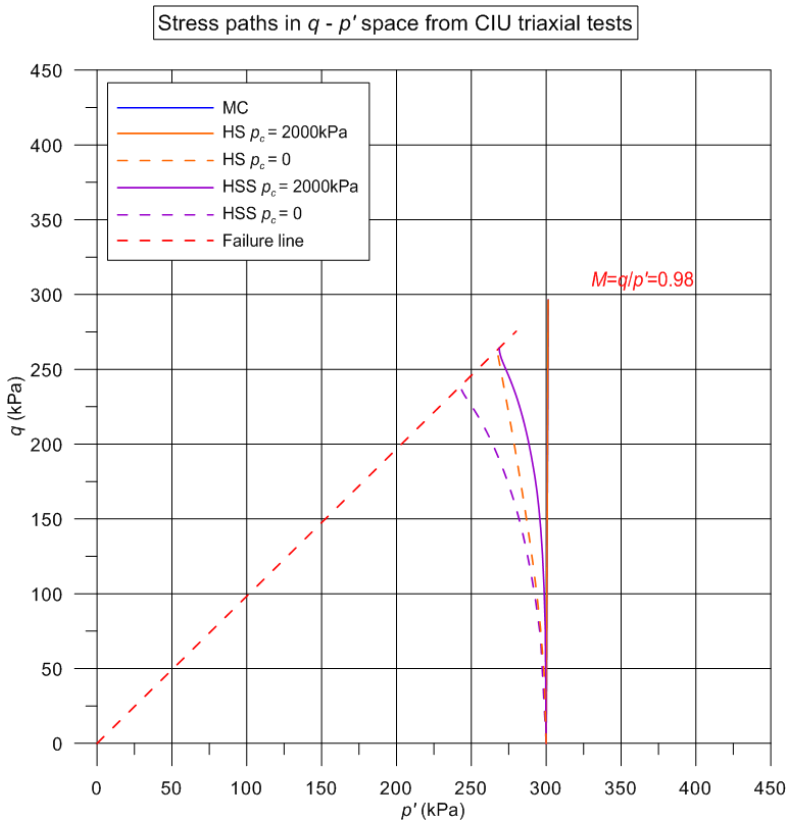

Figure 2.37: Stress paths in q - p' space from CIU triaxial tests at 10m below LC stress level for the MC, HS and HSS

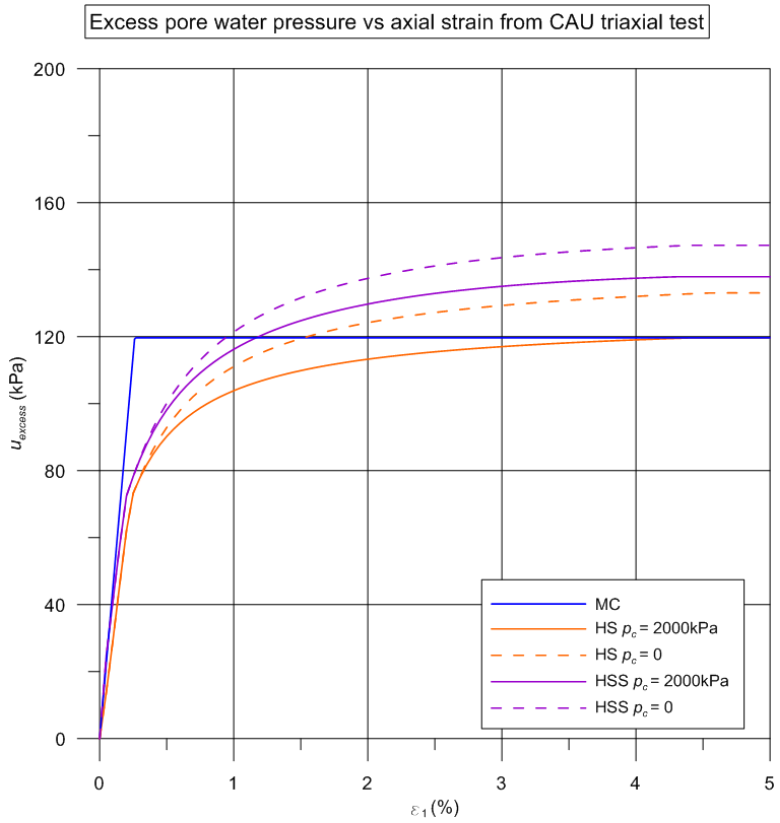

Figure 2.38: Excess pore water pressure vs axial strain from CAU triaxial tests at 10m below LC stress level for the MC, HS and HSS

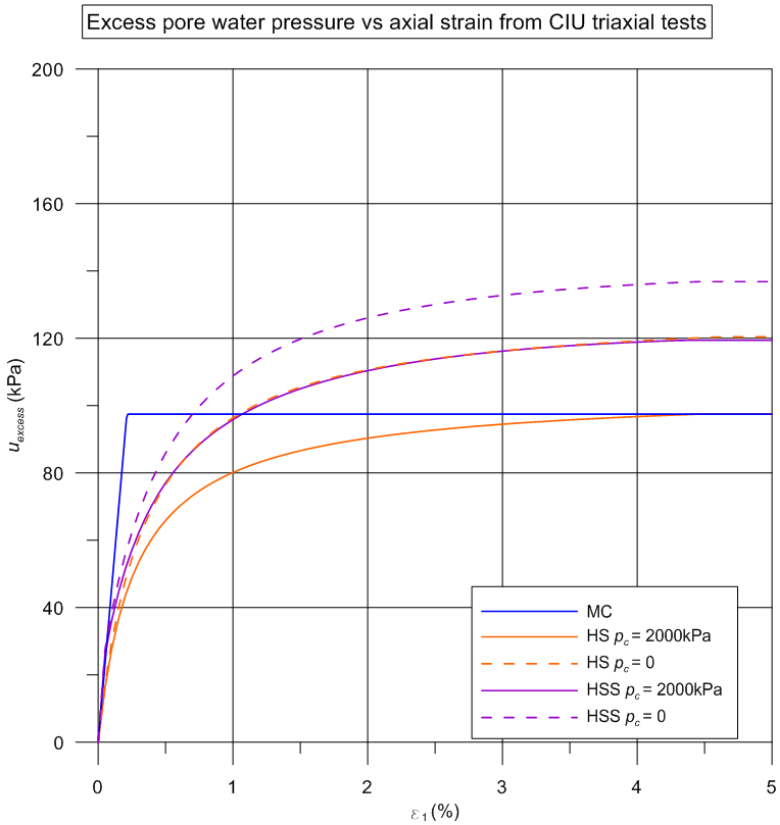

Figure 2.39: Excess pore water pressure vs axial strain from CIU triaxial tests at 10m below LC stress level for the MC, HS and HSS

To better understand the reason for the discrepancies in the stress paths, the Skempton's parameter A, as calculated from Equation 2.41, is plotted against the axial strain in Figure 2.40 for the CAU triaxial test. It can be seen that A is equal to 0.33 for the MC and HS model and 0.41 for the HSS model for p_c = 2000kPa while for zero pre-consolidation pressure, A is equal to 0.39 and 0.46 for the HS and HSS model respectively. Similarly, the parameter A is plotted against the axial strain in Figure 2.41 for all models, at the same stress level but for the CIU triaxial test. It can be seen that A is again equal to 0.33 for the MC and HS model and 0.45 for the HSS model for p_c = 2000kPa while for p_c = 0, A is equal to 0.46 and 0.57 for the HS and HSS model respectively. Overall, the values calculated for the MC model are similar to the theoretical values reported by Skempton (1954) for elastic material behaviour. For more advanced soil models, the parameter A typically varies during shearing. In all cases, the HSS results in higher A values than the MC and HS model.

As discussed earlier and shown in Equation 2.34, the generated pore water pressures depend on the stiffness dependent water bulk modulus and porosity ratio, K_w/n and the volumetric strain, ε_v. For the MC model, the K_w/n ratio at a depth of 10m below the top of London Clay, as calculated by Equation 2.37, is equal to 4589MPa. This value is constant during the triaxial undrained shearing as the soil stiffness is constant. For initial void ratio e_0 = 0.5, the porosity n is equal to 0.3 from Equation 2.35. This results in a bulk modulus of the water K_w = 1,377MPa which is less than the real bulk modulus of pure water. For both the HS and HSS models, the K_w/n ratio at a reference pressure of 100kPa, as calculated from Equation 2.38, is equal to 1,475MPa. However, the ratio varies during triaxial undrained shearing as it depends on the stress dependent soil stiffness. The K_w/n value is 2,905MPa and 11,168MPa for the HS and HSS models respectively with the pre-consolidation pressure having only a minor effect. Moreover, the volumetric strain due to the slightly compressible undrained behaviour is, as expected, negligible with values as low as 0.0026%, 0.0041% and 0.0012% for the MC, HS and HSS model respectively.

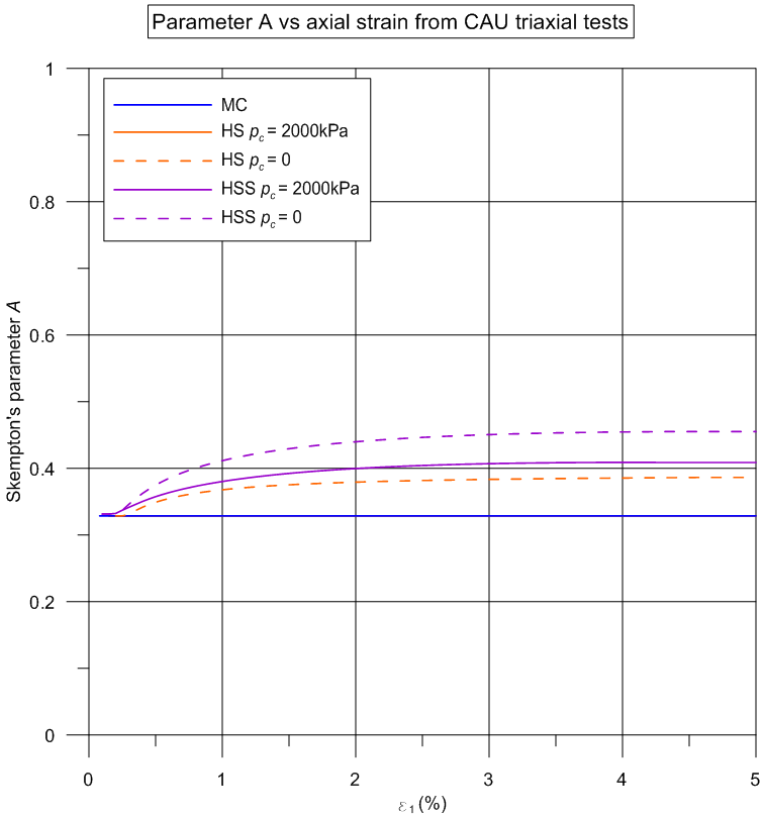

Figure 2.40: Skempton's parameter A vs axial strain from CAU triaxial tests at 10m below LC stress level for the MC, HS and HSS

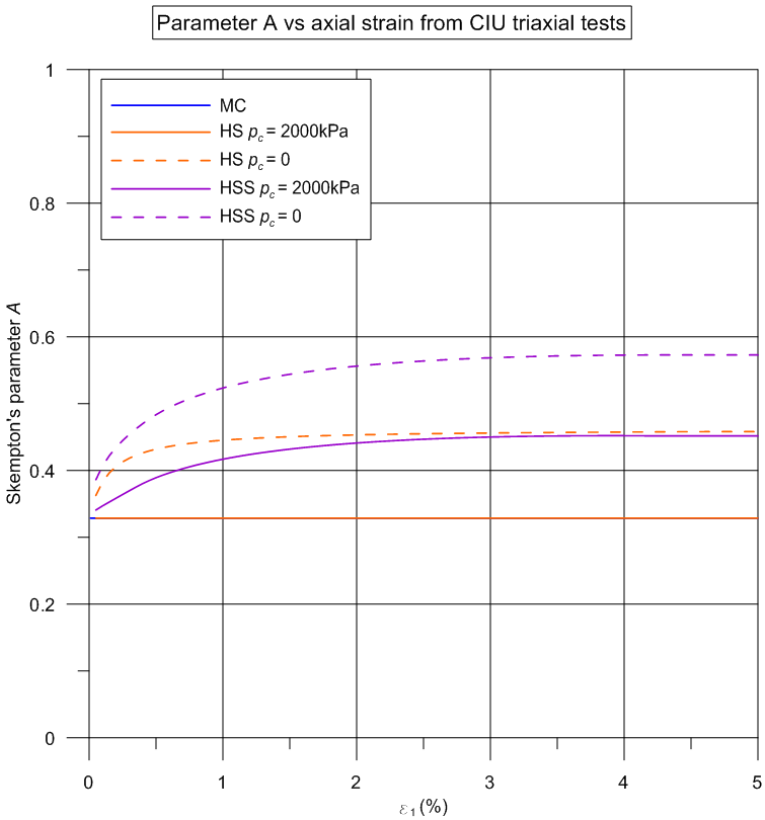

Figure 2.41: Skempton's parameter A vs axial strain CIU triaxial tests at 10m below LC stress level for the MC, HS and HSS

When the undrained shear strength, determined from CAU triaxial compression tests, is plotted in Figure 2.42 at all stress levels, it can be seen that a very good agreement is achieved between the undrained strength profile for the MC and HS soil model (which coincide) and the characteristic c_u profile derived as a cautious estimate of published data, used in this thesis for total stress analysis (see Eq. 2.19). The agreement is also considered satisfactory for the undrained shear strength calculated from the triaxial tests using the HSS model, where the undrained strength at all stress levels is about 7% lower than the value calculated using the MC and HS effective model parameters. Similarly, in Figure 2.43, the undrained shear strength, calculated from CIU triaxial compression tests, is plotted for the MC, HS and HSS models at all stress levels. The undrained strength for the HSS at all stress levels is about 11% lower than the value calculated using the MC and HS. Overall, the agreement with the characteristic c_u profile used for total stress analysis is also considered good, at least up to 20 - 25m below the top of London Clay where most retaining structures are typically constructed.

Overall, it is concluded that the HSS model consistently results in different stress paths, and hence lower undrained shear strength than the HS model. The reason for this is that the generated excess pore water pressure during triaxial shearing is higher than the one predicted for the HS model. As discussed, the excess pore water pressure is calculated based on a relation with the stiffness dependent bulk modulus of water and the volumetric strains which are very low. However, the HSS generates lower volumetric strains but higher K_w/n than the HS model during the undrained triaxial test, which when combined result in the higher excess pore water pressures for the HSS model. Regarding the volumetric strains, it should be noted that the difference also lies in the formulation of the HSS model and the fact that in the model the shear hardening flow rule is defined in a different way than in the HS model as discussed previously.

Although the c_u profiles predicted using the HS and HSS effective model parameters are in good agreement with the published data for London Clay, the stress paths do not match exactly the behaviour reported, for example, by Gasparre (2005) and Pantelidou and Simpson (2007), based on laboratory results. None of these models, can accurately predict the undrained triaxial stress paths in q - p' space for heavily OC samples which typically bend to the right than to the left (see Figure 2.42). Moreover, while OC clays typically exhibit some strain softening after reaching a peak deviatoric stress, the HS and HSS models cannot accurately capture this aspect of soil behaviour. For example, Gasparre (2005) reported that the average stress ratio M drops to a value equal to about 0.85 in the large strain range (as shown in Figure 2.43) while in this study all models result in M = 0.98.

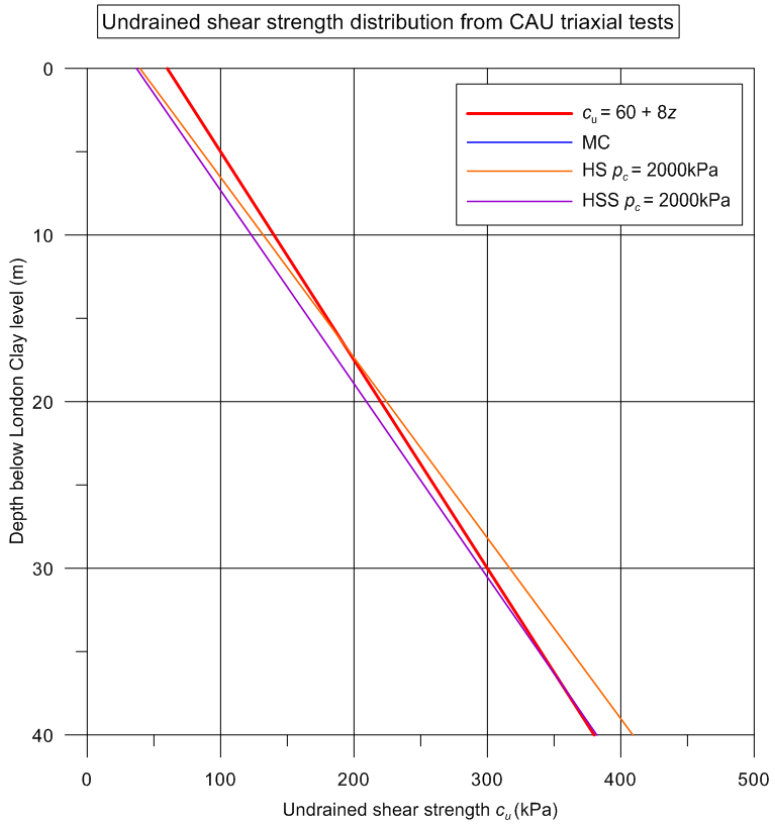

Figure 2.42: Undrained shear strength distribution from CAU triaxial tests for the MC, HS and HSS

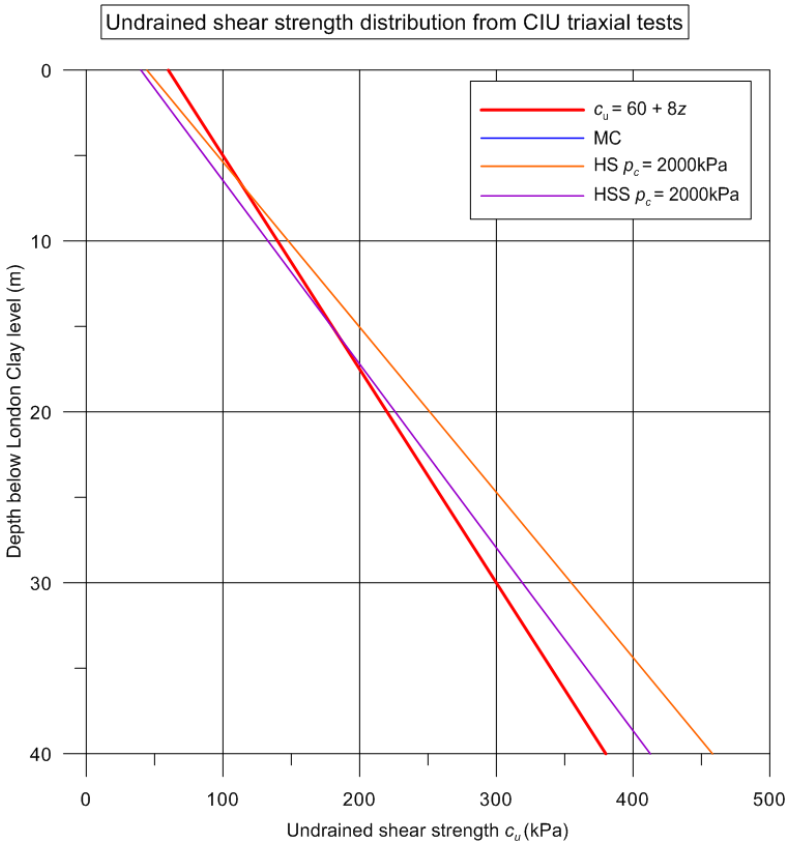

Figure 2.43: Undrained shear strength distribution from CIU triaxial tests for the MC, HS and HSS

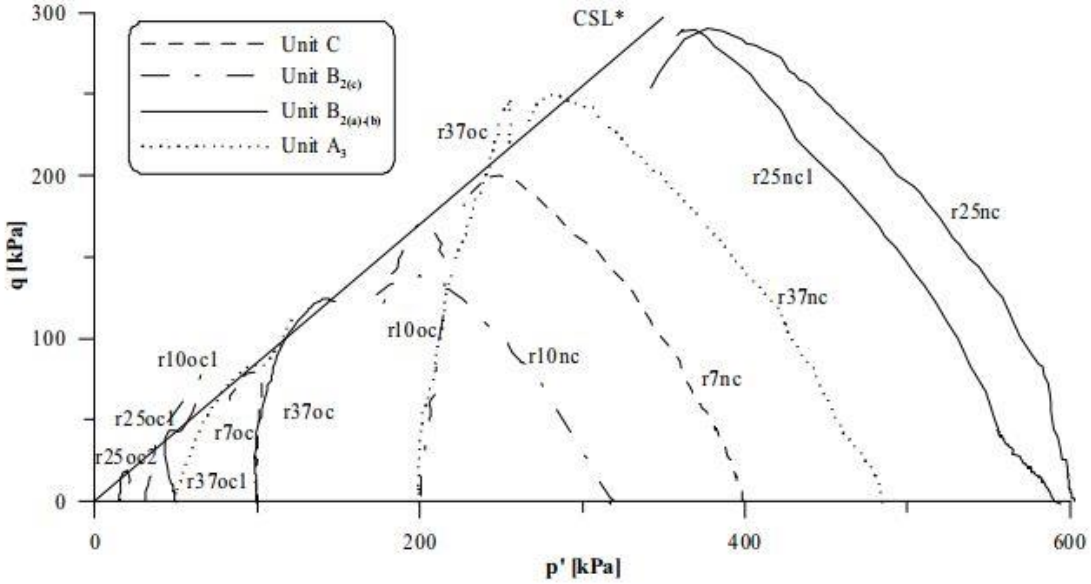

Figure 2.44: Stress paths of reconstituted samples from different London Clay lithological units after Gasparre (2005)

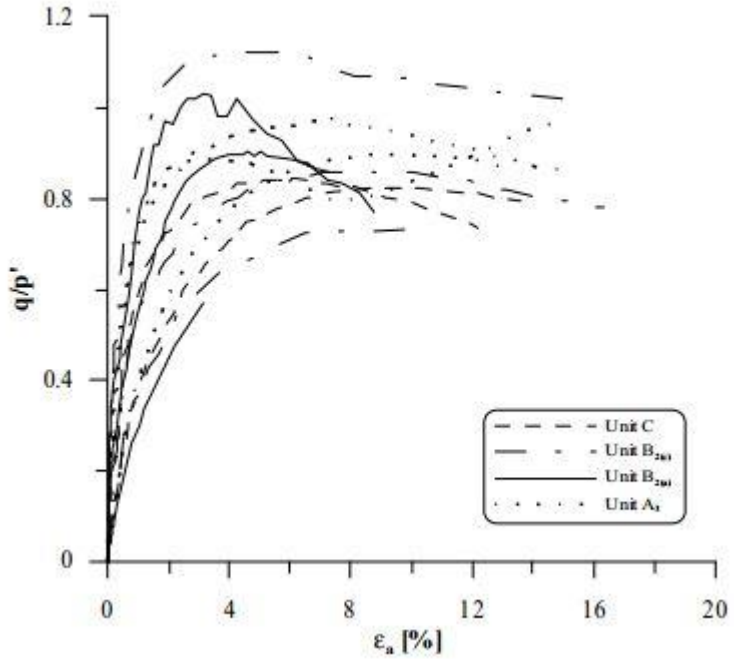

Figure 2.45: Stress ratios for reconstituted samples from different London Clay lithological units after Gasparre (2005)

2.5.4 Factoring the MC, HS and HSS model

One of the most common misinterpretations of EC7 is how to factor the undrained soil strength. When the calculations are carried out assuming total stress conditions, the undrained shear strength, c_u is an input parameter, therefore users are able to simply apply a partial factor equal to 1.4, as the code requires, to the characteristic value. However, when undrained conditions are assumed, using effective stress parameters, the undrained shear strength is not an input parameter but is calculated by the constitutive model. What is usually overlooked during the design is that designers are always required to ensure that the calculated undrained shear strength distribution corresponds to the characteristic one, normally used for SLS, or to the characteristic one, factored by the required value for ULS.

To better understand this, a number of undrained triaxial compression tests were performed with the Plaxis SoilTest, using the Mohr-Coulomb effective stress parameters with a range of angles of shearing resistance, φ'. By trial and error, the required values of the partial factor applied to $\tan\varphi'$, which result in a calculated c_u equal to the characteristic value factored by 1.4, were obtained, for different values of the angle of shearing resistance and plotted in Figure 2.46. This relation, which is independent of the stress level at which the test is performed, enables the designers to use appropriate values of $\gamma_{\tan\varphi'}$ when undrained analysis is performed with effective stress parameters. For example, for the range of values of angle of shearing resistance typically used for London Clay (22 - 25°), using a value of 1.4 for $\gamma_{\tan\varphi'}$ results in an undrained shear strength factored by the about the same value as the code requires. The figure can be used with confidence when the undrained triaxial stress path in the q - p' space is vertical or almost vertical as predicted by the MC or the HS model with p_c = 2000kPa. However, the effect of $\gamma_{\tan\varphi'}$ = 1.4 for non-vertical undrained stress paths as predicted by the HSS model will be further investigated.

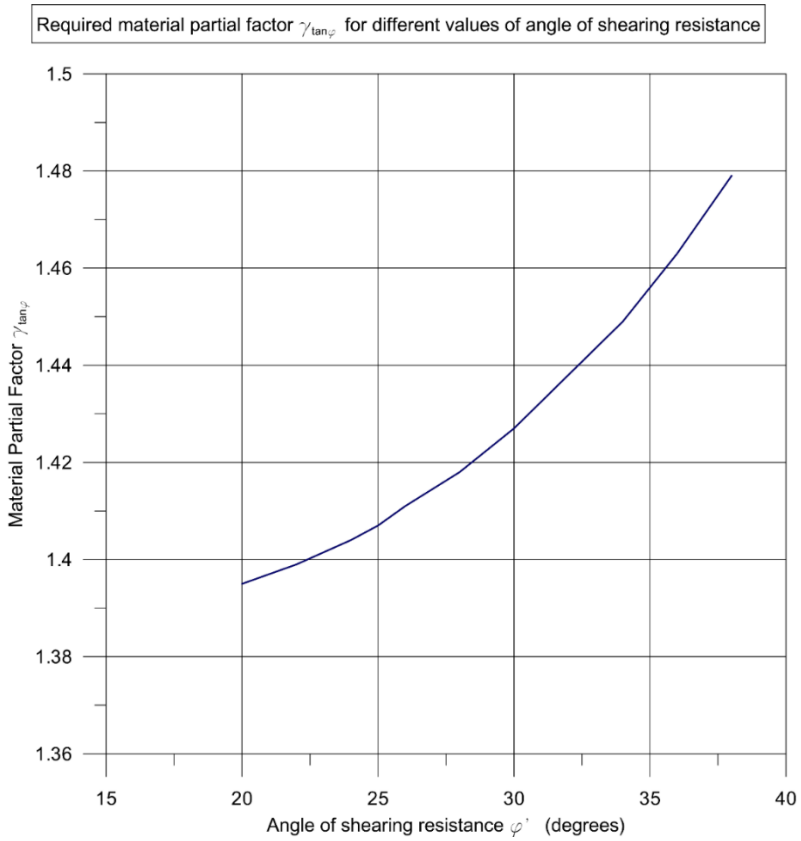

Figure 2.46: Required values of the material partial factor for different angles of shearing resistance

The triaxial undrained compression tests were repeated at different stress levels (corresponding to 0.5, 2, 5, 10, 15, 20, 30 and 40m below the London Clay level) using the MC, HS and HSS effective strength parameters factored by $\gamma_{tan\varphi'} = 1.4$. Again both CAU and CIU triaxial are considered with and without a pre-consolidation pressure of 2000kPa.

In Figures 2.47 and 2.48, the normalised deviatoric stress is plotted against the axial strain for the CAU and CIU triaxial tests respectively. In both cases, the MC, HS and HSS model curves converge to a stress ratio *M* equal to about 0.71 which is less than the corresponding ratio when characteristic (unfactored) effective strength parameters are used.

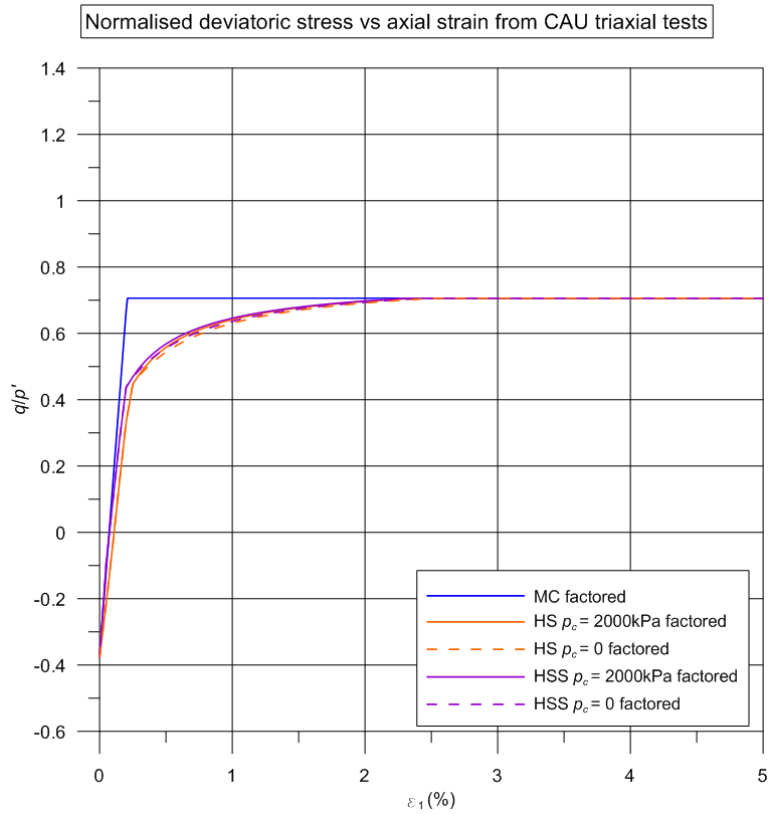

Figure 2.47: Normalised deviatoric stress vs axial strain from CAU triaxial tests at 10m below LC stress level for the factored MC, HS and HSS

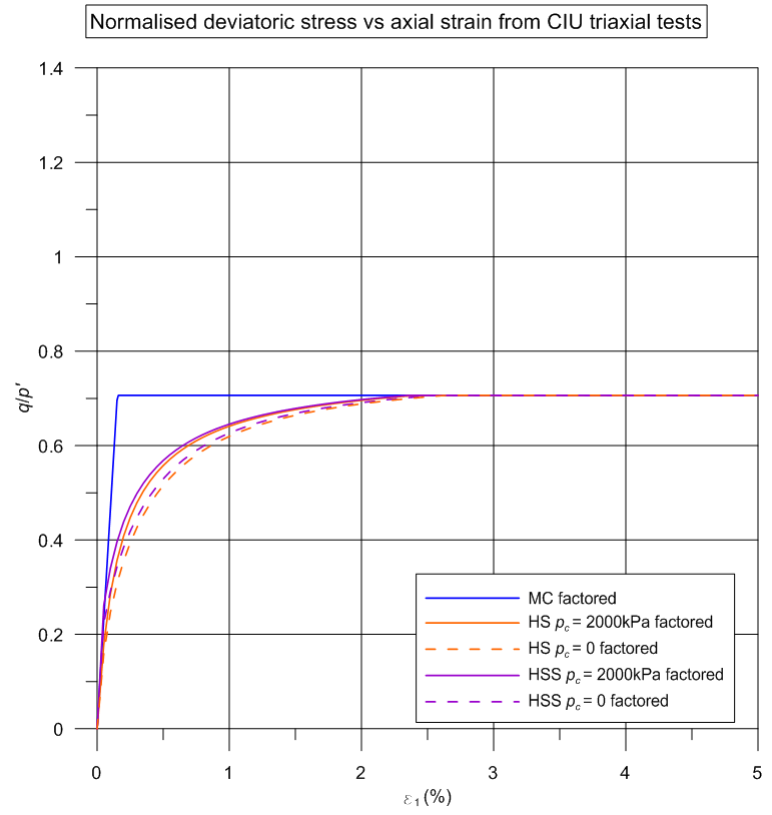

Figure 2.48: Normalised deviatoric stress vs axial strain from CIU triaxial tests at 10m below LC stress level for the factored MC, HS and HSS

In Figure 2.49, the undrained stress paths in the q - p' space are plotted for CAU triaxial tests. The MC stress path is again, as expected, vertical. For p_c = 2000kPa, the HS stress path is also vertical resulting in the same undrained strength, c_u = 94.5kPa. However, the HSS stress path bends slightly to the left, resulting in 4% lower undrained shear strength. For p_c = 0, both the HS and HSS stress paths bend to the left with the HSS resulting in about 3.5% lower undrained shear strength. Overall, it is interesting to note that all stress paths finally reach the same failure line meaning that a factor of 1.4 on tanφ' results in undrained shear strength factored by about 1.4 for all models.

Similarly, in Figure 2.50, the undrained stress paths in the q - p' space are plotted for triaxial tests following isotropic consolidation for p_c = 0 and 2000kPa. Again it can be seen that the MC and the HS for p_c = 2000kPa stress paths are both vertical resulting in c_u = 106kPa, while the HSS results in about 5% lower undrained shear strength. For p_c = 0, both the HS and HSS stress paths again bend to the left with the HSS resulting in about 4% lower undrained strength than the HS.

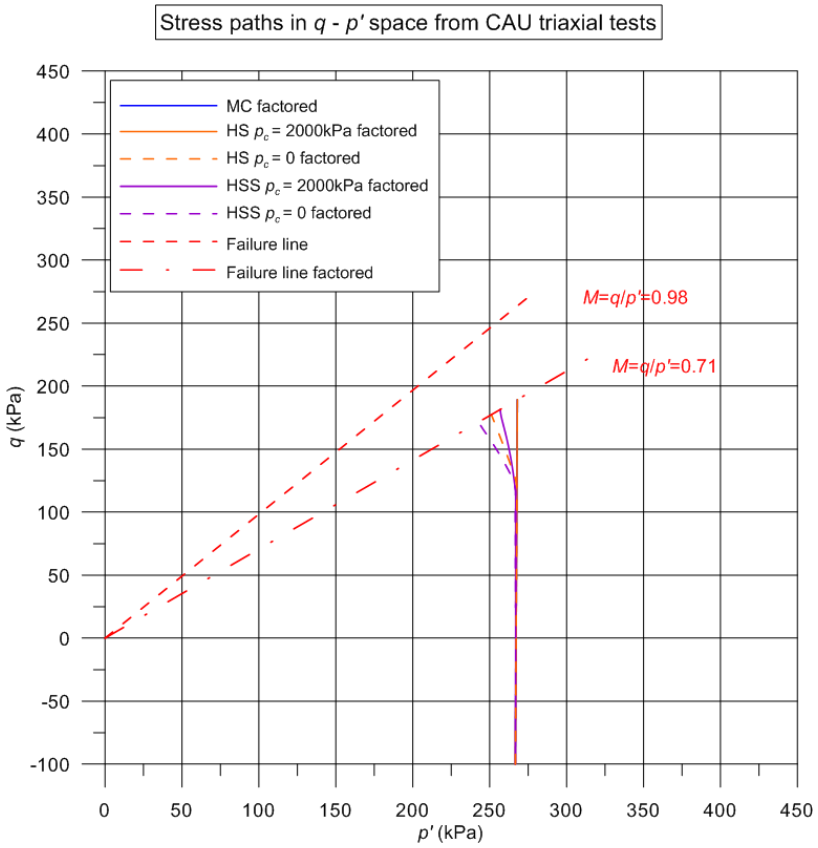

Figure 2.49: Stress paths in q - p' space from CAU triaxial tests at 10m below LC stress level for the factored MC, HS and HSS

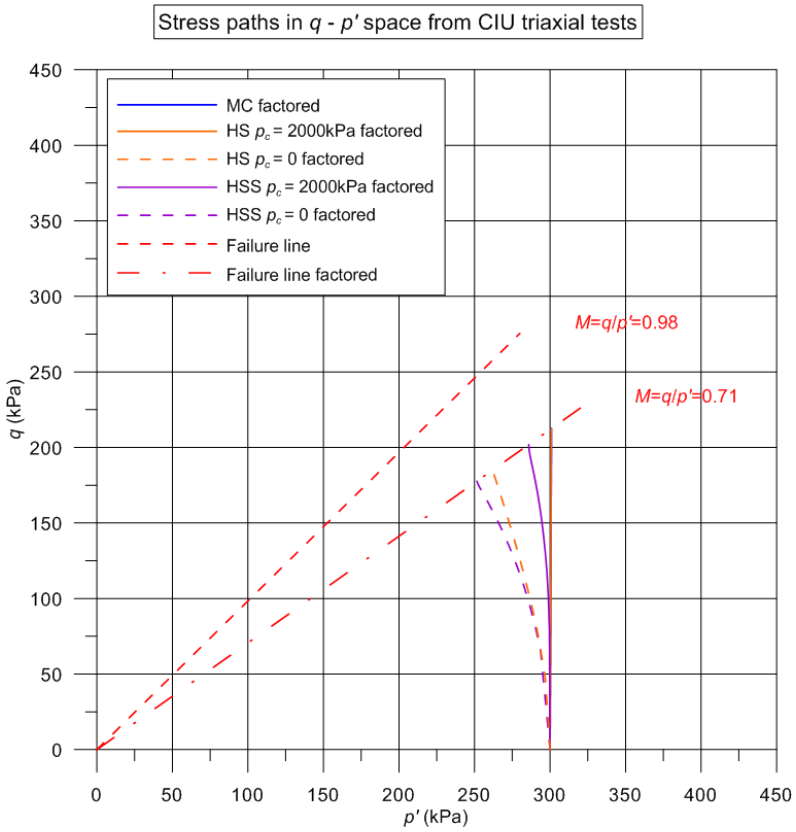

Figure 2.50: Stress paths in q - p' space from CIU triaxial tests at 10m below LC stress level for the factored MC, HS and HSS

The excess pore water pressure generated during the CAU triaxial test is plotted against the axial strain in Figure 2.51. It can be seen that the MC and HS model for p_c = 2000kPa result in similar excess pore water pressure equal to about 95kPa while the HSS predicts a 9% higher pressure. For p_c = 0, the calculated excess pore water pressure is 108kPa and 114kPa for the HS and HSS respectively. For isotropic consolidation, the MC and HS for p_c = 2000kPa result in u_{excess} = 70, while the HSS for p_c = 2000kPa predicts u_{excess} = 81.5kPa, as shown in Figure 2.52. For p_c = 0, the excess pore water pressure is 100kPa and 108kPa for the HS and HSS respectively.

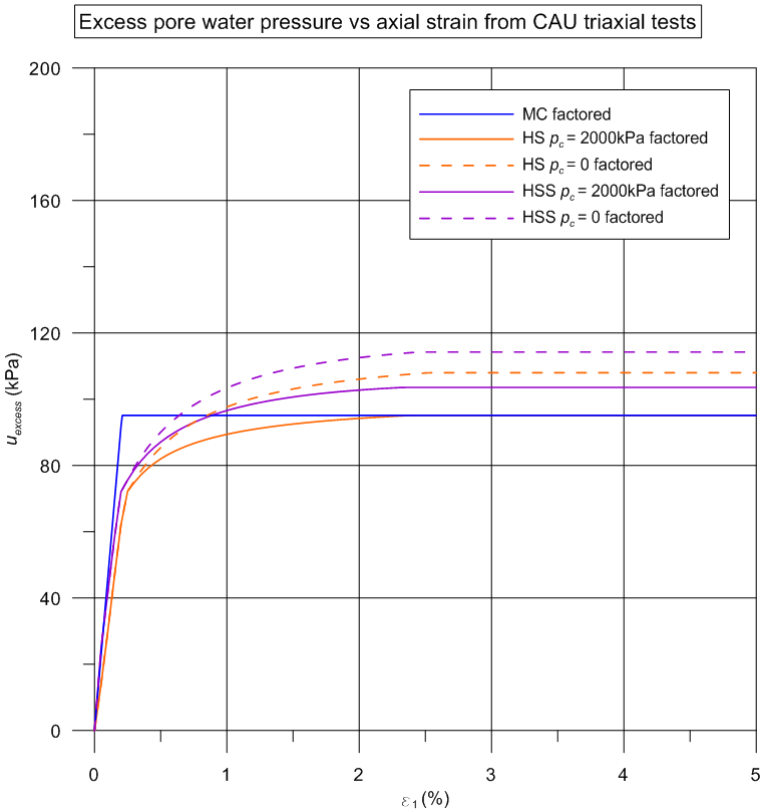

Figure 2.51: Excess pore water pressure vs axial strain from CAU triaxial tests at 10m below LC stress level for the factored MC, HS and HSS

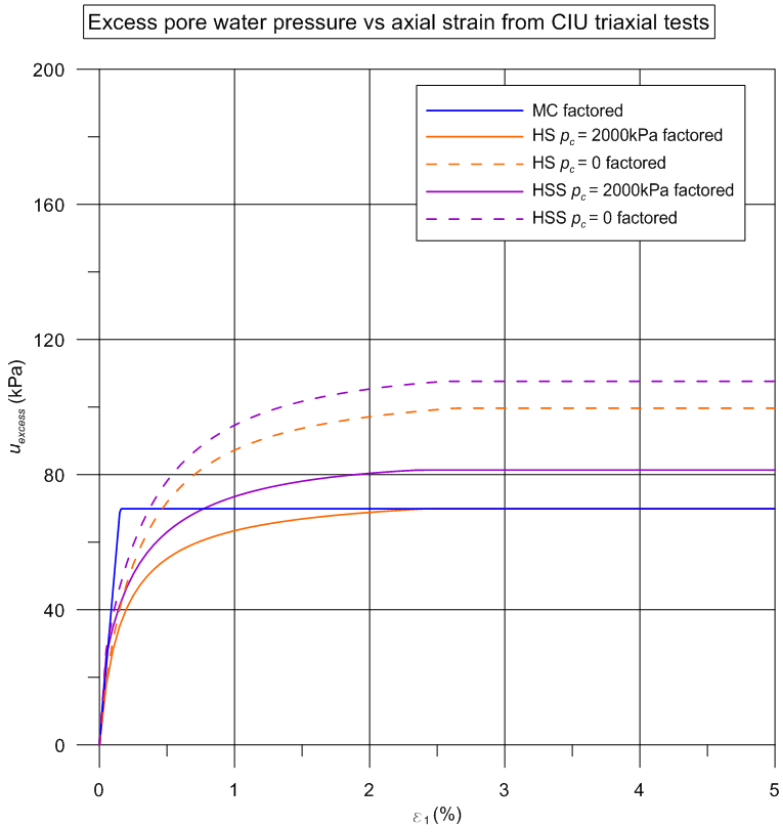

Figure 2.52: Excess pore water pressure vs axial strain from CIU triaxial tests at 10m below LC stress level for the factored MC, HS and HSS

Moreover, the Skempton's parameter A, is plotted against the axial strain in Figure 2.53 for the CAU tests where it can be seen that A is equal to 0.33 for the MC and HS model and 0.37 for the HSS model for p_c = 2000kPa. For p_c = 0, A is equal to 0.39 and 0.42 for the HS and HSS model respectively. Similarly, the parameter A is plotted in Figure 2.54 for the CIU tests where A reaches a value of 0.33, for the MC and HS model and 0.4 for the HSS model for p_c = 2000kPa. For p_c = 0, A is equal to 0.54 and 0.61 for the HS and HSS model respectively. In all cases, the HSS results in higher A values than the MC and HS model.

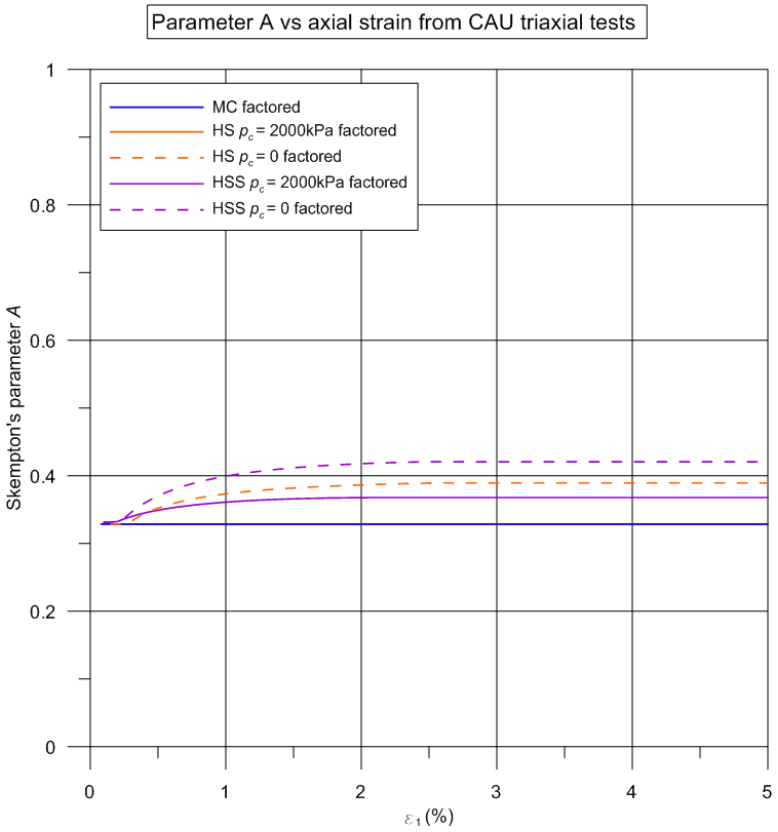

Figure 2.53: Skempton's parameter A vs axial strain from CAU triaxial tests at 10m below LC stress level for the factored MC, HS and HSS

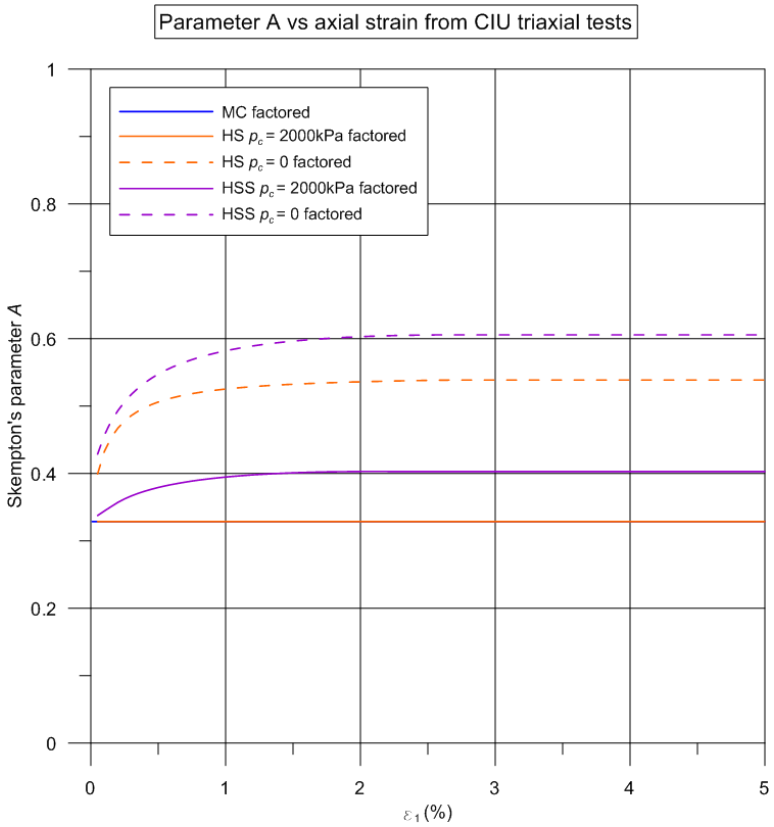

Figure 2.54: Skempton's parameter A vs axial strain from CIU triaxial tests at 10m below LC stress level for the factored MC, HS and HSS

In Figure 2.55, the undrained shear strength profiles for London Clay, calculated from the CAU triaxial compression tests, are shown as dashed lines for the MC, HS and HSS model with effective strength parameters factored by $\gamma_{tan\varphi'} = 1.4$. The red dashed line corresponds to the c_u profile used for total stress analysis factored by 1.4. Overall, for the MC and HS model, a partial factor on the undrained shear strength equal to 1.4 is achieved at all stress levels while the HSS model resulted in an average partial factor of 1.37 which is very close to the value of 1.4 required by EC7. Similarly, in Figure 2.56, the undrained shear strength profiles calculated from the CIU triaxial compression tests are plotted for all models with effective strength parameters factored by $\gamma_{tan\varphi'} = 1.4$. Again, a partial factor on the undrained shear strength equal to 1.4 is achieved for the MC and HS models and about 1.38 for the HSS model.

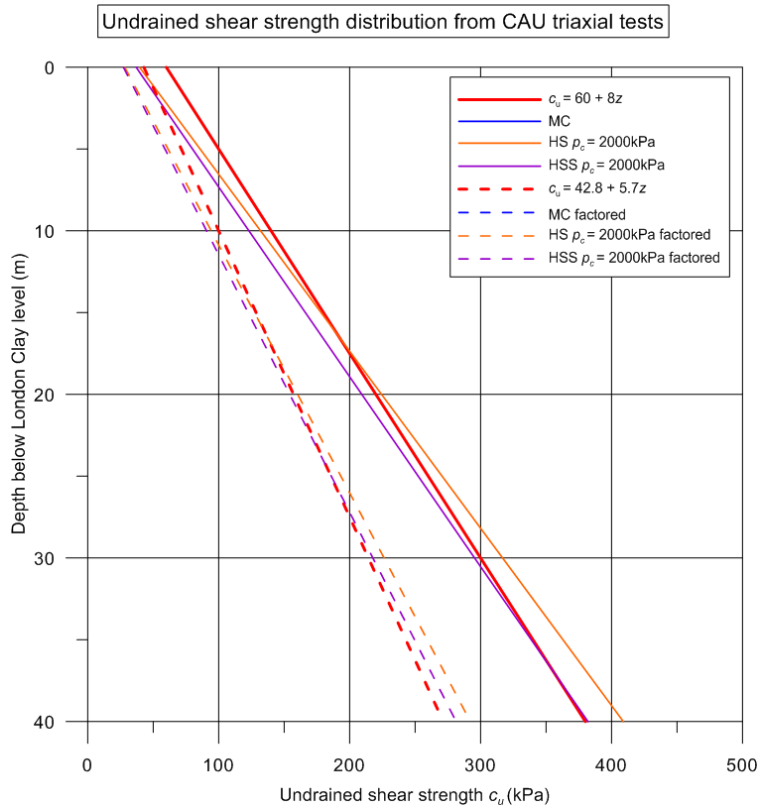

Figure 2.55: Characteristic and factored undrained shear strength profile from CAU triaxial tests for the MC, HS and HSS

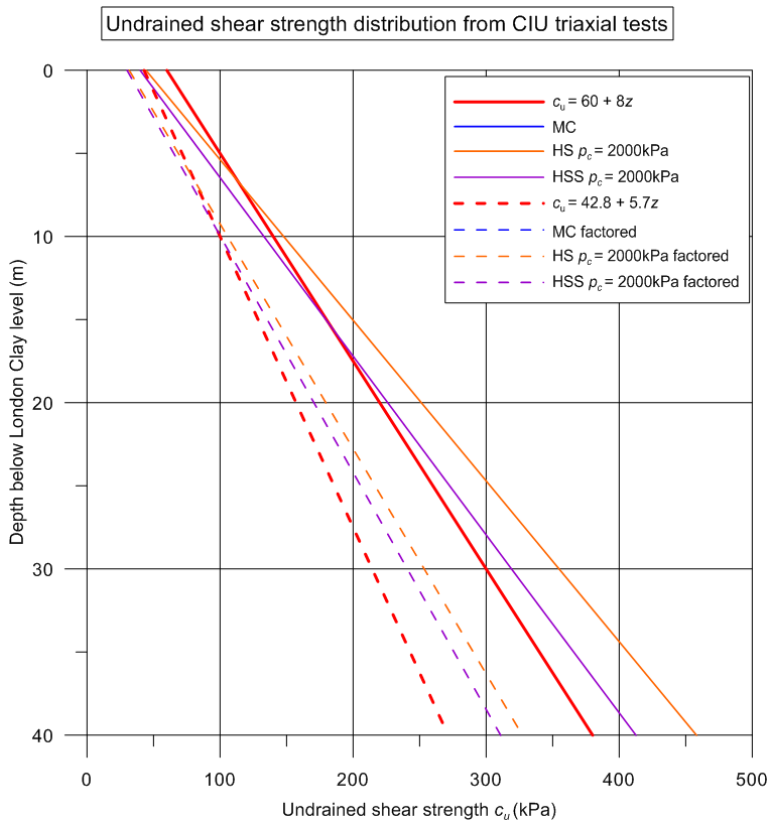

Figure 2.56: Characteristic and factored undrained shear strength profile from CIU triaxial tests for the MC, HS and HSS

As mentioned before, for $c' = 0$, the HS and HSS soil stiffness parameters depend on the stress level but not on the effective strength parameters. For ULS design, this has the benefit that the soil stiffness does not change when the soil strength is factored which is consistent with the EC7 requirements. However, for even small values of cohesion, the soil stiffness reduces when partial factors are applied to the effective strength parameters. For example, for a material with c' = 5 and $\varphi' = 25°$, when a partial factor of 1.4 is applied for undrained conditions, the unloading/reloading Young's modulus, E_{ur} *as* calculated from Equation 2.5, reduces by 27%, 32% and 34% at 10, 20 and 30m below the top of London Clay respectively. Similarly, when a material partial factor of 1.25 is applied for drained conditions, E_{ur} reduces by 33%, 39% and 42% at 10, 20 and 30m below the top of London Clay respectively. Factoring the soil strength affects in the same way the rest of the HS and HSS stiffness parameters so designers should be aware of this effect, usually overlooked when performing ULS analysis for a material with non-zero cohesion.

2.6 BRICK model parameters for London Clay

2.6.1 Characteristic BRICK parameters

The parameters for the BRICK model are based on those given by Pillai (1996), who revised the original set of parameters determined by Simpson (1992). More specifically, Pillai (1996) compared the predictions of the model, using the original parameters, with laboratory data from two case studies: the Heathrow Express trial tunnel and the British Library on Euston Road. The author observing that the model under-predicted the shear modulus in the small strain range, revised the string lengths and achieved a better match for the behaviour of London Clay at small strains. This new set of parameters has been successfully used for modelling the complex behaviour of London Clay for two decades. The BRICK model parameters and the material proportions, R_b and string lengths, L_b, are listed in Table 2.3.

Table 2.3: BRICK model parameters for London Clay (Pillai, 1996).

R_b	L_b
0.00003	0.92
0.000061	0.75
0.000101	0.53
0.000121	0.29
0.00082	0.13
0.00171	0.075
0.00352	0.044
0.00969	0.017
0.02223	0.0035
0.0646	0
Model parameters	
λ	0.1
κ	0.02
$\imath$	0.0019
v	0.2
μ	1.3
β^G	4
β^φ	3

The resulting S-shaped stiffness curve is plotted in Figure 2.57, shown as solid red line, based on the blue discrete lines defined by the material proportions and string lengths.

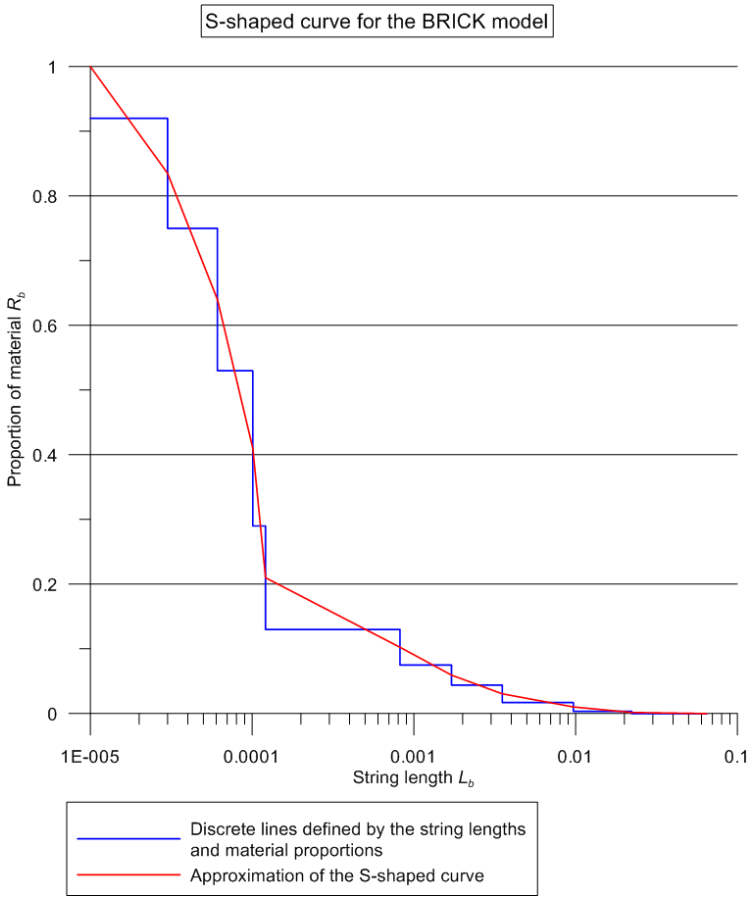

Figure 2.57: Approximated input S-shaped curve for the BRICK

The BRICK Test program which is briefly described in Appendix A, has been widely used in the past two decades within Arup Geotechnics to compute the stress paths under various loading conditions, similarly to Plaxis SoilTest. In this section, the stress paths are calculated from triaxial compression tests using both the BRICK Test program and the PLAXIS SoilTest and the BRICK model parameters listed in Table 2.3. The comparison is necessary because there is no previous experience of using a user-defined soil model such as the BRICK with Plaxis SoilTest. Moreover, this will enable consistent comparisons with the triaxial results for the MC, HS and HSS models as the BRICK Test program gives no information on the excess pore water pressures generated during shearing.

In all cases, a pre-consolidation pressure of 2000kPa is assumed to account for 200m overburden. The simplified soil profile is the same as described before for the rest of the models and hence the total vertical stress and pore water pressure values that correspond to each depth are the same as shown in Figure 2.26. Note that, only CAU triaxial compression tests were considered because as discussed before K_0 is not an input in the BRICK model but is generated based on the geological history of the material.

The results of the runs were post-processed on a spreadsheet and the stress paths in the *q* - *p'* space from the CAU triaxial test at a stress level corresponding to 10m below London Clay are presented in Figure 2.58. It can be seen that the stress path predicted from the BRICK Test program and the Plaxis SoilTest are similar. In Figure 2.59, the normalised deviatoric stress is plotted against the principal axial strain from CAU triaxial test at a stress level corresponding to 10m below London Clay. It can be seen that the BRICK curve finally converges to the same stress ratio *M* equal to about 0.98.

In Figure 2.60, the calculated undrained stress paths in the *q* – *p'* space are plotted from CAU triaxial tests. As the initial stress state before shearing is calculated by the BRICK model based on the modelled geological history, the resulting K_0 is about 1.65 and hence the shearing stress path is to the right of the MC, HS and HSS paths. Moreover, the BRICK stress path bends to the right (i.e. the mean effective stress increases during shearing) resulting in higher deviatoric stress at failure and hence higher undrained shear strength. More specifically, the BRICK stress path results in 35% higher undrained shear strength than the MC and HS and 50% higher than the HSS.

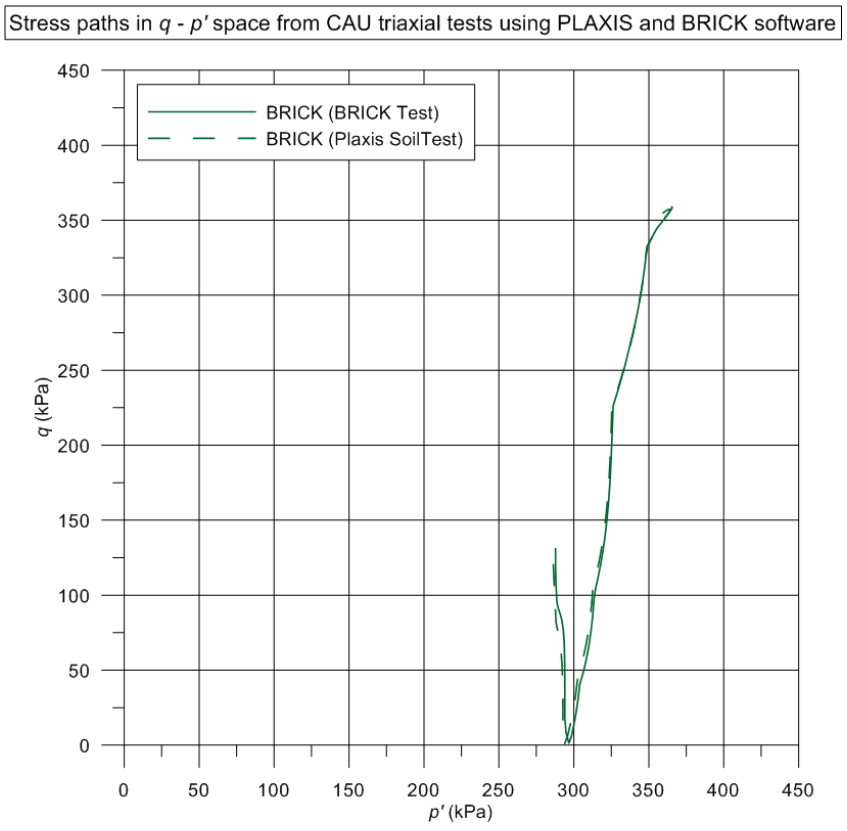

Figure 2.58: Stress paths in q - p' space from CAU triaxial tests at 10m below LC stress level for the BRICK using PLAXIS SoilTest and BRICK Test

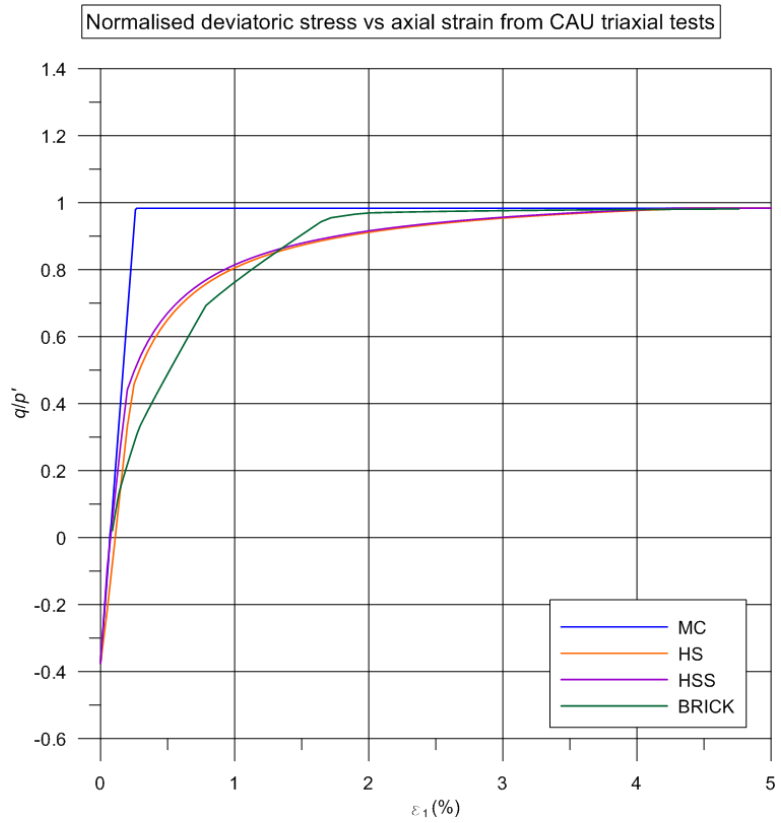

Figure 2.59: Normalised deviatoric stress vs axial strain from CAU triaxial tests at 10m below LC stress level for the MC, HS, HSS and BRICK

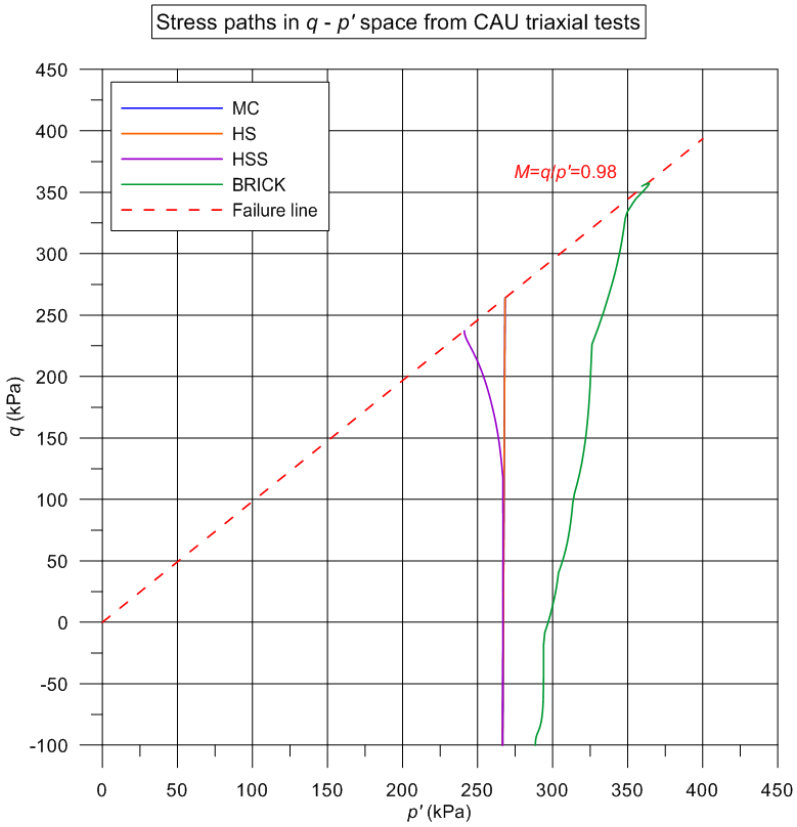

Figure 2.60: Stress paths in q - p' space from CAU triaxial tests at 10m below LC stress level for the MC, HS, HSS and BRICK

The excess pore water pressure generated during the CAU triaxial test is plotted against the axial strain in Figure 2.61. It can be seen that the BRICK model results in 20% lower excess pore water pressure than the MC and HS model and 30% lower than the HSS model. Moreover, the Skempton's parameter A is plotted against the axial strain in Figure 2.62, where it is shown that for the BRICK model, A reaches a final value of 0.19 which is significantly lower than the value predicted by the rest of the soil models. Moreover, the K_w/n ratio is 11,792MPa while the volumetric strain predicted by the model (for the same Poisson's ratio of 0.495 for undrained conditions) is 0.0008% which is again insignificant and even lower than the volumetric strain calculated by the rest of the models.

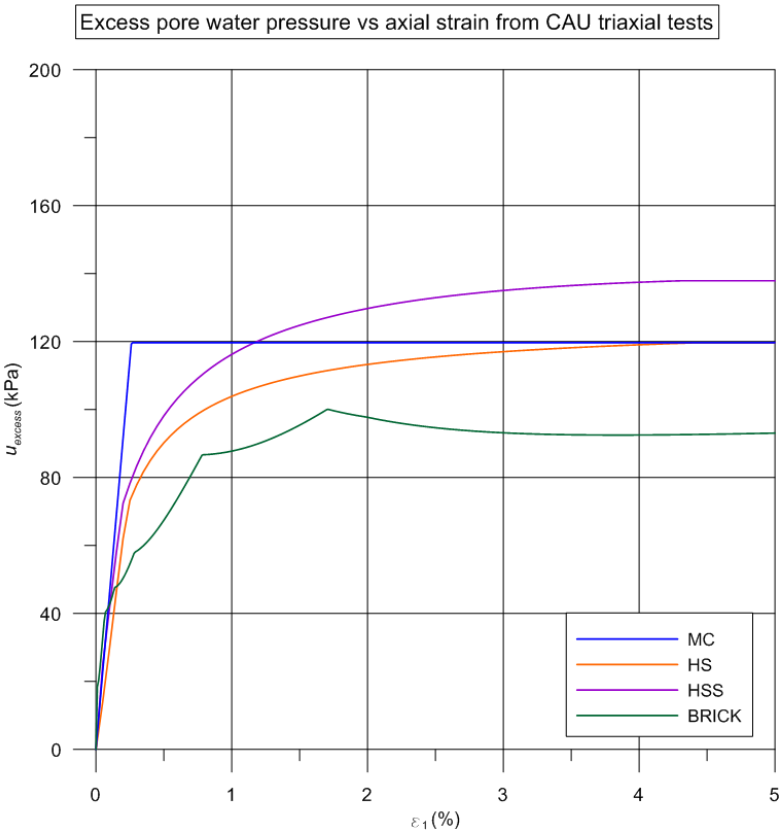

Figure 2.61: Excess pore water pressure vs axial strain from CAU triaxial tests at 10m below LC stress level for the MC, HS, HSS and BRICK

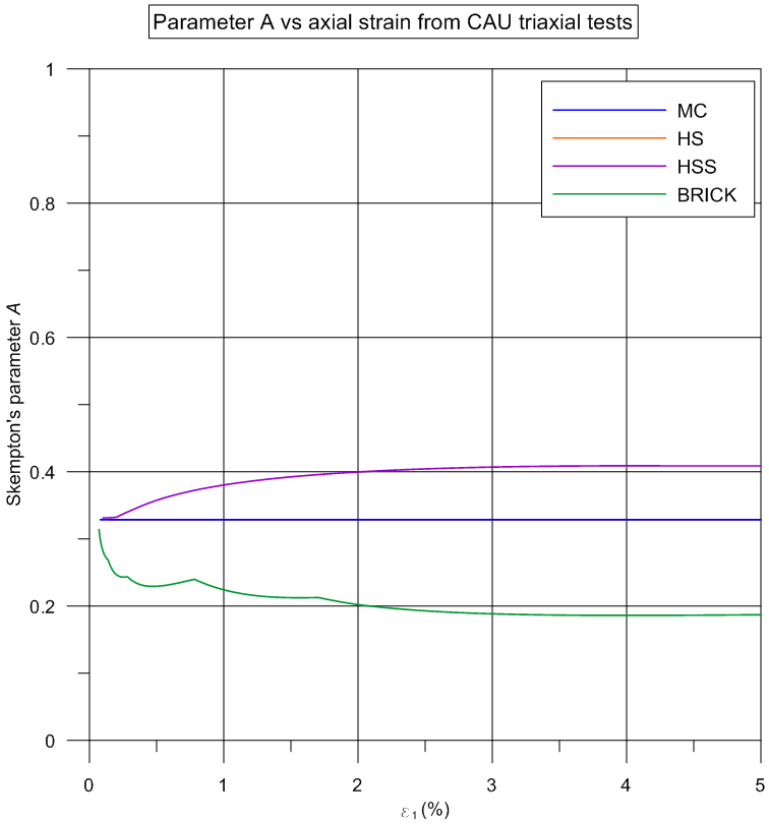

Figure 2.62: Skempton's parameter A vs axial strain from CAU triaxial tests at 10m below LC stress level for the MC, HS, HSS and BRICK

The stress paths in the q - p' space, obtained from the CAU triaxial tests, are shown in Figure 2.63 for the BRICK model for all the stress levels considered in this study. It can be seen that while the stress paths have the same shape, the final stress ratio at failure varies with depth. While the MC, HS and HSS models show a failure line that is constant and independent of the stress level (red dashed line for M = 0.98), the BRICK model has a higher M value for shallow depths and lower value for higher depths. This is also shown in Figure 2.64, where the normalised deviatoric stress is plotted against the axial strain showing that the final stress ratio varies from 1.15 to 0.85. This in principle means that the angle of shearing resistance, which relates to M, as shown in Equation 2.31, also varies with depth. This is attributed, as discussed previously, to the effect of the parameter χ^{φ} which modifies the area under the shear modulus degradation curve and hence the soil strength based on the state of over-consolidation of the material.

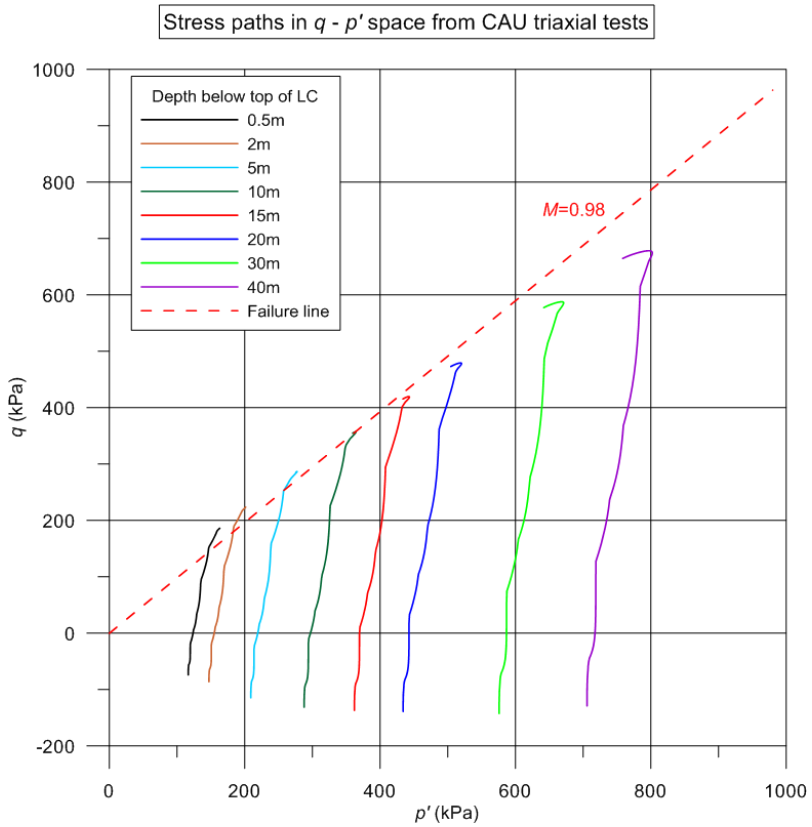

Figure 2.63: Stress paths in the q - p' space from CAU triaxial tests for the BRICK

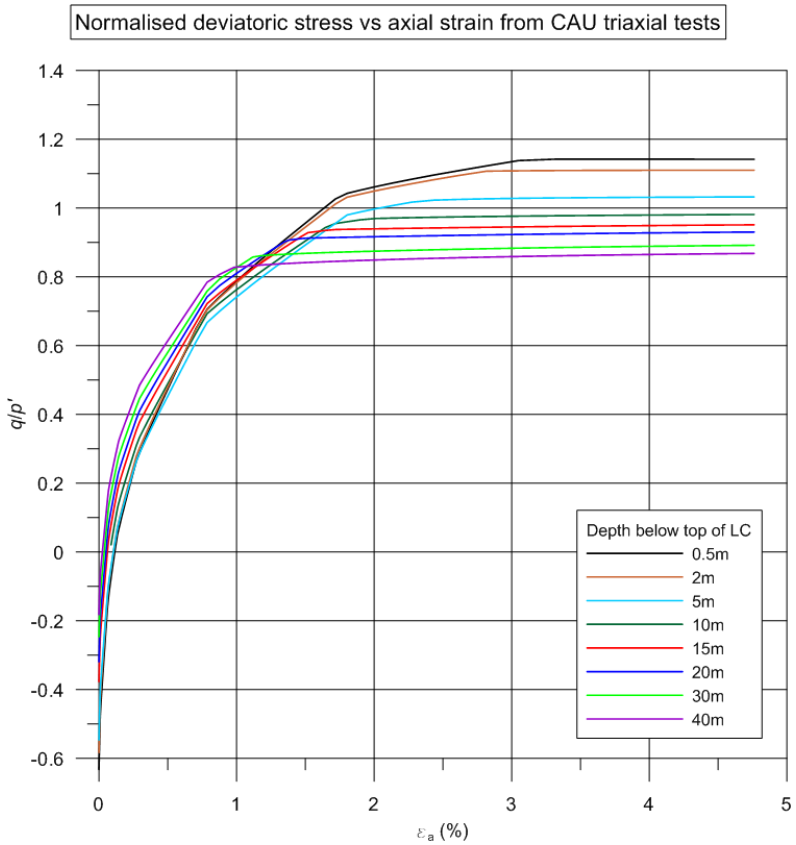

Figure 2.64: Normalised deviatoric stress vs axial strain from CAU triaxial tests for the BRICK

The stiffness degradation curves for the BRICK parameters are plotted in Figure 2.65 for all stress levels. It can be seen that different curves are predicted for different stress levels, with higher elastic stiffness values predicted for shallow depths than for deeper depths. This is attributed to the effect of the parameter χ^G which modifies the elastic soil stiffness based on the state of over-consolidation of the material.

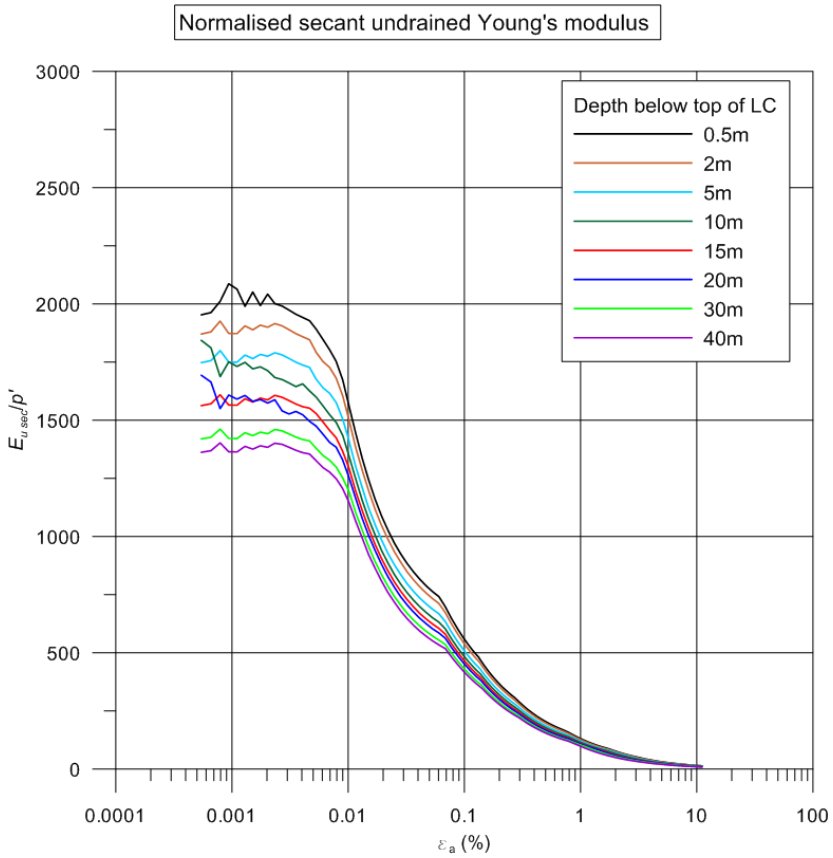

Figure 2.65: Normalised secant undrained Young's modulus vs axial strain from CAU triaxial tests for the BRICK

2.6.2 Factoring BRICK

A new set of material proportions and string lengths has been derived in order to obtain undrained strength results equal to the characteristic strength reduced by a factor of 1.4, as required by EC7. The new set is presented in Table 2.4 where it can be seen that the values of the material proportions for the first six rows are the same as the characteristic values listed in Table 2.3. However, for the last 4 rows, the values of the material proportions are reduced, resulting in an S-shaped soil stiffness degradation curve chopped in the large strain area. The rest of the BRICK model parameters, as given in Table 2.3, remain the same apart from the parameter β^G which is reduced from 4 to 3.5. The reason for this will be explained in more detail later.

Table 2.4: Model parameters for the factored BRICK

R_b	L_b
0.00003	0.92
0.000061	0.75
0.000101	0.53
0.000121	0.29
0.00082	0.13
0.00171	0.075
0.00352	0.044
0.0045	0.017
0.0085	0.0035
0.025	0
Model parameters	
λ	0.1
κ	0.02
ι	0.0019
v	0.2
μ	1.3
β^G	3.5
β^φ	3

The resulting curve is plotted in Figure 2.66 where it can be noted that the curve is reduced in large strains when compared with the curve corresponding to the characteristic BRICK parameters. As mentioned before, the area defined within the S-shaped curve directly relates to the soil strength. Hence, by reducing the material proportions in the large strain area, the area within the curve and hence the corresponding soil strength reduces. Although there are many different ways to reduce the area within the stiffness degradation curve and hence many different combinations of material proportions and string lengths that can result in undrained strength equal to the characteristic undrained strength reduced by 1.4, this approach has the advantage of minimising the effect on the soil stiffness.

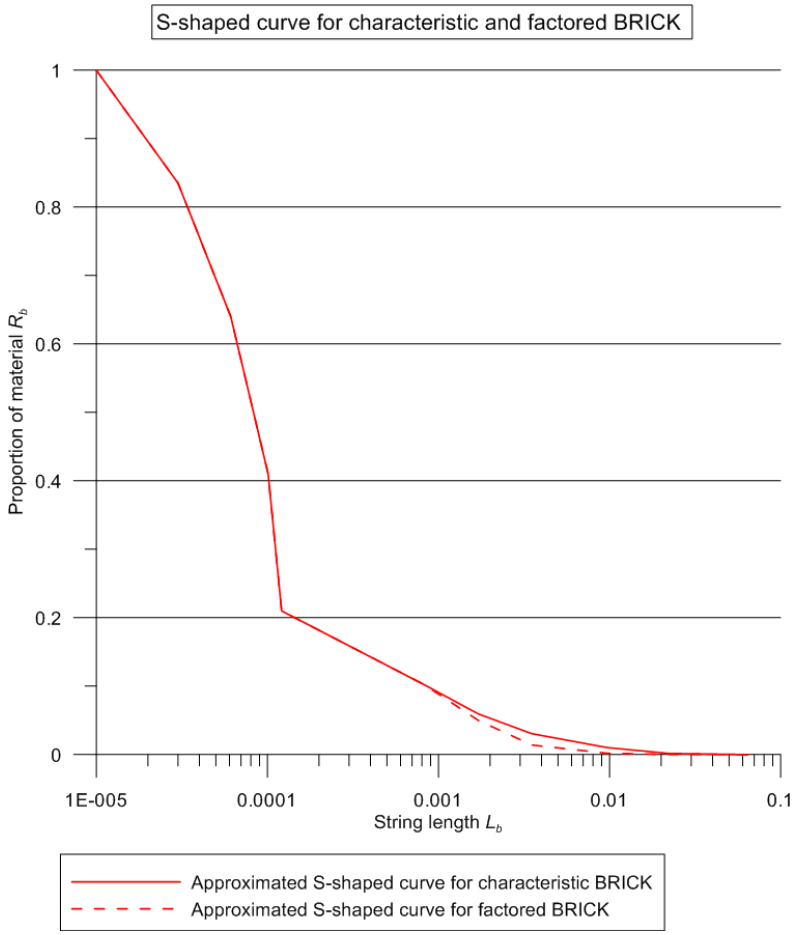

Figure 2.66: Approximated S-shaped input curve for the factored BRICK

In this section, the results from the CAU triaxial tests performed with the BRICK Test and Plaxis SoilTest using the factored BRICK parameters at different stress levels are presented. In Figure 2.67, the normalised deviatoric stress is plotted against the principal axial strain from CAU triaxial test at a stress level corresponding to 10m below London Clay. It can be seen that the BRICK curve finally converges to a stress ratio *M* equal to 0.69. In Figure 2.68, the undrained stress paths is plotted in the *q – p'* stress space are plotted from CAU triaxial tests. It shows that the BRICK stress path bends to the right resulting in 29% higher undrained shear strength than the MC and HS model and 35% higher than the HSS model.

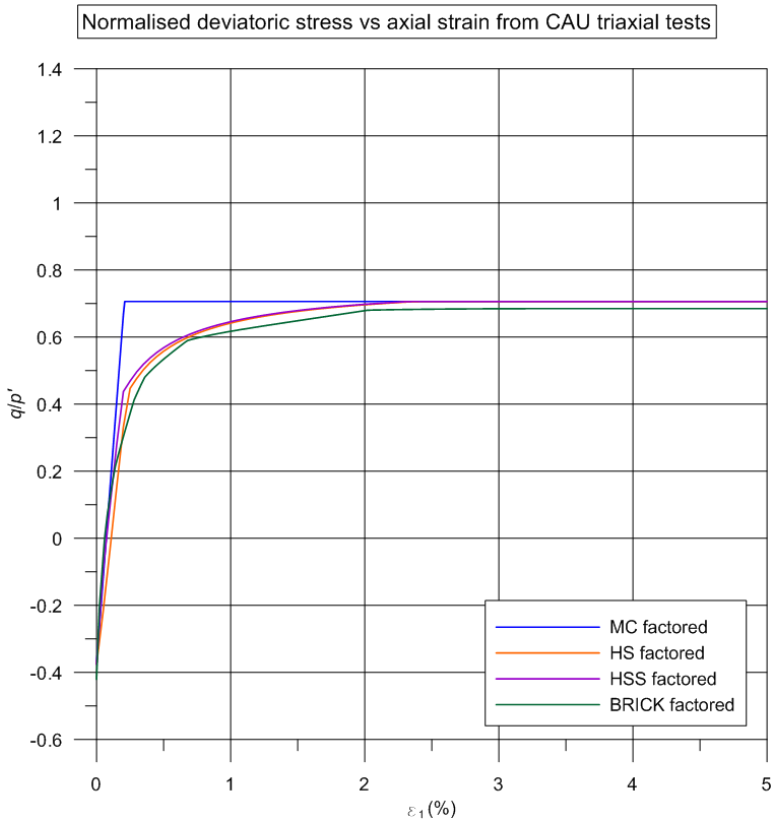

Figure 2.67: Normalised deviatoric stress vs axial strain from CAU triaxial tests at 10m below LC stress level for the factored MC, HS, HSS and BRICK

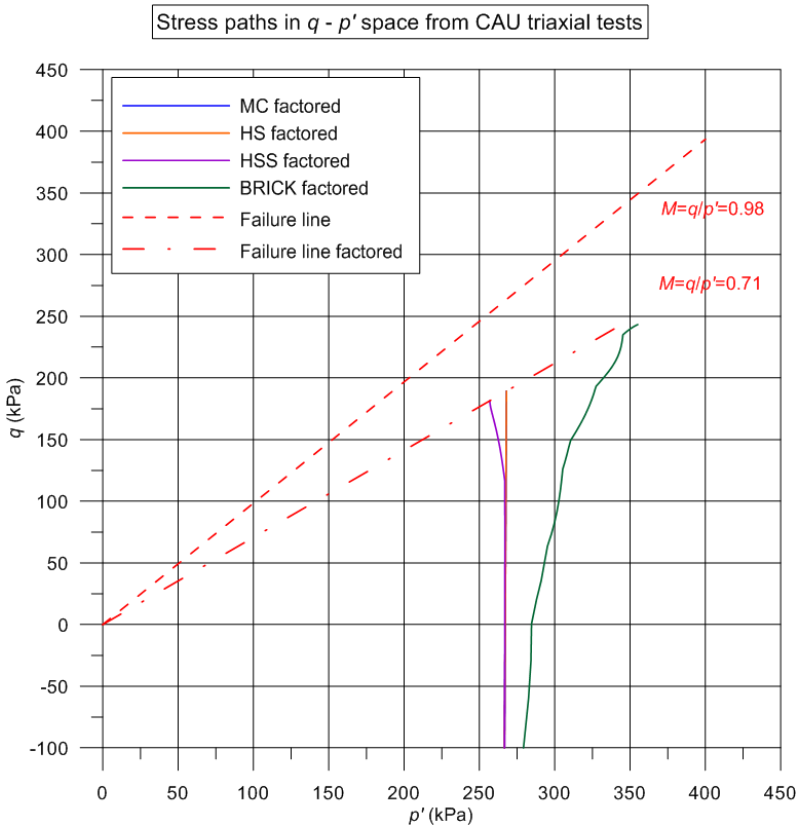

Figure 2.68: Stress paths in q - p' space from CAU triaxial tests at 10m below LC stress level for the factored MC, HS, HSS and BRICK

The excess pore water pressure generated during shearing is plotted against the axial strain in Figure 2.69. It can be seen that the BRICK model results in 40% lower excess pore water pressure than the MC and HS model and 46% lower than the HSS model. The Skempton's parameter A is plotted against the axial strain in Figure 2.70 where it is noted that A reaches a final value of about 0.15 for the BRICK model which is lower than the values predicted by the rest of the models.

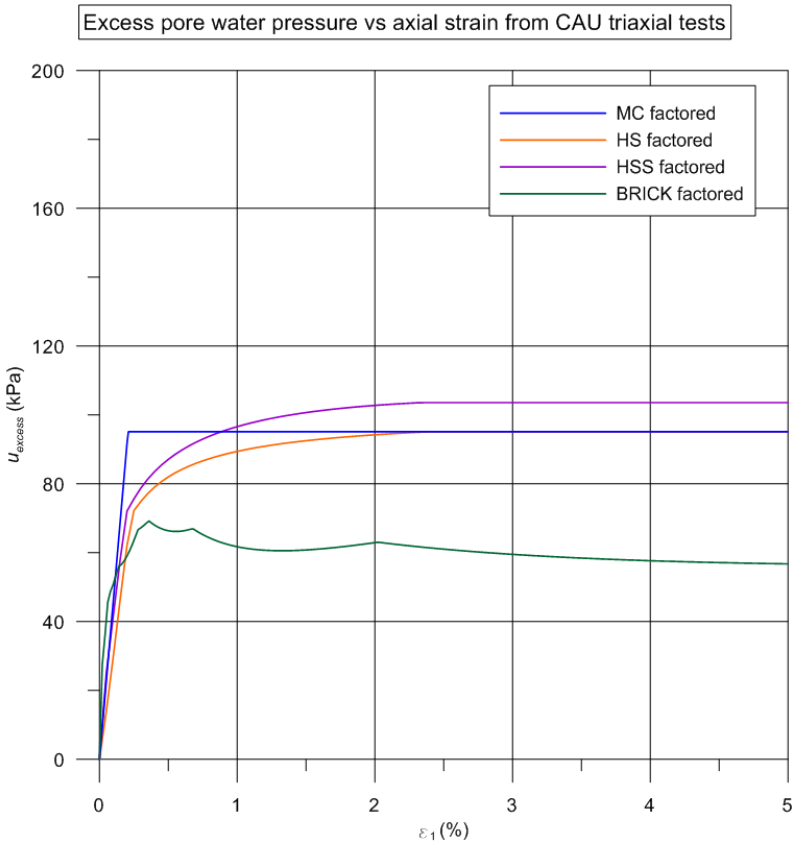

Figure 2.69: Excess pore water pressure vs axial strain from CAU triaxial tests at 10m below LC stress level for the factored MC, HS, HSS and BRICK

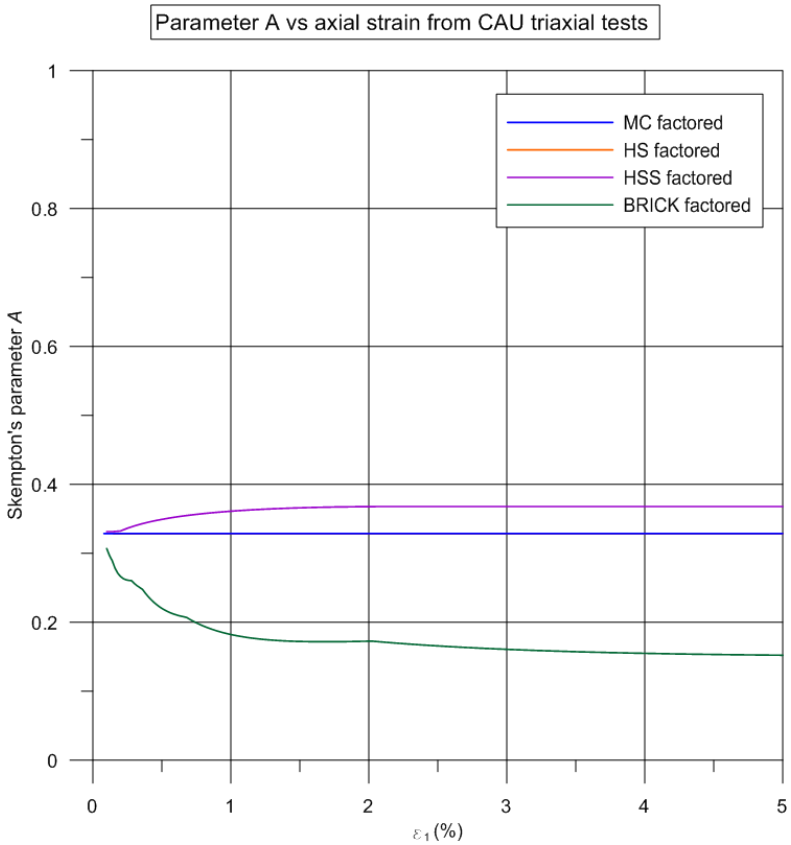

Figure 2.70: Skempton's parameter A vs axial strain from CAU triaxial tests at 10m below LC stress level for the factored MC, HS, HSS and BRICK

The stress paths of all the CAU triaxial tests are plotted in *q* - *p'* space and shown in Figure 2.71 for the factored BRICK model. It can be seen again that the final stress ratio at failure varies with depth. While for the factored MC, HS and HSS models, the failure line for *M* = 0.71, shown as red dashed line, is independent of the stress level, the stress ratio M and hence the angle of shearing resistance depends on the state of over-consolidation for the factored BRICK model. This over-consolidation effect is also illustrated in Figure 2.72, where the normalised deviatoric stress is plotted against the axial strain for the factored BRICK parameters. In Figure 2.73, the normalised deviatoric stress is plotted against the axial strain only at 10m below London Clay stress level for both the characteristic and factored BRICK model.

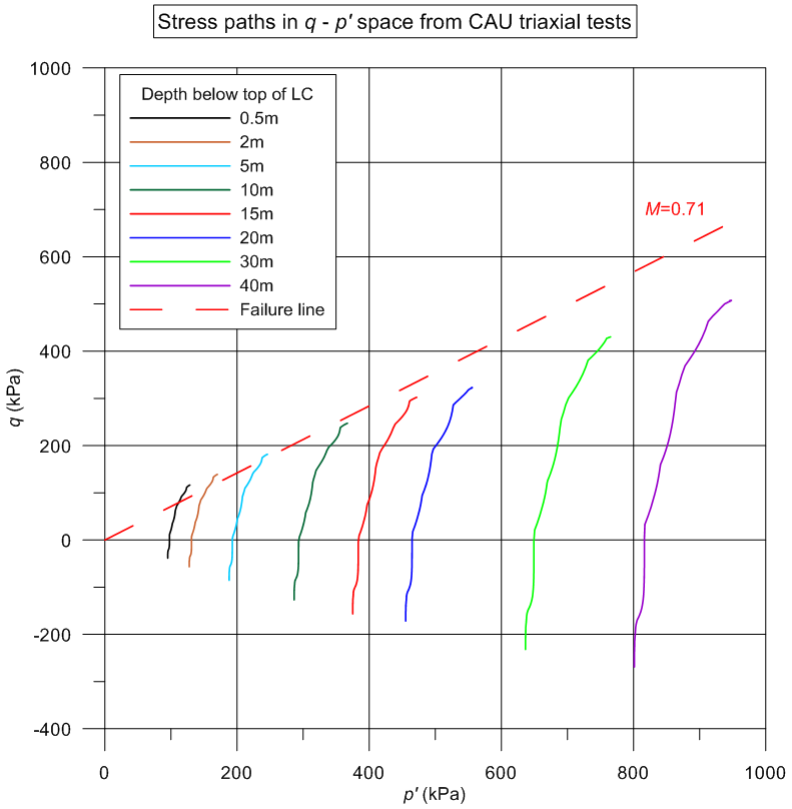

Figure 2.71: Stress paths in the q - p' space from CAU triaxial tests for the factored BRICK

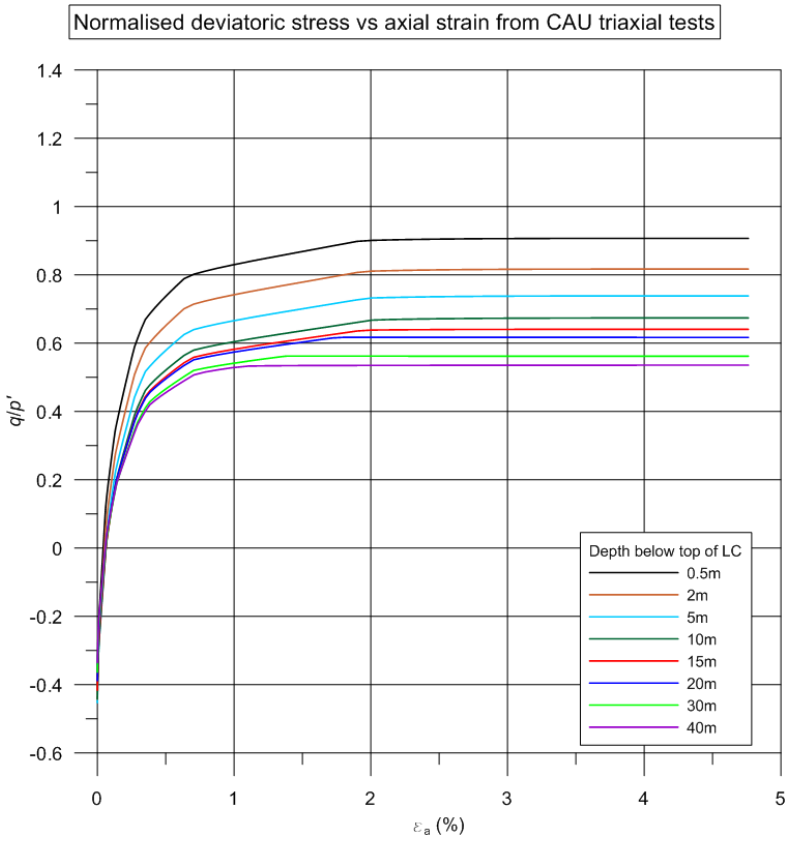

Figure 2.72: Normalised deviatoric stress vs axial strain from CAU triaxial tests for the factored BRICK

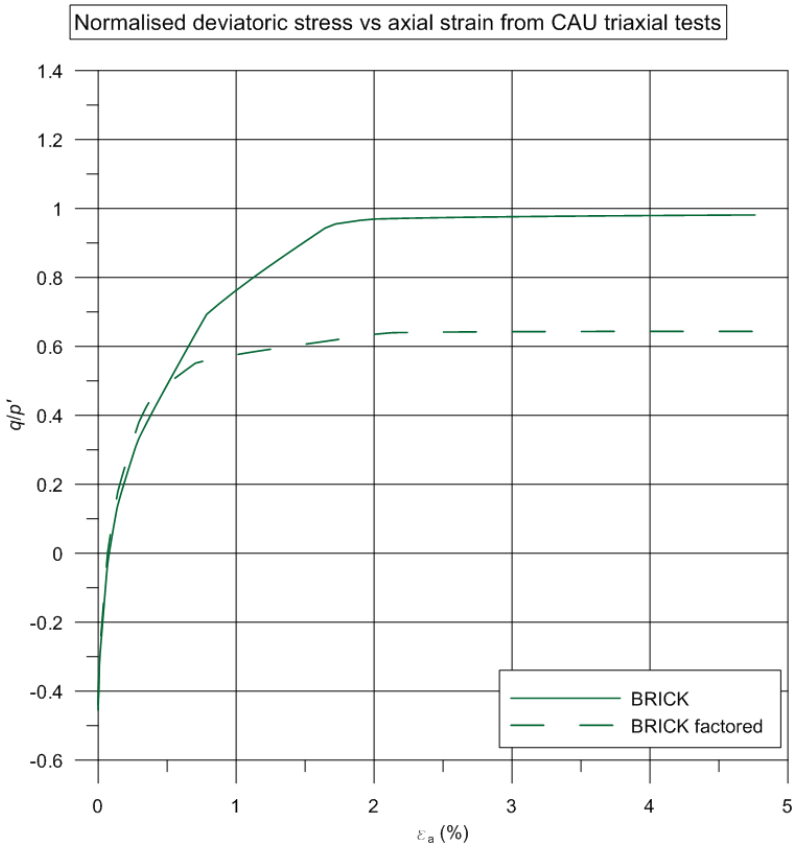

Figure 2.73: Normalised deviatoric stress vs axial strain from CAU triaxial tests at 10m below London Clay stress level for the BRICK

The stiffness degradation curves for the factored BRICK parameters with β_G equal to 4 are plotted for all stress levels in Figure 2.74. It can be seen that the initial height of the curve is different for different depths and hence different states of over-consolidation due to the effect of the parameter χ^G. When compared to the corresponding curves for the characteristic BRICK parameters with $\beta_G = 4$, shown in Figure 2.65, it is noted that there is an increase in the soil stiffness especially in the small strain range The effect is more apparent for shallow depths where the over-consolidation ratio is higher. For this reason, the parameter β_G needs to be slightly reduced to improve the match between the curves for the characteristic and factored BRICK parameters. The stiffness degradation curves for the factored BRICK parameters and $\beta_G = 3.5$ are plotted in Figure 2.75 where it can be seen that the curves are now almost identical to the curves in Figure 2.65. To better illustrate this, in Figure 2.76, the normalised secant undrained Young's modulus, is plotted against the axial strain only for the stress level that corresponds to 10m below the top of London Clay. It is clear that when β_G reduces from 4 to 3.5 for the factored BRICK, there is little difference with the curve corresponding to the characteristic BRICK parameters. This satisfies the EC7 requirement that only the soil strength needs to be factored and not the soil stiffness.

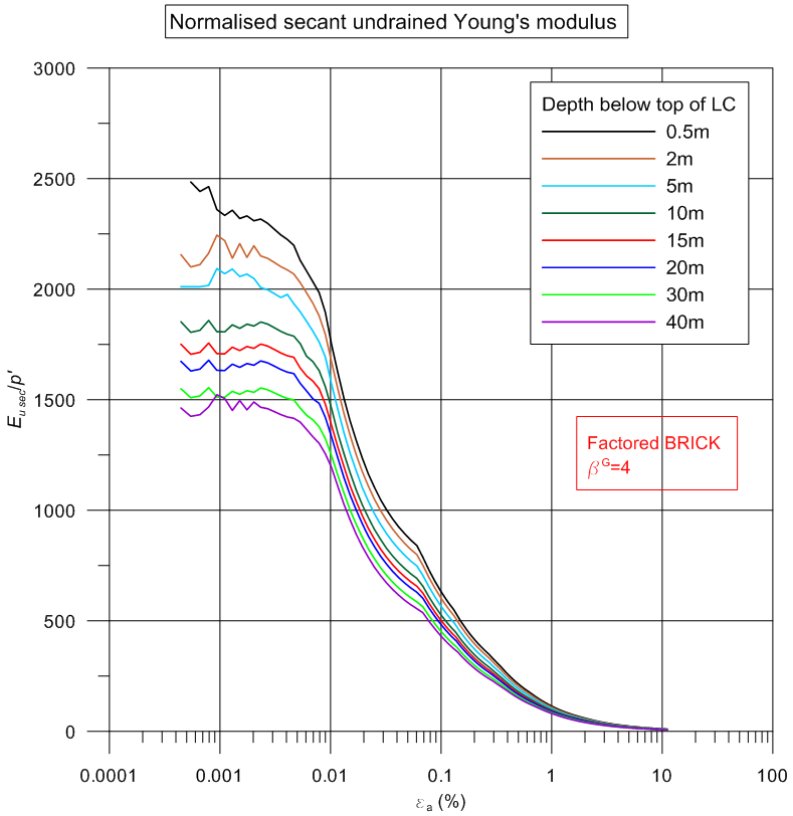

Figure 2.74: Normalised secant undrained Young's modulus vs axial strain from CAU triaxial tests for the factored BRICK with $\beta^G = 4$

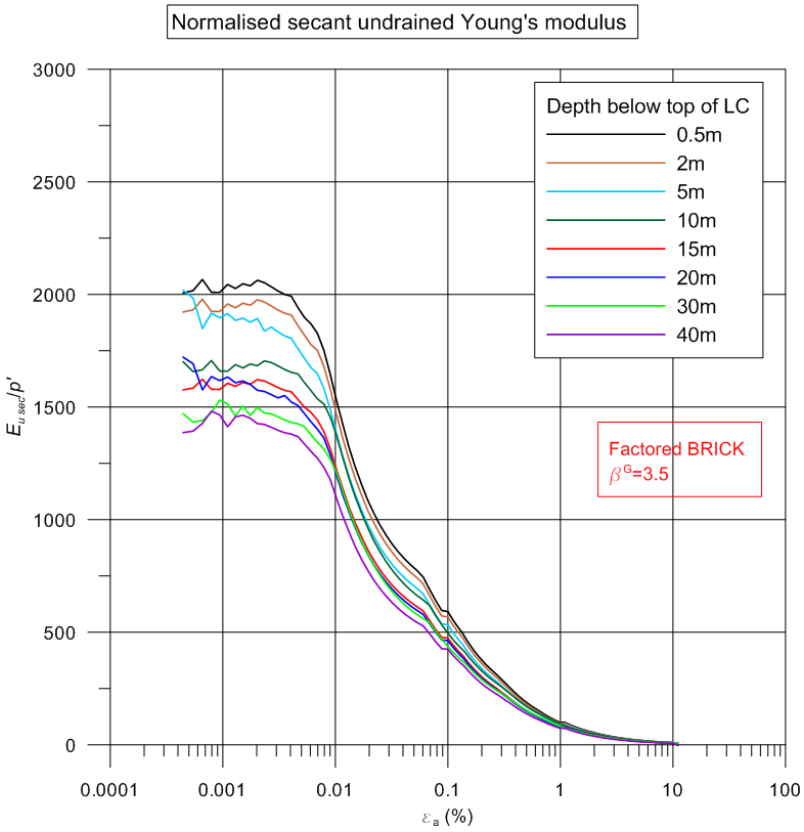

Figure 2.75: Normalised secant undrained Young's modulus vs axial strain from CAU triaxial tests for the factored BRICK with $\beta^G = 3.5$

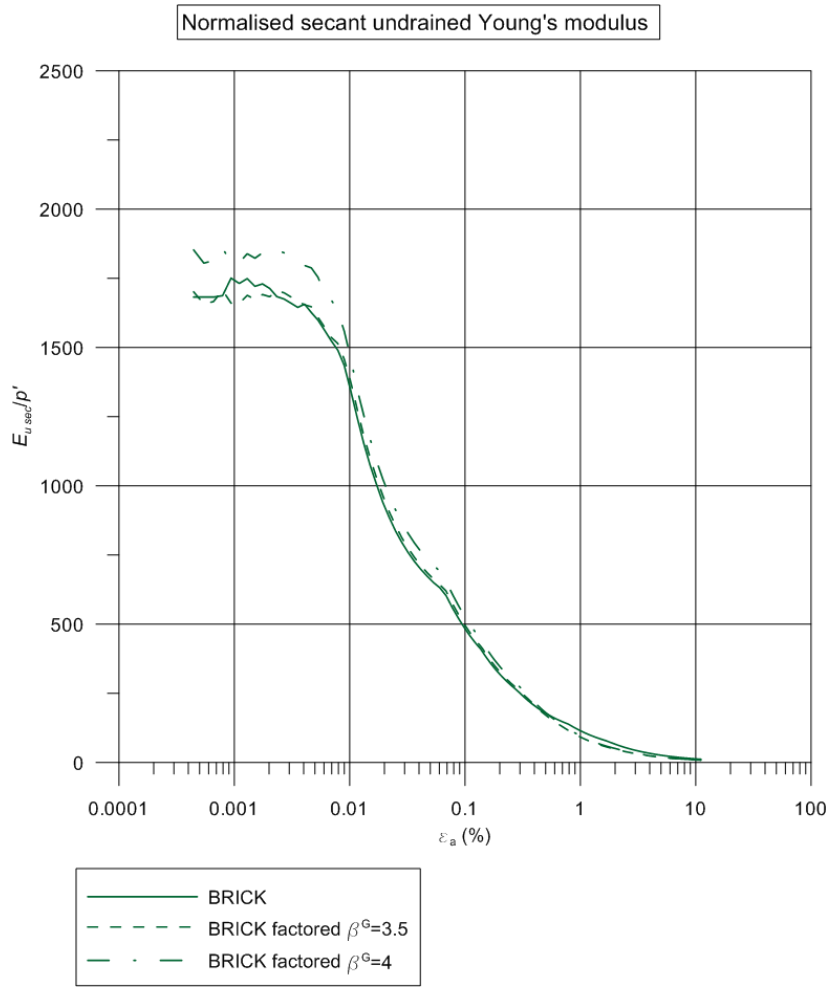

Figure 2.76: Normalised secant undrained Young's modulus degradation at 10m below LC stress level for the BRICK

The undrained shear strength profiles as calculated from the CAU triaxial tests for the characteristic and factored BRICK parameters are presented in Figure 2.77. It can be seen that the resulting factored undrained strength distribution agrees reasonably well with the characteristic undrained strength when factored by 1.4 as EC7 requires. More specifically, the achieved partial factor of safety ranges from 1.42 to 1.35 for depths between 7.5m to 30m below the top of London Clay.

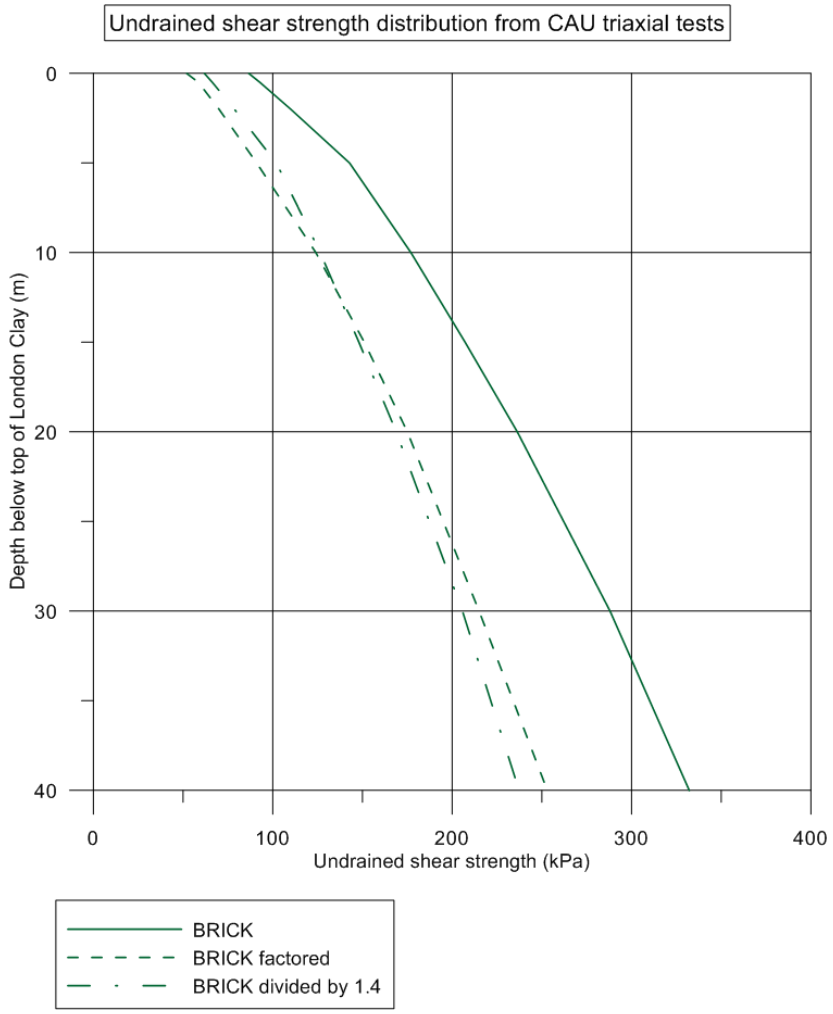

Figure 2.77: Characteristic and design undrained shear strength profiles from CAU triaxial tests for the BRICK

In Figure 2.78, the distribution of the earth coefficient at rest, K_0 is presented for both the characteristic and the factored parameters. As K_0 is not input in the BRICK model but is calculated based on the input parameters and the geological history, there is some discrepancy in the calculated values. Although the average values are similar, the factored BRICK parameters yield lower values (up to a depth of 13m) than those calculated from the characteristic BRICK parameters. It does however yield higher values for higher depths. The maximum difference is about 15% at the top of London Clay and at a depth of 40m below the top. Between 5m and 30m, below the London Clay level, the difference is less than 10%. Differences in the calculated K_0 values between the characteristic and factored BRICK parameters were also reported by Yeow (2014).

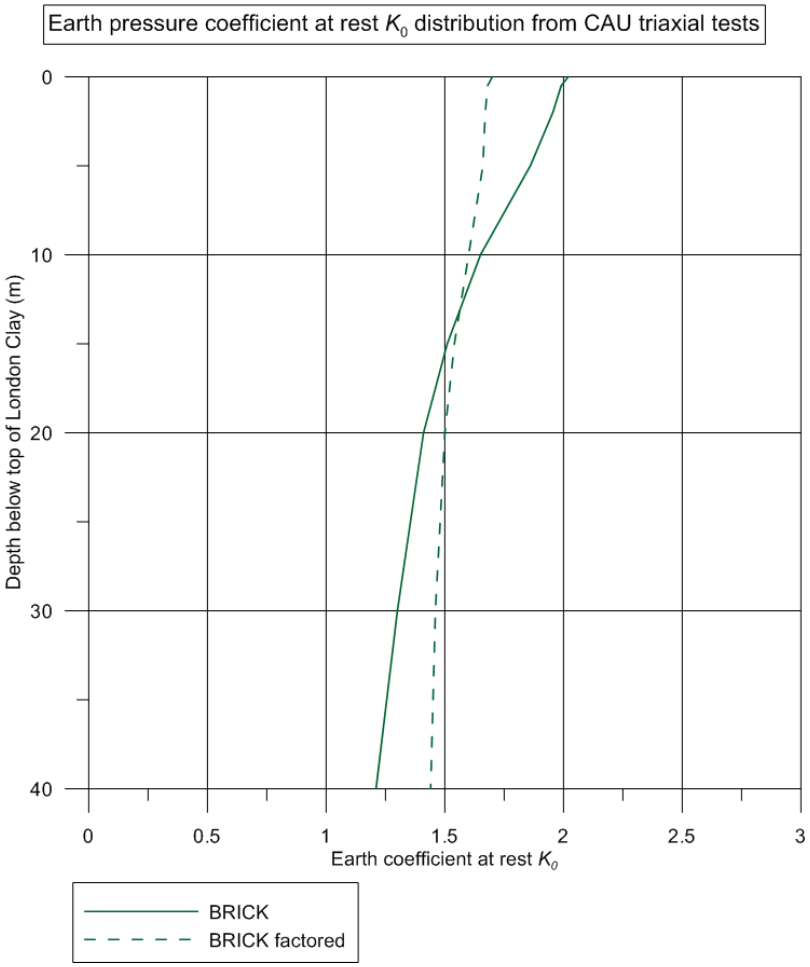

Figure 2.78: K_0 distribution with depth for the BRICK

2.7 Conclusions

In this Chapter, the study focuses on four different constitutive models ranging from the simplest and most widely used, which is a linear elastic, perfectly plastic model such as the Mohr-Coulomb, to more advanced models such as the Hardening Soil (HS) model, the Hardening Soil Small (HSS) and the BRICK model. The material parameters were first derived for all constitutive models for London Clay, based on many studies and high quality field and laboratory data published in the literature.

In the first part of the Chapter, the study focuses on the MC, HS and HSS models where the soil strength is a model input. When undrained conditions are assumed using the HS and HSS model, the effective stress analysis, where the undrained shear strength is not an input parameter but it is calculated by the constitutive model, is preferred to the total stress analysis where the undrained shear strength is an input parameter but the soil stiffness loses its stress dependency. However, in order to ensure that the calculated undrained shear strength profile matches the published data, a series of numerical triaxial undrained compression tests (both CAU and CIU) were performed at different

stress levels. Although, it was found that the undrained shear strength profiles predicted, using the effective stress parameters, are generally in agreement with the published data for all models, the HSS model consistently resulted in different stress paths, and hence about 7% and 11% lower undrained shear strength than the MC and the HS model. The difference lies in the formulation of the HSS model and the fact that the shear hardening flow rule is defined in a different way than in the HS model while the generated excess pore water pressure, during triaxial shearing using the HSS model is higher than the one predicted for the MC and the HS model.

For the ULS analysis, when undrained conditions are assumed using effective stress parameters, designers must ensure that the calculated undrained shear strength distribution corresponds to the characteristic one, factored by the required value. It was found that for the MC, HS and HSS model, for the range of values of angle of shearing resistance typically used for London Clay (22 - 25°), using a value of 1.4 for $\gamma_{tan\varphi'}$ results in an undrained shear strength factored by about the same value as required by the EC7. Moreover, when using the HS and HSS model for ULS design, for materials with $c' = 0$, the soil stiffness does not change when the soil strength is factored which is consistent with the EC7 requirements. However, designers should be aware that even for small values of cohesion, the soil stiffness reduces when partial factors are applied to the effective strength parameters.

In the second part, the study focuses on the BRICK model where the soil strength is not an input but is calculated by the model. Similar to the other models, the stress paths from numerical CAU triaxial compression tests were calculated at different stress levels. It was found that while the stress paths have the same shape, the final stress ratio at failure varies with depth due to the effect of the parameter χ^{Φ} which enables the model to increase the soil strength due to its state of over-consolidation. Similarly, different stiffness degradation curves were predicted at different stress levels, with higher elastic stiffness values typically predicted for shallow depths than for higher depths. This is attributed to the effect of the parameter χ^{G} which modifies the elastic soil stiffness based on the state of over-consolidation of the soil.

For the ULS analysis using the BRICK model, a new set of material proportions and string lengths was derived, which results in an undrained strength equal to the characteristic strength reduced by a factor of 1.4 as EC7 requires. This was achieved by reducing the S-shaped stiffness degradation curve in the large strain area when compared with the curve corresponding to the characteristic BRICK parameters. Because, the area defined within the curve directly relates to the soil strength, when the

material proportions in the large strain area are reduced, the area within the curve and hence the corresponding soil strength reduces accordingly. Moreover, the parameter β_G was reduced from 4 to 3.5 to improve the match between the curves for the characteristic and factored BRICK parameters, satisfying the EC7 requirement that only the soil strength needs to be factored and not the soil stiffness. Although, the derived set of parameters for the factored BRICK satisfies the EC7 requirements with respect to the soil strength and stiffness, there is some discrepancy in the resulting K_0 profile when compared with the characteristic BRICK, as K_0 is not input in the BRICK model but is calculated based on the input parameters and the geological history. However, this limitation can be overcome when using the BRICK model with a software (e.g. LS-Dyna) that allows users to overwrite the K_0 value.

CHAPTER 3

FE analysis of supported excavations using the Mohr-Coulomb model

3.1 Introduction

In this chapter, the challenges of Serviceability Limit State (SLS) and Ultimate Limit State (ULS) FE analysis of embedded walls supporting excavations, are highlighted and discussed. The calculations were performed using the well-known Mohr-Coulomb model, readily available with PLAXIS 2015.02 (Plaxis, 2015), and any other geotechnical FEM software. The chosen geometries, soil profiles and propping system are representative of typical excavations in the greater London area.

Following the description of the construction sequence, material parameters, initial stress conditions and modelling assumptions, the results of the analyses are presented. For the SLS analysis, the main results presented include the wall deflections, the heave at the base of the excavation and the surface settlements behind the wall. For the ULS analysis, the study focuses on the derivation of the design internal structural forces such as prop loads, wall bending moments, shear and axial forces, using different factoring combinations and strategies. As required by Eurocode 7 (EC7), both Combinations of the Design Approach 1 (DA1) were considered while the Combination 2 (DA1-2) was applied with the two alternative strategies discussed in Section 1.7.3. In all cases, the effect of a number of factors, critical to the design, such as the earth pressure coefficient at rest, soil stiffness and prop stiffness on the resulting discrepancies is illustrated.

Moreover, the design prop loads, calculated from the FE analyses, are compared with the values derived from a number of empirical methods (e.g. Twine and Roscoe, 1999; EAB, 2014) for all the geometries considered in this study. The comparisons highlight the limitations and advantages of the different calculation methods.

Finally, the FE analysis was repeated for a deep excavation in a typical Singapore soil profile, to investigate the effect of the material strength on the differences in the results between the different EC7 factoring combinations and strategies for a soft clay.

3.2 FE Modelling of supported excavations

The main types of retaining structures are: gravity walls, embedded walls and composite retaining structures (BS EN1997-1, Section 9.1.2). This study focuses on embedded walls where the stability of the structure is ensured by the passive resistance of the soil in front of the wall below the excavation level. Embedded walls are typically preferred when efficient use of space is required, particularly since they can be incorporated into the permanent structure. When limiting the movements of buildings adjacent to an excavation is of paramount importance, the embedded walls are temporarily supported by structural members such as steel or concrete props, anchors and berms (The Institution of Structural Engineers, 2013). There are different types of embedded walls depending on the structural system between cantilever, single propped and multi propped walls and depending on the construction method between diaphragm walls, sheet pile walls, secant pile walls and contiguous pile walls (Anderson, 2012).

Traditionally, empiricism or simple calculation models, such as Limit Equilibrium (LE) methods, have been used for embedded wall design. Limit Equilibrium can be used for statically determinate systems, such as cantilever and single propped walls, to obtain the embedment depth, the wall bending moments, shear and axial forces and prop loads. Nowadays, Finite Element (FE) methods are increasingly being used for embedded wall design as the advances in available software and constitutive models allow for better approximation of the real field conditions, and especially when ground movements or complex geometry are involved (Gaba et al., 2003; Dong, 2014).

3.2.1 Geometry and construction sequence

Five cross sections were analysed, as presented in Figure 3.1, with increasing excavation depth and number of prop levels. The dashed lines represent the ground level at different excavation stages, while the arrows represent the prop levels. These geometries cover a wide range of retaining structures typically encountered in practice. The soil profile, which is also shown, consists of 4m of Made Ground overlying the London Clay formation, typical of London. The details of the prop levels, the excavation and embedment depth and the excavation width are presented in Table 3.1 for each of the geometries considered in this study. Note that the increased embedment depth for the 5-propped wall case has no effect on the results of the undrained analysis (Potts and Fourie, 1984) but it is required to ensure stability when long term (drained) conditions are considered.

Table 3.1: Details of the geometries considered in this study

Number of prop levels	Excavation depth *H* (m)	Embedment depth *t* (m)	Excavation width *x* (m)	Figure number
1-propped wall	8	4	20	3.1a
2-propped wall	12	4	20	3.1b
3-propped wall	16	4	20	3.1c
4-propped wall	20	4	20	3.1d
5-propped wall	24	7.5	20	3.1e

All geometries have the same support system stiffness (same wall stiffness and same distance between prop levels) and therefore, allow to verify the impact of the rest of the parameters, if it is assumed that systems with similar stiffness present similar strains (Clough et al., 1989; Long, 2001).

A typical bottom-up construction sequence is modelled in all analyses. The benefits of this construction sequence have been extensively discussed by Gaba et al. (2003). Following the initial stress conditions, the embedded wall is constructed and a variable surcharge of 10kPa is applied behind the wall to account for the load due to ancillary construction activities. The wall behaves as an embedded cantilever when the first 4m of soil is excavated. Then the first prop level is installed at 2m below ground level (bgl) and another 4m of soil is excavated. This sequence of soil excavation and prop installation then continues until the formation level is reached (including an overdig of 0.5m for ULS).

- Stage 0: Initial State
- Stage 1: Install wall and apply 10kPa surcharge
- Stage 2: Excavate 4m of soil
- Stage 3: Install prop at 2m bgl
- Stage 4: Excavate another 4m of soil
- Similar for deeper excavations

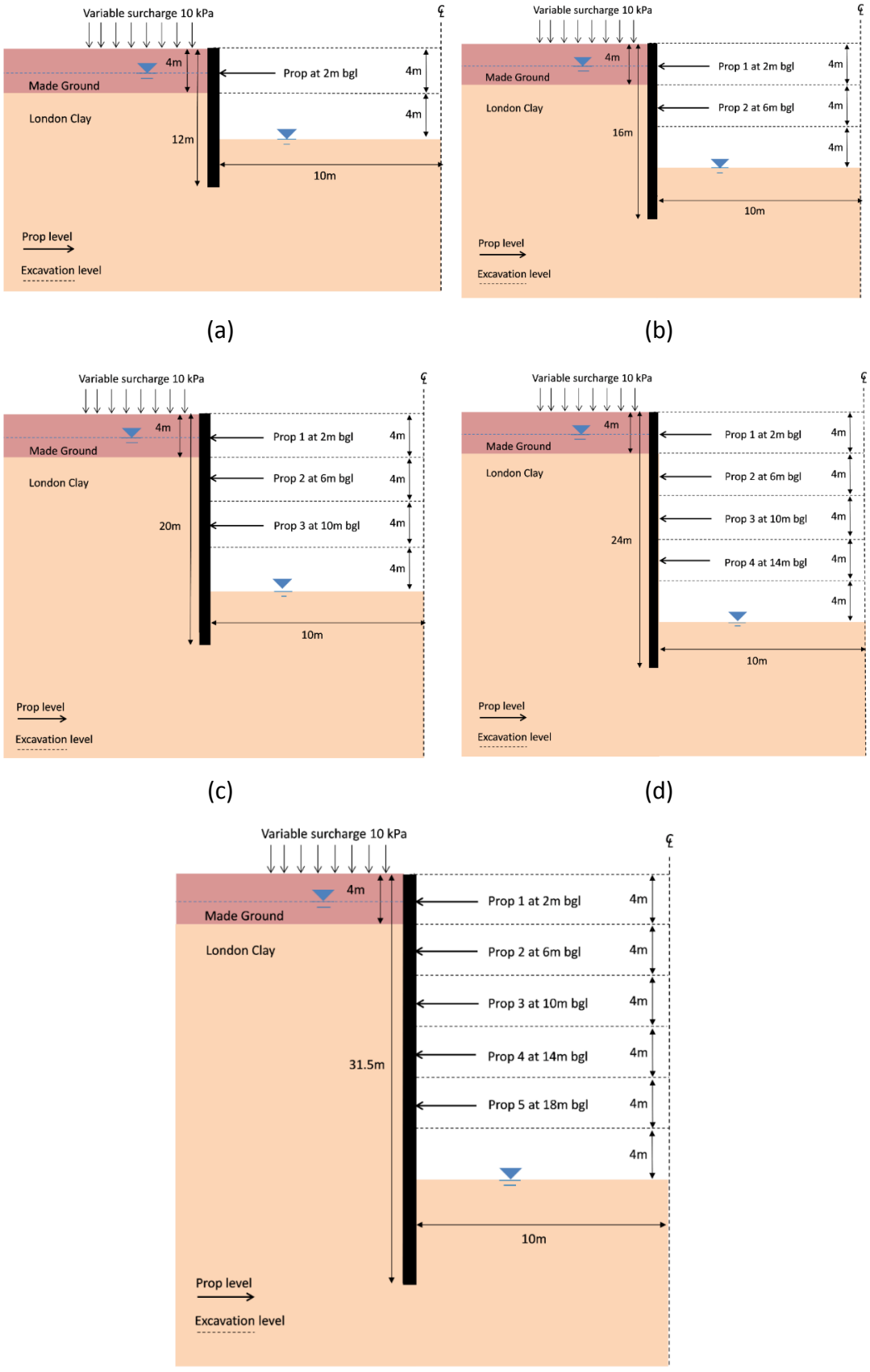

Figure 3.1: Geometry of the supported excavation with 1, 2, 3, 4 and 5 prop levels

3.2.2 Material parameters of soils

In all the analyses, the Mohr-Coulomb constitutive model was used to model the behaviour of both the Made Ground and London Clay. The model parameters for the Made Ground are listed in Table 3.2 while the model parameters for the London Clay have been discussed in detail in Chapter 2, Section 2.5.1.

Table 3.2: Mohr-Coulomb parameters for the Made Ground

Made Ground parameters	
Young´s Modulus, E (MPa)	15
Poisson´s ratio, v	0.2
Angle of internal friction, φ' (°)	25
Angle of dilatancy, ψ (°)	0
Cohesion, c' (kPa)	0
Earth pressure coefficient at rest, K_0	0.577
Unit weight, γ (kN/m^3)	20

3.2.3 Material parameters of the structural elements

In all the analyses the structural elements were modelled as elastic with constant isotropic stiffness. The embedded diaphragm wall, supporting the soil, was wished-in-place, made of concrete and has a thickness of 1m. The material parameters assumed for the wall are listed in Table 3.3.

Table 3.3: Material parameters for the concrete wall

Diaphragm wall properties	
Young´s Modulus, E (GPa)	28
Poisson´s ratio, v	0.2
Cross-section area per m run, A (m)	1
Moment of Inertia, I (m^4)	0.083

The material parameters assumed for the steel, tubular props are listed in Table 3.4. The definition of the prop stiffness, k, is given in Equation 3.1 where E is the Young's modulus, A is the cross section area of the prop, s is the horizontal spacing and l is the effective length of the prop (i.e. half the excavation width when the problem is symmetric). The prop stiffness based on these parameters is k = 100MN/m per m run,

which is considered reasonable for typical excavations in London Clay (Gaba et al., 2003).

$$k = \frac{EA}{sl} \tag{3.1}$$

Table 3.4: Material parameters for the steel props

Prop properties	
Young´s Modulus, *E* (GPa)	200
Cross-sectional area, *A* (m^2)	0.025
Horizontal spacing, *s* (m)	5
Effective length, *l* (m)	10

3.2.4 Initial stress conditions

The initial stress conditions represent the stress state of the soil before any excavation works take place and mostly depend on the coefficient of earth pressure at rest K_0 and the unit weight of the soils. In this study, K_0 was taken as 0.577 and 1.5 for the Made Ground and the London Clay respectively. This choice was based on a number of studies discussed in Chapter 2 and is considered realistic for the London Clay.

3.2.5 Modelling assumptions

The computer software used for the analyses is Plaxis 2015.02 in its two-dimensional version and only half of the excavation was modelled in this plane strain 2D analysis due to symmetry. Tsui and Clough (1974) showed that the plane strain assumption is realistic for diaphragm wall problems. The Finite Element mesh for the 5-propped wall case was 75m x 64m and is shown in Figure 3.2. The side model boundaries were fixed in the horizontal (*x* axis) direction (i.e. horizontal movements are restricted to zero) while the bottom model boundary was fixed in both the horizontal *(x* axis) and vertical (*y* axis*)* directions (i.e. both vertical and horizontal displacements are restricted to zero). Overall, the mesh consists of 2153 15-noded triangular elements. It can be seen that the mesh was refined in the zones where the highest change in stresses and strains are expected. For this reason, the elements near the excavation are much smaller than the elements at the far boundaries.

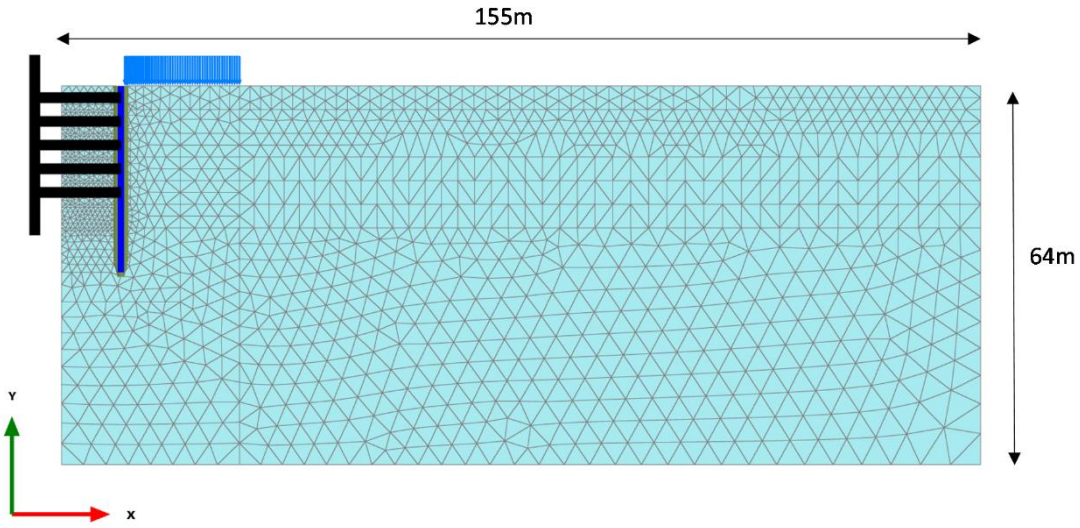

Figure 3.2: Finite Element mesh for the 5-propped wall case

The wall was modelled using plate elements, although these elements do not have thickness in the mesh, the wall input parameters take account of the actual wall thickness. To model the friction interface between wall and soil and to take into account the soil disturbance during construction, impermeable interface elements were used. For the effective stress analysis, it was assumed that $\tan\delta = 2/3 \tan\varphi'$, where δ is the soil/wall friction angle while for the total stress analysis it was assumed that $c_w = 0.5c_u$, where c_w is the wall adhesion and c_u is the undrained shear strength (Gaba et al., 2003). In addition, the props were modelled by fixed-end anchor elements that can transmit only axial forces.

In all the analyses, drained conditions were assumed for the initial stage for both materials. For the rest of the stages, undrained conditions were considered for London Clay on both the active and passive side which is a realistic assumption for temporary excavations where the duration of the construction works is less than a year (Crossrail Ltd, 2009).

There are two modelling strategies in PLAXIS for undrained behaviour, namely the total and effective stress approach with the choice of the approach mainly depending on the intent to calculate the generated excess pore water pressures and the type of constitutive model used. The effective stress approach can be applied either by Method A or Method B while the total stress approach is applied by Method C. In Undrained Method A, effective strength and effective stiffness parameters are used. The undrained shear strength is not an input parameter but a consequence of the constitutive model. The excess pore water pressures and effective stresses are computed while the undrained analysis can be followed by a consolidation analysis. In Undrained Method B,

the undrained shear strength is an input parameter while stiffness parameters in terms of effective stress are used. However, the calculated effective stresses and the generated excess pore water pressures are generally unrealistic and thus the undrained analysis should not be followed by consolidation analysis. Finally, in Undrained Method C, the undrained shear strength is input while undrained stiffness parameters are used. Only the total stresses are obtained in the analysis and the pore pressures and effective stresses are not calculated. Moreover, the undrained analysis cannot be followed by a consolidation analysis. In all FE analyses using the Mohr-Coulomb model, presented in this Chapter, the Undrained Method C was used. This is a reasonable assumption as only the short term post-construction conditions are considered.

3.3 FE analysis of supported excavations using the MC model

Three main parameters were investigated using the Mohr-Coulomb model: earth pressure coefficient at rest (K_0); the soil stiffness expressed as the ratio of the undrained Young's modulus and undrained shear strength (E_u/c_u) and the prop stiffness (k) as the more critical parameters for wall design (GCO, 1990; Yeow and Feltham, 2008).

As embedded walls typically support natural soil, the in situ horizontal stress state, described by the earth pressure coefficient at rest is important. However, wall construction may result in a reduction of the horizontal effective stresses near the wall and alter the stress-strain response during the excavation (Gunn and Clayton, 1992; Symons and Carder, 1992; Powrie et al., 1998). It is generally far from straightforward to model this stress relief in FE analysis (Batten and Powrie, 2000; Powrie and Batten, 2000) and designers often consider this effect empirically by using a reduced K_0 value. For this reason, a parametric study was conducted, using K_0 values of 1.0, 1.25 and 1.5. Note that in a total stress analysis, the undrained shear strength is an input parameter in the Finite Element calculations and hence independent of the specified K_0 value. The K_0 value is required for the initial stage of the construction sequence, when the initial stress field is defined and drained conditions are assumed.

The second parameter that was investigated is the ratio of the undrained Young's modulus and undrained shear strength, E_u/c_u. The MC analysis was repeated using E_u/c_u values of 750, 1000 and 1250, while keeping the rest of the parameters the same. The resulting E_u values, based on the undrained shear strength profile for London Clay discussed in Chapter 2, are shown in Table 3.5.

Table 3.5: Soil stiffness cases to be investigated

Case no	E_u/c_u	c_u (kPa)	E_u (MPa)
1	750	60 + 8*z*	45 + 6*z*
2	1000	60 + 8*z*	60 + 8*z*
3	1250	60 + 8*z*	75 + 10*z*

where *z* (m) is the depth from the top of London Clay

Finally, the analysis was repeated varying the value of the prop stiffness, *k*. Four different cases were considered for tubular steel props with *k* values of 30, 50, 100 and 150 MN/m per m run. The details of the different prop stiffness cases considered in this study are listed in Table 3.6. Designers often specify a requirement for the prop stiffness value that the contractor must achieve to be consistent with the design assumptions. What can reasonably be achieved is a function of the excavation geometry, but for temporary steel props, the values considered in this study, cover reasonably, a wide range of situations from normal to high and very high stiffness. It is worth noting that contractors often achieve stiffness values that are higher than the minimum specified in order to achieve the desired structural capacity. In any case, the value chosen by the designers depends on the degree to which movements need to be controlled.

Table 3.6: Prop stiffness cases to be investigated

Case no	*k* (MN/m/m)	*EA* (MN)	*l* (m)	*s* (m)	Material
1	30	1500	10	5	Steel
2	50	2500	10	5	Steel
3	100	5000	10	5	Steel
4	150	7500	10	5	Steel

3.3.1 SLS analysis using the MC model

As required by EC7, for the SLS analysis, the characteristic values of the material model parameters were used as input in the numerical calculations, without applying any partial factors. In this section, the FE analysis results of the wall deflection, surface settlement behind the wall and the heave at the base of the excavation are presented for all the geometries considered in this study. Moreover, the effect of the K_0, E_u/c_u and prop stiffness *k* on the results is investigated and discussed.

3.3.1.1 Effect of K_0

The wall deflection is one of the main concerns in deep excavations and is typically measured with inclinometers. The pattern and magnitude of the wall deflections depend on a number of factors such as the soil behaviour, the support system, construction method and sequence. The wall deflection profiles for the 5-propped wall case, with varying K_0, are presented in Figure 3.3. It can be seen that the maximum values of wall deflection are 27mm, 35mm and 47mm for K_0 equal to 1.0, 1.25 and 1.5 respectively. These correspond to a ratio of maximum wall deflection and excavation depth of 0.11%, 0.14% and 0.19%. These values fall within the range reported by St John et al. (1992) and Long (2001) for supported excavations in London Clay. The K_0 = 1.5 case is the most critical, as higher K_0 values result in higher horizontal stresses acting on the wall. More specifically, when K_0 increases from 1.0 to 1.25 and 1.5, the maximum wall deflections show an increase of 30% and 74% respectively. In all cases, the curvatures have similar shape and the maximum value is observed at about +15mOD.

The maximum wall deflections for the rest of the geometries are listed in Table 3.7, where it can be seen that the K_0 = 1.5 case consistently resulted in the highest deflection values. In all cases, the ratio of maximum wall deflection and excavation depth ranges from 0.11% to 0.19% for K_0 varying from 1.0 to 1.5 respectively. Overall, the results agree with Potts and Fourie (1984) and GCO (1990) showing that the wall deflections depend on the in-situ stress state, expressed by the earth pressure coefficient at rest.

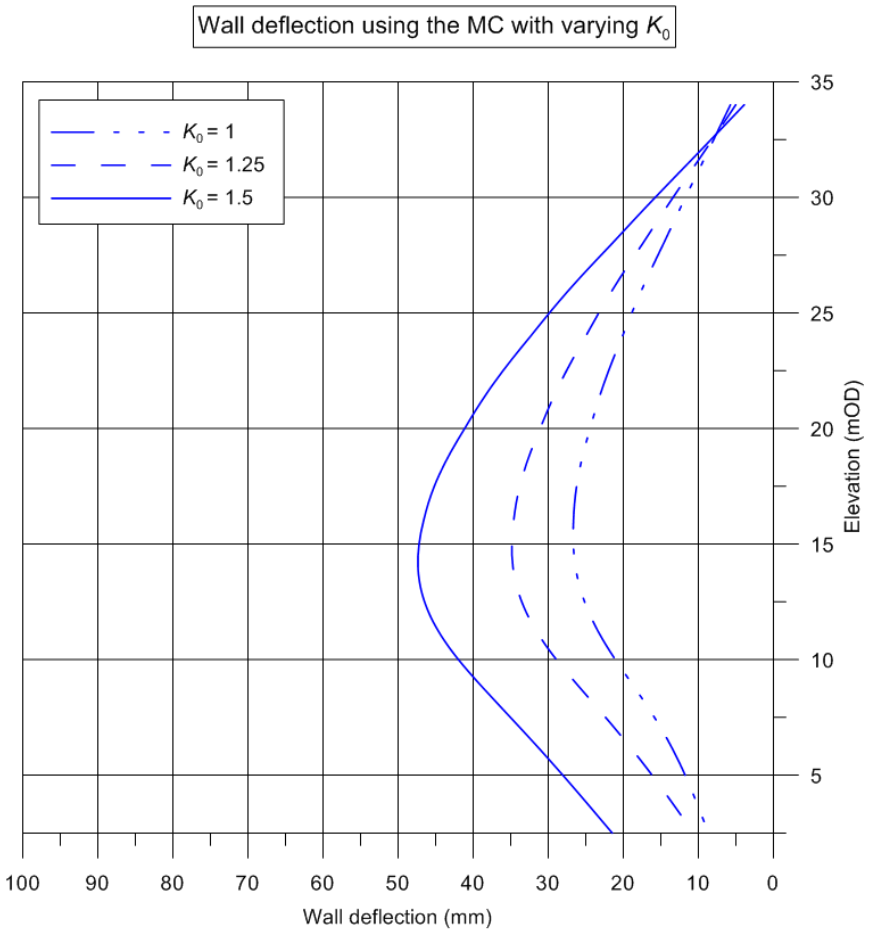

Figure 3.3: Deflection profiles for 5-propped wall using the MC with varying K_0

Table 3.7: Maximum wall deflection with varying K_0

Maximum wall deflection (mm)					
K_0	1-propped wall	2-propped wall	3-propped wall	4-propped wall	5-propped wall
1.0	11	15	19	24	27
1.25	12	17	22	30	35
1.5	14	22	30	39	47

Typically, during an excavation, the soil at the base is under extension due to soil removal and experiences an upward vertical displacement (heave). In Figure 3.4, the vertical soil displacements at the base of the excavation are plotted for the 5-propped wall case. The maximum soil displacements are 22mm, 31mm and 44mm, for K_0 equal to 1.0, 1.25 and 1.5 respectively. In all cases, the lowest heave was observed near the wall, due to the effect of wall friction. The maximum heave values for the rest of the geometries are listed in Table 3.8 where it can be seen that, the K_0 = 1.5 case resulted

in the largest calculated heave at the bottom of the excavation while the smallest heave was obtained for K_0 = 1.0.

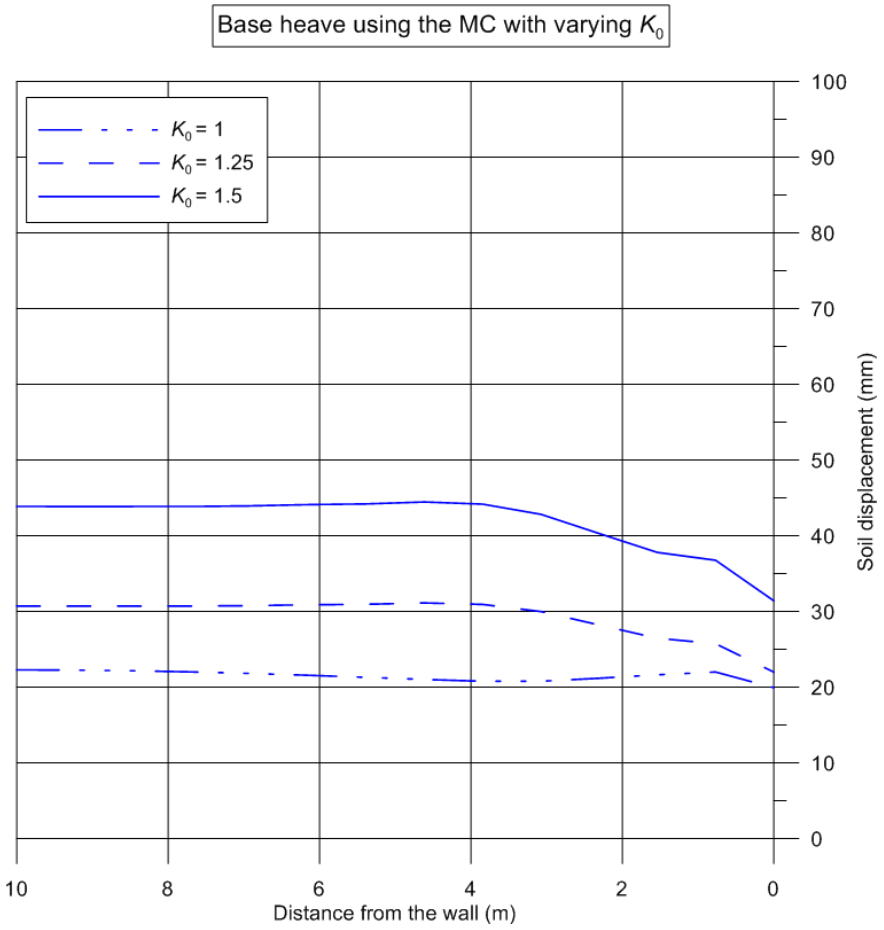

Figure 3.4: Base heave for 5-propped wall using the MC with varying K_0

Table 3.8: Maximum base heave with varying K_0

Maximum heave (mm)					
K_0	1-propped wall	2-propped wall	3-propped wall	4-propped wall	5-propped wall
1.0	13	17	19	20	22
1.25	13.5	18	20	24	31
1.5	14	21	27	34	44

Finally, the surface settlements (i.e. downward vertical soil displacements at the ground level) behind the wall are shown in Figure 3.5 for the 5-propped wall case. The settlement calculation is of paramount importance for the assessment of the stability of adjacent buildings, roads and services. The maximum settlements are 13mm, 15mm and 20mm for K_0 equal to 1.0, 1.25 and 1.5 respectively. The maximum settlement values for

the rest of the geometries are listed in Table 3.9. In all cases, the highest settlements were calculated for K_0 = 1.5 while the smallest settlements were observed for K_0 = 1.0.

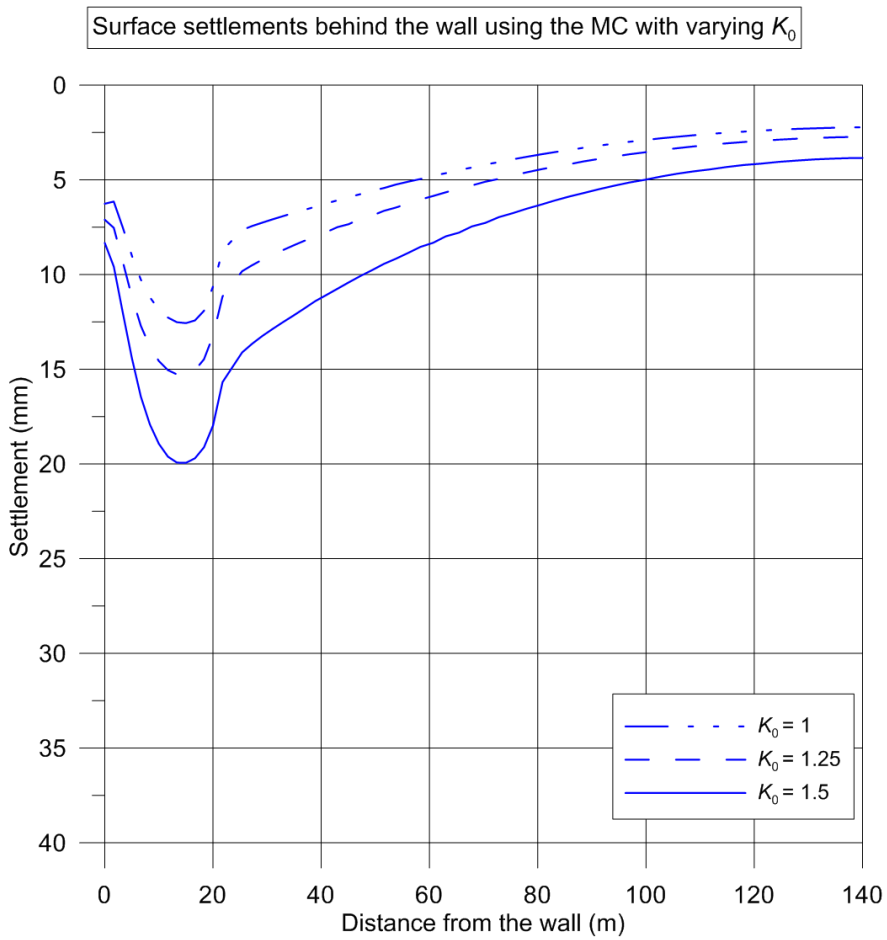

Figure 3.5: Surface settlements behind the wall for 5-propped wall using the MC with varying K_0

Table 3.9: Maximum surface settlement behind the wall with varying K_0

Maximum surface settlement (mm)					
K_0	1-propped wall	2-propped wall	3-propped wall	4-propped wall	5-propped wall
1.0	8	7.5	9	11	13
1.25	8	8	10.5	14	15
1.5	8.5	9.5	13.5	18	20

3.3.1.2 Effect of soil stiffness

The wall deflection profiles for the 5-propped wall case with varying E_u/c_u are shown in Figure 3.6, where it can be seen that the maximum wall deflections are 59mm, 47mm and 40mm for E_u/c_u equal to 750, 1000 and 1250 respectively. These correspond to a ratio of maximum wall deflection and excavation depth of 0.24%, 0.19% and 0.16%. The E_u/c_u = 750 case is the most critical, as the modelled soil has the lowest stiffness resulting in larger deformations of the structural elements of the support system such as the embedded wall. Again, in all cases, the curvatures have similar pattern and the maximum values were observed at about +14mOD to +15mOD. The maximum wall deflections for the rest of the geometries are listed in Table 3.10 where it is noted that the largest wall deflections were observed for E_u/c_u = 750. In all cases, the ratio of maximum wall deflection and excavation depth ranges from 0.15% to 0.24% for E_u/c_u varying from 750 to 1250.

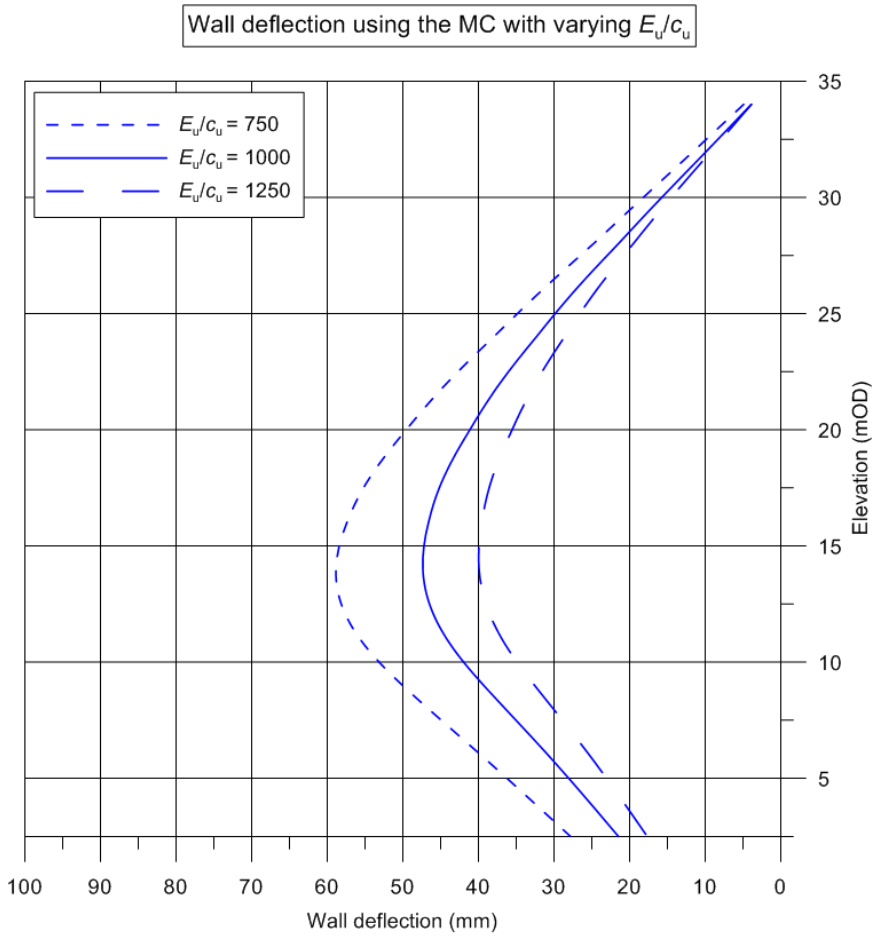

Figure 3.6: Deflection profiles for 5-propped wall using the MC with varying E_u/c_u

Table 3.10: Maximum wall deflection with varying E_u/c_u

Maximum wall deflection (mm)					
E_u/c_u	1-propped wall	2-propped wall	3-propped wall	4-propped wall	5-propped wall
750	18	27	38	46	59
1000	14	22	30	39	47
1250	11	18	26	32	40

In Figure 3.9, the vertical soil displacements at the base of the excavation are shown for the 5-propped wall case. The maximum soil displacements are 57mm, 44mm and 37mm, for E_u/c_u equal to 750, 1000 and 1250 respectively. The maximum heave values for the rest of the geometries are listed in Table 3.11 where it was found that, the E_u/c_u = 750 case resulted in the highest calculated heave at the bottom of the excavation while the lowest heave was obtained for E_u/c_u = 1250.

Table 3.11: Maximum base heave with varying E_u/c_u

Maximum heave (mm)					
E_u/c_u	1-propped wall	2-propped wall	3-propped wall	4-propped wall	5-propped wall
750	19	28	36	48	57
1000	14	21	27	34	44
1250	12	16	22	28	37

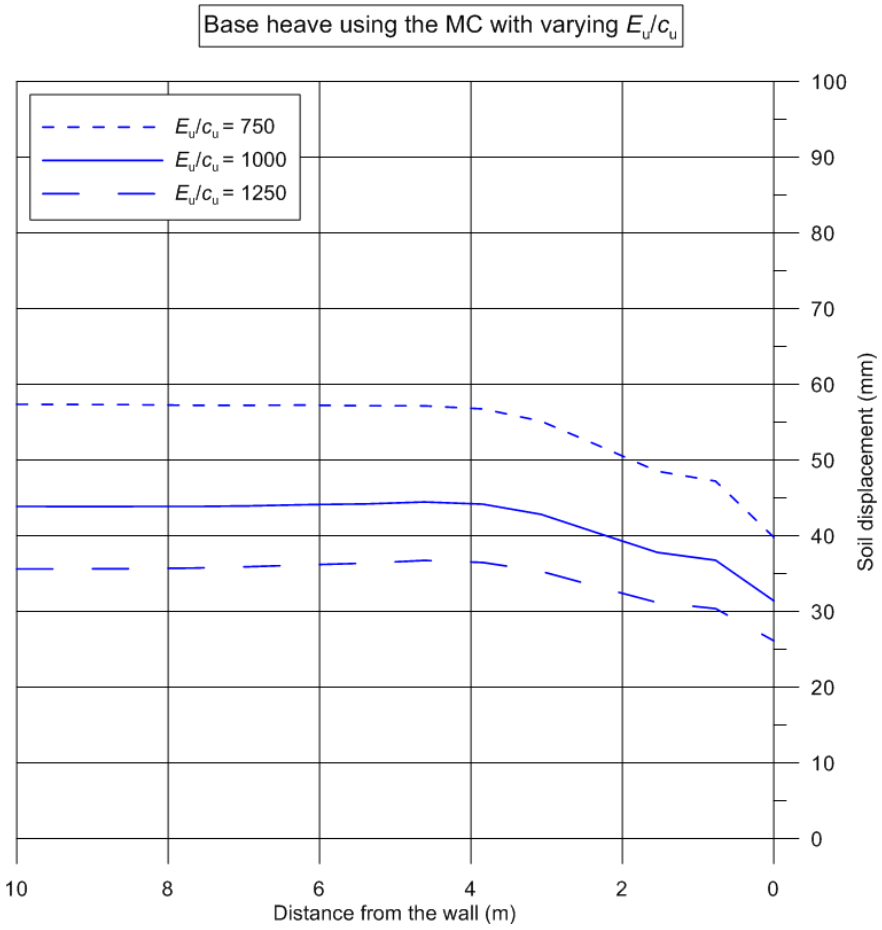

Figure 3.7: Base heave for 5-propped wall using the MC with varying E_u/c_u

The surface settlements behind the wall are shown in Figure 3.8. The maximum settlement values are 27mm, 20mm and 17mm for E_u/c_u equal to 750, 1000 and 1250 respectively. The maximum settlements for the rest of the geometries are listed in Table 3.12, where it can be seen that, the highest settlements were calculated for E_u/c_u = 750 while the lowest settlements were obtained for E_u/c_u = 1250.

Table 3.12: Maximum surface settlements behind the wall with varying E_u/c_u

Maximum surface settlement (mm)					
E_u/c_u	1-propped wall	2-propped wall	3-propped wall	4-propped wall	5-propped wall
750	10	11	17	22	27
1000	8.5	9.5	13.5	18	20
1250	8	8.5	12	15	17

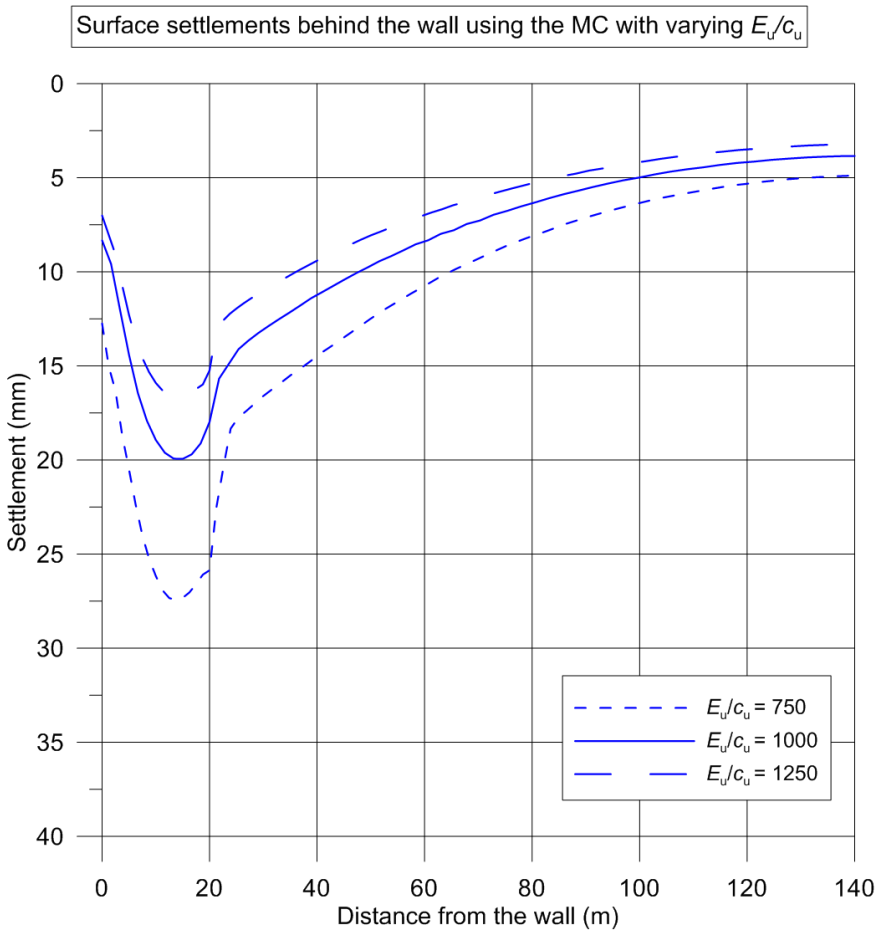

Figure 3.8: Surface settlements behind the 5-propped wall using the MC with varying E_u/c_u

3.3.1.3 Effect of prop stiffness

The wall deflection profiles for the 5-propped wall case with varying the prop stiffness *k* are presented in Figure 3.9. The maximum wall deflections are 59mm, 54mm, 47mm and 44mm for *k* equal to 30, 50, 100 and 150MN/m per m run respectively. These correspond to a ratio of maximum wall deflection and excavation depth of 0.24%, 0.22%. 0.19% and 0.18%. In all cases, the curvatures have similar pattern and the maximum value was observed at about +14 to +16mOD. The maximum deflections for the rest of the geometries are listed in Table 3.13. Overall, the findings agree with GCO (1990) that increasing the prop stiffness generally decreases the movements of the wall.

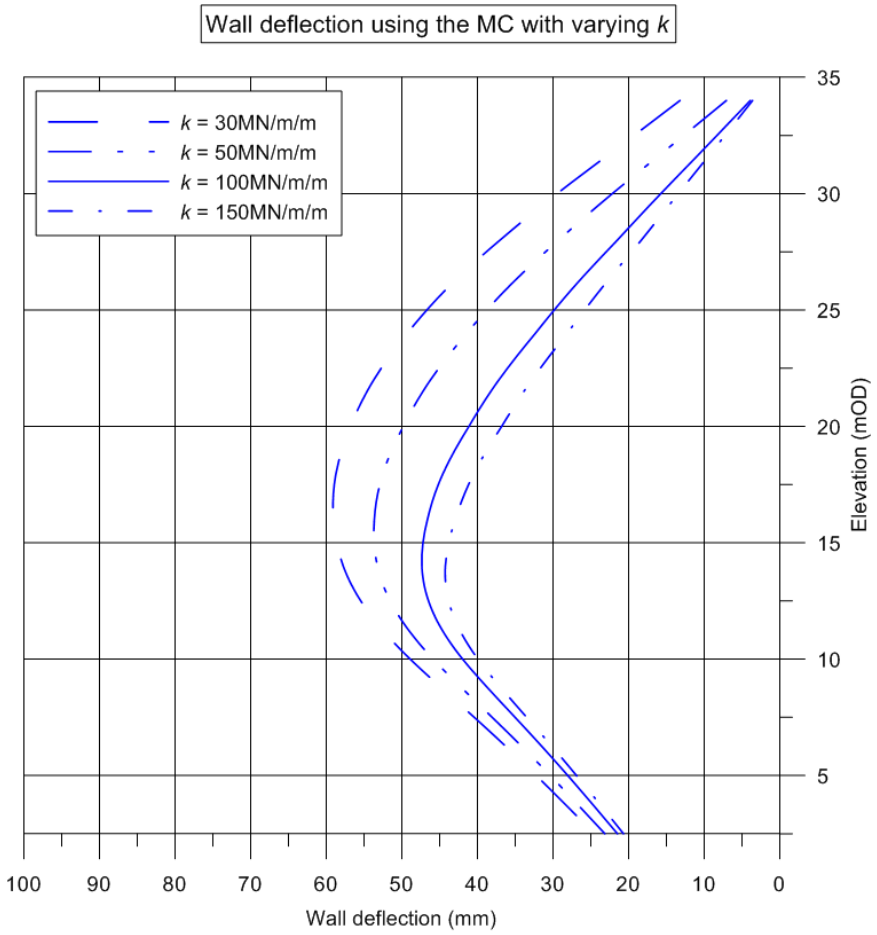

Figure 3.9: Deflection profiles for 5-propped wall using the MC with varying k

Table 3.13: Maximum wall deflection with varying k for all 5 geometries

Maximum wall deflection (mm)					
k (MN/m/m)	1-propped wall	2-propped wall	3-propped wall	4-propped wall	5-propped wall
30	19	26	38	49	59
50	16	24	34	43	54
100	14	22	30	39	47
150	12	20	28	35	44

In Figure 3.10, the vertical soil displacement at the base of the excavation is plotted for the wall supported by 5 levels of props. The maximum soil displacements are 51mm, 48mm, 44mm and 43mm for *k* equal to 30, 50, 100 and 150MN/m per m run respectively. The maximum heave values for the rest of the geometries are listed in Table 3.14 where it can be seen that, the *k* = 30MN/m/m case resulted in the largest calculated heave at the base of the excavation while the smallest heave was obtained for *k* = 150MN/m/m.

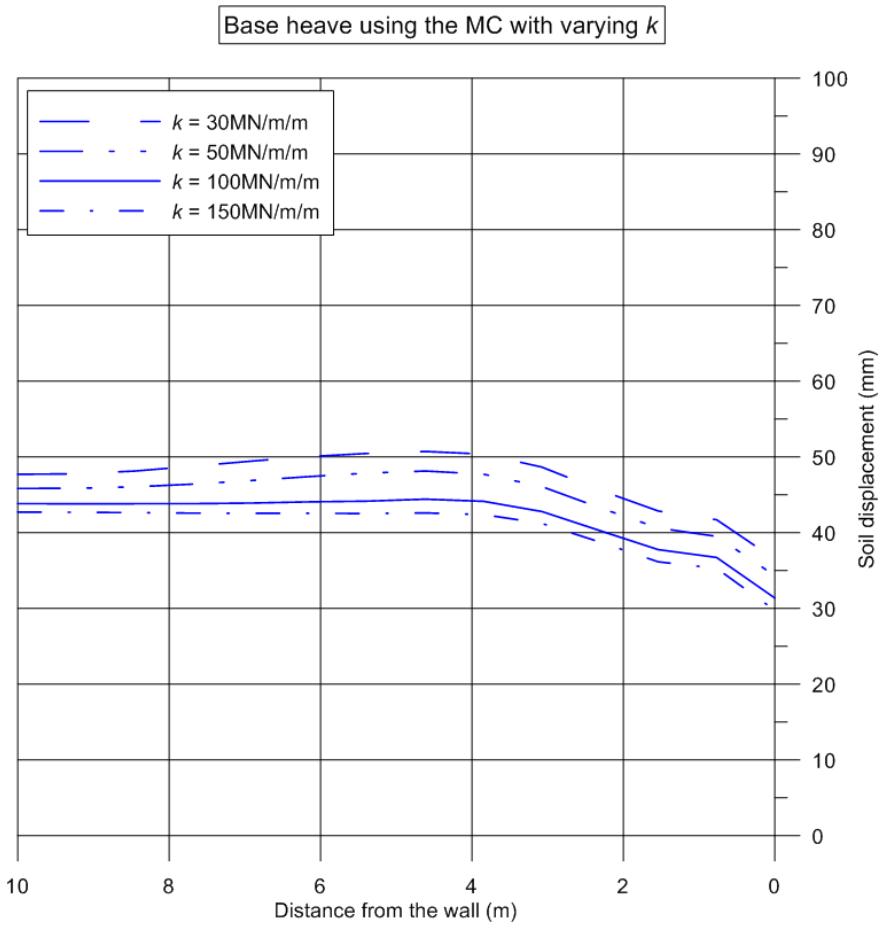

Figure 3.10: Base heave for 5-propped wall using the MC with varying k

Table 3.14: Maximum heave at the base of the excavation with varying k

Maximum heave (mm)					
k (MN/m/m)	1-propped wall	2-propped wall	3-propped wall	4-propped wall	5-propped wall
30	16	23	32	40	51
50	15	22	29	37	48
100	14	21	27	34	44
150	14	19.5	26	33	43

The surface settlements behind the wall are shown in Figure 3.11. The maximum settlement values are 26mm, 23mm, 20mm and 18mm for *k* equal to 30, 50, 100 and 150MN/m per m run respectively. The maximum settlements for the rest of the geometries are listed in Table 3.15, where it is shown that, the largest settlements were calculated for *k* = 30MN/m/m while the smallest settlements were obtained for *k* = 150MN/m/m.

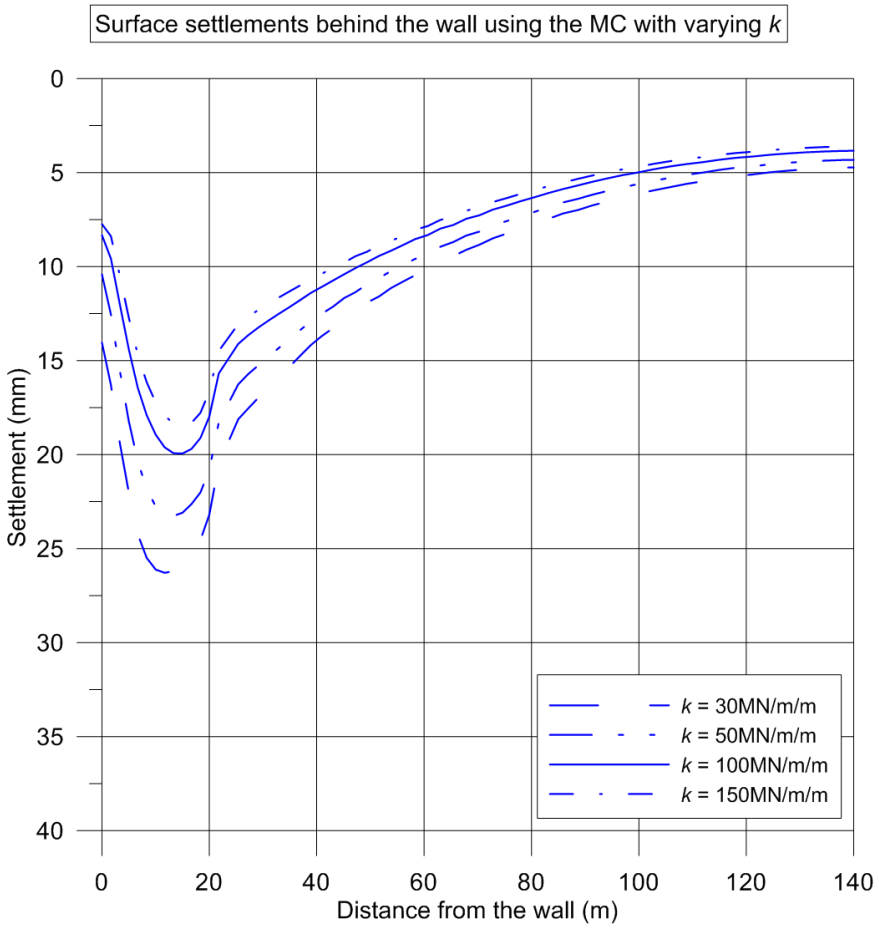

Figure 3.11: Surface settlements behind the 5-propped wall using the MC with varying k

Table 3.15: Maximum surface settlements behind the wall with varying k

Maximum surface settlement (mm)					
k (MN/m/m)	1-propped wall	2-propped wall	3-propped wall	4-propped wall	5-propped wall
30	11	13	17.5	23	26
50	9.5	11	15.5	20	23
100	8.5	9.5	13.5	17	20
150	8	9	12	16	18

3.3.2 ULS analysis using the MC model

The main purpose of the ULS FE analysis is to verify the stability against the GEO and STR Limits States. As required by EC7, both the DA1 Combinations were considered while the DA1-2 was used with two alternative strategies as discussed in

Section 1.7.3. For both Combinations, the safety verification against the GEO limit state is satisfied if the ULS FE analysis converges. For the safety verification against the STR limit state, the design structural forces such as the prop loads, bending moments, shear and axial forces are calculated and compared against the structural capacity of structural elements. For the DA1-1 analysis, the variable surcharge (input) was factored by 1.1 and the outputs (prop loads, wall bending moment, axial and shear force) were factored by 1.35. For the DA1-2 analysis, factored soil properties were used while the variable surcharge (input) was factored by 1.3 and the outputs (prop loads, wall bending moment, axial and shear force) were factored by 1.0. The results from the different factoring combinations and strategies are compared and the influence of the K_0, E_u/c_u and prop stiffness k on the resulting discrepancies are investigated.

3.3.2.1 Effect of K_0

The effect of the in-situ horizontal stresses on the prop loads and wall bending moments was highlighted by Bjerrum et al. (1972). In this section, the design structural forces are compared for varying values of the earth pressure coefficient at rest for all the geometries, to illustrate the effect on the resulting discrepancies between the different factoring combinations and strategies. Three different cases were again considered with K_0 equal to 1.0, 1.25 and 1.5, constant with depth.

In Figure 3.12, the design prop loads are shown for the 1, 2, 3, 4 and 5-propped walls. It can be seen that, the DA1-1 governs the design at all prop levels, apart from the bottom one where the DA1-2 Strategy 2 results in more onerous prop loads. In almost all cases and prop levels, the DA1-2 Strategy 2 is more critical than the DA1-2 Strategy 1.

For $K_0 = 1.5$, the difference in the total force supporting the wall between the two DA1-2 Strategies is 8%, 29%, 27.5%, 26% and 25.5% for the 1, 2, 3, 4 and 5-propped wall case respectively. For walls supported by more than one prop level, the discrepancy between the two DA1-2 Strategies is particularly significant at the bottom level where the difference in the design prop load was 44%, 65%, 77% and 85% for the 2, 3, 4, and 5-propped wall case respectively. Also, the discrepancy becomes more significant with increasing K_0. For the 5-propped wall, the percentage difference in the design prop load at the bottom level is 36.5%, 63% and 85% for K_0 equal to equal to 1.0, 1.25 and 1.5 respectively. The percentage difference in the total force supporting the wall between the two DA1-2 Strategies is 11%, 17% and 25.5%, for the three cases respectively.

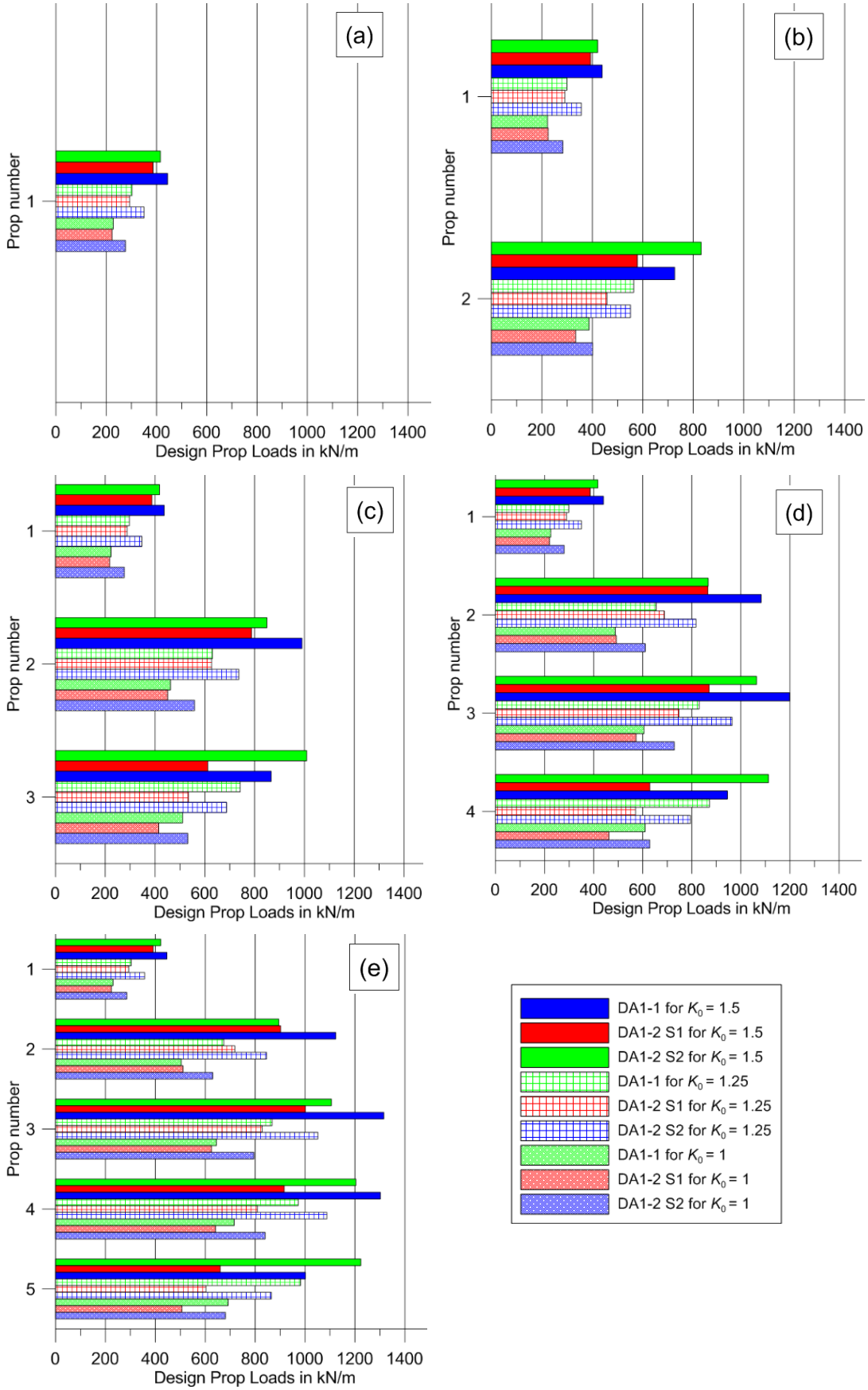

Figure 3.12: Design Prop Loads using the MC with varying K_0 for wall with a) 1, b) 2, c) 3, d) 4 and e) 5 prop levels

It was also found that, the calculated prop loads generally increase, as the K_0 increases. Specifically, when K_0 increased from to 1.0 to 1.5, the total force acting on the wall for the DA1-1, DA1-2 S1 and DA1-2 S2 increased by 61%, 73% and 82% for a 1-propped wall, 70%, 74% and 105% for a 2-propped wall, 68%, 65% and 90% for a 3-propped wall, 63%, 79% and 17% for a 4-propped wall and 61%, 54% and 74% for a 5-propped wall.

Overall, factoring the soil strength from the beginning of the analysis (i.e. DA1-2 Strategy 1), has a small effect on the calculated design prop loads because of the redistribution of the stresses. In DA1-2 Strategy 2, however, the soil strength is suddenly reduced at each excavation stage. Shifting from characteristic to factored soil strength has shown that the lowest prop receives a higher load increment than the props above. The props are installed when the soil strength is unfactored and the developed strains are lower than those developed in the DA1-2 Strategy 1 case. The props enter the analysis with little wall displacement and thus they have a stiffer response and pick up more load when the soil strength is factored. Moreover, the increase of the load at the bottom prop level is due to the development of a plastic zone in front of the wall. Large plastic zones in the area in front of the wall, in stiff highly OC clays, were also observed by Potts and Fourie (1984).

In Figure 3.13, the plastic zones, shown as red, are plotted at the final excavation stage, for the 5-propped wall, using a K_0 value equal to 1.0, 1.25 and 1.5. It is shown that, the plastic zone is small for K_0 = 1.0 but becomes more significant with increasing K_0.

To better understand the effect, in Figure 3.14, the stress paths in q - p space were plotted for the 5-propped wall with varying K_0 at 4 different points: a) 2m, b) 5m, c) 10 and d) 15m below the formation level (shown in Figure 3.13 as black dots). The paths show the variation of the stresses at each point, from the initial state, down to the excavation of the formation level. As expected, the K_0 value has a significant effect on the initial stress state and hence the starting point of the stress path. For K_0 = 1.0, the stress paths start with zero deviatoric stress (i.e. q = 0) and increasing the K_0 value, results in stress paths that start with higher values of deviatoric stress.

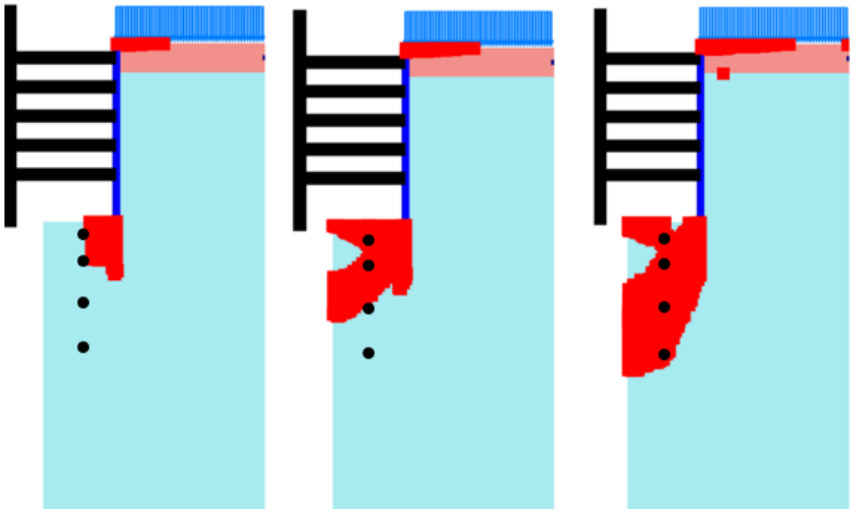

(a) (b) (c)

Figure 3.13: Plastic points at the final excavation stage for 5-propped wall using K_0 equal to a) 1.0, b) 1.25, and c) 1.5

Moreover, in all K_0 = 1.0 cases, the stress paths are within the elastic region and do not reach the failure line. For K_0 = 1.25, only the stress paths at 2m and 5m below the formation level reach the failure line while for K_0 = 1.5, all stress paths reach the failure line and the corresponding points fall within the plastic zone, as shown in Figure 3.13.

Therefore, the results show that the higher the K_0 value, the closer the stress paths are to the failure line and hence the larger the plastic zone. In DA1-2 Strategy 2, when shifting from characteristic to factored soil strength at each excavation stage, the failure line is reduced and thus even more points reach plastification in the zone below the base of the excavation. As a consequence, the lowest prop picks up more load and the difference in the prop loads, between the two DA1-2 Strategies, becomes even more significant.

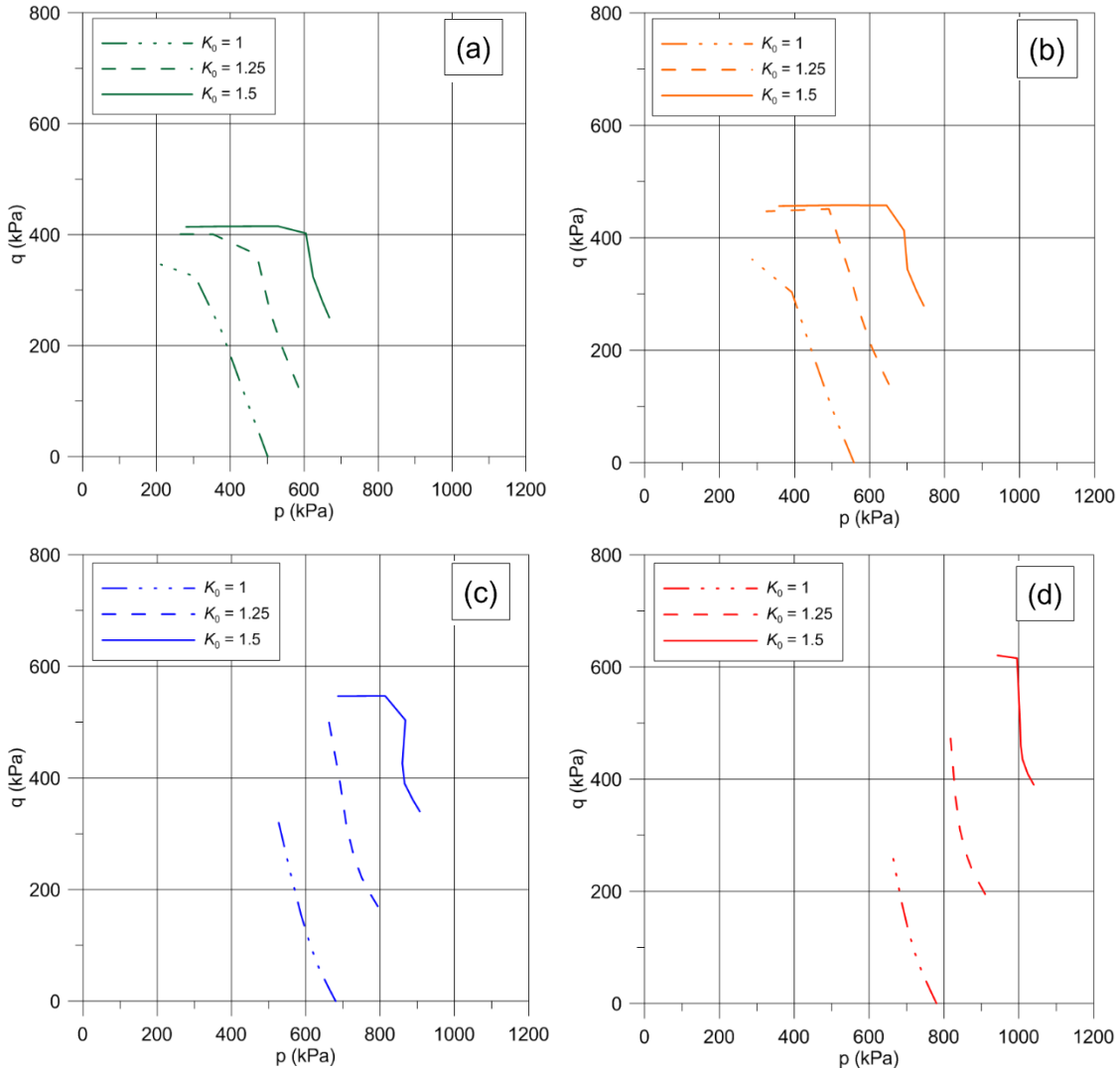

Figure 3.14: Stress paths in q – p space with varying K_0 for integration point at a) 2m, b) 5m, c) 10 and d) 15m below the formation level

In Figure 3.15, the design bending moment envelopes are shown for all the geometries, for K_0 = 1.5. The reason for plotting and comparing the bending moment distributions and not just the maximum values, is that unlike sheet pile walls, concrete walls are not necessarily reinforced equally on both sides or uniformly along their depth, therefore more than one bending moment might be critical to the design. It can be seen that the DA-1 governs the design, not only in terms of the minimum and maximum values of bending moments, but also when the whole distribution is considered. Moreover, the DA1-2 Strategy 2 gives higher maximum sagging and hogging bending moments than the Strategy 1, with the difference becoming more significant for the deeper excavations.

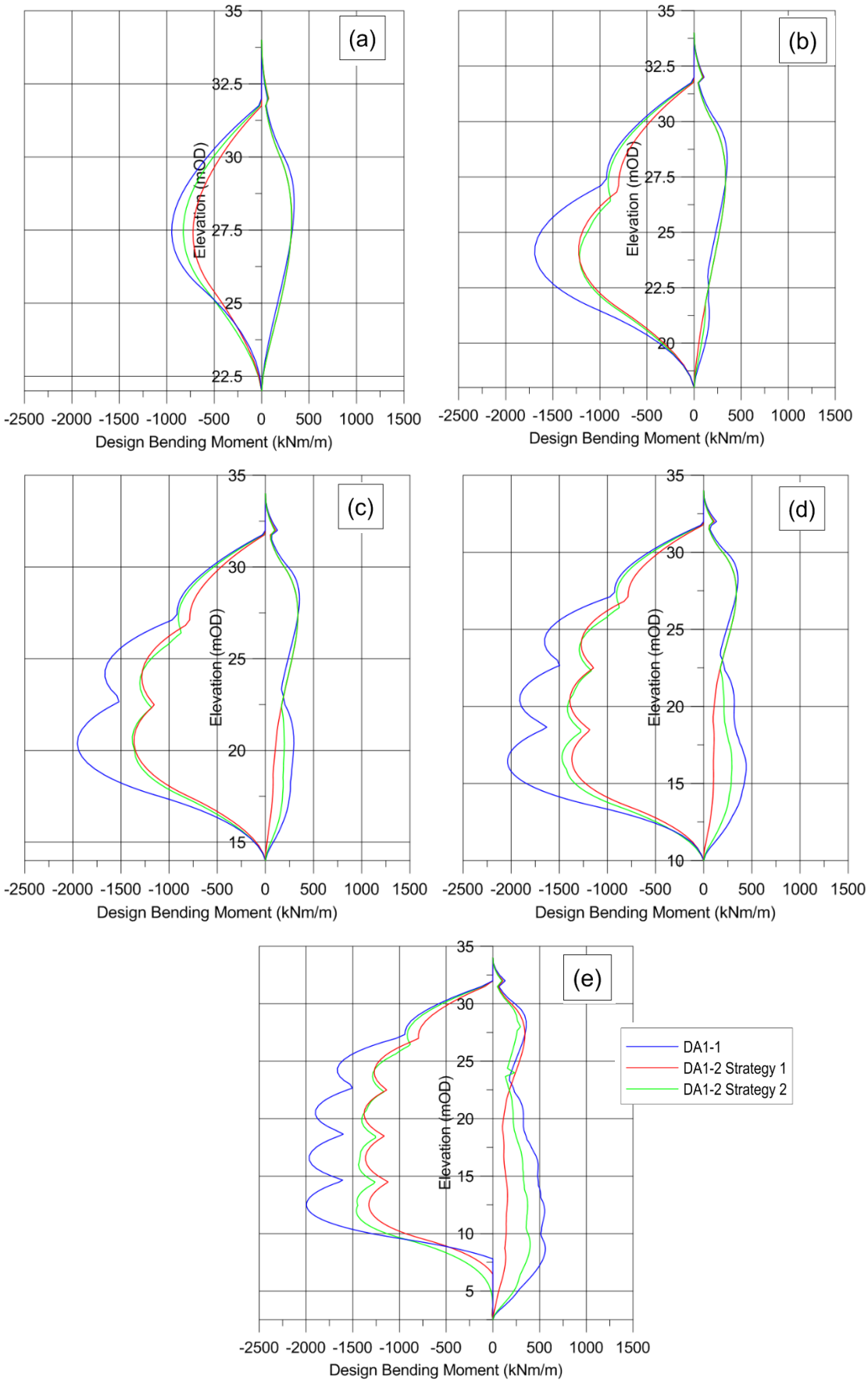

Figure 3.15: Design Bending Moment envelopes for $K_0 = 1.5$ for wall with a) 1, b) 2, c) 3, d) 4 and e) 5 prop levels

The design bending moments for all K_0 cases and geometries are presented in Table 3.16. In all cases, the DA1-1 governs the design while the percentage difference between the two DA1-2 Strategies slightly increases with increasing K_0. For example, for the 5-propped wall case, the difference in the minimum bending moment is 2%, 5% and 6% for K_0 equal to 1.0, 1.25 and 1.5. In all cases, higher K_0 values generally result in higher wall bending moments.

Table 3.16: Design Bending Moments for varying K_0

K_0	M_{max} DA1-1 (kNm/m)	M_{max} DA1-2 S1 (kNm/m)	M_{max} DA1-2 S2 (kNm/m)	M_{min} DA1-1 (kNm/m)	M_{min} DA1-2 S1 (kNm/m)	M_{min} DA1-2 S2 (kNm/m)
1-propped wall						
1.0	334	287	287	-436	-343	-375
1.25	335	305	304	-664	-546	-588
1.5	343	317	316	-949	-724	-826
2-propped wall						
1.0	341	294	293	-960	-742	-750
1.25	342	314	313	-1348	-989	-989
1.5	352	334	333	-1692	-1226	-1217
3-propped wall						
1.0	340	296	295	-1236	-930	-930
1.25	354	316	315	-1582	-1155	-1151
1.5	352	337	337	-1956	-1366	-1383
4-propped wall						
1.0	471	297	313	-1381	-1012	-1020
1.25	524	318	375	-1770	-1211	-1260
1.5	441	339	339	-2039	-1391	-1472
5-propped wall						
1.0	771	434	562	-1372	-1008	-1030
1.25	561	321	575	-1742	-1196	-1258
1.5	770	342	398	-1995	-1379	-1461

While, the influence of the K_0 on the bending moments is significant for all geometries, it was found that the effect generally becomes less pronounced as the excavation depth and the number of prop levels increase. More specifically, when K_0 increases from to 1.0 to 1.5, the difference in the minimum design bending moment for DA1-1, DA1-2 S1 and DA1-2 S2 is 117%, 111% and 120% respectively for a 1-propped

wall, 76%, 65% and 62% for a 2-propped wall, 58%, 47% and 49% for a 3-propped wall, 48%, 38% and 44% for a 4-propped wall and 45%, 37% and 42% for a 5-propped wall. Overall, the results are in agreement with Potts and Burland (1983) and Potts and Fourie (1984) who highlighted that higher K_0 values typically result in higher bending moments on the wall.

Similarly, in Figure 3.16, the design shear force envelopes are shown for all the geometries, for $K_0 = 1.5$. It is shown that while the DA1-1 generally results in higher shear forces along the wall, for the deeper excavation cases, the DA1-2 Strategy 2 generates the highest minimum shear forces. The design shear forces for all K_0 cases are presented in Table 3.17 for the 1, 2, 3, 4 and 5-propped walls. Similar to the bending moments, the percentage difference between the two DA1-2 Strategies increases with increasing K_0. For example, for the 5-propped wall case, the difference in the minimum shear force is 22%, 36% and 41.5% for K_0 equal to 1.0, 1.25 and 1.5 respectively.

It was also found that increasing the K_0 value, generally increases the shear forces. More specifically, when K_0 increases from to 1.0 to 1.5, the difference in the minimum design shear force for DA1-1, DA1-2 S1 and DA1-2 S2 is 72%, 78% and 88% respectively for a 1-propped wall, 73%, 64% and 92% for a 2-propped wall, 56%, 57% and 79% for a 3-propped wall, 57%, 44% and 70% for a 4-propped wall and 49%, 44% and 67% for a 5-propped wall.

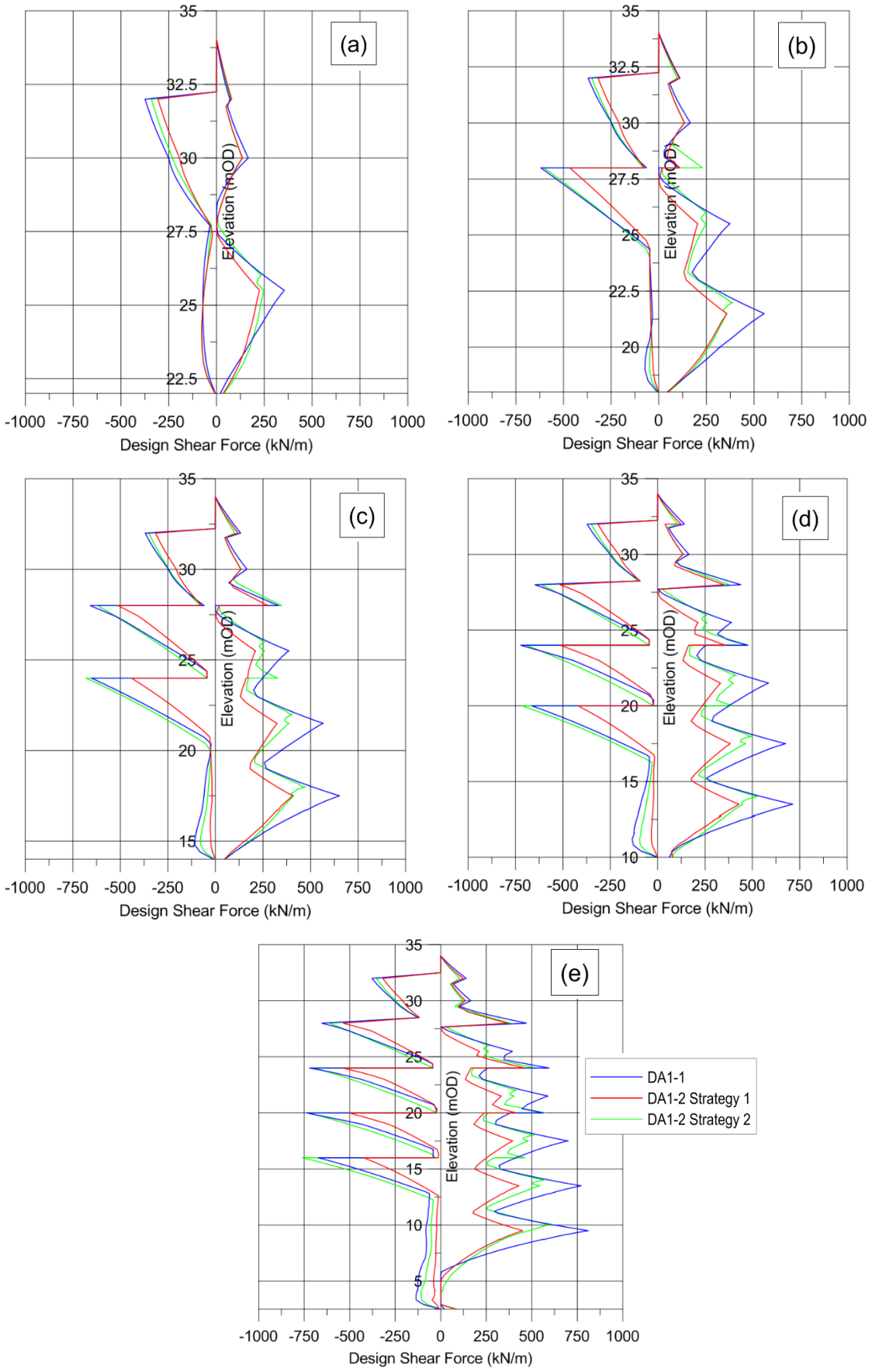

Figure 3.16: Design Shear Force envelopes for $K_0 = 1.5$ for wall with a) 1, b) 2, c) 3, d) 4 and e) 5 prop levels

Table 3.17: Design Shear Forces for varying K_0

K_0	Q_{max} DA1-1 (kN/m)	Q_{max} DA1-2 S1 (kN/m)	Q_{max} DA1-2 S2 (kN/m)	Q_{min} DA1-1 (kN/m)	Q_{min} DA1-2 S1 (kN/m)	Q_{min} DA1-2 S2 (kN/m)
1-propped wall						
1.0	244	163	168	-218	-172	-181
1.25	314	192	208	-288	-235	-248
1.5	355	225	246	-374	-307	-341
2-propped wall						
1.0	431	271	304	-358	-285	-314
1.25	499	312	358	-486	-380	-436
1.5	553	357	388	-619	-468	-603
3-propped wall						
1.0	543	333	404	-422	-327	-381
1.25	581	373	446	-528	-408	-522
1.5	653	407	473	-659	-512	-681
4-propped wall						
1.0	623	372	470	-461	-358	-422
1.25	671	404	500	-592	-454	-577
1.5	714	431	526	-723	-516	-716
5-propped wall						
1.0	808	436	602	-495	-373	-455
1.25	808	439	610	-628	-459	-625
1.5	811	463	607	-738	-538	-761

Finally, in Figure 3.17 the design axial force envelopes are presented for all the geometries for $K_0 = 1.5$ where it can be seen that the DA1-1 governs the design in all cases. The design axial forces for all K_0 cases are presented in Table 3.18 for the 1, 2, 3, 4 and 5-propped walls.

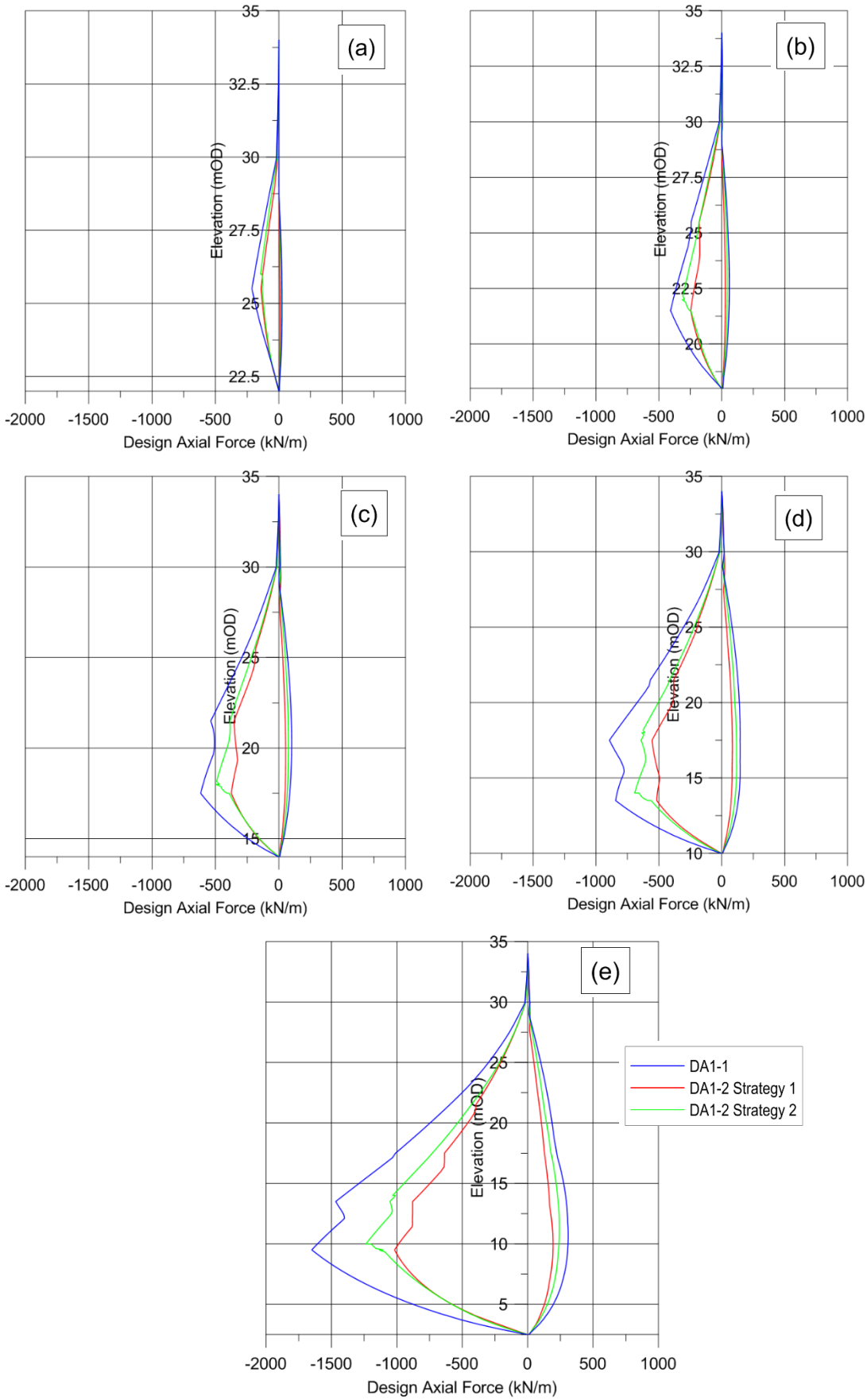

Figure 3.17: Design Axial Force envelopes for $K_0 = 1.5$ for wall with a) 1, b) 2, c) 3, d) 4 and e) 5 prop levels

Overall, the DA1-1 results in higher axial forces while the DA1-2 Strategy 2 is more critical than Strategy 1 in almost all cases with the difference becoming more apparent with increasing K_0 and for deeper excavations. It was again found that increasing the K_0 value increases the axial forces. However, the difference is negligible for the maximum axial force and generally small (less than 10% in most cases) for the minimum axial force.

Table 3.18: Design Axial Forces for varying K_0

K_0	N_{max} DA1-1 (kN/m)	N_{max} DA1-2 S1 (kN/m)	N_{max} DA1-2 S2 (kN/m)	N_{min} DA1-1 (kN/m)	N_{min} DA1-2 S1 (kN/m)	N_{min} DA1-2 S2 (kN/m)
1-propped wall						
1.0	27	16	20	-190	-137	-135
1.25	26	13	20	-200	-141	-138
1.5	25	10	19	-212	-142	-145
2-propped wall						
1.0	62	41	46	-380	-243	-283
1.25	61	37	46	-397	-247	-298
1.5	60	29	44	-407	-248	-315
3-propped wall						
1.0	103	70	76	-574	-353	-458
1.25	103	66	76	-596	-362	-484
1.5	101	54	75	-617	-375	-498
4-propped wall						
1.0	152	102	129	-776	-519	-634
1.25	153	100	128	-816	-549	-664
1.5	146	85	118	-894	-555	-692
5-propped wall						
1.0	345	216	266	-1411	-901	-1045
1.25	338	200	260	-1516	-973	-1196
1.5	311	193	243	-1650	-1017	-1230

Soil/wall interface

As mentioned in Section 3.2.5, to model the friction interface between wall and soil for the total stress analysis it was assumed for London Clay that $c_w = 0.5c_u$ which is the value typically used for practical applications and recommended by CIRIA C580 (Gaba et al., 2003). However, a parametric analysis was performed for the 5-propped wall case with $K_0 = 1.5$ using $c_w/c_u = 0.33$ and 0.66 to investigate the influence on the calculated design structural forces and the discrepancy in the results between the different factoring methods.

It was found that when the value of c_w/c_u decreases form 0.66 to 0.33, the design wall bending moments and shear forces increase by about 13% and 3% respectively. However, the design axial forces decrease by about 90%. The effect is more significant for the axial forces because they directly relate to the friction developed in the soil/wall interface. Nevertheless, the differences in the results among the DA1-1 and the two DA1-2 strategies when varying the c_w/c_u ratio are negligible. The FE analysis results presented in this thesis have been calculated using c_w/c_u=0.5, in line with best practice within Arup Geotechnics.

3.3.2.2 Effect of soil stiffness

The analysis was repeated for all the geometries for E_u/c_u equal to 750, 1000 and 1250. The calculated design structural forces are compared to illustrate the effect of the soil stiffness on the resulting differences between the different factoring combinations and strategies.

In Figure 3.18, the design prop loads are shown for all the geometries. It was found that the DA1-1 governs the design at all prop levels, apart from the bottom one, where the DA1-2 Strategy 2 gives a more critical design prop load. Overall, the DA1-2 Strategy 2 is more critical than the DA1-2 Strategy 1, with the percentage difference, in the total force acting on the wall, between the two DA1-2 Strategies being 24.5%, 25.5% and 26% for E_u/c_u equal to 750, 1000 and 1250 respectively.

It was also found that, regardless of the factoring combination or strategy, the calculated prop loads generally increase as the soil stiffness reduces while the effect on the resulting percentage difference between the two DA1-2 Strategies is negligible. Specifically, when E_u/c_u increases from 750 to 1250, the total force acting on the wall for DA1-1, DA1-2 S1 and DA1-2 S2 decreases by 13% for a 1-propped wall, 18% for a 2-propped wall, 18% for a 3-propped wall, 17% for a 4-propped wall and 16% for a 5-propped wall.

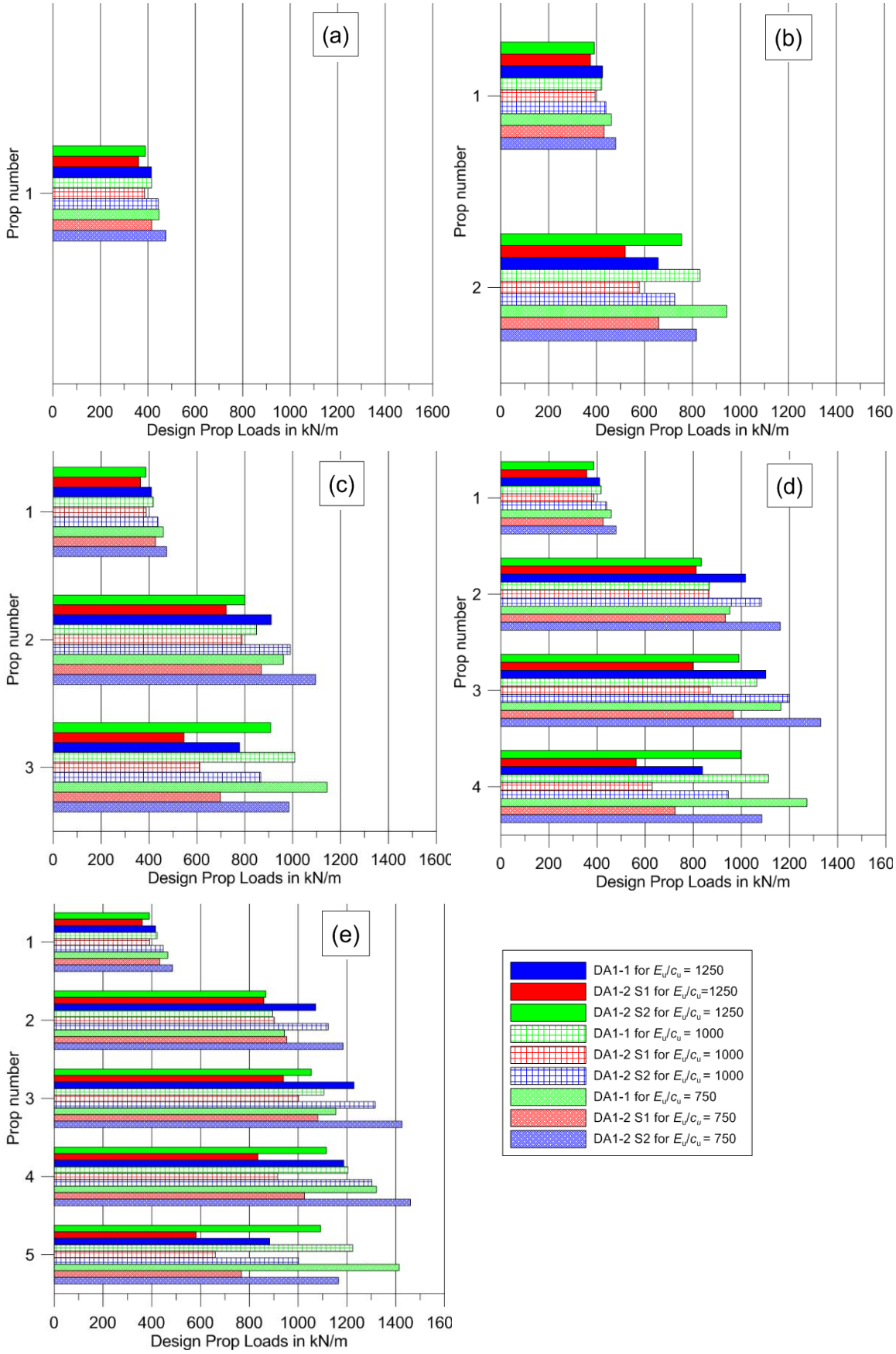

Figure 3.18: Design Prop Loads using the MC model with varying E_u/c_u for wall with a) 1, b) 2, c) 3, d) 4 and e) 5 prop levels

In Table 3.19, the maximum and minimum bending moments are shown for all the geometries with varying E_u/c_u. As the pattern of the bending moment envelopes is similar to Figure 3.15, only the maximum design values are presented here. In all cases, DA1-1 results in higher design bending moments while the DA1-2 Strategy 2 is more critical than the DA1-2 Strategy 1. Varying the E_u/c_u has a very small effect on the resulting percentage difference between the two DA1-2 Strategies.

Table 3.19: Design Bending Moments for varying E_u/c_u

E_u/c_u	M_{max} DA1-1 (kNm/m)	M_{max} DA1-2 S1 (kNm/m)	M_{max} DA1-2 S2 (kNm/m)	M_{min} DA1-1 (kNm/m)	M_{min} DA1-2 S1 (kNm/m)	M_{min} DA1-2 S2 (kNm/m)
1-propped wall						
750	349	324	322	-1039	-789	-897
1000	343	317	316	-949	-724	-826
1250	340	312	311	-864	-664	-762
2-propped wall						
750	361	348	347	-1917	-1384	-1339
1000	352	334	333	-1692	-1226	-1217
1250	345	324	323	-1509	-1093	-1104
3-propped wall						
750	362	353	422	-2307	-1622	-1622
1000	352	337	337	-1956	-1366	-1383
1250	346	326	325	-1688	-1171	-1200
4-propped wall						
750	424	355	443	-2484	-1702	-1786
1000	441	339	339	-2039	-1391	-1472
1250	439	328	327	-1721	-1171	-1250
5-propped wall						
750	581	359	423	-2502	-1716	-1818
1000	771	342	398	-1995	-1379	-1461
1250	533	331	383	-1663	-1166	-1224

Overall, the calculated bending moments generally decrease as E_u/c_u increases, with the difference becoming more profound for the deeper excavations. Specifically, when E_u/c_u increases from to 750 to 1250, the difference in the minimum design bending moment for DA1-1, DA1-2 S1 and DA1-2 S2 is 17%, 16% and 15% respectively for a 1-propped wall, 21%, 21% and 18% for a 2-propped wall, 27%, 29% and 26% for a 3-

propped wall, 31%, 31% and 30% for a 4-propped wall and 34%, 32% and 33% for a 5-propped wall.

Similarly, in Table 3.20, the maximum and minimum design shear forces are presented. As the pattern of the shear force envelopes is similar to Figure 3.16, only the maximum design values are presented here. Again the DA1-1 governs in all cases, resulting in higher shear forces. Moreover, the difference between the two DA1-2 Strategies is apparent, with Strategy 2 being more critical than Strategy 1.

Table 3.20: Design Shear Forces for varying E_u/c_u

E_u/c_u	Q_{max} DA1-1 (kN/m)	Q_{max} DA1-2 S1 (kN/m)	Q_{max} DA1-2 S2 (kN/m)	Q_{min} DA1-1 (kN/m)	Q_{min} DA1-2 S1 (kN/m)	Q_{min} DA1-2 S2 (kN/m)
1-propped wall						
750	374	238	260	-402	-330	-365
1000	355	225	246	-374	-307	-341
1250	340	213	234	-349	-288	-320
2-propped wall						
750	599	391	413	-707	-540	-686
1000	553	357	388	-619	-468	-603
1250	515	328	367	-550	-412	-541
3-propped wall						
750	726	461	517	-783	-572	-805
1000	653	407	473	-659	-512	-681
1250	597	366	443	-597	-462	-591
4-propped wall						
750	807	496	583	-846	-607	-853
1000	714	431	526	-723	-516	-716
1250	649	384	484	-634	-484	-621
5-propped wall						
750	893	500	663	-870	-609	-913
1000	811	463	607	-738	-538	-761
1250	753	456	564	-650	-516	-660

Varying the E_u/c_u has only a small effect on the resulting percentage difference between the two DA1-2 Strategies, particularly for the deeper excavations. It was also found that increasing the E_u/c_u, generally results in a decrease in the shear forces. More specifically, when E_u/c_u increases from to 750 to 1250, the difference in the minimum

design shear force for DA1-1, DA1-2 S1 and DA1-2 S2 is 13%, 14% and 12% respectively for a 1-propped wall, 22%, 24% and 21% for a 2-propped wall, 24%, 19% and 27% for a 3-propped wall, 25%, 20% and 27% for a 4-propped wall and 25%, 15% and 28% for a 5-propped wall.

Finally, in Table 3.21, the maximum and minimum design axial forces are shown for all the geometries. Overall, the DA1-1 governs in all cases resulting in more adverse axial forces, while the DA1-2 Strategy 2 is more critical than DA1-2 Strategy 2. In general, the calculated axial forces slightly increase as E_u/c_u increases, with the difference generally being less than 10%.

Table 3.21: Design Axial Forces for varying E_u/c_u

E_u/c_u	N_{max} DA1-1 (kN/m)	N_{max} DA1-2 S1 (kN/m)	N_{max} DA1-2 S2 (kN/m)	N_{min} DA1-1 (kN/m)	N_{min} DA1-2 S1 (kN/m)	N_{min} DA1-2 S2 (kN/m)
1-propped wall						
750	25	10	19	-203	-136	-140
1000	25	10	19	-212	-142	-145
1250	25	9	10	-220	-146	-151
2-propped wall						
750	60	30	45	-391	-238	-301
1000	60	29	44	-407	-248	-315
1250	59	29	44	-422	-256	-328
3-propped wall						
750	102	55	76	-590	-361	-477
1000	101	54	75	-617	-375	-498
1250	100	53	74	-640	-388	-519
4-propped wall						
750	153	87	124	-848	-541	-662
1000	146	85	118	-894	-555	-692
1250	144	83	119	-928	-565	-715
5-propped wall						
750	327	199	254	-1576	-996	-1181
1000	311	193	243	-1650	-1017	-1236
1250	302	185	238	-1704	-1029	-1270

Overall, the results show that lowering the soil stiffness results, generally, in an increase of the calculated prop loads and the other internal structural forces such as

bending moments and shear forces without any significant effect on the resulting percentage difference between the two DA1-2 Strategies.

3.3.2.3 Effect of prop stiffness

The importance of the effect of prop stiffness on the calculated prop loads, when using numerical methods, was highlighted by Roscoe and Twine (2010). In order to illustrate the influence of the prop stiffness on the resulting differences between the different factoring combinations and strategies, the analysis was repeated for all the geometries for a prop stiffness, *k* equal to 30, 50, 100 and 150 MN/m/m and comparisons are made of the calculated design structural forces.

In Figure 3.19, the design prop loads are shown for all the geometries. It is noted that for all cases, the DA1-1 governs at all prop levels apart from the bottom one, where the DA1-2 Strategy 2 gives a more critical design prop load. Overall, for all cases considered here, the DA1-2 Strategy 2 is more critical than the DA1-2 Strategy 1, with the percentage difference, in the total force acting on the wall, between the two DA1-2 Strategies being 22%, 23%, 25.5% and 26% for *k* equal to 30, 50, 100 and 150 MN/m/m respectively.

It can be also seen, that the calculated prop loads generally increase as the prop stiffness increases. Specifically, when *k* increases from 30 to 150 MN/m/m, the total force acting on the wall for DA1-1, DA1-2 S1 and DA1-2 S2 increases by 33%, 33% and 31% for a 1-propped wall, 58%, 56% and 76% for a 2-propped wall, 66%, 62% and 78% for a 3-propped wall, 66%, 61% and 73% for a 4-propped wall and 67%, 62% and 68% for a 5-propped wall.

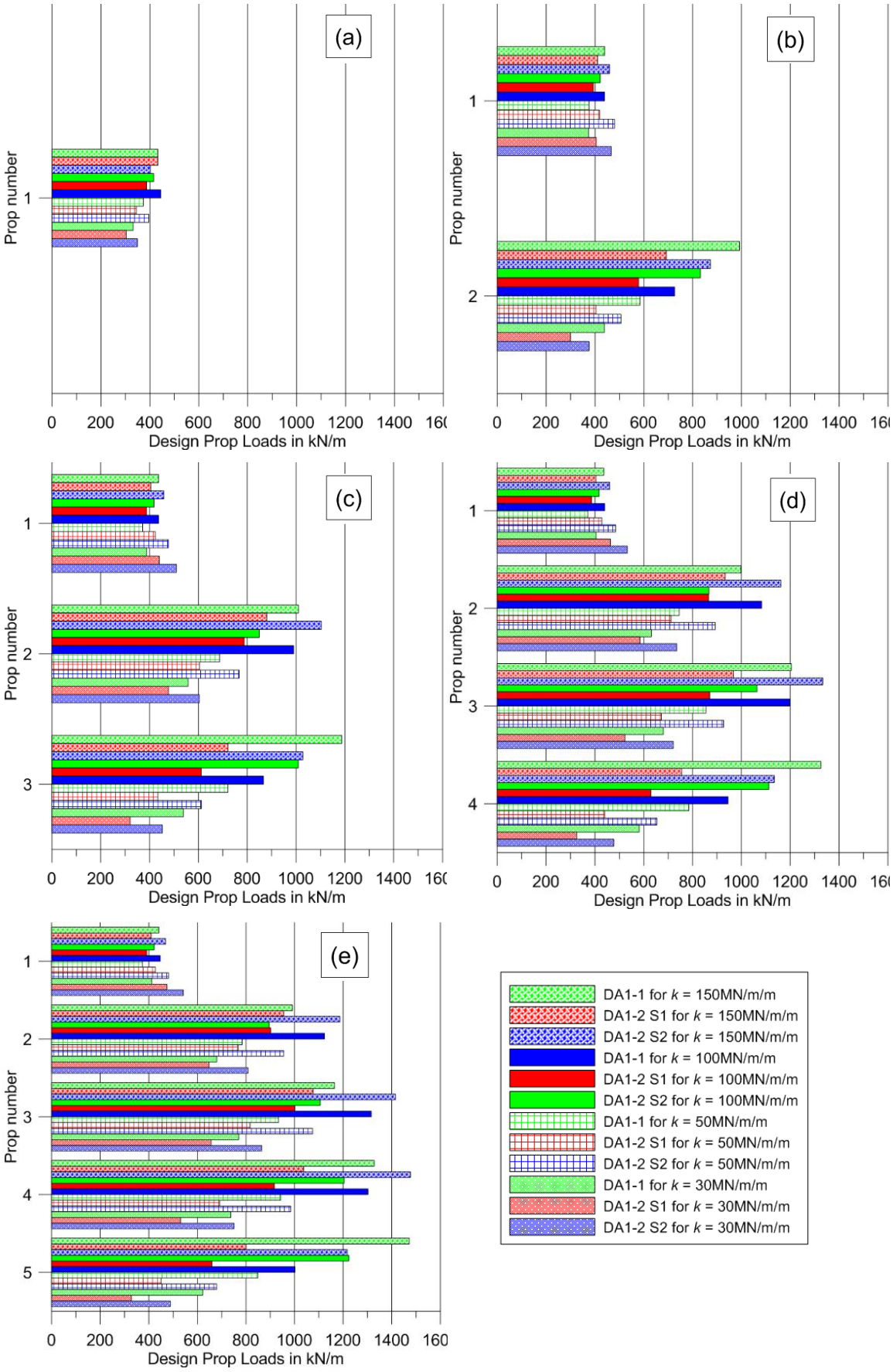

Figure 3.19: Design Prop Loads with varying k for wall with a) 1, b) 2, c) 3, d) 4 and e) 5 prop levels

In Table 3.22, the design bending moments are presented for all the geometries for a prop stiffness equal to 30, 50, 100 and 150 MN/m/m respectively.

Table 3.22: Design Bending Moments for varying prop stiffness

k (MN/m/m)	M_{max} DA1-1 (kNm/m)	M_{max} DA1-2 S1 (kNm/m)	M_{max} DA1-2 S2 (kNm/m)	M_{min} DA1-1 (kNm/m)	M_{min} DA1-2 S1 (kNm/m)	M_{min} DA1-2 S2 (kNm/m)
1-propped wall						
30	344	317	316	-762	-581	-650
50	344	317	316	-863	-653	-744
100	343	317	316	-949	-724	-826
150	343	317	316	-982	-750	-857
2-propped wall						
30	352	334	333	-1587	-1139	-1170
50	352	334	333	-1671	-1208	-1223
100	352	334	333	-1692	-1226	-1217
150	352	334	333	-1675	-1212	-1188
3-propped wall						
30	352	337	337	-1854	-1280	-1332
50	352	337	337	-1920	-1334	-1369
100	352	337	337	-1956	-1366	-1383
150	352	337	337	-1958	-1372	-1379
4-propped wall						
30	559	339	389	-1862	-1283	-1362
50	506	339	347	-1947	-1346	-1416
100	441	339	339	-2039	-1391	-1472
150	465	339	445	-2078	-1404	-1495
5-propped wall						
30	679	342	507	-1783	-1279	-1302
50	633	342	465	-1867	-1337	-1366
100	771	342	398	-1995	-1379	-1461
150	517	343	489	-2061	-1404	-1517

Overall, it was found that, the DA1-1 results in higher hogging and sagging bending moments along the wall. In all cases, the DA1-2 Strategy 2 results in higher design bending moments than the DA1-2 Strategy 1. Moreover, the calculated wall bending moments generally increase as the prop stiffness becomes higher. However, the difference is only considered significant for the 1-propped wall. More specifically, when *k* increases from to 30 to 150 MN/m/m, the difference in the minimum design bending moment for DA1-1, DA1-2 S1 and DA1-2 S2 is 29%, 29% and 32% respectively for a 1-propped wall, 6%, 6% and 2% for a 2-propped wall, 6%, 7% and 4% for a 3-propped wall, 12%, 10% and 10% for a 4-propped wall and 16%, 10% and 17% for a 5-propped wall.

Similarly, in Table 3.23, the design shear forces are presented. Again, the DA1-1 governs in all cases resulting in higher shear forces. The difference between the two DA1-2 Strategies is apparent in all cases but it becomes more significant for higher values of the prop stiffness *k,* with the Strategy 2 being more critical than the Strategy 1. Overall, the calculated shear forces generally increase with increasing prop stiffness. More specifically, when *k* increases from to 30 to 150 MN/m/m, the differences in the minimum design shear force for DA1-1, DA1-2 S1 and DA1-2 S2 was 31%, 31% and 31% respectively for a 1-propped wall, 65%, 70% and 77% for a 2-propped wall, 56%, 48% and 103% for a 3-propped wall, 57%, 45% and 108% for a 4-propped wall and 56%, 37% and 108% for a 5-propped wall.

Table 3.23: Design Shear Forces for varying prop stiffness

k (MN/m/m)	Q_{max} DA1-1 (kN/m)	Q_{max} DA1-2 S1 (kN/m)	Q_{max} DA1-2 S2 (kN/m)	Q_{min} DA1-1 (kN/m)	Q_{min} DA1-2 S1 (kN/m)	Q_{min} DA1-2 S2 (kN/m)
1-propped wall						
30	315	193	211	-298	-244	-271
50	336	210	229	-337	-275	-307
100	355	225	246	-374	-307	-341
150	362	231	253	-390	-319	-354
2-propped wall						
30	528	336	378	-422	-310	-388
50	546	351	387	-499	-371	-470
100	553	357	388	-619	-468	-603
150	550	355	384	-696	-528	-686
3-propped wall						
30	622	382	460	-493	-371	-395
50	638	395	469	-568	-433	-486
100	653	407	473	-659	-512	-681
150	657	411	474	-768	-548	-801
4-propped wall						
30	672	405	501	-510	-396	-408
50	692	414	513	-576	-456	-504
100	714	431	526	-723	-516	-716
150	725	439	531	-803	-576	-849
5-propped wall						
30	782	433	587	-533	-430	-437
50	796	438	596	-593	-490	-535
100	811	463	607	-738	-538	-761
150	819	487	638	-833	-590	-907

In Table 3.24, the design axial forces are shown. Overall, the DA1-1 governs in all cases resulting in more adverse axial forces. The discrepancy between the two DA1-2 Strategies is apparent in all cases, with Strategy 2 being more critical than Strategy 1 with the difference generally being less than 10%. Overall, it was found that the minimum axial forces generally decrease with increasing prop stiffness.

Table 3.24: Design Axial Forces for varying prop stiffness

k (MN/m/m)	N_{max} DA1-1 (kN/m)	N_{max} DA1-2 S1 (kN/m)	N_{max} DA1-2 S2 (kN/m)	N_{min} DA1-1 (kN/m)	N_{min} DA1-2 S1 (kN/m)	N_{min} DA1-2 S2 (kN/m)
1-propped wall						
30	25	10	19	-243	-160	-165
50	25	10	10	-229	-152	-155
100	25	10	19	-212	-142	-145
150	25	10	19	-205	-138	-141
2-propped wall						
30	60	29	44	-469	-280	-368
50	60	29	44	-439	-265	-343
100	60	29	44	-407	-248	-315
150	60	29	44	-394	-240	-303
3-propped wall						
30	101	54	75	-712	-423	-582
50	101	54	75	-668	-403	-544
100	101	54	75	-617	-375	-498
150	101	54	75	-592	-362	-479
4-propped wall						
30	146	85	115	-1056	-606	-809
50	146	85	115	-984	-586	-755
100	146	85	118	-894	-555	-692
150	149	85	120	-849	-538	-662
5-propped wall						
30	284	177	200	-1941	-1115	-1469
50	295	186	230	-1820	-1075	-1369
100	311	193	243	-1650	-1017	-1236
150	317	196	248	-1570	-989	-1174

3.4 Numerical Vs Empirical methods for deriving prop loads

3.4.1 Empirical methods

For multi-propped walls, there are a number of empirical methods, represented graphically that allow the derivation of the design prop loads. Traditional methods (e.g. Terzaghi and Peck 1967; Peck 1969) are simple to use and have been widely adopted in practice. They are based on field measurements of prop loads and provide the designer with conservative lateral earth pressures distributions. Peck (1969) considered a number of case studies in stiff clays supported only by flexible walls so he only provided tentative pressure graphs for excavations in stiff clays, supported by stiff walls. However, he stated at an ASCE conference in 1990 that these graphs might not be conservative (Twine and Roscoe, 1999).

CIRIA C517 (Twine and Roscoe, 1999), enhancing Terzaghi's work and making it more relevant in the UK practice, suggested the Distributed Prop Load (DPL) method, based on 81 case histories and field measurements of prop loads. Soils are classified in 4 classes, named A, B, C and D, corresponding to normally consolidated and slightly over-consolidated clays, heavily over-consolidated clays, granular soils and mixed soils respectively. A distinction is also made between flexible (e.g. sheet pile) and stiff walls (e.g. diaphragm, bored pile). Note that the DPL is not the real lateral stress distribution but provides values of prop forces unlikely to be exceeded for any temporary system in a similar excavation (Twine and Roscoe, 1999). There are also several conditions that the designer should check before using the empirical graphs (e.g. excavation depth and width, number of prop levels, sufficient toe embedment etc.). CIRIA C517 gives characteristic values of prop loads in accordance with the Eurocode's definitions. The guide adopts the *limit state* approach and is compliant with the ENV 1997-1. It is suggested that the ENV 1997-1 Case B (equivalent to EN1997-1 DA1 Combination 1) is likely to govern the design.

BS8002 (1994), for multi-propped walls, recommends the use of Peck's diagrams without mentioning how they should be used for ULS and SLS calculations. CIRIA C580 (Gaba et al., 2003), which is included in the EC7 UK National Annex as a NCCI (Non Contradictory Complementary Information) document, encourages the use of soil-structure interaction methods (beam-spring, beam continuum, FEM etc.) for multi-propped wall design, mentioning that the results should always be checked with comparable experience and past practice. The guide also makes reference to the CIRIA C517 and clearly encourages the use of the DPL method which means that both

documents are still in use along with EC7 and many designers still refer to the CIRIA DPLs for the design of supported walls.

Similar guidance and pressure graphs exist in other European countries. The 3rd edition of the German EAB Recommendations on Excavations (EAB, 2014) has been recently published and included in the EC7 German National Annex as an NCCI. Note that the guidance provides the shapes of the redistributed pressure diagrams but not the dimensions. The dimensions are problem dependent (i.e. based on lateral earth coefficient values) as the area of the trapezoid should be equivalent to the area of the classical triangular earth pressure distribution.

3.4.2 Comparing the results from the FEM and the empirical methods

In Figure 3.20, the design prop loads calculated from the FE analyses and the empirical methods are presented for a supported wall with 1, 2, 3, 4 and 5 prop levels. The detailed calculations of the prop loads, based on the CIRIA C517 and EAB diagrams, are shown in Appendix B. The results from both the DA1-1 and the DA1-2 Strategy 1 and 2 are shown and not just the maximum calculated value from all cases, to allow for better comparison. In all analyses, a value of K_0 equal to 1.5 was used while the prop stiffness was taken as k = 100 MN/m/m.

It can be seen that the agreement between the different calculation methods is reasonable for the cases with 1 and 2 prop levels. However, for deeper excavations and more prop levels, the DPL results in significantly higher values of the design prop loads at the top prop level, when compared to the values from both the EAB method and the FEM. While the total force acting on the wall is similar for both empirical methods, the EAB guide generally results in conservative prop loads at all prop levels, showing a better agreement with the pattern seen on the FEM values. This highlights that the uniform distribution assumed by the CIRIA C517 report is challenged for the cases with more than two prop levels.

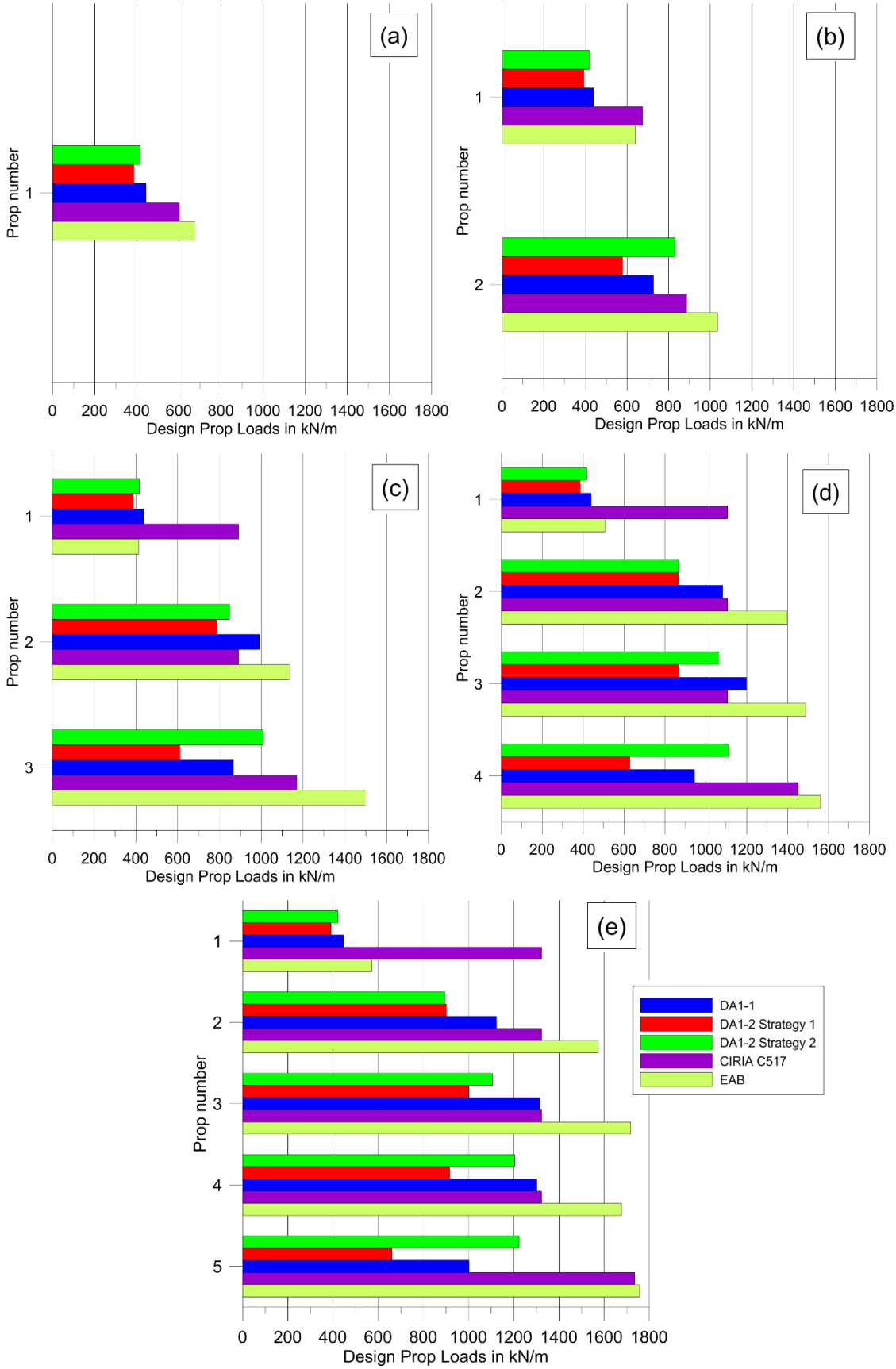

Figure 3.20: Design prop loads from FE and empirical methods for wall with a) 1, b) 2, c) 3, d) 4 and e) 5 prop levels

It was found that CIRIA C517 and FEM calculations provide different prop force values for multi-propped wall geometries, with the differences being particularly apparent for the upper prop levels where CIRIA's assumption of uniform distribution of the pressure load with depth results in significantly higher design prop loads. FEM results in lower values of loads at the upper prop level, increasing with excavation depth for the geometries with two or more props considered here. This raises the question of how accurate is C517's assessment stating that the force in the upper props will be equal to that in the lower props for multi propped geometries. On the other hand, FE methods and the German EAB guidance provide prop force values that are in better agreement.

As previously discussed, CIRIA C517 does not provide the real lateral stress distribution but values of prop forces unlikely to be exceeded for any temporary system in a similar excavation. For excavations in stiff clays supported by stiff walls and props, the CIRIA's assessment was based on ten case studies, most of them in London clay. Five case studies were supported by only one level of props, one case study by two levels of props and the rest by three prop levels. The pressure distributions for each case are presented in the Appendix of the guide (Twine and Roscoe, 1999). Single-propped geometries result, as expected, in uniform pressure distributions (e.g. BS1, BS3, BS5 case studies). As the number of prop levels increase, the pressure distribution becomes stepped, increasing with depth. However, when the pressure distributions from all the case studies are plotted in a single graph, the resulting characteristic (i.e. cautious estimate) DPL is uniform with depth and equal to $0.5\gamma H$. The resulting diagram might be sufficient for single-propped or even double-propped excavations but can be too conservative for walls supported by more prop levels. Half of the case studies considered are singly supported walls and the resulting pressure distributions are uniform with depth. Plotting all the pressure distributions, results in uniform DPL which ignores (or does not explicitly takes into account) the stepped pressure distributions of the case studies with more levels of props.

The German EAB Recommendations on Excavations suggests different shapes of pressure distribution for supported walls with different number of prop levels. The distribution is uniform (rectangular) for singly supported walls and becomes trapezoidal as the number of prop levels increases. This assessment is more reasonable and results in design prop loads in better agreement with the FEM results for the range of geometries considered here.

Singly supported excavations are statically determinate problems and conventional analytical methods are sufficient to calculate the structural forces. However, for multi-

supported excavations, where the analytical methods are not relevant, empirical pressure distributions based on field measurements and good practice can be of great value. It might be worth adopting the German thinking and considering separately the CIRIA C517 case studies. This would result in different characteristic DPLs for different numbers of prop levels and more realistic predictions of the upper prop load values, particularly in deep excavations. It might be also worth including more case studies (with higher excavation depths and more prop levels). Conventionally one or two levels of props used to be sufficient for supported excavations in the London area. However, in the last few years, in many projects (e.g. Crossrail station boxes) the excavation depth is higher and hence more prop levels are needed to ensure that the SLS and ULS requirements are met. CIRIA C580 and C517 should be in line with the current practice in deep excavations.

3.5 Accidental prop loss

In deep supported excavations, the most typical example of an accidental design situation is the loss of a single prop. As described in Section 1.6, there are two methods of accounting for a single props loss: a) incorporating the loss of prop into the design of the support system and b) a risk assessment and management strategy to eliminate the risk of accidentally damaging a prop.

In this section, this study focuses on the first method and particularly how the prop loss effect can be accounted for in 2D and 3D FE analysis for a deep excavation in London Clay, supported by 5 levels of props. As discussed in Section 1.3.5, for accidental design situations, a partial factor of 1.0 shall be used according to EC7. Hence, the accidental prop loss effect can be easily investigated in conjunction with the SLS FE analysis.

3.5.1 2D FE analysis

For the 2D FE analysis, the 5-propped wall case shown in Figure 3.1e, was studied. Only the reference case using the MC model was considered with K_0 = 1.5, E_u/c_u = 1000 and k = 100MN/m/m. The modelling assumptions and the construction sequence down to the formation level are the same as discussed previously in Section 3.2. However, for the accidental prop loss analysis, five separate stages were included after the excavation to the formation level for the SLS FE analysis. In each of these separate stages, one individual prop was deactivated and the forces allowed to redistribute until the model reached equilibrium.

Figure 3.21 shows the maximum prop load at each level, level from all the accidental prop loss stages simulated. These are plotted together with the design prop

loads from the corresponding ULS analysis (i.e. the highest loads from the DA1-1 and the two DA1-2 Strategies). It can be seen that, for the upper two levels, the prop loads are higher for the accidental conditions while for the bottom three levels, the calculated prop loads are higher for the ULS conditions.

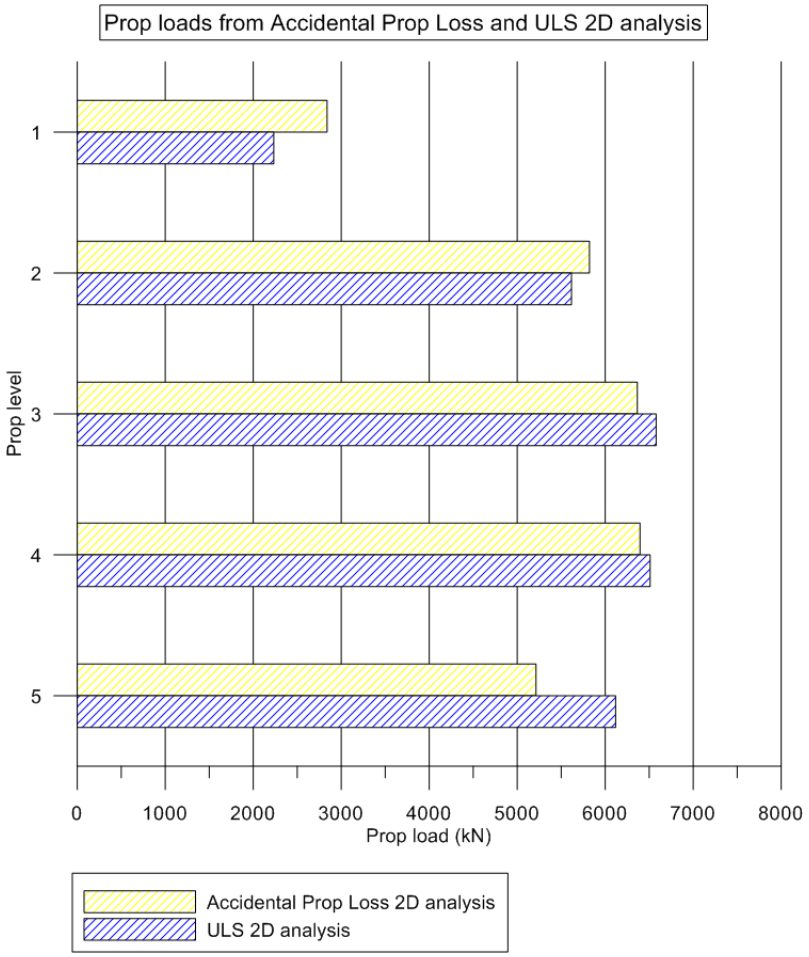

Figure 3.21: Prop loads for accidental prop loss and ULS 2D analysis

This highlights that the ULS analysis is not always sufficiently conservative to account for the single prop loss effect and designers need to include separate stages in the analysis accounting for the loss of each one of the props. The maximum value obtained from the ULS or from the prop loss analysis should be the design value of each prop.

3.5.2 3D FE analysis

The single prop loss is, in principle, a three-dimensional problem as the prop load of the deactivated prop is redistributed to the adjacent props not only in the vertical but also in the horizontal direction. For this reason, the prop loss effect is investigated using 3D FE methods for a deep excavation model, based on the 5-propped wall geometry studied in the 2D FE analysis.

3.5.2.1 Soil profile and geometry

The soil profile and the material parameters are the same as in the 2D analysis. The excavation is 24m deep, supported by 1m thick concrete diaphragm wall and 5 levels of horizontal hollow steel props with 8 props at each level. The diaphragm wall is 7.5m embedded in the London Clay. The dimensions of the excavation are 20m x 40m in plan view and the horizontal spacing of the props is 5m centre to centre as shown in Figure 3.22.

3.5.2.2 Modelling assumptions

The software used is PLAXIS 2016 in its three-dimensional version. The FE mesh of the 3D model, consisting of 15-noded triangular elements, is shown in Figure 3.23. The mesh was generated initially using the automatic mesh generation facility and the areas of interest in the potential active and passive zones, around the props and adjacent to these, were refined to give greater node density. The boundary conditions adopted were the standard fixities offered by PLAXIS. The ground level horizontal boundary was free both horizontally and vertically. The bottom horizontal boundary was fixed both horizontally and vertically while the vertical boundaries each side of the model were fixed horizontally but free vertically.

In Figure 3.24 a cross-section of the model, perpendicular to the *y* axis, is presented. The rest of the modelling assumptions, including the wall and prop properties as well as the Mohr-Coulomb model parameters assumed, for the London Clay and the Made Ground, are the same as discussed previously in Section 3.2.

For the SLS analysis, the construction sequence down to the formation level is the same as discussed in Section 3.2. However, for the accidental prop loss analysis, 20 separate stages were included, following the excavation to the formation level, where each of the individual props prop was deactivated (i.e. one prop deactivated at each stage). Due to symmetry, only the prop loss effect of half the props was considered. More specifically, at each of the five prop levels, four prop locations were considered with increasing distance from the side wall: A, B, C and D as shown in Figure 3.22.

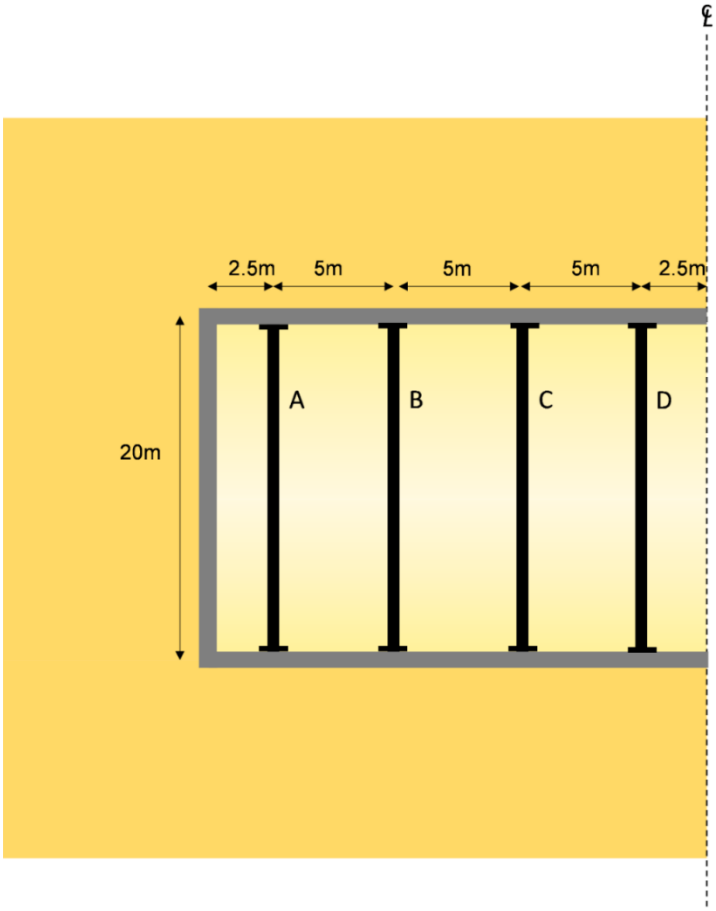

Figure 3.22: Plan view of half the 3D excavation geometry

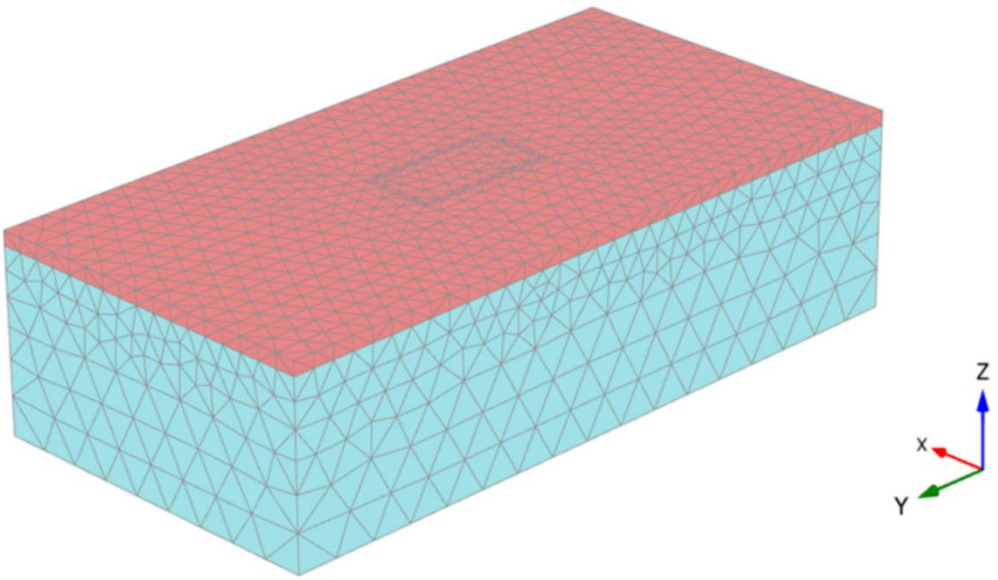

Figure 3.23 Finite Element mesh of the 3D model

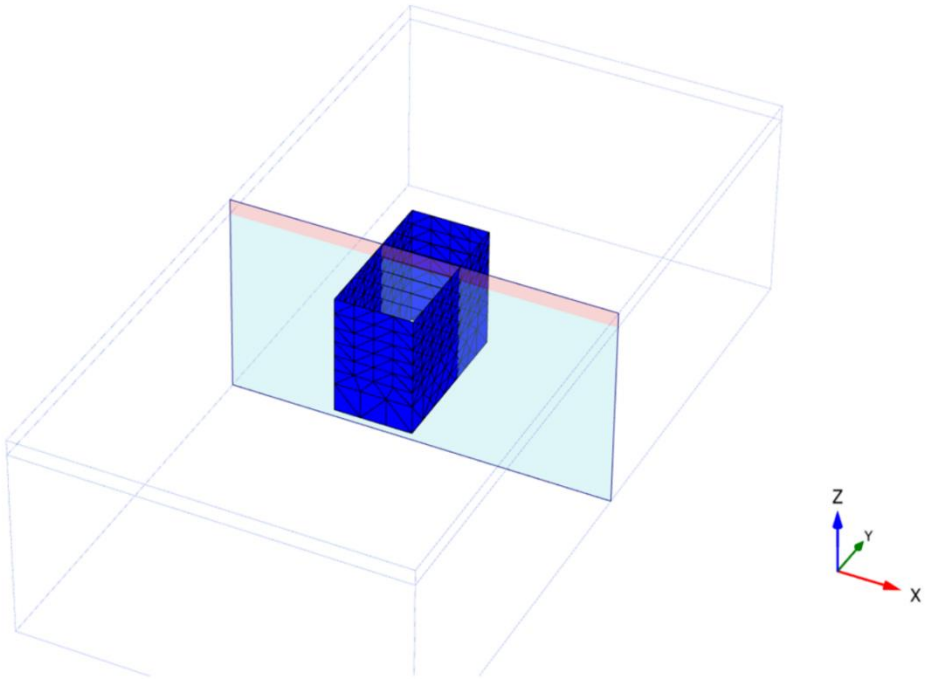

Figure 3.24 Cross-section perpendicular to *y* axis

First, the results of the 3D FE analysis are presented for the SLS conditions. In Figures 3.25 and 3.26, the plastic points shown in red (i.e. points where the soil exhibits plastic behaviour) and the corresponding zone of fully mobilised soil strength, at the final excavation stage, are shown respectively on *x*-*z* cross section. Similarly, in Figures 3.27 and 3.28, the plastic points and the zone of fully mobilised soil strength are shown respectively on *y*-*z* cross section.

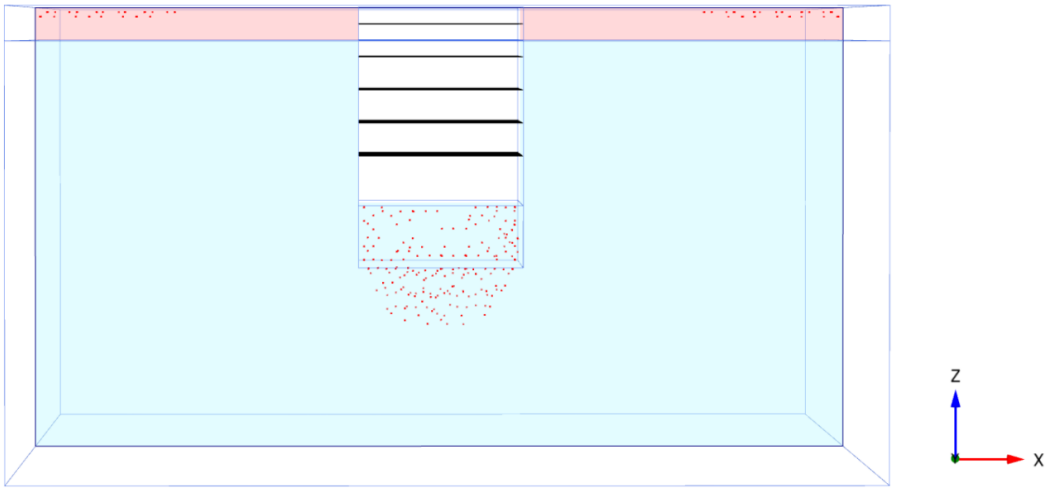

Figure 3.25: Plastic points on *x*-*z* cross section

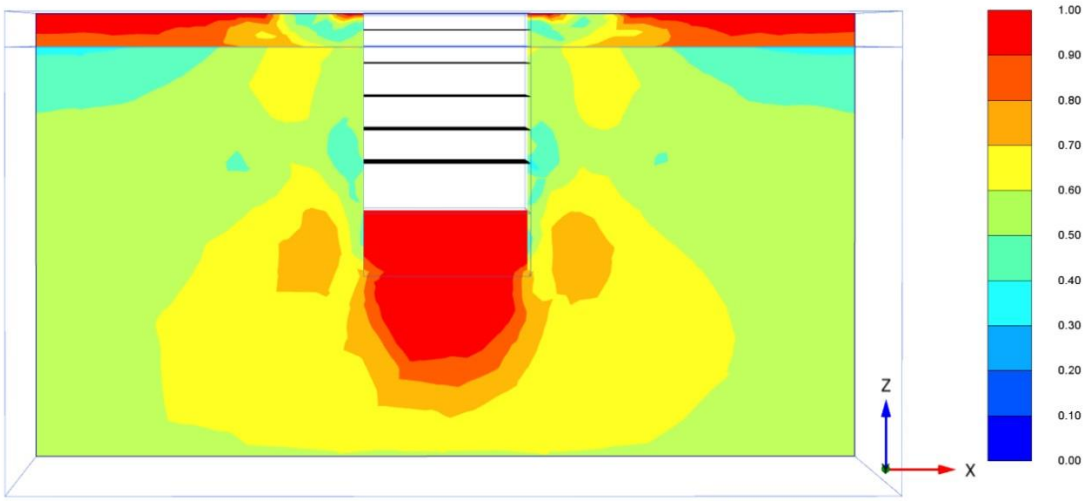

Figure 3.26: Mobilised soil strength on *x-z* cross section

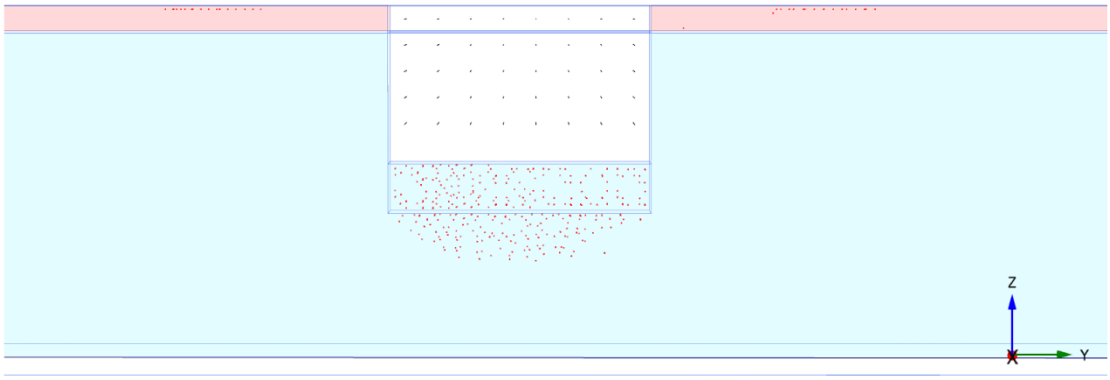

Figure 3.27: Plastic points on *y-z* cross section

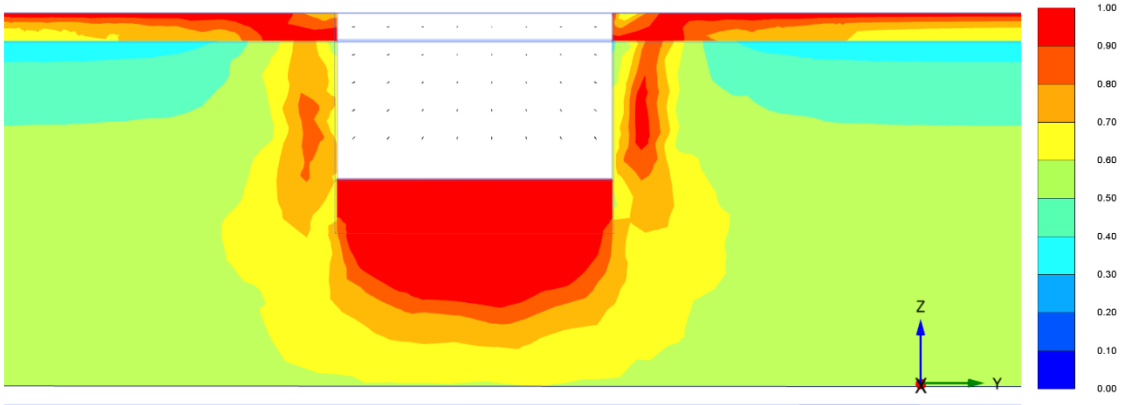

Figure 3.28: Mobilised soil strength on *y-z* cross section

It can be seen that there is a large plastic zone, defined by the contour equal to 1.0 and shown in red, at the base of the excavation in front of the wall, which is in agreement with the findings in section 3.3.2. It can be also seen that the strength of the soil on the active side is more mobilised on the *y-z* cross section than on the *x-z* cross section. This is because, in the 3D model, only the long sides of the embedded wall are supported by props because, as shown in Figure 3.29, this is where the highest horizontal stresses (and hence the highest total force acting on the wall) are generated.

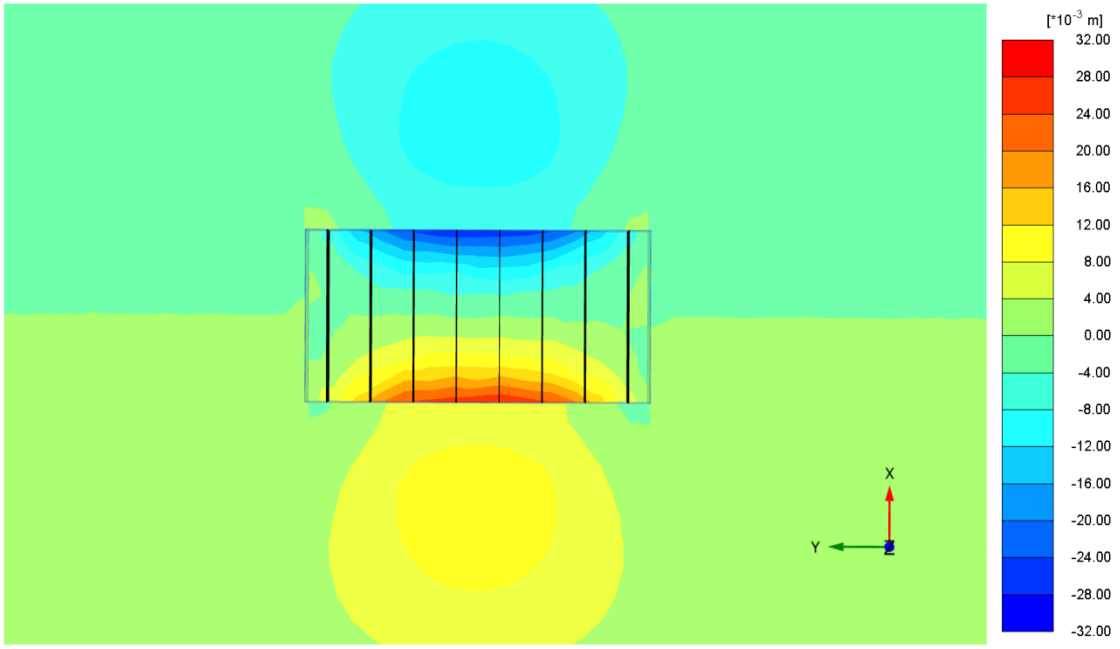

Figure 3.29: Horizontal effective stresses (plan view)

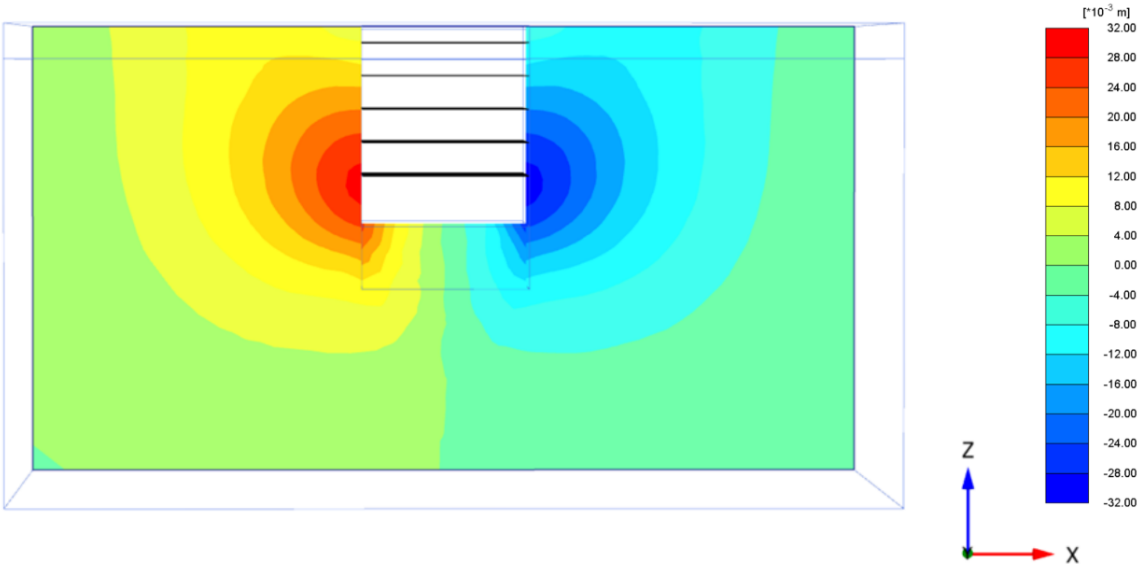

Figure 3.30: Horizontal soil displacements on *x-z* cross section

For the SLS analysis, the maximum prop loads obtained from the 3D FE analysis are presented in Figure 3.31. Please note that, the prop loads shown are the axial loads in kN per prop while the 2D analysis results were previously shown in kN per m run along the line of the wall. It can be seen that the prop loads, at all prop levels, are higher at the prop locations C and D, in the centre of the excavation box, and much lower at the prop location A, close to the corner of the excavation box. Moreover, for all prop locations, higher prop loads were observed at the lower prop levels where the effective horizontal stresses and the horizontal soil displacements, shown in Figure 3.29 and 3.30 respectively, are higher.

In Figure 3.32, the design prop loads are presented from the 3D ULS analysis along the results from the corresponding 2D analysis. Again, only the maximum values from both the DA1-2 and DA1-2 are shown. It can be seen that, for the props in the centre of the excavation box (i.e. prop locations C and D), the design loads calculated from the 3D analysis are very similar to the values obtained from the 2D analysis. This illustrates that the plane strain conditions considered in the 2D analysis is a reasonable assumption for the props located in the centre of the excavation where the corner effects are negligible. However, for the props closer to the corner of the excavation box (i.e. prop location A and to a lesser extend B), the design loads obtained from the 3D analysis are lower than the corresponding loads from the 2D analysis.

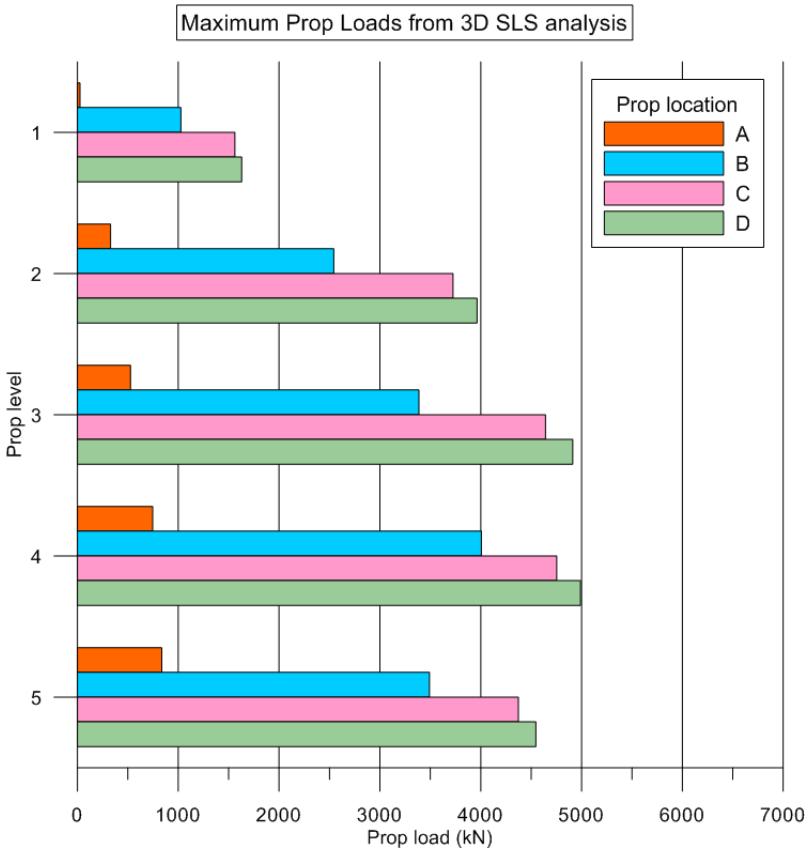

Figure 3.31: Maximum Prop loads for the 3D SLS analysis

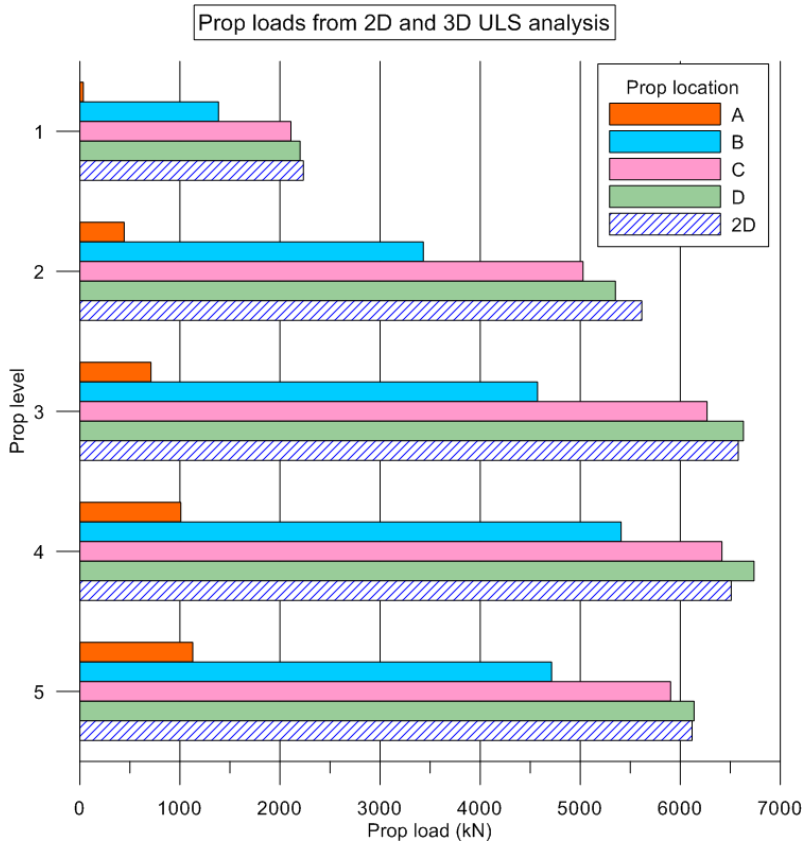

Figure 3.32: Prop loads for 2D and 3D ULS analysis

In Figure 3.33, the maximum prop loads are shown from the accidental prop loss 3D analysis along with the values from the 2D case. It can be seen that, for the props at locations C and D, the prop loads from the 3D analysis are not similar to the values from the 2D analysis. This illustrates that the prop loss is a complex three-dimensional problem and the plane strain assumption in the 2D analysis is no longer reasonable even in the centre of the excavation box.

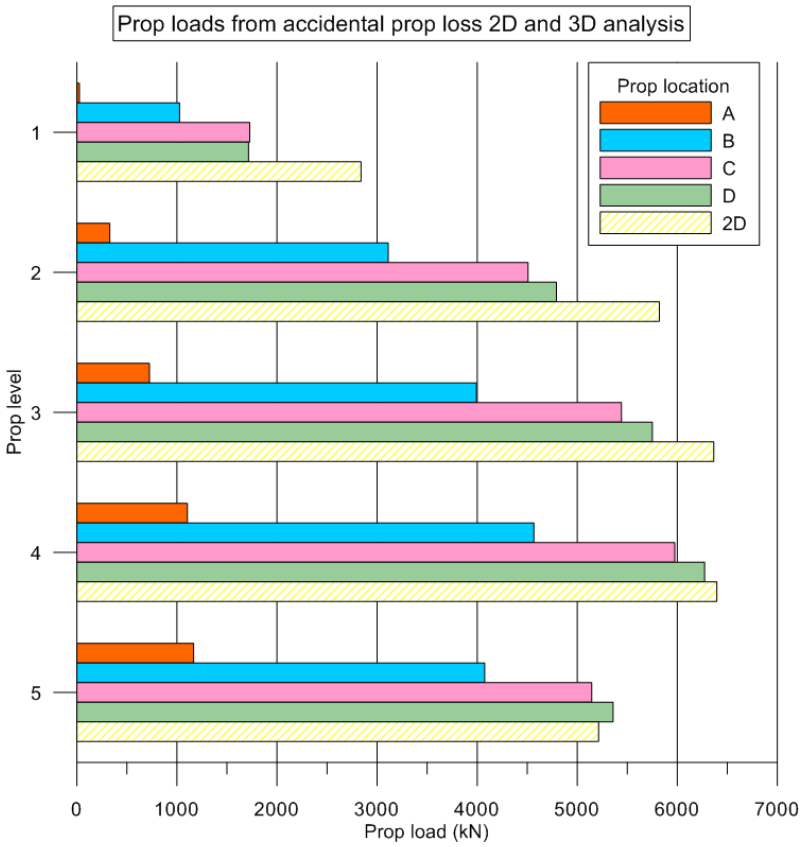

Figure 3.33: Prop loads for accidental prop loss 2D and 3D analysis

When comparing the prop loads from the accidental prop loss 3D analysis (Figure 3.33) with the design values obtained from the 3D ULS analysis (Figure 3.32), it can be seen that the latter values are higher than the first in all cases apart from the location A prop load at the bottom three levels. This again illustrates that the ULS analysis cannot sufficiently account for the effects of the single prop loss case and separate analysis stages need to be performed to investigate the effect. The prop loads that govern the design are the maximum values obtained from both the ULS and the accidental prop loss analysis.

3.6 Supported Excavation in Soft Marine Clay

3.6.1 Introduction

The 2D FE analysis was repeated for the 5-propped wall case for a typical soil profile in Singapore. This profile was selected because it typically consists of a soft and weak clay of marine origin. This allows a comparison of the calculated design structural forces between the different EC7 factoring combinations and methods as well as an investigation of the influence of the material's strength, since these results are also compared with those discussed previously for a typical London Clay profile.

3.6.2 Typical soil profile in Singapore

A typical soil profile in mainland and offshore areas of Singapore consists of about 40m of soft soils of the Kallang Formation; a quaternary deposit that lies within valleys cut in the Old Alluvium deposits (Arulrajah and Bo, 2008). There are two major units in the Kallang Formation, namely the Upper and Lower Marine Clay which are underlain by Estuarine/Fluvial clays and sands. The oldest major unit, the Lower Marine Clay (LMC), was deposited about 120,000 years ago, while the Upper Marine Clay (UMC), and other facies of the Kallang Formation, date from 10,000 years ago (Bird et al., 2003). Varying sea levels had a profound impact on the deposition environment of the terrestrial and marine facies of the Kallang Formation as shorelines advanced and retreated from the mainland. Both units are highly plastic silty clays and have high compressibility and moisture content (Choa et al., 2001). The major clay mineral is kaolinite, with some presence of illite and smectite. A more detailed description of the material properties is given by Bo et al. (1998); Bo et al. (2000); and Arulrajah and Bo (2008).

While the two units of Marine Clay have generally similar features and properties, the top layer of the LMC was weathered, as the sea level dropped, to a stiff mottled clay unit (typically referred to as F2) which is over-consolidated and has low compressibility and moisture content. This intermediate layer that separates the two Marine Clay units forms a sub-horizontal unit that lies about 15m below current sea level (Bird et al., 2003 and Choa et al., 2001). The Old Alluvium is typically a very dense cemented silty and clayey sand with a few stiff clay layers (Simpson et al., 2008). A simplified soil profile in Singapore was used for this study which consists of 4m of Fill, 15m of UMC, 4m of F2 and 11m of LMC overlying the Old Alluvium (Simpson and Junaideen, 2013). The Mohr-Coulomb model parameters for all the materials are listed in Tables 3.25 to 3.28 and are based on the studies discussed here.

Table 3.25: Mohr-Coulomb parameters for Upper Marine Clay

Upper Marine Clay parameters	
Unit weight of soil, γ_{sat} (kN/m^3)	16
Undrained shear strength, c_u (kPa)	20 + 1 z
Effective Young's modulus, E' (MPa)	333 c_u
Earth pressure coefficient at rest, K_0	1
Poisson's ratio, v'	0.2
where z is the depth below 14m bgl	

Table 3.26: Mohr-Coulomb parameters for F2

F2 parameters	
Unit weight of soil, γ_{sat} (kN/m^3)	19
Undrained shear strength, c_u (kPa)	25 + 1.3 z
Effective Young's modulus, E' (MPa)	333 c_u
Earth pressure coefficient at rest, K_0	1
Poisson's ratio, v'	0.2
where z is the depth below 14m bgl	

Table 3.27: Mohr-Coulomb parameters for Lower Marine Clay

Lower Marine Clay parameters	
Unit weight of soil, γ_{sat} (kN/m^3)	16.5
Undrained shear strength, c_u (kPa)	42 + 1.4 z,
Effective Young's modulus, E' (MPa)	333 c_u
Earth coefficient at rest, K_0	1
Poisson's ratio, v'	0.2
where z is the depth below 23m bgl	

Table 3.28: Mohr-Coulomb parameters for Alluvium

Alluvium parameters	
Unit weight of soil, γ_{sat} (kN/m^3)	21
Effective cohesion, c' (kPa)	25
Angle of shearing resistance, φ' (°)	35
Effective Young's modulus, E' (MPa)	200
Earth coefficient at rest, K_0	0.7
Poisson's ratio, v'	0.2

3.6.3 ULS analysis of 5-propped embedded wall

The analysis was repeated for the reference 5-propped wall case for a typical soil profile in Singapore as shown in Figure 3.34. The excavation depth is 24m and the excavation width is 30m similar to the cases considered before for the stiff clay profile. The wall is supported by 5 levels of props with a prop stiffness equal to k = 100MN/m/m. The embedment depth of the wall is 20m, significantly larger when compared to the supported excavations in London Clay. This is because the marine clay is extremely soft and the wall needs to be well embedded into the much stiffer and stronger Alluvium.

Moreover, jet grouting in the area below the formation level and in front of the wall, as shown in Figure 3.34, was needed to ensure stability against excessive wall deflection and soil deformations; a common practice for deep excavations in soft marine clays. The calculated design structural forces are plotted to illustrate the effect of the soil type on the resulting differences between the different factoring combinations and strategies.

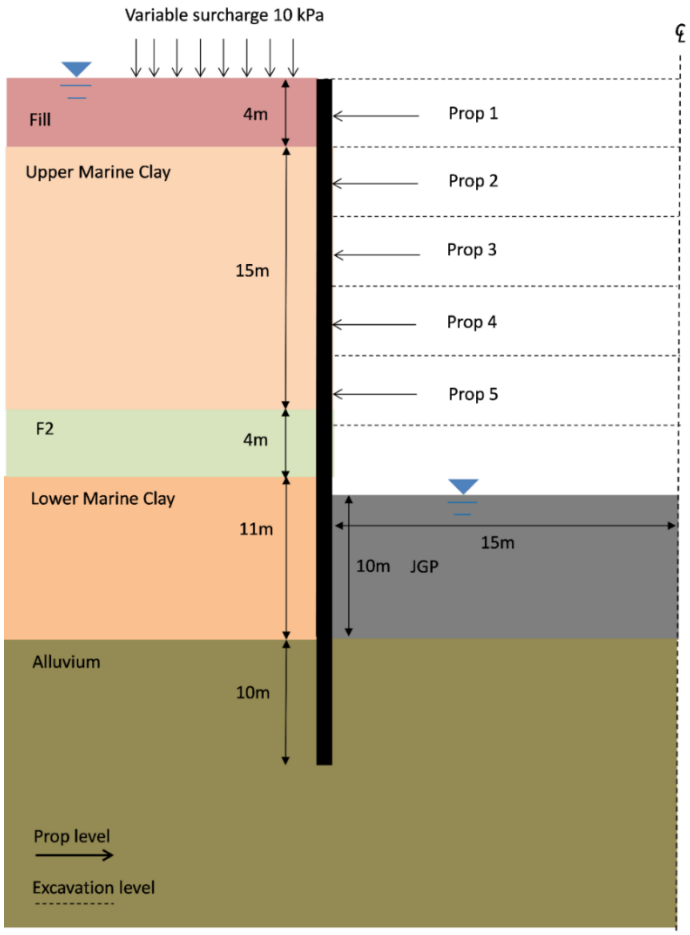

Figure 3.34: Geometry of a deep excavation in a typical Singapore soil profile

In Figure 3.35, the design prop loads are shown and it can be seen that the DA1-2 Strategy 2 governs at all prop levels. More specifically, the DA1-2 Strategy 2 is more

critical than the DA1-2 Strategy 1, with the percentage difference in the prop load between the two DA1-2 Strategies, being 19%, 22%, 32%, 34% and 46% for the for the first, second, third, fourth and bottom prop level respectively. Overall, the percentage difference in the total force acting on the wall between the two DA1-2 Strategies is about 30%. The DA1-1 is more critical than the DA1-2 Strategy 1 for the upper 4 prop levels with the difference in the total force acting on the wall being 3.5%.

Overall, the Material Factoring Approach, expressed by the DA1-2 Strategy 2, is more critical than the DA1-1, showing that factoring the soil strength of a weak soil such as this, has a more profound effect than factoring the strength of a hard soil, such as the London Clay. In DA1-2 Strategy 2, when shifting from characteristic to factored soil strength at each excavation stage, the lowest prop level receives a higher load increment than the rest of the prop levels. This increase is due to the development of a large plastic zone in front of the wall, as shown in red in Figure 3.36. The props are installed when the soil strength is unfactored and the developed strains are much lower than those developed in the DA1-2 Strategy 1 case. While the effect is the same as the one discussed before, for a similar excavation in London Clay, now it becomes more profound as the soil is weaker and when the soil strength is factored, much larger strains are developed and hence the props have a stiffer response and pick up higher loads.

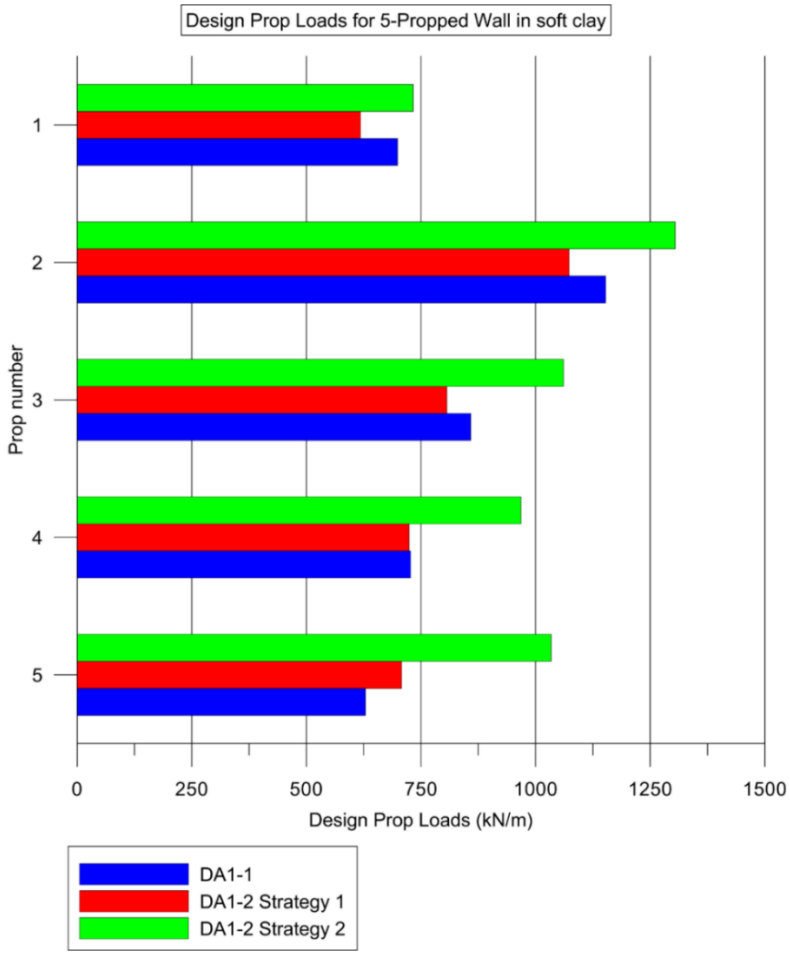

Figure 3.35: Design Prop Loads for 5-propped wall in typical Singapore soil profile

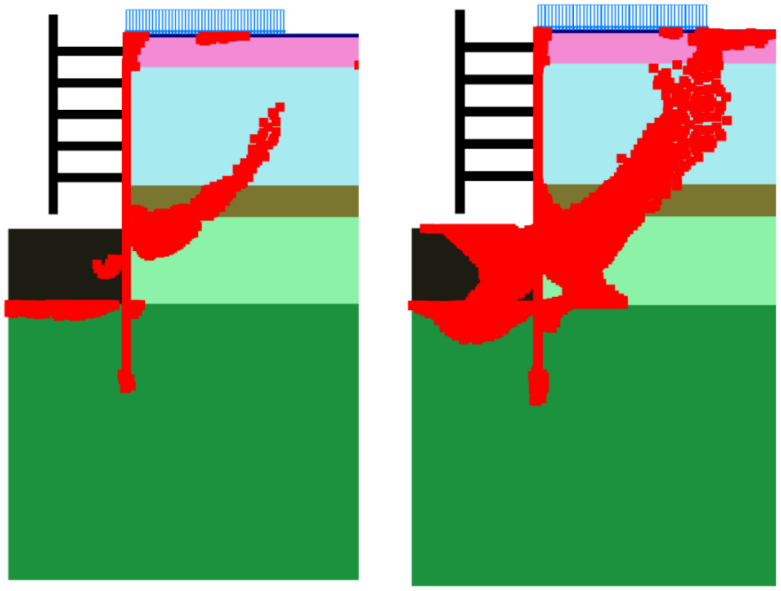

Figure 3.36: Plastic points developed at the final excavation stage for the 5-propped wall: a) before the excursion and b) after the excursion

In Figure 3.37, the design bending moment envelopes are plotted. It can be seen that the minimum and maximum bending moments are -5132kNm/m and 5281kNm/m respectively, for DA1-1; -3475kNm/m and 7063kNm/m for DA1-2 Strategy 1 and -4327kNm/m and 4001kNm/m for DA1-2 Strategy 2. It was found that the DA1-2 Strategy 1 generates the highest maximum bending moment. More specifically, the DA1-2 Strategy 1 results in much higher maximum bending moment than the DA1-2 Strategy 2 with the difference being 76.5% while the DA1-1 is more critical than the DA1-2 Strategy 2, with the difference in the maximum bending moment being 32%. Overall, in DA1-2 Strategy 1, the soil strength is factored right from the beginning of the analysis and the developed strains are much higher than those developed when the strength is unfactored, resulting in a higher maximum design bending moment.

Moreover, the DA1-1 governs the design in terms of the minimum bending moment. The DA1-1 is more critical than the DA1-2 Strategy 2, with the difference in the minimum bending moment being 19%. The DA1-2 Strategy 2 results in a more onerous minimum bending moment than the DA1-2 Strategy 1, with the difference being 24.5%.

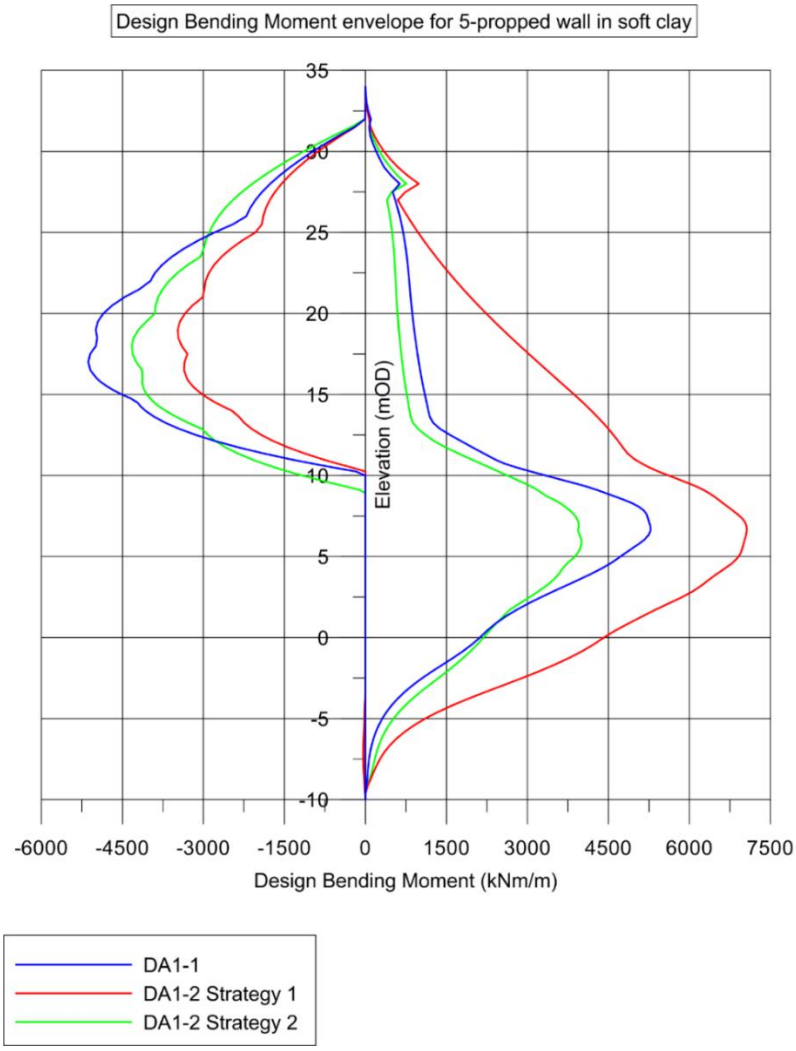

Figure 3.37: Design Bending Moment envelopes for 5-propped wall in typical Singapore soil profile

In Figure 3.38, the design shear force envelopes are presented. The minimum and maximum shear forces are -1098kN/m and 2070kN/m for DA1-1, -1082kN/m and 1553kN/m for the DA1-2 Strategy 1 and -1145kN/m and 1531kN/m for the DA1-2 Strategy 2. It was found that the DA1-1 results in the most critical maximum shear force. The DA1-1 generates a higher maximum shear force than the DA1-2 Strategy 1, with the difference being 33%, while the difference between the two DA1-2 Strategies is negligible. Moreover, the DA1-2 Strategy 2 governs the design in terms of the minimum shear force resulting in about 4% and 6% higher force than the DA1-1 and the DA1-2 Strategy 1 respectively.

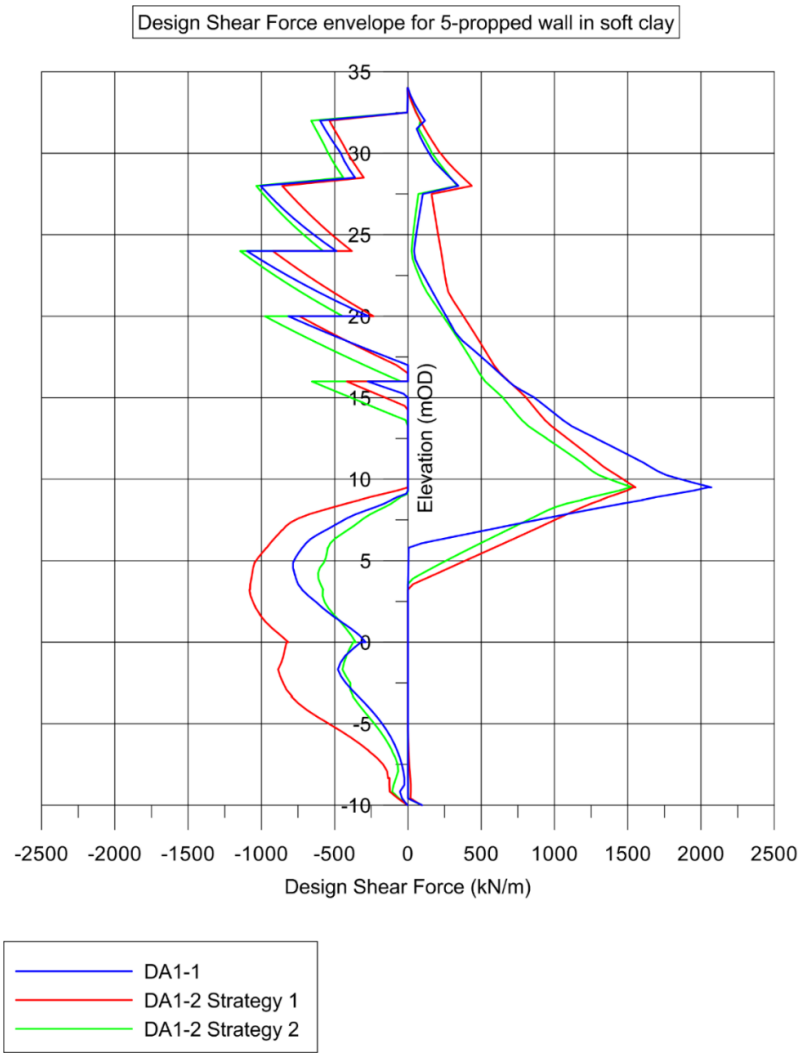

Figure 3.38: Design Shear Force envelopes for 5-propped wall in typical Singapore soil profile

The design axial force envelopes are shown in Figure 3.39. The minimum and maximum axial forces are -538kN/m and 1587kN/m for the DA1-1, -297kN/m and 1291kN/m for the DA1-2 Strategy 1 and -397kN/m and 1175kN/m for the DA1-2 Strategy 2. Overall, the DA1-1 governs the design, resulting in more adverse minimum and maximum axial forces. The DA1-2 Strategy 2 results in about 34% higher minimum axial force than the DA1-2 Strategy 1 while the DA1-2 Strategy 1 is more critical than the DA1-2 Strategy 2 in terms of the maximum axial force, with the difference being about 10%.

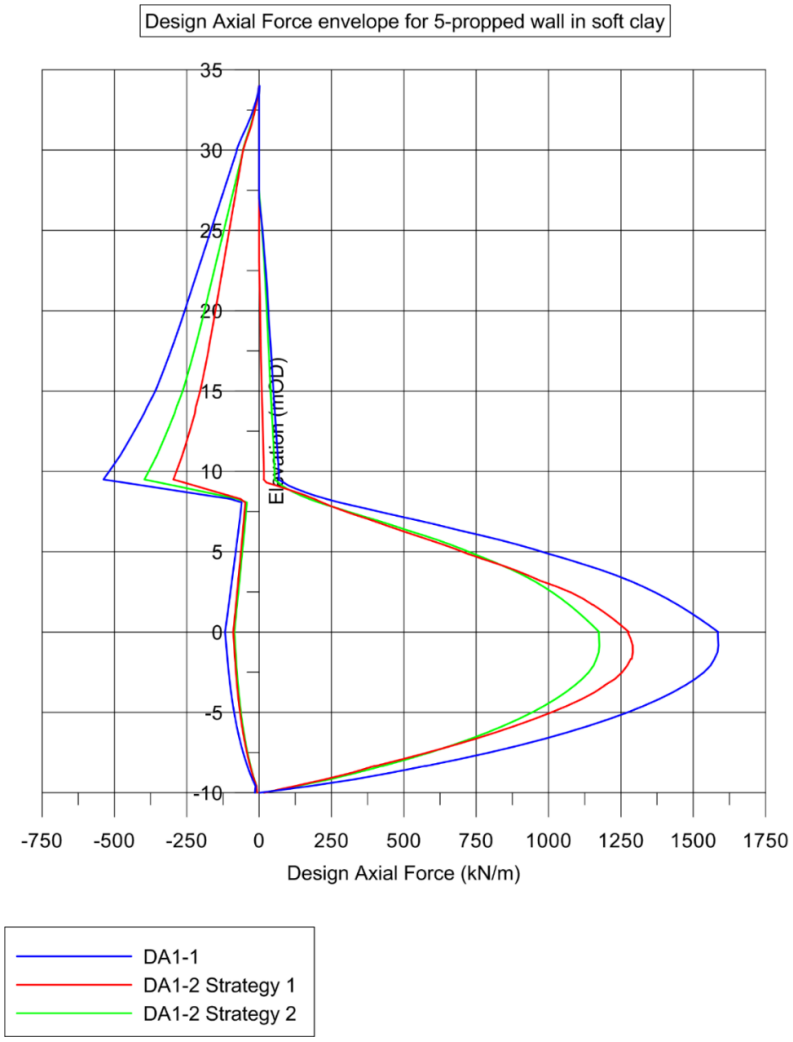

Figure 3.39: Design Axial Force envelopes for 5-propped wall in typical Singapore soil profile

3.7 Conclusions

In this chapter, the challenges of the SLS and ULS analysis of five different embedded wall geometries of increasing excavation depth in plane strain (2D) finite element analysis, were illustrated. The main parameters that were investigated using the Mohr-Coulomb model, are the earth pressure coefficient at rest, K_0, the soil stiffness expressed as the ratio of the undrained Young's modulus and undrained shear strength, E_u/c_u and the prop stiffness, k.

For the SLS analysis, it was found that for all geometries, increasing K_0 and decreasing E_u/c_u generally results in higher wall deflections and more onerous heave at the excavation base and surface settlement behind the wall. Lower values of the prop stiffness generally result in higher wall deflections and more adverse surface settlements behind the wall while the effect is less significant on the heave at the bottom of the excavation.

For the ULS analysis, as required by EC7, both Combinations of the DA1 were considered while the Combination 2 was applied with two alternative strategies. It was found that, the DA1-1 generally results in the highest values of the design internal structural forces for a stiff OC clay such as the London Clay where the soil strength is not very critical for the design. Increasing the value of K_0 or the prop stiffness generally results in higher differences between the two DA1-2 Strategies, particularly for deeper excavations with many prop levels. However, varying the soil stiffness has only a modest effect on the resulting percentage difference in the results between the two DA1-2 Strategies.

Overall, the dual approach of the DA1, expressed as a combination of DA1-1 and DA1-2 Strategy 2, generally governs the design decisions for a wide range of geometries and values of strength parameters, critical for the design. DA1-2 Strategy 2 is preferred to Strategy 1 because it is generally more critical; it is a more intuitive way of accounting for the uncertainty in the soil strength; and because it can be easily applied in conjunction with the SLS analysis. In any case, the choice of the factoring strategy, for the design of the wall bending moments, is less important than for prop design because retaining walls typically display some plasticity and redistribute the bending moment. However, Strategy 2 is preferable for the design of prop loads, because props can exhibit brittle behaviour and the DA1-2 Strategy 1 might not be adequately conservative.

Moreover, the design prop loads calculated from the FE analyses, were compared with the values derived from the empirical methods suggested by CIRIA C517 and EAB. CIRIA C517 and FEM calculations provided different prop loads, particularly for the upper prop levels where CIRIA's assumption of uniform pressure distribution, results in significantly higher prop loads. On the other hand, FEM and the EAB guide result in prop load values that are in better agreement. This is because the EAB guide suggests different patterns of pressure distribution for walls supported by different number of prop levels which is a more reasonable assumption.

The study also focuses on how the accidental prop loss effect can be accounted for in both 2D and 3D FE analysis, illustrating that the single prop loss is a three-dimensional problem with the load of the deactivated prop being redistributed to the adjacent props both in the vertical and horizontal direction. It was found that the ULS analysis is not always more critical than the prop loss analysis. Thus, the prop loads that govern the design are the maximum values calculated from both analyses.

Finally, the FE analysis was repeated for a deep excavation in a soft marine clay, typically encountered in Singapore, showing that factoring the soil strength of a soft clay

has a more significant influence on the calculated design structural forces, than factoring the strength of a stiff clay. DA1-2 Strategy 2 governs the design of prop loads and results in more onerous minimum shear forces while DA1-2 Strategy 1 results in more critical maximum wall bending moments.

CHAPTER 4

FE analysis of supported excavations using advanced soil models

4.1 Introduction

When performing FE analysis using advanced constitutive models, it has been common practice for designers to perform the SLS analysis using the advanced model parameters and then switch to the design values of the Mohr-Coulomb parameters to verify safety against the ULS (Simpson, 2012).

In this chapter, the challenges of both the SLS and ULS FE analysis of embedded walls supporting excavations, using advanced soil models such as the Hardening Soil (HS), Hardening Soil Small (HSS) and BRICK, are highlighted and discussed. The effect of the soil model on the serviceability and ultimate limit state analysis was investigated.

As, there is limited reference in the literature as to what soil stiffness parameters are appropriate for London Clay when using the HS and HSS models, the effect of a number of model parameters such as the power law exponent *m,* the secant stiffness in a standard drained triaxial test, the tangent stiffness for primary oedometer loading and the strain $\gamma_{0.7}$ on the resulting discrepancies was investigated.

As in Chapter 3, the main results presented for the SLS analysis include the wall deflections, the heave at the base of the excavation and the surface settlements behind the wall. For the ULS analysis, the study focused on the derivation of the design internal structural shear and axial forces, bending moments and prop loads, using as required by EC7, both the DA1 Combinations, while the DA1-2 was applied with the two alternative strategies discussed in Section 1.7.3. Overall, the type of results presented in this Chapter are similar to the Mohr-Coulomb analysis to allow for the comparison of the results and discussion.

4.2 Modelling assumptions

The computer software used for all the analyses is PLAXIS 2015.02 in its two-dimensional version. The geometries and soil profile are the same as used in Chapter 3.

The modelling assumptions, including: the Finite Element mesh; the wall and prop properties; the construction sequence as well as the Mohr-Coulomb material parameters, assumed for the Made Ground, were also discussed in detail in Chapter 3. The London Clay parameters for the constitutive models used in this study were discussed in detail in Chapter 2.

In all the analyses using the HS, HSS and BRICK soil models, undrained conditions were considered, using an effective stress approach (e.g. Undrained Method A for HS and HSS) while an under-drained pore water profile was assumed for London clay. The excavation was modelled in PLAXIS as a dry excavation using the phreatic method, according to which, the pore water pressures are directly generated based on a linear distribution from defined water levels taking only the unit weight of the water into account. For every undrained excavation phase, 4m of soil was excavated and the excavated area was set dry while the phreatic level outside the excavation remained unchanged. This method is suitable for short term excavations.

The K_0 profile used in the HS and HSS analysis was constant with a value of 1.5, based on a number of studies discussed in Chapter 2. However, when the BRICK model is used, K_0 is not an input parameter but is calculated based on the stress history of the soil. In all analyses, a pre-consolidation pressure of 2000kPa was applied accounting for an eroded strata thickness of 200m. Moreover, in all cases the prop stiffness was taken as k = 100MN/m/m which is considered reasonable for typical excavations in London Clay.

4.3 Methodology

The stiffness parameters required for the HS and HSS model are not readily available for London Clay. For this purpose, a parametric analysis was carried out to investigate the influence of a number of input model parameters.

Three main parameters were investigated using the HS model: the power law exponent m which controls the stress-level dependency of stiffness; the secant stiffness in standard drained triaxial test E^{ref}_{50} and the tangent stiffness for primary oedometer loading E^{ref}_{oed}. Moreover, the additional parameter investigated using the HSS model was the shear strain $\gamma_{0.7}$, which is the strain at which the secant shear modulus is reduced to 72.2% of its initial value.

More specifically, the analysis was repeated for all the geometries using the HS model with varying the parameter m as shown in Table 4.1 (considered to be a typical range of values for clay materials according to Benz, 2007), while keeping all the rest of

the model parameters the same. Moreover, a sensitivity analysis was performed, with the cases shown in Table 4.2, to investigate the effect of the HS stiffness parameters E^{ref}_{50} and E^{ref}_{oed} on the results.

For the shear strain $\gamma_{0.7}$, a reference value of 0.0001 was selected in Chapter 2, which was considered to result in realistic stiffness degradation curve shapes for a wide range of materials (Brinkgreve et al., 2007). In order to assess the influence of $\gamma_{0.7}$ on the shear modulus degradation curves and consequently the FEM results for both SLS and ULS conditions, the analysis was repeated for the range of $\gamma_{0.7}$ values shown in Table 4.3.

Table 4.1: Power law exponent m values to be investigated

Case	*m*
1	0.7
2	0.85
3	1

Table 4.2: E^{ref}_{50} and E^{ref}_{oed} cases to be investigated

Case	E^{ref}_{50} (MPa)	E^{ref}_{oed} (MPa)
1	15	15
2	15	10
3	10	5

Table 4.3: $\gamma_{0.7}$ values to be investigated

Case	$\gamma_{0.7}$
1	0.001
2	0.0002
3	0.0001
4	0.00001

4.4 SLS analysis using advanced soil models

In this section, the FE analysis was repeated for all the geometries using more advanced constitutive models such as the HS, HSS and BRICK, to investigate the effect of the model on the calculated wall deflection, heave at the base of the excavation and surface settlement behind the wall.

4.4.1 Wall deflections

4.4.1.1 Hardening Soil (HS) model

Effect of the power law exponent *m*

The wall deflection profiles for the 5-propped wall case, using the HS model with varying *m*, are presented in Figure 4.1. It can be seen that the maximum wall deflections are 88mm, 77mm and 67mm for *m* equal to 0.7, 0.85 and 1.0 respectively. These correspond to a ratio of maximum wall deflection and excavation depth of 0.36%, 0.31% and 0.27%. These values are higher than the values predicted with the Mohr-Coulomb model. The *m* = 0.7 case is the most critical, as lower *m* values result in lower soil stiffness profiles. In all cases, the profiles exhibit similar pattern and the maximum value was observed at about +12.5mOD. The maximum wall deflections for the rest of the geometries are listed in Table 4.4 where it can be seen that the *m* = 0.7 case consistently results in the highest deflection values. In all cases, the ratio of maximum wall deflection and excavation depth ranges from 0.20% to 0.32%.

Table 4.4: Maximum wall deflection using the HS with varying *m*

Maximum wall deflection (mm)					
m	1-propped wall	2-propped wall	3-propped wall	4-propped wall	5-propped wall
0.7	28	42	56	71	88
0.85	27	38	49	61	77
1.0	26	36	46	55	67

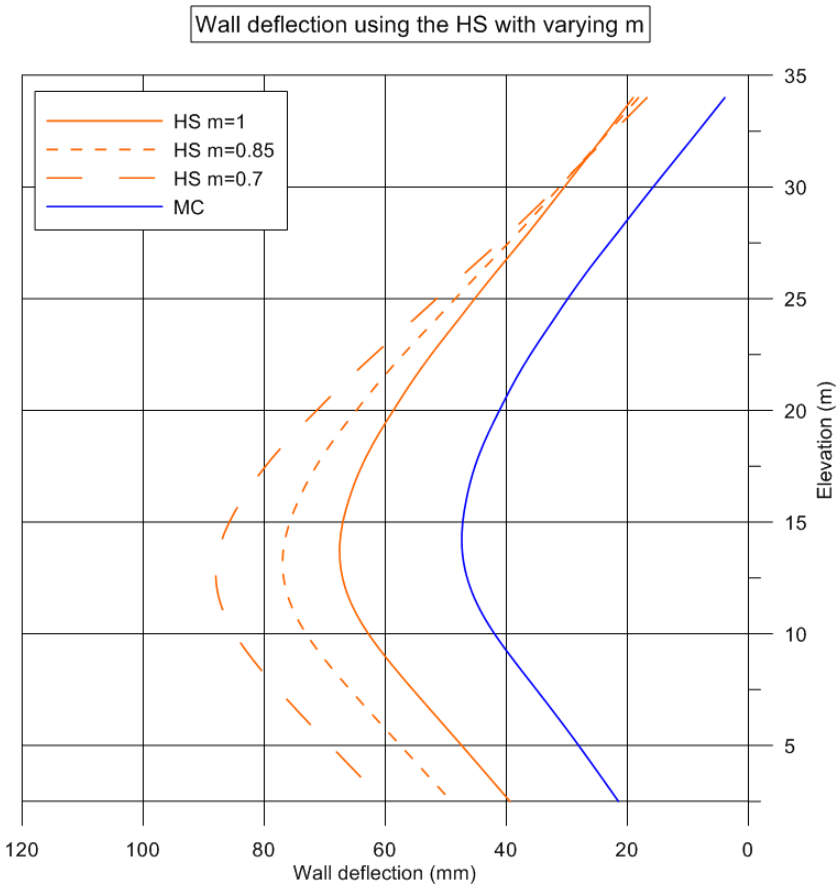

Figure 4.1: Deflection profiles for 5-propped wall using the HS with varying *m*

Effect of the E^{ref}_{50} and E^{ref}_{oed}

The wall deflection profiles for the 5-propped wall case, using the HS model with varying the E^{ref}_{50} and E^{ref}_{oed}, are presented in Figure 4.2. It can be seen that varying the reference E^{ref}_{50} and E^{ref}_{oed} results in only marginally lower wall deflections. Overall, it was found that the influence of the E^{ref}_{50} and E^{ref}_{oed} on the wall deflections is insignificant and the conclusion applies for the rest of the geometries.

In excavation problems, due to the soil removal, there is vertical unloading at the bottom of the excavation and horizontal unloading behind the wall. For this reason, the most critical soil stiffness parameter is the unloading Young's Modulus, E_{ur}. The effect of the secant soil stiffness during shearing is less significant while the primary oedometer loading soil stiffness becomes more relevant in excavations supported by pre-stressed anchors.

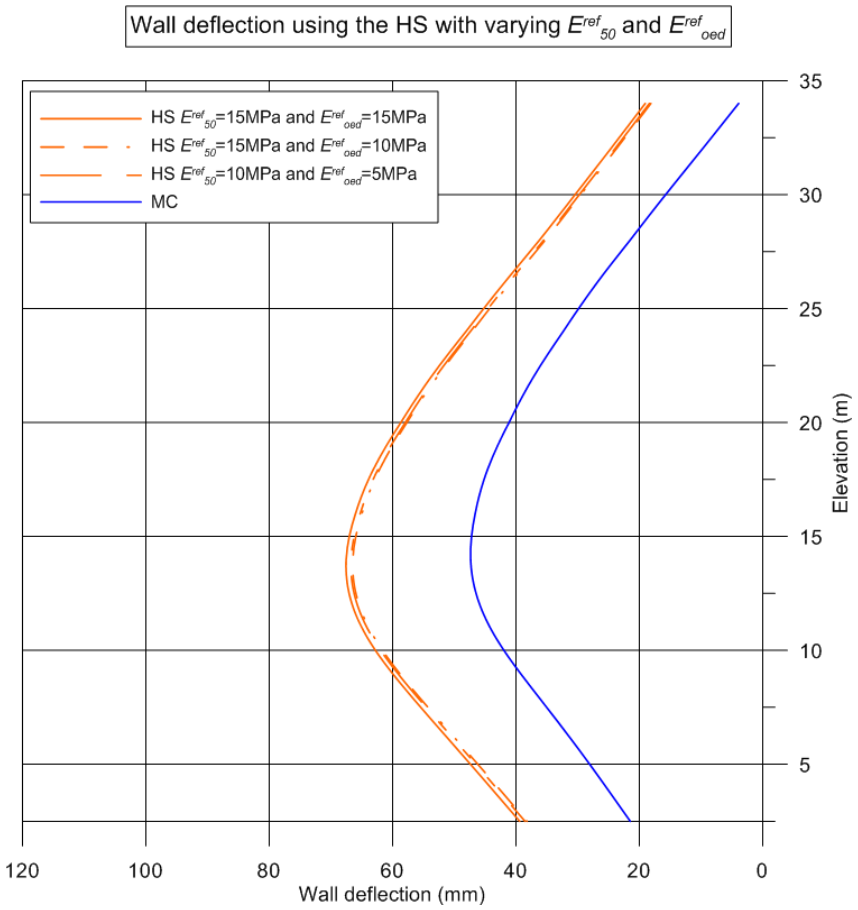

Figure 4.2: Deflection profiles for 5-propped wall using the HS with varying E^{ref}_{50} and E^{ref}_{oed}

4.4.1.2 Hardening Soil Small (HSS) model

Effect of the power law exponent *m*

The wall deflection profiles for the 5-propped wall case, using the HSS model with varying *m*, are presented in Figure 4.3. It is shown that the maximum wall deflections are 62mm, 53mm and 48mm for *m* equal to 0.7, 0.85 and 1.0 respectively. These correspond to a ratio of maximum wall deflection and excavation depth of 0.25%, 0.22% and 0.2%. These values are lower than the values predicted with the HS model. The *m* = 0.7 case is the most critical, as lower *m* values result in lower soil stiffness profiles. In all cases, the curvatures have similar shape and the maximum value is observed at about +12.5mOD. The maximum wall deflections for the rest of the geometries are listed in Table 4.5 where it can be seen that the *m* = 0.7 case consistently results in the highest deflection values. In all cases, the ratio of maximum wall deflection and excavation depth ranges from 0.2% to 0.26%.

Table 4.5: Maximum wall deflection using the HSS with varying *m*

	Maximum wall deflection (mm)				
m	1-propped wall	2-propped wall	3-propped wall	4-propped wall	5-propped wall
0.7	20	31	42	53	62
0.85	19	28	38	45	53
1.0	18	26	34	42	48

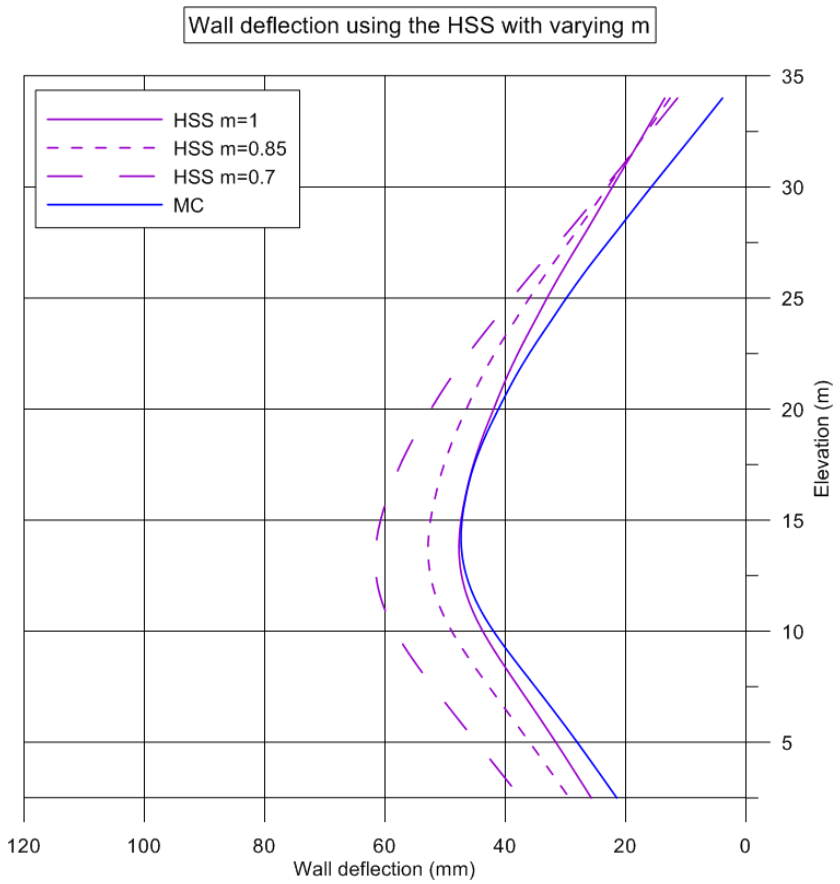

Figure 4.3: Deflection profiles for 5-propped wall using the HSS with varying *m*

Effect of the strain $\gamma_{0.7}$

The wall deflection profiles for the 5-propped wall case, using the HSS model with varying $\gamma_{0.7}$, are presented in Figure 4.4. It can be seen that the maximum wall deflections are 27mm, 42mm, 48mm and 66mm for $\gamma_{0.7}$ equal to 0.001, 0.0002, 0.0001 and 0.00001 respectively. These correspond to a ratio of maximum wall deflection and excavation depth of 0.11%, 0.17%, 0.2% and 0.27% respectively. The $\gamma_{0.7}$ = 0.00001 case is the

most critical, as the lower $\gamma_{0.7}$ value results in quicker degradation of the soil stiffness while for $\gamma_{0.7}$ = 0.001, the soil shows a much stiffer response due to the slower degradation of the soil stiffness. In all cases, the curvatures show a similar pattern and the maximum values are at about +12.5mOD.

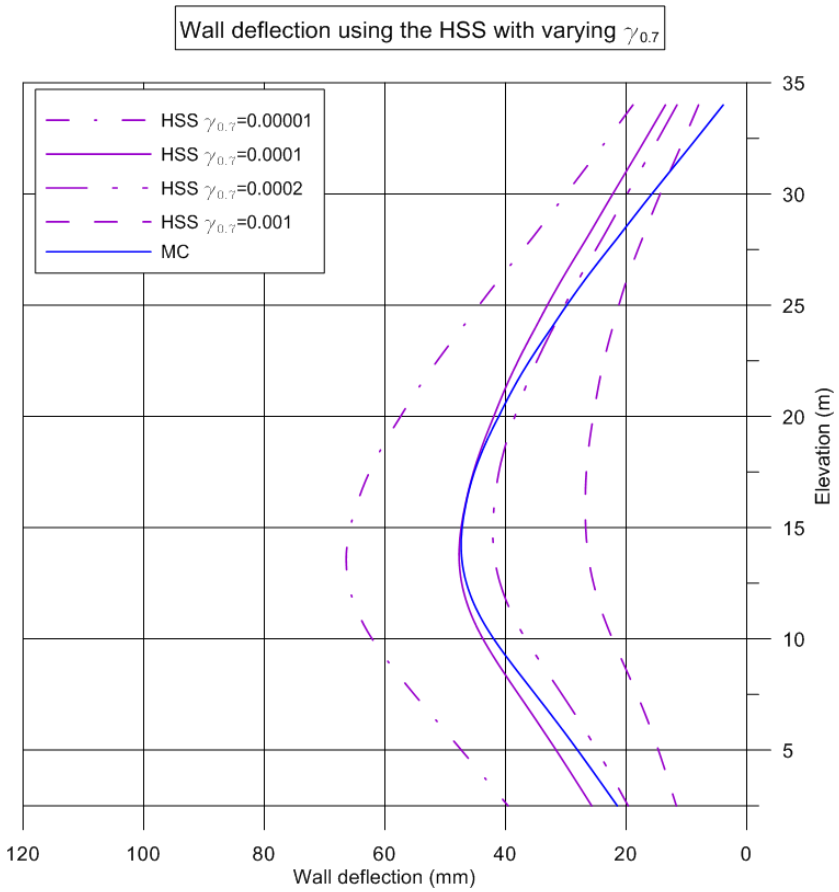

Figure 4.4: Deflection profiles for 5-propped wall using the HSS with varying $\gamma_{0.7}$

The maximum wall deflections for the rest of the geometries are listed in Table 4.6 where it can be seen that the $\gamma_{0.7}$ = 0.00001 case consistently results in the most critical deflection values. In all cases, the ratio of maximum wall deflection and excavation depth ranges from 0.1% to 0.32%.

Table 4.6: Maximum wall deflection using the HSS with varying $\gamma_{0.7}$

Maximum wall deflection (mm)					
$\gamma_{0.7}$	1-propped wall	2-propped wall	3-propped wall	4-propped wall	5-propped wall
0.001	10	15	20	24	27
0.0002	15	22	30	38	42
0.0001	18	26	34	42	48
0.00001	27	38	49	58	66

4.4.1.3 BRICK model

In this section, the analysis was repeated for all the geometries using the BRICK model. The maximum wall deflections, presented in Table 4.7, correspond to a ratio of maximum wall deflection and excavation depth of about 0.20%, 0.20%, 0.21%, 0.21% and 0.22% for the 1, 2, 3, 4 and 5-propped wall respectively. In all cases, the curvatures have similar pattern with the curves for the HS and HSS model cases. For the 5-propped wall, the maximum value is observed at about +14mOD.

Table 4.7: Maximum wall deflection using the BRICK

Maximum wall deflection (mm)				
1-propped wall	2-propped wall	3-propped wall	4-propped wall	5-propped wall
17	25	34	43	53

4.4.1.4 Comparison

In this section, the SLS results using the different constitutive models are compared. Only the results for the 5-propped wall case are compared but the conclusions can be applied to all the geometries considered in this study. For the MC model, the results for the reference case with K_0 = 1.5 and E_u/c_u = 1000, are presented. For the HS model, only the case for m = 1.0 was considered for the comparison. For the E^{ref}_{50} and E^{ref}_{oed} parameters, values of 15MPa were used although the effect of these parameters was found to be insignificant on the results. For the HSS model, similarly to the HS, only the m = 1.0 case was considered. A value for the strain $\gamma_{0.7}$ equal to 0.0001 was found to be reasonable and also in line with the values quoted in the literature. For $\gamma_{0.7}$ equal to 0.00001, the HSS practically loses the small strain stiffness feature and

reduces to the HS model while for $\gamma_{0.7}$ equal to 0.001, the soil shows an extremely stiff response.

In Figure 4.5, the deflection profiles of the retaining wall are plotted for the different soil models. The maximum wall deflection is 47mm, 67mm, 48mm and 53mm for the MC, HS, HSS and BRICK model respectively. These correspond to a ratio of maximum wall deflection and excavation depth of 0.19%, 0.26%, 0.20% and 0.22%. In all cases, the curvatures have similar pattern and the maximum values are observed at about +12.5mOD to +15mOD.

As discussed in Chapter 2, the soil stiffness in the HS and HSS models depends on the effective horizontal stress. In excavation problems, the horizontal unloading governs the behaviour of the soil behind the wall where due to the removal of soil there is some stress relief (i.e. reduction of the effective horizontal stress below its initial value). For this reason, the HS and HSS models show a less stiff response when compared to the MC model where the soil stiffness is constant and independent of the stress level. Moreover, the HSS model results in smaller wall deflection than the HS model. This is because, in supported excavations, the generated strains behind the wall are not large enough to reduce the soil stiffness to its unloading/reloading value. Moreover, the HSS model assumes a non-linear elastic unloading/reloading soil behaviour which represents an advance over the linear behaviour predicted by the HS model.

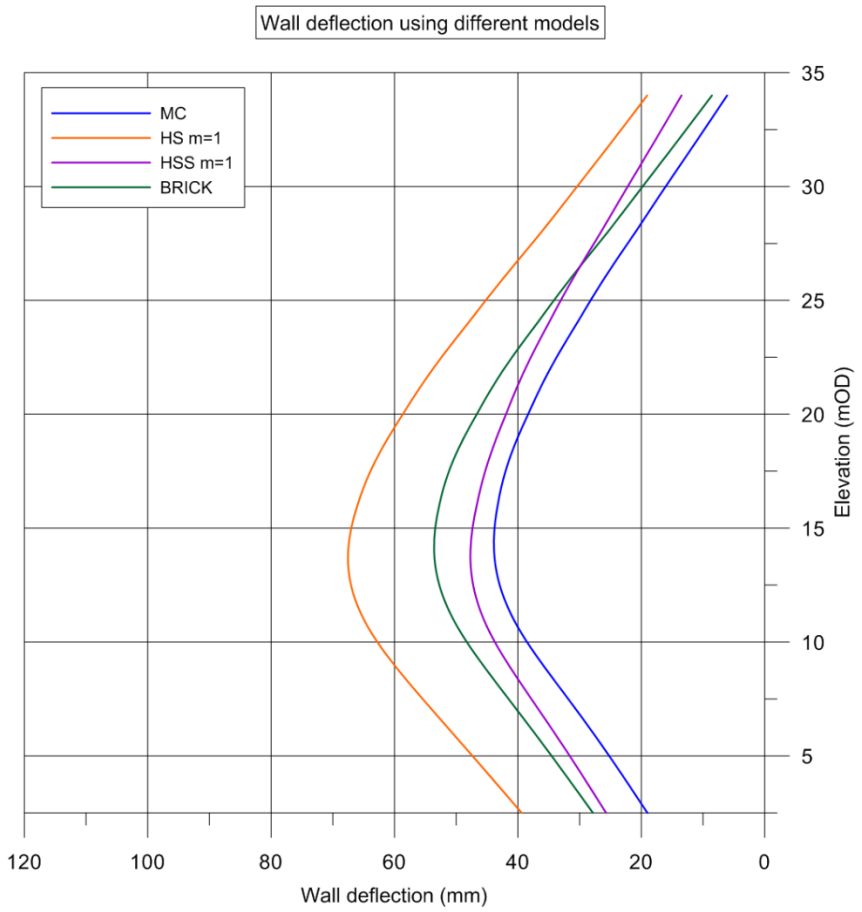

Figure 4.5: Deflection profiles for 5-propped wall for different constitutive models

4.4.2 Soil heave at the base of the excavation

4.4.2.1 Hardening Soil (HS) model

Effect of the power law exponent *m*

In Figure 4.6, the vertical soil displacements at the base of the excavation are shown for the 5-propped wall case. The maximum soil displacements are 130mm, 108mm and 88mm, for *m* equal to 0.7, 0.85 and 1.0 respectively. In all cases, the lowest heave is observed near the wall, due to the effect of wall friction. The maximum heave values for the rest of the geometries are listed in Table 4.8 where it can be seen that, the *m* = 0.7 case results in the highest calculated heave at the bottom of the excavation while the lowest heave is obtained for *m* = 1.0.

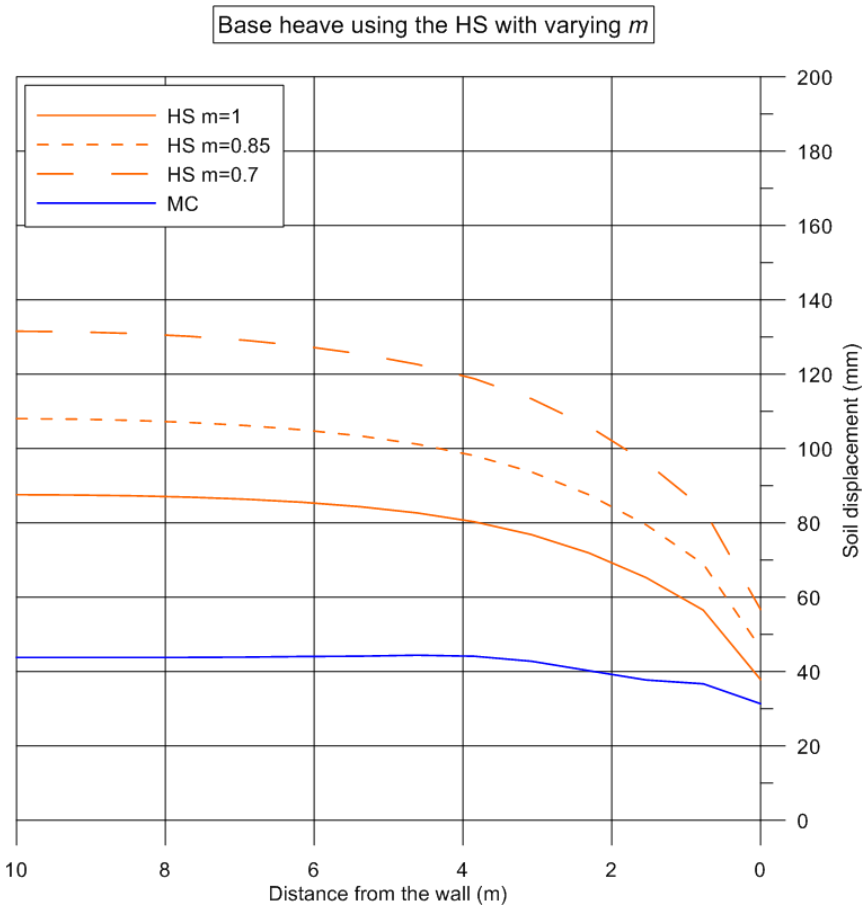

Figure 4.6: Base heave for 5-propped wall using the HS with varying *m*

Table 4.8: Maximum base heave using the HS with varying *m*

Maximum heave (mm)					
m	1-propped wall	2-propped wall	3-propped wall	4-propped wall	5-propped wall
0.7	41	62	81	100	130
0.85	36	54	71	86	108
1.0	33	47	60	72	88

Effect of the E^{ref}_{50} and E^{ref}_{oed}

In Figure 4.7, the vertical soil displacements at the base of the excavation, using the HS model with varying the E^{ref}_{50} and E^{ref}_{oed}, are shown for the 5-propped wall case. Overall, it was found that the effect of the E^{ref}_{50} and E^{ref}_{oed} on the base heave is insignificant and the conclusion applies for the rest of the geometries.

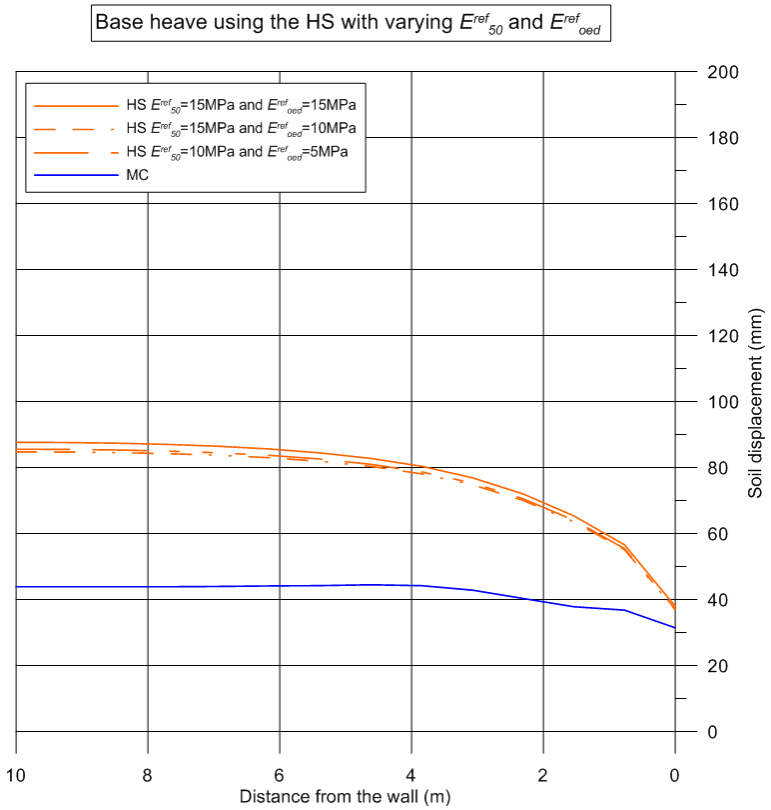

Figure 4.7: Base heave for 5-propped wall using the HS with varying E^{ref}_{50} and E^{ref}_{oed}

4.4.2.2 Hardening Soil Small (HSS) model

Effect of the power law exponent *m*

In Figure 4.8, the vertical soil displacements at the base of the excavation, using the HSS model with varying *m*, are shown for the 5-propped wall case. The maximum heave is 81mm, 63mm and 56mm, for *m* equal to 0.7, 0.85 and 1.0 respectively. In all cases, the lowest heave value is observed near the wall due to the effect of wall friction. The maximum heave values for the rest of the geometries are listed in Table 4.9 where it can be seen that, the *m* = 0.7 case results in the largest calculated heave at the bottom of the excavation while the smallest soil heave value is obtained for *m* = 1.0.

Table 4.9: Maximum base heave using the HSS model with varying *m*

Maximum heave at the base of the excavation (mm)					
m	1-propped wall	2-propped wall	3-propped wall	4-propped wall	5-propped wall
0.7	22	37	54	73	81
0.85	20	31	44	55	63
1.0	18	27	36	46	56

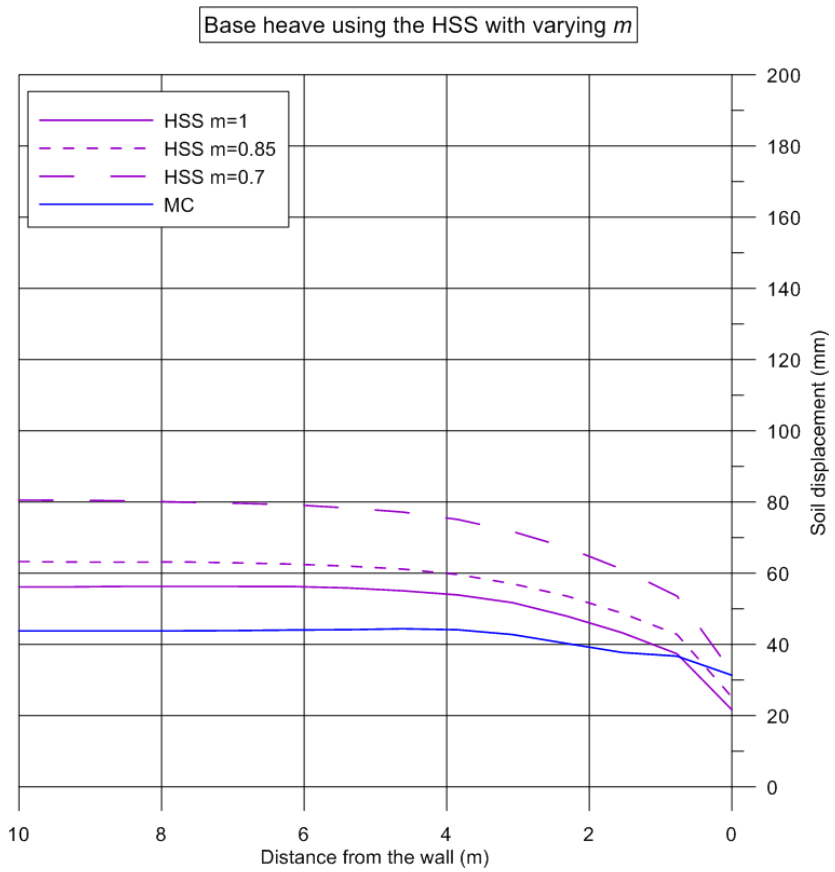

Figure 4.8: Base heave for 5-propped wall using the HSS model with varying *m*

Effect of the strain $\gamma_{0.7}$

In Figure 4.9, the vertical soil displacements at the base of the excavation, using the HSS model with varying $\gamma_{0.7}$, are shown for the 5-propped wall case. The maximum soil displacements are 29mm, 46mm 56mm and 87mm, for $\gamma_{0.7}$ equal to 0.001, 0.0002, 0.0001 and 0.00001 respectively. The maximum heave values for the rest of the geometries are listed in Table 4.10 where it can be seen that, the $\gamma_{0.7}$ = 0.00001 case

results in the highest calculated heave at the bottom of the excavation while the lowest heave is obtained for $\gamma_{0.7}$ = 0.001.

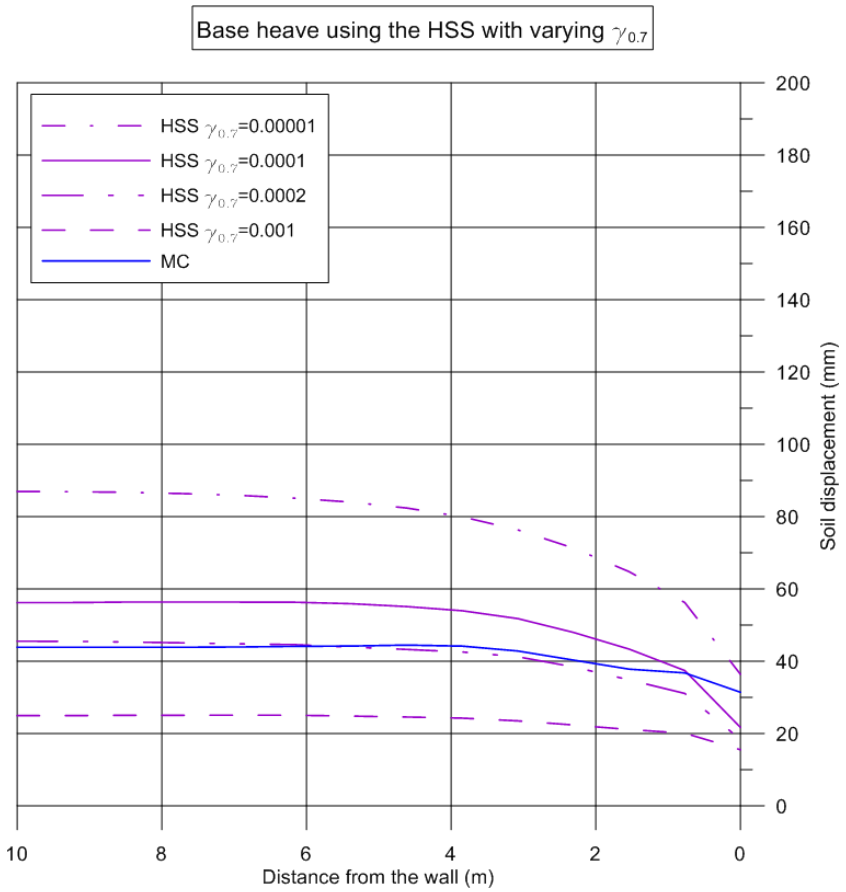

Figure 4.9: Base heave for 5-propped wall using the HSS with varying $\gamma_{0.7}$

Table 4.10: Maximum base heave using the HSS with varying $\gamma_{0.7}$

Maximum heave at the base of the excavation (mm)					
$\gamma_{0.7}$	1-propped wall	2-propped wall	3-propped wall	4-propped wall	5-propped wall
0.001	10	15	20	23	25
0.0002	15	24	32	42	46
0.0001	18	27	36	46	56
0.00001	33	50	66	80	87

4.4.2.3 BRICK model

Similarly, the maximum heave values for all geometries using the BRICK model are listed in Table 4.11.

Table 4.11: Maximum base heave using the BRICK

Maximum heave (mm)				
1-propped wall	2-propped wall	3-propped wall	4-propped wall	5-propped wall
18	31	43	56	69

4.4.2.4 Comparison

In Figure 4.10, the short-term vertical soil displacements at the base of the excavation are shown for the 5-propped wall case. The maximum heave is 44mm, 88mm, 56mm and 69mm for the MC, HS, HSS and BRICK model respectively. In excavation problems, where the vertical unloading governs the behaviour of the heaving soil at the base of the excavation, it is found that the MC model results in smaller heave than the rest of the models. As discussed before, the soil stiffness shows significant anisotropy with the horizontal values typically being much higher than the vertical values. However, in the MC model the soil stiffness is assumed to be isotropic, constant and independent of the stress level. In all the analyses, the undrained Young's modulus was taken equal to $1000c_u$ which, as discussed in Chapter 2, corresponds to the horizontal undrained soil stiffness and is appropriate for the soil behind the wall where the horizontal unloading governs. However, this value is less appropriate when the vertical unloading governs the soil behaviour (e.g. for the calculation of the short-term vertical soil displacement at the base of the excavation), thus the MC predicts lower heave values than the rest of the soil models.

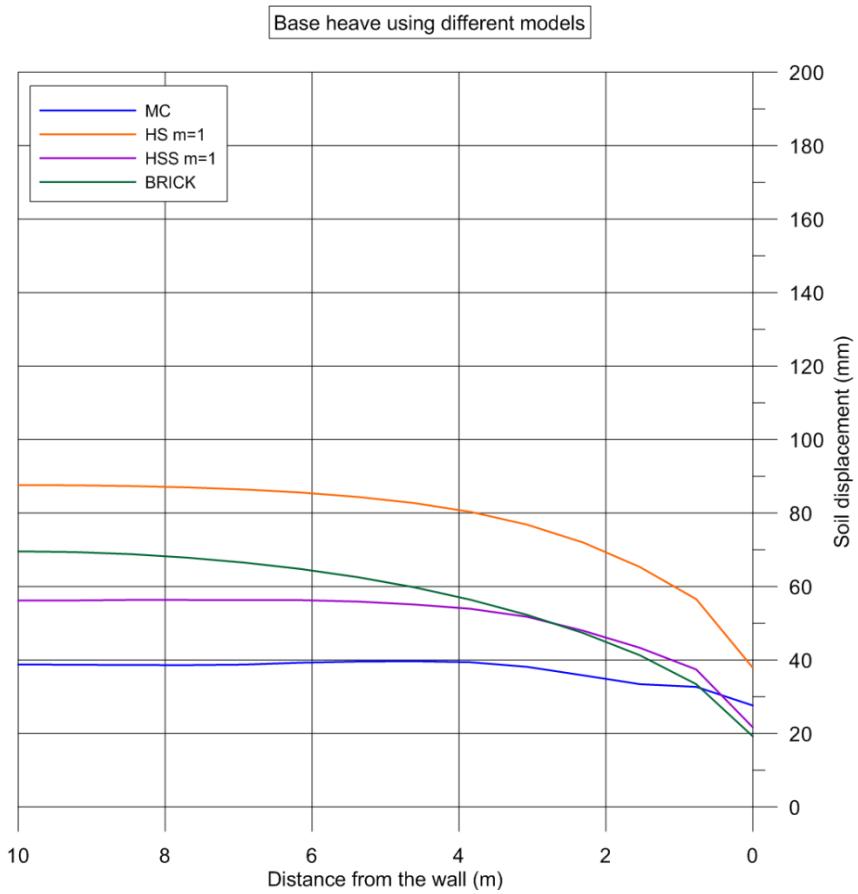

Figure 4.10: Base heave for 5-propped wall for different constitutive models

4.4.3 Surface settlement

4.4.3.1 Hardening Soil (HS) model

Effect of the power law exponent *m*

The surface settlements behind the wall predicted using the HS model are shown in Figure 4.11 for the 5-propped wall case. The maximum settlements are 34mm, 32mm and 29mm for *m* equal to 0.7, 0.85 and 1.0 respectively. The maximum settlement values for the rest of the geometries are listed in Table 4.12. In all cases, the highest settlements are calculated for *m* = 0.7 while the smallest settlements are observed for *m* = 1.0.

Table 4.12: Maximum surface settlement behind the wall using the HS with varying *m*

Maximum surface settlement (mm)					
m	1-propped wall	2-propped wall	3-propped wall	4-propped wall	5-propped wall
0.7	15	17	23	29	34
0.85	17	17	22	28	32
1.0	18	18	21	25	29

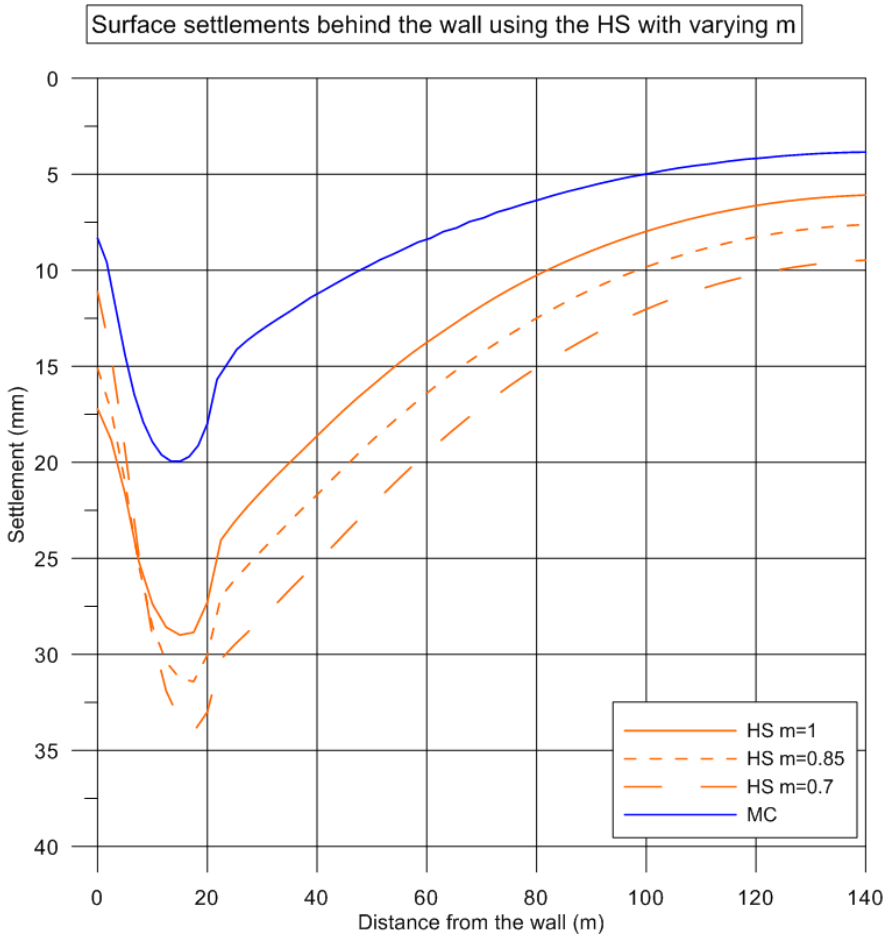

Figure 4.11: Surface settlements behind the 5-propped wall using the HS with varying *m*

Effect of the E^{ref}_{50} and E^{ref}_{oed}

The surface settlements behind the wall, using the HS model with varying the E^{ref}_{50} and E^{ref}_{oed}, are shown in Figure 4.12 for the 5-propped wall. Overall, it was found that the effect of the E^{ref}_{50} and E^{ref}_{oed} on the results is negligible and the conclusion applies for the rest of the geometries.

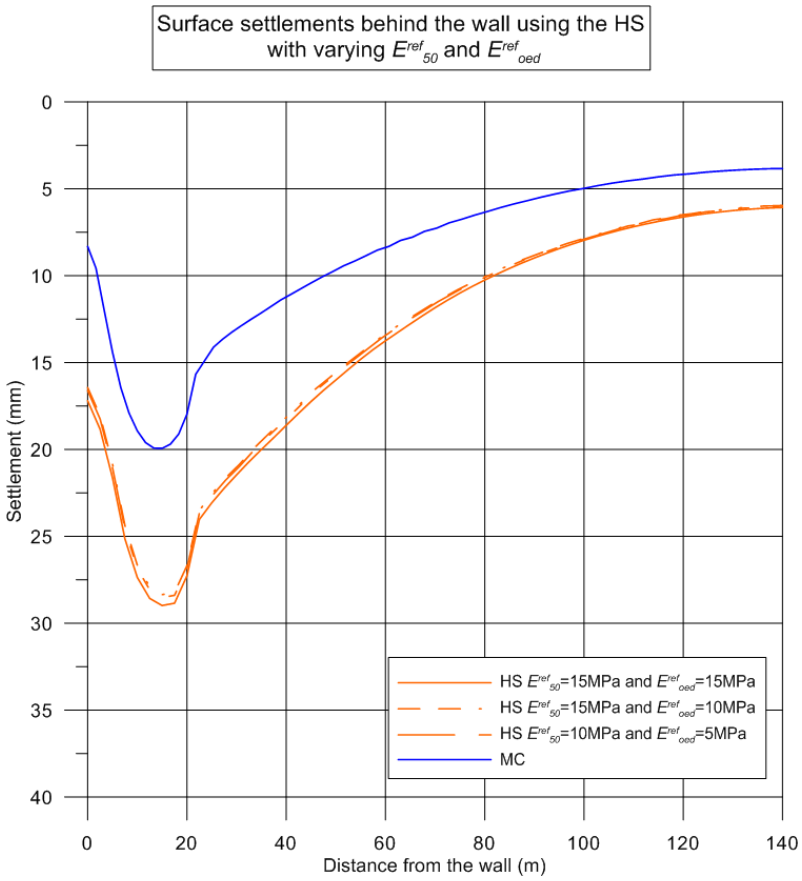

Figure 4.12: Surface settlements behind the 5-propped wall using the HS with varying E^{ref}_{50} and E^{ref}_{oed}

4.4.3.2 Hardening Soil Small (HSS) model

Effect of the power law exponent *m*

The surface settlements behind the wall using the HSS model with varying *m* are shown in Figure 4.13 for the 5-propped wall case. The maximum settlements are 34mm, 31mm and 29mm for *m* equal to 0.7, 0.85 and 1.0 respectively. The maximum settlement values for the rest of the geometries are listed in Table 4.13. In all cases, the highest settlements are calculated for *m* = 0.7 while the lowest settlements are observed for *m* = 1.0.

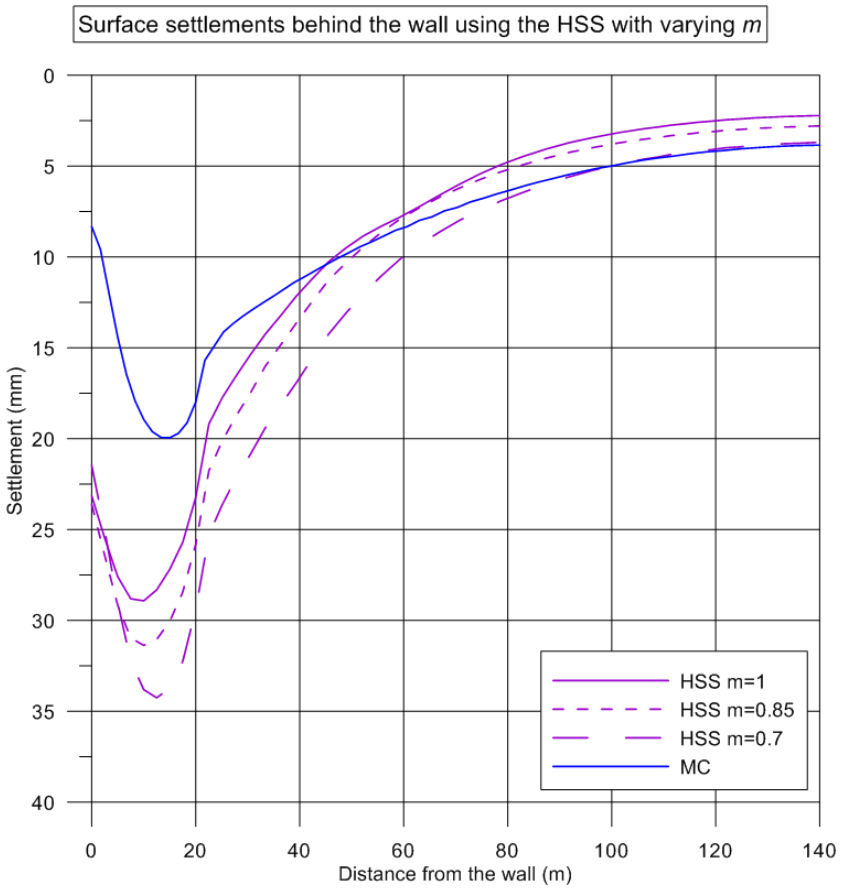

Figure 4.13: Surface settlements behind the 5-propped wall using the HSS with varying *m*

Table 4.13: Maximum surface settlement behind the wall using the HSS with varying *m*

Maximum surface settlement (mm)					
m	1-propped wall	2-propped wall	3-propped wall	4-propped wall	5-propped wall
0.7	18	20	26	30	34
0.85	18	20	25	28	31
1.0	18	20	24	26	29

Effect of the strain $\gamma_{0.7}$

The surface settlements behind the wall, using the HSS model with varying $\gamma_{0.7}$, are shown in Figure 4.14 for the 5-propped wall case. The maximum settlements are 14.5mm, 26mm, 29mm and 30mm for $\gamma_{0.7}$ equal to 0.001, 0.0002, 0.0001 and 0.00001 respectively. The maximum settlement values for the rest of the geometries are listed in

Table 4.14. In all cases, the highest settlements are calculated for $\gamma_{0.7}$ = 0.00001 while the lowest settlements are obtained for $\gamma_{0.7}$ = 0.001.

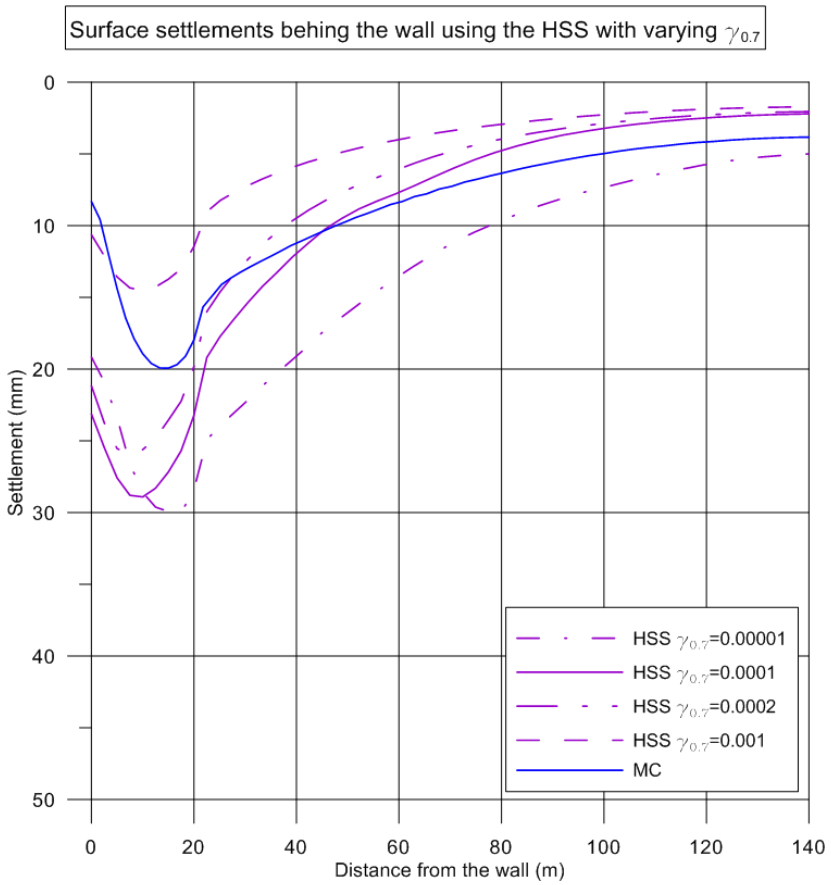

Figure 4.14: Surface settlements behind the 5-propped wall using the HSS with varying $\gamma_{0.7}$

Table 4.14: Maximum surface settlement behind the wall using the HSS with varying $\gamma_{0.7}$

Maximum surface settlement (mm)					
$\gamma_{0.7}$	1-propped wall	2-propped wall	3-propped wall	4-propped wall	5-propped wall
0.001	9	10	11	13	14.5
0.0002	14	16	21	24	26
0.0001	18	20	24	26	29
0.00001	19	20	23	28	30

4.4.3.3 BRICK model

The maximum settlement values for all the geometries using the BRICK model are shown in Table 4.15. As expected, the deeper the excavation, the higher the calculated value of the settlement of the soil behind the wall.

Table 4.15: Maximum surface settlement behind the wall using the BRICK

Maximum surface settlement (mm)				
1-propped wall	2-propped wall	3-propped wall	4-propped wall	5-propped wall
12	13	19	22	26

4.4.3.4 Comparison

The surface settlements behind the wall, calculated from the FE analyses using the different soil models, are shown in Figure 4.15, for the 5-propped wall case. The maximum settlements are 20mm, 29mm, 29mm and 26mm for the MC, HS, HSS and BRICK model respectively.

It was found that the MC model predicts the lowest settlement value again due to the assumption that the soil stiffness is isotropic and equal to values typically used for the horizontal undrained Young's modulus. Moreover, it can be seen that the settlement trough predicted by the HS model is too wide when compared to the rest of the models and particularly the HSS and BRICK. The small strain stiffness is relevant for the soil far away from the excavation zone, so the better settlement trough prediction by these small strain models is due to the higher far-field soil stiffness.

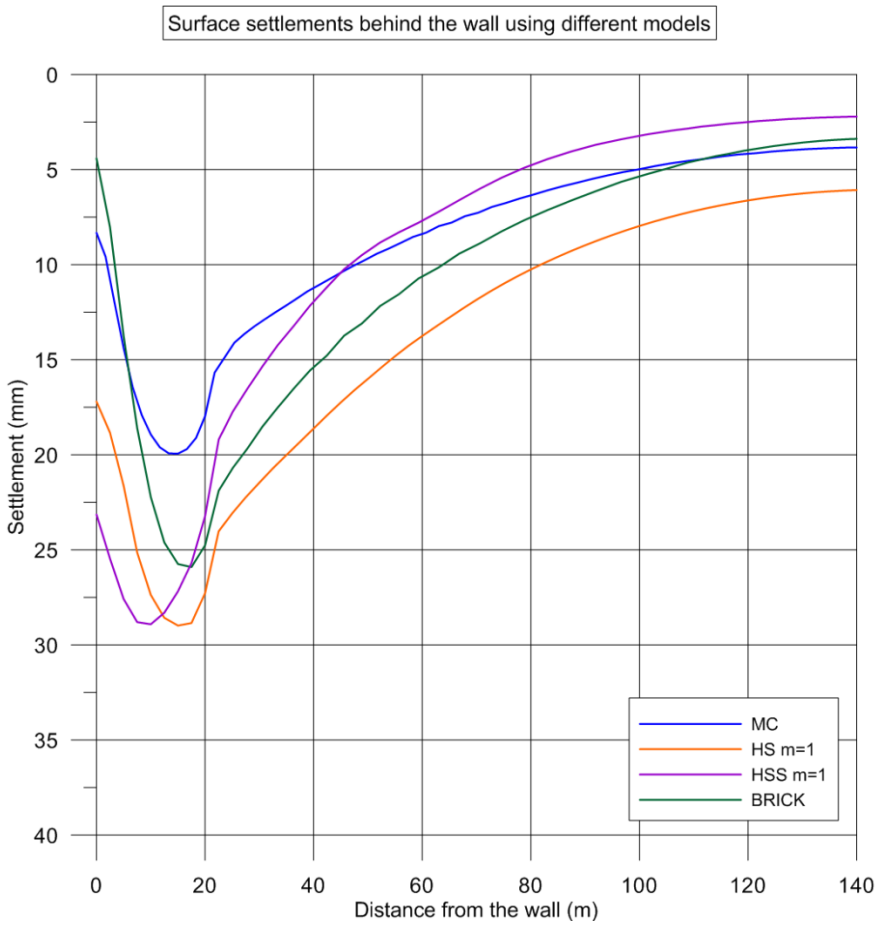

Figure 4.15: Surface settlements behind the wall for 5-propped wall for different constitutive models

4.5 ULS analysis using advanced soil models

In this section, the results from the Finite Element analyses for all the geometries using the HS, HSS and BRICK model are presented in terms of the design structural forces (i.e. prop loads, bending moments, shear and axial forces). The results from the different EC7 factoring combinations and strategies are compared and the influence of a number of model parameters on the resulting discrepancies is discussed.

4.5.1 Prop loads

4.5.1.1 Hardening Soil (HS) model

For the HS model, in the first part of the parametric analysis, three different cases were considered to investigate the effect of the power law exponent (*m* equal to 0.7, 0.85 and 1) on the calculated design internal structural forces. In the second part of the parametric analysis, three different combinations of E^{ref}_{50} and E^{ref}_{oed} were considered: E^{ref}_{50} = 15MPa and E^{ref}_{oed} = 15MPa; E^{ref}_{50} = 15MPa and E^{ref}_{oed} = 10MPa and E^{ref}_{50} =10MPa and E^{ref}_{oed} = 5MPa.

Effect of the power law exponent *m*

In Figure 4.16, the design prop loads are shown for the 1, 2, 3, 4 and 5-propped walls. It can be seen that, the DA1-1 governs the design at all prop levels for the 1, 2, 3 and 4 propped wall case. For the 5-propped wall case, the DA1-1 results in higher loads at all prop levels apart from the bottom one where the DA1-2 Strategy 2 is more critical. In almost all cases and prop levels, the DA1-2 Strategy 2 is more critical than the DA1-2 Strategy 1. For m = 1.0, the percentage difference in the total force supporting the wall between the two DA1-2 Strategies is 7%, 15%, 12%, 11% and 11% for the 1, 2, 3, 4 and 5-propped wall case respectively. For walls supported by more than one prop level, the discrepancy between the two DA1-2 Strategies is particularly significant at the bottom level where the percentage difference in the design prop load is 19%, 29%, 33% and 40% for the 2, 3, 4, and 5-propped wall case respectively.

Also, the discrepancy between the two DA1-2 Strategies remains almost the same when varying the power m. For example, for the 5-propped wall, the percentage difference in the design prop load at the bottom level is 43%, 42% and 40% for m equal to equal to 0.7, 0.85 and 1.0 respectively. The percentage difference in the total force supporting the wall between the two DA1-2 Strategies is about 11% for all three cases.

It can be also seen that the calculated prop loads generally decrease as m increases. More specifically, when m increases from to 0.7 to 1.0, the total force acting on the wall for DA1-1, DA1-2 S1 and DA1-2 S2 reduces by about 6% for a 1-propped wall, 11% for a 2-propped wall, 10.5% for a 3-propped wall, 10.5% for a 4-propped wall and 11% for a 5-propped wall.

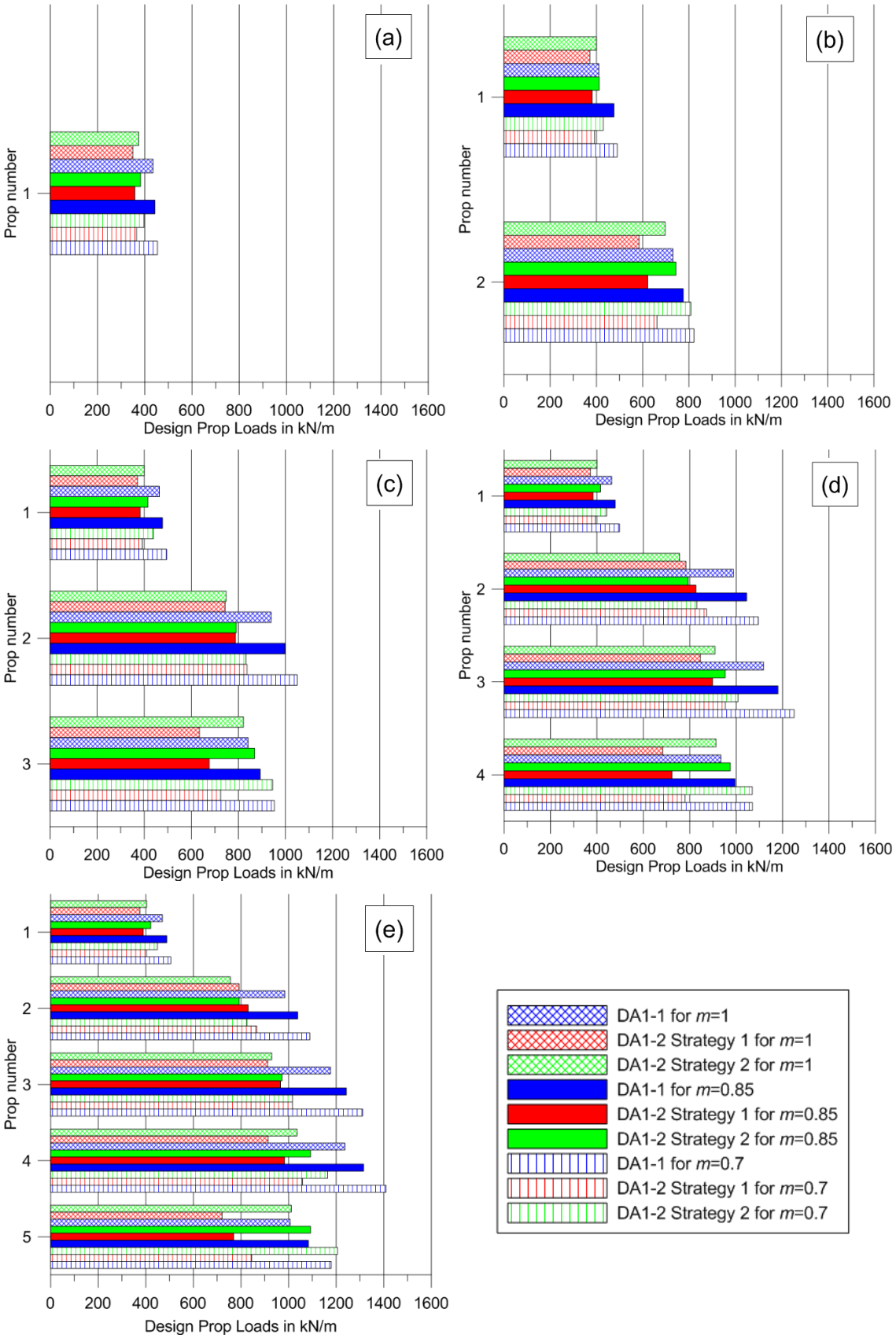

Figure 4.16: Design Prop Loads using the HS with varying *m* for wall with a) 1, b) 2, c) 3, d) 4 and e) 5 prop levels

Effect of the E^{ref}_{50} and E^{ref}_{oed}

The design prop loads for the 5-propped wall case using the HS model with varying the E^{ref}_{50} and E^{ref}_{oed} are presented in Figure 4.17. It can be seen that varying the reference E^{ref}_{50} and E^{ref}_{oed} results in only marginally different prop loads. As discussed before, for excavation problems, the most critical soil stiffness parameter is the unloading Young's modulus (E_{ur}) due to the vertical unloading at the bottom of the excavation and horizontal unloading behind the wall.

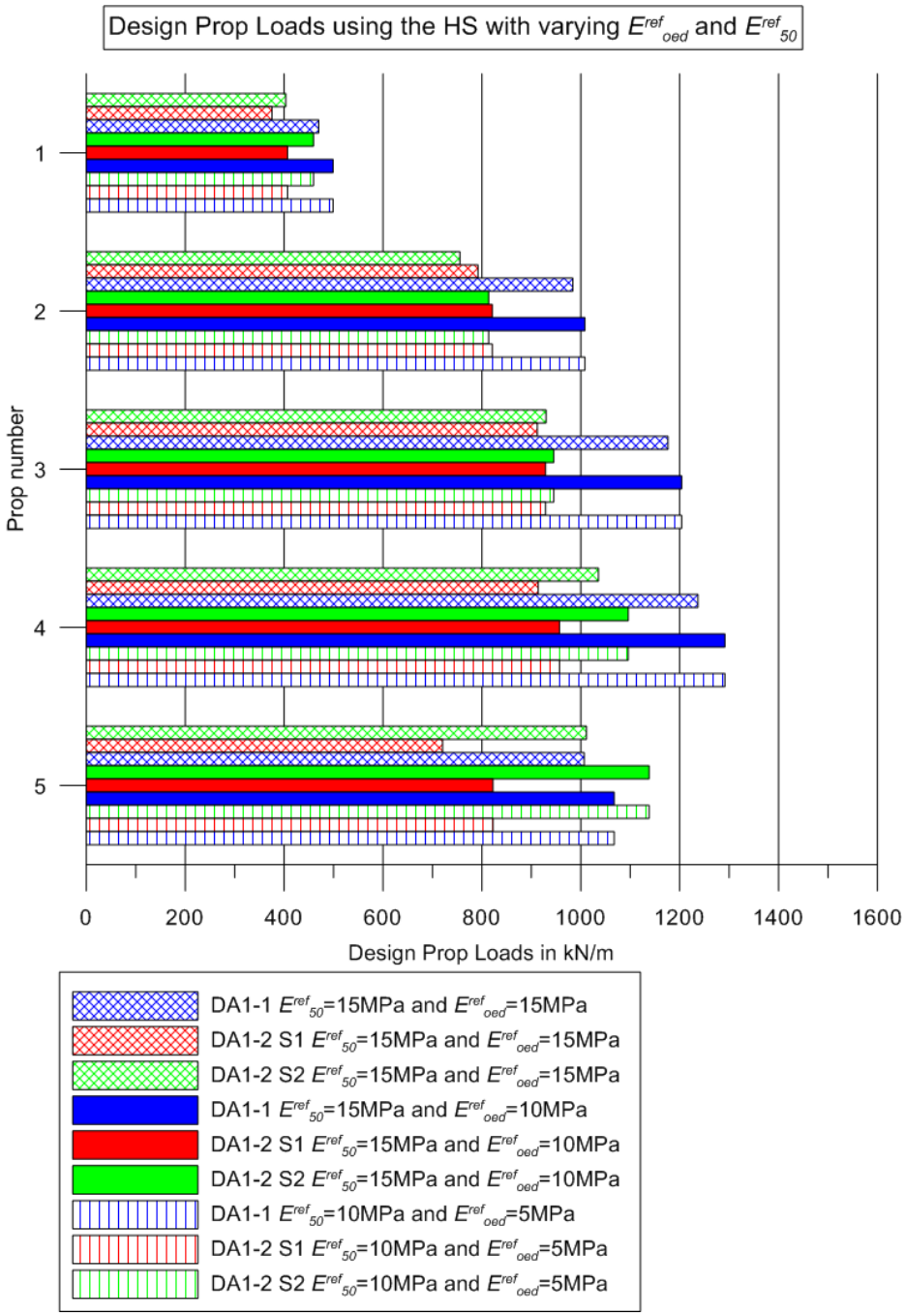

Figure 4.17: Design Prop Loads for 5-propped wall using the HS with varying E^{ref}_{50} and E^{ref}_{oed}

4.5.1.2 Hardening Soil Small (HSS) model

For the HSS model, in the first part of the parametric analysis, three different cases were considered to investigate the effect of the power law exponent on the calculated design internal structural forces with *m* equal to 0.7, 0.85 and 1.0. In the second part of the parametric analysis, four different cases were considered with the strain $\gamma_{0.7}$ equal to 0.001, 0.0002, 0.0001 and 0.00001. The power *m* is taken as 1.0 while all the other parameters remain unchanged.

Effect of the power law exponent *m*

In Figure 4.18, the design prop loads are presented for the 1, 2, 3, 4 and 5-propped wall respectively. It is shown that, DA1-1 governs the design, generally resulting in higher prop loads at almost all prop levels for the 1, 2, 3 and 4-propped wall. For the 5-propped wall, DA1-1 results in higher prop loads at all levels apart from the bottom one where the DA1-2 Strategy 2 is more critical. Moreover, in all cases and prop levels, the DA1-2 Strategy 2 is more critical than the DA1-2 Strategy 1. For *m* = 1.0, the percentage difference in the total force supporting the wall between the two DA1-2 Strategies is 6%, 12%, 9%, 7% and 9% for the 1, 2, 3, 4 and 5-propped wall case respectively. For walls supported by more than one prop level, the discrepancy between the two DA1-2 Strategies is particularly significant at the bottom level where the percentage difference in the design prop load is 16%, 21%, 28% and 32% for the 2, 3, 4, and 5-propped wall case respectively.

Also, the discrepancy between the two DA1-2 Strategies does not vary significantly with increasing *m*. For example, for the 5-propped wall, the percentage difference in the design prop load at the bottom level is 39%, 36% and 32% while the percentage difference in the total force supporting the wall between the two DA1-2 Strategies is about 12.5%, 10.5% and 9% for *m* equal to equal to 0.7, 0.85 and 1.0 respectively. It was also found that the calculated prop loads generally decrease with increasing *m*.

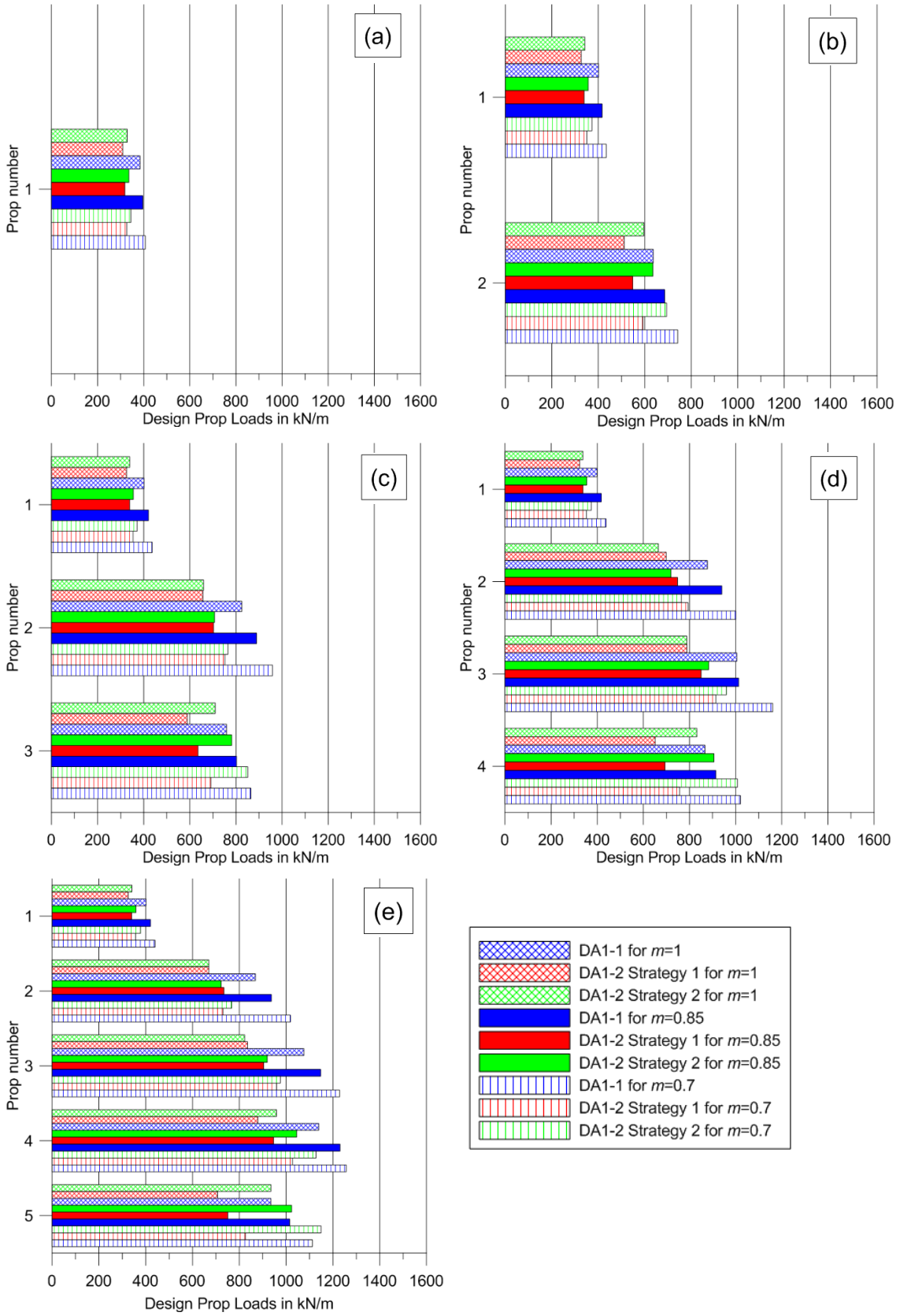

Figure 4.18: Design Prop Loads using the HSS with varying *m* for wall with a) 1, b) 2, c) 3, d) 4 and e) 5 prop levels

Effect of the strain $\gamma_{0.7}$

In Figure 4.19, the design prop loads, using the HSS model with varying $\gamma_{0.7}$, are shown for the 1, 2, 3, 4 and 5-propped walls. It can be seen the DA1-1 generally governs the design at all prop levels with the DA1-2 Strategy 2 resulting in more onerous prop loads only for the 5-propped wall case and for $\gamma_{0.7}$ equal to 0.0001 and 0.00001.

In almost all cases and prop levels, the DA1-2 Strategy 2 is more critical than the DA1-2 Strategy 1 and the discrepancy between the two DA1-2 Strategies does not vary greatly when varying $\gamma_{0.7}$. For example, for the 5-propped wall, the percentage difference in the design load at the bottom prop level is 17%, 28%, 36% and 40% while the percentage difference in the total force supporting the wall between the two DA1-2 Strategies is 7%, 10%, 11% and 11% for $\gamma_{0.7}$ equal to 0.001, 0.0002, 0.0001 and 0.00001 respectively. It can be also seen that the calculated prop loads generally increase with decreasing $\gamma_{0.7}$.

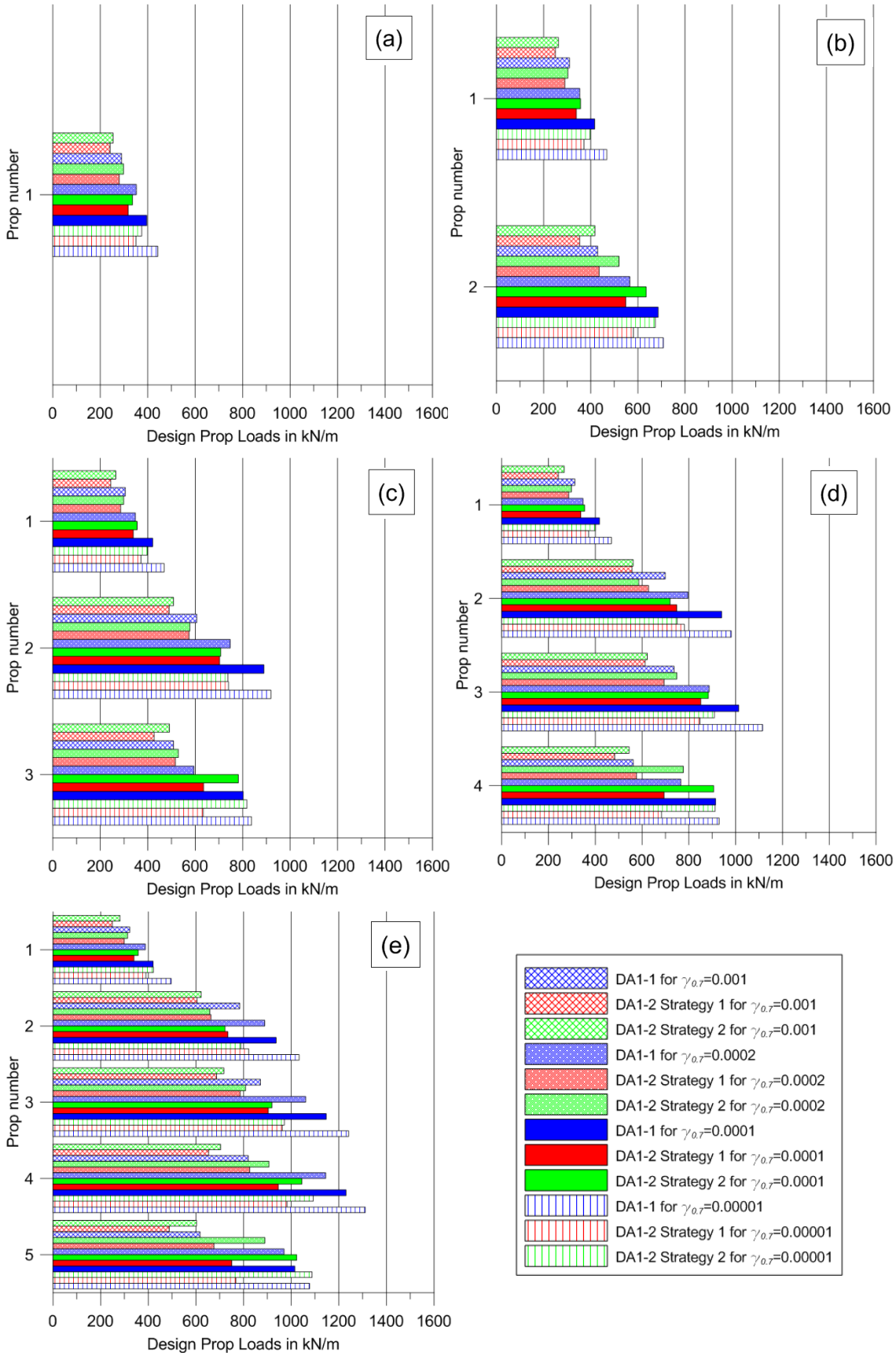

Figure 4.19: Design Prop Loads using the HSS with varying $\gamma_{0.7}$ for wall with a) 1, b) 2, c) 3, d) 4 and e) 5 prop levels

4.5.1.3 BRICK model

In Figure 4.20, the design prop loads using the BRICK model are presented for the 1, 2, 3, 4 and 5-propped walls. It is shown that, the DA1-1 governs the design generally resulting in higher prop loads at almost all prop levels for all geometries while in all cases and prop levels, the DA1-2 Strategy 2 is more critical than the DA1-2 Strategy 1. The percentage difference in the total force supporting the wall between the two DA1-2 Strategies is 10%, 10%, 8%, 8% and 8% for the 1, 2, 3, 4 and 5-propped wall case respectively.

Moreover, the percentage difference in the total force supporting the wall between the DA1-1 and the DA1-2 Strategy 1 and 2 is 44% and 30%, 41% and 28%, 37% and 27%, 34% and 25% and 33% and 23% respectively for the 1, 2, 3, 4 and 5-propped wall case respectively. For walls supported by more than one prop level, the discrepancy between the two DA1-2 Strategies is particularly significant at the bottom level where the percentage difference in the design prop load is 12%, 16%, 23% and 30% for the 2, 3, 4, and 5-propped wall case respectively.

4.5.1.4 Comparison

In this section, the ULS results using the different constitutive models are compared. For the MC model, the reference case is considered to the one with $K_0 = 1.5$, $E_u/c_u = 1000$ and $k = 100$MN/m/m. For the HS model, only the case with $m = 1$ and for the HSS model, only the case with $m = 1.0$ and $\gamma_{0.7} = 0.0001$ is considered for the comparison.

It was found that for the MC, HS and HSS models, DA1-1 governs the design of the prop loads for the 1, 2, 3 and 4 propped wall geometry. In the 5-propped wall case, DA1-1 results in higher loads at top 4 prop levels, while at the bottom level the DA1-2 Strategy 2 is more critical. For the BRICK model, DA1-1 governs the design generally resulting in higher prop loads at all prop levels for all geometries. In all cases and prop levels, the DA1-2 Strategy 2 is more critical than the DA1-2 Strategy 1 with the percentage difference in the total force supporting the wall, between the two DA1-2 Strategies for the 5-propped wall, being 25.5%, 11%, 11% and 8% for the MC, HS, HSS and BRICK model respectively.

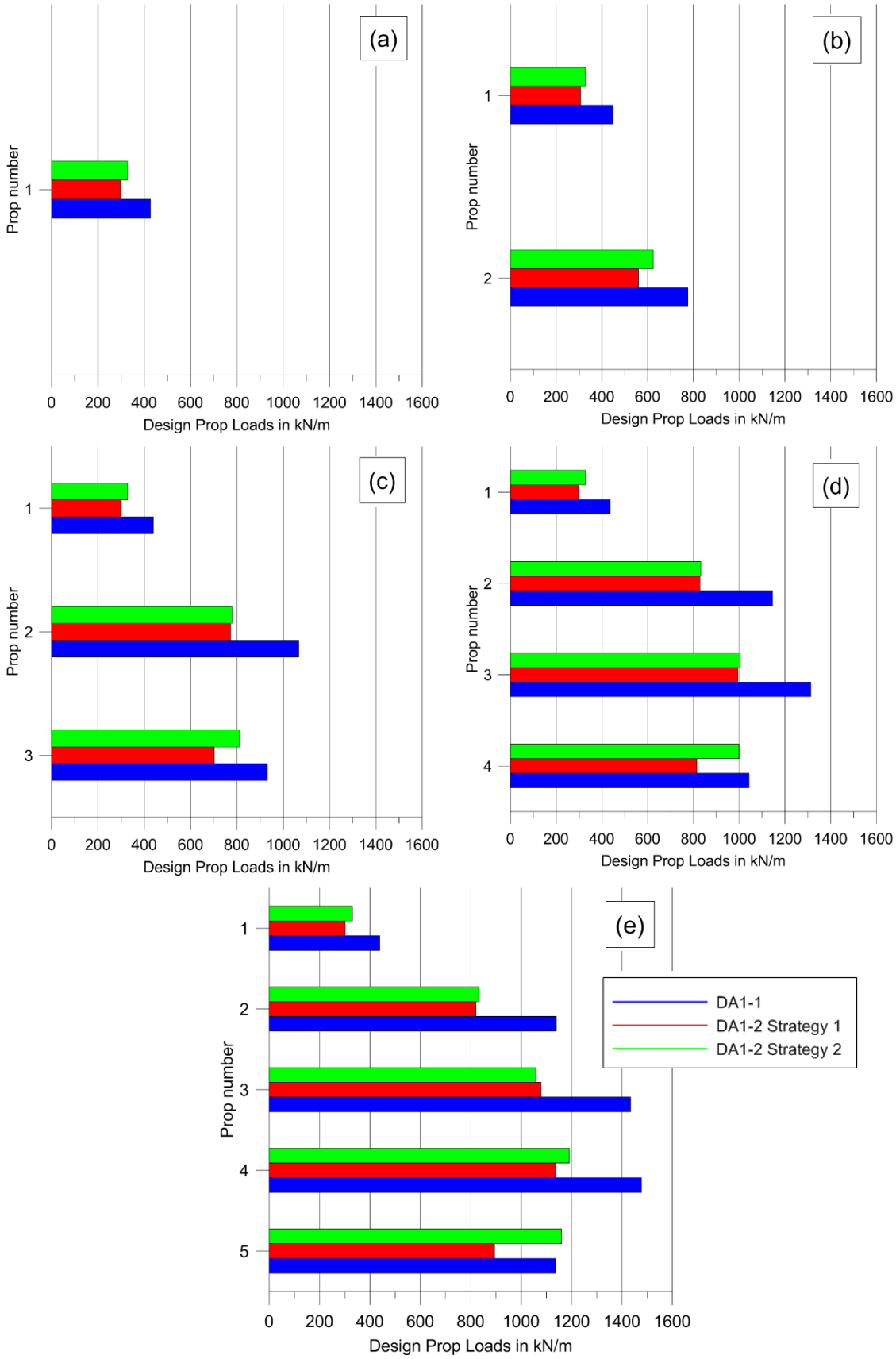

Figure 4.20: Design Prop Loads using the BRICK for wall with a) 1, b) 2, c) 3, d) 4 and e) 5 prop levels

Overall, it was found that the discrepancy in the results between the two DA1-2 Strategies is more apparent for the MC model than the more advanced models. As discussed in Chapter 2, for an elastic-perfectly plastic model such as the Mohr-Coulomb, the soil behaves in an elastic way in the area within the yield surface and becomes plastic when the stress path intersects with the yield surface. In the DA1-2 Strategy 2, when shifting from characteristic to factored soil strength parameters at each excavation stage, the failure line is reduced and the stress state of the plastic points (i.e. the stress points along the failure line) is abruptly changed to be compatible with the new failure line as there is no permissible stress states outside the failure line. Moreover, the stress points that were within the elastic zone but close to the failure line, also become plastic points.

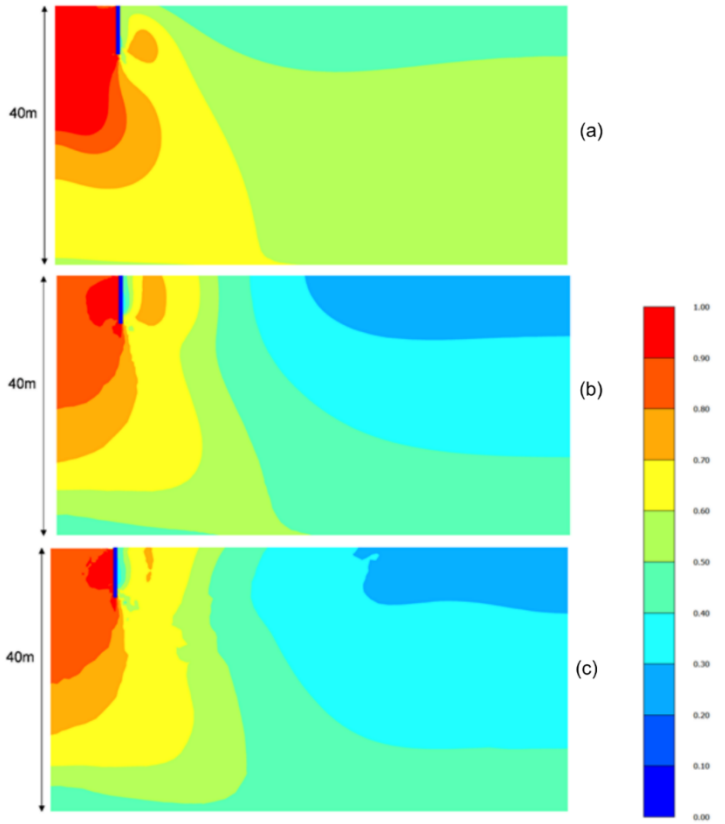

Figure 4.21: Contours of mobilised strength before the excursion at the final excavation stage using the (a) MC; (b) HS; (c) HSS model

The effect is particularly significant for the Mohr-Coulomb model, where a large plastic zone (i.e. zone of fully mobilised strength) is developed at the bottom of the excavation and in front of the wall. The larger the zone, the more abrupt the change in the stress state of the integration points when shifting from the characteristic to factored strength. As shown in Figure 4.21, the plastic zones developed with the HS and HSS model, which are defined by the contour equal to 1.0 and shown as red, are smaller when compared to the MC case and confined only to an area near the wall. Outside this zone,

the soil experiences elasto-plastic hardening and the soil strength is not yet fully mobilised. Please note that as the BRICK model is not readily available with PLAXIS but is a user-defined model, the plastic zone cannot be generated in the output of the programme.

4.5.2 Bending moments

4.5.2.1 Hardening Soil (HS) model

As discussed before, the effect of the E^{ref}_{50} and E^{ref}_{oed} parameters on the structural forces is negligible and not shown here again.

Effect of the power law exponent *m*

In Figure 4.22, the design bending moment envelopes, using the HS model with *m* = 1.0, are shown for the 5-propped wall. It can be seen that the DA-1 governs the design, not only in terms of the minimum and maximum values of bending moments, but also when the whole distribution is considered. Moreover, the DA1-2 Strategy 2 gives higher maximum sagging and hogging bending moments than the Strategy 1. The design bending moments for all *m* cases are presented in Table 4.16 for the 1, 2, 3, 4 and 5-propped walls.

In all cases, DA1-1 governs the design in terms of the minimum bending moment while the percentage difference between the two DA1-2 Strategies is negligible and does not vary with increasing *m*. For example, for the 5-propped wall case, the differences in the minimum bending moment are 0.3%, 1% and 0.5% for *m* equal to 0.7, 0.85 and 1.0. In all cases, higher *m* values generally result in lower wall bending moments, with the effect generally becoming more profound as the excavation depth and the number of prop levels increased. More specifically, when *m* increases from to 0.7 to 1.0, the difference in the minimum design bending moment is about 5% for a 1-propped wall, 7% for a 2-propped wall, 12% for a 3-propped wall, 16% for a 4-propped wall and 26% for a 5-propped wall.

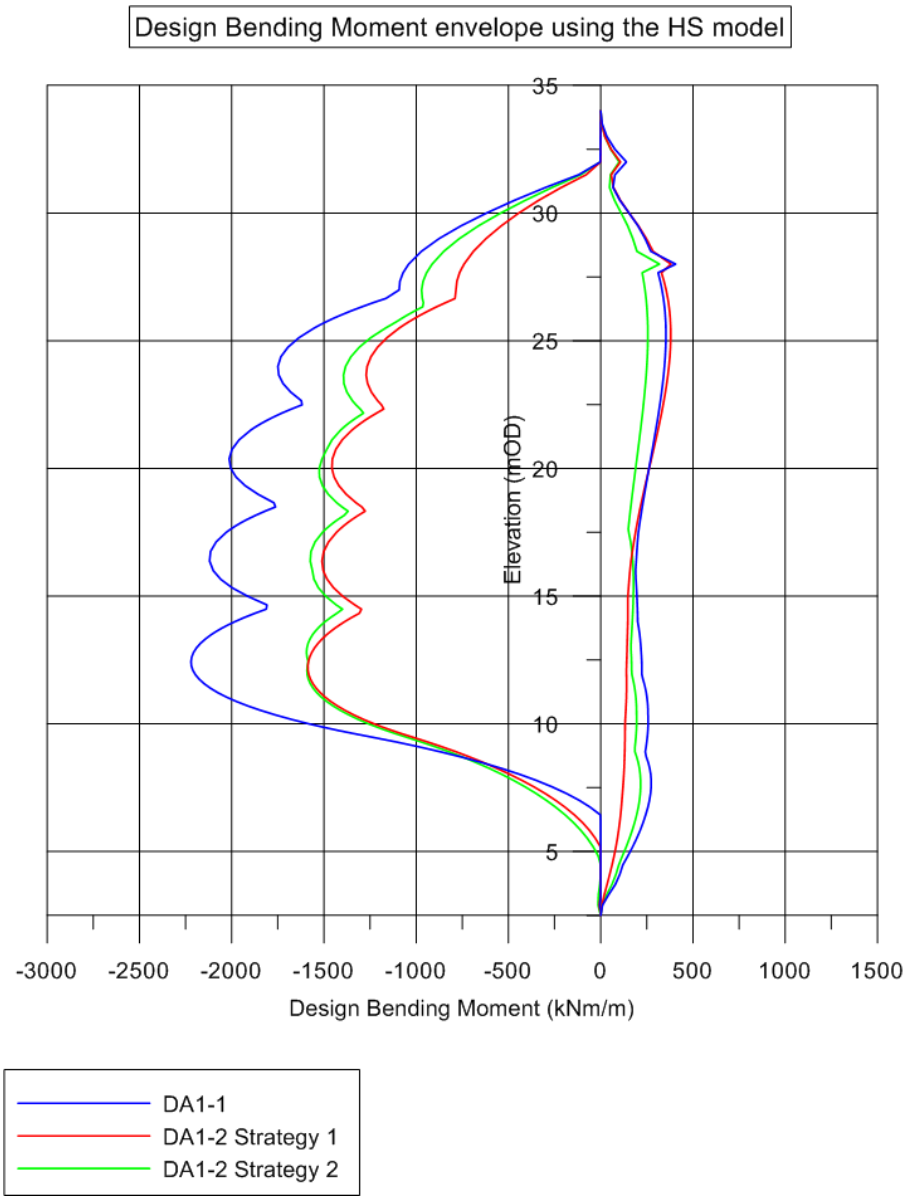

Figure 4.22: Design Bending Moment envelopes for 5-propped wall using the HS with m = 1.0

Table 4.16: Design Bending Moments using the HS with varying *m*

m	M_{max} DA1-1 (kNm/m)	M_{max} DA1-2 S1 (kNm/m)	M_{max} DA1-2 S2 (kNm/m)	M_{min} DA1-1 (kNm/m)	M_{min} DA1-2 S1 (kNm/m)	M_{min} DA1-2 S2 (kNm/m)
1-propped wall						
0.7	259	297	296	-922	-598	-747
0.85	266	302	301	-898	-585	-728
1.0	276	310	337	-879	-569	-718
2-propped wall						
0.7	297	328	369	-1715	-1148	-1272
0.85	309	342	372	-1658	-1114	-1231
1.0	326	355	379	-1598	-1075	-1190
3-propped wall						
0.7	312	346	388	-2179	-1477	-1616
0.85	328	360	390	-2057	-1400	-1526
1.0	345	374	396	-1939	-1318	-1442
4-propped wall						
0.7	542	523	462	-2462	-1737	-1825
0.85	443	421	418	-2269	-1599	-1681
1.0	355	377	399	-2122	-1464	-1578
5-propped wall						
0.7	622	561	479	-2801	-2008	-2014
0.85	502	462	389	-2465	-1755	-1771
1.0	406	381	318	-2221	-1587	-1595

4.5.2.2 Hardening Soil Small (HSS) model

Effect of the power law exponent *m*

In Figure 4.23, the design bending moment envelopes, using the HSS model with *m* = 1.0, are shown for the 5-propped wall.

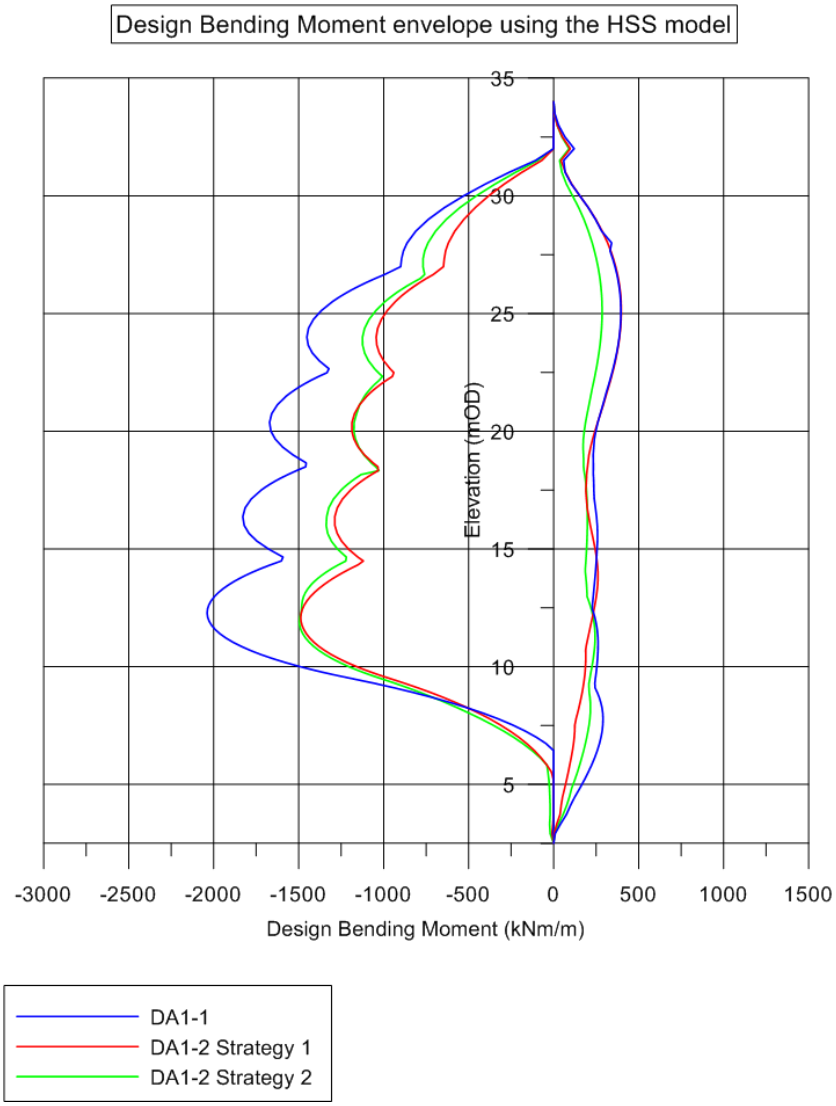

Figure 4.23: Design Bending Moment envelopes for 5-propped wall using the HSS with *m* = 1.0

It is shown that the DA-1 governs the design, not only in terms of the highest values of bending moments, but also when the whole distribution is considered. Moreover, DA1-2 Strategy 2 results in more critical minimum bending moments than Strategy 1 with the difference becoming smaller for the excavation cases with higher number of props. The design bending moments for all *m* cases are presented in Table 4.17 for the 1, 2, 3, 4 and 5-propped walls.

Table 4.17: Design Bending Moments using the HSS with varying *m*

m	M_{max} DA1-1 (kNm/m)	M_{max} DA1-2 S1 (kNm/m)	M_{max} DA1-2 S2 (kNm/m)	M_{min} DA1-1 (kNm/m)	M_{min} DA1-2 S1 (kNm/m)	M_{min} DA1-2 S2 (kNm/m)
1-propped wall						
0.7	279	302	338	-804	-529	-641
0.85	290	311	340	-784	-513	-631
1.0	301	320	342	-756	-496	-629
2-propped wall						
0.7	342	349	380	-1513	-1023	-1125
0.85	358	364	378	-1432	-983	-1078
1.0	376	380	384	-1359	-932	-1029
3-propped wall						
0.7	359	364	393	-1953	-1340	-1447
0.85	376	379	391	-1833	-1254	-1356
1.0	394	396	396	-1714	-1163	-1275
4-propped wall						
0.7	501	471	428	-2237	-1550	-1657
0.85	377	387	392	-1910	-1408	-1437
1.0	395	397	400	-1877	-1312	-1379
5-propped wall						
0.7	549	492	452	-2441	-1826	-1887
0.85	444	390	347	-2326	-1607	-1670
1.0	396	398	285	-2039	-1488	-1496

In all cases, the DA1-1 governs the design while the percentage difference between the two DA1-2 Strategies is negligible and does not particularly vary with increasing *m*. For example, for the 5-propped wall case, the percentage difference in the minimum bending moment is 3%, 4% and 1% for *m* equal to 0.7, 0.85 and 1.0. In all cases, higher *m* values generally result in lower bending moments, with the effect generally becoming more pronounced as the excavation depth and the number of prop levels increase.

Effect of the strain $\gamma_{0.7}$

The design bending moments for all cases are shown in Table 4.18. It was found that the DA1-1 governs the design while DA1-2 Strategy 2 results in more critical minimum bending moments than Strategy 1 with the difference becoming less apparent for deeper excavations with higher number of prop levels.

Table 4.18: Design Bending Moments using the HSS with varying $\gamma_{0.7}$

$\gamma_{0.7}$	M_{max} DA1-1 (kNm/m)	M_{max} DA1-2 S1 (kNm/m)	M_{max} DA1-2 S2 (kNm/m)	M_{min} DA1-1 (kNm/m)	M_{min} DA1-2 S1 (kNm/m)	M_{min} DA1-2 S2 (kNm/m)
1-propped wall						
0.001	280	307	336	-548	-386	-461
0.0002	310	323	340	-687	-450	-585
0.0001	301	320	342	-756	-496	-629
0.00001	279	312	343	-885	-565	-710
2-propped wall						
0.001	294	314	349	-927	-679	-700
0.0002	355	364	367	-1164	-792	-865
0.0001	376	380	384	-1359	-932	-1029
0.00001	336	360	387	-1578	-1057	-1172
3-propped wall						
0.001	295	314	353	-1058	-823	-781
0.0002	359	371	372	-1459	-997	-1082
0.0001	394	396	396	-1714	-1163	-1275
0.00001	358	381	402	-1883	-1288	-1406
4-propped wall						
0.001	295	314	354	-1124	-905	-848
0.0002	359	371	373	-1721	-1175	-1190
0.0001	395	397	400	-1877	-1312	-1379
0.00001	363	384	407	-2061	-1428	-1531
5-propped wall						
0.001	441	314	317	-1046	-828	-839
0.0002	556	371	286	-1698	-1395	-1398
0.0001	396	398	285	-2039	-1488	-1496
0.00001	433	387	300	-2334	-1566	-1586

For example, for the 5-propped wall case, the percentage difference in the minimum bending moment is 1.5%, 0.5%, 0.5% and 1% for $\gamma_{0.7}$ equal to 0.001, 0.0002, 0.0001 and 0.00001 respectively. In all cases, higher $\gamma_{0.7}$ values result in lower wall bending moments, with the effect generally becoming more apparent for deeper excavations.

4.5.2.3 BRICK model

In Figure 4.24, the design bending moment envelopes using the BRICK model are shown for the 5-propped wall. It can be seen that the DA-1 governs the design in terms of the minimum and maximum values of bending moments. Moreover, the DA1-2 Strategy 2 gives higher maximum bending moments than the Strategy 1. The design bending moments are presented in Table 4.19 for the 1, 2, 3, 4 and 5-propped walls. In all cases, the DA1-1 governs the design while the percentage difference in the minimum bending moment between the two DA1-2 Strategies is 17%, 6%, 1%, 1% and 3% for the 1, 2, 3, 4 and 5-propped wall case respectively.

Table 4.19: Design Bending Moments using the BRICK

No of prop levels	M_{max} DA1-1 (kNm/m)	M_{max} DA1-2 S1 (kNm/m)	M_{max} DA1-2 S2 (kNm/m)	M_{min} DA1-1 (kNm/m)	M_{min} DA1-2 S1 (kNm/m)	M_{min} DA1-2 S2 (kNm/m)
1	356	327	310	-931	-574	-673
3	385	361	332	-1685	-1127	-1190
3	388	364	333	-1986	-1452	-1463
4	390	365	334	-2133	-1610	-1627
5	479	444	335	-2109	-1669	-1722

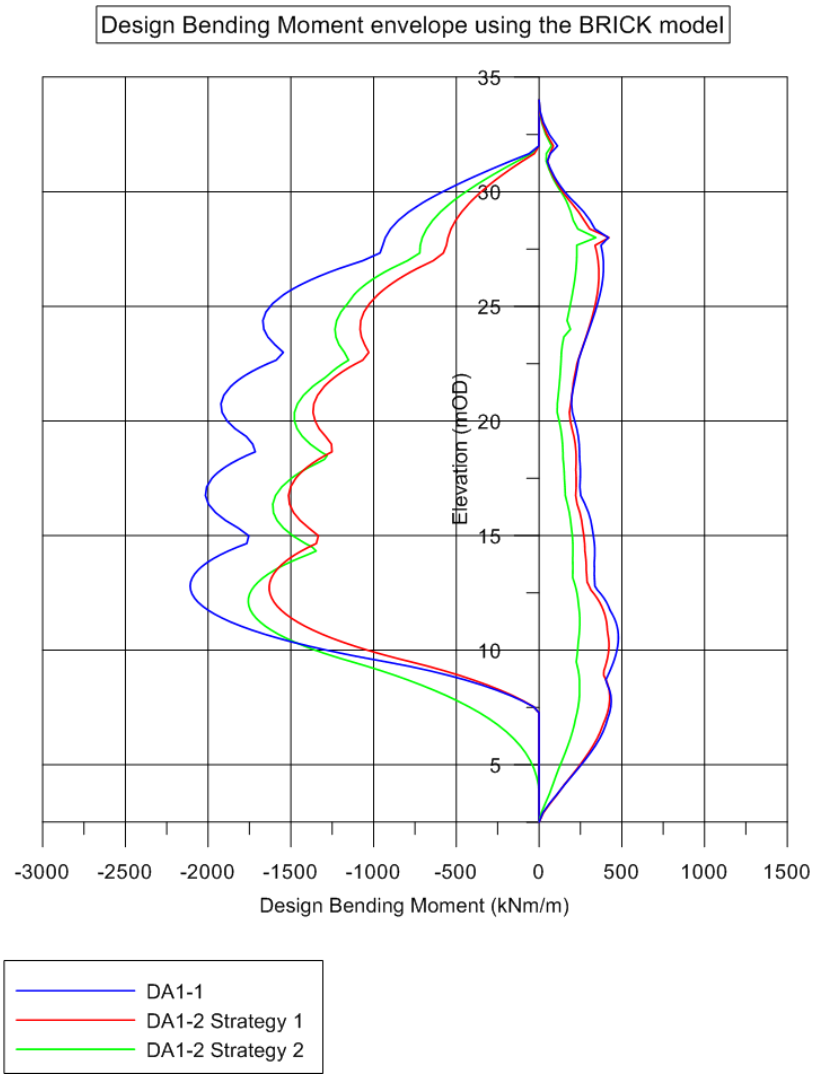

Figure 4.24: Design Bending Moment envelopes for 5-propped wall using the BRICK

4.5.2.4 Comparison

In all cases and for all models, the DA1-1 governs the design in terms of the wall bending moments. Overall, it was found that the discrepancy in the bending moments between the two DA1-2 Strategies is more apparent for the MC model than the more advanced models. More specifically, the difference in the minimum bending moment between the two DA1-2 Strategies for the 5-propped wall is 6%, 0.5%, 0.5% and 3% for the reference cases using the MC, HS, HSS and the BRICK model.

4.5.3 Shear forces

4.5.3.1 Hardening Soil (HS) model

Effect of the power law exponent *m*

In Figure 4.25, the design shear force envelopes, using the HS model with m = 1.0, are shown for the 5-propped wall. It is shown that the DA1-1 results in higher shear forces while the DA1-2 Strategy 2 is more critical than the Strategy 1.

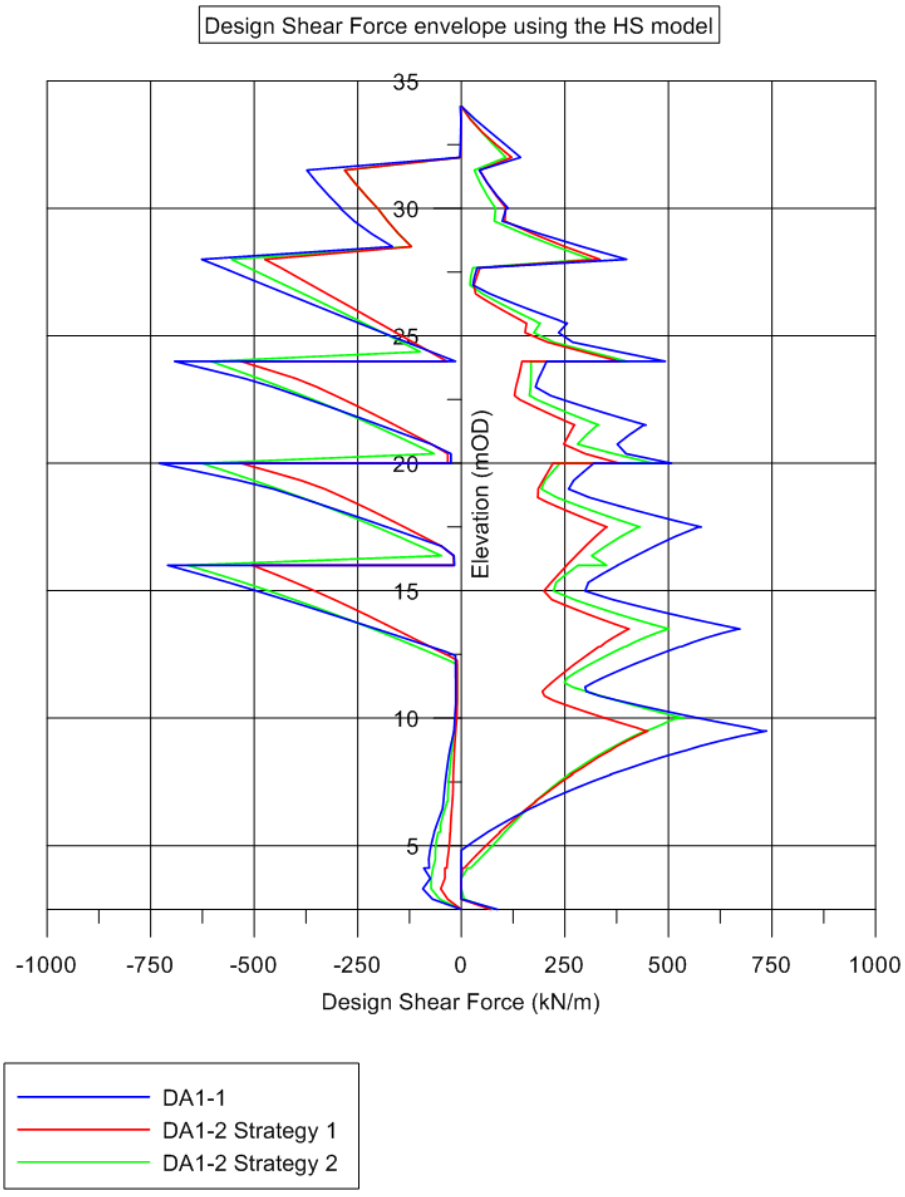

Figure 4.25: Design Shear Force envelopes for 5-propped wall using the HS with m = 1.0

The design shear forces for all m cases are presented in Table 4.20 for the 1, 2, 3, 4 and 5-propped walls. Similar to the bending moments, the change in the percentage difference between the two DA1-2 Strategies is insignificant when varying the power m.

For example, for the 5-propped wall case, the percentage difference in the minimum shear force is 26%, 23% and 24% for *m* equal to 0.7, 0.85 and 1.0 respectively. It was also found that increasing the *m* value, generally decreases the shear forces.

Table 4.20: Design Shear Forces using the HS with varying *m*

m	Q_{max} DA1-1 (kN/m)	Q_{max} DA1-2 S1 (kN/m)	Q_{max} DA1-2 S2 (kN/m)	Q_{min} DA1-1 (kN/m)	Q_{min} DA1-2 S1 (kN/m)	Q_{min} DA1-2 S2 (kN/m)
1-propped wall						
0.7	287	176	215	-364	-275	-312
0.85	283	174	211	-356	-270	-302
1.0	278	171	207	-351	-264	-297
2-propped wall						
0.7	502	327	373	-686	-514	-599
0.85	490	320	363	-654	-488	-562
1.0	477	312	356	-621	-463	-533
3-propped wall						
0.7	643	422	478	-770	-577	-692
0.85	618	404	460	-711	-529	-631
1.0	589	383	438	-657	-487	-587
4-propped wall						
0.7	754	492	560	-821	-622	-739
0.85	710	459	528	-767	-578	-661
1.0	680	435	506	-714	-534	-610
5-propped wall						
0.7	792	483	576	-881	-654	-826
0.85	758	462	550	-791	-591	-728
1.0	737	451	538	-729	-532	-660

4.5.3.2 Hardening Soil Small (HSS) model

Effect of the power law exponent *m*

In Figure 4.26, the design shear force envelopes, using the HSS model with *m* = 1.0, are shown for the 5-propped wall. It is shown that the DA1-1 governs the design while the DA1-2 Strategy 2 is more critical than the Strategy 1. The design shear forces for all *m* cases are presented in Table 4.21 for the 1, 2, 3, 4 and 5-propped walls. Similar

to the bending moments, the change in the percentage difference between the two DA1-2 Strategies is not significant when varying the power *m*. For example, for the 5-propped wall case, the percentage difference in the minimum shear force is 21%, 23% and 21% for *m* equal to 0.7, 0.85 and 1.0 respectively. It was also found that increasing the *m* value, generally results in lower design shear forces.

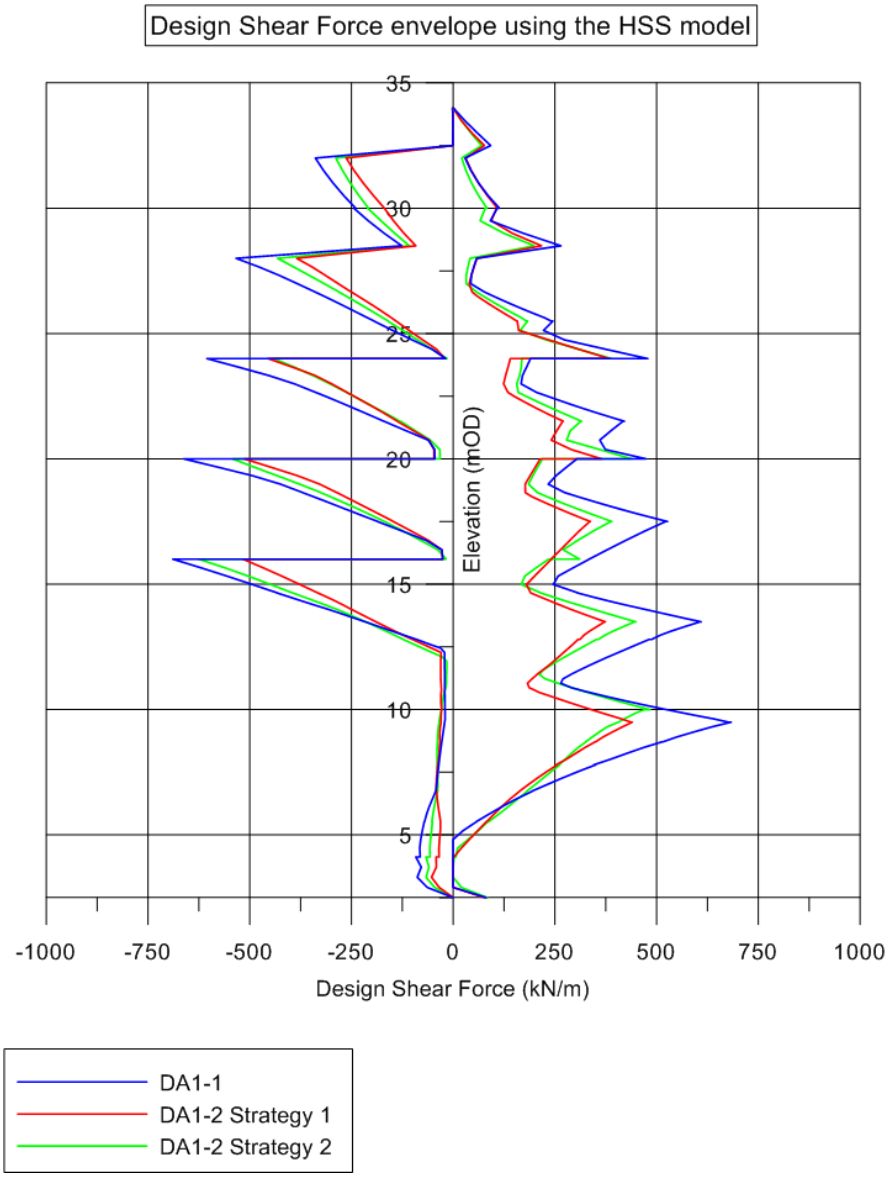

Figure 4.26: Design Shear Force envelopes for 5-propped wall using the HSS with *m* = 1.0

Table 4.21: Design Shear Forces using the HSS with varying *m*

m	Q_{max} DA1-1 (kN/m)	Q_{max} DA1-2 S1 (kN/m)	Q_{max} DA1-2 S2 (kN/m)	Q_{min} DA1-1 (kN/m)	Q_{min} DA1-2 S1 (kN/m)	Q_{min} DA1-2 S2 (kN/m)
1-propped wall						
0.7	256	158	189	-329	-249	-275
0.85	255	156	187	-320	-243	-269
1.0	253	153	186	-311	-237	-265
2-propped wall						
0.7	450	299	335	-605	-451	-516
0.85	433	289	326	-567	-423	-481
1.0	423	276	315	-529	-397	-455
3-propped wall						
0.7	586	392	437	-695`	-542	-632
0.85	561	371	416	-635	-492	-574
1.0	532	348	395	-593	-450	-513
4-propped wall						
0.7	693	464	520	-785	-581	-712
0.85	633	428	464	-649	-534	-602
1.0	617	407	462	-637	-484	-569
5-propped wall						
0.7	712	465	543	-812	-648	-781
0.85	708	419	524	-763	-558	-684
1.0	683	441	484	-689	-516	-625

Effect of the strain $\gamma_{0.7}$

Similarly, the design shear forces for all cases are shown in Table 4.22 for the 1, 2, 3, 4 and 5-propped walls where it can be seen that the DA1-1 again results in higher forces. Moreover, the DA1-2 Strategy 2 is more critical than the Strategy 1, with the difference between the two DA1-2 Strategies becoming more apparent when decreasing the $\gamma_{0.7}$. For example, for the 5-propped wall case, the percentage difference in the minimum shear force is 1.5%, 12%, 21% and 23% for $\gamma_{0.7}$ equal to 0.001, 0.0002, 0.0001 and 0.00001 respectively. It was also found that decreasing the $\gamma_{0.7}$, generally results in higher design shear forces.

Table 4.22: Design Shear Forces using the HSS with varying $\gamma_{0.7}$

$\gamma_{0.7}$	Q_{max} DA1-1 (kN/m)	Q_{max} DA1-2 S1 (kN/m)	Q_{max} DA1-2 S2 (kN/m)	Q_{min} DA1-1 (kN/m)	Q_{min} DA1-2 S1 (kN/m)	Q_{min} DA1-2 S2 (kN/m)
1-propped wall						
0.001	217	143	161	-240	-192	-210
0.0002	235	144	176	-288	-217	-245
0.0001	253	153	186	-311	-237	-265
0.00001	272	169	203	-355	-265	-297
2-propped wall						
0.001	335	228	248	-329	-259	-293
0.0002	374	245	278	-443	-329	-379
0.0001	423	276	315	-529	-397	-455
0.00001	466	306	348	-603	-457	-516
3-propped wall						
0.001	409	286	302	-372	-300	-306
0.0002	489	313	365	-495	-383	-390
0.0001	532	348	395	-593	-450	-513
0.00001	568	374	425	-643	-480	-585
4-propped wall						
0.001	469	331	355	-413	-340	-349
0.0002	581	378	416	-584	-436	-534
0.0001	617	407	462	-637	-484	-569
0.00001	653	425	486	-703	-528	-604
5-propped wall						
0.001	566	293	415	-497	-353	-358
0.0002	690	422	481	-600	-486	-549
0.0001	683	441	484	-689	-516	-625
0.00001	723	442	510	-771	-532	-657

4.5.3.3 BRICK model

In Figure 4.27, the design shear force envelopes using the BRICK model are shown for the 5-propped wall. It is shown that the DA1-1 governs the design while the DA1-2 Strategy 2 is more critical than the Strategy 1. The design shear forces are presented in Table 4.23 for the 1, 2, 3, 4 and 5-propped walls. Similar to the bending moments, the percentage difference between the two DA1-2 Strategies is not significant. The difference in the minimum shear force is 13%, 9%, 10%, 5% and 9% for the 1, 2, 3, 4 and 5-propped wall case respectively.

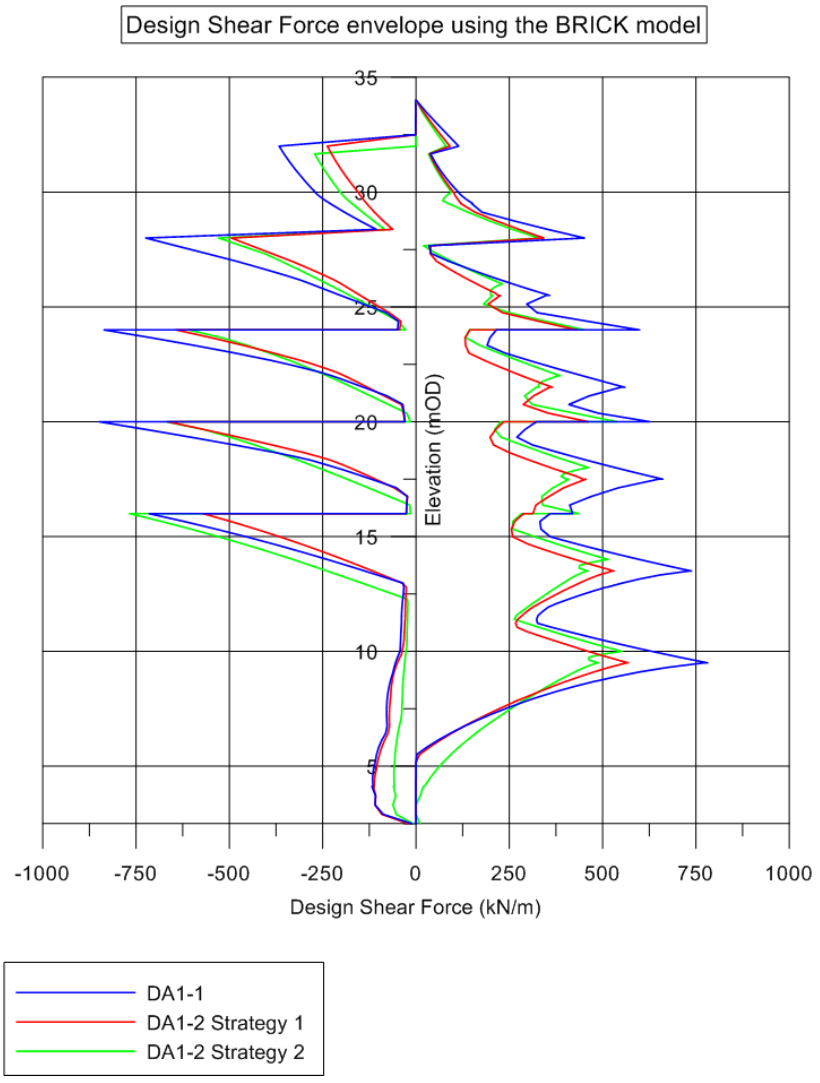

Figure 4.27: Design Shear Force envelopes for 5-propped wall using the BRICK

Table 4.23: Design Shear Forces using the BRICK

No of prop levels	Q_{max} DA1-1 (kN/m)	Q_{max} DA1-2 S1 (kN/m)	Q_{max} DA1-2 S2 (kN/m)	Q_{min} DA1-1 (kN/m)	Q_{min} DA1-2 S1 (kN/m)	Q_{min} DA1-2 S2 (kN/m)
1	343	210	225	-361	-242	-274
2	552	359	382	-640	-451	-493
3	650	451	454	-733	-526	-579
4	720	518	505	-815	-633	-663
5	781	576	552	-849	-674	-738

4.5.3.4 Comparison

In all cases and for all models, the DA1-1 governs the design in terms of the wall shear forces. Overall, it was found that the discrepancy in the shear forces between the two DA1-2 Strategies is more apparent for the MC model than the more advanced models. More specifically, the difference in the minimum shear force between the two DA1-2 Strategies for the 5-propped wall is 41.5%, 24%, 23% and 9% for the reference cases using the MC, HS, HSS and the BRICK model.

4.5.4 Axial forces

4.5.4.1 Hardening Soil (HS) model

Effect of the power law exponent *m*

In Figure 4.28, the design axial force envelopes using the HS model with m = 1.0 are presented for the 5-propped wall. It can be seen that the DA1-1 governs the design. The design axial forces for all m cases are presented in Table 4.24 for the 1, 2, 3, 4 and 5-propped walls.

Overall, the DA1-1 results in higher axial forces while the DA1-2 Strategy 2 is more critical than the Strategy 1 in almost all cases with the difference not varying significantly with increasing m. It was also found that increasing the m value results in an increase in the axial forces with the difference becoming apparent only in the minimum axial force for deeper excavations.

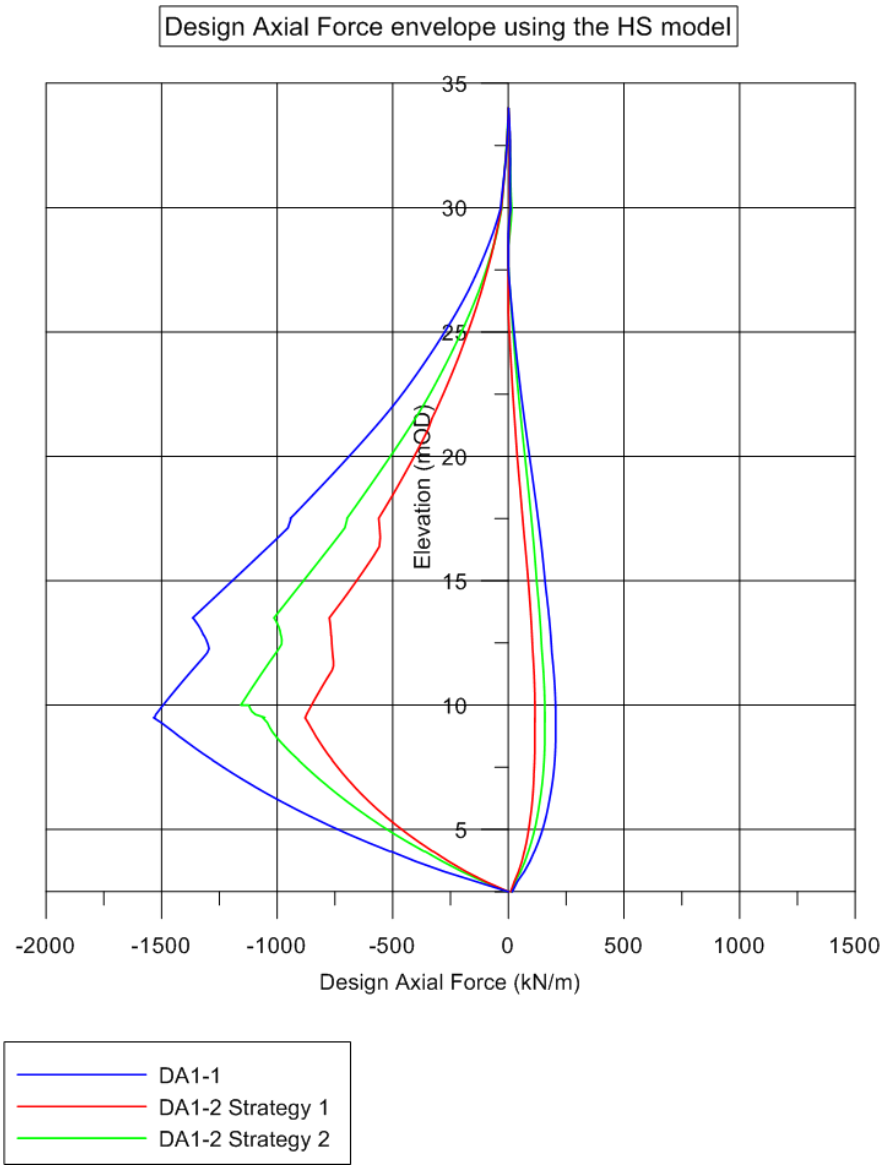

Figure 4.28: Design Axial Force envelopes for 5-propped wall using the HS with m = 1.0

Table 4.24: Design Axial Forces for 1-propped wall using the HS with varying *m*

m	N_{max} DA1-1 (kN/m)	N_{max} DA1-2 S1 (kN/m)	N_{max} DA1-2 S2 (kN/m)	N_{min} DA1-1 (kN/m)	N_{min} DA1-2 S1 (kN/m)	N_{min} DA1-2 S2 (kN/m)
1-propped wall						
0.7	6	5	5	-181	-102	-133
0.85	5	5	4	-185	-102	-136
1.0	5	5	4	-189	-102	-141
2-propped wall						
0.7	19	9	15	-346	-192	-256
0.85	15	8	12	-354	-195	-262
1.0	14	7	11	-363	-199	-270
3-propped wall						
0.7	49	20	37	-523	-293	-390
0.85	43	18	33	-537	-302	-399
1.0	38	16	31	-555	-310	-414
4-propped wall						
0.7	92	46	70	-775	-458	-572
0.85	86	42	66	-799	-459	-590
1.0	81	38	64	-826	-459	-615
5-propped wall						
0.7	243	132	182	-1426	-841	-1074
0.85	225	125	164	-1485	-865	-1111
1.0	205	115	158	-1535	-880	-1157

4.5.4.2 Hardening Soil Small (HSS) model

Effect of the power law exponent *m*

Finally, in Figure 4.29 the design axial force envelopes using the HSS model with *m* = 1.0 are presented for the 5-propped wall. It is shown that the DA1-1 governs the design resulting in more onerous axial forces. The design axial forces for all *m* cases are presented in Table 4.25 for the 1, 2, 3, 4 and 5-propped walls. Overall, the DA1-1 results in higher axial forces while the DA1-2 Strategy 2 is more critical than the Strategy 1 in almost all cases with the difference becoming more apparent for higher values of *m* and for deeper excavations.

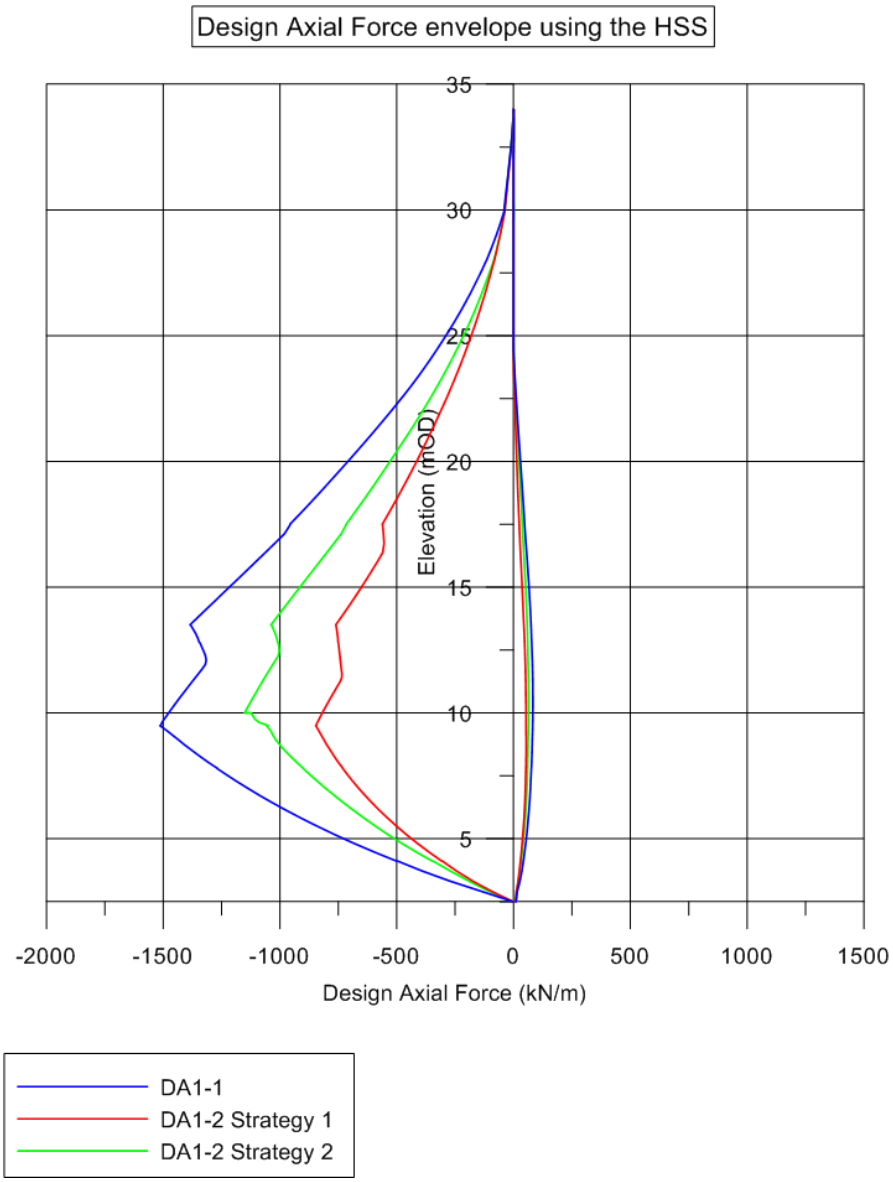

Figure 4.29: Design Axial Force envelopes for 5-propped wall using the HSS with m = 1.0

Table 4.25: Design Axial Forces using the HSS with varying *m*

m	N_{max} DA1-1 (kN/m)	N_{max} DA1-2 S1 (kN/m)	N_{max} DA1-2 S2 (kN/m)	N_{min} DA1-1 (kN/m)	N_{min} DA1-2 S1 (kN/m)	N_{min} DA1-2 S2 (kN/m)
1-propped wall						
0.7	3	4	4	-168	-106	-123
0.85	3	4	3	-170	-107	-127
1.0	3	4	2	-173	-107	-129
2-propped wall						
0.7	5	4	4	-331	-194	-245
0.85	6	4	5	-332	-196	-247
1.0	6	4	4	-342	-199	-260
3-propped wall						
0.7	15	9	12	-509	-296	-377
0.85	13	8	10	-517	-298	-384
1.0	13	7	10	-525	-305	-396
4-propped wall						
0.7	34	17	26	-761	-469	-562
0.85	31	16	23	-795	-468	-581
1.0	31	16	23	-820	-465	-615
5-propped wall						
0.7	89	54	70	-1449	-804	-1078
0.85	85	51	64	-1467	-844	-1113
1.0	83	50	62	-1515	-847	-1152

Effect of the strain $\gamma_{0.7}$

The effect of $\gamma_{0.7}$ on the design axial forces for all cases is presented in Table 4.26 for the 1, 2, 3, 4 and 5-propped walls. Overall, the DA1-1 results in higher axial forces while the DA1-2 Strategy 2 is more critical than the Strategy 1 in all cases. Moreover, it was found that increasing the $\gamma_{0.7}$ value results in a decrease in the axial forces, with the difference becoming more apparent for deep excavations.

Table 4.26: Design Axial Forces using the HSS with varying $\gamma_{0.7}$

$\gamma_{0.7}$	N_{max} DA1-1 (kN/m)	N_{max} DA1-2 S1 (kN/m)	N_{max} DA1-2 S2 (kN/m)	N_{min} DA1-1 (kN/m)	N_{min} DA1-2 S1 (kN/m)	N_{min} DA1-2 S2 (kN/m)
1-propped wall						
0.001	6	6	5	-136	-100	-103
0.0002	5	5	4	-165	-107	-125
0.0001	3	4	2	-173	-107	-129
0.00001	4	5	4	-183	-100	-137
2-propped wall						
0.001	15	10	12	-296	-178	-222
0.0002	10	7	7	-327	-194	-245
0.0001	6	4	4	-342	-199	-260
0.00001	11	7	9	-350	-199	-262
3-propped wall						
0.001	30	18	23	-458	-267	-346
0.0002	19	10	15	-516	-294	-388
0.0001	13	7	10	-525	-305	-396
0.00001	30	16	24	-536	-309	-402
4-propped wall						
0.001	50	31	38	-687	-426	-516
0.0002	38	22	29	-797	-455	-578
0.0001	31	16	23	-820	-465	-615
0.00001	65	31	51	-811	-462	-605
5-propped wall						
0.001	136	88	101	-1149	-751	-1002
0.0002	110	72	76	-1350	-830	-1139
0.0001	83	50	62	-1515	-847	-1152
0.00001	179	98	132	-1357	-872	-1155

4.5.4.3 BRICK model

Finally, in Figure 4.30 the design axial force envelopes using the BRICK model are presented for the 5-propped wall. It can be seen that the DA1-1 governs the design resulting in more onerous axial forces. The design axial forces for are presented in Table 4.27 for the 1, 2, 3, 4 and 5-propped walls. Overall, the DA1-1 results in higher axial

forces while the DA1-2 Strategy 2 results in most cases in similar axial forces with the Strategy 1.

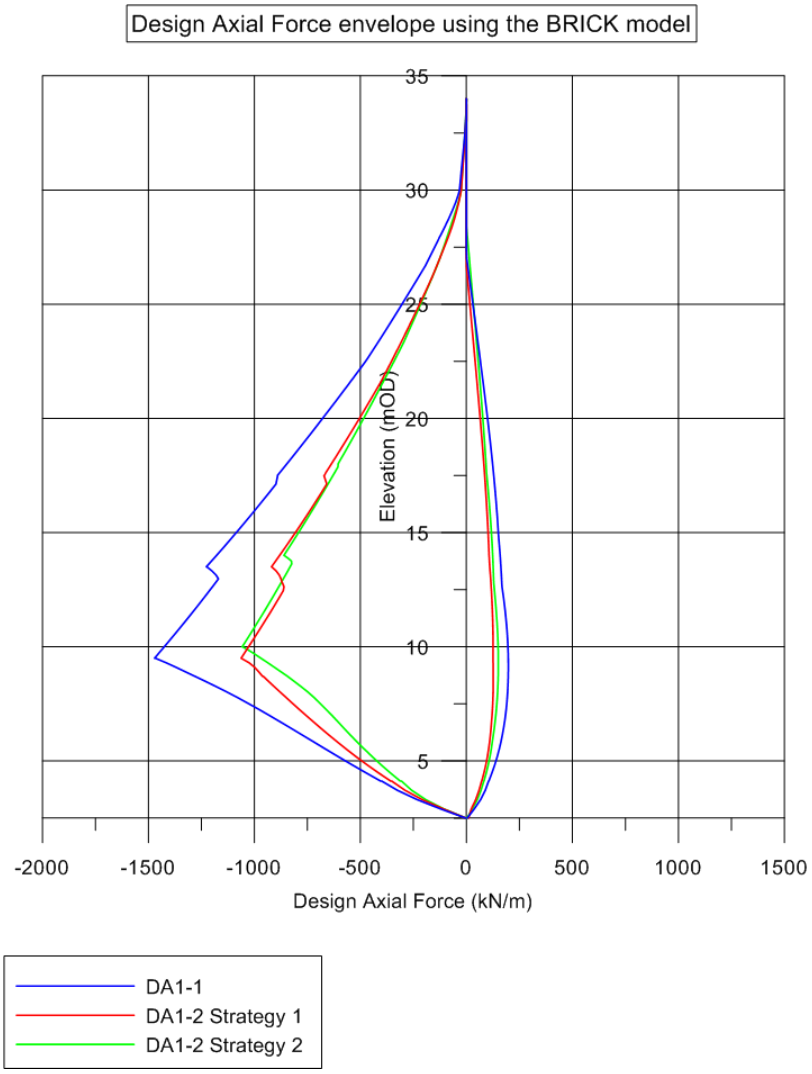

Figure 4.30: Design Axial Force envelopes for 5-propped wall using the BRICK

Table 4.27: Design Axial Forces using the BRICK

No of prop levels	N_{max} DA1-1 (kN/m)	N_{max} DA1-2 S1 (kN/m)	N_{max} DA1-2 S2 (kN/m)	N_{min} DA1-1 (kN/m)	N_{min} DA1-2 S1 (kN/m)	N_{min} DA1-2 S2 (kN/m)
1	6	4	7	-237	-165	-166
3	20	13	18	-448	-314	-315
3	45	30	36	-675	-462	-489
4	80	55	60	-917	-611	-677
5	198	130	149	-1472	-1060	-1062

4.5.4.4 Comparison

In all cases and for all models, the DA1-1 governs the design in terms of the wall axial forces. Moreover, it was found that the discrepancy in the axial forces between the two DA1-2 Strategies is more apparent for the MC model than the more advanced models. More specifically, the difference in the minimum axial force between the two DA1-2 Strategies for the 5-propped wall is 21%, 31%, 36% and 0.5% for the reference cases using the MC, HS, HSS and the BRICK model.

4.6 Conclusions

Overall, it was found that the SLS results from the analyses using the HSS model, and to a lesser extent, the HS model, with the model parameters derived in Chapter 2, are in reasonable agreement with the results from the analysis using the BRICK model which has been long successfully used to model the behaviour of the London Clay. However, the settlement trough predicted by the HS model was too wide when compared to the HSS and BRICK models. The small strain stiffness governs the behaviour of the soil far away from the excavation zone, so the more realistic prediction, by the small strain models, is due to the higher far-field soil stiffness.

For the ULS analysis, it was found that, in almost all cases and for all models, the DA1-1 governs the design in terms of the prop loads, wall bending moments, shear and axial forces. It was also found that the discrepancy in the results between the two DA1-2 Strategies is more significant for the MC model than the more advanced models. While designers can possibly be more relaxed about the choice of the DA1-2 Strategy when using more advanced models, the Strategy 2 is still more critical than the Strategy 1. Overall, the dual approach currently required in the DA1, expressed as a combination of the DA1-1 and the DA1-2 Strategy 2, governs the design decisions for the materials and the range of geometries considered in this study.

CHAPTER 5

FE analysis of deep excavation case histories

5.1 Introduction

In this Chapter, the design challenges of deep supported excavations in London Clay, using Finite Element Methods, are illustrated and discussed using two deep excavation case histories. The first project is the Moorgate Crossrail Station excavation, part of one of the largest infrastructure projects that, at time this document was being written it was under construction. This is an exceptionally deep excavation in central London, supported by 7 levels of temporary props. The second project, referred to as the Exhibition Road Building, is a new exhibition space currently being constructed within the courtyard area of the Victoria & Albert Museum. The development comprises the construction of a deep basement supported by a multi-propped secant pile wall.

The study focuses on the ULS FE analysis of the two case histories, using both EC7 DA1 Combinations, and the derivation of the design internal structural forces similar to what was done in the previous chapters. Both analyses were repeated using the MC, HS, HSS and the BRICK model parameters for the London Clay. The different factoring combinations and strategies are compared and the effect of the soil model on the resulting discrepancies is discussed. Moreover, for the Victoria & Albert excavation, the calculated design prop loads are compared with the available field measurements, in order to assess the conservatism of the FEM assumptions and the constitutive models.

The reason for studying such deep multi-propped excavations is that, as shown in Chapters 3 and 4, the differences in the calculated design values of the internal structural forces, between the different factoring methods, become more apparent for deeper excavations and higher number of prop levels.

5.2 The Moorgate Crossrail Station Case Study

5.2.1 Description of the project

One of the largest infrastructure projects currently under construction in London, is the Crossrail project, a new high capacity railway aiming to connect the east and west sides of London. Tunnels of 19 km length are being constructed, driven from deep shafts to get access to the underground sites. One of the biggest challenges of the project is

the depth of the launching platforms for the Tunnel Boring Machines (TBM) because the rail lines have to run beneath the existing metro lines. This study focuses on a proposed deep excavation at the Moorgate site in central London, part of the Crossrail project.

The total depth of the Moorgate excavation (i.e. 40.7m) is deeper than most common excavations in the greater London urban area because the site is supposed to be used both as a launching platform for the tunnel boring machine and as part of a future Crossrail passenger station with escalators.

The geometry and soil conditions are shown in Figure 5.1 and were based on the proposal made by Zdravkovic et al. (2005). The soil profile, which consists of a sequence of different layers, is shown in Figure 5.1. The construction sequence is also shown, where the dashed lines show the ground level at each excavation stage, and the arrows indicate the prop levels.

The groundwater table is located 7.2m below the ground surface. The excavation geometry consists of a 35m by 35m square in plan-view with the diaphragm wall being 47.6m deep. The concrete wall is 1.2m thick, supported by 7 levels of steel tube props.

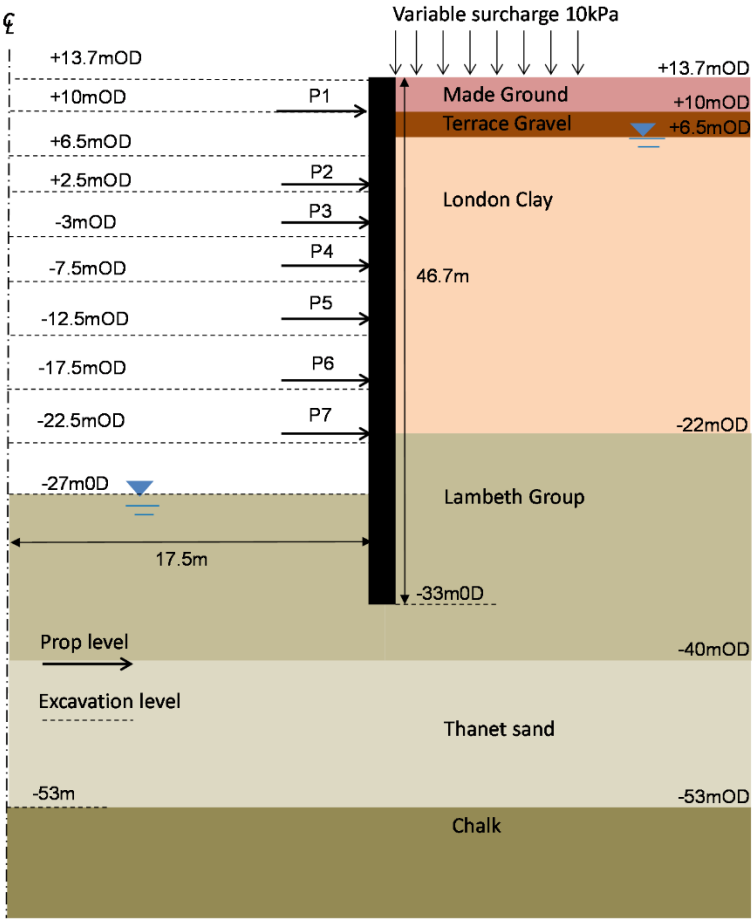

Figure 5.1: Geometry and soil profile based on Zdravkovic et al. (2005)

5.2.2 Modelling assumptions

The following assumptions were made in the model:

- The wall is wished-in-place.
- Half the excavation width is only modelled, due to symmetry.
- The side model boundaries are fixed in the *x* direction while the bottom model boundary is fixed in both *x* and *y* directions.
- The unit weight of the soil *γ* is equal to 20kN/m^3
- Interface elements are used between the soil and the wall with tanδ = 2/3 tanφ', where δ is the soil/wall friction angle.
- In all analyses drained conditions are assumed for only the initial stage. For the rest of the stages undrained conditions were considered.

The following modeling sequence was analysed:

- Stage 0 Initial State
- Stage 1 Install wall and apply 10kPa surcharge
- Stage 2 Excavation to +16mOD
- Stage 3 Install prop 1 at +10mOD
- Stage 4 Excavation to +2.5mOD
- Stage 5 Install prop 2 at +3.3mOD
- Stage 6 Excavation to -3mOD
- Stage 7 Install prop 3 at -1.6mOD
- Stage 8 Excavation to -7.5mOD
- Stage 9 Install prop 4 at -6.5mOD
- Stage 10 Excavation to -12.5mOD
- Stage 11 Install Prop 5 at -11.2mOD
- Stage 12 Excavation to -17.5mOD
- Stage 13 Install prop 6 at -16.2mOD
- Stage 14 Excavation to -22.5mOD
- Stage 15 Install prop 7 at -21.2mOD
- Stage 16 Excavation to -27mOD

The computer software PLAXIS 2015.02 was used for the analysis in its 2D version. The FE mesh, which is shown in Figure 5.2, consists of 1050 15-noded elements. The coarseness of the mesh increases with the distance from the axis of symmetry (i.e. the left hand side boundary). A finer mesh was used for the area of the excavation whereas the mesh gets coarser in the areas far from the excavation. The

dimensions of the model (i.e. 100m and 66.7m in the x and y direction respectively), are large enough to minimize the influence of the boundary conditions.

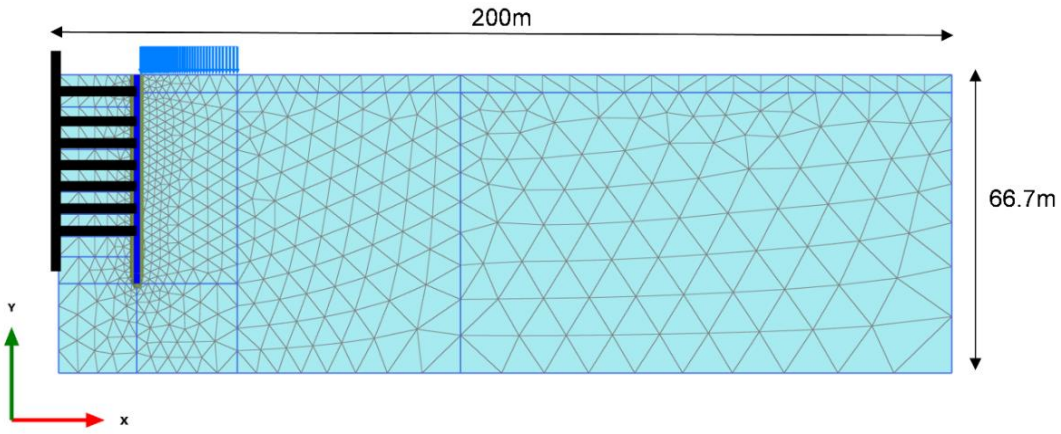

Figure 5.2: FE mesh for the Moorgate excavation

The ground water table is at +6.5mOD and an under-drained pore water profile was assumed with an increment equal to 6kN/m^2/m to account for the water extraction of the London Clay formation from the underlain Chalk layer.

For the Made Ground, Terrace Gravel and Thanet Sand, the Mohr-Coulomb model was used in the analysis with the parameters listed in Table 5.1, based on Zdravkovic et al. (2005). For the London Clay, the parameters derived in this study and discussed in Chapter 2, were used. The London Clay model parameters were also used for the Lambeth Group, consistent with the assumption made by Zdravkovic et al. (2005). The top of the Chalk is below the bottom boundary level of the model.

Table 5.1: Characteristic parameters for the Made Ground and Terrace Gravel

Stratum	Top Level (mOD)	Unit weight γ (kN/m^3)	φ' (°)	c' (kPa)	E' (kPa)	v
Made Ground	+13.7mOD	19	25	0	10,000	0.2
Terrace Gravel	+10mOD	19	35	0	30,000	0.2
Thanet Sand	-40mOD	20	32	0	300,000	0.2

For all structural elements (i.e. concrete wall, steel tubular props), an elastic behaviour was assumed with a constant stiffness.

Parameters for the diaphragm wall:

- Young's modulus E = 28000MN/m²
- Poisson's ratio v = 0.2
- Cross sectional area A = 1.2m²
- Moment of inertia I = 0.144m^4

Parameters for the steel props:

- Young's modulus E = 200GPa
- Spacing = 5m
- Cross sectional area A = 0.04375m²
- Prop stiffness k = 100MN/m/m

5.2.3 ULS analysis

In this section, the results from the ULS FE analyses are presented in terms of the design structural forces (i.e. prop loads, bending moments, shear and axial forces). The FE ULS analysis was repeated using the MC, HS, HSS and BRICK model parameters for the London Clay, discussed in Chapter 2.

5.2.3.1 Comparison of the different factoring methods

In Figure 5.3, the design prop loads are presented. For the MC model case, it can be seen that the DA1-1 governs at the upper 6 prop levels while the DA1-2 Strategy 2 results in higher loads at the bottom prop level. The discrepancy in the results between the two DA1-2 Strategies, is negligible at the upper prop levels, but becomes particularly apparent at the lower prop levels. More specifically, the percentage difference in the calculated prop load is 15%, 25%, 40% and 75% for the 4th, 5th, 6th and 7th prop level respectively. The difference in the total force supporting the wall, between the two DA1-2 Strategies, is 19%. Moreover, the differences in the total force supporting the wall, between the DA1-1 and the DA1-2 Strategy 1 and 2, are 41% and 20% respectively. Factoring the soil strength from the beginning (i.e. DA1-2 Strategy 1) has very little effect on the calculated prop loads. This highlights that the soil strength is not critical for the material and the geometry considered, which is in agreement with the findings for the benchmark examples studied in Chapters 3 and 4. In the DA1-2 Strategy 2, shifting from the unfactored to the factored soil strength, has shown that the lowest prop, receives a higher load increment.

For the HS model case, the DA1-1 governs at all prop levels. It was also found that the difference in the results between the two DA1-2 Strategies, is insignificant at the upper prop levels, but becomes more apparent at the lower prop levels. More specifically, the percentage difference in the calculated prop load is 6%, 11%, 19% and 41% for the 4^{th}, 5^{th}, 6^{th} and 7^{th} prop level respectively. The percentage difference in the total force supporting the wall between the two DA1-2 Strategies is about 9%. Moreover, the differences in the total force supporting the wall, between the DA1-1 and the DA1-2 Strategy 1 and 2, are 35% and 24% respectively.

For the HSS model case, it can be seen that the DA1-1 governs at all prop levels, apart from the bottom one where the DA1-2 Strategy 2 governs, similar to the MC model case. The discrepancy in the calculated prop loads between the two DA1-2 Strategies, is generally insignificant with the difference in the total force supporting the wall, between the two DA1-2 Strategies, being about 6%. Moreover, the differences in the total force supporting the wall, between the DA1-1 and the DA1-2 Strategy 1 and 2, are 28% and 20% respectively.

Finally, for the BRICK model case, it was found that, the DA1-1 governs at the upper six prop levels while the DA1-2 Strategy 2 governs at the bottom prop level. It was also found that the difference in the prop loads between the two DA1-2 Strategies, is insignificant at the upper 5 prop levels, but becomes more apparent at the lower prop levels. More specifically, the difference in the calculated prop load is 15% and 60% for the 6^{th} and 7^{th} prop level respectively. The difference in the total force supporting the wall, between the two DA1-2 Strategies, is 8% while the differences between the DA1-1 and the DA1-2 Strategy 1 and 2, are 26% and 16% respectively.

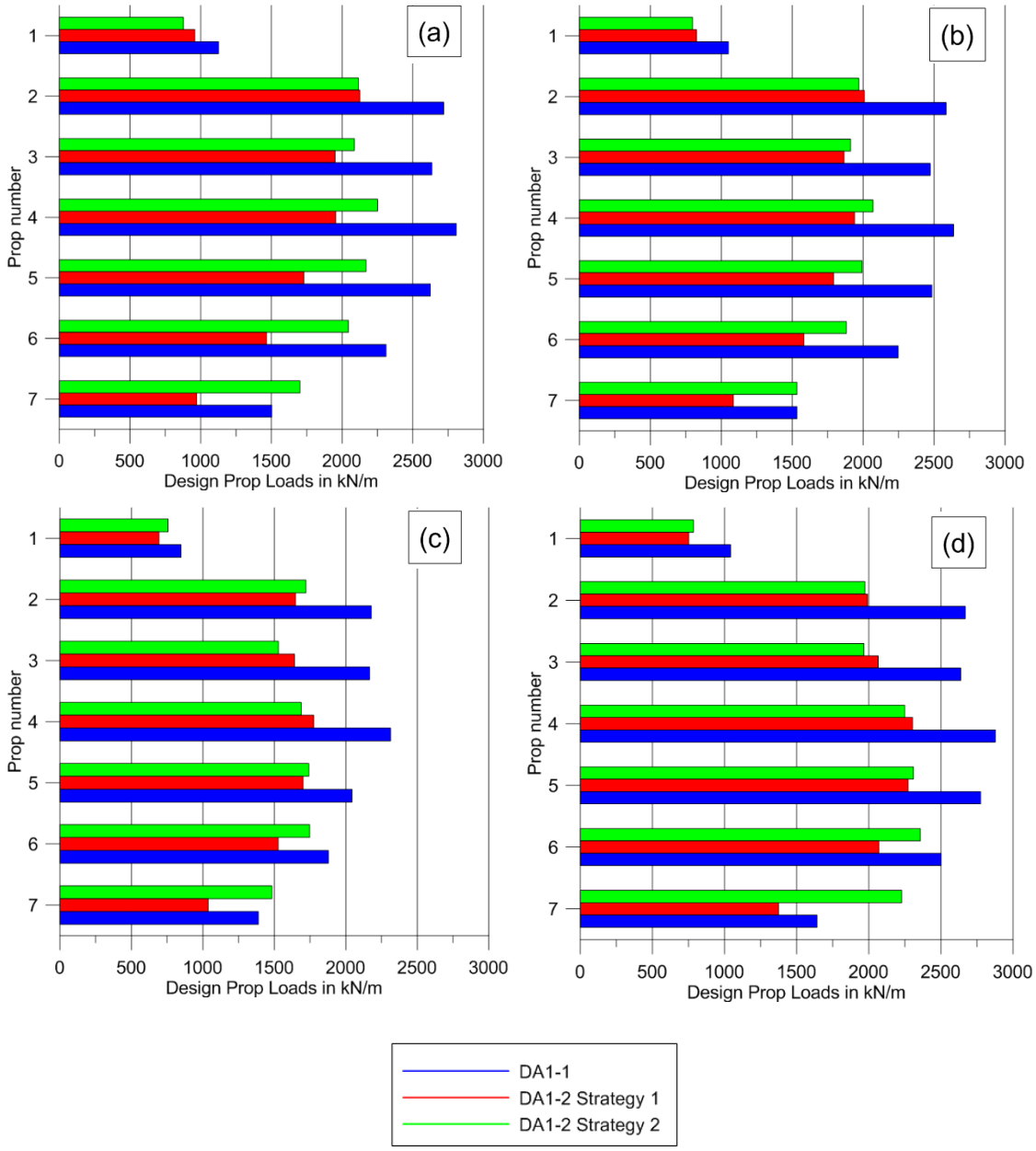

Figure 5.3: Design Prop Loads for the Moorgate excavation using the a) MC, b) HS, c) HSS and d) BRICK model

In Table 5.2, the maximum and minimum design bending moments are shown while in Figure 5.4 the design bending moment envelopes are presented. It was found, that the DA1-1 governs the design, resulting in the highest design bending moments in all cases. Moreover, the DA1-2 Strategy 1 results in more critical maximum bending moment than the Strategy 2 for all models except the MC, with the difference being 15%, 37% and 4% for the HS, HSS and the BRICK model respectively. On the other hand, the DA1-2 Strategy 2 results in higher minimum bending moment than the Strategy 1 in all cases, with the difference being 12%, 3%, 0.5% and 10% for the MC, HS, HSS and the BRICK model respectively.

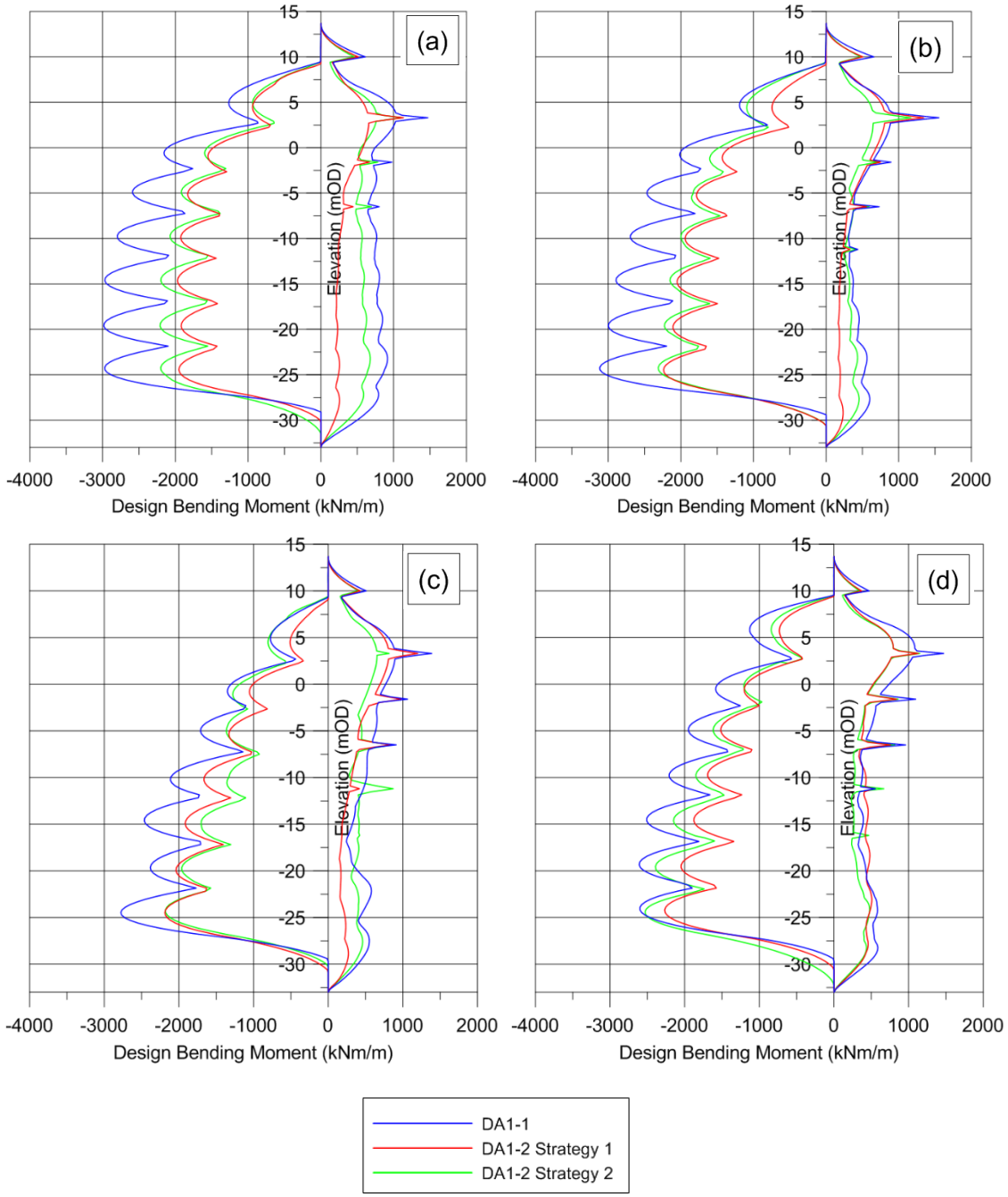

Figure 5.4: Design Bending Moment envelopes for the Moorgate excavation using the a) MC, b) HS, c) HSS and d) BRICK model

Note that the peaks in the envelopes of the positive bending moments, which are observed at the levels of the props, indicate that the most critical bending moments at those levels are generated at the excavation stage following the installation of the corresponding prop. However in some cases (for example for the MC model) there are less than 5 peaks in the envelopes showing that the maximum bending moment at the level of the missing peak is generated at a different stage of the analysis.

Table 5.2: Design bending moments with different constitutive models

Model	M_{max} DA1-1 (kNm/m)	M_{max} DA1-2 S1 (kNm/m)	M_{max} DA1-2 S2 (kNm/m)	M_{min} DA1-1 (kNm/m)	M_{min} DA1-2 S1 (kNm/m)	M_{min} DA1-2 S2 (kNm/m)
MC	1471	1134	1167	-2985	-1971	-2211
HS	1554	1342	1166	-3117	-2239	-2312
HSS	1388	1200	871	-2778	-2180	-2187
BRICK	1470	1196	1150	-2610	-2292	-2530

In Table 5.3, the maximum and minimum design shear forces are presented while in Figure 5.5, the design shear force envelopes are shown. In all cases, the DA1-1 governs the design, resulting in the highest shear forces. Moreover, the DA1-2 Strategy 2 is more critical than the Strategy 1, with the difference in the maximum shear force being 2.5%, 2.5%, 6% and 0.5% and the difference in the minimum shear force being 7%, 1.5%, 1.5% and 4.5% for the MC, HS, HSS and the BRICK model respectively.

Similarly, in Table 5.4, the maximum and minimum design axial forces are presented while in Figure 5.6 the design axial force envelopes are shown. It was found that the DA1-1 governs the design resulting in more critical axial forces. Moreover, the DA1-2 Strategy 2 is more critical than the Strategy 1, with the difference in the maximum axial force being 61%, 43%, 17% and 10% and the difference in the minimum axial force being 21%, 22%, 23% and 4% for the MC, HS, HSS and the BRICK model respectively.

Overall, the DA1-1 governs the design in all cases, resulting in more adverse structural forces. When using the MC model, the discrepancy between the two DA1-2 Strategies is apparent, with the Strategy 2 being more critical than the Strategy 1. However, it was found that when the more advanced models were used, the differences in the calculated design prop loads, bending moments, shear and axial forces between the two DA1-2 Strategies are generally lower when compared to the Mohr-Coulomb case.

Table 5.3: Design shear forces with different constitutive models

Model	Q_{max} DA1-1 (kN/m)	Q_{max} DA1-2 S1 (kN/m)	Q_{max} DA1-2 S2 (kN/m)	Q_{min} DA1-1 (kN/m)	Q_{min} DA1-2 S1 (kN/m)	Q_{min} DA1-2 S2 (kN/m)
MC	1389	1086	1111	-1429	-1059	-1140
HS	1304	994	1020	-1359	-1035	-1050
HSS	1157	851	902	-1196	-963	-978
BRICK	1411	1133	1138	-1490	-1211	-1268

Table 5.4: Design axial forces with different constitutive models

Model	N_{max} DA1-1 (kN/m)	N_{max} DA1-2 S1 (kN/m)	N_{max} DA1-2 S2 (kN/m)	N_{min} DA1-1 (kN/m)	N_{min} DA1-2 S1 (kN/m)	N_{min} DA1-2 S2 (kN/m)
MC	480	220	355	-3249	-2004	-2416
HS	330	179	256	-3202	-1945	-2387
HSS	137	77	90	-3220	-1914	-2385
BRICK	301	200	222	-2653	-2028	-1958

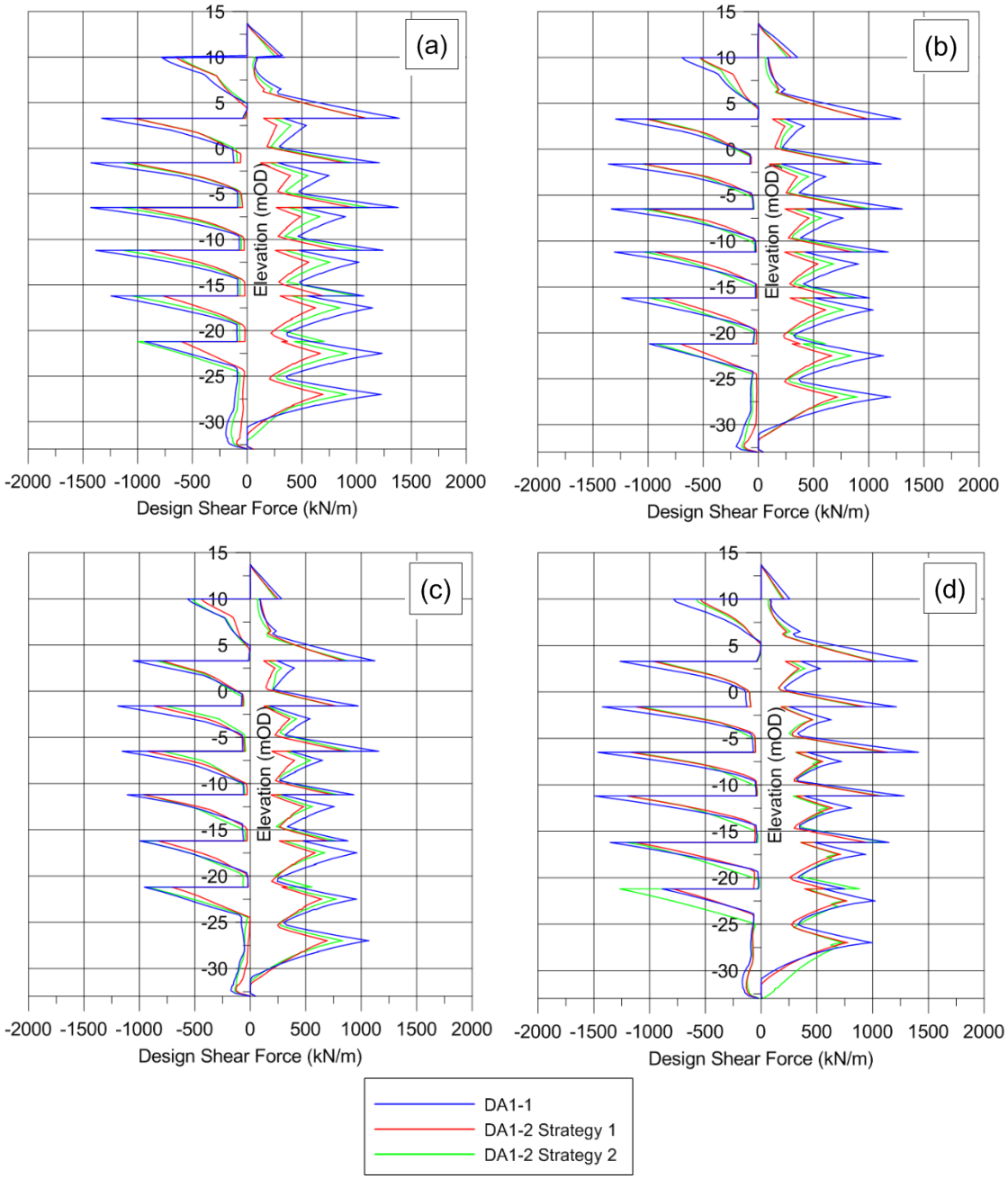

Figure 5.5: Design Shear Force envelope for the Moorgate excavation using the a) MC, b) HS, c) HSS and d) BRICK model

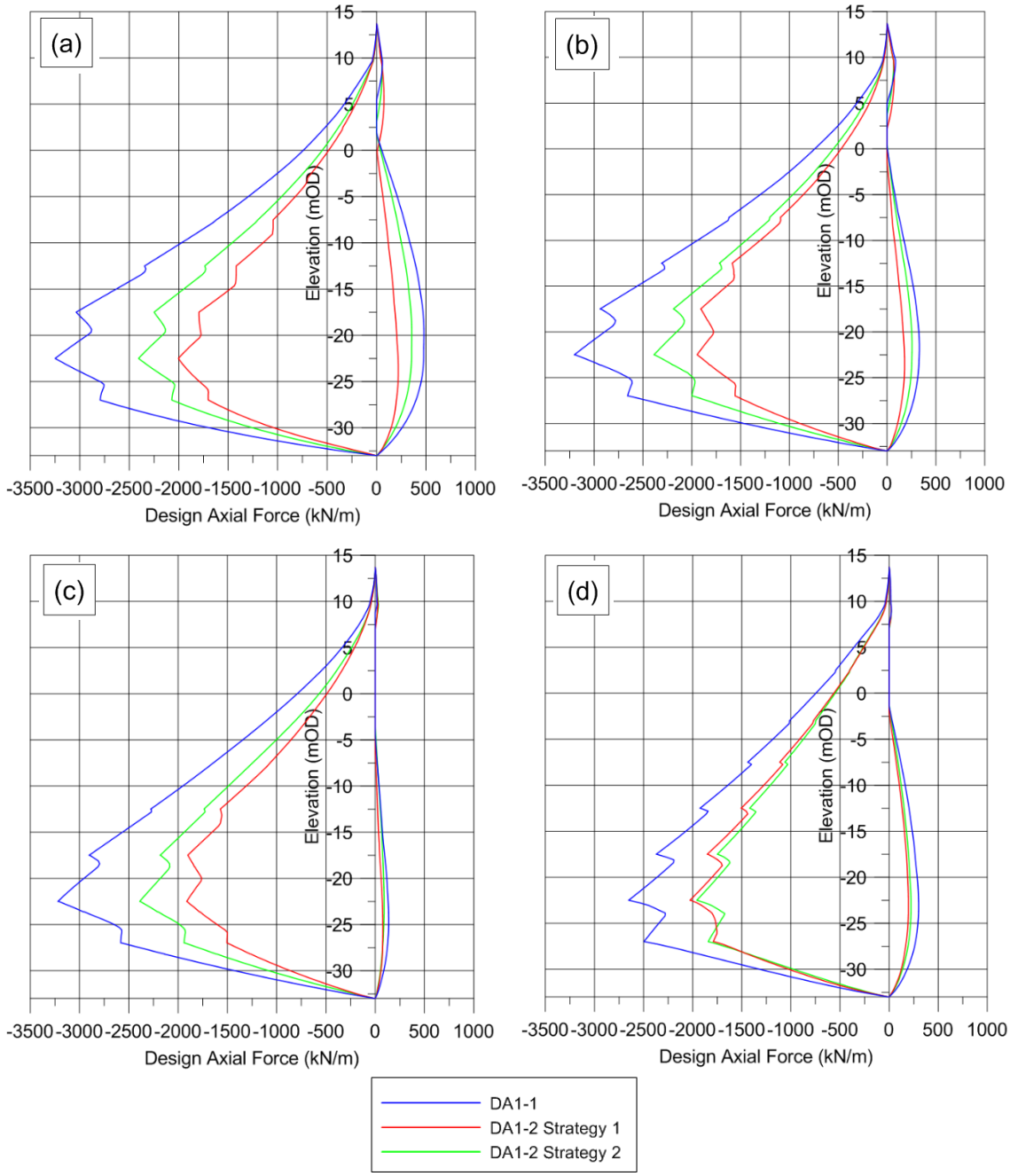

Figure 5.6: Design Axial Force envelope for the Moorgate excavation using the a) MC, b) HS, c) HSS and d) BRICK model

5.3 Victoria & Albert Museum - The Exhibition Road building

5.3.1 Description of the project

A new exhibition space is currently being constructed within the courtyard area of the Victoria & Albert Museum. The development, referred to as the Exhibition Road Building, comprises the construction of a new two-level deep basement, approximately 15m deep and occupying an area of approximately 1700m^2, to provide new gallery space for temporary exhibitions and associated plant rooms. The basement is supported by a multi-propped secant pile wall and the main design features are listed below:

- The basement extends to a depth of approximately 15m below the current street level of Exhibition Road and is founded in London Clay;
- A propped secant pile wall supports the excavation;
- It was decided that the alignment of the secant pile wall has to be as close to the footings of the existing structures as possible, in order to maximize the available space;
- The level of propping and construction sequence for the basement has been designed to control the movement of the surrounding buildings
- The superstructure and basement floors are supported by the secant pile wall and extra bearing piles;
- In the long term condition, the basement walls are propped by the floor structures.

5.3.2 Site location

The site is located within the Victoria & Albert Museum in South Kensington, London. The different areas of the site are shown in Figure 5.7, where it can be seen that the majority of the basement is constructed in the courtyard space between three existing buildings owned by the V&A Museum: the Henry Cole building to the north, the Western Range building to the west, and the Aston Webb building to the south. A small part of the new basement, forming a new staircase, extends under part of the Western Range to a reduced depth of 8m.

The surrounding buildings are all of load bearing masonry construction and are founded on strip footings; they generally date from the 1860s to 1890s, with various minor alterations and additions throughout the 20th century. In addition, the Henry Cole building is Grade II* listed and the Aston Webb building is Grade I listed.

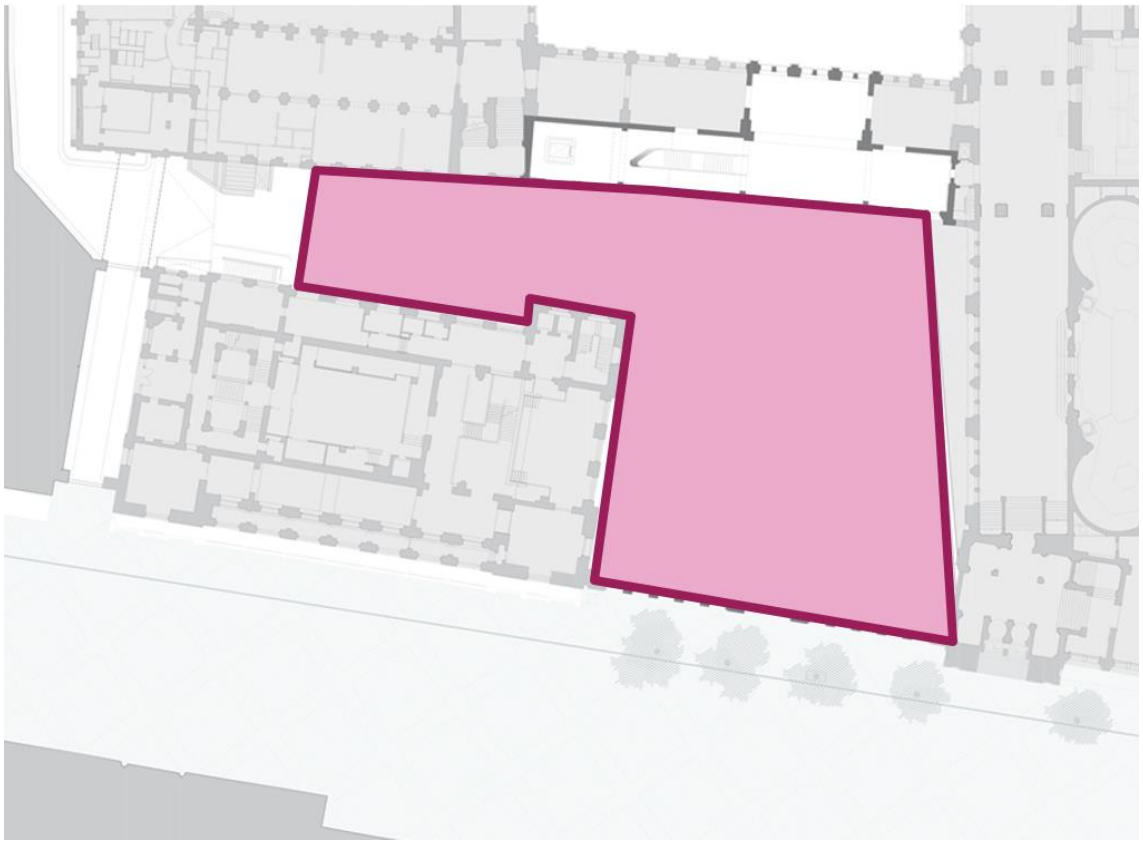

Figure 5.7: Site layout of the V&A Exhibition Road building

5.3.3 Regional geology and soil parameters

A significant thickness of Made Ground is expected to cover the site as a result of development of the area in recent history. Underlying this, is late Pleistocene age River Terrace Deposits, London Clay, Lambeth Group, Thanet Sand and Chalk. A brief description of the main features of each stratum is given in this section while the characteristic material properties are listed in Table 5.5.

The Made Ground in the area is variable and generally consists of dark brown or black, sandy gravely clay, with brick and sandstone fragments. Typically it is 1m to 2.5m thick with the base level at approximately +6mOD. The River Terrace Deposits are described as medium dense to dense, fine to course gravel with varying amounts of brown sand or fine to course gravely sand with occasional thin seams of clay in parts. The thickness of the River Terrace Deposits is typically between 2m and 7m. The London Clay is described as firm to very stiff, brown (weathered) becoming dark grey with depth, fissured, sometimes laminated silty clay. The top level of the stratum was found to vary between +3.0mOD and -2.5mOD and its thickness is expected to be up approximately 60m. The London Clay formation overlies the Lambeth Group, which is comprised of a highly variable sequence of very stiff to hard fissured clays, sands and pebble beds, locally cemented into sandstone or conglomerate. The stratum could be up to 20m thick

with a top level of approximately -58.5mOD. Given the depth of this stratum, it is not expected to be encountered as part of the site works. The geotechnical design parameters are assumed to be a continuation of the Lower London Clay layer.

Table 5.5: Characteristic values of the material properties

Stratum	Top Level (mOD)	Unit Weight (kN/m³)	φ' (°)	c_u (kPa)	K_0 (-)	Horizontal		Vertical	
						E'_h (MPa)	$E_{u,h}$ (MPa)	E'_v (MPa)	$E_{u,v}$ (MPa)
Made Ground	Ground level	19	25	-	0.58	5	N/A	5	N/A
River Terrace Deposits	+6.0	20	36	-	0.41	75	N/A	75	N/A
Upper London Clay	+0.0	20	24	$100+7.5z_1$	1.5	$750c_u$	$1000c_u$	$300c_u$	$500c_u$
Lower London Clay	-15.0	20	24	$225+2z_2$	1.5	$750c_u$	$1000c_u$	$300c_u$	$500c_u$
Lambeth Group	-58.5	20	24	$225+2z_2$	1.5				
Thanet Sand	-75	20	36			300	N/A	300	N/A
Chalk	-81	Assumed Rigid Layer							

Where z_1 is the depth below 0mOD and z_2 is the depth below -15mOD

5.3.4 Design and construction considerations

A secant pile retaining wall was used to support a retained height of soil of up to 15m, roughly half of which is within the London Clay and the other half within the Made Ground and River Terrace Deposits.

The spacing of the secant piles was chosen to maintain a minimum 25mm secant overlap between the male and female piles down to a level of -2.5mOD (2.5m into the London Clay). Overlap was not required beneath this level since the London Clay is sufficiently impermeable that water ingress will be negligible. The required spacing of the male piles is 850mm c/c for 600mm diameter piles (dog leg basement area) and 1400mm c/c for 880mm diameter piles (main basement area). For secant pile walls, the female piles are considered non-structural elements and their contribution to the flexural stiffness of the wall was therefore conservatively neglected. The bending stiffness of the piled retaining wall was calculated based on Equation 5.1, where E is the Young's

Modulus of concrete, taken as 28GPa, *r* is the pile radius and *s* is the spacing between the male piles.

$$EI_{short\ term} = \frac{0.7\ E\ \pi\ r^4}{4\ s} \tag{5.1}$$

In the main basement area, the construction sequence is semi-top down, supported with temporary props at the top level and a permanent doughnut slab at the B2 level. In the dog leg area, the construction sequence is bottom up, with multiple levels of temporary props. A total of 12 cross sections, as shown in Figure 5.8, were considered by the Arup design team: 6 in main basement area; 3 in the dog leg area and 3 in the staircase area. The locations of the props in plan-view along with the location of the strain gauges for the monitoring of the prop loads are shown in Figure 5.9. The support system in the dog leg basement area can be seen in the photos taken by Arup engineers during the excavation stage and shown in Figure 5.10.

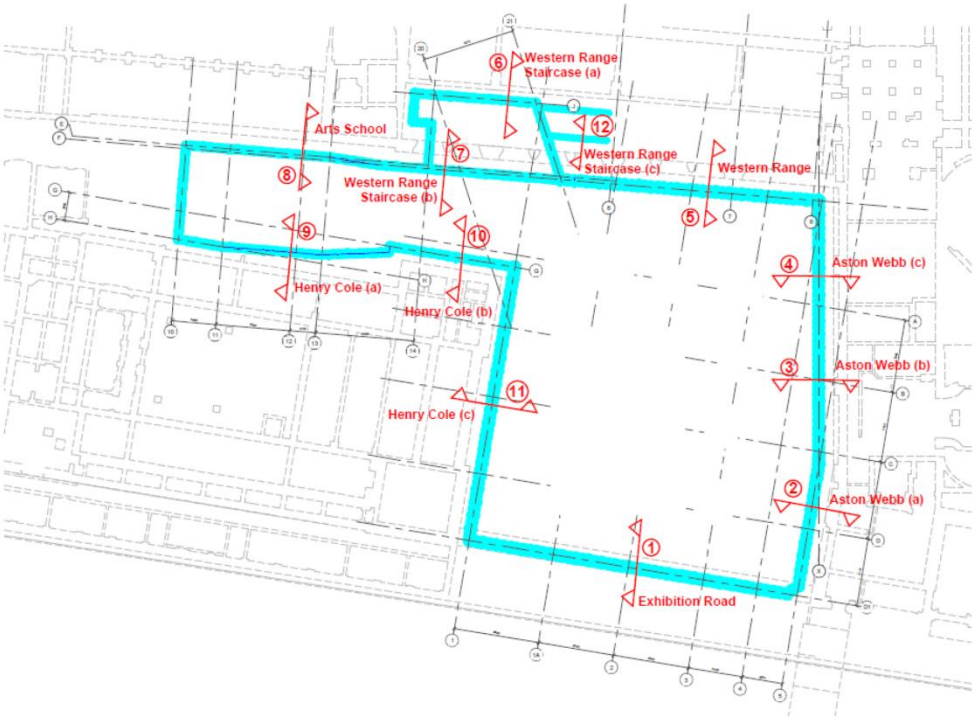

Figure 5.8: Cross section locations

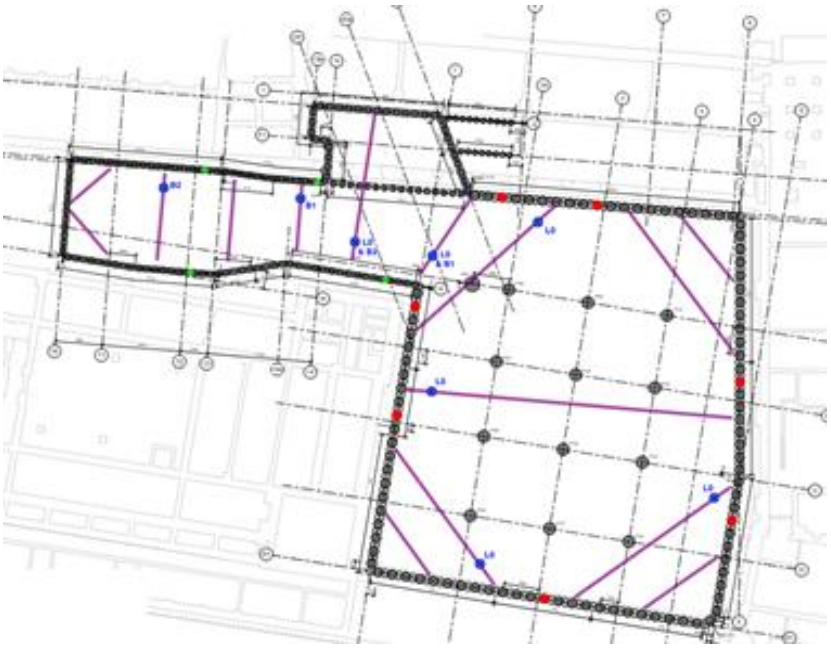

Figure 5.9: Location of temporary props and strain gauges

Figure 5.10: The dog leg basement excavation area (courtesy of Arup Geotechnics)

5.3.5 Methodology

For this study, only the Section 8 in the dog leg basement area (see Figure 5.8) was considered. The reason for this, is that in this section, the excavation is deeper as the lift pit requires lower formation level (-8.1mOD). Moreover, as in all sections in the dog leg basement area, the secant pile wall is supported by more levels of steel props. As discussed previously, the differences in the resulting design values of the internal structural forces between the different factoring methods become more apparent for deeper excavations and larger number of prop levels.

In this section, the active ground level is at approximately +7.7mOD (ground floor level) while the initial passive ground level is at +7.2mOD (modelled as 10kPa surcharge). Three lines of Arts School footings modelled at +6.75mOD. The groundwater table is located at +3.5mOD. The excavation geometry, as shown in Figure 5.11, is approximately 10m wide and the secant pile wall is 23m deep, supported by 4 levels of steel tube props.

The following assumptions were made in the model:

- The wall is wished-in-place.
- Half the excavation width is only modelled, due to symmetry.
- The side model boundaries are fixed in the *x* direction while the bottom model boundary is fixed in both *x* and *y* directions.
- The unit weight of the soil γ is equal to 20kN/m^3
- Interface elements are used between the soil and the wall with $\tan\delta = 2/3 \tan\varphi'$, where δ is the soil/wall friction angle.
- In all analyses drained conditions are assumed for only the initial stage. For all the rest of the stages undrained conditions were considered.
- Only short term conditions are considered.

The following construction sequence was used in the analyses for the dog leg basement area:

- Stage 0 Initial conditions (include surcharge from existing building footings)
- Stage 1 Install wall and apply 10kPa surcharge
- Stage 2 Excavate to +6.2mOD
- Stage 3 Install temporary prop at +6.7mOD
- Stage 4 Excavate to +2.7mOD
- Stage 5 Install temporary prop at +3.2mOD
- Stage 6 Excavate to -1.1mOD

- Stage 7 Install temporary prop at -0.6mOD
- Stage 8 Excavate to -4.9mOD
- Stage 9 Install temporary prop at -4.4mOD
- Stage 10 Excavate to -6.37mOD, locally to -8.1mOD in lift pit areas (overdig to -8.6mOD for ULS)

The computer software PLAXIS 2015.02 was used for the analysis in its 2D version. The analyses was repeated using the MC, HS, HSS and BRICK constitutive models. For the MC analysis, the characteristic material properties listed in Table 5.5 were used while for the more advanced models, the parameters derived for London Clay in Chapter 2 were employed.

The finite element mesh for the cross section at dog leg basement excavation area is shown in Figure 5.12. A finer mesh was used for the area of the excavation whereas the coarseness of the mesh increases with the distance from the excavation. The dimensions of the model are large enough to minimize the influence of the boundary conditions.

A constant value for the coefficient of lateral earth pressure at rest, K_0, equal to 1.5 was assumed for the London Clay in all the analyses. The ground water pressure profile was assumed to be under-drained, diverging from the hydrostatic profile at the top level of the Upper London Clay (i.e. 0mOD), with a pore-water increment equal to 6kN/m^2/m. The props were modelled as tubular steel pipes with prop stiffness, *k* equal to 100 MN/m/m. The behaviour of all structural elements was assumed to be elastic.

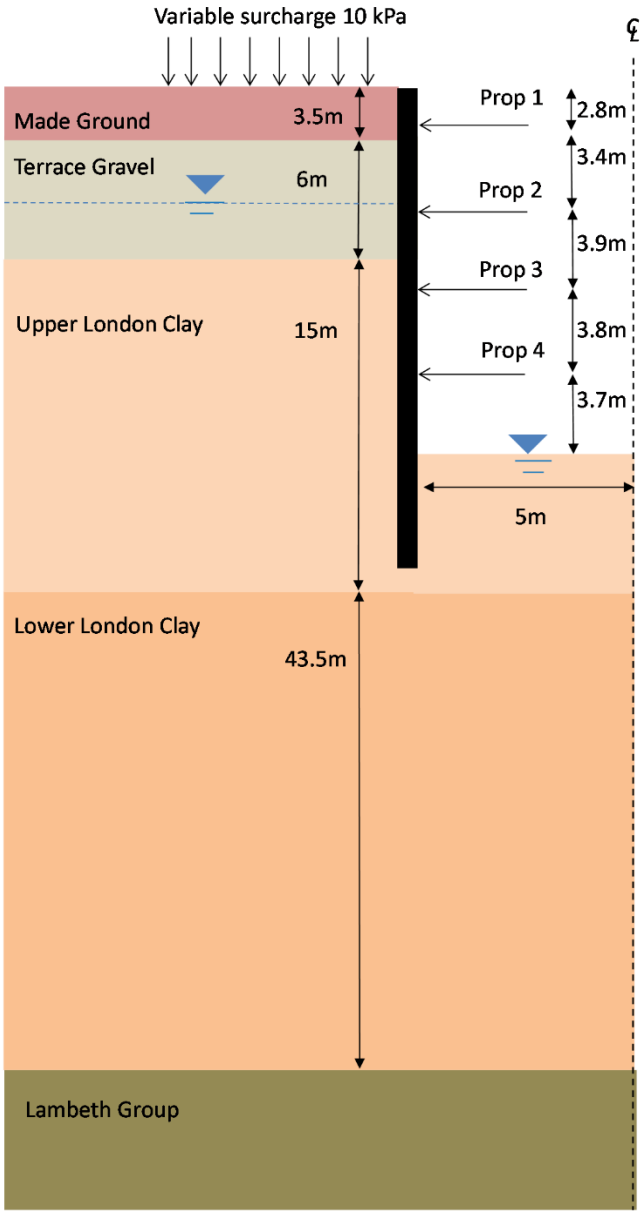

Figure 5.11: Geometry of the Cross Section 8 in the dog leg excavation area

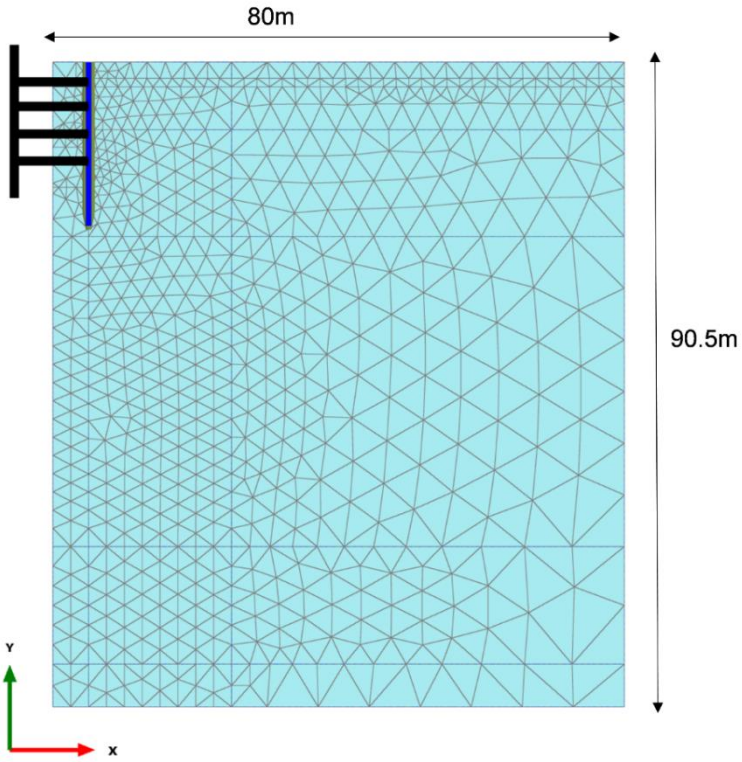

Figure 5.12: FE mesh for the Cross Section 8 in the dog leg excavation area

5.3.6 ULS analysis

For the ULS, a set of analyses was carried out for both the EC7 DA1 Combination 1 and Combination 2. In this section, the results from the Finite Element analyses are presented in terms of the design structural forces (i.e. prop loads, bending moments, shear and axial forces), using the MC, HS, HSS and BRICK constitutive models.

In Figure 5.13, the design prop loads are presented. For the MC model case, it can be seen, the DA1-2 governs at the upper prop level while the DA1-1 governs at the other three levels. It is noted that the discrepancy in the results between the two DA1-2 Strategies, is negligible at the upper prop levels, but becomes particularly apparent at the bottom prop level. More specifically, the percentage difference in the calculated prop load is 31% at the bottom prop level while the difference in the total force supporting the wall is 11%. Similarly to the MC case, it can be seen that the DA1-1 governs the design at all prop levels. The percentage differences between the two DA1-2 Strategies, in the calculated prop load at the bottom prop level, are 9.5%, 3% and 12% while the percentage differences in the total force acting on the wall are 3%, 2% and 5% for the HS, HSS and BRICK model case respectively. Overall, it can been seen, that the difference in the prop loads between the two DA1-2 Strategies reduces when compared to the Mohr-Coulomb case.

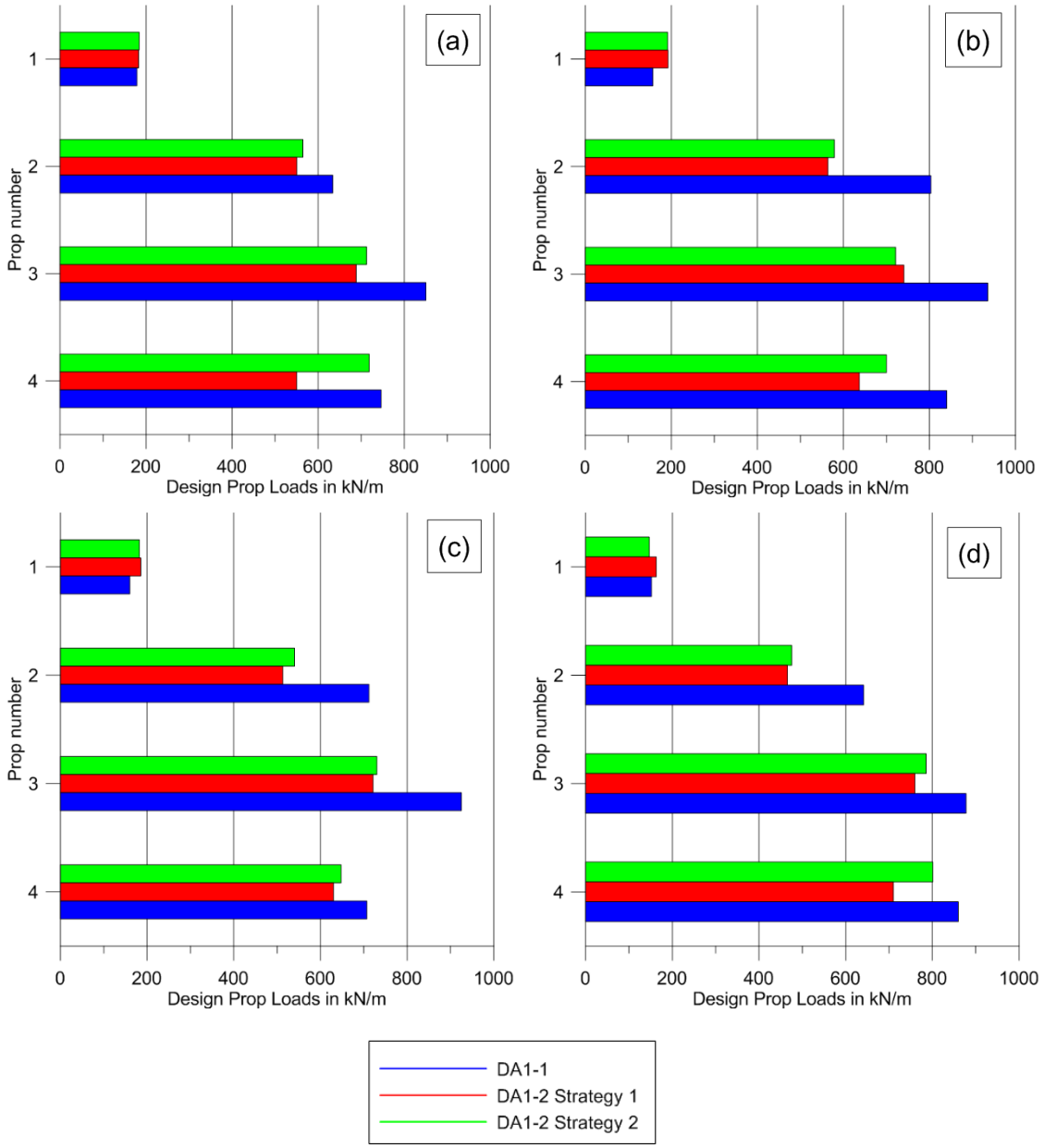

Figure 5.13: Design prop loads for the V&A Exhibition Building excavation using the a) MC, b) HS, c) HSS and d) BRICK model

In Figures 5.14, 5.15 and 5.16, the calculated design prop loads are compared with the field measurements for the 1st, 2nd and 3rd prop level respectively, in order to assess the conservatism of the FEM assumptions and compare the results between the different constitutive models. Please note that, no data were available for the prop loads at the bottom level as there were no strain gauges installed on these props.

In all cases, the prop load values, calculated at each stage of the FE analysis, were plotted against the date on which the corresponding construction stage was undertaken on site. It can be seen that in all cases, the maximum prop loads measured on site, are lower than the design values predicted by the FE calculations, regardless the constitutive

model. Moreover, the variation of the calculated prop loads with time generally follows the pattern of the field measurements.

In Figure 5.14, it can be seen that the maximum measured prop load value for the upper prop level is 701kN and the maximum calculated prop loads are 674kN, 713kN, 694kN and 604kN for the MC, HS, HSS and BRICK model respectively. Similarly, in Figure 5.15, for the second prop level, the maximum measured prop load is 2171kN and the maximum calculated design prop loads are 2364kN, 2974kN, 2636kN and 2407kN for the MC, HS, HSS and BRICK model respectively. Finally, in Figure 5.16, for the third prop level, the maximum measured prop load is 3404kN and the maximum calculated design prop loads are 3150kN, 3467kN, 3427kN and 3222kN for the MC, HS, HSS and BRICK model respectively. The HS and to a lesser extent the HSS model, over-predicted the load at the 2nd prop level while the BRICK model under-predicted the load at the upper level.

The actual design axial capacities of the steel props are 4048kN, 6044kN and 6080kN for the 1st, 2nd and 3rd prop level respectively. Comparing the capacities with the corresponding measured values of the prop loads gives an achieved factor of safety equal to 5.7, 2.8 and 1.8 for the three levels respectively. This shows that particularly the upper prop level is overdesigned and a reduction in the capacity and hence the prop section, could result in a more economic design.

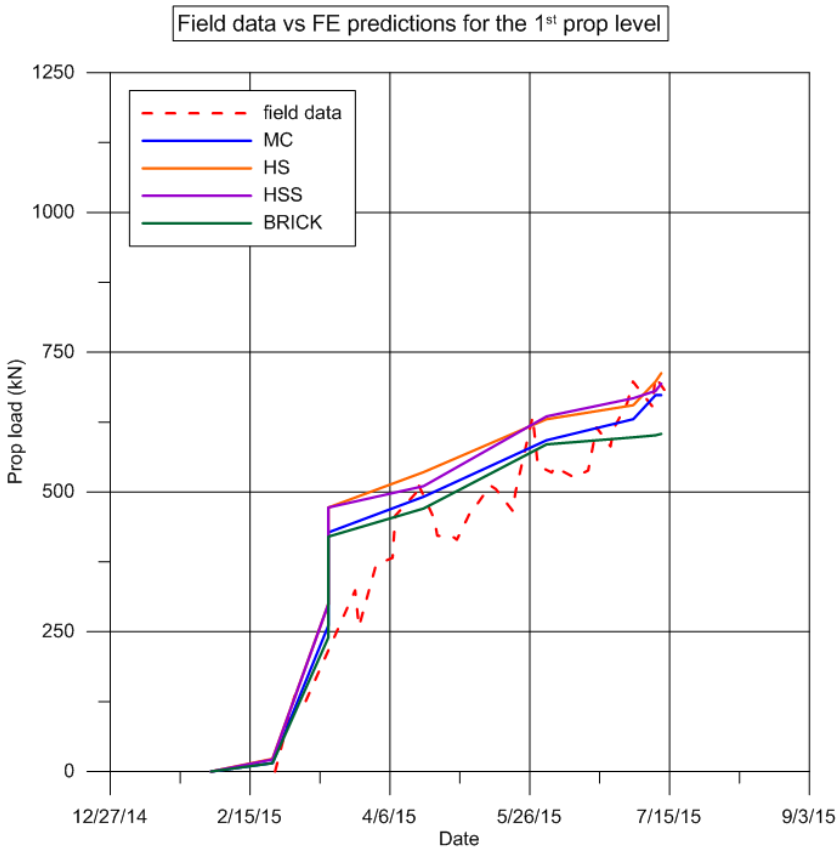

Figure 5.14: Field data vs FE predictions for the 1st prop level

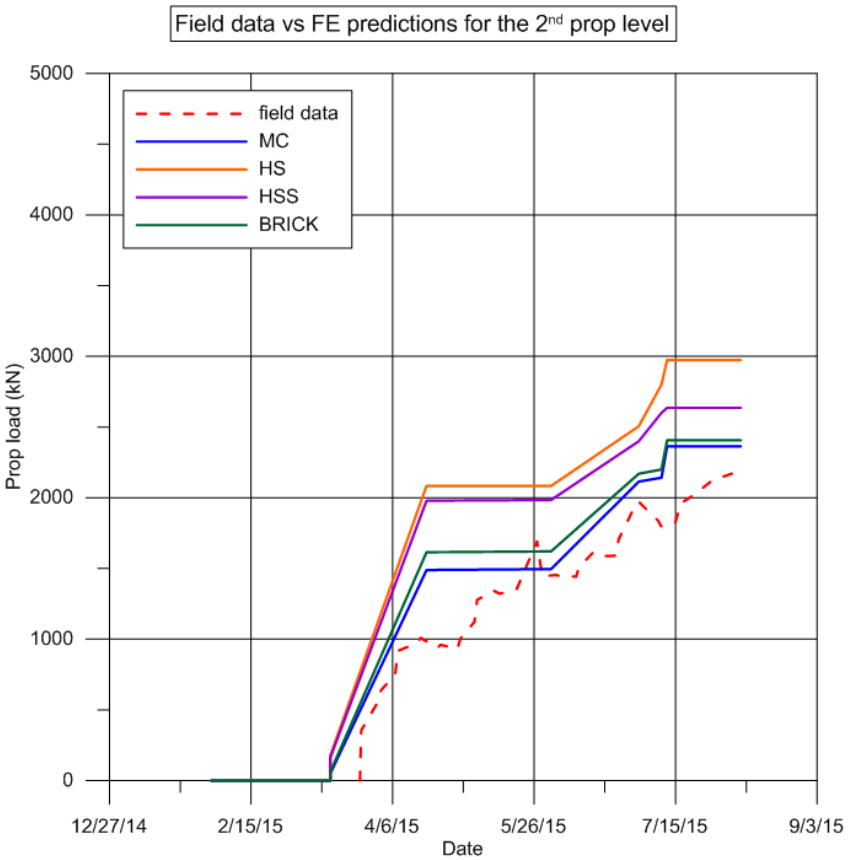

Figure 5.15: Field data vs FE predictions for the 2nd prop level

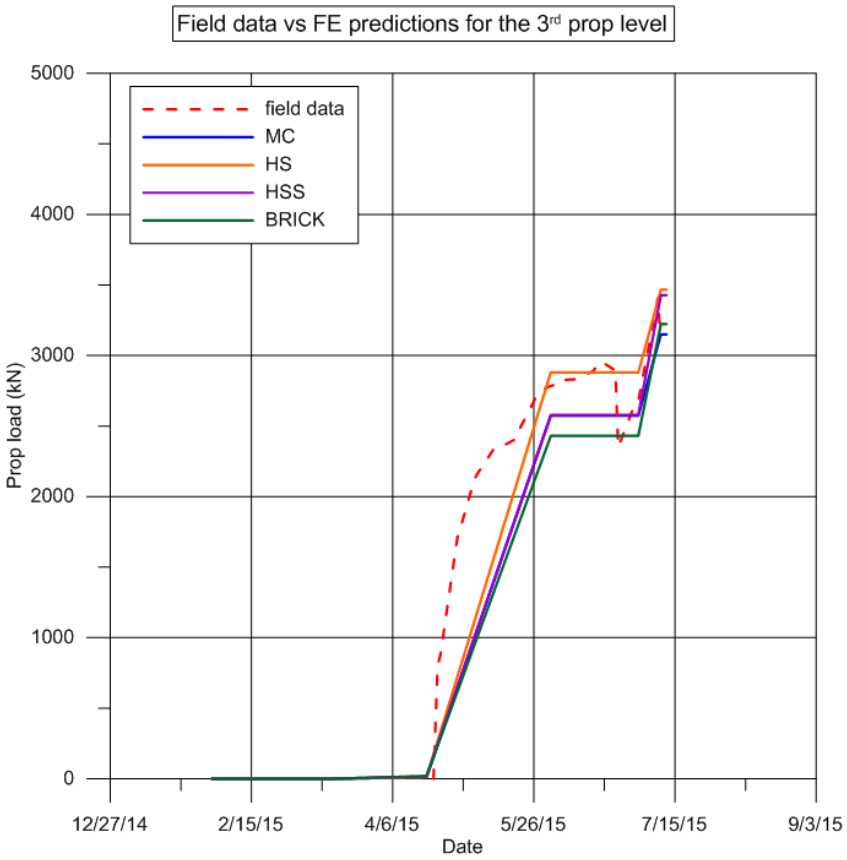

Figure 5.16: Field data vs FE predictions for the 3rd prop level

In Table 5.6, the maximum and minimum design bending moments, calculated from the FE analysis, are shown while in Figure 5.17, the design bending moment envelopes are presented. It can be seen, that the DA1-1 governs the design, resulting in the most onerous wall bending moments. The DA1-2 Strategy 2 is generally more critical than the Strategy 1, with the difference in the maximum bending moment being 10%, 12%, 45% and 12% and the difference in the minimum bending moment being 6%, 7%, 7% and 11% for the MC, HS, HSS and the BRICK model respectively.

Table 5.6: Design bending moments with different constitutive models

Model	M_{max} DA1-1 (kNm/m)	M_{max} DA1-2 S1 (kNm/m)	M_{max} DA1-2 S2 (kNm/m)	M_{min} DA1-1 (kNm/m)	M_{min} DA1-2 S1 (kNm/m)	M_{min} DA1-2 S2 (kNm/m)
MC	245	239	218	-498	-339	-358
HS	350	189	212	-674	-481	-515
HSS	293	139	202	-580	-405	-433
BRICK	255	192	215	-610	-424	-470

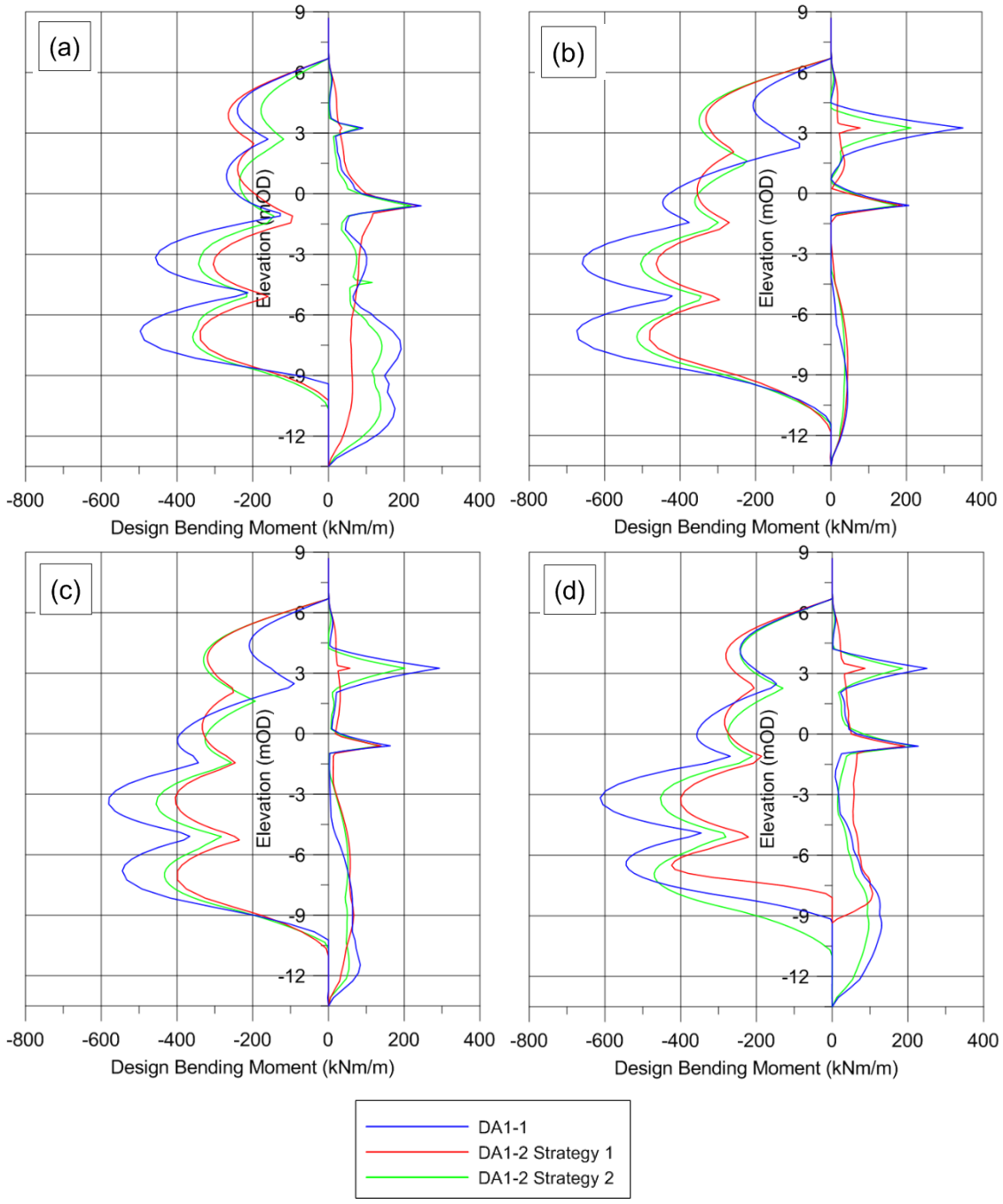

Figure 5.17: Design Bending Moment envelopes for the V&A Exhibition Building excavation using the a) MC, b) HS, c) HSS and d) BRICK model

In Table 5.7 the maximum and minimum design shear forces are presented while in Figure 5.18 the design shear force envelopes are shown. Overall, the DA1-1 governs in all cases, resulting in more critical shear forces. The DA1-2 Strategy 2 is more critical than the Strategy 1, with the difference in the maximum shear force being 13%, 5%, 9% and 13% and the difference in the minimum shear force being 10%, 5%, 10% and 9% for the MC, HS, HSS and the BRICK model respectively.

Table 5.7: Design shear forces with different constitutive models

Model	Q_{max} DA1-1 (kN/m)	Q_{max} DA1-2 S1 (kN/m)	Q_{max} DA1-2 S2 (kN/m)	Q_{min} DA1-1 (kN/m)	Q_{min} DA1-2 S1 (kN/m)	Q_{min} DA1-2 S2 (kN/m)
MC	374	286	324	-494	-353	-389
HS	422	299	313	-548	-393	-414
HSS	383	269	293	-521	-355	-390
BRICK	423	336	378	-540	-454	-496

Similarly, in Table 5.8 the maximum and minimum design axial forces are shown while in Figure 5.19 the design axial force envelopes are presented. Overall, the DA1-1 governs in all cases, resulting in more adverse axial forces. In all cases, the discrepancy between the two DA1-2 Strategies is apparent, with the Strategy 2 being more critical than the Strategy 1. More specifically, the difference in the minimum axial force is about 14%, 14%, 12% and 0.5% for the MC, HS, HSS and the BRICK model respectively.

Table 5.8: Design axial forces with different constitutive models

Model	N_{max} DA1-1 (kN/m)	N_{max} DA1-2 S1 (kN/m)	N_{max} DA1-2 S2 (kN/m)	N_{min} DA1-1 (kN/m)	N_{min} DA1-2 S1 (kN/m)	N_{min} DA1-2 S2 (kN/m)
MC	5	3	4	-785	-508	-580
HS	5	3	4	-739	-487	-556
HSS	5	4	4	-731	-484	-541
BRICK	5	3	3	-761	-567	-570

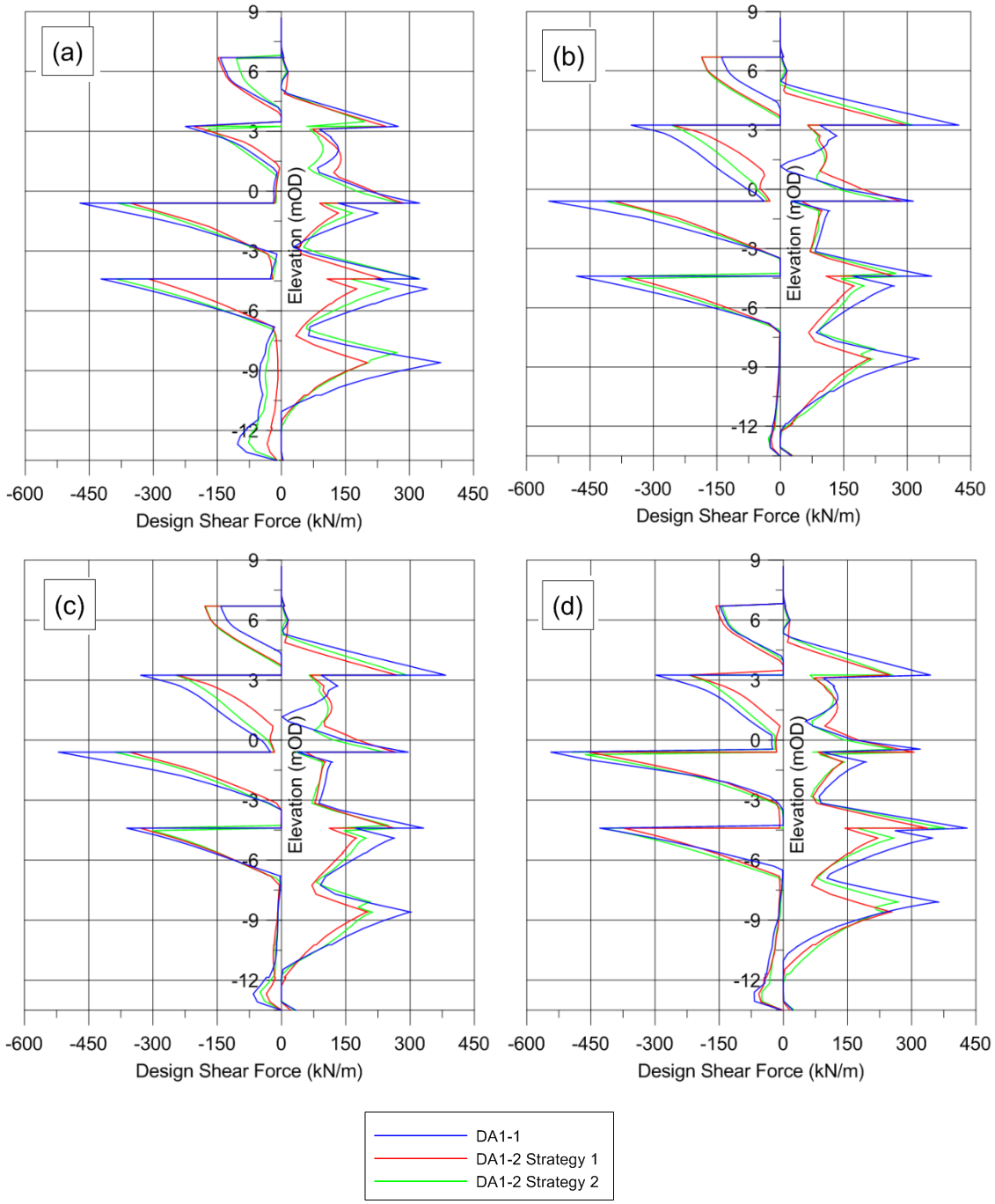

Figure 5.18: Design Shear Force envelopes for the V&A Exhibition Building excavation using the a) MC, b) HS, c) HSS and d) BRICK model

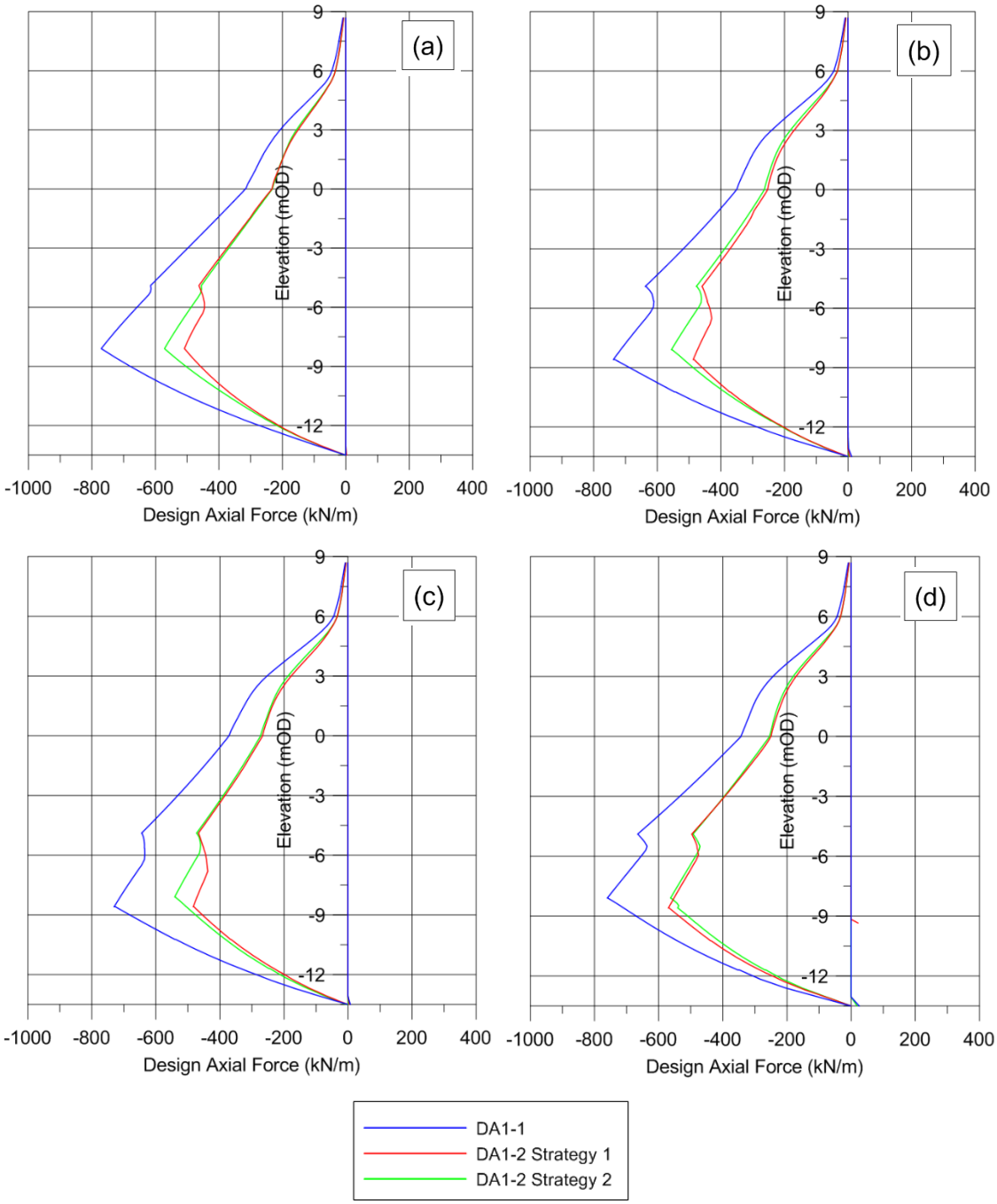

Figure 5.19: Design Axial Force envelopes for the V&A Exhibition Building excavation using the a) MC, b) HS, c) HSS and d) BRICK model

5.4 Conclusions

In this Chapter, the ULS FE analysis of two deep excavation case histories was repeated using the MC, HS, HSS and the BRICK model to investigate the effect of the model on the results.

For the Moorgate excavation, the DA1-1 governs the design in all cases resulting in more adverse structural forces. In most cases, the DA1-2 Strategy 2 is more critical than the Strategy 1, with the difference being more apparent for the MC model case. It was found that when the more advanced model parameters were used for the London Clay, the differences in the calculated design prop loads, bending moments, shear and axial forces between the two DA1-2 Strategies are lower when compared to the Mohr-Coulomb case.

For the V&A excavation, in all cases, the DA1-1 also generates the most critical structural forces. The DA1-2 Strategy 2 generally results in higher prop loads, bending moments, shear and axial forces than the Strategy 1 for all constitutive models. When the HS, HSS and the BRICK model parameters were used for the London Clay, the differences in the calculated prop loads, between the two DA1-2 Strategies, become lower when compared to the Mohr-Coulomb case. However, no particular trend was observed regarding the bending moments, shear and axial forces.

Overall, the effect of the model on the differences between the factoring combinations and methods is more pronounced for the Moorgate excavation analysis due to the much higher depth of the excavation and larger number of prop levels, which agrees well with the findings in Chapters 2 and 3.

Moreover, for the V&A excavation, the calculated design prop loads were compared with the measured values from the strain gauge data. It was shown that the variation of the calculated prop loads with time generally follows the pattern of the field measurements. While generally the FE results agree with the measured values, the HS and to a lesser extent the HSS, over-predicted the load at the 2nd prop level while the BRICK model under-predicted the load at the upper level. By comparing the structural capacities with the measured values of the prop loads, the achieved factor of safety was calculated showing that the prop at the top level is heavily overdesigned.

Overall, this study confirms that the dual approach currently required in the DA1 expressed as a combination of the DA1-1 and the DA1-2 Strategy 2 governs the design

decisions, not only for the benchmark examples studied in Chapters 2 and 3, but also for the more realistic geometries and soil profiles considered in this Chapter.

CHAPTER 6

HYD verifications using FEM

6.1 Introduction

This chapter describes and discusses the HYD limit state. HYD, as described in Eurocode 7, is related to the upward flow of water through the soil towards a free surface, such as in front of a retaining wall or in the base of an excavation. The hydraulic heave stability problem is caused by hydraulic gradients and is one of the most dangerous Ultimate Limit States, resulting in sudden failure with serious consequences for people and structures.

In recent years, with the advances in software and hardware, more designers are willing to use Finite Element (FE) methods, to verify safety against hydraulic heave. The HYD verification using FEM can be performed with two different approaches, namely the *soil block* approach and the *integration point* approach (Evolution Group 9 - Water Pressures, 2014).

The first approach is the conventional approach where safety may be checked by studying the equilibrium of a rectangular block of soil. In the *integration point* approach, stability can be verified at every integration point by checking the equilibrium of a soil column of negligible width. The results are plotted as contours, rendering the checks of whether the equilibrium is fulfilled at every integration point an easy task. In this chapter, the two approaches are described and their advantages and disadvantages are discussed. Comparisons made using benchmark geometries, extensively studied and discussed between the members of the EC7 Evolution Group 9 on Water Pressures, illustrate that the HYD verification using numerical methods is very promising. Thorough comparisons between the factors from the two approaches, allow designers to better understand the benefits of using more advanced and robust approaches for such stability verifications.

6.2 The HYD problem

The HYD limit state is described in Eurocode 7 (EC7) in relation to the *hydraulic heave, internal erosion and piping in the ground, caused by hydraulic gradients* (BS EN 1997-1, 2004). This covers a wide range of situations related to stability problems

caused by hydraulic gradients. McNamee (1949) made a distinction between two types of failure relating to water pressures; piping that usually initiates locally and heave which involves a greater soil mass.

This chapter focuses on part of the EC7 definition, hydraulic heave, which is illustrated in EC7 and shown here as Figure 6.1. Hydraulic heave relates to the ground movement of a free surface caused by a vertical upward flow of water. Requirements for hydraulic heave are expressed in EC7 which states that the stability of a soil against heave shall be checked in terms of seepage forces and buoyant weights, or in terms of total stresses and pore-water pressures. A particular case where hydraulic heave is relevant is in front of a retaining wall. It represents an Ultimate Limit State, potentially resulting in sudden failure with serious consequences for people and structures. Simpson et al. (1989) discuss problems caused by water pressures due to rising water levels while Stroud (1987) refers to a number of situations where unforeseen water pressures led to critical failures. Other authors have also discussed similar issues related to safety considerations in relation to the ground water pressures (e.g. Orr, 2005; Simpson et al., 2009; and Simpson, 2011).

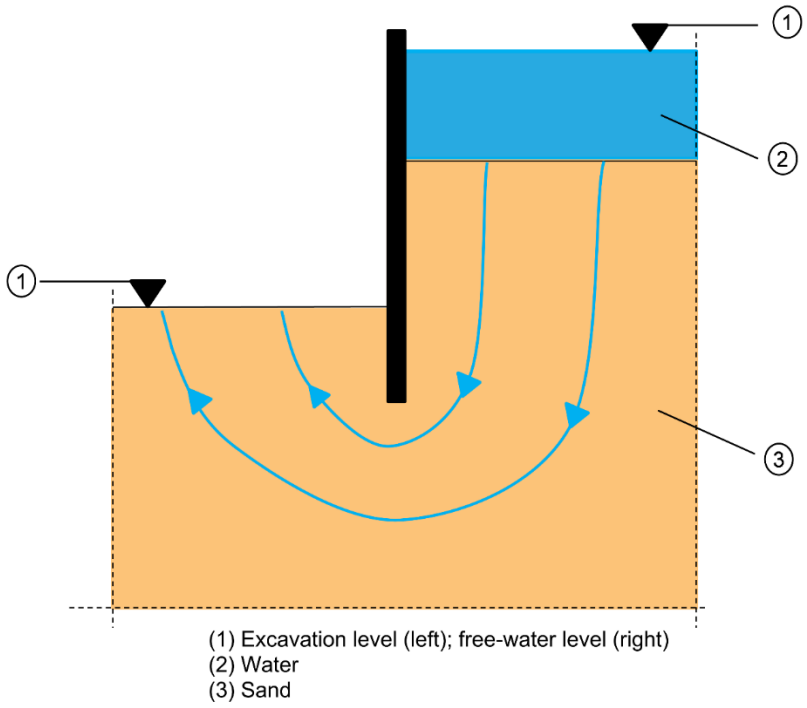

Figure 6.1: Example of situation where heave might be critical

6.3 Eurocode 7 Requirements

Safety against failure by hydraulic heave can be verified with Equation 6.1 or 6.2 as given by EC7 (BS EN 1997-1, 2004), where stability shall be checked in terms of

seepage forces and buoyant weights or in terms of total stresses and pore-water pressures. Equation 6.1 (2.9a as referred to in BS EN1997-1, 2004) requires the design pore water pressure, $u_{dst;d}$ at the bottom of a relevant soil column to be less than the design total vertical stress, $\sigma_{stb;d}$. Equation 6.2 (2.9b as referred to in BS EN1997-1, 2004) requires the design seepage force caused by the excess pore water pressures, $S_{dst;d}$ to be less than the design buoyant weight of the column, $G'_{stb;d}$.

$$u_{dst;d} \leq \sigma_{stb;d} \tag{6.1}$$

$$S_{dst;d} \leq G'_{stb;d} \tag{6.2}$$

Both equations already incorporate safety using *design values* (subscript *d*), without further factors being shown in the requirements. The subscripts *dst* and *stb* refer to destabilising and stabilising effects respectively.

For the HYD Limit State, the typical partial factors are specified with $\gamma_{G;dst}$ =1.35 for permanent unfavourable actions, $\gamma_{G;stb}$ =0.9 for permanent favourable actions and $\gamma_{Q;dst}$ =1.5 for variable unfavourable actions (see Table 6.1). However, EC7 does not state precisely how these factors are to be applied in Equations 6.1 or 6.2.

Table 6.1: Partial factors for HYD

Action	Symbol	Value
Permanent		
Unfavourable[a]	$\gamma_{G;dst}$	1.35
Favourable[b]	$\gamma_{G;stb}$	0.90
Variable		
Unfavourable[a]	$\gamma_{Q;dst}$	1.50

a Destabilising
b Stabilising

Some designers apply the partial factors to the characteristic values of the stabilising and destabilising parameters, misinterpreting the Equations 6.1 and 6.2 to mean:

$$\gamma_{G;dst}\, u_{dst;k} \leq \gamma_{G;stb}\, \sigma_{stb;k} \tag{6.3}$$

$$\gamma_{G;dst}\, S_{dst;k} \;\leq\; \gamma_{G;stb}\, G'_{stb;k} \qquad (6.4)$$

Here, the subscript *k* refers to characteristic values of the parameters. Orr (2005) pointed out that if the two equations are used in this way they can lead to markedly different results for the same values of partial factors. Simpson (2012) argues that this is a misunderstanding of the code requirement, and in particular of the concept of design values, and suggested that if the load partial factors are to be used in this context they should be applied to the excess water pressures only, not to the hydrostatic component. Orr (2005) also concluded that the partial actions factors should only be applied to the excess pore water pressure and not the hydrostatic pressure.

EC7 notes that the load factors might not be always appropriate for ground water pressures and allows for direct assessment of the design value or application of a safety margin to the characteristic ground water table. Thus, by allowing three alternative approaches, the UK National Annex leaves much of the responsibility for calculation of the design value of water pressures with the designers (Simpson et al., 2011). Simpson and Katsigiannis (2015) argue that factoring water pressures should generally be avoided and favour the direct assessment of the design water pressures or the design water table level.

6.4 Methodology

The two approaches for HYD verification using FE methods, are now illustrated for the two simple problems presented in Figure 6.2, a 10m deep excavation and a cofferdam geometry. The software used is PLAXIS 2015.02 and the following assumptions were made in the model:

- The wall is wished-in-place, impermeable and not allowed to deform in any direction.
- Only half of the excavation width is modelled due to symmetry.
- The calculations are performed assuming steady state conditions while the soil is considered fully drained; constant hydraulic head is used by to specify a fixed water table behind the retaining wall. In front of the wall, the water level is lowered to the formation level at the end of the excavation.
- The side and bottom model boundaries are considered to be impermeable.

- The side model boundaries are fixed in the x direction while the bottom model boundary is fixed in both x and y directions.
- The unit weight of the soil γ is equal to 20kN/m^3
- Initial stress field conditions are based on hydrostatic water pressures and K_0=1-sinφ'.
- Interface elements are used between the soil and the wall with tanδ = 0.5tanφ', where δ is the soil/wall friction angle.

The properties of the soil are given in Table 6.2 for an elastic-perfectly plastic soil model such as the Mohr-Coulomb. The stiffness of the soil, which varies with depth, has no effect on this problem. Examples of the Finite Element meshes, which consist of 15-node triangular elements, used for the simulations are given in Figure 6.3 and Figure 6.4 for the 10m deep excavation and cofferdam case respectively. Please note that for the cofferdam case only the embedded part of the sheet pile wall is modelled. The mesh sizes are adequate for this type of problem.

Table 6.2: Soil properties of uniform soil

Mohr-Coulomb model parameters	
Young's Modulus, E' (MPa)	25+6.5z
Angle of shearing resistance, φ' (°)	35
Effective cohesion, c' (kPa)	0
Poisson's ratio, ν'	0.2
Permeability (m/s)	10^{-5}
where z is the depth below the ground level (m)	

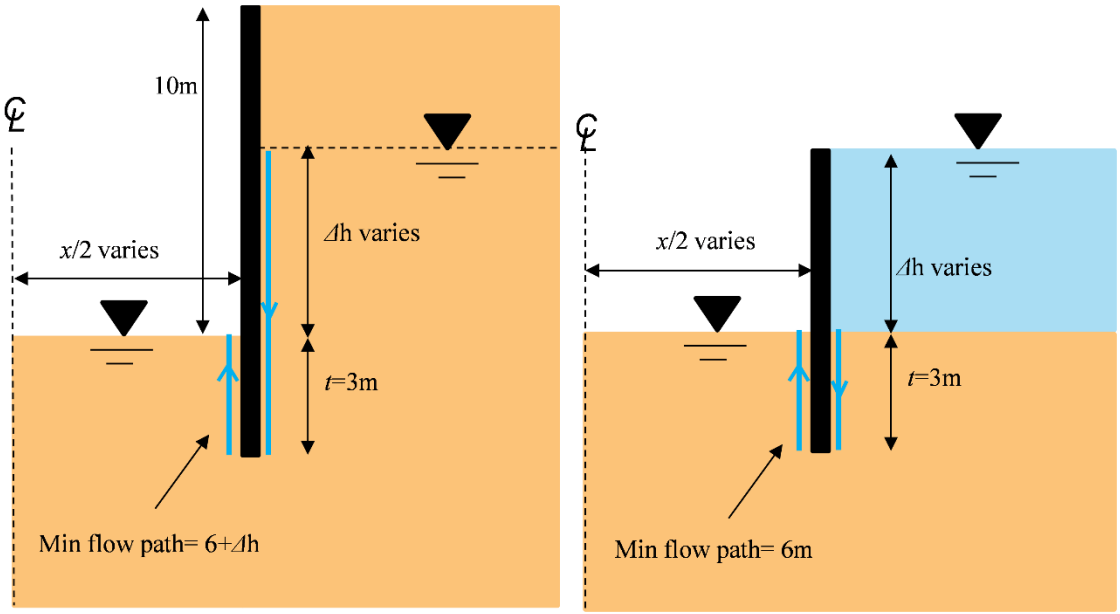

Figure 6.2: Geometry of the 10m deep excavation and the cofferdam models

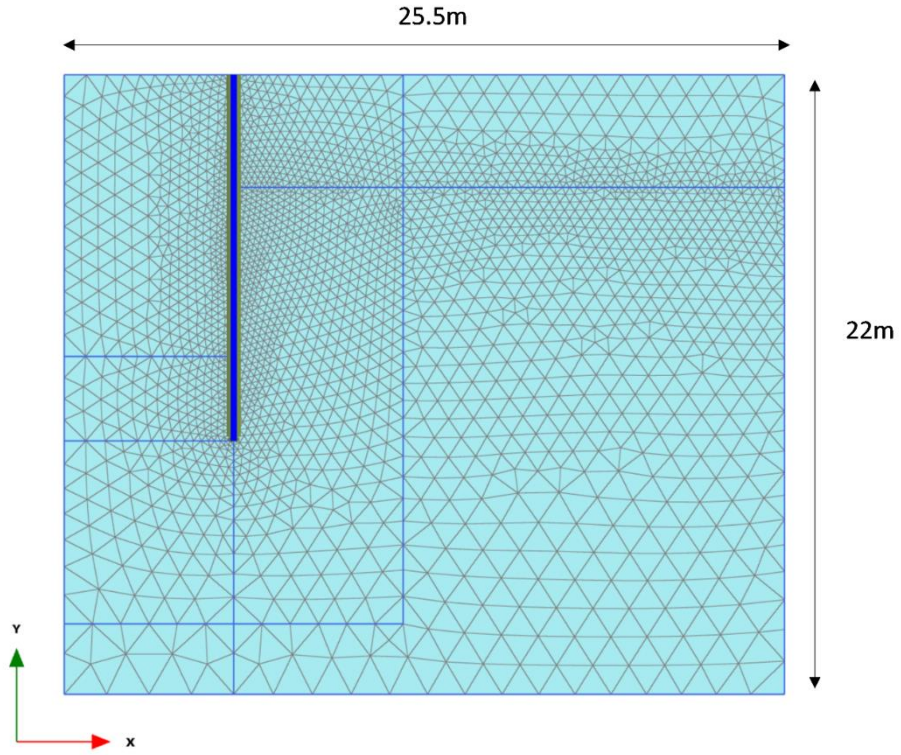

Figure 6.3: FE mesh for the 10m deep excavation model

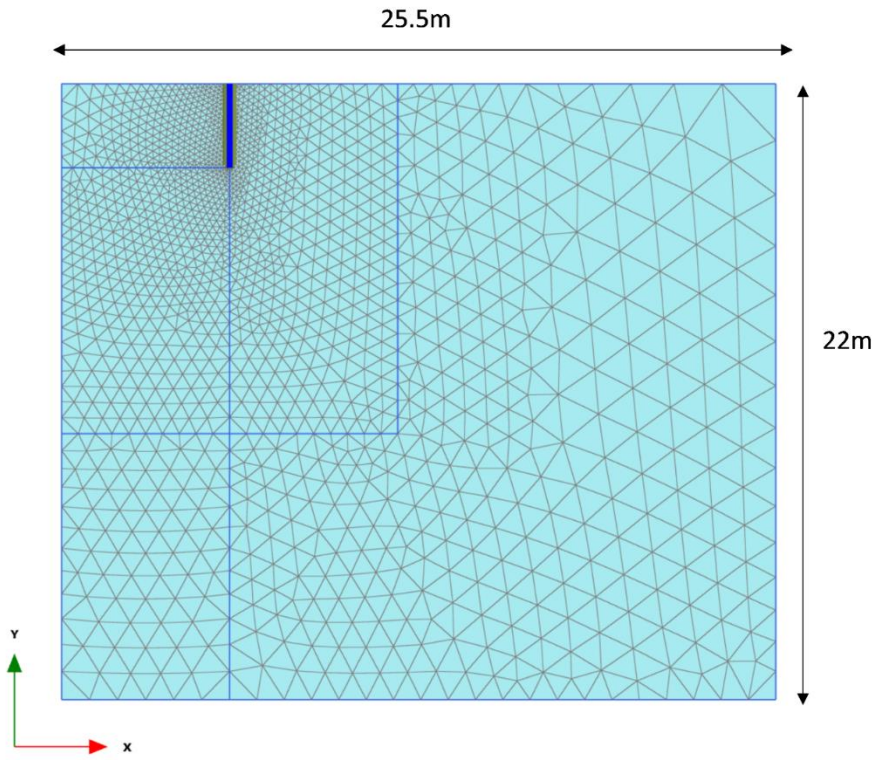

Figure 6.4: FE mesh for the cofferdam model

6.5 The Soil Block Approach

6.5.1 Terzaghi's criterion

According to experimental evidence for isotropic and uniform soils, it is sufficient to check the stability of a rectangular soil block of dimensions $b=t/2$, where b is the block's width and t the embedment depth (Terzaghi, 1922 and 1943), by ensuring that the seepage force is less than the buoyant weight of the block (see Figure 6.5). The friction on both sides of the block is not taken into account. Terzaghi proposed that a factor of safety should be calculated as $F_T = G'/S$, where G' is the buoyant weight of the block and S is the upwards seepage force. Other authors also presented results from tests on homogeneous sands. Marsland (1953) also observed that the soil fails as a block while Davidenkoff (1954) highlighted that the shear forces on the sides of the block should be ignored.

Although Terzaghi et al. (1996), gives a worked example in which the acceptable factor required is $F_T = 2.5$, no direct recommendation from Terzaghi has been found, in previous publications, with the specification of a minimum factor of safety. Values taken

from a survey of publications, generally based on the use of Terzaghi's diagram, are summarised in Table 6.3 (Simpson and Katsigiannis, 2015).

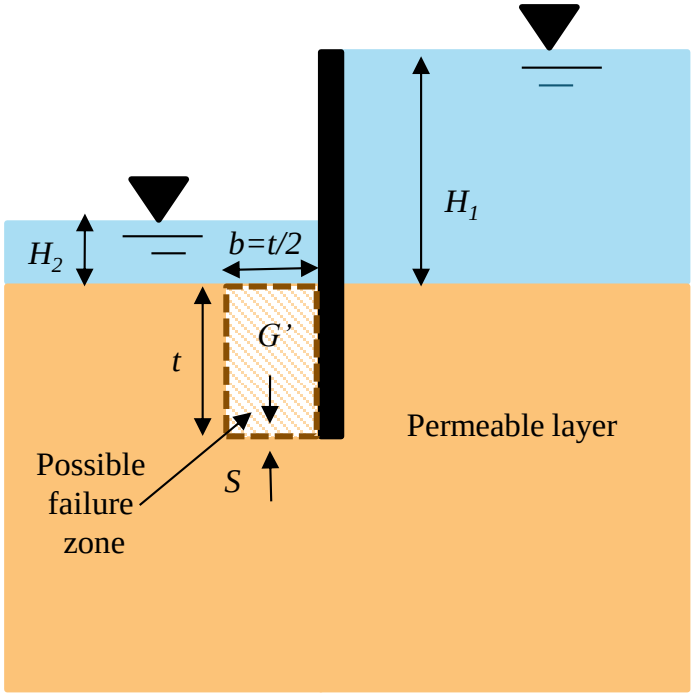

Figure 6.5: Terzaghi's calculation

Table 6.3: Published values for Terzaghi's factor of safety F_T (after Simpson and Katsigiannis, 2015)

Publication and any limitations		Values
Williams & Waite (1993)		1.5 to 2
For clean sands		
Kashef, Abdel-Aziz Ismail (1986)		4 to 5
Harr (1962)		4 to 5
German practice	– unfavourable soils	1.9
(DIN 1054/A2 2014)	– favourable soils	1.42
Swedish practice	– coarse soils	1.5
(Ryner et al., 1996)	– silty material	2.5
Dutch practice		2.8
Das (1983), quoting Harr (1962)		4 to 5

The values for the required factor of safety shown in Table 6.3, range from 1.42 to 5. While some authorities require larger factors for finer soils than for coarser soils, no explanation of this range has been given by the above mentioned authors.

Skempton and Brogan (1994) illustrated the significance of the grading curves of the materials in relation to safety considerations in the presence of hydraulic gradients. Even if water pressures are known with confidence, the achieved levels of safety highly depend on the grading curve of the material with poorly graded materials generally tolerating lower hydraulic gradients. This is because, in poorly graded materials, the effective stress may vary locally over distances of the order of a few soil particles, leaving some particles subject to much lower effective stresses than calculated from the depth of overburden and assuming a uniform hydraulic gradient.

Similarly, the German guide on erosion (BAW, 2013) makes a distinction between poorly graded soils that are internally unstable and well graded soils where the soil particle mixtures are internally stable. The critical failure mechanism depends on the grading curve with internal erosion and particularly suffusion (migration of fines due to seepage forces through the pores of a coarse particles structure) being critical for poorly graded soils and hydraulic heave for well graded soils.

This variability of the grading curves and the governing failure mechanisms among different soils, may explain why different authors have proposed quite different values for the Terzaghi's factor with higher values typically suggested as an empirical way to account for anomalies in the grading curve or internally unstable soils.

6.5.2 The soil block approach with FEM

The soil block approach relates directly to the conventional Terzaghi's approach where safety may be checked by studying the equilibrium of a rectangular block of soil. In the soil block approach, the Terzaghi's factor (F_T) at steady state directly relates to the $\gamma_{dst}/\gamma_{stb}$ ratio where γ_{dst} is the partial factor applied to the destabilising seepage force and γ_{stb} the partial factor applied to the stabilising buoyant weight of the block. Expressing the partial factors as a ratio enables comparisons with the global safety factor values traditionally used for similar problems in a number of countries and for a range of different materials.

Calculating the Terzaghi's factor (F_T) with FE methods is straightforward. The definition of the factor is given in Equation 6.5 where W is the weight of the soil block, H is the force on the base of the block due to hydrostatic pressure, U is the water force on the base of the block, W-H is the buoyant weight and U-H is the seepage force.

$$F_T = \frac{W-H}{U-H} \tag{6.5}$$

The weight of the soil block *W* and the hydrostatic force on the base of the block *H,* and hence the buoyant weight of the block *W-H*, can be easily calculated as the unit weight of the soil and the water are known. The water force on the soil block *U* is obtained from the output of the FE analysis.

As mentioned before, Terzaghi recommended that a column of width *b*=*t*/2 should be used in the calculations of the factor of safety, taking no account of friction forces on its vertical sides. It could be that Terzaghi considered that a narrower column is unlikely to fail because the favourable effect of the friction forces on its vertical sides would become significant. The reason for this, however, is unclear, therefore for this study, all the soil block calculations are based on the Terzaghi's block dimensions, where the depth of the block is equal to the embedment depth *t* and the width *b* is equal to *t*/2.

As the buoyant weight, which is a stabilising force, only depends on the unit weight of the soil, *γ,* and can be easily calculated for the Terzaghi's block as defined in Figure 6.5, the Terzaghi's factor is more sensitive to variations of the destabilising force which is the seepage force caused by the pore water pressures. The effects of different parameters on the pore water pressures and hence the Terzaghi's factor, are investigated in this study.

6.5.2.1 Effect of Δh/t

In this section, the effect of varying the ratio *Δ*h/*t* on the calculated Terzaghi's factor is investigated for the 10m excavation and cofferdam reference geometries (see Figure 6.2). In the cofferdam case, there is no excavation of the soil so that the ground surface is at the same level on both sides of the wall and the water flows around the wall because of the difference in the hydraulic head.

By increasing gradually the *Δ*h/*t* ratio, both analyses were driven to failure. Different hydraulic heads were used by specifying different water table levels behind the retaining wall. At the end of each analysis, the Terzaghi's factor was calculated by integrating the pore water pressures acting along the base of the soil block, from the output of the calculations.

In Figure 6.6, the calculated Terzaghi's factor is plotted against the ratio *Δ*h/*t.* It can be seen that in both cases, the factor decreases with increasing *Δ*h/t with the factor values being consistently higher for the 10m deep excavation case. Moreover, the cofferdam and excavation problems become unstable, i.e. $F_T = 1$, for a ratio of *Δ*h/t equal

to 2.25 and *Δ*h/t = 3.3 respectively. In both cases, the pore pressures become high, reducing the effective stresses, and making the values of wall friction insignificant.

Simpson and Katsigiannis (2015), also considering a 10m deep excavation, wide enough to give only minor lateral restraint to the flow (*x* = 4*t*), observed that the factor of safety becomes, as expected, lower as the difference in the hydraulic head becomes higher. It was observed that the FE analysis becomes unstable for a *Δ*h/*t* ratio in excess of 3.3 which is consistent with this study.

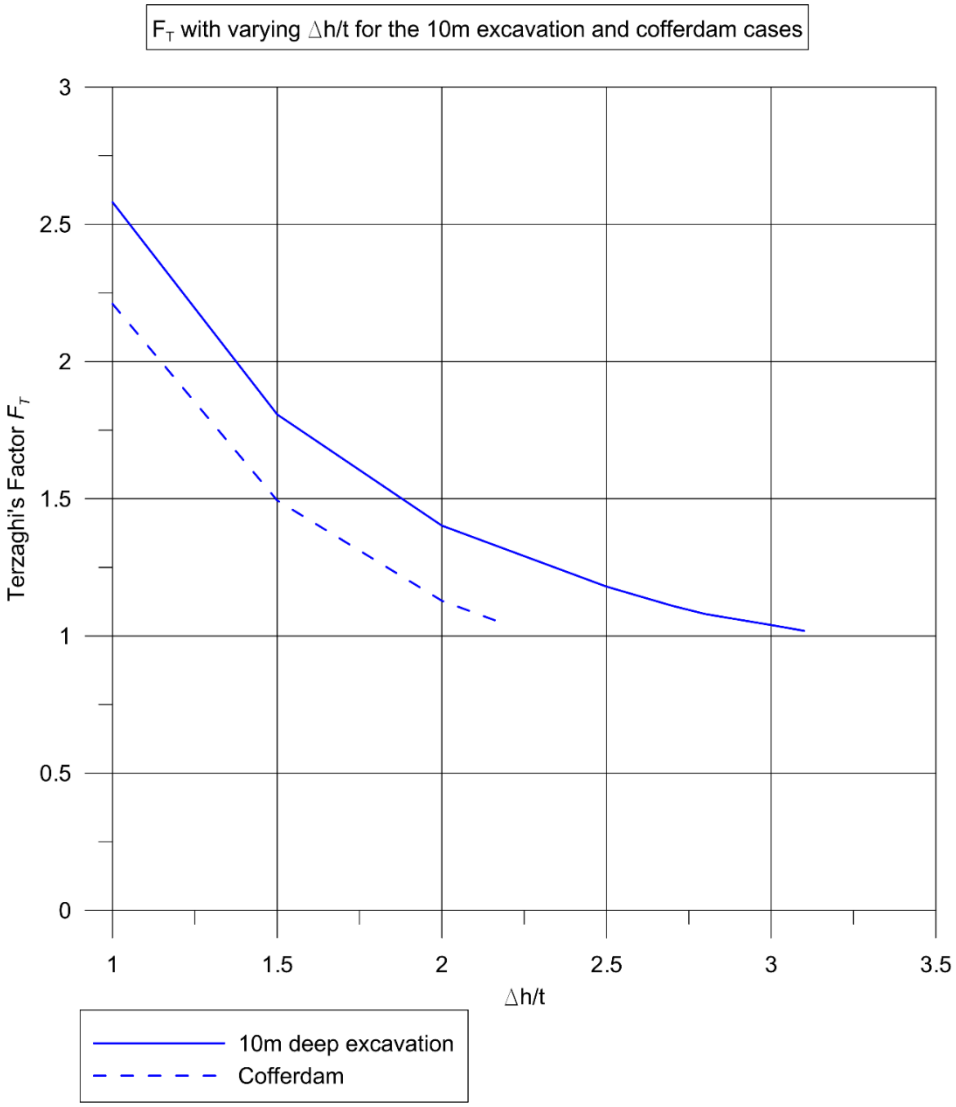

Figure 6.6: Calculated Terzaghi's factor F_T with varying *Δ*h/*t* for the 10m deep excavation and cofferdam cases

6.5.2.2 Effect of minimum flow path

The reason that in Figure 6.6, the 10m deep excavation case gives higher values of the Terzaghi's factor than the cofferdam case for the same ratios of *Δ*h/t, is that the minimum flow paths are different. The minimum flow path which can be defined as the

shortest subsurface path a water particle would follow, in a given groundwater regime, is equal to the sum of the distance from the tip of the wall to the groundwater table level in front of the wall, and the distance from the tip of the wall to the groundwater table level behind the wall. This means that for a given ratio of $\Delta h/t$, the minimum flow path relates directly to the height of the retained soil behind of the wall.

In Figure 6.2, the minimum flow paths are illustrated with the light blue solid lines around the wall for the 10m excavation and the cofferdam problem respectively. For example, for $\Delta h/t = 1.5$, the minimum flow path is 6m for the cofferdam case and 10.5m for the 10m deep excavation case. Longer flow paths for the same $\Delta h/t$, indicate higher loss of energy through the voids formed by the soil particles and hence relief in the pore water pressures acting at the bottom of the soil block.

To better illustrate this effect, the analyses were repeated for variations in the minimum flow paths, achieved by increasing gradually the height of the soil retained behind the retaining wall. The calculated values of Terzaghi's factor are plotted in Figure 6.7 against the minimum flow path for the different ratios of $\Delta h/t$. It can be seen that the minimum flow path is 6m for the cofferdam case, regardless of the level of the water behind the wall, while for the 10m deep excavation, the minimum flow path was measured as 9, 10.5 and 12 for ratios of $\Delta h/t$ equal to 1, 1.5 and 2 respectively. Moreover, for the same $\Delta h/t$, the Terzaghi's factor becomes lower as the minimum flow path decreases with the cofferdam case being the most critical.

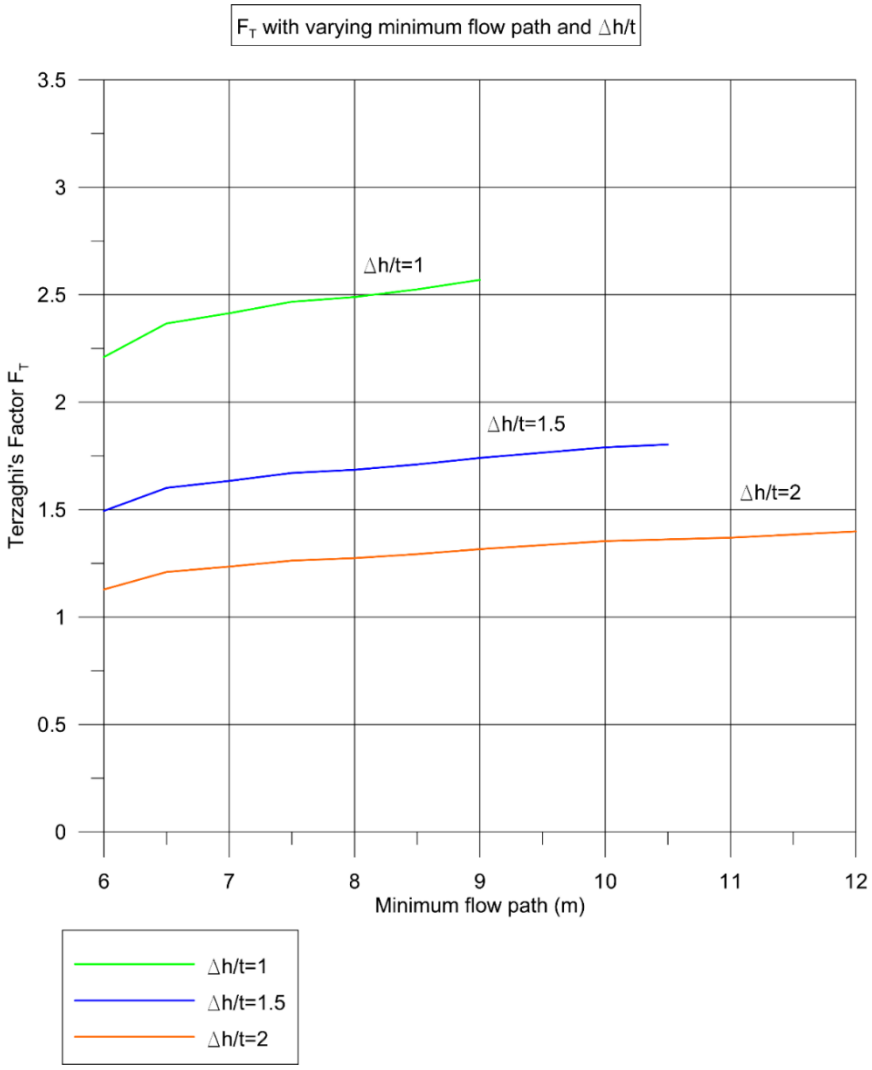

Figure 6.7: Calculated Terzaghi's factor F_T with varying minimum flow path

6.5.2.3 Effect of excavation width

In this section, the effect of varying the excavation width on the calculated Terzaghi's factor is investigated for the two reference geometries.

Figure 6.8 shows the head equipotential lines for three cases: (a) a wide excavation (width $x = 12t$), (b) a narrow trench ($x = t$), and (c) a circular excavation (diameter $d = t$). In all cases, the seepage is generated from a side boundary located at 18m ($6t$) from the wall, where a constant head is applied. For $\Delta h = 1.5t$, the Terzaghi's factor of safety F_T is: (a) 2.89; (b) 1.33 and (c) 0.97, respectively (Simpson and Katsigiannis, 2015).

Similarly, Aulbach and Ziegler (2013) found that when water is flowing upwards, beneath a narrow excavation, the upward hydraulic gradients are higher than in the cases of wider excavations with little or no lateral restraint.

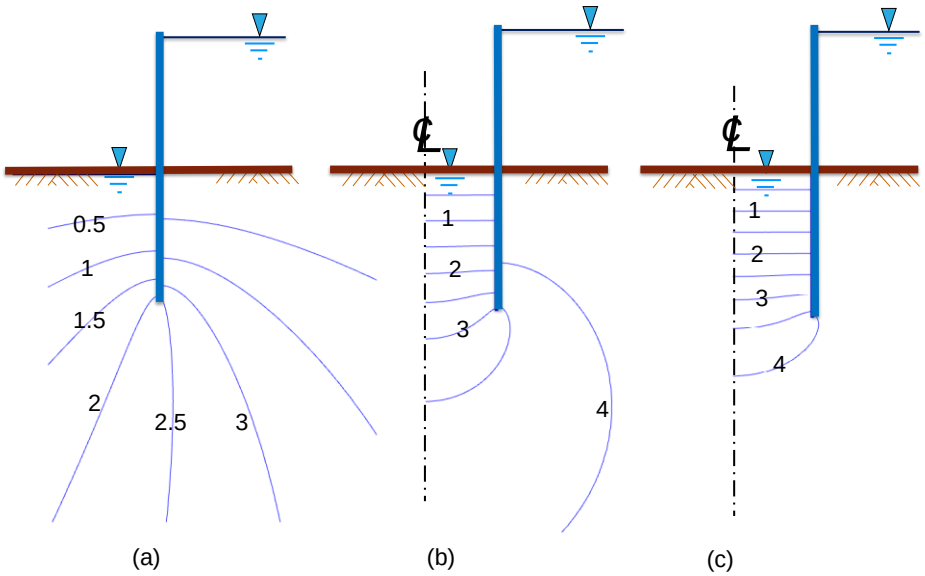

Figure 6.8: Equipotential lines for three cases: (a) a wide excavation (width x = 12t), (b) a narrow trench (x = t), and (c) a circular excavation (diameter d = t) after Simpson and Katsigiannis (2015)

To better illustrate this effect, the analysis is repeated for different *x*/*t* ratios where *x* is the excavation width in the horizontal direction (only half the excavation is modelled due to symmetry) and *t* is the embedment depth in the vertical direction while the rest of the model parameters remain the same. More specifically, 5 different cases were considered for plain strain conditions: *x*/*t* = 12, 8, 4, 2 and 1. At the end of each analysis, the Terzaghi's factor was calculated using the values of the pore water pressures acting at the bottom of the soil block from the output of the calculations. This study includes 10 different geometries each simulated using three different values of *Δ*h/*t*, totalling 30 analyses.

In Figure 6.9, the Terzaghi's factor is plotted against the ratio *x*/*t* for *Δ*h/t = 1.5. It can be seen, that the narrower the excavation is, the lower the factor of safety becomes. The factor of safety values show larger drops for values of *x*/*t* lower than 4 on both geometries. Figure 6.10 presents the values of the Terzaghi's factor for different values of *x*/t and *Δ*h/t for the excavation case. Again, it can be seen that the factor of safety drops significantly as the excavation becomes narrower.

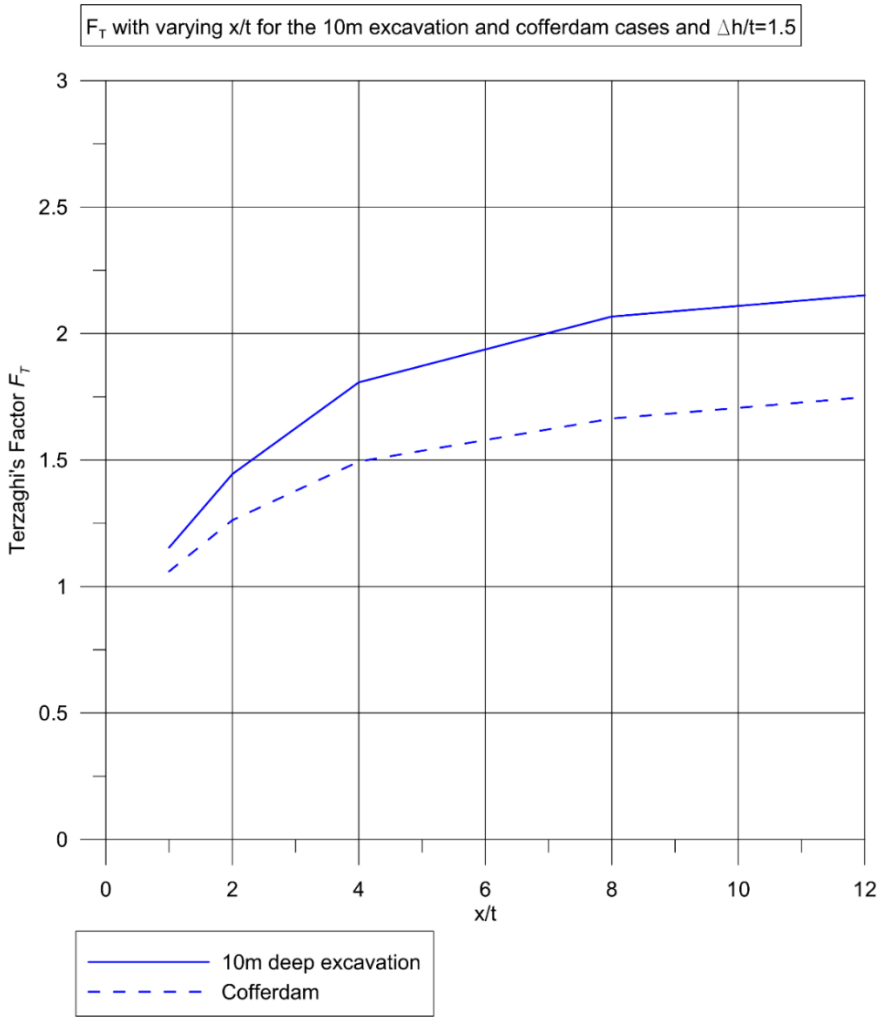

Figure 6.9: Calculated Terzaghi's factor with varying *x*/*t* for the 10m deep excavation and cofferdam cases with *Δ*h/*t*=1.5

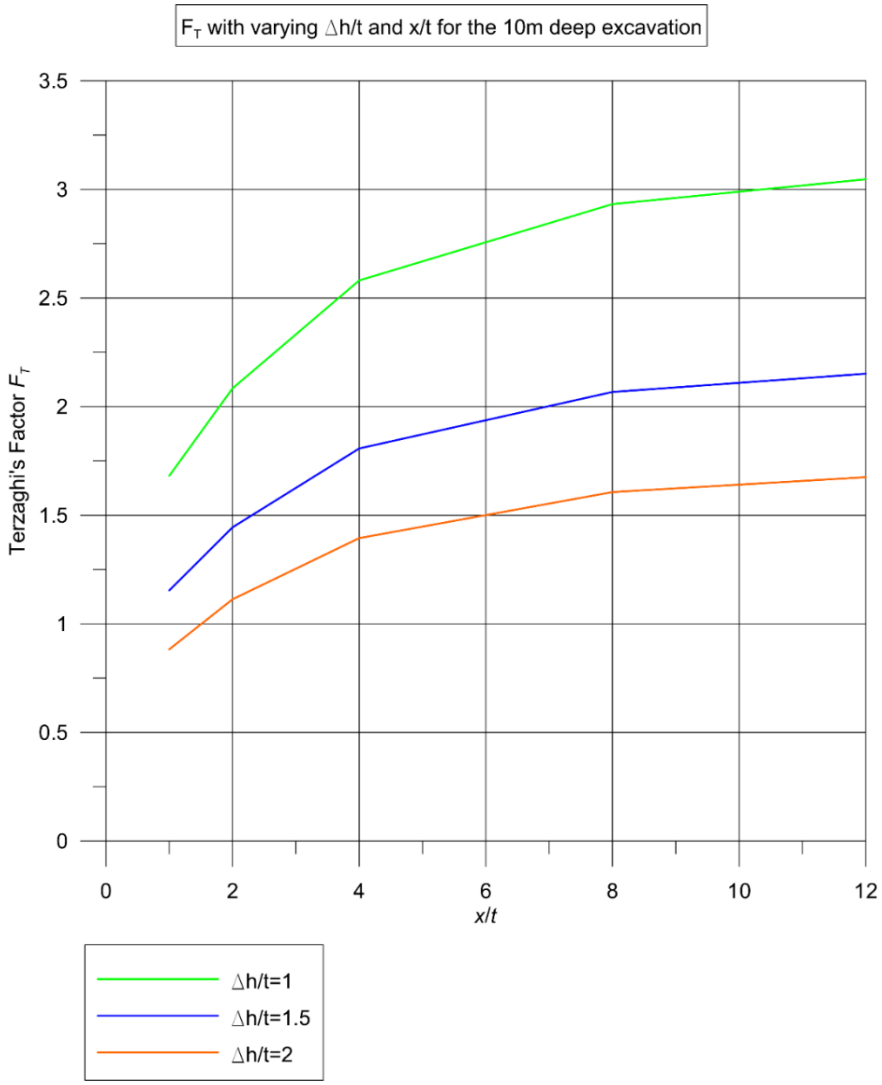

Figure 6.10: Calculated Terzaghi's factor for varying *x*/*t* and *Δ*h/t for the 10m deep excavation problem

6.5.3 Discussion

It can be concluded that the use of the soil block approach with FE methods is straightforward, requiring only the pore water pressure from the numerical analysis for the calculation of the Terzaghi's factor of safety. The calculated Terzaghi's factor directly depends on the upstream and downstream groundwater levels as specified by the ratio *Δ*h/t. It was also noted that for a given difference in the hydraulic head, the system becomes more critical for shorter minimum flow paths and narrow excavations, where confined spaces result in an increase in the groundwater pressures within the excavation and hence greater hydraulic gradients.

The obvious disadvantage of the soil block approach is that it provides no useful information about the critical failure mechanism and it is only applicable to very specific situations of upward flow towards a horizontal surface. In practice, more complex

situations are encountered, including flow beneath sloping surfaces in embankments and cuttings.

6.6 The integration point approach

The second approach for verifying stability against HYD using FEM, is the *integration point approach* which can be expressed in two different forms, depending on how safety is introduced into the calculations.

In the first form of the integration point approach, safety is verified at every integration point for a given set of partial load factors applied to the destabilising and stabilising actions. Hence, the design water pressures are calculated after applying the corresponding factor to their characteristic values, derived from the output of the FE calculations.

In the second form, no factors are applied to the water pressures but their design values are derived by directly assessing the design water table which is input in the numerical calculations. Thus, the values derived from the output of the FE analysis are already design values and no further factors need to be applied. Afterwards, the stabilising and destabilising pressures are combined at every integration point to give the achieved factor of safety as an estimate of the level of safety and economy.

6.6.1 Apply partial factors to the excess water pressures

In the first form of the approach, stability is verified at every integration point by checking that a relevant criterion with a given combination of partial factors, is fulfilled for a soil column of negligible width above each point. Then contours of the criterion values can be plotted downstream, in front of the wall, to check whether the criterion is fulfilled.

Simpson (2012) shows that when water pressures have to be factored, γ_{dst} should be applied to the excess pore water pressure because the destabilizing seepage force is only caused due to the excess pore water and not the hydrostatic component of the water pressure. Similarly, the stabilising factor, γ_{stb} should be applied to the buoyant density of the soil γ'. Based on the above, this study only focuses on the comparison of the two criteria, namely the D_γ and D_σ, defined in Equation 6.6 and 6.7 respectively. The values of the partial factors γ_{stb} and γ_{dst}, used in both Equations, correspond to the values required by EC7 and are given in Table 6.1.

$$D_\gamma = \gamma_{stb}(\gamma z - \gamma_w z) - \gamma_{dst}(u_k - \gamma_w z) > 0 \tag{6.6}$$

$$D_\sigma = \gamma_{stb}(\sigma_v - \gamma_w z) - \gamma_{dst}(u_k - \gamma_w z) > 0 \quad (6.7)$$

The difference between the two criteria is that in D_γ, the total vertical stress, σ_v, is equal to γz, while in D_σ the value is taken from the output of the numerical analysis (i.e. it includes other elements such as friction). No evidence is presented in the literature on which criterion is more suitable. Stelzer and Odenwald (2015) used the D_σ criterion (referred to as simply *D* in their paper) for verifying safety against HYD for a cofferdam geometry as a way to take into consideration the stress redistribution and the friction. However, a thorough comparison of the two criteria is needed to better understand their advantages and limitations.

In Figures 6.11 to 6.14, the contours of the D_γ and D_σ criteria are presented for the two extreme cases considered in Section 6.4: the 10m deep excavation and the cofferdam case with *x*/*t* = 4. For illustration purposes, only the contours for the cases that correspond to a Terzaghi's factor equal to 1.5 are presented here while the full list of the contours for the parametric analysis are included in Appendix C. It can be seen in Figure 6.6, that the Terzaghi's factor becomes 1.5 for *Δ*h/*t* = 1.8 and *Δ*h/*t* = 1.5 for the 10m excavation and the cofferdam case respectively. This is because the minimum flow path is shorter for the cofferdam geometry and hence the hydraulic heave problem becomes more critical.

Note that the contours are only plotted for the area of interest in front of the wall, where the vertical dimension of the area in the *y* axis direction is twice the embedment depth and the horizontal dimension in the *x* axis direction is half the excavation width.

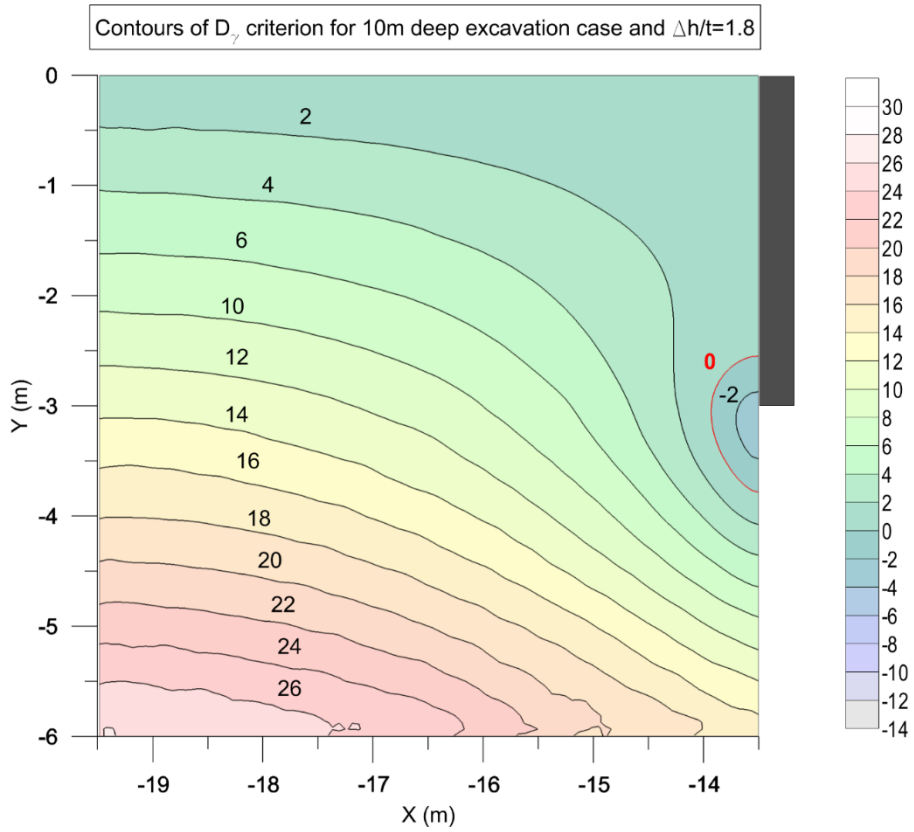

Figure 6.11: Contours of D_γ for the 10m excavation case with Δh = 1.8*t*

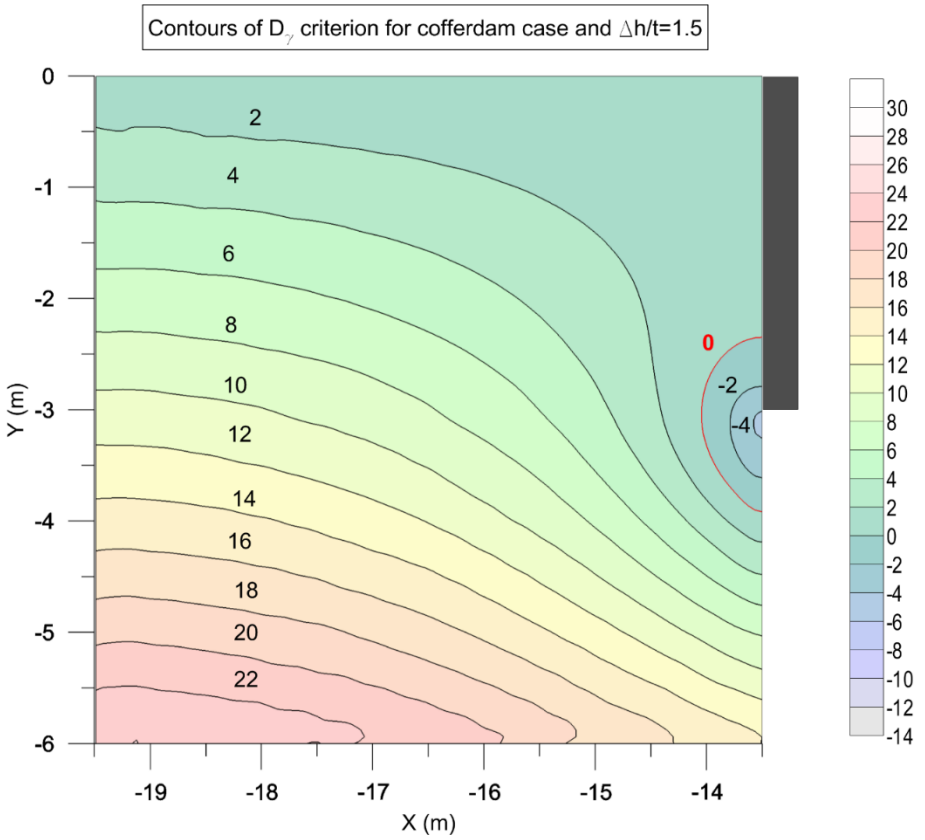

Figure 6.12: Contours of D_γ for the cofferdam case with Δh = 1.5t

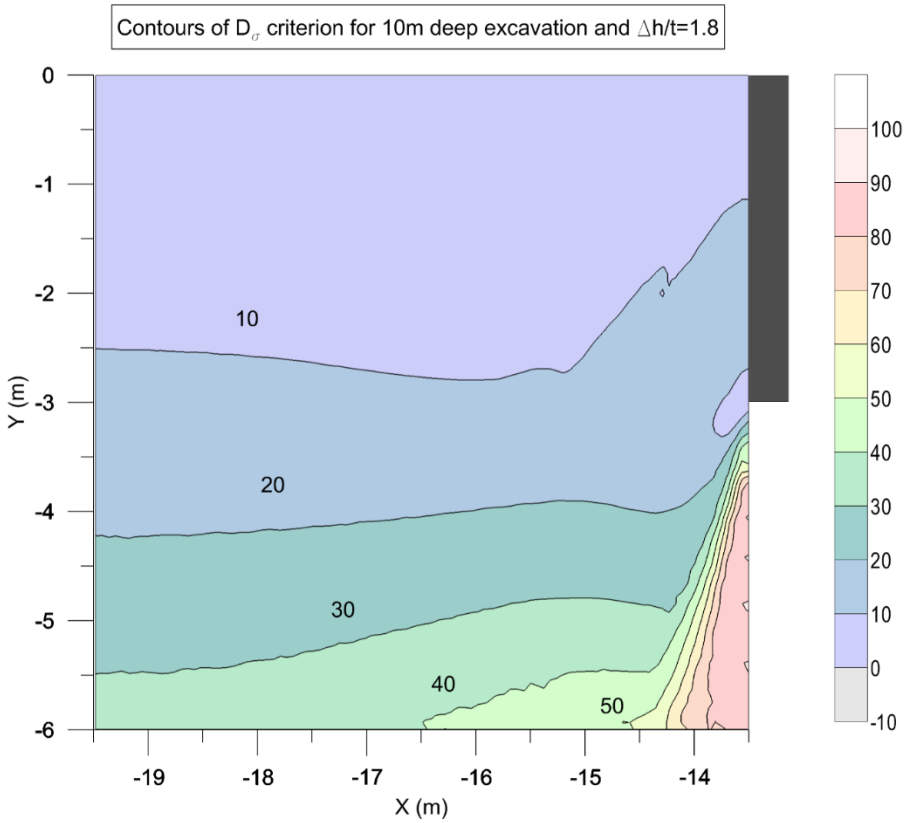

Figure 6.13: Contours of D_σ for the 10m excavation case with Δh = 1.8t

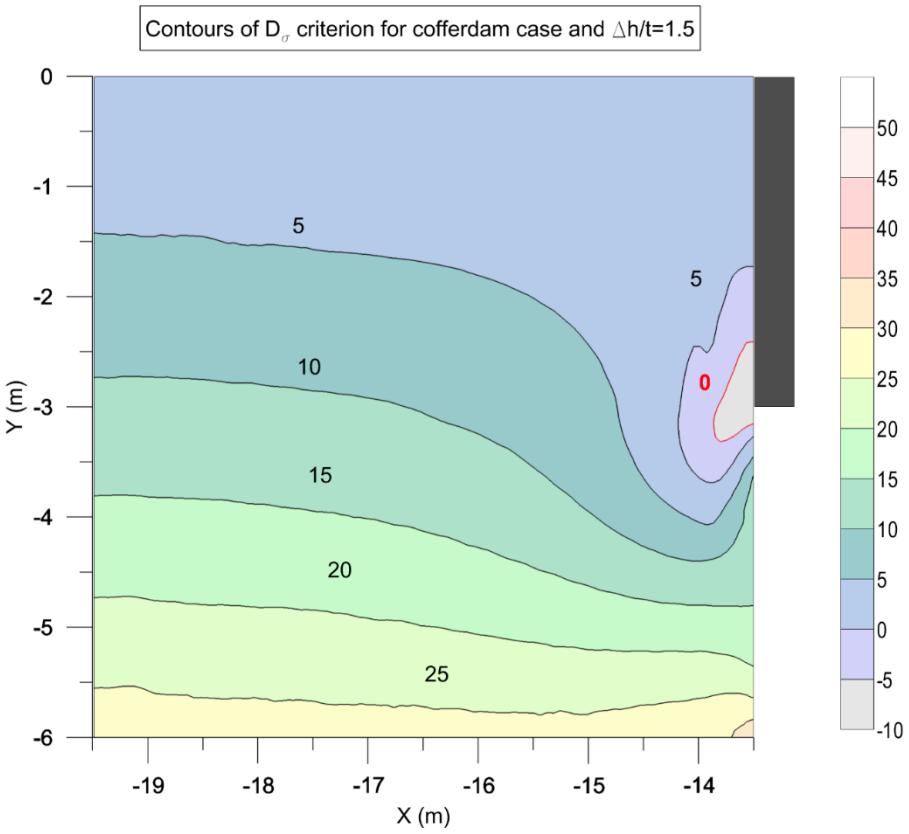

Figure 6.14: Contours of D_σ for the cofferdam case with Δh = 1.5t

It can be seen from Figures 6.11 and 6.12 that while both cases correspond to a value of Terzaghi's factor equal to 1.5, when the contours of D_γ are plotted using the partial factors required by EC7 (where $\gamma_{dst}/\gamma_{stb}$ = 1.5), there is an area close to the wall where the safety criterion is not fulfilled (zone with negative values).

In Figures 6.13 and 6.14, the contours of D_σ are plotted using again the EC7 partial factors and the effect of using the σ_v values from the output of the FE analysis instead of γz, is illustrated. For the 10m excavation case, it can be seen from Figure 6.13 that the contours of D_σ are everywhere positive and the criterion everywhere fulfilled. This means that using σ_v instead of γz to calculate the stabilizing stresses has a significantly favourable effect. On the other hand, for the cofferdam case, when the contours of D_σ are plotted (Figure 6.14), it is observed that while the negative area is smaller compared to the contours of D_γ in Figure 6.12, the criterion is still not fulfilled everywhere. It is obvious that while γz is uniquely defined, σ_v varies and can have a favourable effect when being used instead of γz.

Please note that negative values of either D_γ or D_σ relate to a local failure at the specific integration point and not to the global failure of the soil in the area in front of the wall. That is why an essential part of the HYD verification using the integration point approach is the contour plotting of the criteria values.

6.6.2 Direct assessment of the design water table

EG9 of EC7, in its final report, has proposed that no factors should be applied to water pressures, so in effect γ_{dst} = 1.0 (Evolution Group 9 - Water Pressures, 2014). The members of EG9 have recommended that in situations of this type, partial factors should not be applied to water pressures or to forces derived from water pressures, such as the seepage force *S*. Instead, engineers must take an appropriately cautious view of the piezometric water table level and the water pressures that could occur in the ground. According to EG9, the characteristic piezometric water levels and accordingly the characteristic values of water pressures shall correspond to a return period at least equal to the duration of the design life span of the structure (e.g. 100 years) while the ultimate limit state piezometric water levels and accordingly the ultimate limit state values of water pressures shall have a rare probability (e.g. 1%) of occurrence in the duration of the design situation of the structure. This also implies that a careful review of the possible range of distributions of permeability must be undertaken (e.g. even thin layers of lower permeability can cause the generation of high water pressures) and the design must be based on the worst that is credible. Afterwards, the code requirement is simply to prove that equilibrium exists under those design conditions.

An alternative form of the integration point approach described previously, can be used in combination with such directly specified design water table, to give an estimate of the achieved level of safety at every integration point of the FE mesh in the area in front of the wall. Based on the definitions of D_γ and D_σ (Equations 6.6 and 6.7), the integration point approach factors of safety, namely $F_{D\gamma}$ and $F_{D\sigma}$ are defined in Equations 6.8 and 6.9.

$$F_{D\gamma} = \frac{\gamma z - \gamma_w z}{u_k - \gamma_w z} \tag{6.8}$$

$$F_{D\sigma} = \frac{\sigma_v - \gamma_w z}{u_k - \gamma_w z} \tag{6.9}$$

According to these definitions, $F_{D\gamma}$ and $F_{D\sigma}$ are equal to the ratio $\gamma_{dst}/\gamma_{stb}$ when the criteria D_γ and D_σ respectively are equal to zero. Hence, the contours of $F_{D\gamma}$ and $F_{D\sigma}$, provide the safety factor value achieved at each integration point. Again, the two Equations differ in the way they include the total vertical stress in the calculations. Equation 6.8 ignores the mobilised friction effects whilst Equation 6.9 introduces σ_v directly from the output of the FE analysis, hence accounting for the friction developed along the soil/wall interface.

In Figures 6.15 and 6.16, the contours of $F_{D\gamma}$ are plotted for the 10m deep excavation and the cofferdam case for a ratio of Δh/t equal to 1.8 and 1.5 respectively. It can be seen that, in both cases, a minimum value of $F_{D\gamma}$ equal approximately to 1.3 is achieved. The lowest value of the factor of safety is close to the toe of the wall where the excess pore water pressures have their highest values.

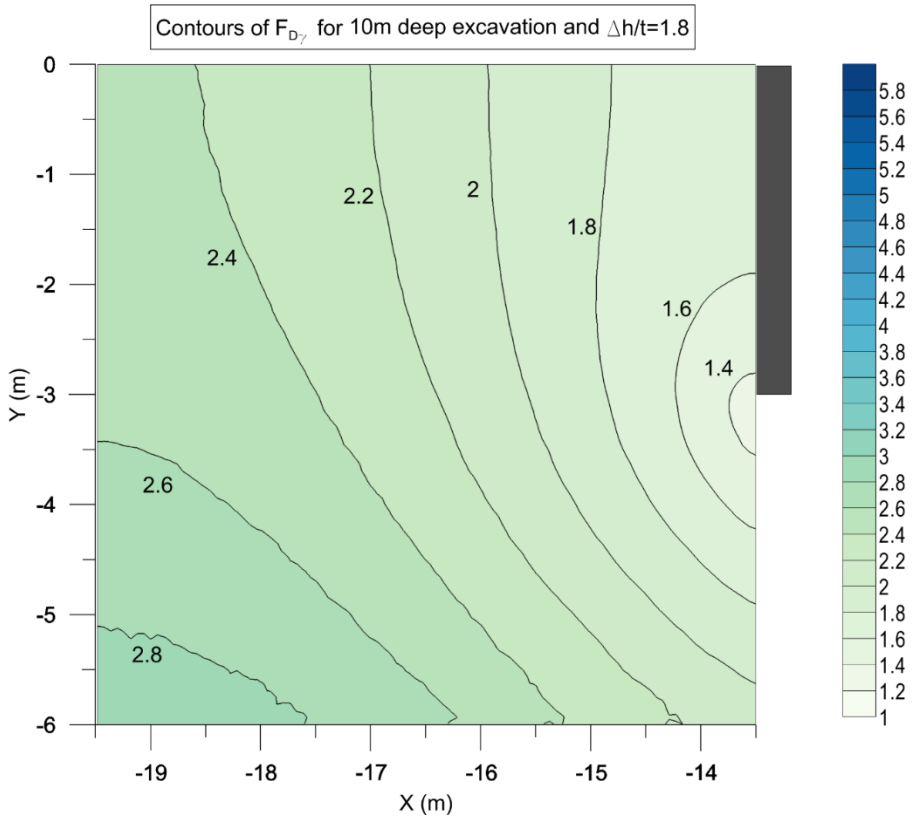

Figure 6.15: Contours of F_{DY} for the 10m excavation case with Δh = 1.8t

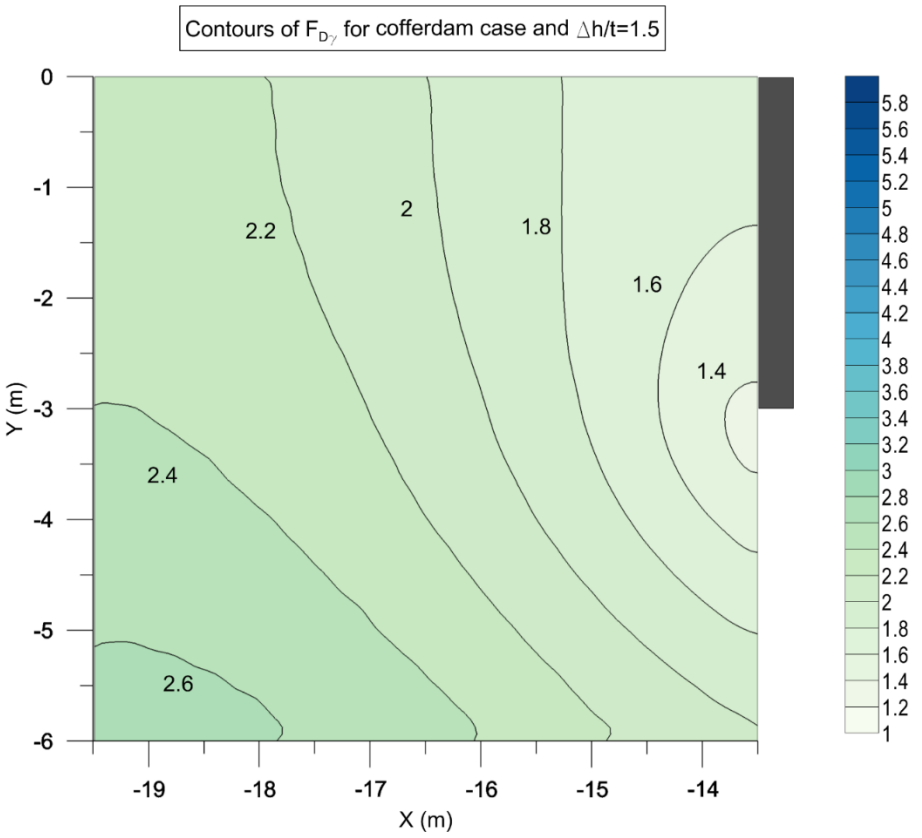

Figure 6.16: Contours of F_{DY} for the cofferdam case with Δh = 1.5t

Similarly, in Figures 6.17 and 6.18, the contours of $F_{D\sigma}$ are plotted for the same cases. However, the calculated values of the safety factor are now different for the two problems. For the 10m excavation case, the minimum factor is 1.8 as shown in Figure 6.17 while for the cofferdam case it is 1.4 as shown in Figure 6.18. Both values are higher than the corresponding minimum $F_{D\gamma}$ value observed in Figure 6.15 and 6.16 for the same $\Delta h/t$. However, $F_{D\sigma}$ is much higher for the 10m excavation than the cofferdam case because of the favourable effect of the mobilised friction.

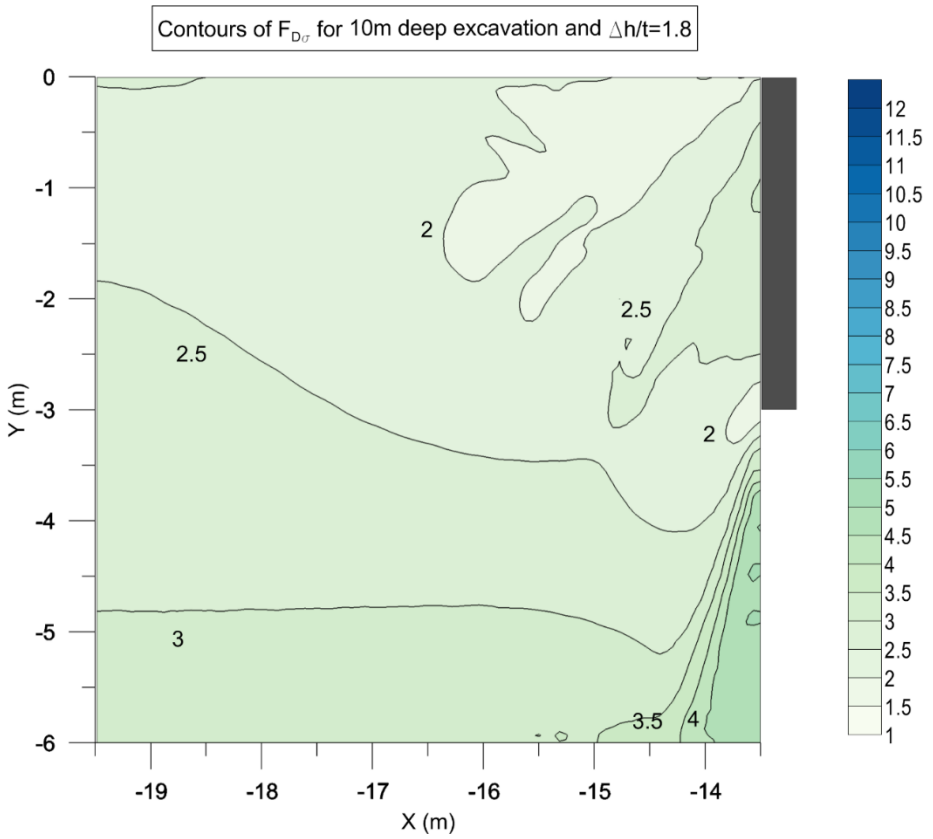

Figure 6.17: Contours of $F_{D\sigma}$ for the 10m excavation case with $\Delta h = 1.8t$

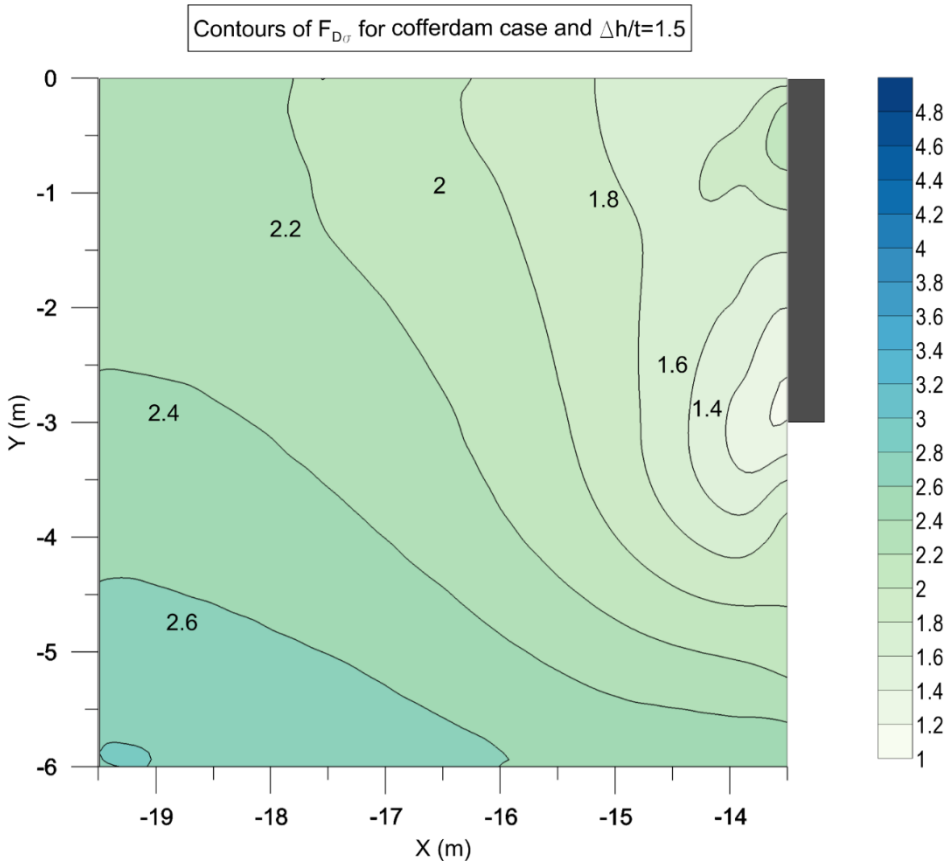

Figure 6.18: Contours of $F_{D\sigma}$ for the cofferdam case with Δh = 1.5t

6.7 Comparison of the Factors

It was observed above that for cases corresponding to a Terzaghi's factor of 1.5, there is an area close to the wall where $F_{D\gamma}$ is less than 1.5 while when calculating the $F_{D\sigma}$ values it was observed that the factor varies depending on the effect of the mobilised friction. It is clear that there is a need for a more thorough comparison between the calculated values of the safety factors from the soil block and the integration point approaches, together with a better understanding of the resulting differences.

In this section, the minimum integration point factors $F_{D\gamma}$ and $F_{D\sigma}$ (i.e. close to the toe of the wall) are plotted against the Terzaghi's factor F_T for the 10m excavation and cofferdam cases with varying x/t, $\Delta h/t$ and the soil/wall interface friction angle δ. In Figure 6.19, the relationship between $F_{D\gamma}$ and F_T is presented. As can be seen, the points follow a linear trend, where $F_T = 1.15F_{D\gamma}$, with an R^2 value of 0.98. Since friction is not considered, only one line defines the relationship between the two factors. According to their definition, both factors are calculated using γz as the stabilizing stress. However, as the factor $F_{D\gamma}$ is calculated at every integration point of the FE mesh, instead of a soil

block, a value of 1.0 is only related to a very local failure at the specific integration point and not the global failure of the soil in the area in front of the wall.

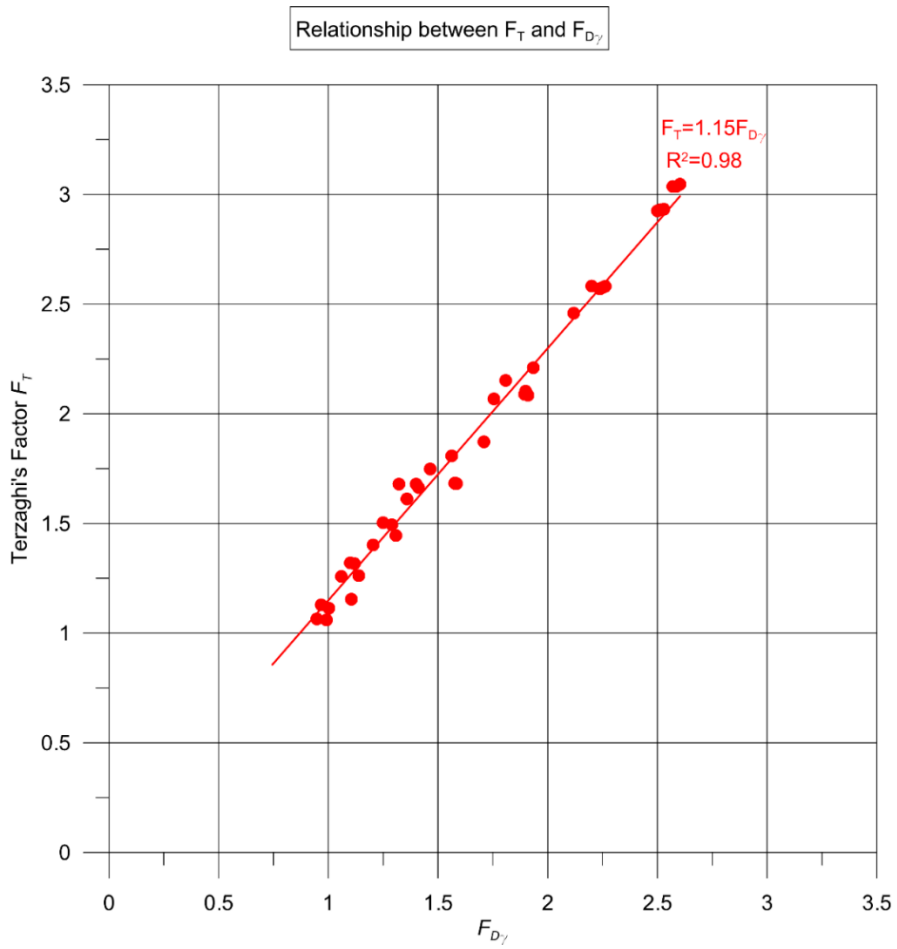

Figure 6.19: Relationship between the Terzaghi's factor F_T and the integration point approach factor $F_{D\gamma}$

In Figure 6.20, the relationships are given between the Terzaghi's factor F_T and the integration point approach factor, $F_{D\sigma}$ for both geometries. Straight lines are a good approximation (with R^2 values between 0.89 and 0.98). However, due to the presence of friction, the relation is not unique. $F_{D\sigma}$ is higher for the 10m excavation case (blue line) than the cofferdam case (orange line) as the friction effect is more significant. When tanδ increases from 0.5tanφ' to tanφ', both lines move to the right as $F_{D\sigma}$values increase (dashed lines).

The reason for this is that the effective horizontal stresses, and therefore, the mobilised friction, are different. While the earth coefficient at rest is the same and equal to 1-sinφ', the initial effective horizontal stresses are different as they are calculated at different depths. Since the initial stresses are calculated before the excavation is made, the toe of the wall is 13m and 3m below the ground level for the 10m deep excavation

and the cofferdam case respectively. After the excavation of 10m of soil, the horizontal effective stresses are ‘locked-in’. They don’t completely disappear when the loading is removed.

To illustrate this effect, Figure 6.21 presents the horizontal stress profiles in front of the wall and the resultant forces for all cases. It can be noted, that the effective stresses are much higher for the 10m excavation than the cofferdam case. Moreover, when tanδ increases from 0.5tanφ' to tanφ', the total force increases from 13.1kN/m to 21.8kN/m in the case of the cofferdam and from 69.4kN/m to 137.5kN/m in the case of the 10m deep excavation. This increase in horizontal stresses is directly proportional to the friction between soil and wall. The findings agree with the results of Benmebarek et al. (2005) who carried out parametric analysis to investigate the effect of wall friction for a similar problem and Stelzer and Odenwald (2015) who observed a higher effect of friction in a supported excavation, when compared to a cofferdam geometry, resulting in higher stresses in the proximity of the wall.

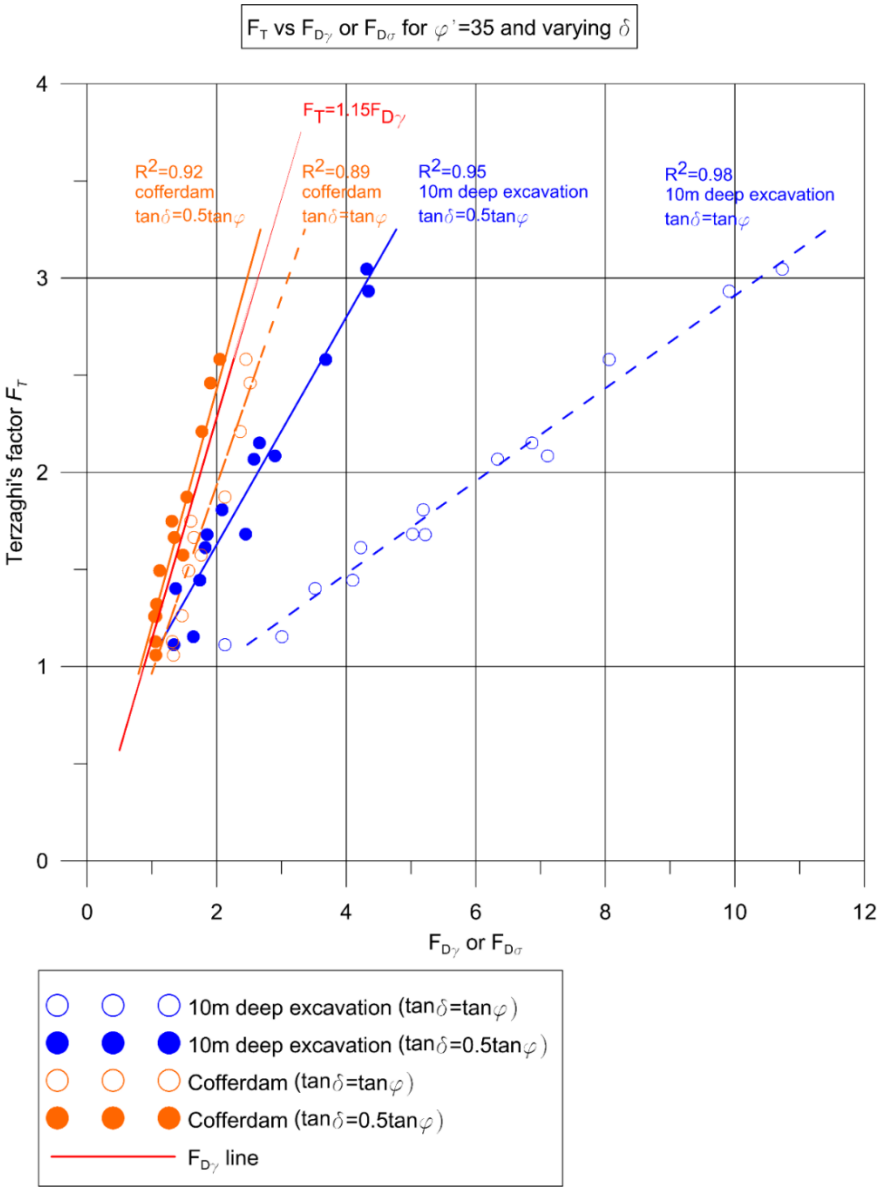

Figure 6.20: Relationship between the Terzaghi's factor F_T and the integration point approach factors $F_{D\gamma}$ and $F_{D\sigma}$ for $\varphi' = 35°$ and varying soil/wall friction angle δ

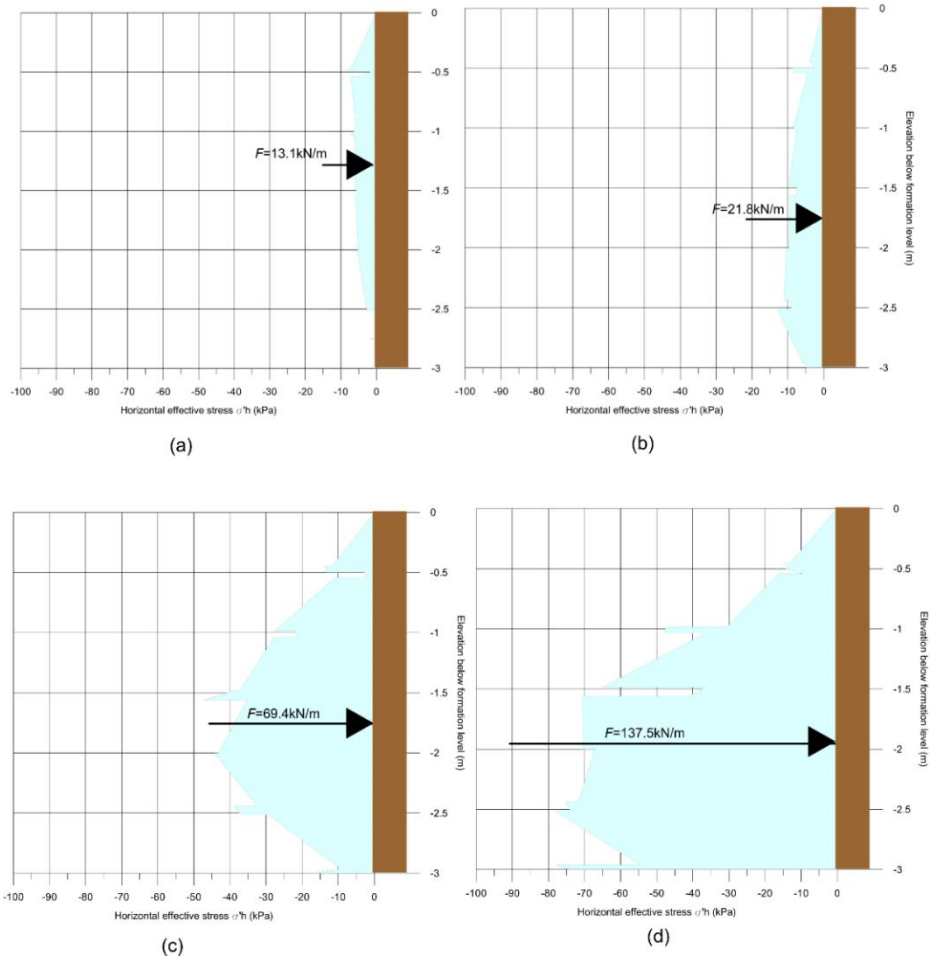

Figure 6.21: Horizontal effective stresses and resultant forces for a) cofferdam with tanδ = 0.5tanφ', b) cofferdam with δ' = φ', c) 10m deep excavation with tanδ = 0.5tanφ' and d) 10m deep excavation with $\delta = \varphi'$

The analysis was also repeated for a weaker soil to investigate the effect of the soil strength parameters on the calculated values of $F_{D\gamma}$ and $F_{D\sigma}$ and the relationship with F_T. The new soil has an angle of shearing resistance equal to φ' = 25° while the rest of the soil parameters, listed in Table 6.2, remain the same. The analysis is repeated for both the 10m excavation and the cofferdam case with varying $\Delta h/t$, x/t and δ.

Since $F_{D\gamma}$ is not related to the friction angle but to the unit weight of the soil, the relationship determined in Figure 6.19 can be used for this soil. However, as illustrated in Figure 6.22, the effect is significant for $F_{D\sigma}$. It can be seen that the solid $F_{D\sigma}$ lines for the 10m excavation and the cofferdam case, have moved to the left of the graph and hence the $F_{D\sigma}$ values have decreased when compared to Figure 6.20. The decrease in the angle of shearing resistance and hence the decrease in soil/wall friction angle, reduces the calculated factor of safety $F_{D\sigma}$ and therefore has an unfavourable effect on

the calculated $F_{D\sigma}$ values. It is worth noting that when tanδ increases from 0.5tanφ' to tanφ', both $F_{D\sigma}$ lines move to the right as $F_{D\sigma}$ values increase (dashed lines).

The effect is again particularly significant for the 10m excavation case where σ_v is much higher than γz due to the friction component. It is important to mention that all the other geometries considered, for the minimum flow path parametric analysis, yielded values that fell between the $F_{D\sigma}$ lines in Figures 6.20 and 6.22.

In all cases considered, for the same F_T value, the calculated values of $F_{D\sigma}$ are higher than the corresponding values of $F_{D\gamma}$ (red solid line), meaning in principle that $\sigma_v > \gamma z$. As the effect of friction becomes more significant, either by increased effective horizontal stresses or soil/wall interface friction angle δ, σ_v becomes much higher than γz and hence $F_{D\sigma}$ is much higher than $F_{D\gamma}$.

However, it is interesting that the range of $F_{D\sigma}$ values from all cases considered, narrows down for lower values of F_T (especially lower than 1.5) and also their values become closer to the corresponding $F_{D\gamma}$ values. In fact, they almost have a common point at $F_{D\sigma} = F_{D\gamma} = 1$, $F_T = 1.15$. At this point, friction against the wall is destroyed by water pressure.

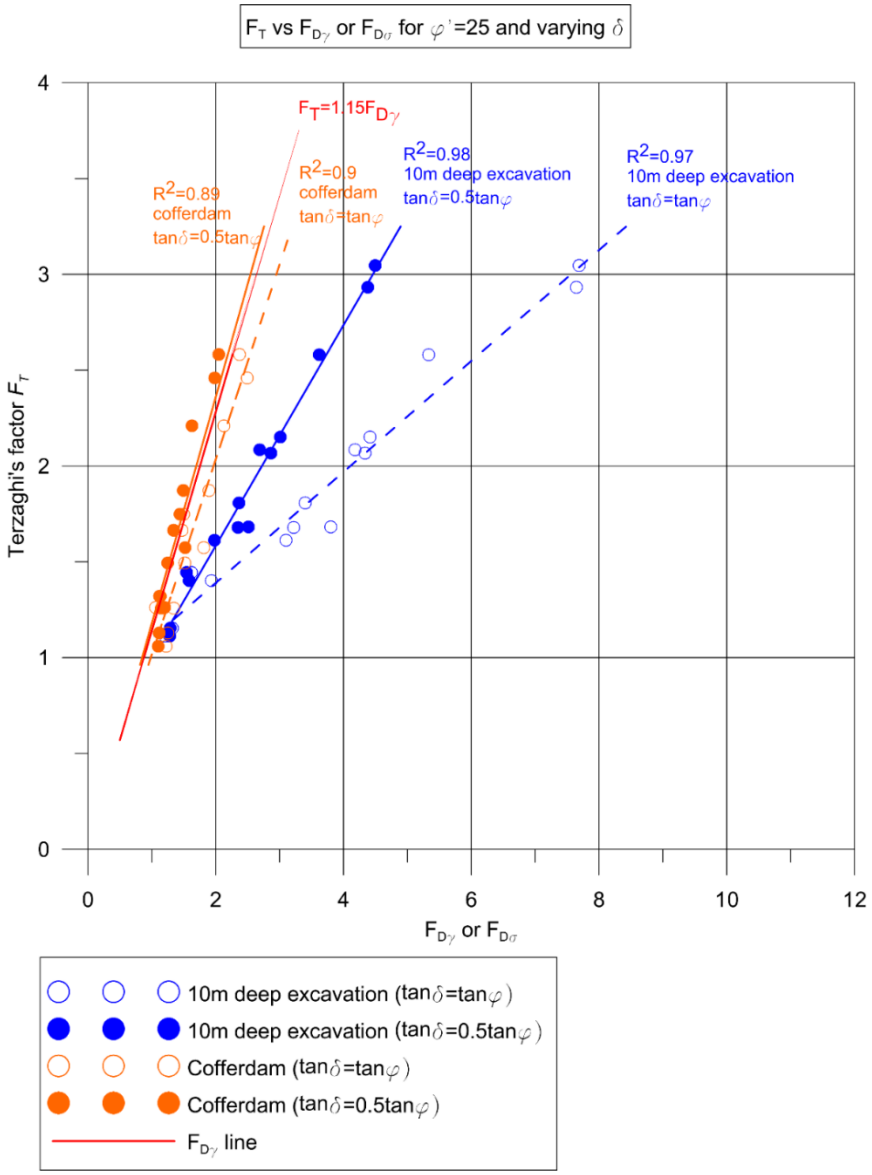

Figure 6.22: Relationship between the Terzaghi's factor F_T and the integration point approach factors $F_{D\gamma}$ and $F_{D\sigma}$ for φ' = 25° and varying soil/wall friction angle δ

6.8 Discussion

The results show that there is a unique and simple relationship between F_T and $F_{D\gamma}$, proportional to the unit weight of the soil. With regards to $F_{D\sigma}$, the calculations using two extreme geometries and variations of the angle of shearing resistance φ' and the soil/wall interface friction angle δ, have shown that the range of relationships between the factors is broad and very sensitive to effect of friction along the wall.

Moreover, the $F_{D\gamma}$ values are lower than those of $F_{D\sigma}$ for all cases considered and hence they provide a conservative verification of the HYD Limit State. However, when pore water pressures rise, the effective stresses decrease and the friction effect is lost.

In this instance, the HYD Limit State becomes more critical and all the $F_{D\sigma}$ lines tend to converge towards the $F_{D\gamma}$ line.

The use of the $F_{D\gamma}$ factor of safety presents advantages over the use of the $F_{D\sigma}$ factor as, in general, designers should not just rely on the favourable friction effect to verify stability against HYD. Remote from the limit state wall friction appears to enhance safety, increasing $F_{D\sigma}$. But at the limit state this is no longer so because the water pressure destroys the friction. This illustrates the fact that carrying out calculations for conditions remote from the limit state and then relying on a factor of safety can be misleading.

6.9 Conclusions

The verification of stability against HYD using FE methods is straightforward and very promising. While designers might be more familiar with the soil block approach and the Terzaghi's calculation, the more advanced integration point approach has the advantage that it is readily applicable not only to the simple cases considered here, but also to more complicated situations such as water approaching sloping ground surfaces. Moreover, it provides insights into the stability of the soil at a very local level, instead of assuming a pre-defined failure mechanism (e.g. a block of soil mass with specific dimensions).

There are two ways to introduce the design values of the destabilising pore water pressures into the integration point approach calculations; either by applying the HYD partial load factors suggested by EC7 to the characteristic values or by directly assessing the design water table. As it is very likely, based on the suggestions of the EG9 (Evolution Group 9 - Water Pressures, 2014), that the next version of the Eurocode 7, due in 2020, will move away from factoring the pore water pressures, the calculation of the integration point factors, based on a direct assessment of the groundwater conditions, might become more relevant in the future compared to the verification using the D_γ and D_σ criteria, which involve the application of partial factors. The use of the $F_{D\gamma}$ safety factor to get an estimate of the safety margin has significant advantages, since there is no friction available at the limit state.

Moreover, the integration point approach criteria and factors of safety, are calculated based on the excess pore water pressures. Therefore, the integration point approach addresses the misinterpretation mentioned above regarding which component of the pore water pressure needs to be factored.

CHAPTER 7

Conclusions and suggestions for further research

7.1 Conclusions

The work presented in this thesis, has addressed critical issues and challenges associated with the routine use of FE methods for the ULS analysis of supported excavations and represents a significant step forward in demonstrating the benefits and limitations of implementing the Eurocode 7 in advanced numerical analysis, and consequently producing a code compliant and economic design. The effect of several key parameters and constitutive models has been investigated through parametric studies on simplified supported excavation geometries and FE analyses of two deep excavation case histories. While the detailed conclusions and the practical implications on the design have been discussed separately in each Chapter, these conclusions are summarised here in a more comprehensive way.

The study has focused on the derivation of the model parameters for London Clay of different constitutive models, ranging from the Mohr-Coulomb (MC), to more advanced models such as the Hardening Soil (HS) model, the Hardening Soil Small (HSS) model and the BRICK model. The model parameters were derived based on studies and high quality field and laboratory data published in the literature. Note that other constitutive models have not been selected for this study either due to time constraints or because they are rarely used within Arup Geotechnics and generally in the industry or in the case of the Modified Cam-Clay (Roscoe and Burland, 1968) because the use of the model in practical applications is not recommended as the model may allow for extremely large shear stresses and softening behaviour that can lead to mesh dependency and convergence issues (Plaxis, 2015).

In the first part, the study was concerned with the MC, HS and HSS models where the soil strength is a model input. When undrained conditions are considered for the soil behaviour using the effective stress approach, the undrained shear strength is not input but is calculated by the constitutive model. Thus, in order to ensure that the calculated strength profile matches the published data, a series of numerical triaxial undrained compression tests (both CAU and CIU) were performed at different stress levels using the MC, HS and HSS effective stress model parameters. It was found that the undrained

shear strength profiles predicted generally accord with the profile derived from the data published in the literature. While, the MC and the HS models predicted the same undrained shear strength, the HSS model consistently resulted in different stress paths, and consequently lower undrained shear strength. The discrepancy is due to the formulation of the HSS model and the different definition of the shear hardening flow rule when compared to the HS model. Moreover, the excess pore water pressures, generated during the triaxial tests, are higher than those predicted by the MC and the HS models.

For the ULS analysis, when undrained conditions are assumed using effective stress parameters, designers must ensure that the calculated undrained shear strength distribution is equal to the characteristic one, reduced by the required value of the partial factor. It was found that for values of angle of shearing resistance representative of London Clay, applying a factor of 1.4 to the effective stress parameters results in an undrained shear strength factored by about the same value as required by the EC7.

For the ULS analysis, EC7 does not suggest factoring the soil stiffness. While this can be easily achieved with the Mohr-Coulomb model, where the soil strength and stiffness are independent parameters, it was shown that when using the HS and HSS model, even for small values of cohesion, the soil stiffness reduces when partial factors are applied to the effective strength parameters. However, for cohesionless materials, the soil stiffness remains unchanged when the soil strength is reduced which is consistent with the EC7 requirements.

For the ULS FE analysis using constitutive models, such as the BRICK model, where the soil strength is not an input but is calculated by the model, it is not possible to apply the partial factor required by EC7. For this reason, a new set of material proportions and string lengths was derived, which results in an undrained strength equal to the characteristic value reduced by a factor of 1.4, consistent with the code requirements. The corresponding S-shaped stiffness degradation curve is reduced in the large strain area when compared with the curve obtained from the characteristic BRICK parameters. According to the formulation of the BRICK model, the area defined within the curve directly relates to the soil strength. Consequently, when the material proportions in the large strain area are reduced, the area within the curve, corresponding to the soil strength, also reduces. Moreover, in order to satisfy the EC7 requirement that only the soil strength shall be factored and not the soil stiffness, the parameter β_G was slightly reduced to improve the match between the curves that correspond to the characteristic and factored BRICK parameters.

Although, the new set of BRICK parameters for the ULS analysis is consistent with the EC7 requirements regarding the soil strength and stiffness, the resulting K_0 profile does not exactly match the profile corresponding to the characteristic BRICK parameters. This is because K_0 is not input in the BRICK model but is calculated based on the input model parameters and the geological history. This limitation though can be addressed by using the BRICK model with a FE software (such as the LS-Dyna) that allows the K_0 value to be overwritten.

Following the derivation of the model parameters, the challenges of the SLS and ULS FE analysis of five supported excavations in London Clay of increasing excavation depth, were illustrated using the Mohr-Coulomb model.

For the SLS analysis, it was found that for all geometries, higher K_0 and lower soil stiffness values generally result in higher wall deflections and more critical soil heave at the base of the excavation and surface settlement behind the wall. Lower values of the prop stiffness generally result in higher wall deflections and more adverse surface settlements behind the wall with the influence being less significant on the heave at the bottom of the excavation.

For the ULS analysis, it was found that, the DA1-1 governs the design resulting in higher values of the design internal structural forces. This illustrates that the soil strength is not critical for the design for a stiff material such as the London Clay. Moreover, the DA1-2 Strategy 2 is generally more critical than the Strategy 1. It was shown that higher values of K_0 and prop stiffness generally result in larger differences between the two DA1-2 Strategies, particularly for the deep excavation cases with many prop levels while varying the soil stiffness only has a minor effect on the discrepancy in the results between the two DA1-2 Strategies.

More specifically, it was found that the higher the K_0 value, the closer the stress paths are to the failure line and hence the larger the plastic zone. In DA1-2 Strategy 2, when shifting from characteristic to factored soil strength at each excavation stage, the failure line is reduced and thus even more points reach plastification in the zone below the base of the excavation. As a consequence, the lowest prop picks up more load and the difference in the prop loads, between the two DA1-2 Strategies, becomes even more significant.

Moreover, when the FE analysis was repeated using the MC model for a deep excavation in a soft marine clay, typically encountered in Singapore, it was shown that

factoring the soil strength of a soft clay has a more significant effect on the calculated design structural forces, than factoring the strength of a stiff clay.

The design prop loads calculated from the FE analyses, were compared with the values derived from the graphs based on the empirical graphs suggested by CIRIA C517 and EAB. The FEM results are in better agreement with the values derived from the EAB than the CIRIA guide. This is due to the assumption made by the EAB guide that different pressure distributions apply to walls supported by different number of prop levels, as opposed to the uniform distribution proposed by the CIRIA.

The study has also focused on how the accidental prop loss effect can be considered in the FE analysis, illustrating that the single prop loss is a three-dimensional problem with the load of the deactivated prop being redistributed to the adjacent props both in the vertical and horizontal direction. It was also found that the ULS analysis is not always more critical than the prop loss analysis. Thus, the prop loads that govern the design are the maximum values calculated from both analyses.

When the FE analysis was repeated, using the more advanced model parameters for the London Clay, it was found that the SLS results from the analyses using the HSS reference model parameters reasonably agree with the results from the analysis using the BRICK model which has been long successfully used to model the behaviour of the London Clay. The results are less promising for the HS model as for example the predicted settlement trough is too wide when compared to models, such as the HSS and the BRICK, which can more realistically account for the small strain stiffness of the soil far away from the excavation zone. In any case, designers must be aware that the soil stiffness in the HS and HSS models is strongly dependent on the effective stress profile, hence it is practically impossible to derive a single set of input parameters for London Clay which is appropriate for every problem. Users need to carefully select the stiffness parameters taking always into account the effective horizontal and vertical stress profiles.

For the ULS analysis, it was found that the DA1-1 governs the design in terms of the prop loads, wall bending moments, shear and axial forces. It was also found that the DA1-2 Strategy 2 is generally more onerous than the Strategy 1 with the discrepancy in the results being more apparent for the MC model than the rest of the models. The results show that the use of advanced constitutive models for the ULS FE analysis is not only feasible but it also has advantages and is very also promising.

The ULS FE analysis of two deep excavation case histories in London Clay, such as the Moorgate Crossrail and the V&A Exhibition Building excavation, using the MC,

HS, HSS and the BRICK model, confirms the findings that the DA1-1 governs the design in all cases resulting in more adverse structural forces. Moreover, in most cases, the DA1-2 Strategy 2 is more critical than the Strategy 1, with the difference being more apparent when the MC model is used. It was shown that when the more advanced models were used, the differences in the calculated design structural forces between the two DA1-2 Strategies are lower when compared to the Mohr-Coulomb case with the effect being more pronounced for the Moorgate excavation due to the higher depth of the excavation.

Moreover, for the V&A excavation, the calculated design prop loads were compared with the measured values from the strain gauges showing that, in most cases, the FE results agree with the measured values and the variation of the values with time follows the pattern of the field measurements. The comparison between the structural capacities of the props with the measured values of the prop loads, reveals that particularly the upper prop was heavily overdesigned.

Overall, it is concluded from the study that the dual approach, currently required by the DA1, expressed as a combination of the DA1-1 and the DA1-2 Strategy 2, governs the design decisions, not only for the simple examples, but also for the more realistic geometries and soil profiles of the two case histories. The DA1-2 Strategy 2 is preferred to the Strategy 1 because it is generally more critical; it is a more intuitive way of accounting for the uncertainty in the soil strength; and because it can be easily applied in conjunction with the SLS analysis. In any case, the choice of the factoring strategy, for the design of the wall bending moments, is less important than for prop design because retaining walls typically display some plasticity and redistribute the bending moment. However, the Strategy 2 is preferable for the design of prop loads, because props can exhibit brittle behaviour and the DA1-2 Strategy 1 might not be adequately conservative.

While in this study only the DA1, currently adopted in the UK, was considered and the partial factor values suggested in the UK National Annex were used, the conclusions regarding the DA1-1 and DA1-2 apply, in broader context, to the Load Resistance Factoring Approach (LRFA) and the Material Factoring Approach (MFA) respectively for the materials considered.

In the final Chapter, the study focuses on the verification of the stability against the HYD Limit State using FE methods for the analysis of supported excavations. While the conventional soil block approach, based on the well-known Terzaghi's calculation, has the obvious advantage of simplicity, the more advanced integration point approach can

be used for more complex geometries to provide an insight into the stability of the soil at a very local level.

There are two ways to introduce the design values of the destabilising pore water pressures into the integration point approach calculations; either by applying the HYD partial load factors, suggested by EC7, to the characteristic values and perform the verification using the D_γ and D_σ criteria or by directly assessing the design water table and calculate the integration point factors $F_{D\gamma}$ and $F_{D\sigma}$. The use of the $F_{D\gamma}$ safety factor to calculate the margin of safety is generally preferred because there is no friction available at the limit state.

7.2 Further Research

Although, a comprehensive study on the SLS behaviour, predicted by the HS and HSS models, for London Clay, is beyond the scope of this thesis, the results are promising. Further research and calibration with laboratory test results is needed to confirm the applicability of these models.

The study on the ULS analysis of deep supported excavations using FE methods needs to be extended to include more advanced constitutive models, not only for stiff OC clays such as the London Clay but for a wider range of materials (e.g. sandy materials), and particularly models where the soil strength is not an input parameter but is calculated by the model. Similar to the approach used for the BRICK model, a new set of parameters needs to be derived that results in an undrained shear strength equal to the characteristic strength reduced by 1.4 and the knock-on effects on the soil stiffness need to be investigated.

More deep excavation case histories need also to be studied, in both 2D and 3D FE analysis, to confirm the findings on the effect of the soil model on the discrepancies in the calculated design values of the structural forces, between the different factoring combinations and strategies.

Moreover, the study of case histories where a prop was accidentally lost will enable comparisons between the prop loads from the field measurements with the values predicted from the 3D FE analysis using different constitutive models. This will facilitate a comprehensive investigation of the findings of this thesis and provide a better insight into the three-dimensional prop loss effect.

The work on the HYD verification using FE methods presents a comprehensive study on the subject focusing on plane strain two dimensional problems. Further studies

need to address the applicability of the conclusions for axi-symmetry problems (e.g. circular excavations). Moreover, Aulbach and Ziegler (2014) have investigated that hydraulic heave is most critical in the corners of excavation pits. Therefore, a further study should also examine whether the conclusions are also applicable for 3D problems.

REFERENCE LIST

AASHTO (2007). *LRFD Bridge Design Specifications (4th Edition).* American Association of State Highway and Transportation Officials.

Alpan, I., (1970). *The Geotechnical Properties of Soils*. Earth Science Reviews, Elsevier, (6), pp 5-49.

American Petroleum Institute (2003). *Recommended practice for planning, designing and constructing fixed offshore platforms - Load and Resistance Factor Design*. American Petroleum Institute.

Anagnostopoulos, A.G. and Frank, R. (2010). *EC7: Eurocode 7: an "umbrella code" its implementation, evolution and impact worldwide.* Proc. 6th Hellenic Conference on Geotechnical & Geoenvironmental Engineering, Volos.

Anderson, S. (2012). *Geotechnical design of retaining wall support systems.* ICE Manual of Geotechnical Engineering. Volume II Geotechnical Design, Construction and Verification. Chapter 65, pp. 1001-1009. Institution of Civil Engineers. London.

Arulrajah, A. and Bo, M.W. (2008). *Characteristics of Singapore Marine Clay at Changi.* Geotech Geol Eng (2008) 26, pp. 431-441.

Arup (1991). *End of Construction (Undrained) Settlement of Structures on London Clay. Addendum Report on Settlement of Structures on Overconsolidated Clays.* Arup Geotechnics, October 1991, London.

Atkinson, J.H. and Sallfors, G. (1991). *Experimental determination of soil properties*. In: Proceedings of the 10th ECSMFE, vol. 3, Florence, pp. 915-956.

Aulbach, B. and Ziegler, M. (2013). Simplified design of excavation support and shafts for safety against hydraulic heave. *Geotechnics and Tunnelling*, pp. 362-374.A

Aulbach, B. and Ziegler, M. (2014). Versagensform und Nachweisform beim hydraulischen Grundbruch – Plädoyer für den Terzaghi-Körper, Geotechnik, pp. 6-18.

Batten, M. and Powrie, W. (2000). *Measurement and Analysis of Temporary Prop Loads at Canary Wharf Underground Station, East London*. Proceedings of the Institution of Civil Engineers, Geotechnical Engineering, Vol. 143, pp. 151-163.

Bauduin, C., De Vos, M., Simpson, B., (2000). *Some Considerations on the Use of Finite Element Methods in Ultimate Limit State Design.* LSD 2000 International Workshop on Limit State Design in Geotechnical Engineering Melbourne, Australia.

Bauduin, C., Bakker, K.J., Frank, R. (2005). *Use of Finite Element Methods in Geotechnical Ultimate Limit State Design.* Proc. XVI ICSMGE, Osaka, pp. 2775-2779.

BAW (2013). *Code of Practice: Internal Erosion (MMB).* German Federal Waterways Engineering and Research Institute, Karlsruhe.

Beeby, A.W. and Simpson, B. (2001). *A proposal for partial safety factors for soil pressures in BS 8110.* The Structural Engineer. Vol. 79, 2001.

Bélidor B.F. (1729). *La science des ingenieurs dans la conduite des travaux de fortifications et d'architecture civil.* Jombert, Paris

Benmebarek, N., Benmebarek, S., and Kastner, R. (2005). *Numerical studies of seepage failure of sand within a cofferdam.* Computers and Geotechnics, pp. 264-273.

Benz, T. (2007). *Small-strain stiffness of soils and its numerical consequences*. PhD, Universitat Stuttgart.

Bird, M.I., Chang, C.H., Shirlaw, J.N., Tan, T.S. and The, T.S. (2003). *The age and origin of the Quaternary sediments of Singapore, with emphasis on the marine clay. Workshop 'Updating the Engineering Geology of Singapore*. In Proc. Underground Singapore 2003. November. NTU. Singapore. pp. 428-440.

Bishop, A.W., Webb, D.L. and Lewin, P.I. (1965). *Undisturbed samples of London Clay from the Ashford Common shaft: strength-effective stress relationships*. Géotechnique. Vol. 15, No.1, pp. 1-31.

Bjerrum, L., Clausen, C.J. and Duncan, J.M. (1972). *Earth pressures on flexible structures.* 5th European conference on Soil Mechanics and Foundation Engineering. Madrid, Spain, Vol. 2.

Bo M.W, Arulrajah A. and Choa V. (1998). *Hydraulic conductivity of Singapore marine clay*. Q J Eng Geol 31(4), pp. 291-299.

Bo M.W., Chang M.F., Arulrajah A. and Choa V. (2000). *Undrained shear strength of the Singapore marine clay at Changi from in situ tests*. Geotech Eng J Southeast Asian Geotech Soc 31(2), pp. 91-107.

Bolton M.D. (1993a)*. What are partial factors for?* Proc. International Symposium on Limit State Design in Geotechnical Engineering, Copenhagen, Danish Geotechnical Society for ISSMFE TC 23, in DGF Bulletin 10, May, 3, pp. 565-583.

Bolton M.D. (1993b). *Codes, standards and design guides, Proceedings International Conference on Retaining Structures.* Institution of Civil Engineers, Robinson College, Cambridge, July 1992; in Retaining Structures, pp. 387-402, Thomas Telford, London.

Bond, A. (2013)*. Implementation and evolution of Eurocode 7.* Modern Geotechnical Design Codes of Practice, P. Arnold et al. (Eds.), IOS Press.

Bond, A. (2016). *Towards the second generation of Eurocode 7*. ISSMGE – ETC 3 International Symposium on Design of Piles in Europe. Leuven, Belgium, April 2016.

Bond A. and Harris A. (2008)*. Decoding Eurocode 7.* Taylor & Francis London.

Brinch Hansen, J. (1956). *Limit design and safety factors in soil mechanics,* Danish Geotechnical Institute, Bulletin No. 1.

Brinkgreve, R.B.J., and Bakker, H.L. (1991). *Non-linear finite element analysis of safety factors.* Proc. of the 7th International Conference on Computer Methods and Advances in Geomechanics, Beer, Booker and Carter eds. Bakelma, Rotterdam, pp. 1117-1122.

Brinkgreve, R.B.J. and Post, M. (2015). *Geotechnical Ultimate Limit State Design Using Finite Elements.* Geotechnical Safety and Risk V T. Schweckendiek et al. (Eds.), pp. 464-469.

Brinkgreve, R.B.J., Kappert, M.H. and Bonnier, P.G. (2007). *Hysteretic damping in a small-strain stiffness model.* Numerical Models in Geomechanics. NUMOGX. Pande and Pietruszczak (eds). Taylor & Francis Group, London.

British Geological Survey, (2004). *Geology of London*, Special Memoir 256, 257, 270 and 271 (England and Wales). Keyworth, Nottingham.

Brooker, E.W. and Ireland, H.O. (1965). *Earth pressures at rest related to stress history.* Canadian Geotechnical Journal, Vol. 2, No. 1, pp. 1-15.

BS 8002 (1994). *Code of practice for earth retaining structures,* British Standards Institution, London.

BS 8002 (2015). *Code of practice for earth retaining structures.* British Standards Institution, London.

BS 8004 (2015). *Code of practice for foundations.* British Standards Institution, London.

BS 8081 (1989). *Code of practice for grouted anchors.* British Standards Institution, London.

BS 8081 (2015). *Code of practice for grouted anchors.* British Standards Institution, London.

BS EN 1990 (200*2*). *Eurocode – Basis of structural design.* British Standards Institution, London.

BS EN 1997-1 (2004). *Eurocode 7 – Geotechnical design, Part 1 – general rules,* British Standards Institution, London.

BS NA EN 1991-1-7 (2006). *UK National Annex to Eurocode 1 Actions on Structures-Accidental Conditions*. British Standards Institution, London.

Burland, J.B. (1989). *The Ninth Bjerrum Mem. Lecture: Small is beautiful - the stiffness of soils at small strains*. Can. Geotech. Journ., Vol. 26, pp. 499-516.

Burland, J.B. and Kalra, C.J. (1986). *Queen Elizabeth II Conference Centre: Geotechnical Aspects.* Proc. Institution of Civil Engineers, Part 1, 80, pp. 1479-1503.

Burland, J.B., Simpson, B. and St John, H.D. (1979). *Movements around excavations in London Clay*. Proc. 7th Eur. Conf. Soil Mech., Brighton 1, pp. 13-30.

Butler, F.G. (1975). *General report and state-of-the art review*. Session 3-Proceedings of the Conference on settlement of structures, Cambridge. Pentech Press. London 1975, pp. 531-78.

Canadian Geotechnical Society (2006). *Canadian Foundation Engineering Manual (4th Edition)*. Canadian Geotechnical Society.

Carter, J.P., Desai, C.S., Potts, D.M., Schweiger, H.F. and Sloan, S.W. (2000*). Computing and computer modelling in geotechnical engineering.* Proc. GeoEng 2000,

Int. Conf. on Geotechnical and Geological Engineering, Melbourne. Technomic, pp. 1157-1252.

CEN/TC 250 (2013). Response to Mandate M/515, 'Towards a second generation of EN Eurocodes', CEN/TC250, document N993.

Chambers, P., Augarde, C.E., Reed, S. and Dobbins, A. (2016). *Temporary propping at Crossrail Paddington station*. Geotechnical research, 3 (1), pp. 3-16.

Chandler, R.J. and Apted, J.P. (1988). *The effects of weathering on the strength of London Clay*. Quart. Journal of Engineering Geology, London, Vol. 21, pp. 59-68.

Chandler, R.J. (2000). *Clay sediments in Depositional Basin: the Geotechnical Cycle.* Quart. Journal of Engineering Geology and Hydrogeology, Vol.33, pp. 7-39.

Choa, V., Bo, M.W. and Chu J. (2001). *Soil improvement works for Changi East Reclamation Project*. Ground Improvement. Vol. 5, No. 4, pp. 141-153.

Clarke, S. (2009). *Enhancement of the BRICK constitutive model to incorporate viscous soil behaviour*. PhD thesis. University of Sheffield.

Clough, G.W., Smith, E. W. and Sweeney, B. P. (1989). *Movement control of excavation support system by iterative design.* Foundation Engineering Current Principles and Practices, Vol.2 ASCE, New York, NY, 1989, pp.869-882.

Collins, I.F. and Kelly, P.A. (2002). *A thermo-mechanical analysis of a family of soil models*. Géotechnique. Vol. 52, No. 7, pp. 507-518.

Cooling, L. F. and Skempton, A. W. (1942). *A Laboratory Study of London Clay*. J. Inst. Civ. Eng. 17, pp. 251-276.

Coulomb, C. A. (1773*). Essai sur une application des regles des maximis et minimis a quelquels problemesde statique relatifs, a la architecture.* Mem. Acad. Roy. Div. Sav., vol. 7, pp. 343–387.

Crossrail Ltd (2009). *Underground Box Structures and Deep Foundations. Civil Engineering Standard - Part 3*. Document number CR-STD-303-3. August 2009. London.

Das, B. (1983). *Advanced Soil Mechanics.* McGraw-Hill. New York.

Davidenkoff, RN. (1954). *Zur berechnung des hydraulischen grundbruches*. Wasserwirtschaft 1954(46), pp. 298–307.

Dong, Y. (2014). *Advanced Finite Element Analysis of Deep Excavation Case Histories.* PhD Thesis, Oxford University.

DS 415 (1965). *Code of practice for foundation engineering*. Dansk Ingeniørforening.

Duncan, J.M. and Chang, C.M. (1970). *Nonlinear analysis of stress and strain in soils.* Journal of Soil Mechanics and Foundations Division, ASCE, 96 (SM5), pp. 1629-1653.

EAB (2014). *Recommendations on Excavations.* 3rd Edition. Edited by the German Geotechnical Society. Ernst & Sohn.

Ellison, K.C. (2012). *Constitutive modelling of a heavily overconsolidated clay. PhD thesis.* Cambridge University.

Ellison, K.C. and Soga, K. and Simpson, B. (2012). *A strain space soil model with evolving stiffness anisotropy.* Géotechnique, Vol. 62, pp. 627-641.

Ellison, K.C., Soga, K. and Simpson, B. (2010). *An examination of strain space versus stress space for the formulation of elastoplastic constitutive models*. Proc. 7th European Conference on Numerical Methods in Geotechnical Engineering, pp. 33-38.

European Commission (2016). *The European Construction Sector – A Global Partner*. http://ec.europa.eu/growth/tool-sdatabases/newsroom/cf/itemdetail.cfm?item_id=8753

Evolution Group 9 - Water Pressures. (2014). *Final report to TC250/SC7 Evolution of Eurocode 7 Part 1*. July 2014.

Frank, R. (2006). *Some aspects of soil-structure interaction according to Eurocode 7 'Geotechnical design'.* Engenharia Civil. UM 2006/25, pp. 5-16.

Frank, R., Bauduin, C., Kavvadas, M., Krebs Ovesen, N., Orr, T., and Schuppener, B. (2004). *Designers' guide to EN 1997-1: Eurocode 7: Geotechnical design – General rules.* London: Thomas Telford.

Fuentes, R., Pillai, A. and Devriendt, M. (2010). Short term three dimensional back-analysis of the One New Change basement in London. *Proc. 7th European Conference on Numerical Methods in Geotechnical Engineering*, pp. 741-748.

Gaba, A, Hardy, S, Doughty, L, Powrie, W, Selemetas, D. (2016). Guidance on embedded retaining wall design. CIRIA Report C760, London: CIRIA.

Gaba, A. R., Simpson, B., Powrie, W., and Beadman, D. R. (2003). *Embedded retaining walls - guidance for economic design.* CIRIA Report C580, London: CIRIA.

Gasparre, A. (2005*). Advanced laboratory characterization of London Clay*. PhD thesis, Imperial College London (downloadable from www.imperial.ac.uk/geotechnics).

Gasparre, A., Nishimura, S., Coop, M.R. and Jardine, R.J. (2007a). *The influence of structure on the behaviour of London Clay*. Géotechnique. Vol. 57, No. 1, pp. 19-31.

Gasparre, A., Nishimura, S., Minh, N.A., Coop, M.R. and Jardine, R.J. (2007b). *The stiffness of natural London Clay.* Géotechnique. Vol. 57, No. 1, pp. 33-47.

GCO (1990). *Review of Design Methods for Excavations*. GCO Publication No. 1/90, Geotechnical Control Office, Hong Kong, 192p.

Gray, D.A. and Foster, S.S.D. (1972). *Urban influences upon groundwater conditions in the Thames flood plain deposits of central London.* Philosophical Transactions of the Royal Society of London A 272, pp. 245-257.

Gunn, M.J. and Clayton, C.R.I. (1992). *Installation effects and their importance in the design of earth-retaining structures.* Géotechnique. Vol. 42(1), pp. 137-141.

Hardin, B.O. and Drnevich, V.P. (1972). *Shear modulus and damping in soils: design equations and curves.* Journal of the Soil Mechanics and Foundations Division (ASCE), Vol. 98, No. SM7, pp. 667-691.

Harr, M. (1962). *Groundwater and Seepage.* McGraw-Hill. New York.

Heibaum, M. and Herten, M. (2009). *Geotechnical verifications using the finite-element method?* Ernst & Sohn Verlag für Architektur und technische Wissenschaften GmbH & Co. KG, Berlin, Bautechnik Special issue 2009 – Geotechnical Engineering, pp. 7-15.

Heibaum, M. and Herten, M. (2010). *Verifications in accordance with EC7/DIN 1054 using numerical methods.* Proc. 14th Danube-European Conference on Geotechnical Engineering, Bratislava, Slovak Republic, June 2-4, 2010.

Henkel, D.J. (1957). *Investigations of two long-term failures in London Clay slopes at Wood Green and Northolt*. Proc. 4th Int. Conf. Soil Mech. Found. Engng, London 2, pp. 315-320.

Hewitt, P. (1989). *Settlements of Structures on Overconsolidated Clay*. Master of Engineering Thesis. School of Civil and Mining Engineering. The University of Sydney.

Hight, D.W. and Jardine, R.J. (1993). *Small strain stiffness and strength characteristics of hard London Clay Tertiary clays*. Proc. Int. Symp. On Hard Soils-Soft Rocks, Athens, Greece, Vol. 1, pp. 533-522, Balkema, Rotterdam.

Hight, D.W., Gasparre, A., Nishimura, S., Minh, N. A., Jardine, R. J. & Coop, M.R. (2007). *Characteristics of the London Clay from the Terminal 5 site at Heathrow Airport.* Géotechnique. Vol. 57, No. 1, pp. 3-18.

Hight, D.W., McMillan, F., Powell, J.J.M., Jardine, R.J. and Allenou, C.P. (2003). *Some characteristics of London Clay*. Proc. Conf. Characterisation and Engineering, National University Singapore. Tan T.S., Phoon, K.K., Hight D.W., Lerouil S. (eds). Balkema, Vol. 2, pp. 851-907.

Hooper, J.A. (1974). Observations on the behaviour of a piled raft foundation on London Clay. Proceedings of the Institution of Civil Engineers. Volume 55 Issue 4, December 1973, pp. 855-877, Part 2.

Houlsby, G.T. (1981). *A Study of Plasticity Theories and Their Applicability to Soils.* Ph.D. Thesis, University of Cambridge.

Houlsby, G.T. and Wroth, C.P. (1991). *The variation of shear modulus of a clay with pressure and overconsolidation ratio*. Soils and Foundations. Vol. 31, No. 3, pp. 138-143.

Jaky, J. (1944). *The coefficient of earth pressure at rest.* Journal of the Society of Hungarian Architects and Engineers. Vol. 78, 22, pp. 355-358.

Jardine, R.J., Potts, D.M., Fourie, A.B. and Burland, J.B. (1986). *Studies of the influence of non-linear stress strain characteristics in soil structure interaction*. Géotechnique, Vol. 36, No 3, pp. 377-396.

Jardine, R.J., Symes, M.J.R.P. and Burland, J.B. (1984). *The measurement of soil stiffness in the triaxial apparatus*. Géotechnique, Vol. 34, No. 3, pp. 232-340.

Jovicic, V., Coop, M. and Simpson, B. (2006). *Interpretation and modelling of deformation characteristics of a stiff North Sea clay*. Canadian Geotechnical Journal. Vol. 35, No. 1, pp. 115-130.

JRC Science for Policy Report. (2015). State of Implementation of the Eurocodes in the European Union. European Commission.

Kashef, A. (1986). *Groundwater Engineering.* McGraw Hill. New York.

Katsigiannis, G., Ferreira, P. and Fuentes, R. (2014). *Ultimate Limit State design of retaining walls with numerical methods*, Numerical Methods in Geotechnical Engineering 2014 – Hicks, Brinkgreve & Rohe (Eds), Vol. 1, pp 385-390, Taylor & Francis Group, London.

Katsigiannis, G., Schweiger, H.F., Ferreira, P. and Fuentes, R. (2015b). *Design of deep supported excavations: comparison between numerical and empirical methods*. Geotechnical Safety and Risk V T. Schweckendiek et al. (Eds.) IOS Press. doi: 10.3233/978-1-61499-580-7-479.

Katsigiannis, G, Schweiger, H.F., Simpson, B., Ferreira, P. and Fuentes, R. (2015a). *Eurocode 7 and new design challenges using numerical methods with different soil models.* In XVI European Conference on Soil Mechanics and Geotechnical Engineering, 13-17 Sep 2015, Edinburgh. ICE Publishing, pp. 4277-4282.

King, C. (1981). *The stratigraphy of the London Basin and associated deposits*. Tertiary Research Special Paper, Vol. 6, Backhuys, Rotterdam.

King, C. (1991). *Stratigraphy of the London Clay (Early Eocene) in the Hampshire Basin*. PhD Thesis, Kingstone Polytechnic.

Kolymbas, D. (1991). *An outline of hypoplasticity*, Arch. Appl. Mech. 61, pp. 143-151.

Lees, A. (2013). *Using numerical analysis with geotechnical design codes.* Modern Geotechnical Design Codes of Practice. P. Arnold et al. (eds.), IOS Press 2013, pp. 157-170.

Lees, A. (2016). *Can FE analysis be used with design codes?* Geotechnical Finite Element Analysis - A Practical Guide. ICE Publishing, London.

Lees, A. and Perdikou, S. (2010). *Embedded cantilever retaining wall ULS design by FEA in accordance with EN 1997-1.* Numerical Methods in Geotechnical Engineering – Benz & Nordal (eds). Taylor & Francis Group, London, ISBN 978-0-415-59239-0.

Lehane, B. and Simpson, B. (2000). *Modelling glacial till conditions using a BRICK soil model*. Canadian Geotechnical Journal 37, No. 5, pp. 1078-1088.

Li, X.S. and Dafalias, Y.F. (2000). *Dilatancy for cohensioless soils.* Géotechnique. Vol. 50, No 4, pp. 449-460.

Long, M. (2001). *Database for Retaining Wall and Ground Movements due to Deep Excavations.* J. Geotech. Geoenviron. Eng., 127(3), pp. 203-224.

LTA (2010). *Civil design criteria for road and rail transit systems*. Land Transport Authority, Singapore.

M/515 EN Mandate for amending existing Eurocodes and extending the scope of Structural Eurocodes. (2012). European Commission Enterprise and Industry Directorate-General, Brussels, 12 December 2012.

Marsland, A. (1953). *Model experiments to study the influence of seepage on the stability of a sheeted excavation in sand*. Géotechnique. The Institution of Civil Engineers. London. 4(7), pp. 223-41.

Mayne, P. W. and Kulhawy, F.H. (1982). *K_0-OCR relationships in clay.* J. Geotech. Engng Div. ASCE 108, No. GT6, pp 851-870.

McNamee, J. (1949). *Seepage into a sheeted excavation*. Géotechnique. The Institution of Civil Engineers. London 1949; 4(1), pp. 229-41.

Meyerhof G.G. (1994). *Evolution of Safety Factors and Geotechnical Limit State Design,* The Second Spencer J. Buchanan Lecture, Texas A&M University

Minh, N. (2006). The anisotropic stress-strain-strength characteristics of London Clay in hollow cylinder apparatus. PhD Thesis, Imperial College London.

Niemunis, A. and Herle, I. (1997). *Hypoplastic Model for Cohesionless Soils with Elastic Strain Range.* Mechanics of Cohesive-Frictional Materials, Vol. 2, pp. 279-299.

Nishimura, S. (2005). *Laboratory study on anisotropy of natural London Clay*. PhD thesis, Imperial College, University of London, London, UK.

Nishimura, S., Minh, A.N. and Jardine, R.J. (2007). *Shear strength anisotropy of natural London Clay*. Géotechnique, Vol. 57, No. 1, pp. 49-62.

O'Brien, A.S. and Sharp, P. (2001). *Settlement and heave of over-consolidated clays - a simplified non-linear method of calculation.* Ground Engineering. October 2001, pp 28-32.

Odenwald, B., and Stelzer, O. (2013). *Nachweis gegen hydraulischen Grundbruch mit FEM auf Grundlage des EC7.* Workshop Bemessen mit numerischen Methoden. Veröffentlichungen des Institutes Geotechnik und Baubetrieb TU Hamburg, pp. 88-110.

Orr T.L.L. and Farrell E.R. (1999). *Geotechnical design to Eurocode 7.* London: Springer Verlag, 1999.

Orr T.L.L. (2000). *Selection of characteristic values and partial factors in geotechnical designs to Eurocode 7.* Computers and Geotechnics, Vol. 26(3), pp. 263-279.

Orr T.L.L. (2005). *Model Solutions for Eurocode 7 Workshop Examples.* Dublin: Trinity College.

Orr T.L.L. (2007). *The Development and Implementation of Eurocode 7.* Meeting of the Geotechnical Society of Ireland Society at Engineers, Ireland, 6th November 2007.

Orr T.L.L. (2012). *How Eurocode 7 has affected geotechnical design: a review,* Proceedings of the ICE - Geotechnical Engineering, Vol. 165, Issue 6, December 2012, pp. 337-350.

Orr T.L.L. (2013). *Implementing Eurocode 7 to achieve reliable geotechnical designs.* Modern Geotechnical Design Codes, P. Arnold et al. (eds.), IOS Press 2013, pp. 72-86.

Orr T.L.L. (2017). *Defining and selecting characteristic values of geotechnical parameters for designs to Eurocode 7.* Georisk: Assessment and Management of Risk for Engineered Systems and Geohazards Vol. 11, Iss. 1, 2017.

Padfield, C.J. and Mair, R.J. (1984). Design of Retaining Walls Embedded in Stiff Clay. Construction Industry Research and Information Association. CIRIA Report R104.

Pantelidou, H. and Simpson, B. (2007). *Geotechnical variation of London clay across central London*. Géotechnique. Vol. 57, No. 1, pp. 101–112.

Patel, D.C. (1992). *Interpretation of results of pile tests in London Clay*. Piling European practice and worldwide trends. pp. 100-110. Thomas Telford, London.

Peck, R.B. (1969). *Deep excavations and tunnelling in soft ground*. Proc. 7th Int. Conf. SMFE. Mexico City. State-of-the-art vol., pp. 225-290.

Pillai (Kanapathipillai), A. (1996). *Review of the BRICK model of soil behaviour*. MSc dissertation, Imperial College, London.

Plaxis (2015). Plaxis 2D Material Models Manual. Plaxis bv. Delft, the Netherlands.

Potts, D.M. (2003). *Numerical analysis: a virtual dream or a practical reality?* Géotechnique, Vol. 53, No. 6, pp. 535-573.

Potts, D.M. and Burland, J.B. (1983). *A parametric study of the stability of embedded retaining structures.* TRRL Supplementary Report 813, Transport and Road Research Laboratory, Crowthorne, Berkshire, 50p.

Potts, D.M. and Fourie, A.B. (1984). *The behaviour of a propped retaining wall: results of a numerical experiment*. Géotechnique. Vol. 34, pp. 383-404.

Potts, D.M. and Zdravkovic, L. (1999). *Finite element analysis in geotechnical engineering: theory,* London, Thomas Telford.

Potts, D.M. and Zdravkovic, L. (2012). *Accounting for partial material factors in numerical analysis,* Géotechnique, Vol. 62, ISSN:0016-8505, Pages:1053-1065.

Powrie, W. and Batten, M. (2000). *Comparison of measured and calculated temporary prop loads at Canada Water station*. Géotechnique. Vol. 50(2), pp. 127-140.

Powrie, W., Chandler, R.J., Cardner, D.R. and Watson, G.V.R. (1999). *Back-analysis of an embedded retaining wall with stabilizing base slab*. Proc. Instn. Civ. Engrs. Geot. Eng. 137, pp. 75-86.

Powrie, W., Pantelidou, H. and Stallebrass, S.E. (1998). *Soil stiffness in stress paths relevant to diaphragm walls in clay*. Géotechnique. Vol. 48(4), pp. 483-494.

Price, M. and Reed, D.W. (1989). *The influence of mains leakage and urban drainage on groundwater levels beneath conurbations in the UK.* Proceedings Institution of Civil Engineers 86 (1), pp. 31–39.

Roscoe, H. and Burland, J.B. (1968). *On the generalised stress-strain behaviour of wet clay*. Engineering Plasticity, edited by J. Heyman and F.A. Leckie, pp. 535-609, Cambridge University Press.

Roscoe, H. and Twine, D. (2010). *Design and performance of retaining walls.* Proceedings of the Institution of Civil Engineers. Vol. 163, Issue 5. October 2010, pp. 279-290.

Rowe, P.W. (1962). *The stress dilatancy relation for static equilibrium of an assembly of particles in contact.* Proc. R. Sot. 269A, pp. 500-527.

Royse, K.R., de Freitas, M., Burgess, W.G., Cosgrove, J., Ghail, R.C., Gibbard, P., King, C., Lawrence, U., Mortimore, R.N., Owen, H. and Skipper, J. (2012). *Geology of London, UK.* Proc. Geol. Ass. 123, pp. 22-45.

Ryner, A., Fredriksson, A., and Stille, H. (1996). *Sponthandboken: handbok för konstruktion och utformning av sponter.* Byggforskningsrådet T18:1996.

Santos, J.A. and Correia, A. (2001). *Reference threshold shear strain of soil. Its application to obtain a unique strain-dependent shear modulus curve for soil*. XV International Conference on Soil Mechanics and Geotechnical Engineering, Istanbul, Turkey.

Schanz, T. (1998). *Zur Modellierung des Mechanischen Verhaltens von Reibungsmaterialen*. Habilitation. Stuttgart University.

Schanz, T., Vermeer, P.A. and Bonnier, P.G. (1999). The hardening soil model: formulation and verification. Beyond 200 in Computational Geotechnics – 10 years of Plaxis, Balkelma, Rotterdam.

Schweiger, H.F. (2002). *Some Remarks on pore pressure parameters A and B in undrained analyses with the Hardening Soil model.* Plaxis Bulletin No 12, June 2002. Delft, the Netherlands.

Schweiger, H.F. (2005). *Application of FEM to ULS design (Eurocodes) in surface and near surface geotechnical structures.* Proc. 11th Int. Conf. Computer Methods and Advances in Geomechanics (G. Barla, M. Barla eds.), Patron Editore, Bologna, 2005, Vol.4, pp. 419-430.

Schweiger, H.F. (2009). *Influence of constitutive model and EC7 design approach in FEM analysis of deep excavations.* Proceeding of ISSMGE International Seminar on Deep Excavations and Retaining Structures, Budapest, pp. 99 – 114.

Schweiger, H.F. (2010). *Design of deep excavations with FEM - Influence of constitutive model and comparison of EC7 design approaches,* Proc. of the 2010 Earth Retention Conference (Finno, R.J., Hashash, Y.M.A., Arduino, P., eds.) Bellevue, Washington, USA, 1.-4. August 2010, ASCE, pp. 804-817.

Schweiger, H.F. (2014). *Influence of EC7 design approaches on the design of deep excavations with FEM.* Ernst & Sohn Verlag für Architektur und technische Wissenschaften GmbH & Co. KG, Berlin, geotechnik 37 (2014), Heft 3, pp. 169-176.

SCOUT. (2007). D18 Report on Observational Method under the Framework of Eurocodes. European Commission Sixth Framework Programme. Project no: 516290. Report ref no: SB.DTTAP-NOT- 6.045. Arup Geotechnics.

Shohet, D.C. (1995). *Prediction of in-situ horizontal stresses in clay soils from the measurement of undrained shear strength, plasticity index and vertical effective stress.* Geotechnical Engineering, Vol. 13, pp. 206-214.

Simpson, B. (1992). *Retaining Structures: Displacement and Design*. Géotechnique. Vol. 42, No 4, pp. 541-576.

Simpson, B. (2007). *Approaches to ULS design - The merits of Design Approach 1 in Eurocode 7.* ISGSR2007 First International Symposium on Geotechnical Safety & Risk, pp. 527-538. Shanghai Tongji University, China.

Simpson, B. (2011). *Water pressures.* Proc. 2nd International Workshop on Evaluation of Eurocode 7. Pavia. 12-14 April 2010.

Simpson, B. (2012). *Eurocode 7 – fundamental issues and some implications for users.* 16th Nordic Geotechnical Meeting. Copenhagen: Danish Geotechnical Society. pp. 29-52.

Simpson, B. and Driscoll, R. (1998). *Eurocode 7 - a commentary.* Construction Research Communications Ltd, Watford, UK.

Simpson, B. and Yazdchi, M. (2003). *Use of finite element methods in ultimate limit state design,* LSD 2003: International workshop in Limit State Design in Geotechnical Engineering Practice, Cambridge, Massachusetts.

Simpson, B. and Hocombe, T. (2010). *Implications of modern design codes for earth retaining structures.* Proc. ER2010, ASCE Earth Retention Conference 3, Seattle, August 2010.

Simpson, B. and Junaideen, S.M. (2013). *Use of numerical analysis with Eurocode 7.* 18th Southeast Asian Geotechnical & Inaugural AGSSEA Conference 29 - 31 May 2013. Singapore Leung. Goh & Shen (eds).

Simpson, B., and Katsigiannis, G. (2015). *Safety Considerations for the HYD Limit State.* XVI European Conference on Soil Mechanics and Geotechnical Engineering. Edinburgh: ICE Publishing, pp. 4325-4330.

Simpson, B., O' Riordan, N.J. and Croft, D.D. (1979). *A computer model for the analysis of ground movements in London Clay*. Géotechnique, Vol. 29, No. 2, pp. 149-175.

Simpson, B., Calbresi, G., Sommer, H. and Wallays, M. (1981). *Design parameters for stiff clays.* Proc. Of 7th Eur. Conf. on Soil Mech. And Found. Eng., Brighton, British Geotechnical Soc., London. Vol. 5, pp. 91-125.

Simpson, B., Blower, T., Craig, R.N. and Wilkinson, W. B. (1989). *The engineering implications of rising groundwater levels in the deep aquifer beneath London*. CIRIA Special Publication 89, 1989, London.

Simpson, B., Nicholson, D.P., Banfi, M., Grose, W.G. and Davies, R.V. (2008). *Collapse of the Nicoll Highway excavation, Singapore.* Proc. Fourth International Forensic Engineering Conference. Thomas Telford.

Simpson, B., Morrison, P., Yasuda, S., Townsend, B., and Gazetas, G. (2009). *State of the art report: Analysis and design*. Proc. 17th Int. Conf. SMGE, Alexandria, Vol. 4, pp. 2873-2929.

Simpson, B, Vogt, N. and van Seters A.J. (2011). *Geotechnical safety in relation to water pressures.* Proc. 3rd International Symposium on Geotechnical Safety and Risk, Munich.

Skempton, A.W. (1954). *The Pore-Pressure Coefficients A and B*. Géotechnique. Vol. 4, pp 143-147.

Skempton, A.W. (1961). Horizontal stresses in an overconsolidated Eocene clay, Proc. 5th ICSMFE, Paris 1, pp. 351-357.

Skempton, A.W. (1964). *The Long-term stability of clay slopes*. 4th Rankine Lecture. Géotechnique. Vol. 14, No. 2, pp. 77-101, doi:10.1680/geot.1964.14.2.77.

Skempton, A.W. and Henkel, D.J. (1957). *Tests on London Clay from deep borings at Paddington, Victoria, and South Bank.* Proceedings of 4th International Conference on Soil Mechanics, London, Vol. 1, pp. 100-106.

Skempton, A.W. and La Rochelle, P. (1965). *The Bradwell slip: a short-term failure in London Clay.* Géotechnique, Vol. 15, No 3, pp. 221-242.

Skempton, A. W., and Brogan, J. M. (1994). *Experiments on piping in sandy gravels.* Géotechnique. 44, No. 3, pp. 449-460.

Skempton, A.W., Schuster, F.R.S. and Petley D.J. (1969). *Joints and fissures in the London Clay at Wraysbury and Edgware*. Géotechnique. Vol. 19, No 2, pp. 205-217.

St John, H.J. (1975). *Field and theoretical studies of the behaviour of ground around deep excavations in London Clay*. PhD Thesis, University of Cambridge.

St. John, H.D., Potts, D.M., Jardine, R.J. and Higgins, K.G. (1992). *Prediction and performance of ground response due to construction of a deep basement at 60 Victoria Embankment.* Predictive soil mechanics. Proc. of the Wroth memorial symposium, Oxford, 1992, pp. 581-608.

Standing, J.R. and Burland, J.B. (2005). *Investigating variations in tunnelling volume loss -a case study*. Proc. Int. Conf. Geotechnical Aspects of Underground Construction in Soft ground, Amsterdam, Balkema, in print.

Stelzer, O., and Odenwald, B. (2015). *A New Stress-Based Approach for Verification of Safety Against Hydraulic Heave Based on EC7.* XVI European Conference on Soil Mechanics and Geotechnical Engineering, Edinburgh: ICE Publishing, pp. 4073-4078.

Stroud, M.A. (1987). *The Control of Groundwater*. General Report and State of the Art Review to Session 2 of IX ECSMFE Dublin.

Symons, I. and Carder, D.R. (1992). *Field measurements of embedded retaining walls.* Géotechnique. Vol. 42(1), pp. 117-126.

Tan, T. S., Phoon, K. K., Hight, D. W., Leroueil, S. (2003). *Characterisation and Engineering Properties of Natural Soils.* Swets & Zeitlinger, Netherlands.

Taylor, D. W. (1948). *Fundamentals of soil mechanics*. New York: J. Wiley.

Terzaghi, K. (1922). Der Grundbruch an Stauwerken and seine Verhiltung. *Die Wasserkraft*, pp. 445-449.

Terzaghi, K. (1943). *Theoretical Soil Mechanics,* J. Wiley and Sons, New York

Terzaghi, K. and Peck, R.B. (1967). *Soil mechanics in engineering practice (2nd edition).* John Wiley & Sons, Inc.

Terzaghi, K., Peck, R., and Mesri, G. (1996). *Soil Mechanics in Engineering Practice, 3rd edition.* John Wiley & Sons, Inc.

The Institution of Structural Engineers. (2013). *Manual for the geotechnical design of structures to Eurocode 7*. IStructE Ltd. May 2013. London.

TR26 (2010). *Technical Reference for Deep Excavation.* Spring Singapore, Singapore.

Tsui, Y. and Clough, G.W. (1974). *Plane strain approximations in finite element analysis of temporary walls.* Proceedings of the ASCE Conference on Analysis and Design in Geotechnical Engineering, Austin, Texas, Vol. 1, pp 173-198.

Twine, D. and Roscoe, H. (1999). *Temporary propping of deep excavations-guidance on design, CIRIA C517.* CIRIA, London.

Vardenega, P. and Bolton, M. (2011). *Predicting shear strength mobilisation of London Clay.* In Proceedings of the 15th European Conference on Soil Mechanics and Geotechnical Engineering. Athens, Greece. IOS Press, Amsterdam, the Netherlands, Vol. 1, pp 487-492.

Wagner, H. (2007). *Numerical Analysis of a Deep Excavation in London*. MSc Thesis. Graz University of Technology, Graz, Austria.

Ward, W.H., Marsland A. and Samuels S.G. (1965). *Properties of the London Clay at the Ashford Common shaft: in-situ and undrained strength tests*. Géotechnique. Vol. 15, No 4, pp 321-344.

Ward, W.H., Samuels S.G. and Butler, M.E. (1959). *Further studies of the proprieties of London Clay*. Géotechnique. Vol. 9, No 2, pp 33-58.

Water Resources Board. (1972). *The Hydrogeology of London Basin: With special reference to artificial recharge*. Water Resources Board, Reading, United Kingdom.

Webb, D. L. (1964). *The mechanical proprieties of undisturbed samples of London Clay and Pierre shale*. PhD. Thesis, University of London.

Williams, B., and Waite, D. (1993). *The design and construction of sheet-piled cofferdams.* London: Special publication 95. Construction Industry Research and Information Association.

Yeow, H. C. (2014). *Ultimate limit state using an advanced 'Brick' model in the finite-element method.* Proceedings of the Institution of Civil Engineers. Geotechnical Engineering. 167 December 2014. Issue GE6, pp. 537-546.

Yeow, H., and Feltham, I. (2008). *Case histories back analyses for the application of the Observational Method under Eurocodes for the SCOUT project*. 6th International Conference on Case Histories in Geotechnical Engineering. August 11-16 2008, Arlington, VA, pp. 1-13.

Yeow, H. C., Nicholson, D. P. and Simpson, B. (2006). *Comparison and Feasibility of Three-dimensional finite element modelling of deep excavations using non-linear soil models.* Proc. Int. Conf. Numerical Simulation of Construction Processes in Geotechnical Eng. for Urban Environment, pp. 29-34.

Zdravkovic, L. Potts, D.M. and St John, H.D. (2005). *Modelling of a 3D excavation in finite element analysis*, Géotechnique. Vol. 55, pp. 497-513.

APPENDIX A

The BRICK Test Program

The input of the BRICK Test program consists of three sections as shown in Figure A.1. The first section is the *Soil Parameters* section, where users enter the values of the BRICK model parameters and the stress state from which the soil will be consolidated by large strains. At this initial state of low stress, the strings are totally loose and the soil has no history. Values of the mean stress and the shear component equal to 2kPa and zero respectively are typically used. Users can also specify in this section, the number of stress iterations (i.e. the program iterates to find the correct strain increments for each stress increment) and the tolerance (i.e. the maximum permitted ratio between the apparent error in the stress increment and the magnitude of the stress increment. For all the runs performed in this study, the number of stress iterations is taken equal to 30 and the tolerance equal to 0.02. In the second section of the input, the string lengths and the ratios of the tangent shear modulus, G, to its maximum value, G_0 are specified. Each pair of values corresponds to the bottom of a step. The string lengths are specified in order of increasing magnitude and the last value of G/G_0 must be equal to zero. From the data in this section and the value of i, the critical state angle of shearing resistance, φ'_{crit} is calculated.

Finally, in the final section of the input, users can specify the stress-strain path which consists of a number of steps, each of which corresponds to one row of data. Steps can be defined as either strain steps or target stresses or a combination of both.

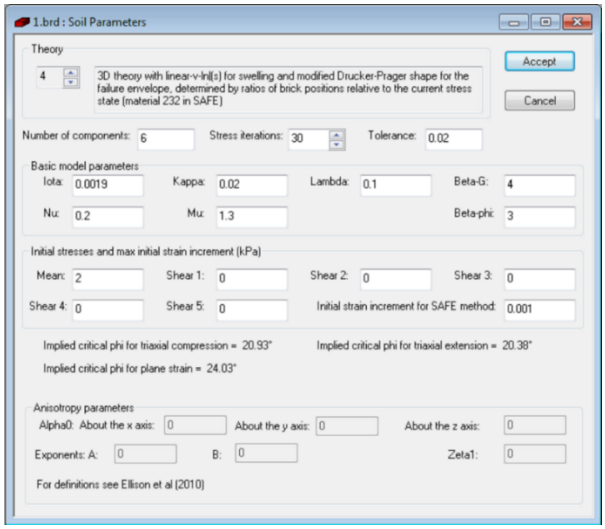

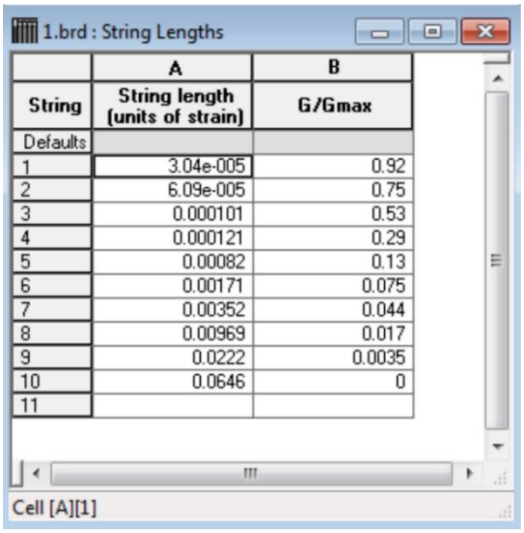

String	A: String length (units of strain)	B: G/Gmax
Defaults		
1	3.04e-005	0.92
2	6.09e-005	0.75
3	0.000101	0.53
4	0.000121	0.29
5	0.00082	0.13
6	0.00171	0.075
7	0.00352	0.044
8	0.00969	0.017
9	0.0222	0.0035
10	0.0646	0
11		

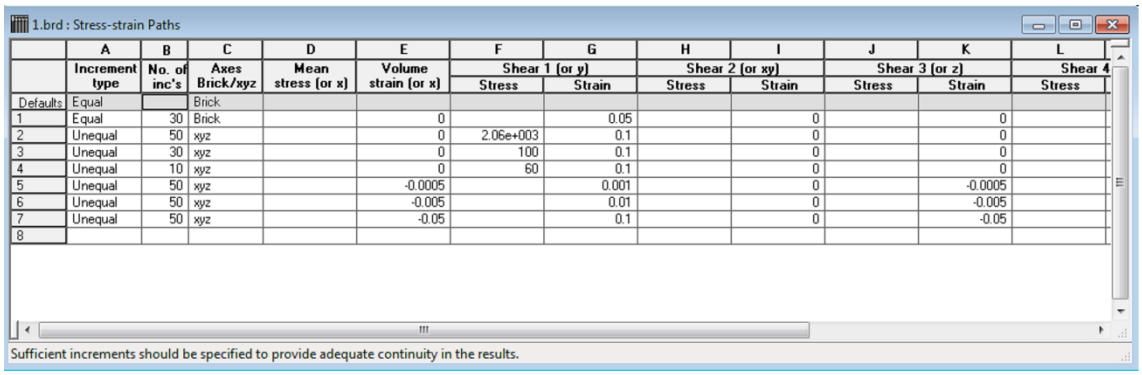

	A: Increment type	B: No. of inc's	C: Axes Brick/xyz	D: Mean stress (or x)	E: Volume strain (or x)	F: Shear 1 (or y) Stress	G: Shear 1 (or y) Strain	H: Shear 2 (or xy) Stress	I: Shear 2 (or xy) Strain	J: Shear 3 (or z) Stress	K: Shear 3 (or z) Strain	L: Shear 4 Stress
Defaults	Equal		Brick									
1	Equal	30	Brick		0		0.05		0		0	
2	Unequal	50	xyz		0	2.06e+003	0.1		0		0	
3	Unequal	30	xyz		0	100	0.1		0		0	
4	Unequal	10	xyz		0	60	0.1		0		0	
5	Unequal	50	xyz		-0.0005		0.001		0		-0.0005	
6	Unequal	50	xyz		-0.005		0.01		0		-0.005	
7	Unequal	50	xyz		-0.05		0.1		0		-0.05	
8												

Figure A.1: BRICK Test input parameters

APPENDIX B

Design prop load calculations based on pressure diagrams

In this section, the design prop loads are calculated from the empirical graphs of CIRIA C517 and EAB for the 5 different geometries: propped wall with 1, 2, 3, 4 and 5 prop levels. The use of the DPL graphs is extended tentatively for the deeper excavation cases for illustration and comparison purposes. The Distributed Pressure Loads (DPLs) suggested by Twine and Roscoe (1999) are shown in Figure B.1 while the pressure diagrams for different geometries suggested by EAB (2014) are shown in Figures B.2, B.3 and B.4.

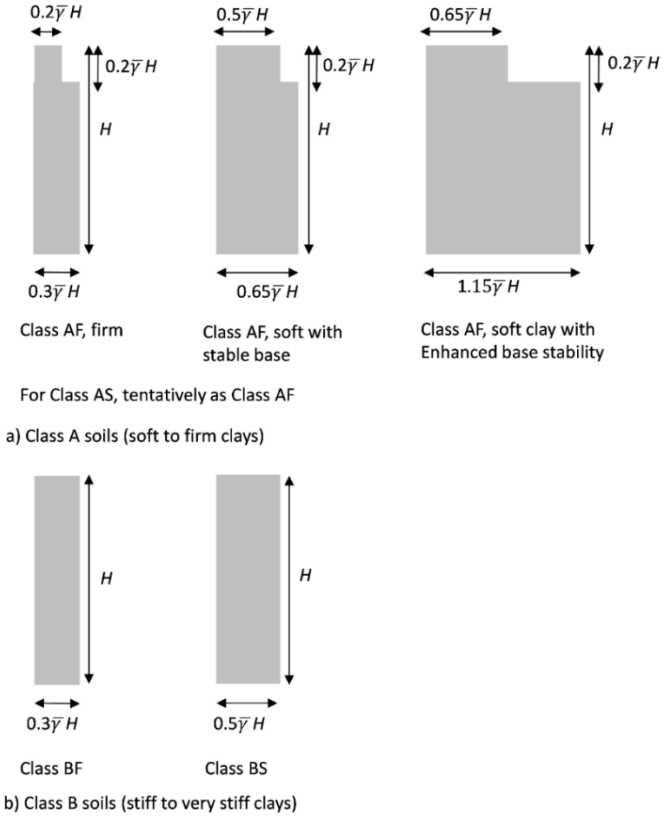

Figure B.1: Distributed Pressure Loads (DPLs) suggested by Twine and Roscoe (1999)

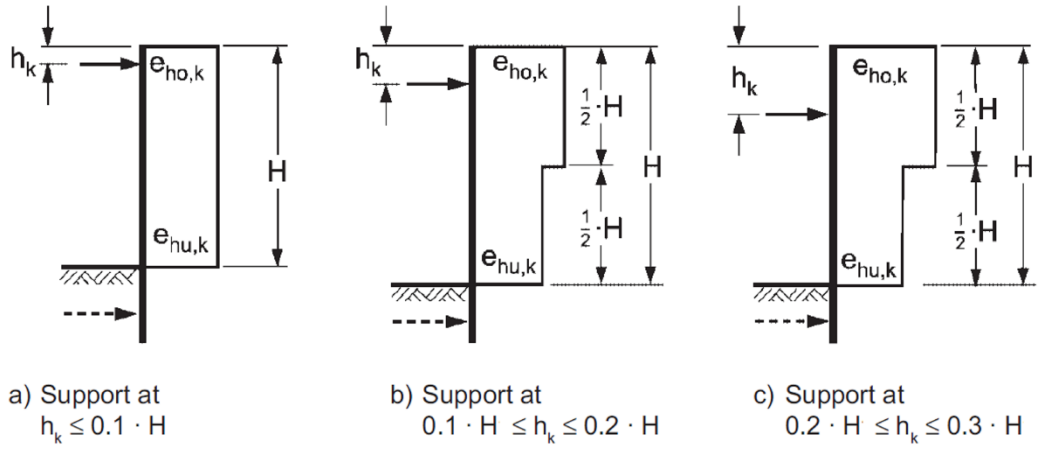

Figure B.2: Pressure diagrams for single-supported sheet pile and concrete walls after EAB (2014)

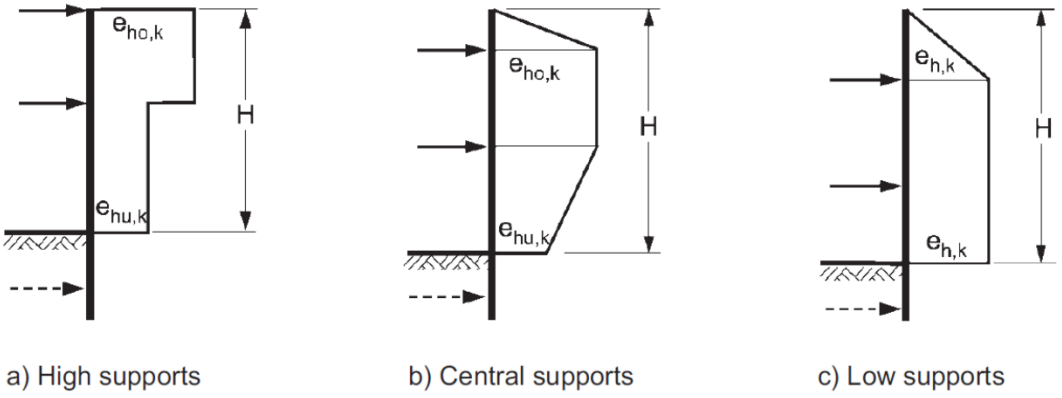

Figure B.3: Pressure diagrams for double-supported sheet pile and concrete walls after EAB (2014)

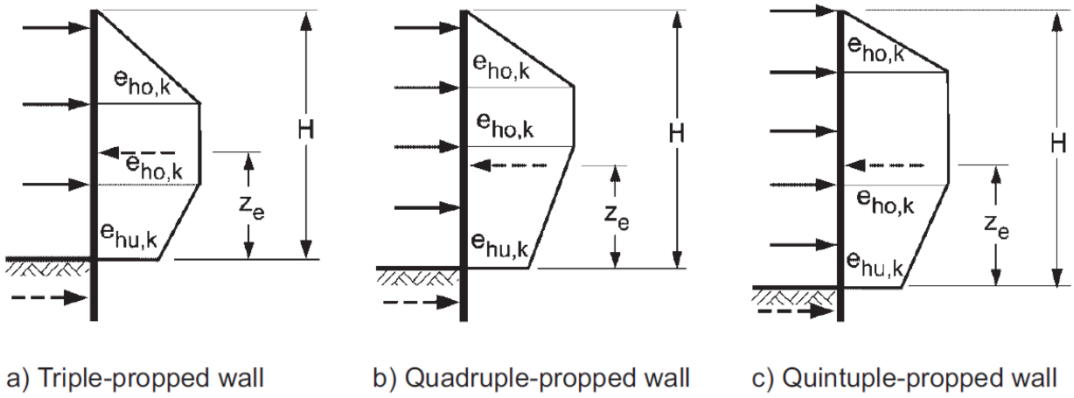

Figure B.4: Pressure diagrams for triple- and multiple-supported sheet pile and concrete walls after EAB (2014)

The process of the calculation is discussed in detail by Twine and Roscoe (1999) and is illustrated in Figure B.5. Note that the horizontal distance supported by each individual prop is not considered here and the prop loads are calculated by multiplying the pressure only with the corresponding vertical distance supported by each prop level. For the bottom prop level, only half of the distance between the prop level and the formation level of the excavation is considered, to account for the contribution of the soil on the passive side of the wall in the support of the system. In all cases, a load factor of 1.35 is introduced to the characteristic pressure values given by the diagrams to derive the design values of the pressures.

As the EAB guide provides only the way that the stresses are redistributed (i.e. the shape of the diagrams) but it does not recommend any values (i.e. the actual size of the diagrams), in this study, the area of the EAB trapezoids is taken to be equal with the corresponding area of the CIRIA rectangular. This allows for better comparisons of the way the two methods assume that the lateral pressures act on the wall.

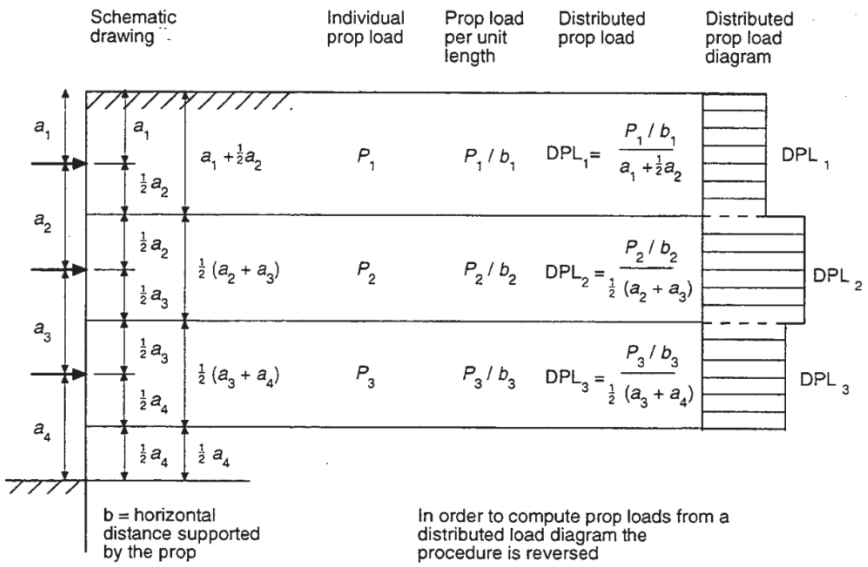

Figure B.5: Calculating the Distributed Prop Loads (after Twine and Roscoe, 1999)

DPL calculations

The characteristic DPL is given by Equation B.1 where H (m) is the excavation depth and $\bar{\gamma}$ (kN/m^3) is the average unit weight of the soils retained by the wall. The design DPL is equal to the characteristic value multiplied by a load factor of 1.35 (Twine and Roscoe, 1999).

$$DPL = 0.5\bar{\gamma}H \quad \text{(B.1)}$$

1 - Propped Wall

The average unit weight of the soils is 20kN/m^3 and the excavation depth (including the overdig) is 8.5m. From Equation B.1:

DPL = 0.5 $\bar{\gamma}H$ = 85kPa

Design value DPL = 1.35 * 85 = 114.75kPa

The vertical distance supported by the prop level based on the calculation process discussed above is 5.25m. Hence, the design prop load is calculated as follows:

P_1 = 114.75 * 5.25 = 602.4kN/m

2 - Propped Wall

Similarly, for the 2-propped wall geometry the excavation depth (including the overdig) is 12.5m. From Equation B.1:

DPL = 0.5 $\bar{\gamma}H$ = 125kPa

Design value DPL = 1.35 * 125 = 168.75kPa

The vertical distances supported by the two prop levels based on the calculation process discussed above are 4m and 5.25m respectively. Hence, the design prop loads are calculated as follows:

P_1 = 168.75 * 4 = 675kN/m

P_2 = 168.75 * 5.25 = 885.9kN/m

3 - Propped Wall

Similarly, for the 3-propped wall geometry the excavation depth (including the overdig) is 16.5m. From Equation B.1:

DPL = 0.5 $\bar{\gamma}H$ = 165kPa

Design value DPL = 1.35 * 165 = 222.75kPa

The vertical distances supported by the three prop levels based on the calculation process discussed above are 4m, 4m and 5.25m respectively. Hence, the design prop loads are calculated as follows:

P_1 = 222.75 * 4 = 891kN/m

P_2 = 222.75 * 4 = 891kN/m

P_3 = 222.75 * 5.25 =1169.4kN/m

4 - Propped Wall

Similarly, for the 4-propped wall geometry the excavation depth (including the overdig) is 20.5m. From Equation B.1:

DPL = 0.5 $\bar{\gamma}H$ = 205kPa

Design value DPL = 1.35 * 205 = 276.75kPa

The vertical distances supported by the four prop levels based on the calculation process discussed above are 4m, 4m, 4m and 5.25m respectively. Hence, the design prop loads are calculated as follows:

P_1 = 276.75 * 4 = 1107kN/m

P_2 = 276.75 * 4 = 1107kN/m

P_3 = 276.75 * 4 = 1107kN/m

P_4 = 276.75 * 5.25 = 1452.9kN/m

5 - Propped Wall

Similarly, for the 5-propped wall geometry the excavation depth (including the overdig) is 24.5m. From Equation B.1:

DPL = 0.5 $\bar{\gamma}H$ = 245kPa

Design value DPL = 1.35 * 205 = 330.75kPa

The vertical distances supported by the five prop levels based on the calculation process discussed above are 4m, 4m, 4m, 4m and 5.25m respectively. Hence, the design prop loads are calculated as follows:

P_1 = 330.75 * 4 = 1323kN/m

P_2 = 330.75 * 4 = 1323kN/m

P_3 = 330.75 * 4 = 1323kN/m

P_4 = 330.75 * 4 = 1323kN/m

P_5 = 330.75 * 5.25 = 1736kN/m

EAB calculations

The calculation process of the design prop loads based on the EAB pressure diagrams is similar to the one discussed by Twine and Roscoe (1999). As shown in Figure B.5, the design prop loads are equal to the corresponding areas of the pressure diagram. Again, only half of the distance between the prop level and the formation level of the excavation is considered, to account for the contribution of the soil on the passive side of the wall in the support of the system. This vertical distance, *H'*, for all the geometries considered in this study, is calculated as shown in Equation 3.3 and is equal to 3.25m.

$$H' = \frac{H - h_k}{2} \tag{B.2}$$

1 - Propped Wall

For the 1-propped geometry the excavation depth *H* (including the overdig) is 8.5m while the vertical distance of the prop level form the ground level h_k is 2m. The ratio h_k/H is 0.235 and hence $0.2 \leq h_k/H \leq 0.3$ which corresponds to case (c) in Figure B.2. For this case, the ratio between the upper and lower horizontal stress e_{ho}/e_{hu} is equal to 1.5 (EAB §6.2, 2014). By trial and error, the values of e_{ho} and e_{hu} are derived such as they result in a total horizontal force acting on the wall equal to the design force calculated from CIRIA C517. This, in principle, means that in this study the areas of the EAB diagrams and the CIRIA's DPL are equal, allowing for a consistent comparison of the two different ways of stress distribution. The design values of e_{ho} and e_{hu} are 137.7kPa and 91.8kPa respectively. Note that the calculated values of e_{ho} and e_{hu} are already design values so there is no need for a load factor to be applied. The design prop load is then equal to the considered area of the EAB pressure diagram and is calculated as follows:

$P_1 = 137.7 * 4.25 + 91.8 * 1 = 677kPa$

2 - Propped Wall

The 2-propped geometry corresponds to case (b) in Figure B.3 (i.e. central supports). For this case, the ratio between the upper and lower horizontal stress e_{ho}/e_{hu} is equal to 2 (EAB §6.2, paragraph 3, 2014). Again, by trial and error, the values of e_{ho} and e_{hu} are derived such as they result in a total horizontal force acting on the wall equal to the design force calculated from CIRIA C517. The design values of e_{ho} and e_{hu} are 213.6kPa and 106.8kPa respectively. The design prop loads, which are equal to the corresponding areas of the EAB pressure diagram, are then calculated as follows:

$P_1 = 213.6 * 0.5 * 2 + 213.6 * 2 = 640.8kN/m$

$P_2 = 213.6 * 2 + [213.6 + (213.6 + 106.8) / 2] * 3.25 / 2 = 1034.6kN/m$

3 - Propped Wall

For the 3-propped geometry, the ratio between the upper and lower horizontal stress e_{ho}/e_{hu} is equal to 2 (EAB §6.2, paragraph 4, 2014). By trial and error, the design values of e_{ho} and e_{hu} are 309.5kPa and 154.75kPa respectively. The design prop loads are equal to the corresponding areas of the EAB pressure diagram and are calculated as follows:

$P_1 = 309.5 * 4 / 6 * 4 / 2 = 412.6kN/m$

$P_2 = (309.5 + 309.5 * 4 / 6) * 2 / 2 + 309.5 * 2 = 1134.8kN/m$

$P_3 = 309.5 * 2 + [309.5 + (309.5 + 154.75) / 2] * 3.25 / 2 = 1499.1kN/m$

4 - Propped Wall

For the 4-propped geometry, the ratio between the upper and lower horizontal stress e_{ho}/e_{hu} is equal to 2 (EAB §6.2, paragraph 4, 2014). By trial and error, the design values of e_{ho} and e_{hu} are 381.4kPa and 190.7kPa respectively. The design prop loads which are equal to the corresponding areas of the EAB pressure diagram, are calculated as follows:

$P_1 = 381.4 * 4 / 6 * 4 / 2 = 508.5kN/m$

$P_2 = (381.4 + 381.4 * 4 / 6) * 2 / 2 + 381.4 * 2 = 1398.5kN/m$

$P_3 = 381.4 * 2 + [381.4 + (190.7 + 190.7 * 8.5 / 10.5)] * 2 / 2 = 1489.3kN/m$

$P_4 = [190.7 + 190.7 * 3.25 / 10.5 + 190.7 + 190.7 * 8.5 / 10.5)] * 5.25 / 2 = 1561.4kN/m$

5 - Propped Wall

For the 5-propped geometry, the ratio between the upper and lower horizontal stress e_{ho}/e_{hu} is equal to 2 (EAB §6.2, paragraph 4, 2014). By trial and error, the design values of e_{ho} and e_{hu} are 429.3kPa and 214.65kPa respectively. The design prop loads are then calculated as follows:

$P_1 = 429.3 * 4 / 6 * 4 / 2 = 572.4kN/m$

$P_2 = (429.3 + 429.3 * 4 / 6) * 2 / 2 + 429.3 * 2 = 1574.1kN/m$

P_3 = 429.3 * 4 = 1717.2kN/m

P_4 = 429.3 * 2 + [429.3 + (214.65 + 214.65 * 8.5 / 10.5)] * 2 / 2 = 1676.3kN/m

P_5 = [214.65 + 214.65 * 3.25 / 10.5 + 214.65 + 214.65 * 8.5 / 10.5)] * 5.25 / 2 = 1757.5kN/m

APPENDIX C

Full list of contours for HYD verification using FEM

In this Section, the full list of the contours for the parametric analysis discussed in Chapter 6, are included for completeness.

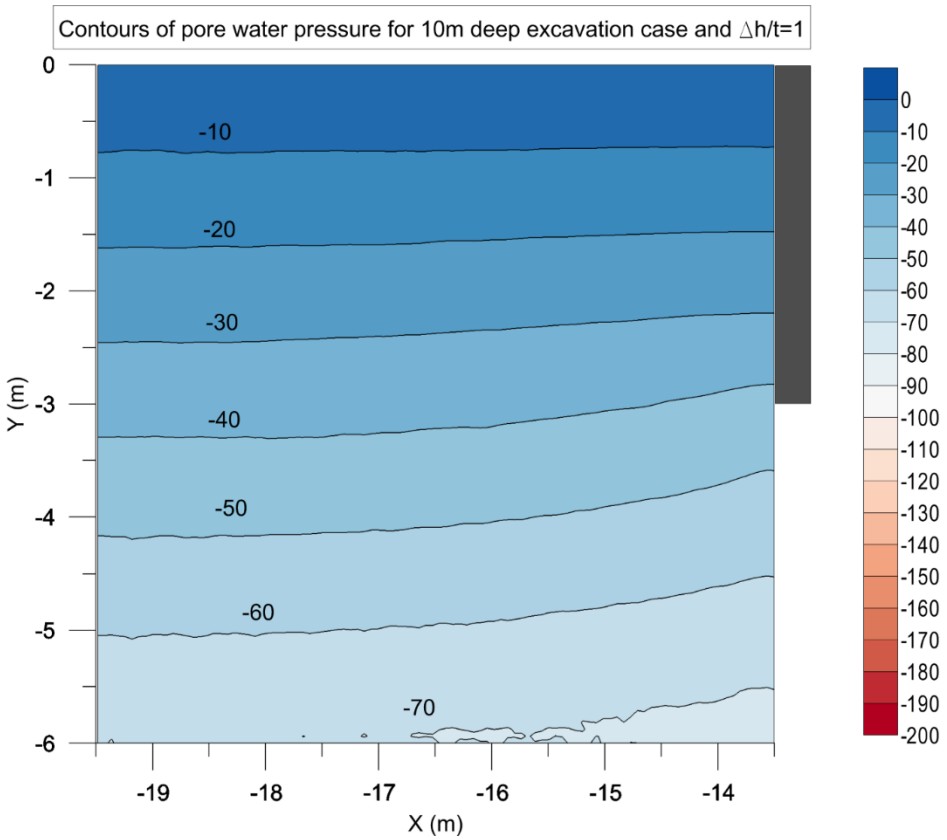

Figure C.1: Contours of pore water pressure for 10m deep excavation with *Δ*h=1t

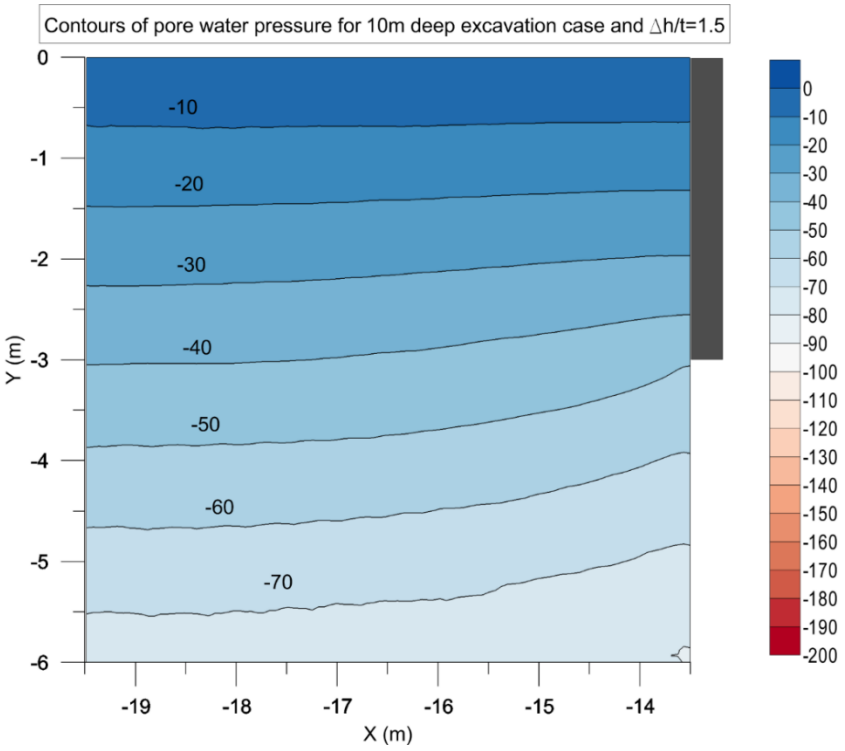

Figure C.2: Contours of pore water pressure for 10m deep excavation with Δh=1.5t

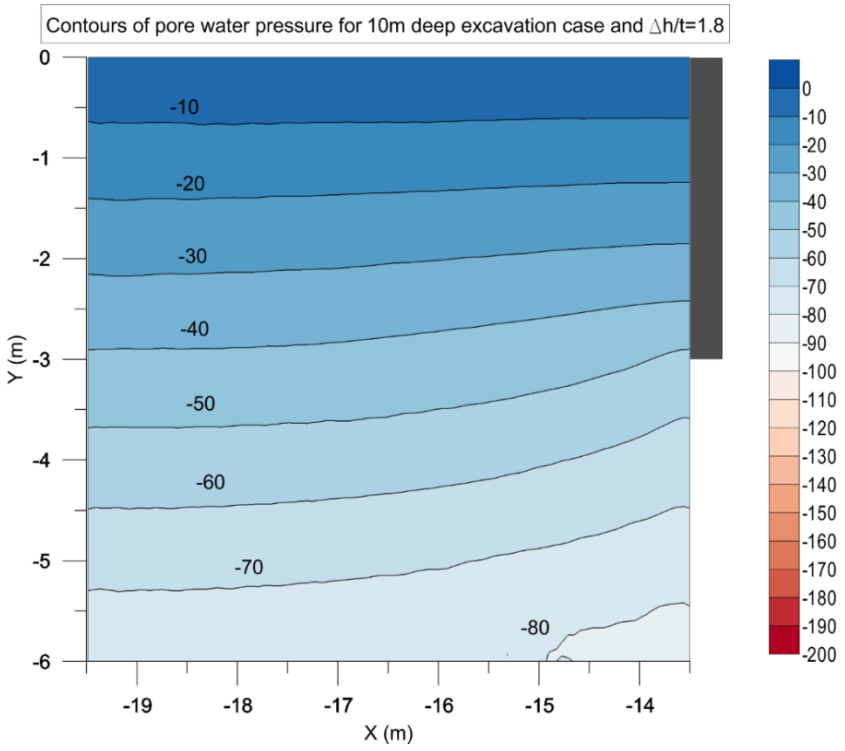

Figure C.3: Contours of pore water pressure for 10m deep excavation with Δh=1.8t

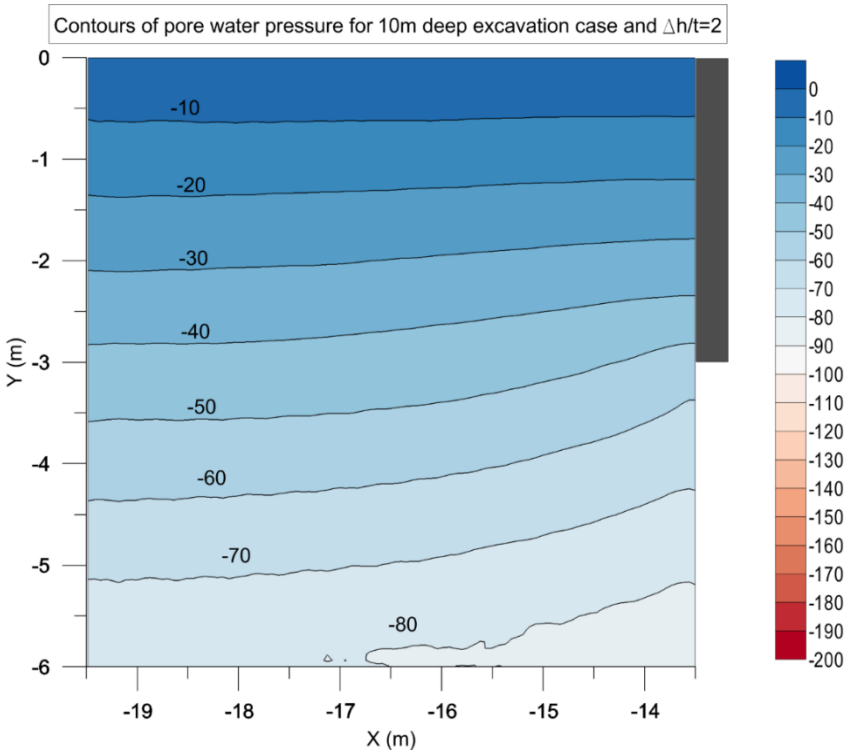

Figure C.4: Contours of pore water pressure for 10m deep excavation with *Δ*h=2t

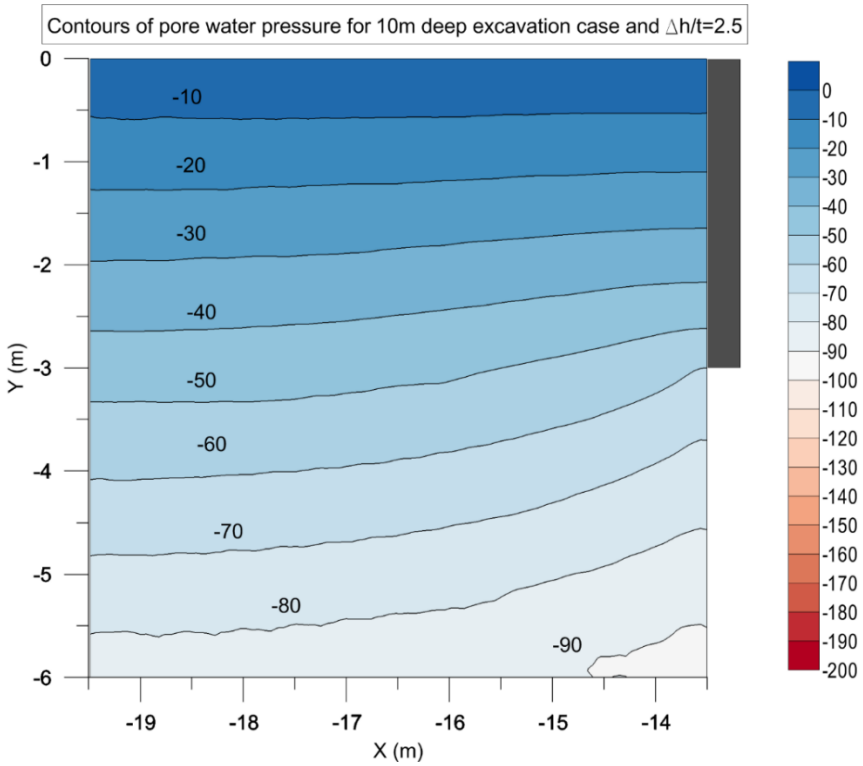

Figure C.5: Contours of pore water pressure for 10m deep excavation with *Δ*h=2.5t

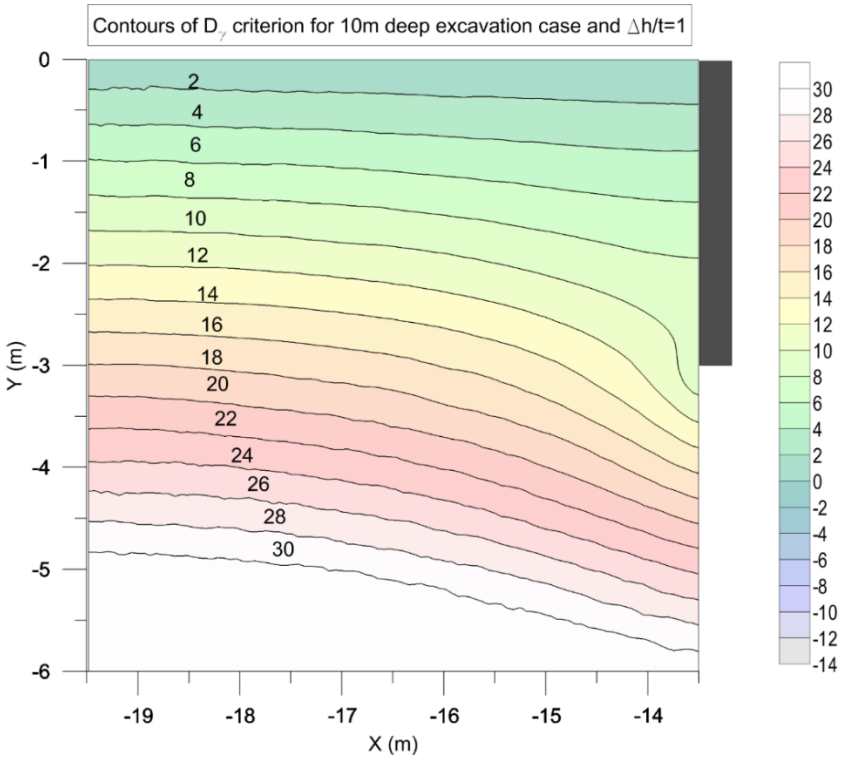

Figure C.6: Contours of D_γ for 10m deep excavation with Δh=1t

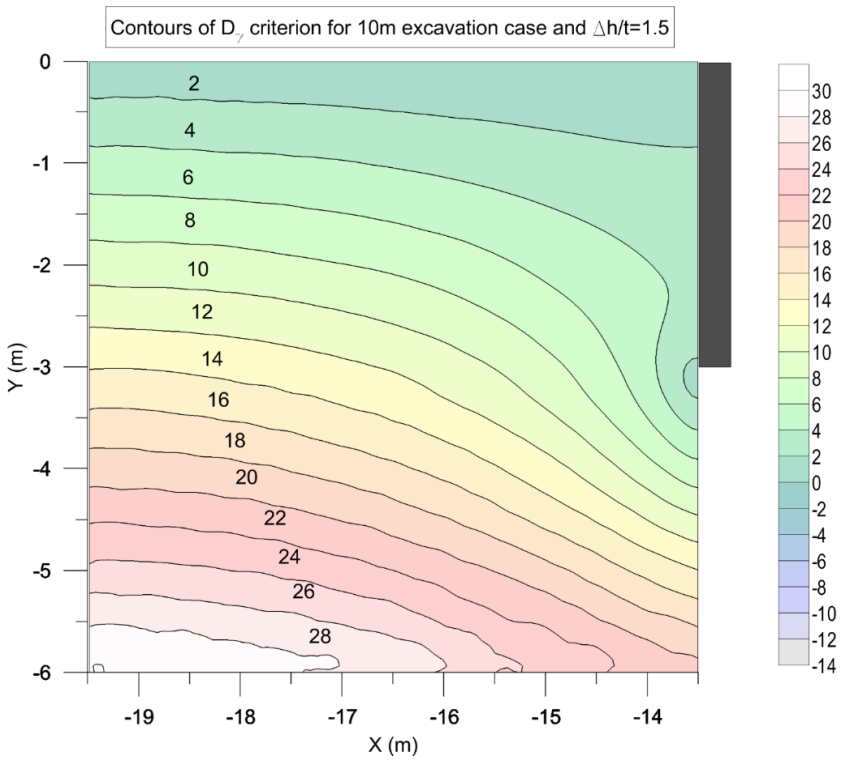

Figure C.7: Contours of D_γ for 10m deep excavation with Δh=1.5t

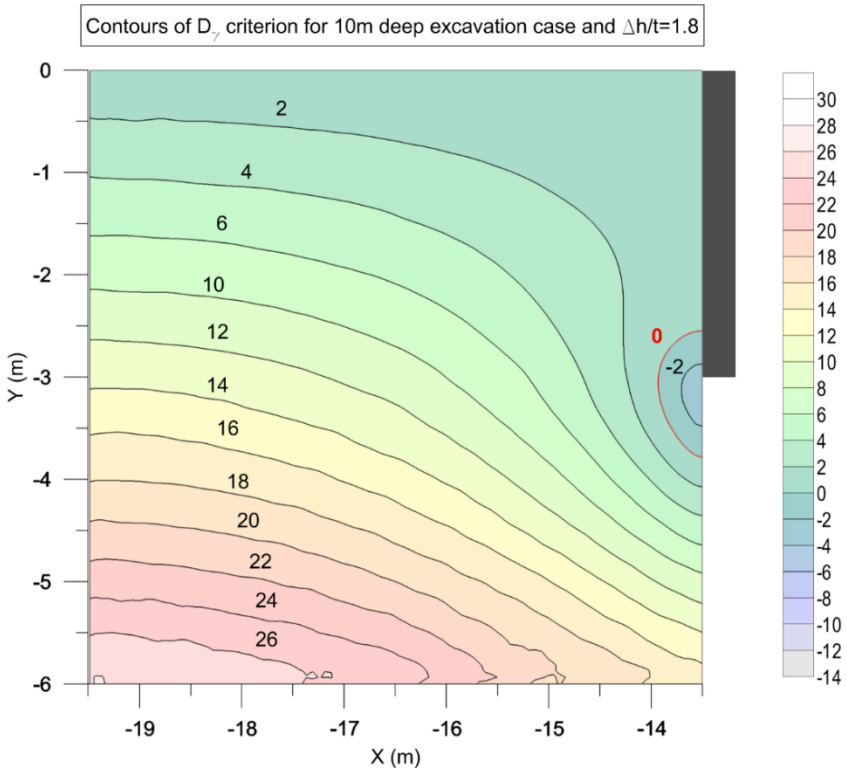

Figure C.8: Contours of D_γ for 10m deep excavation with $\Delta h=1.8t$

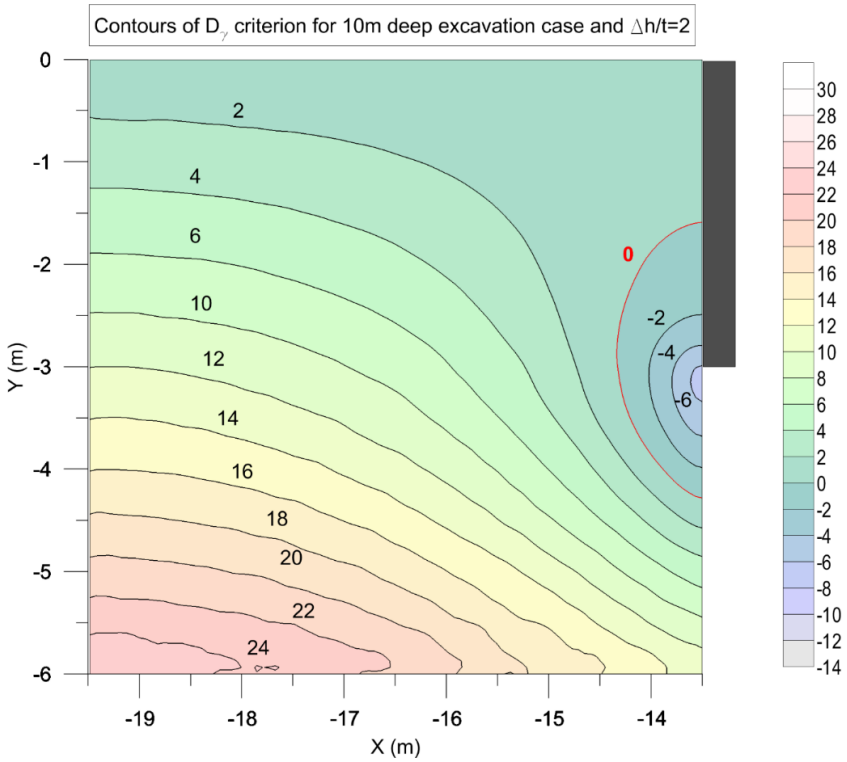

Figure C.9: Contours of D_γ for 10m deep excavation with $\Delta h=2t$

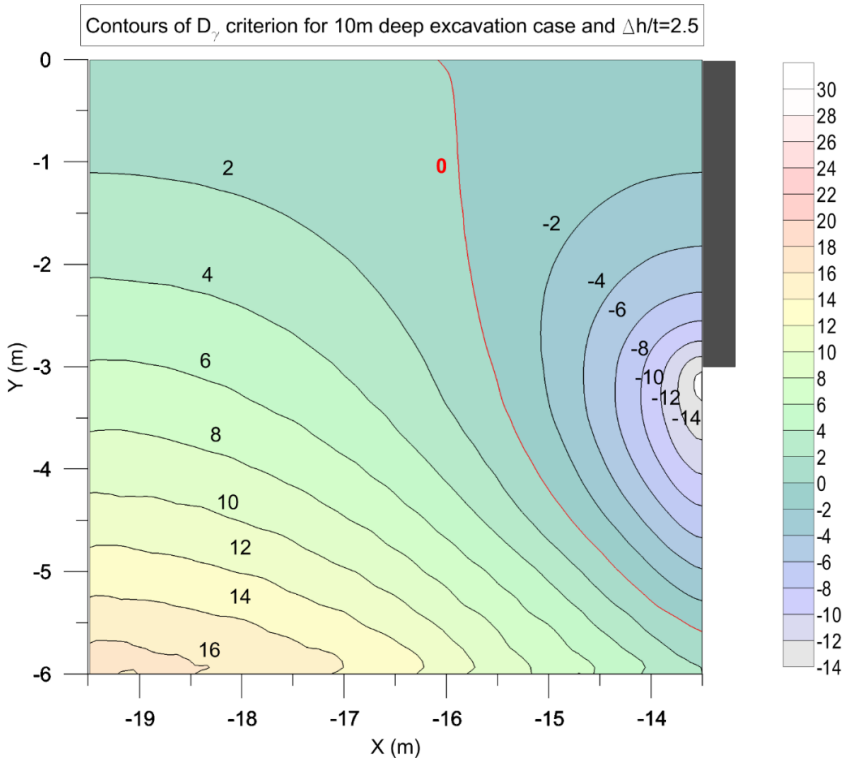

Figure C.10: Contours of D_γ for 10m deep excavation with Δh=2.5t

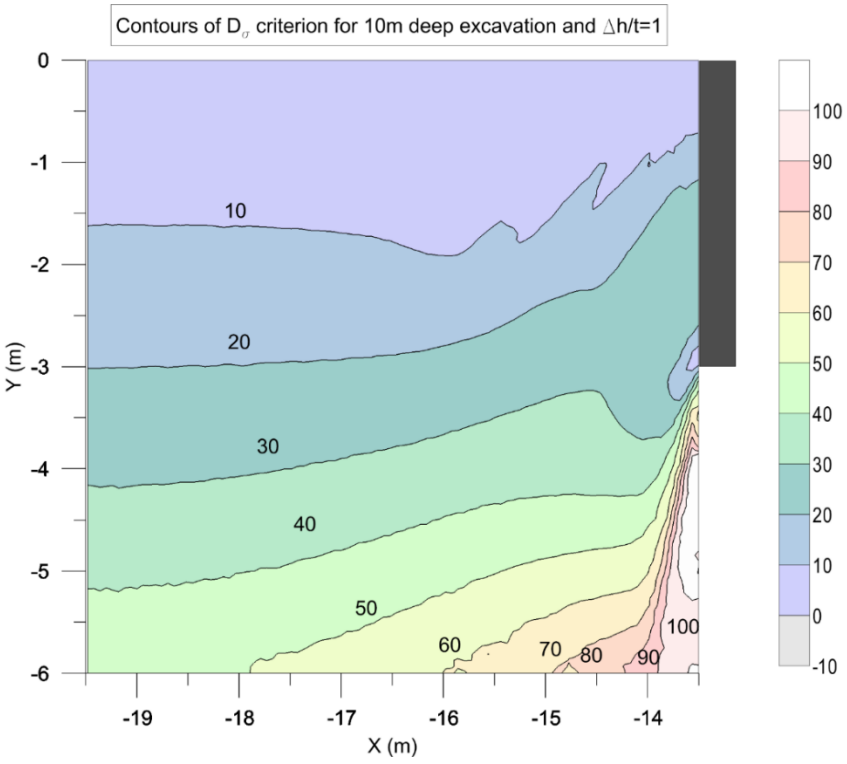

Figure C.11: Contours of D_σ for 10m deep excavation with Δh=1t and tanδ/tanφ'=0.5

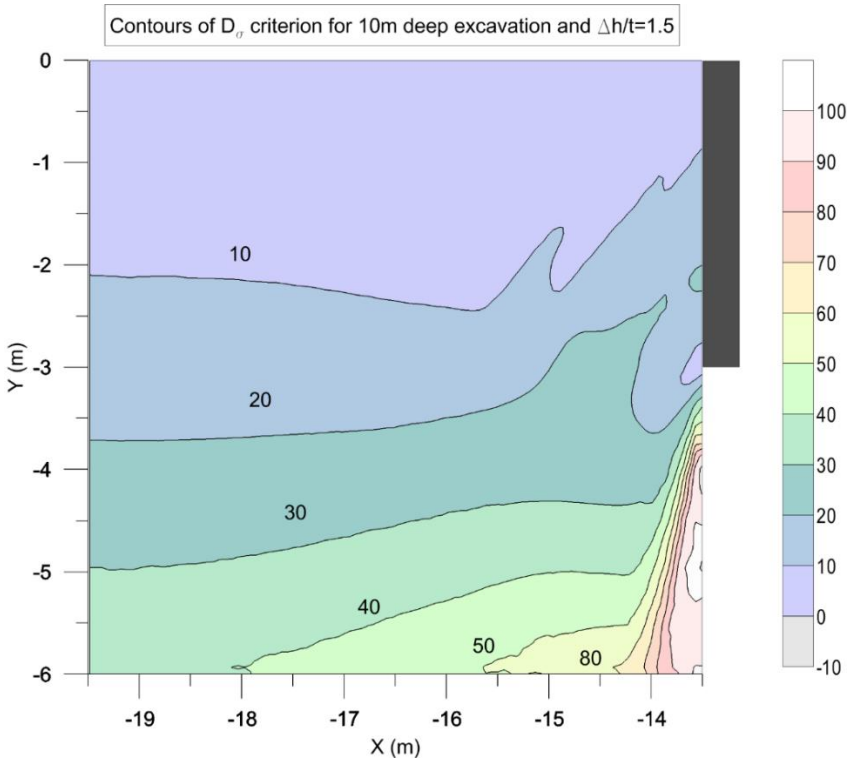

Figure C.12: Contours of D_σ for 10m deep excavation with Δh=1.5t and tanδ/tanφ'=0.5

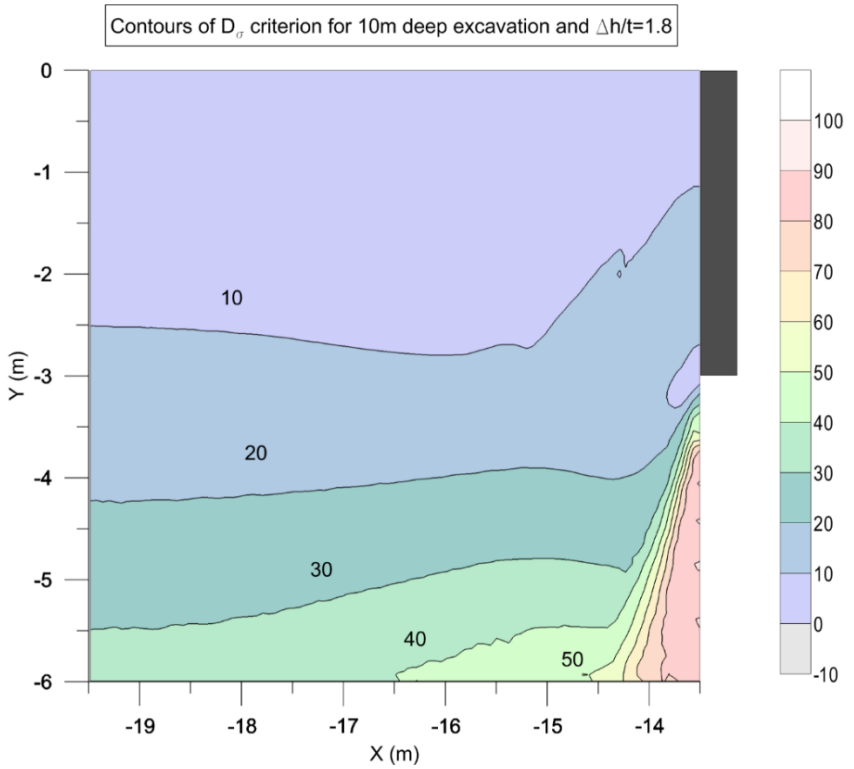

Figure C.13: Contours of D_σ for 10m deep excavation with Δh=1.8t and tanδ/tanφ'=0.5

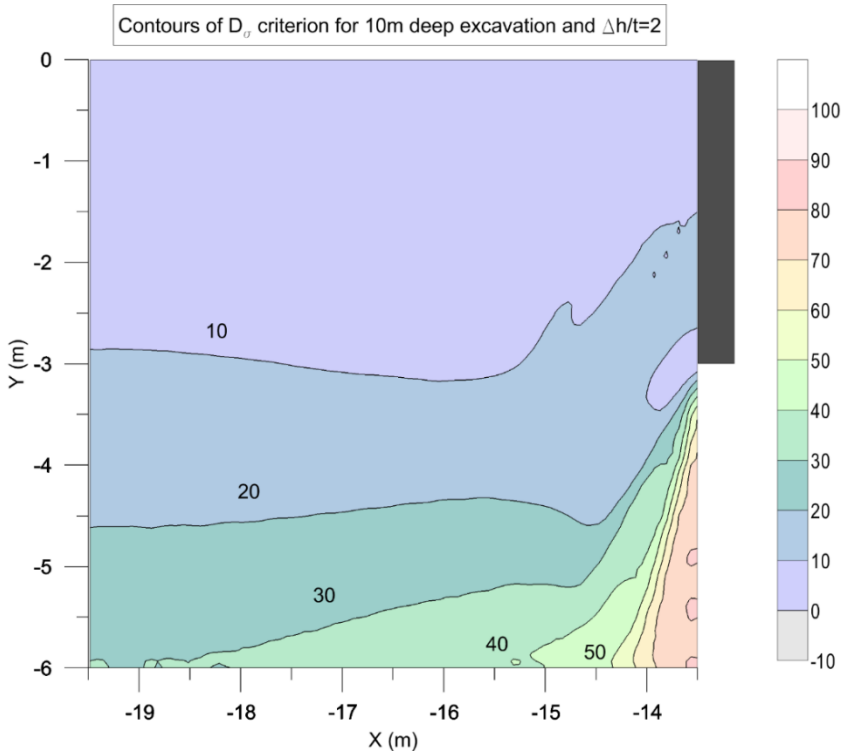

Figure C.14: Contours of D_σ for 10m deep excavation with Δh=2t and tanδ/tanφ'=0.5

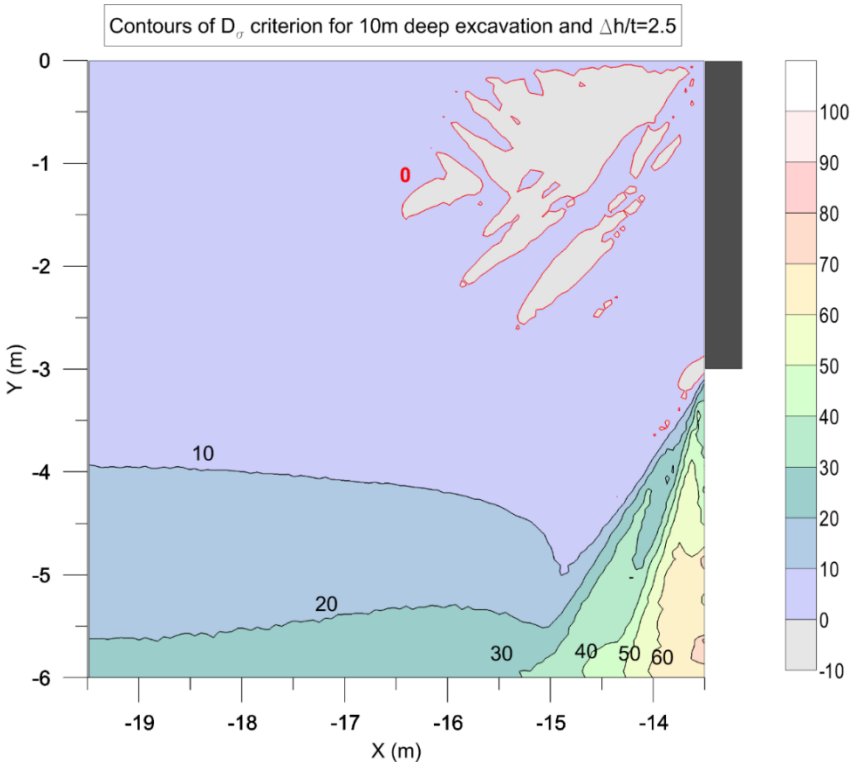

Figure C.15: Contours of D_σ for 10m deep excavation with Δh=2.5t and tanδ/tanφ'=0.5

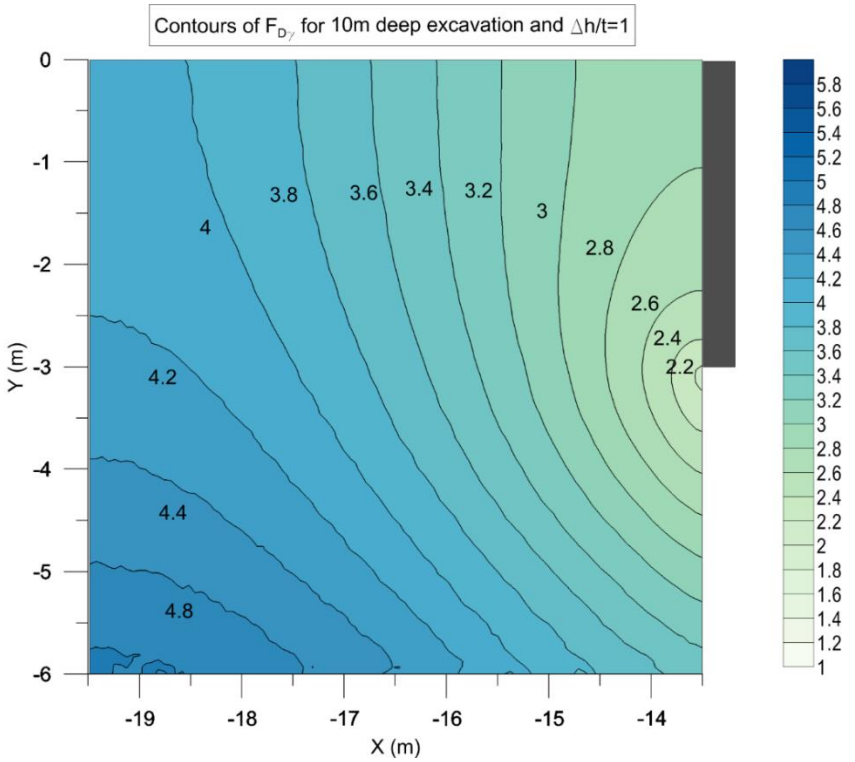

Figure C.16: Contours of F_{DY} for 10m deep excavation with Δh=1t

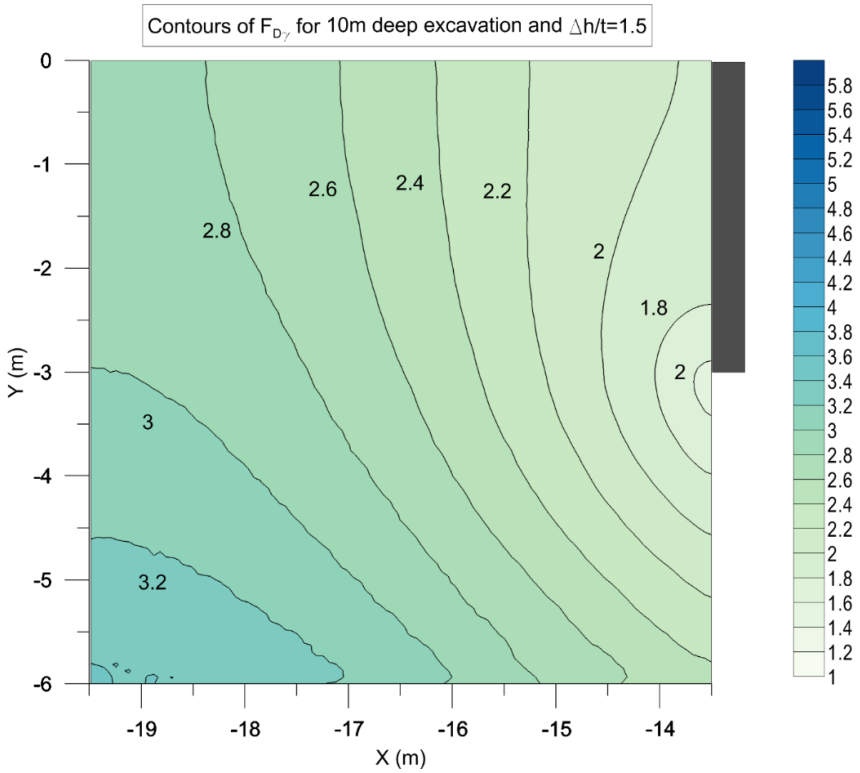

Figure C.17: Contours of F_{DY} for 10m deep excavation with Δh=1.5t

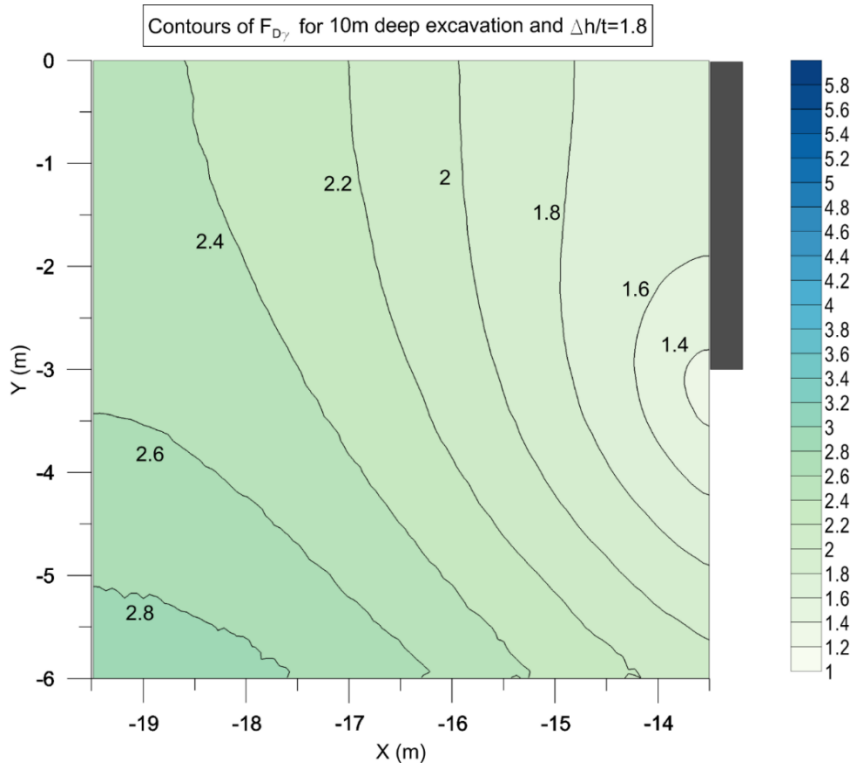

Figure C.18: Contours of $F_{D\gamma}$ for 10m deep excavation with Δh=1.8t

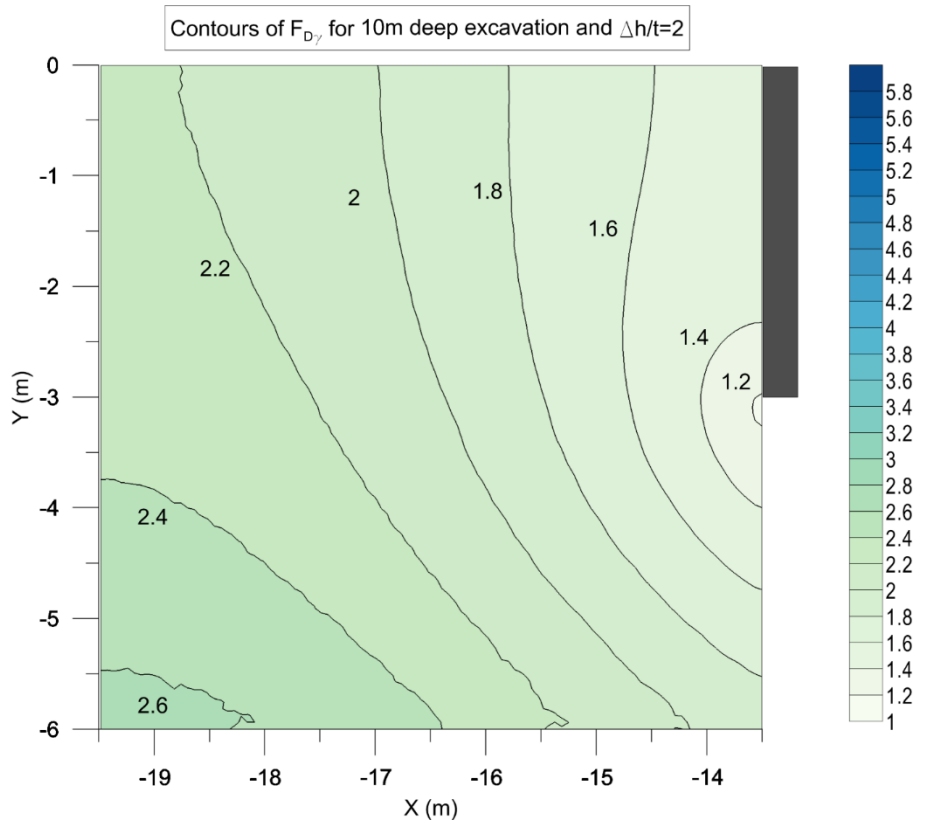

Figure C.19: Contours of $F_{D\gamma}$ for 10m deep excavation with Δh=2t

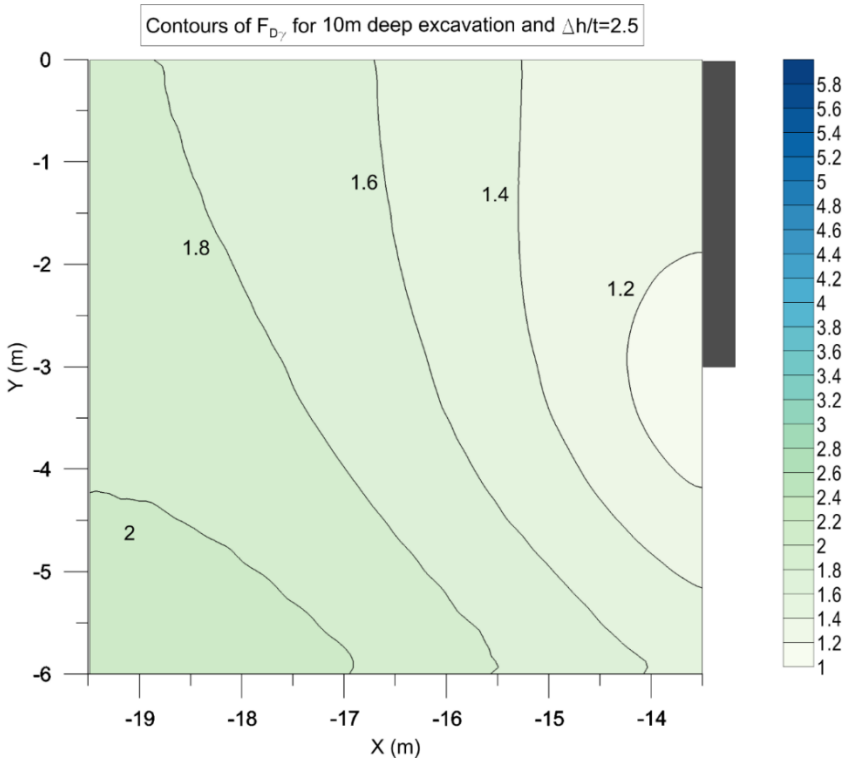

Figure C.20: Contours of $F_{D\gamma}$ for 10m deep excavation with Δh=2.5t

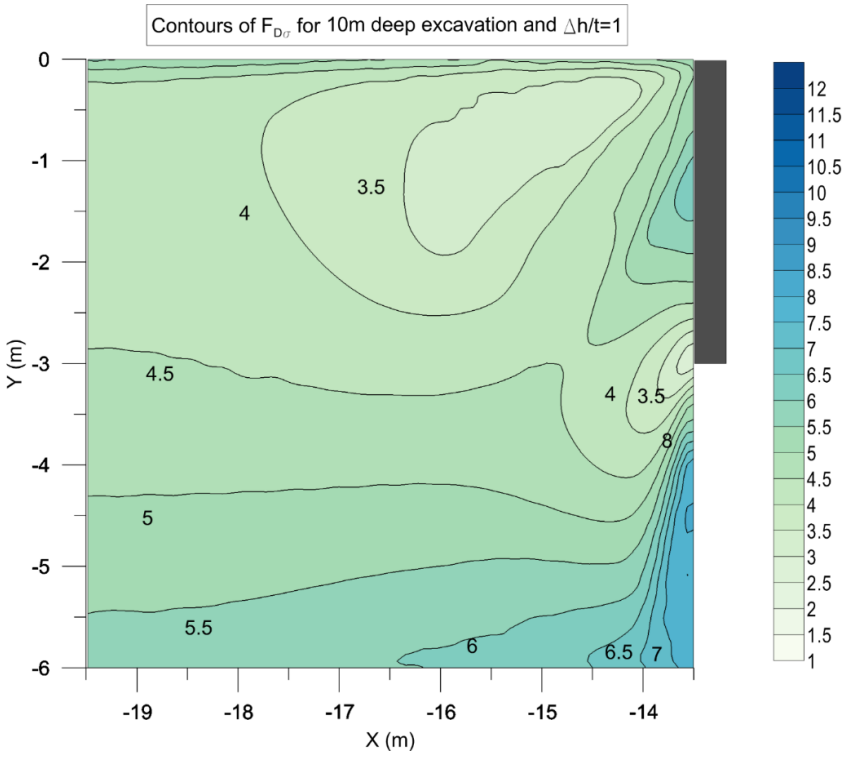

Figure C.21: Contours of $F_{D\sigma}$ for 10m deep excavation with Δh=1t and tanδ/tanφ'=0.5

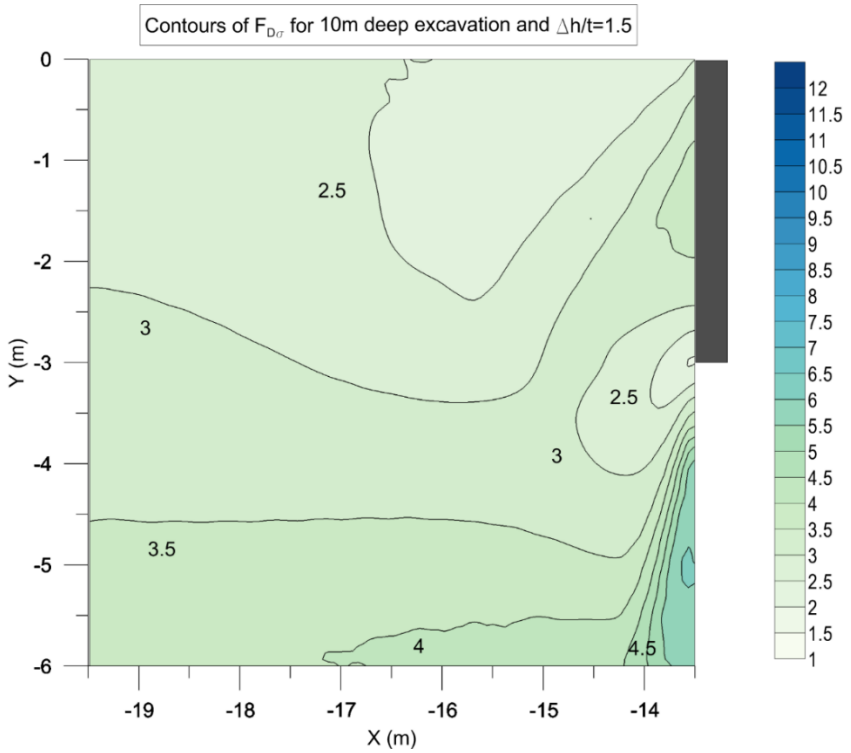

Figure C.22: Contours of $F_{D\sigma}$ for 10m deep excavation with Δh=1.5t and tanδ/tanφ'=0.5

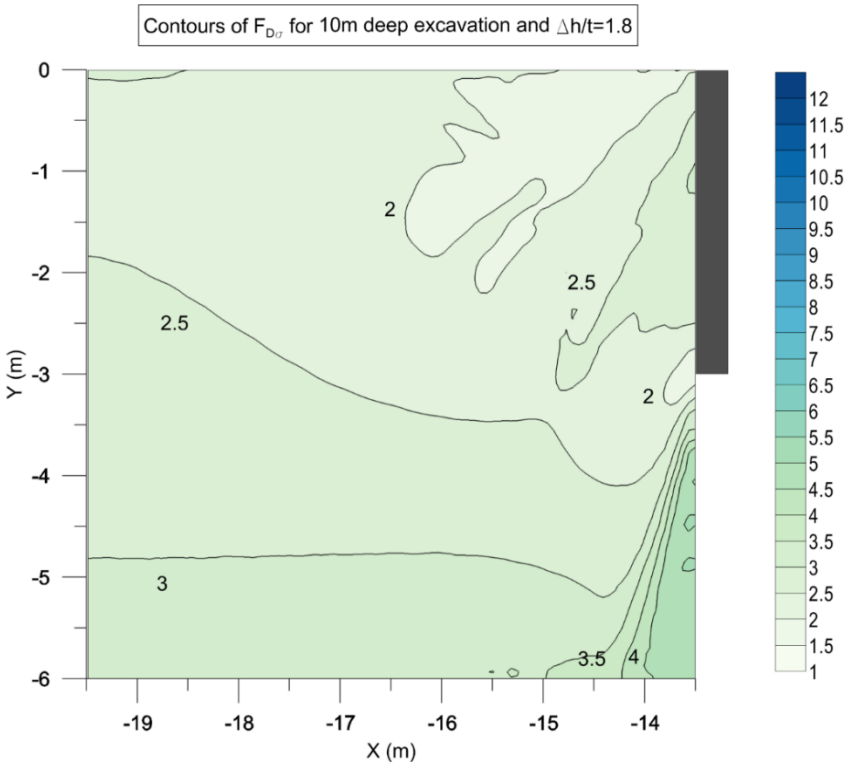

Figure C.23: Contours of $F_{D\sigma}$ for 10m deep excavation with Δh=1.8t and tanδ/tanφ'=0.5

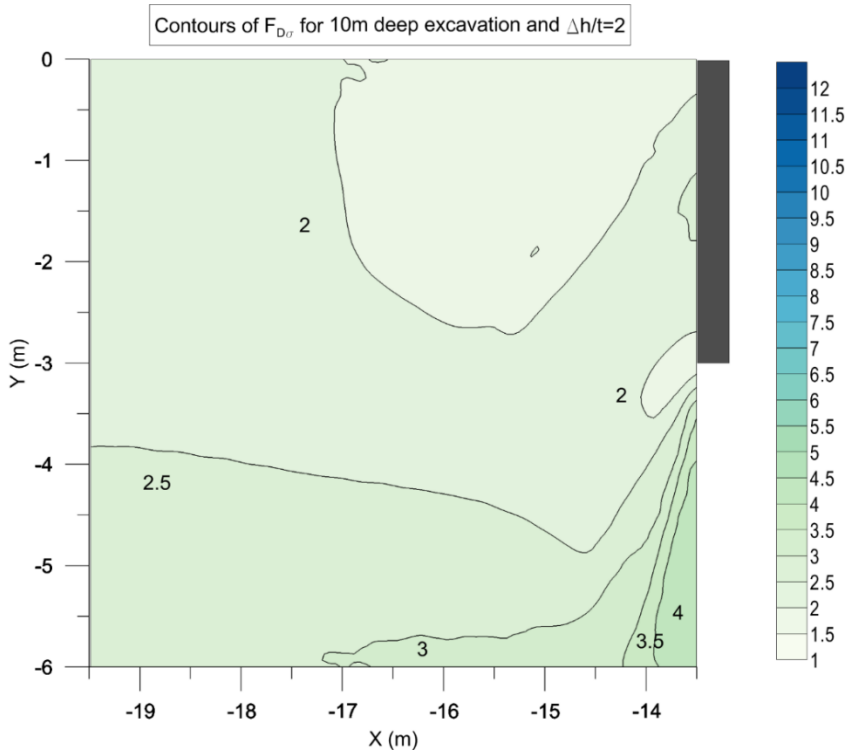

Figure C.24: Contours of $F_{D\sigma}$ for 10m deep excavation with Δh=2t and tanδ/tanφ'=0.5

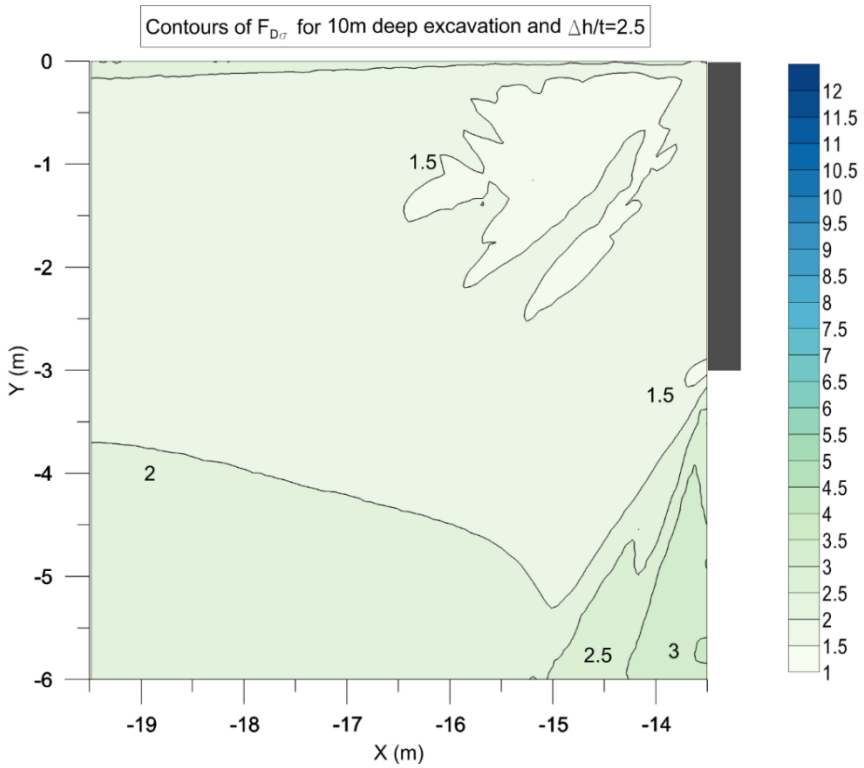

Figure C.25: Contours of $F_{D\sigma}$ for 10m deep excavation with Δh=2.5t and tanδ/tanφ'=0.5

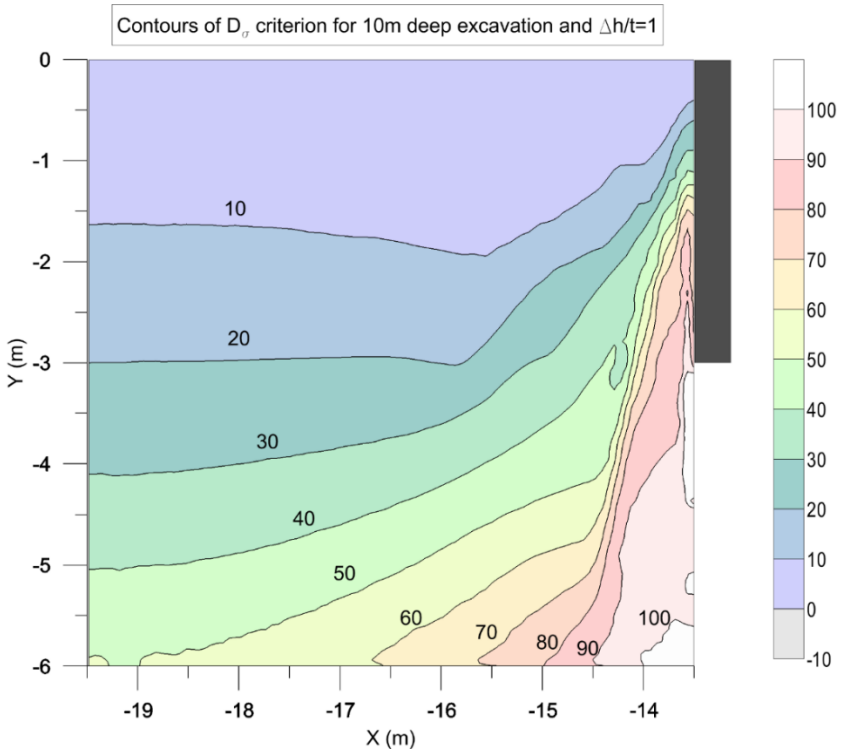

Figure C.26: Contours of D_σ for 10m deep excavation with Δh=1t and tanδ/tanφ'=1

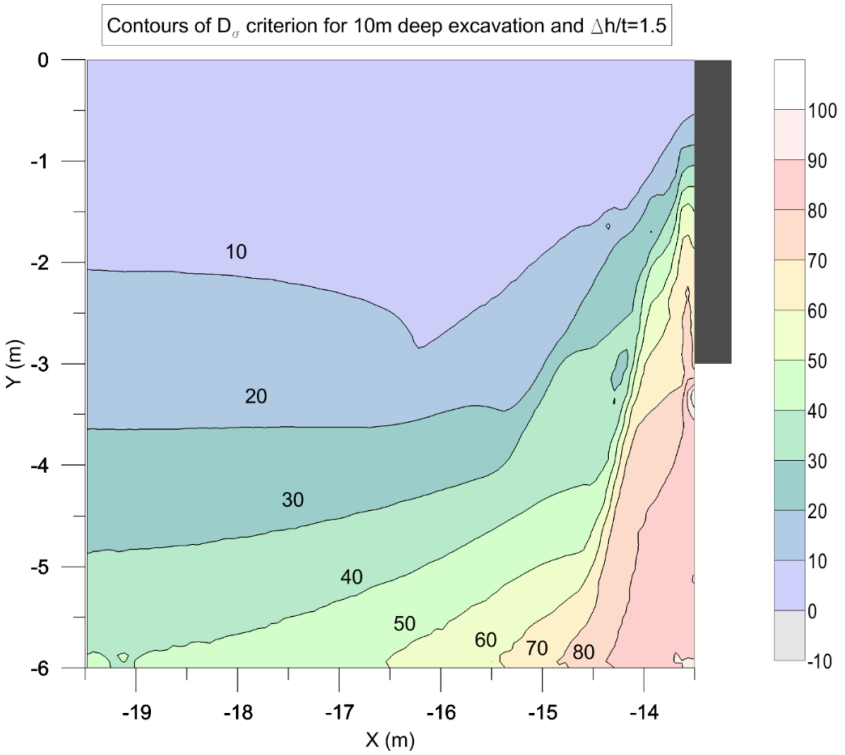

Figure C.27: Contours of D_σ for 10m deep excavation with Δh=1.5t and tanδ/tanφ'=1

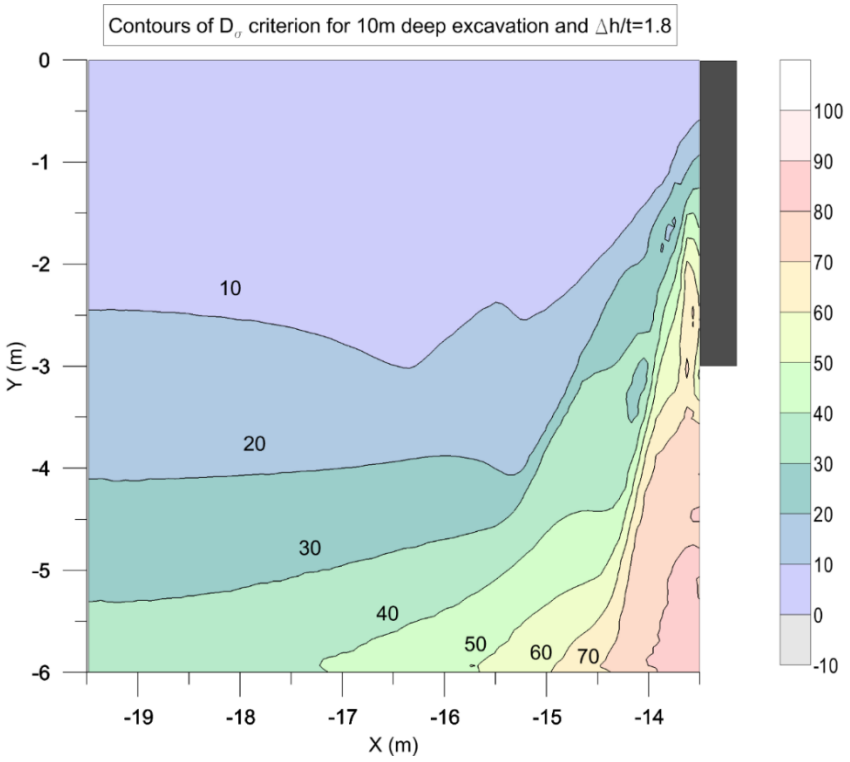

Figure C.28: Contours of D_σ for 10m deep excavation with Δh=1.8t and tanδ/tanφ'=1

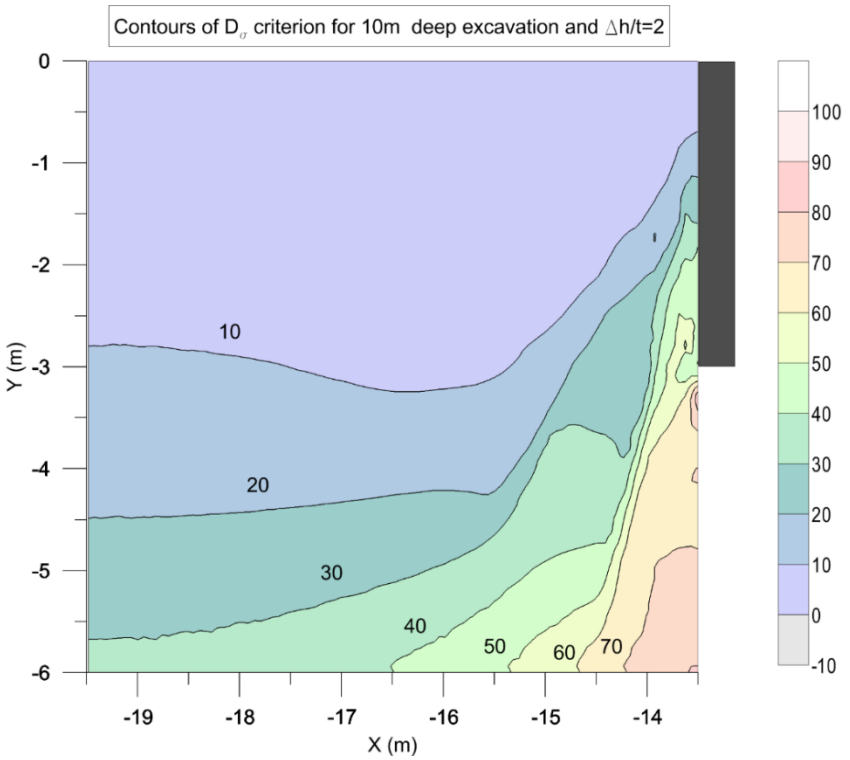

Figure C.29: Contours of D_σ for 10m deep excavation with Δh=2t and tanδ/tanφ'=1

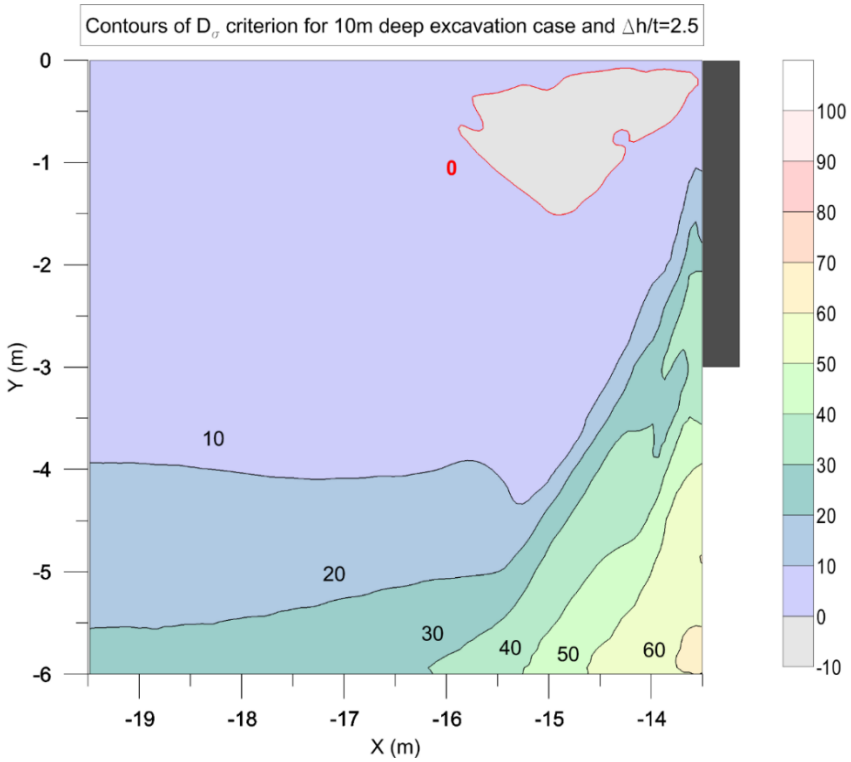

Figure C.30: Contours of D_σ for 10m deep excavation with Δh=2.5t and tanδ/tanφ'=1

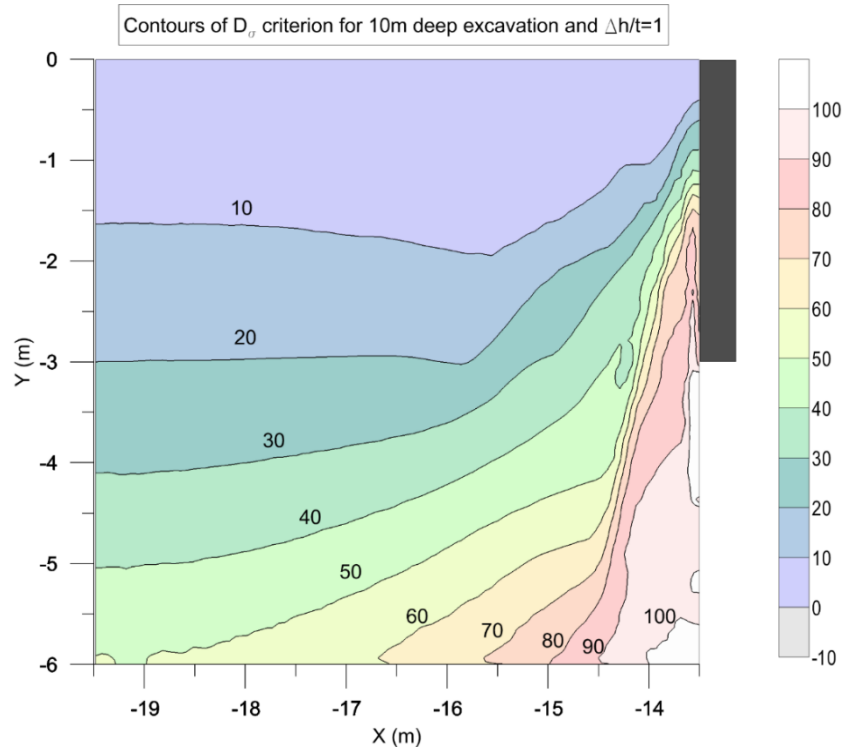

Figure C.31: Contours of $F_{D\sigma}$ for 10m deep excavation with Δh=1t and tanδ/tanφ'=1

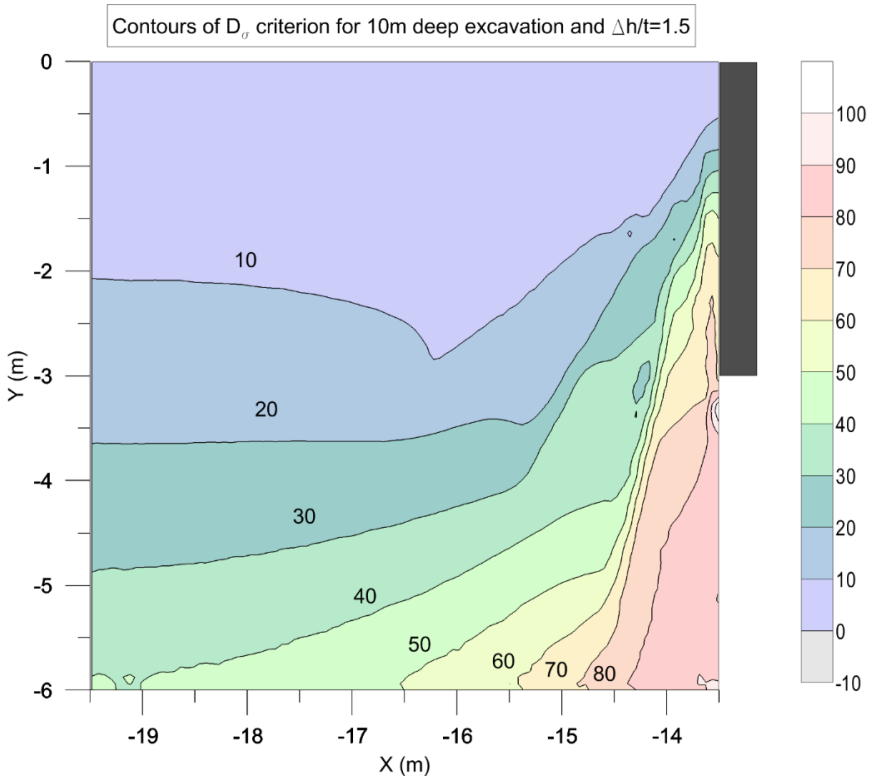

Figure C.32: Contours of $F_{D\sigma}$ for 10m deep excavation with $\underline{\Delta}$h=1.5t and tanδ/tanφ'=1

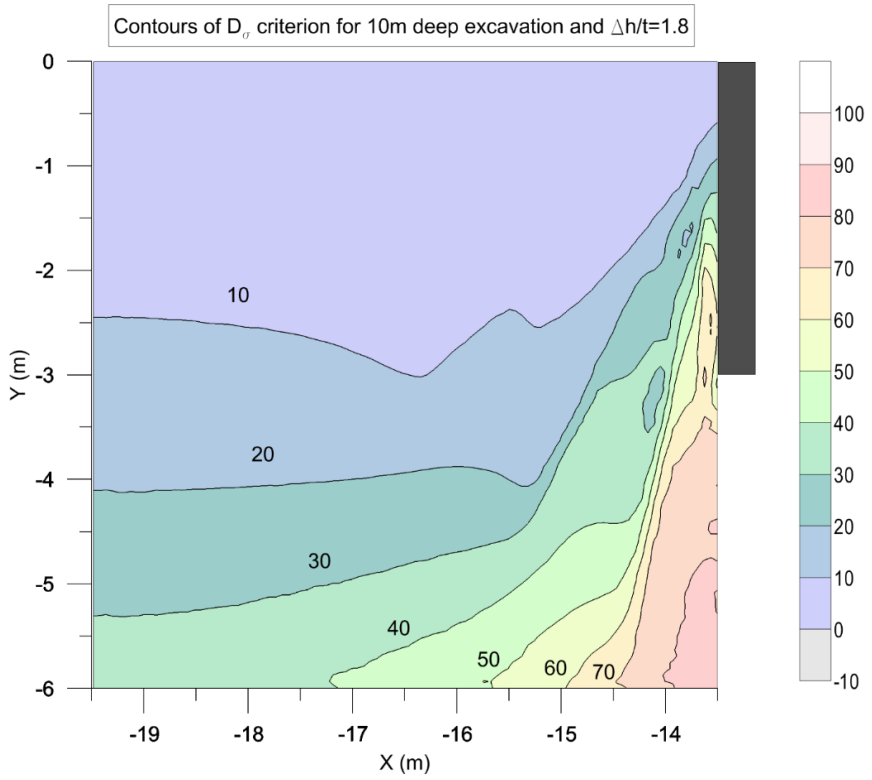

Figure C.33: Contours of $F_{D\sigma}$ for 10m deep excavation with Δh=1.8t and tanδ/tanφ'=1

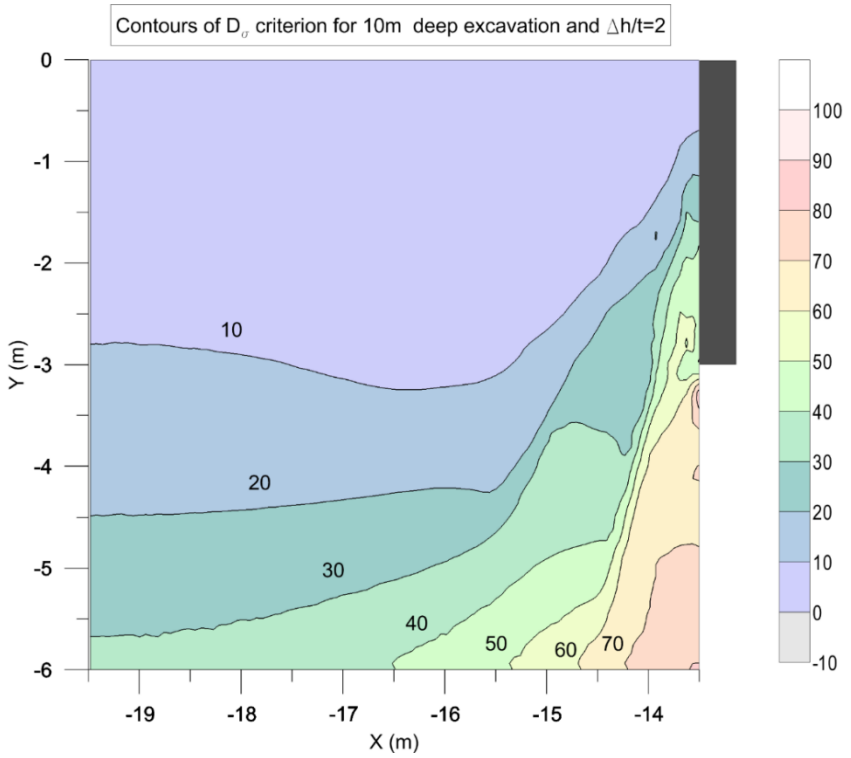

Figure C.34: Contours of $F_{D\sigma}$ for 10m deep excavation with Δh=2t and tanδ/tanφ'=1

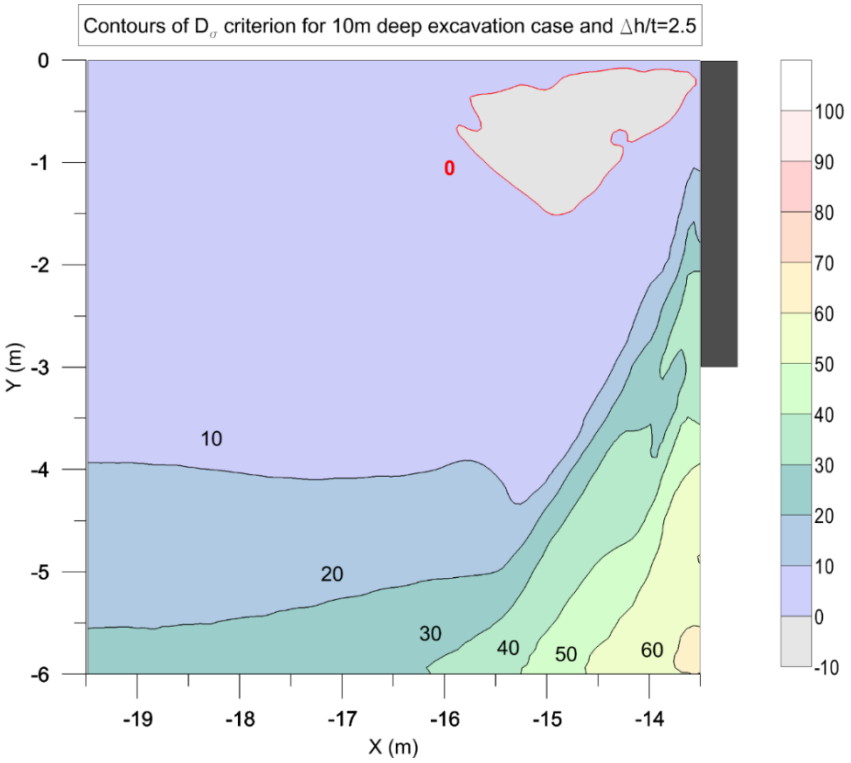

Figure C.35: Contours of $F_{D\sigma}$ for 10m deep excavation with Δh=2.5t and tanδ/tanφ'=1

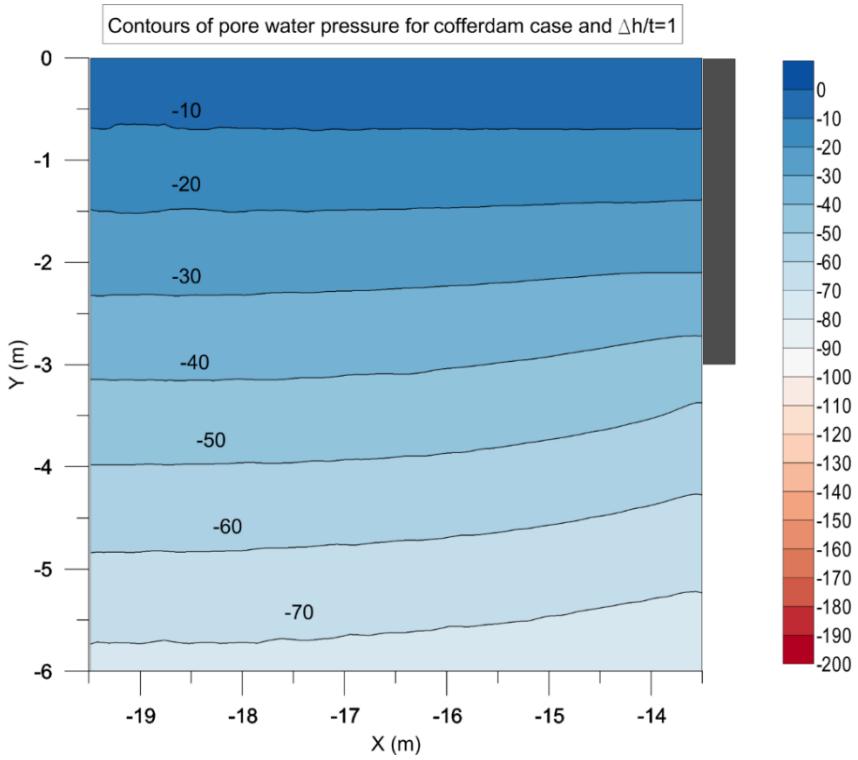

Figure C.36: Contours of pore water pressure for the cofferdam case with *Δ*h=1t

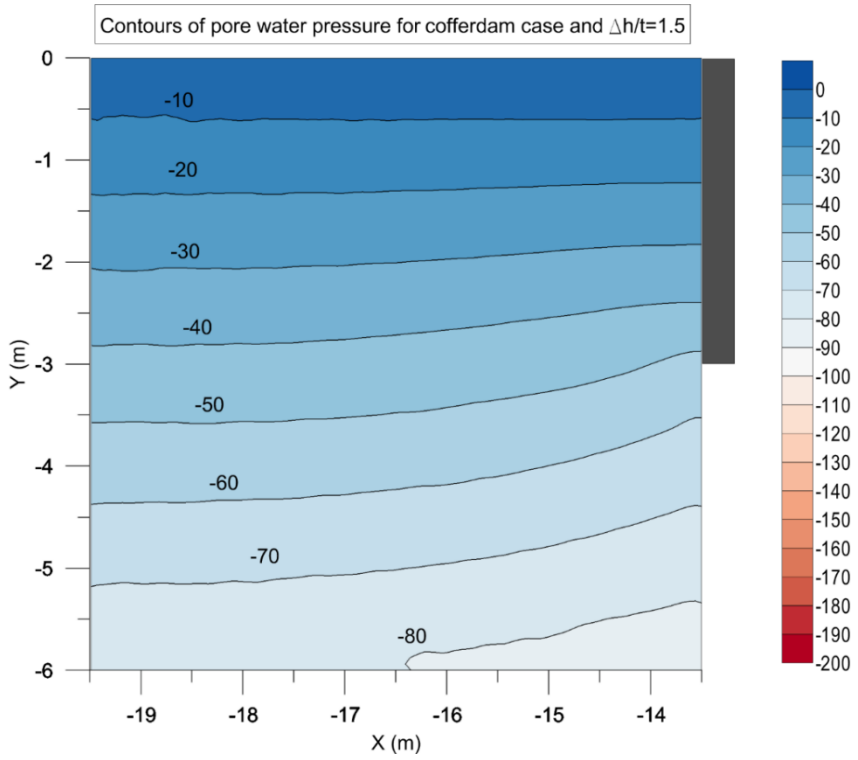

Figure C.37: Contours of pore water pressure for the cofferdam case with *Δ*h=1.5t

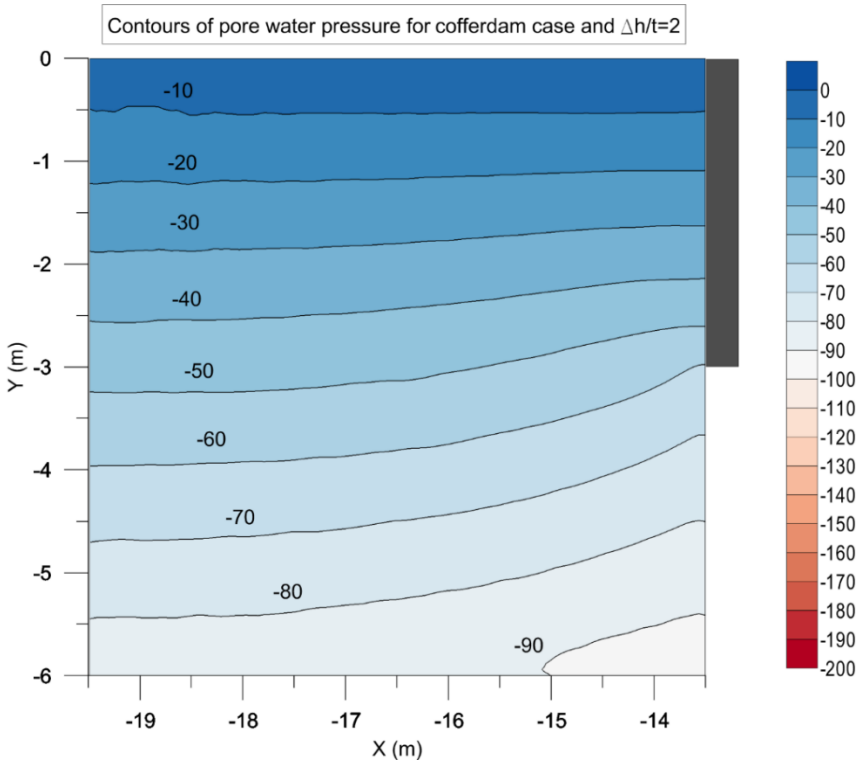

Figure C.38: Contours of pore water pressure for the cofferdam case with Δh=2t

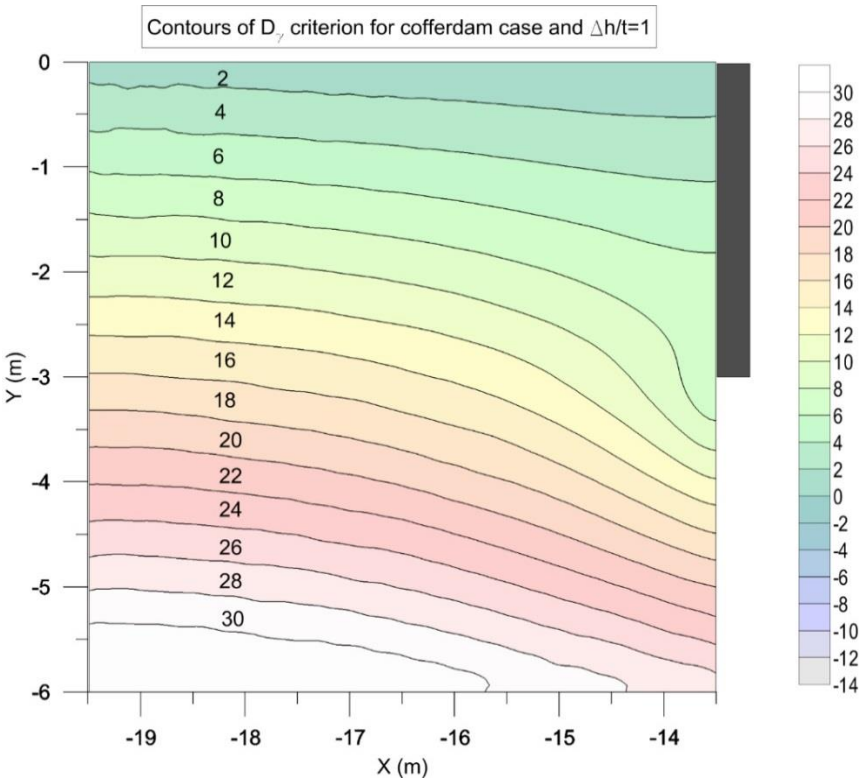

Figure C.39: Contours of D_Y for the cofferdam case with Δh=1t

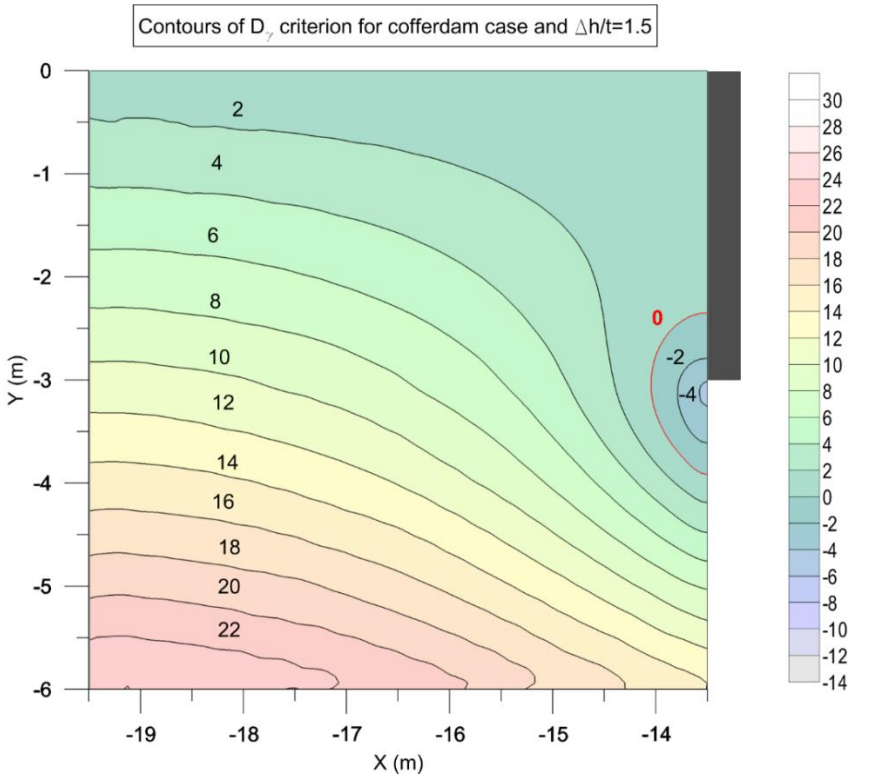

Figure C.40: Contours of D_Y for the cofferdam case with Δh=1.5t

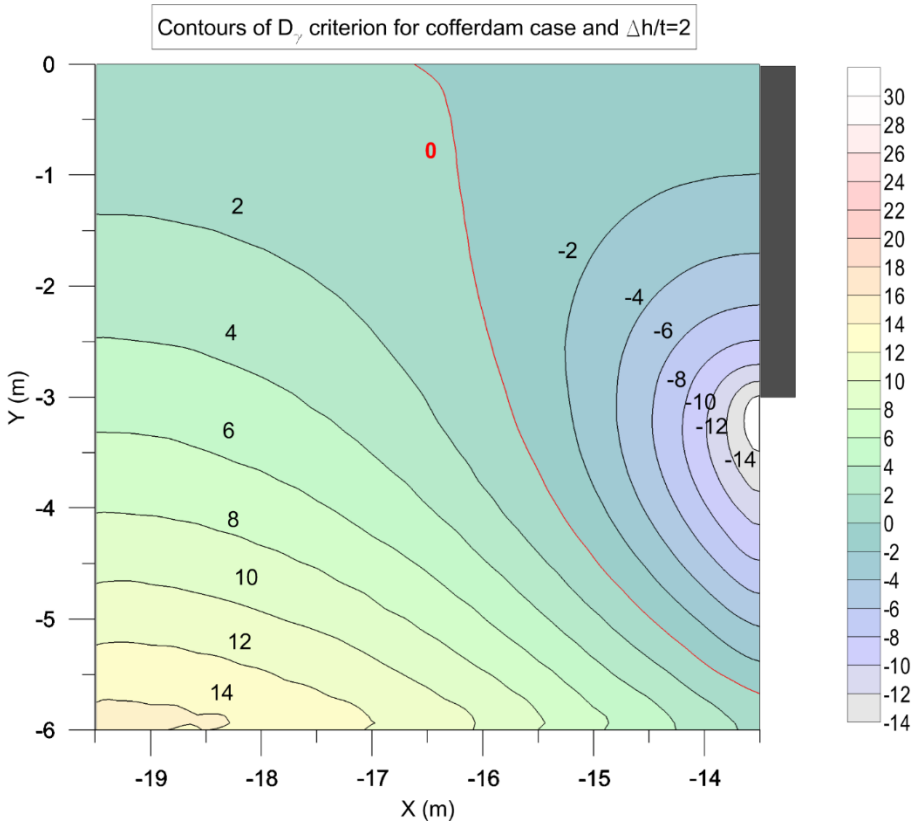

Figure C.40: Contours of D_Y for the cofferdam case with Δh=2t

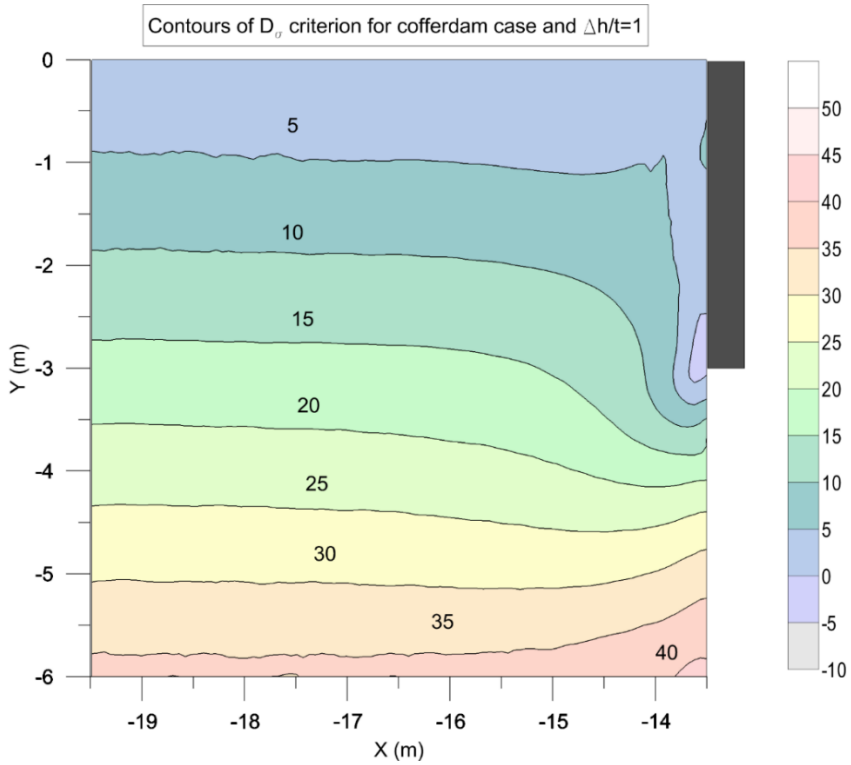

Figure C.41: Contours of D_σ for the cofferdam case with Δh=1t and tanδ/tanφ'=0.5

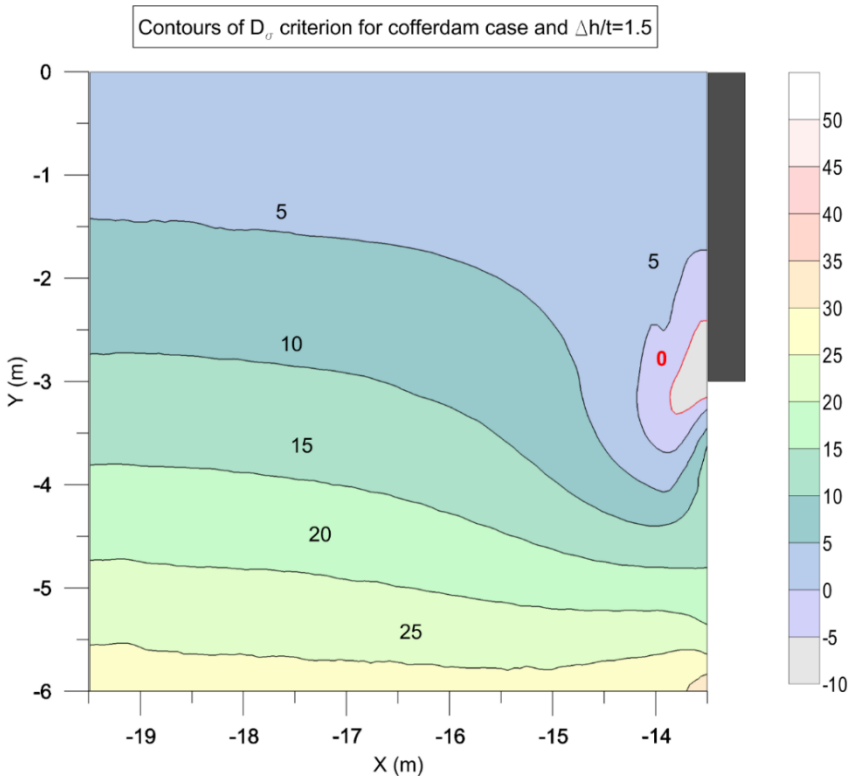

Figure C.42: Contours of D_σ for the cofferdam case with Δh=1.5t and tanδ/tanφ'=0.5

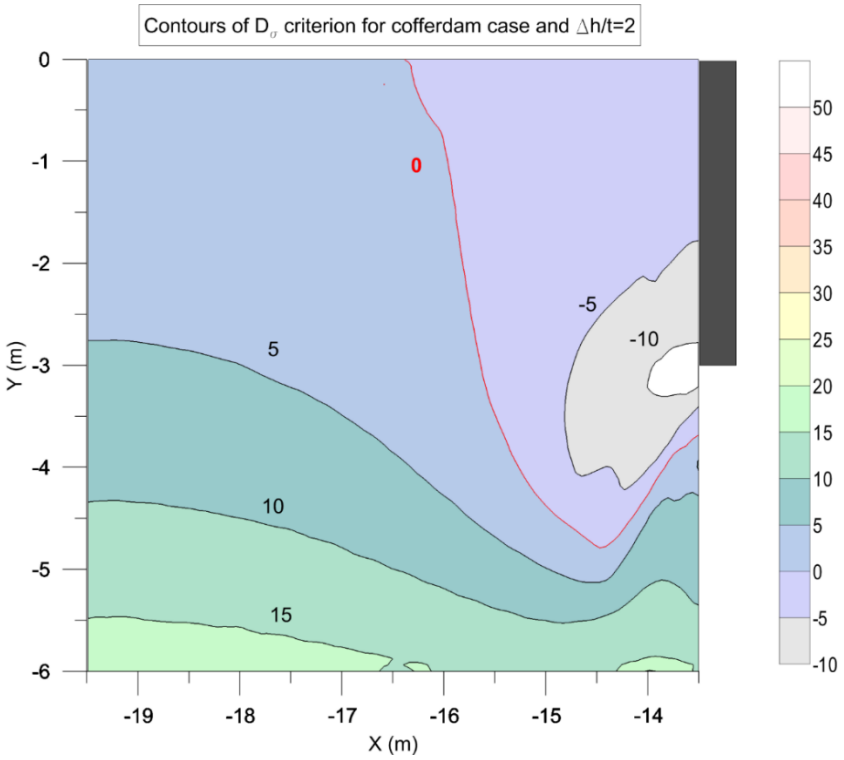

Figure C.43: Contours of D_σ for the cofferdam case with Δh=2t and tanδ/tanφ'=0.5

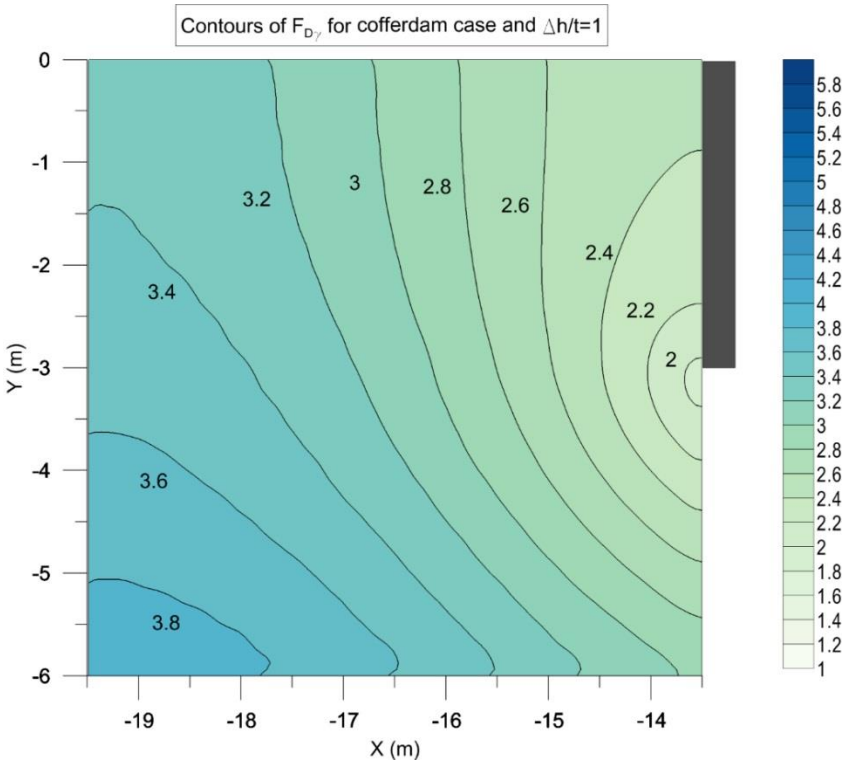

Figure C.44: Contours of F_{DY} for the cofferdam case with Δh=1t

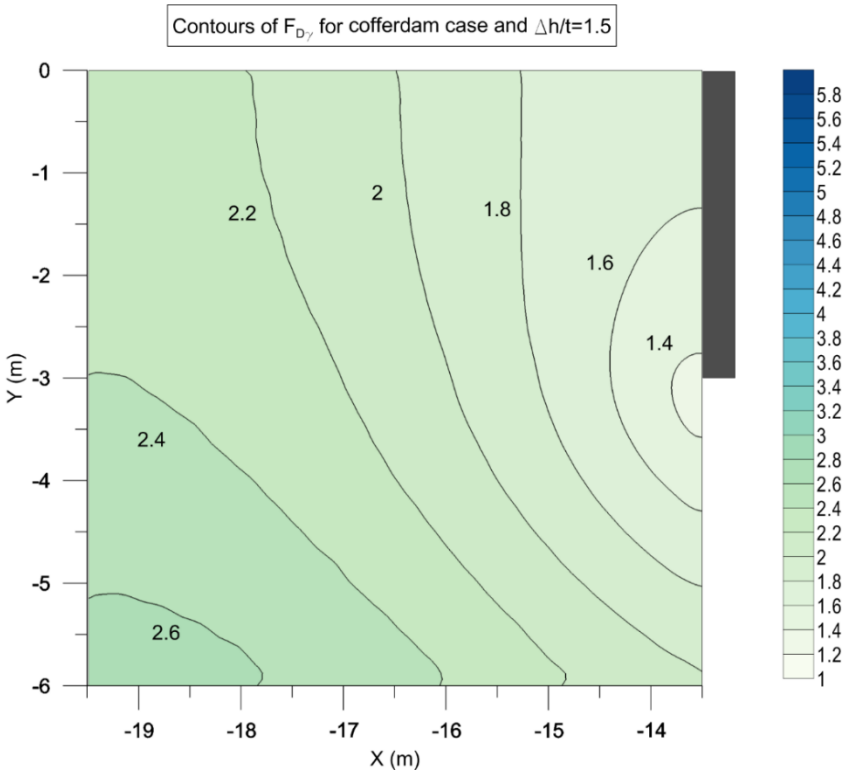

Figure C.45: Contours of F_{DY} for the cofferdam case with Δh=1.5t

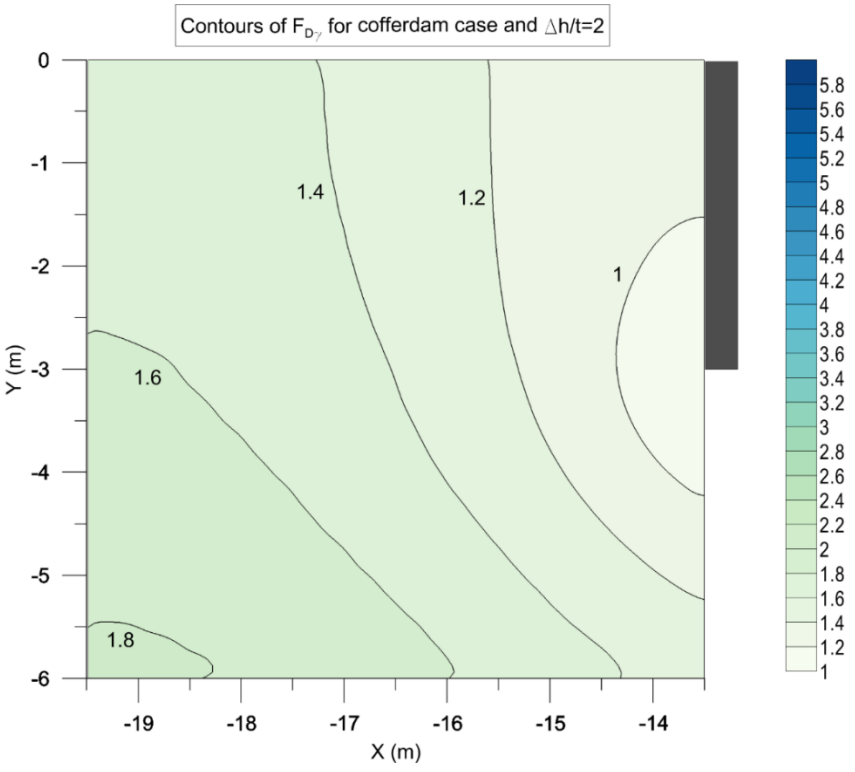

Figure C.46: Contours of F_{DY} for the cofferdam case with Δh=2t

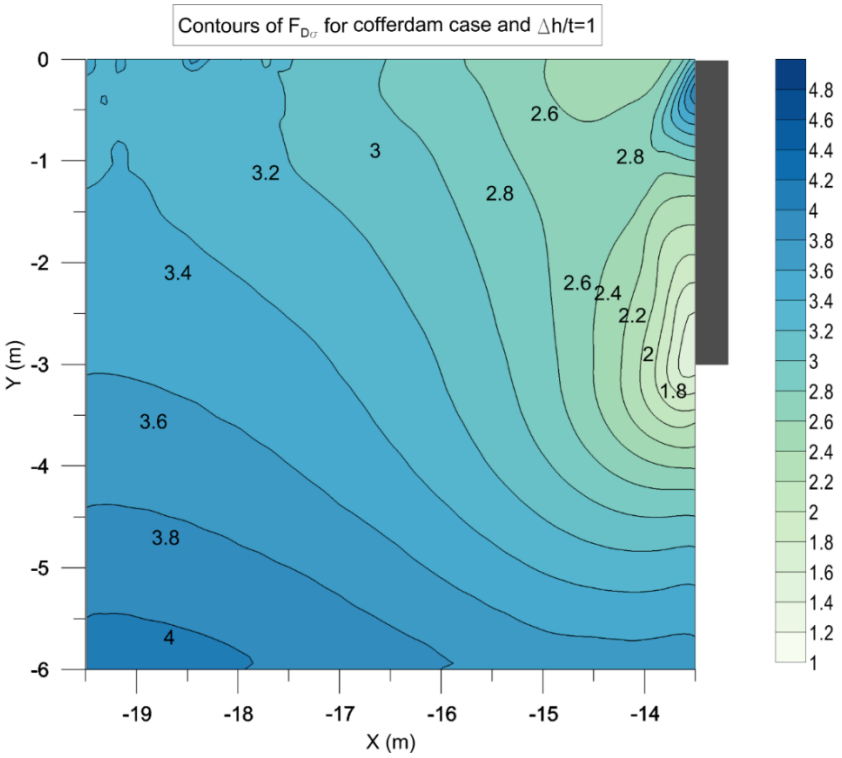

Figure C.47: Contours of $F_{D\sigma}$ for the cofferdam case with Δh=1t and tanδ/tanφ'=0.5

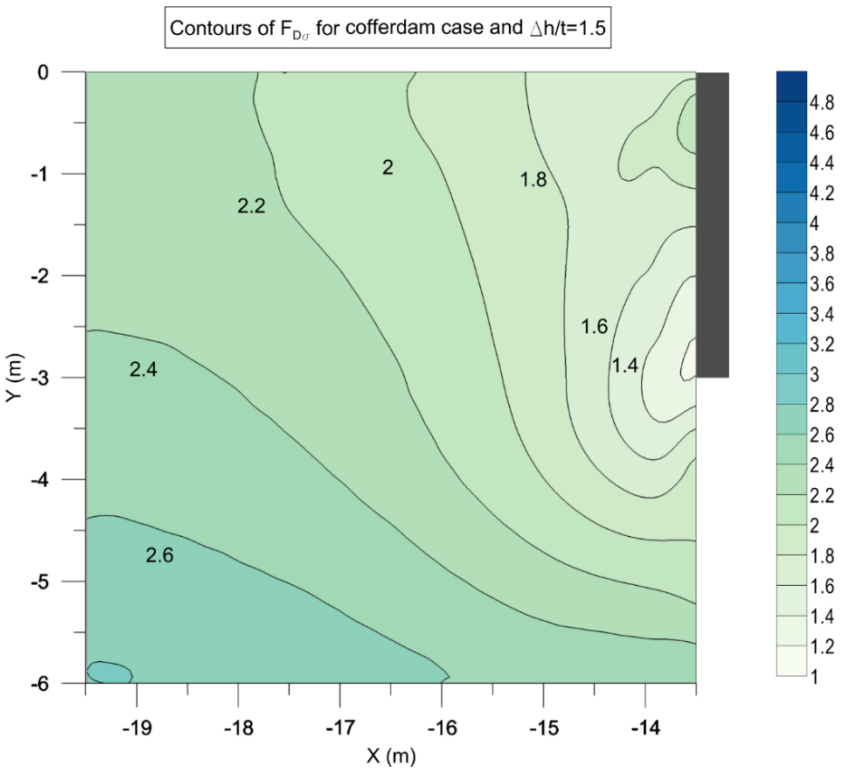

Figure C.48: Contours of $F_{D\sigma}$ for the cofferdam case with Δh=1.5t and tanδ/tanφ'=0.5

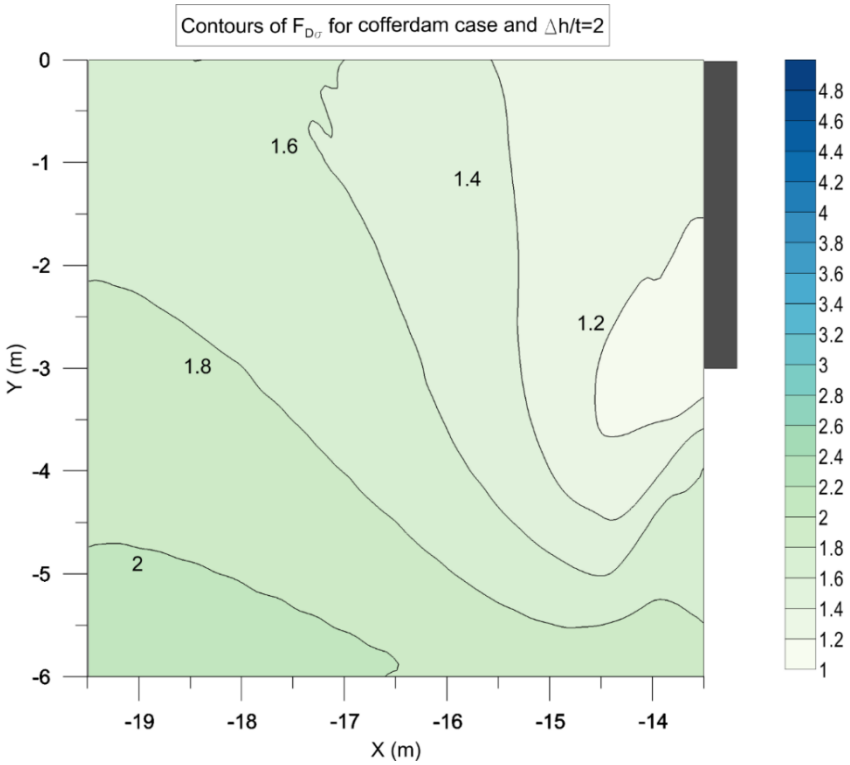

Figure C.49: Contours of $F_{D\sigma}$ for the cofferdam case with Δh=2t and tanδ/tanφ'=0.5

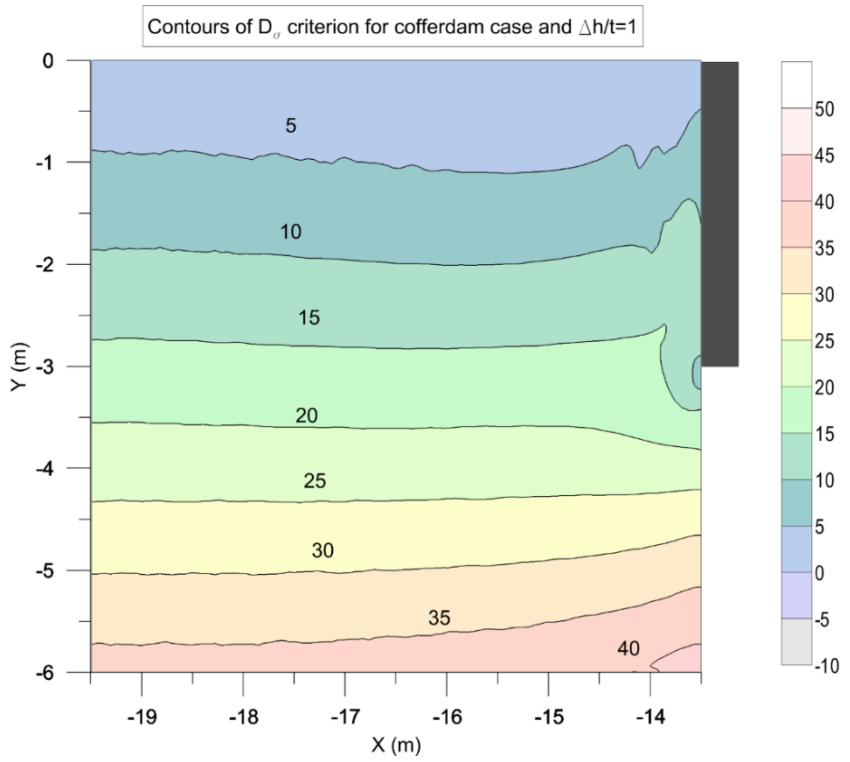

Figure C.50: Contours of D_{σ} for the cofferdam case with Δh=1t and tanδ/tanφ'=1

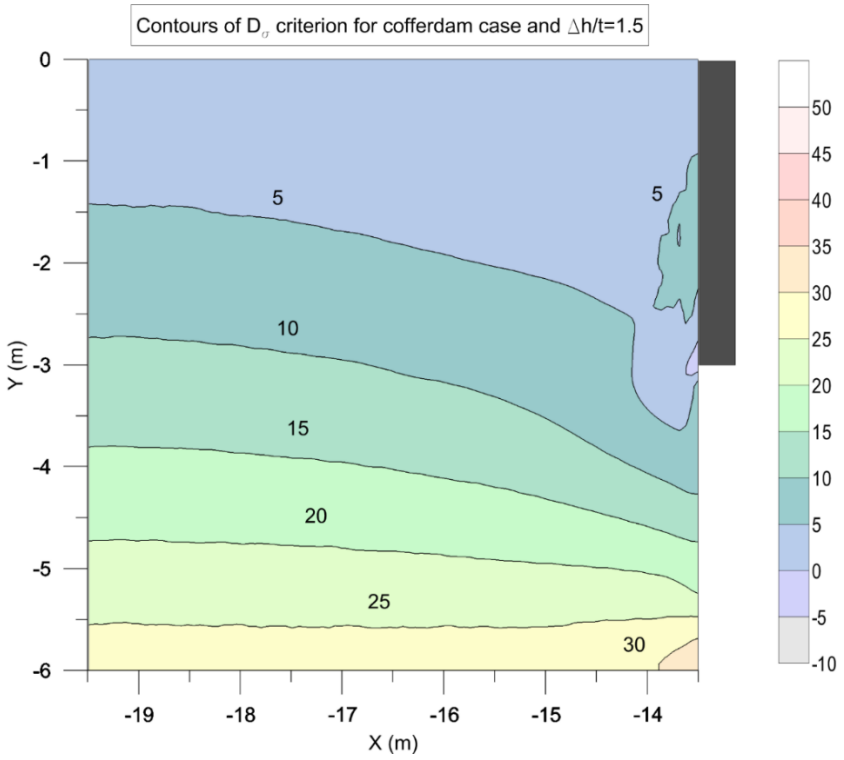

Figure C.51: Contours of D_σ for the cofferdam case with Δh=1.5t and tanδ/tanφ'=1

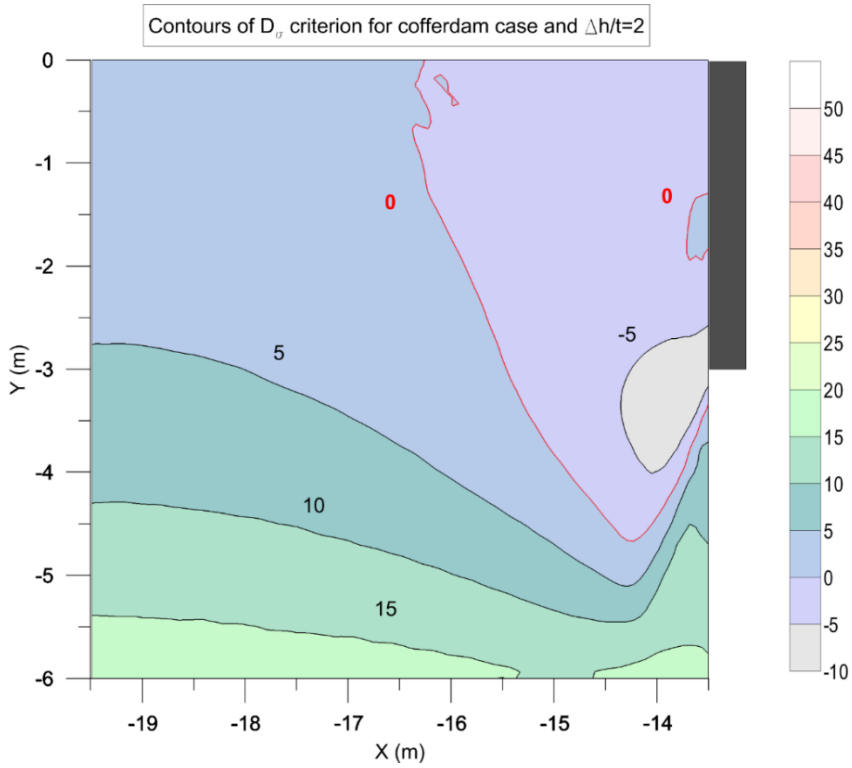

Figure C.52: Contours of D_σ for the cofferdam case with Δh=2t and tanδ/tanφ'=1

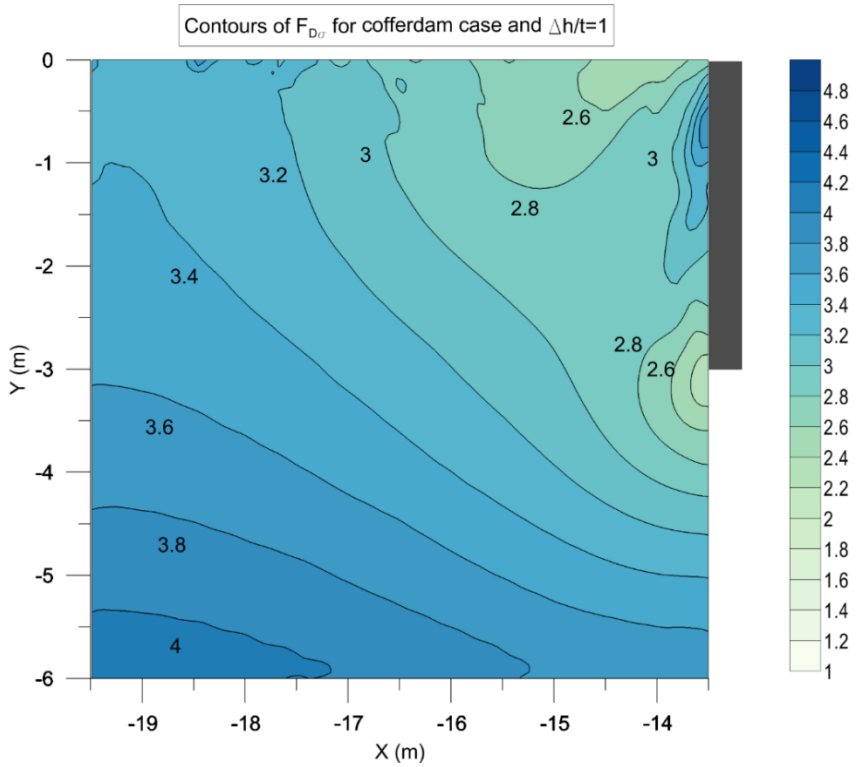

Figure C.53: Contours of $F_{D\sigma}$ for the cofferdam case with Δh=1t and tanδ/tanφ'=1

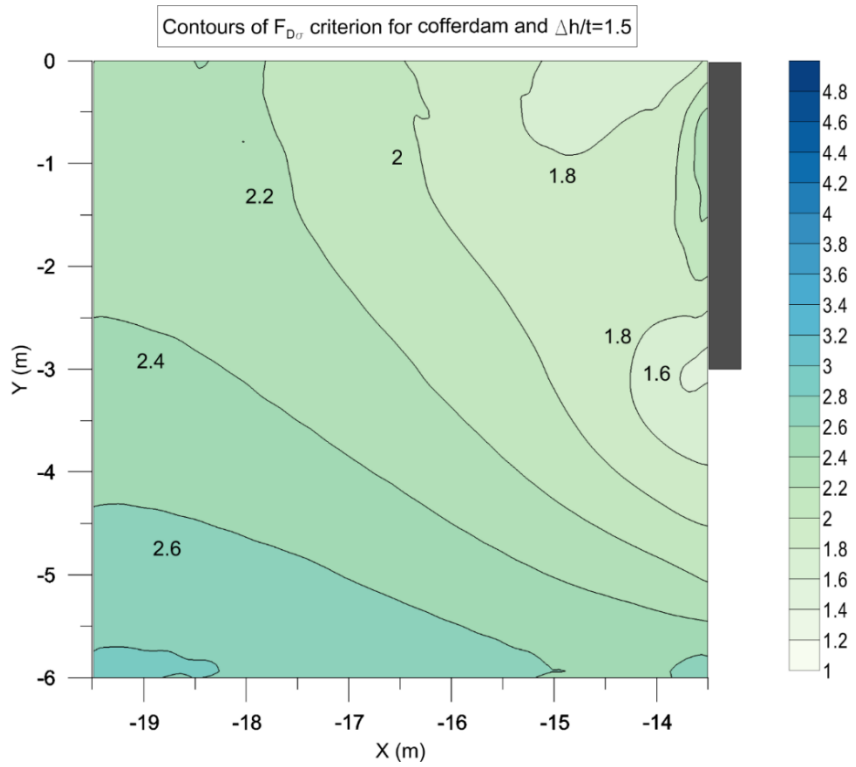

Figure C.54: Contours of $F_{D\sigma}$ for the cofferdam case with Δh=1.5t and tanδ/tanφ'=1

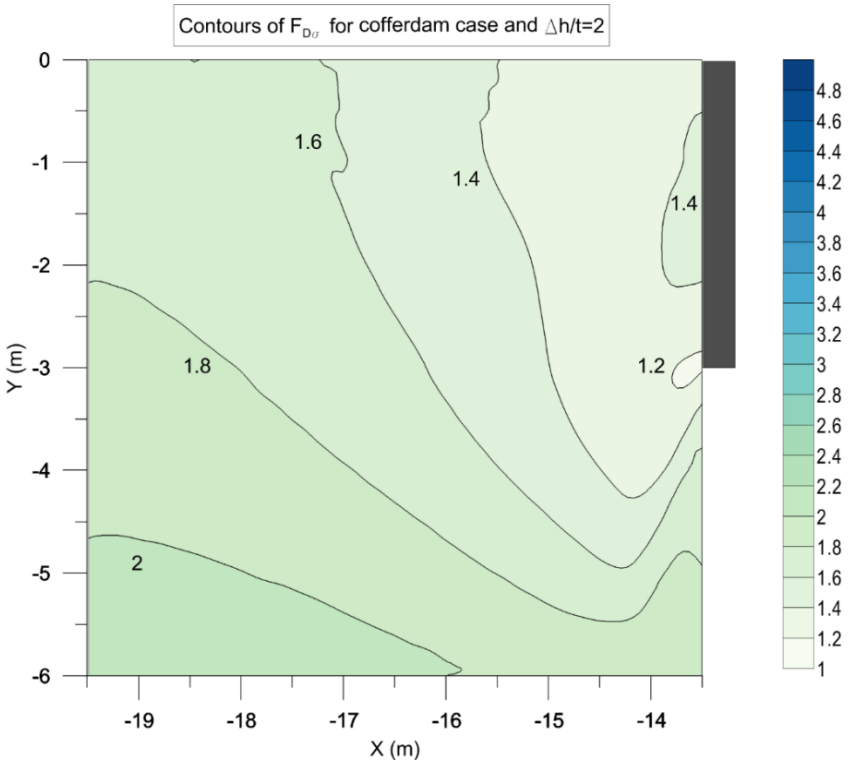

Figure C.55: Contours of $F_{D\sigma}$ for the cofferdam case with Δh=2t and tanδ/ tanφ'=1